ASPECTS OF ASTROPHYSICAL MASS LOSS

by

John Peter Phillips B.Sc., F.R.A.S.

December, 1977

A thesis submitted for the degree of
Doctor of Philosophy of the University of London
and for the
Diploma of Imperial College

Blackett Laboratory
Imperial College
London S.W.7.

ASPECTS OF ASTROPHYSICAL MASS LOSS

Abstract

The development of supersonic flows in late type stars is considered. The possibility of these arising from drag by radiatively accelerated grains receives particular attention. A discussion of planetary nebulae is concerned with how observed shell structures may originate, and the structures of particular nebulae are investigated using a wide range of observational techniques.

There is discussion of the structural development of novae shells, and the origins of transition zone oscillations. A likely 10.2 μm source in M15 is considered, and its possible nature examined. A more general discussion considers the limits which may be placed upon planetary nebulae as a primary mass loss mode in globular clusters.

Mass loss in binary star systems is briefly reviewed, with more detailed discussion of certain typical systems; new infrared observations of binaries are presented. A preliminary description of observations of comet West is presented in an appendix. Finally, a brief discussion is given of the primary instrumental systems employed in the acquisition of the data presented, with some consideration of certain error sources prevalent in infrared photometry.

CONTENTS

PUBLICATIONS:

A. D. MacGregor, J. P. Phillips, M. J. Selby, 1973. The Detection of M15 at 10.2 μm, Monthly Notices Roy. Astron. Soc., 164, 31p.

T. R. Hicks, J. P. Phillips, N. K. Reay, 1976. The Structure and Internal Extinction in N.G.C. 7027, Monthly Notices Roy. Astron. Soc., 176, 409.

J. P. Phillips, M. J. Selby, 1977. The Inception of Novae Transition Zone Oscillations, Astrophys. Space Sci., 49, 339.

C. Sanchez Magro, J. D. Needham, J. P. Phillips, M. J. Selby, 1977. Observations of β Persei at 4.8 μm, Monthly Notices Roy. Astron. Soc., 180, 461.

J. P. Phillips, N. K. Reay, 1977. On the Structural Development of the Shells of Novae and Planetary Nebulae, Astron. Astrophys., 59, 91.

J. P. Phillips, N. K. Reay, S. P. Worswick, 1977. The Structure of N.G.C. 6543, Astron. Astrophys.

TABLES

FIGURES

Acknowledgements

Most of the work in this thesis was initiated and completed within the last 3 years, although both data and experience acquired during a preceding period with the infrared astronomy group have also contributed. During such a period one inevitably acquires many debts of gratitude. To Dr. N. K. Reay I am indebted for many stimulating discussions concerning nebular structure, as well as help and encouragement over the last two years. Although most of the infrared data was both obtained and reduced by myself, the acquisition of this data would have been impossible without the expert instrumental and observational help provided by past and present members of the Imperial College, and Universidad de la Laguna groups. To all these, I extend a corporate thanks. Professor J. Ring and Dr. A. D. MacGregor are to be thanked in particular for many favours, as is Dr. Carlos Sanchez Magro, who has given much friendly help during my sojourns in Tenerife. Mrs. Maureen Puplett is also to be congratulated for her splendid typescript, completed against the almost insuperable odds presented by my handwriting.

Dr. M. J. Selby has provided help and advice, both during and after my tenure with his group. To him go particular thanks for consistent support, as well as for a critical reading of the thesis. Finally, I would like to thank personal friends, and above all my parents, who had begun to despair that this thesis would ever see the light of day.

Introduction

One of the major astronomical achievements of the last half century has been the realisation that a considerable fraction of the mass in stars and interstellar clouds has been through several stages of processing. Gas condenses to form stars, is enriched with heavy elements and (in part) ejected back to the interstellar medium, where it constitutes material for further stellar formation. The accretion stage of the process is understood in mainly theoretical terms; there is little direct observational evidence of phenomena which can be incontrovertibly attributed to this stage of the cycle. In contrast, the observational evidence for mass loss in stars is considerable, and it is aspects of this behaviour which we are mainly concerned with in this thesis.

On a broader canvas, mass loss is known also to occur within planetary systems, and from galaxies, although it is doubtful whether either of these latter cases represent evidence of mass recycling. A short list of situations where large scale mass loss is important would contain the following details:

(a) Planetary systems - cases include mass loss by comets, evaporative loss of planetary atmospheric constituents, etc.

(b) Stars - mass loss from supernovae; novae (including recurrent and dwarf varieties); binary star components. Mass loss by stellar winds (probably applies to most stars), flares ("flare stars", U.V. Ceti stars, W UMa stars, etc.)

(c) Galaxies, etc. - mass loss from the nuclei of Seyfert, N-type galaxies (from spectroscopic data), giant elliptical galaxies (c.f. optical jet in M87) and other galaxy types (c.f. ejected radio emission components). Mass loss from quasars (optical jets, extended radio emission components).

In addition, gravitational radiation (particularly in exploding stars, and close binary systems), electromagnetic radiation, and subatomic particles may contribute to mass depreciation to a more or less significant degree.

The very profligacy of the mechanisms involved, and objects to which they apply, places restrictions upon the generality of any discussion which is to make useful comments within this field. For this reason, the present work covers only certain problems associated with these mechanisms, and applies to a broad, but nevertheless similarly restricted range of objects.

Specifically, mass loss in red giants, supergiants, dwarfs, in novae and the progenitors of planetary nebulae, and finally in binary systems and globular clusters will be considered. Since much of the work is substantially based on new and recently published observations however, we begin with a consideration of the instrumental systems employed in the acquisition of this data, and sources of error in the infrared photometry.

CHAPTER 1

INFRARED AND ELECTRONOGRAPHIC OBSERVATIONS

1.1 Telescope and Site

All observations of the Imperial College infrared astronomy group have been obtained with the 60" flux collector at the Observatorio del Teide, Izaña, Tenerife. This is located at longitude 01h 05m 48s W, latitude +28° 17' 32" at a height 2400 m above sea level. This height, combined with a local temperature inversion at ~1400 m conspires to reduce precipitable water vapour levels to, on occasions <1 mm, although (with some uncertainty) it is probably more typically ~3 mm. Seeing of <2 arcseconds has been claimed for ~77% of observing time by site testers (Bennet McInnes, Royal Observatory Edinburgh, Personal Communication). In reality, it appears to be more typically 3-4" in the visible on the 60" flux collector, even on nights regarded as possessing good (<2") seeing by testers. This difference may arise from turbulence due to the dome, or in the lee of the Izaña ridge. The flux collector mirror was design specified to provide ~90% intensity within an image disk ~3-4 arcseconds diameter. In fact, sub-arcsecond visual images have been recorded on several occasions.

The site is prone to temporary incursions of wind-borne Saharan dust. These have usually plagued the summer months, and have at the least introduced restrictions upon visual guiding on faint sources. The effects upon infrared extinction have not been noted, but can hardly be negligible. This question is expanded upon later.

In winter, a particular difficulty arises from the instability

of the inversion layer, and experience indicates observing to be possible in only ~50% of nights during the November-February period.

1.2 Infrared Photometry

The instrumental package is placed at the Cassegrain focus of the telescope. The photometric system consists of an aluminium alloy framework for instrumental support, a mirror chopper, and a cooled cryostat containing detector elements and filters. A schematic diagram of the system, and its placement on the flux collector, is provided in figure 1.1.

Two cryostats are used to cover the spectral range 1.25 μm - ~22 μm. For wavelengths $\lambda \leq 4.8$ μm a B.O.C. multifilter nitrogen cooled cryostat, developed and described by A. D. MacGregor (1973) is used. Early results were obtained at H and K bands using a PbS detector cooled with a CO_2/Alcohol mixture. Certain of these are presented in the discussion of binary stars. The capabilities of the cryostat were subsequently expanded to include J, H, K, L and M bands using InSb detectors and a CaF window, with liquid nitrogen coolant. Filters are mounted on a rotating wheel coupled to a nitrogen cooled shield.

The second (Mullard) cryostat, used at λ = 10.2 μm and longer wavelengths is less versatile, permitting the use of only one filter for any one observing period. A Thor cryostat with slide capable of containing three filters has been under consideration for this spectral region, but is not yet operational. Measurements with the Mullard cryostat have been carried out primarily in the 8 - 13 μm band, with a helium cooled Cu:Ge detector. A nitrogen cooled shield reduces

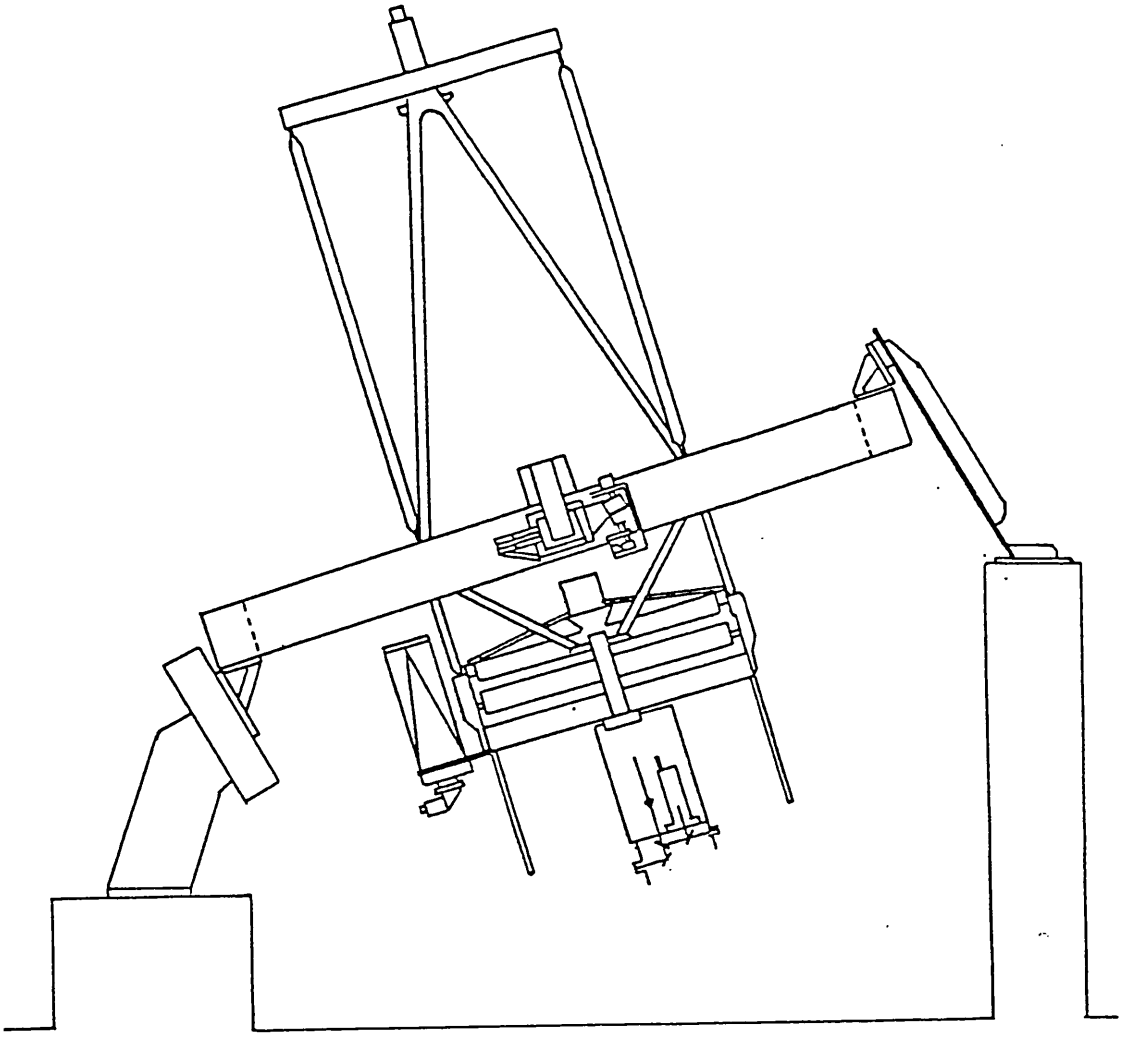

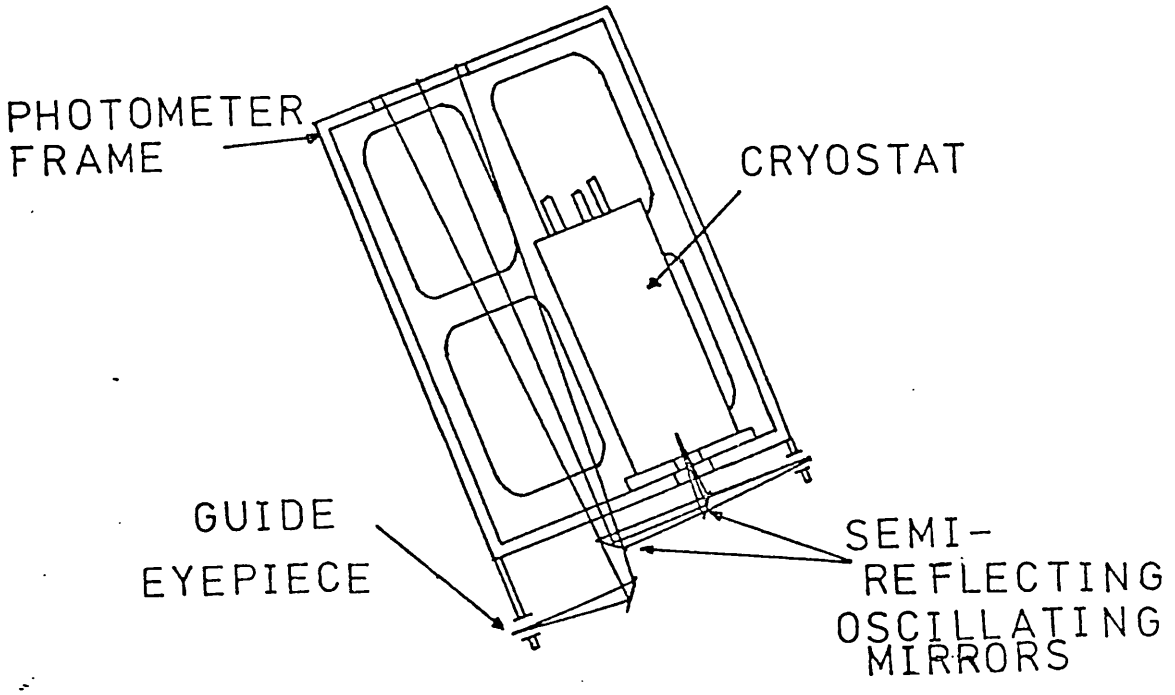
PHOTOMETER
FRAME
CRYOSTAT
GUIDE
EYEPIECE
SEMI-
REFLECTING
OSCILLATING
MIRRORS

FIGURE 1.1

radiation leaks. Initial pumping to ~10^{-6} torr, with diffusion pump (and backing rotary pump), and subsequent freezing out of gaseous contaminants (cryopumping) reduce vapour heat transport to acceptable levels. At present, it is found that the detector can be maintained at helium temperature for ~24 hours, providing care is taken in maintaining a reasonable level in the nitrogen chamber. A cross-section of a helium cooled cryostat is provided in figure 1.2.

The chopping system has also undergone several important modifications during the period covered by observations presented in this thesis. At the time of initial development, two designs for near focal plane chopping were commonly in use; a rotating mirror sector chopper (used and described by for instance Murray and Wildey 1964), and a small gold coated oscillating plane mirror (details may be found in Selby 1973). In addition, wobbling of the telescope secondary mirror had been used on the f45 61" telescope at the Catalina Observing Station, Lunar and Planetary Laboratory (Low and Riecke 1974) to provide a reasonable square wave chop. The 60" flux collector at Tenerife was not however provided with this facility.

A major difficulty with the rotating chopper was the tendency for thermal spikes to occur whenever an interface between sectors crossed the detector field. An oscillatory chop mode was finally adopted for much of the early photometry. This has been superceded by a two mirror focal-plane chopper, permitting larger image displacements for smaller amplitudes of mirror displacement. Operated at resonance, microphonic noise arising from vibrations in the cryostat are reduced to a minimum. Details of the chopping system are provided by Jorden, Long, MacGregor and Selby (1976). Optimum chop frequencies of ~5 Hz were used for the PbS detectors, but more recent use of InSb

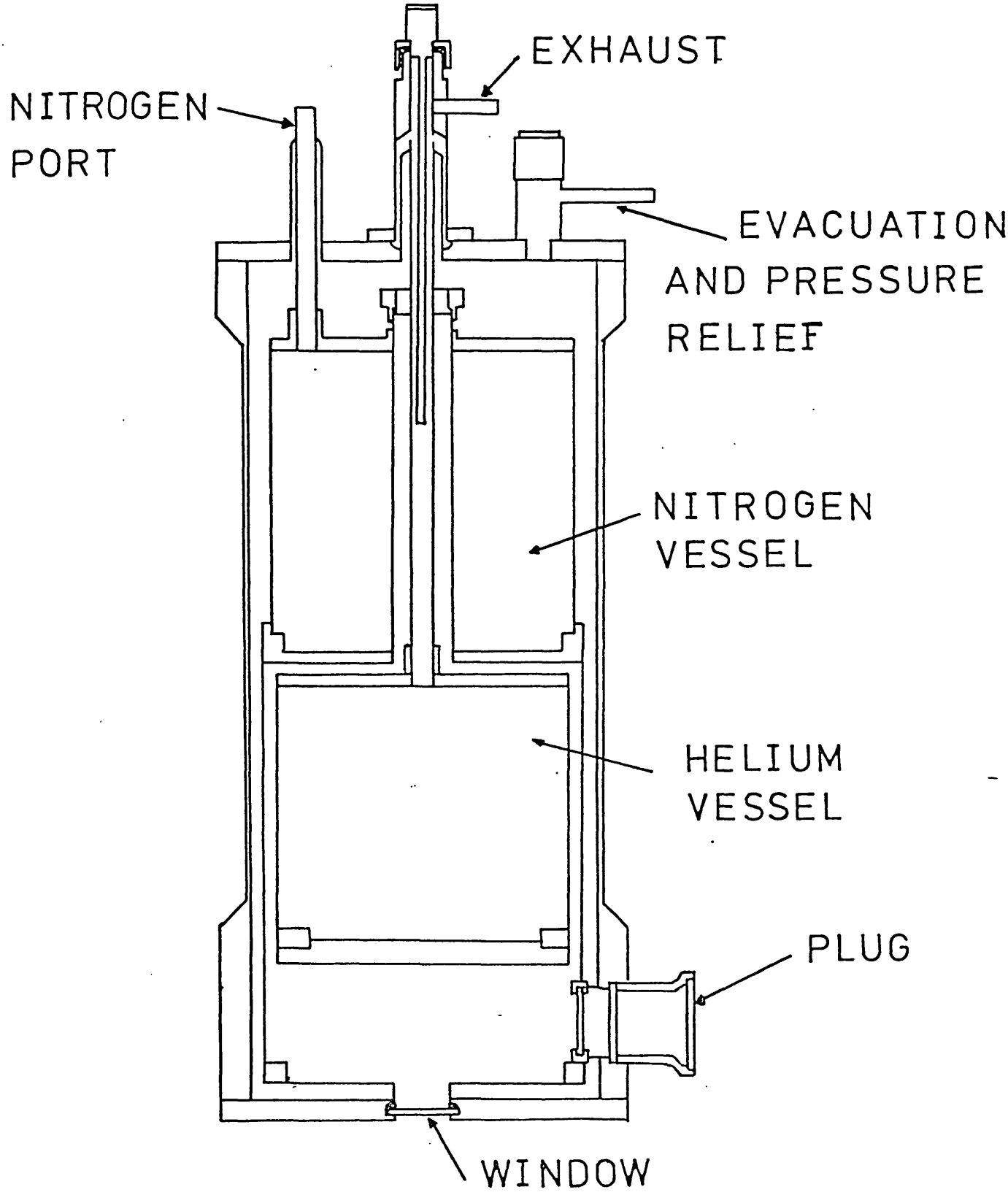

HELIUM COOLED CRYOSTAT

FIGURE 1.2

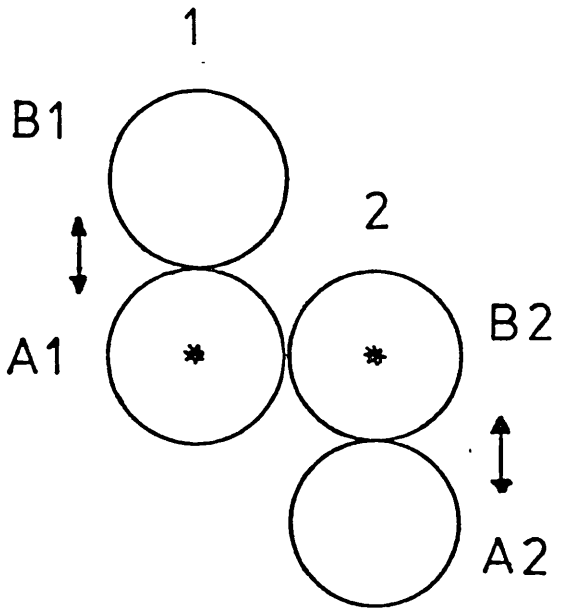

FIGURE 1.3

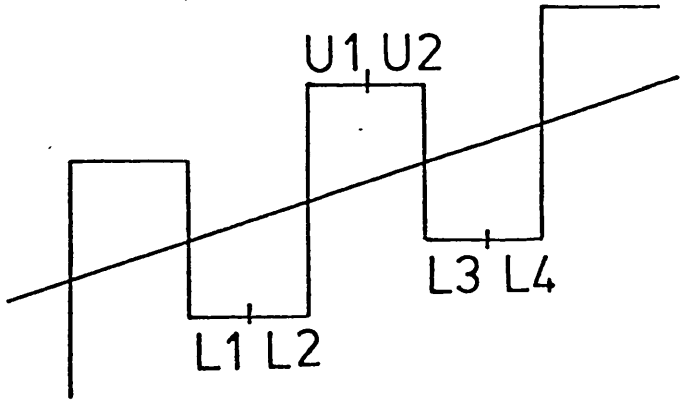

FIGURE 1.4

and CuGe detectors has necessitated frequencies ~300 Hz.

An originally sinusoidal mirror motion was employed for the chopper. Although this reduced microphonic noise, it also reduced the effective time spent by the source upon the detector. The system electronics has now been modified to permit square wave chopping.

As a result of chopping, the detector element alternately sees areas of sky separated by an angular distance determined by the chop amplitude, and of size defined by cooled detector apertures. It is usually desirable to reduce chop amplitude to a minimum, both to reduce microphonics, and eliminate spurious signal arising from sky emissivity gradients. For this reason, angular chop amplitude is usually made the same as the sky beam diameter. Even with this arrangement, however, the usefulness of the system would be greatly impaired through the detection of sky emission gradients, and this problem is usually overcome by further nodding the telescope.

The procedure is illustrated in figure 1.3. This shows the two beams as seen by the detector, with in (1) a source in the lower beam, and in (2) the source in the upper beam as a result of nodding the telescope. In position (1) the measured signal is $I_{B1}-I_{A1}$ (I_{B1} = intensity in beam B1). Since $I_{A1} = I_* + I_{SA1}$, where I_* = stellar emission, I_{SA1} = sky emission in beam A, nod position (1); and $I_{B1} = I_{SB1}$, then $(I_{B1} - I_{A1}) = (I_{SB1} - I_{SA1}) - I_*$. Similar consideration of the other nod position gives $I_{B2} - I_{A2} = (I_{SB2} - I_{SA2}) + I_*$. Whence $(I_{B2} - I_{A2}) - (I_{B1} - I_{A1}) = 2I_*$, providing $I_{SB2} - I_{SA2} \simeq I_{SB1} - I_{SA1}$. Since for even a relatively bright infrared source (N = +0.0), $I_{A1}/I_* \simeq 10^4$ at $\lambda \simeq 10.2$ μm, the last relation must be met with some stringency, and we will find that the second differential of the variation of sky emissivity with zenith angle may under certain

circumstances introduce spurious signals at a power level similar to the shot noise limit of the sky emission.

The signal from the detector is first preamplified within the cryostat, and subsequently amplified by a further factor ~10^3 to a voltage ~1 volt by a main amplifier attached to the photometer framework. This is subsequently filtered (to a 3 Hz bandwidth) with a tunable filter, a reference signal defining the chop frequency, and full wave rectified and smoothed in a P.S.D., to give a D.C. output voltage level directly proportional to input signal. The voltage is recorded on a chart recorder and, through a digital voltmeter on an Anadex printer, paper tape punch, and Nova computer. Sampling rate is independently determined by a sampling control box, which also controls telescope nod and scan facilities through an R.O.E. console. The Nova computer may be programmed to give on-line reduction of the photometry, scan summation, etc., which may in turn be recorded on magnetic tape, at the teletype, and on a small display C.R.O.

The result of sky nodding upon the chart record of output signal is given in figure 1.5, for a good night and bright source.

In a normal photometry mode ten measurements are taken in each nod position, with a usual time constant $\tau \simeq 0.1$ sec. The data is processed to remove gradients arising from temporal changes in the D.C. background level (the causes of drifts are investigated later). To effect this, the data from any one nod position is split into two equal parts, containing five samples each - labelled in the schematic diagram (figure 1.4) L1 and L2 (L for lower beam). Results L2 are averaged, and subtracted from similarly treated upper beam measurements U2, to record a total signal level (U1-L2). This is then added to

FIGURE 1.5

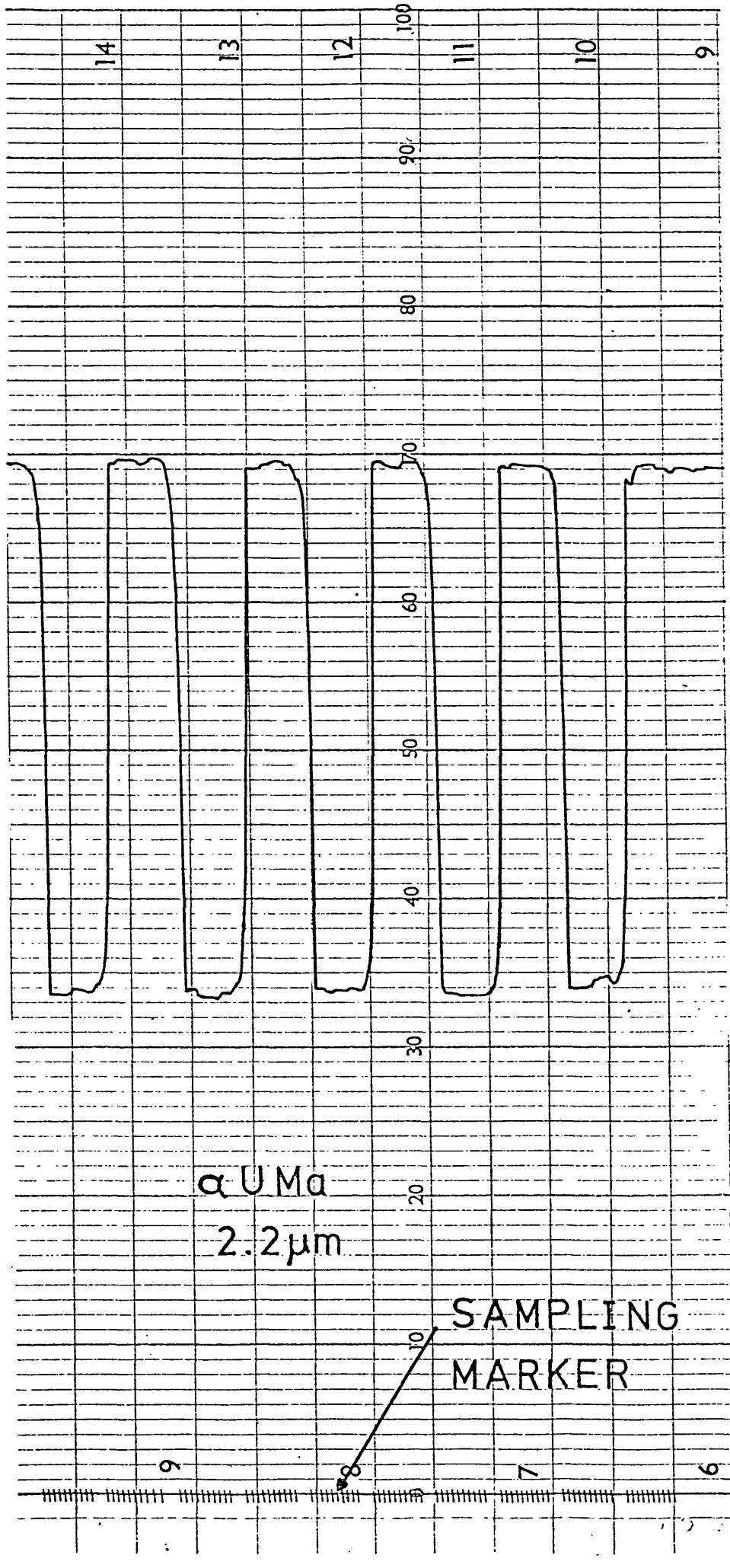
14
13
12
11
10
9
100
90
80
70
60
50
40
30
20
10
9
8
7
6
αUMα
2.2μm
SAMPLING
MARKER

(U2-L3). For a strong "D.C. drift" of the kind illustrated, (U1-L2) will be larger than the intrinsic signal strength by an amount Δ_1, say whereas (U2-L3) will be smaller by Δ_2. For a sufficiently slow or linear drift, $\Delta_1 \simeq \Delta_2$, and (U1-L2) + (U2-L3) gives a result close to that obtained in the absence of drifts. When measuring weak sources however, the influence of second differential drift terms becomes pertinent.

Maximum information is retrieved for a sampling rate $\nu_s = 2F \text{ sec}^{-1}$, where F is the maximum frequency within the signal. If such a rule is adhered to, the power spectrum of noise in the recorded signal levels should fall to zero at the Nyquist frequency. In reality, electronic filters do not provide complete filtering of higher frequencies, and some aliasing will occur. This might be usefully reduced by oversampling, although the consequent burgeoning data levels makes this most advantageous where on-line computer processing is available. Too low a sampling rate will lead to significant power spectrum amplitude at the Nyquist frequency, unacceptable aliasing, and significant loss of signal information content.

After subtracting mean levels, we have assessed power spectra for sets of typical photometric upper and lower beam data. An example from good photometry is shown in figure 1.6. The noise power is primarily concentrated at frequencies ~0.07 Hz, falling off rapidly at higher frequencies. Errors due to poor guiding, variable seeing, etc., may introduce higher frequency noise, and examples of power spectra in these conditions are presented in figure 1.6.

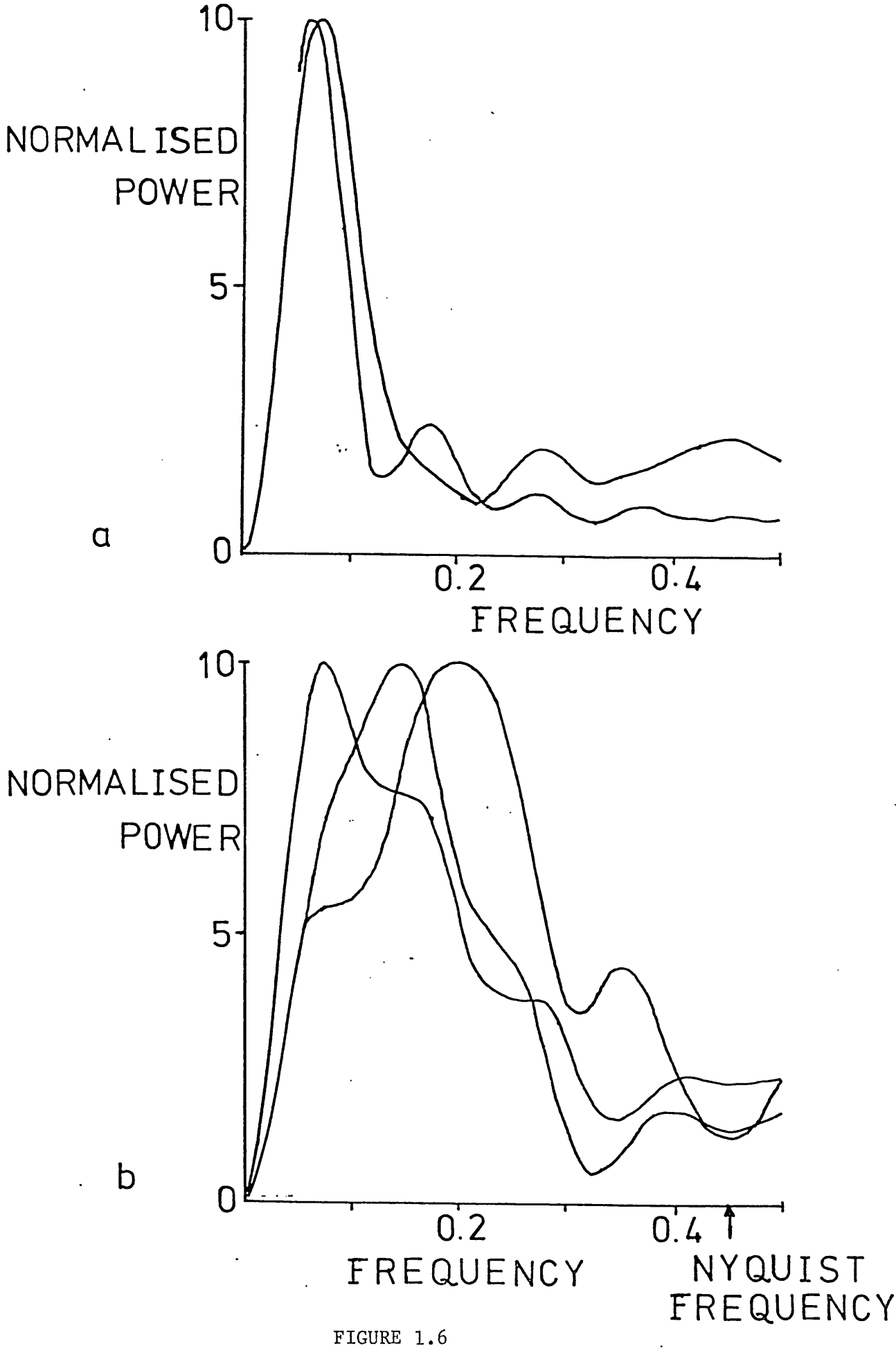

FIGURE 1.6

a GOOD OBSERVING CONDITIONS
b POOR OBSERVING CONDITIONS

1.3 Sources of Electronic and Signal Noise

There are several noise sources of relevance to near infrared photometry, relating to the electronics, or intrinsic properties of the signal. We briefly itemise these.

Johnson noise arises from random change fluctuations within resistors. It contributes a minimum mean square voltage noise $\overline{V_n^2} \simeq 4kTR\Delta\nu$, where $\Delta\nu$ is the noise bandwidth, T the absolute temperature, k the Boltzmann constant and R is resistance (ohms). Assessed for the system as a whole, Johnson noise falls significantly short of sky photon shot noise at all wavelengths in ideal systems.

A potentially more important noise source is Generation-Recombination Noise, arising from fluctuations in carrier lifetimes. For photoconductor type detectors it is given by

$$V_n = R\ I \frac{2\ \tau\ \Delta\ \nu}{h(1 + 4\ \pi^2\ \nu^2\ \tau^2)}$$

where τ is carrier lifetime, I is D.C. current and n carrier density. V_n is constant to $\nu \simeq (2\pi\tau)^{-1}$, and then falls with increasing frequency. Ideally, it is less than shot noise. Generally, it makes a significant contribution to detector N.E.P's.

I/f noise has uncertain origin, but dominates at low frequencies. It is one reason for adopting high chopper frequencies.

Thermal noise will arise from variations in detector temperature. This can be reduced to insignificant levels.

Microphonic noise covers those sources of voltage fluctuations generated by mechanical vibrations of the system. Vibration will normally originate primarily from the chopper system and may to some extent be eliminated with appropriate antivibration mounts, or

designing the chopper to work at low power levels.

Since voltage fluctuations arise primarily through moving conductors, capacitances, etc., in weak fields, securing of such items (c.f. stray leads) to firm surfaces will also help.

Finally, and ideally the most important source of noise is photon shot noise originating from radiation incident upon the detector. The mean square photon fluctuation level is

$$\overline{\Delta n^2} = \frac{\bar{n}\, e^{hc/\lambda kT}}{(e^{hc/\lambda kT} - 1)}$$

in the limit $\lambda kT/hc \to 0$ however $\overline{\Delta n^2} \simeq \bar{n}$.

In the 8 - 13 μm window, the equivalent noise is ~2 x 10^{-14} W, decreasing to ~5 x 10^{-15} W in the 4.5 - 5.5 μm window and ~10^{-16} W for the 2.0 - 2.2 μm window. State of the art detectors generally have N.E.P's similar (at short waves), or significantly better than these limits ($\lambda \geq 10$ μm), and the detectors used at Imperial College are now essentially background limited at $\lambda \geq 10.2$ μm. At 2 μm, practical N.E.P's (and this is true for Imperial College detectors) are about ten times greater than background shot noise levels.

1.4 Evaluation of Extinction

The intensity I of astrophysical sources is usually assumed to vary as $I = I_o\, e^{-\kappa \sec \phi}$ in the infrared, where ϕ is the zenith angle. The relation implies plane parallel absorption by an atmosphere optically thin at all wavelengths. Plotting the magnitude of a source with respect to sec ϕ should then produce a straight, sloping line with gradient -1.086 κ. An example of such a procedure applied to a

night of 5 μm observations is presented in figure 1.7. To evaluate the extinction for an uncalibrated source, it is generally considered advisable to measure a nearby calibration star at similar air mass and at about the same time. The intrinsic relative intensities of calibrated and uncalibrated sources may then be established with reasonable accuracy using extinction rates determined by this, or other calibrated sources. Calibrated sources are in turn determined by measuring intensities relative to α Lyrae (taking α Lyrae to have magnitude 0.0 at all bands), or adopting C.I.T. standards. Where these overlap, magnitudes rarely differ by ≳ 0.03 magnitudes. The magnitudes adopted for calibration stars used in this thesis are quoted later. This extinction evaluation procedure minimises errors arising from uncertain or varying extinction. There are various questions which must however be raised with respect to this method.

First we note that for an absorbing atmosphere with scale height h, and radius R, air mass varies not as sec ϕ, but closely as

$$AM = \left\{\frac{\pi R}{2h}\right\}^{\frac{1}{2}} \exp\left\{\frac{R\cos^2\phi}{2h}\right\} \operatorname{erf}\left\{\left(\frac{R\cos^2\phi}{2h}\right)^{\frac{1}{2}}\right\}$$

Young (1974a) finds the relation to be accurate providing $R = 1\frac{1}{6} R_{\oplus}$, where $R_{\oplus}$ is Earth radius, and the factor 1/6 allows for refraction. This leads to serious deviations from the sec ϕ law at very high air mass (approaching 0.2 air masses by sec $\phi = 6$, and 1 air mass at sec $\phi = 10$), although at the smaller air masses (sec $\phi \lesssim 3$) used in infrared photometry, the error is probably quite small ($\lesssim$0.02 air masses). This "geometrical" effect may be complicated, since extinction in most windows arises from two primary atmospheric constituents (CO_2 and H_2O) having rather different scale heights h.

FIGURE 1.7 CALIBRATION STARS ON A NIGHT OF 4.8 μm PHOTOMETRY.

A. β GEM; B. α CMi; C. γ DRAC; D. μ UMa; E. α UMa; F. μ CEP; G. α BOO; H. α HER; I. α SCO.

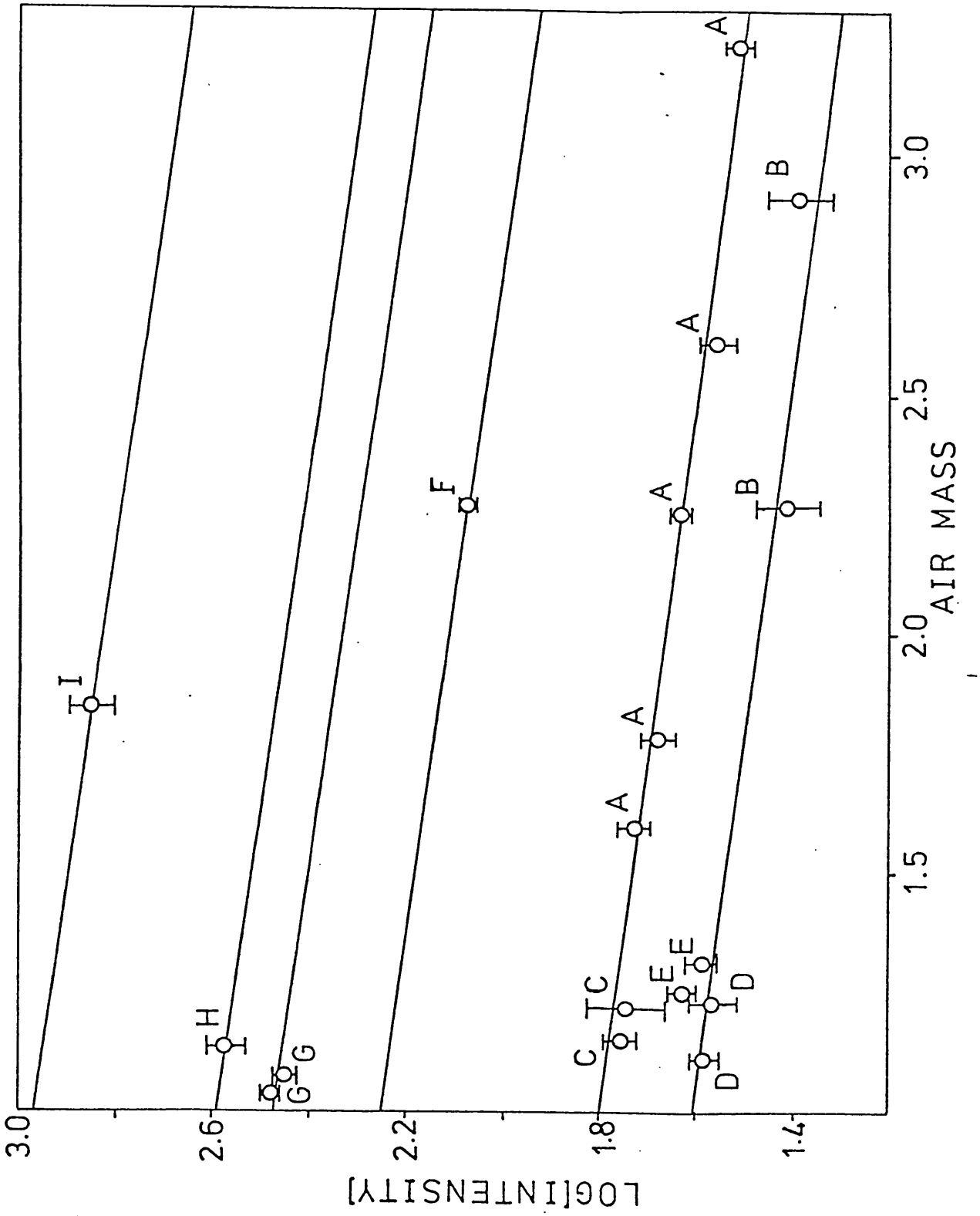

In addition, the 8 - 13 μm window has a strong band at ~9.6 μm. This latter arises from a relatively thin ozone layer at height ~30 km above the Earth's surface, and will lead to absorption varying as sec ϕ (assuming the band to be optically thin).

Of more considerable interest is the relevance of the assumption that atmospheric band absorption is optically thin at all wavelengths, within the standard infrared windows. There have been various studies of atmospheric band absorption (see for instance Elsasser 1938; Plass and Yates 1965 and references therein). These generally predict an extinction varying as sec ϕ for a plane parallel, "weak line approximation" atmosphere (i.e. absorption at line centres is optically thin); but asymptotically approaching a $\sec^{\frac{1}{2}} \phi$ law as lines become saturated. Sinton and Strong (1960) used a $\sec^{\frac{1}{2}} \phi$ law in early measurements of Venus in the 7 - 13 μm band, and this was subsequently carried over by Murray and Wildey (1964) in 8 - 13 μm measurements of the Moon. Subsequently, Wildey and Murray (1964) were to transfer to a sec ϕ law on the (unpublished) evidence that Westphal had found this most appropriate. This is surprising since Strong (1941) had apparently convincingly demonstrated that particular segments of the 8 - 13 μm band, apparently reasonably well isolated from the edges of the atmospheric window, have extinction varying most closely as $\sec^{\frac{1}{2}} \phi$, and even earlier measurements by Adel (1939, 1940) for this window yielded a similar law. Similarly, in a classic paper on sky emissivity, Bell et al. (1960) clearly demonstrated that emission in the 4.3 - 6 μm window varied as $(1 - e^{-\kappa \sec^{\frac{1}{2}} \phi})$ (where they found $\kappa = 0.44$ for their particular set of measurements at Sacramento Peak, New Mexico, 9200 feet above sea level). A similar law was apparently also obtained for the 8 - 13 μm window. Although sky emissivity will differ from the

absorption optical depth, the atmospheric temperature-density-compositional structure is such as to preferentially weight the emission contribution of the lower atmospheric layers; the same layers as are primarily responsible for absorption. More recent measurements of emissivity in the J, H, K and L bands using the Tenerife flux collector (MacGregor - personal communication) appear to further support this relation for emissivity.

The consequences of using a $\sec^{\frac{1}{2}} \phi$ law in place of a sec ϕ law may be serious, particularly when defining an absolute calibration. Consider measurements of a star at air masses sec ϕ_1, and sec ϕ_2 > sec ϕ_1. A magnitude difference ΔM is measured and extinction laws $e^{-\kappa_1 \sec^{\frac{1}{2}} \phi}$, $e^{-\kappa_2 \sec \phi}$ are fitted. It is found that

$$\kappa_2 = \kappa_1 \left\{ \frac{\sec^{\frac{1}{2}} \phi_1 - \sec^{\frac{1}{2}} \phi_2}{\sec \phi_1 - \sec \phi_2} \right\}$$

Extinction at an air mass sec ϕ_3 is now assessed. Setting $\kappa_1 = 0.3$, sec $\phi_1 = 1.0$, sec $\phi_2 = 1.5$ gives $\kappa_2 = 0.135$. For the two extinction laws we now obtain relative extinctions between sec ϕ_1 and sec $\phi_3 = 3.0$ of $\Delta M_1 = 1.086\ \kappa_1\ (\sec^{\frac{1}{2}} \phi_3 - \sec^{\frac{1}{2}} \phi_1) = 0.239$, $\Delta M_2 = 1.086\ \kappa_2\ (\sec \phi_3 - \sec \phi_1) = 0.293$; that is, an error of 0.054 magnitudes (i.e. ~20% of total extinction). This is for a night of reasonable extinction. For $\kappa_1 = 1.0$, $\kappa_2 = 0.45$, the corresponding extinction differences are $\Delta M_1 = 0.80$ magnitudes, $\Delta M_2 = 0.98$ magnitudes, and the consequences of applying the wrong extinction law become quite unacceptable. It should be noted that the high extinction limit at 10.2 μm and 4.8 μm just quoted is based on experience at Imperial College; it is larger than rates given by Riecke and Low. The difference is probably to be ascribed to differing filter bandwidths. More generally,

the errors at any particular air mass arising from application of an inappropriate extinction law are increased as sec ϕ_2 approaches sec ϕ_1, and κ_2 asymptotically approaches 0.5 κ_1. Thus for $\kappa_1 = 1$, the error at three air masses may approach 0.29 magnitudes. Extrapolation to zero air mass from one air mass therefore leads to differences $1.086\ (\kappa_1-\kappa_2) \simeq 0.5$ magnitudes under the best circumstances on a high extinction night, and increases as (sec ϕ_2 - sec ϕ_1) increases.

The situation at L and shorter wave bands is less clear. Higher transparencies within the windows may imply the applicability of a sec ϕ law. In any case, extinction rates are usually sufficiently low that errors arising from these uncertainties are probably not too large.

This discussion is of course idealised to make more clearly the requisite points. In reality extinction is determined from several measurements at differing air masses. Nevertheless, it seems clear that there is firm evidence for a $\sec^{\frac{1}{2}} \phi$ extinction law in the 4.8 μm, 10.2 μm and (probably) 20 μm windows. The application of a sec ϕ law will lead to a roughly straight line relation when extinction is plotted against air mass, for a reasonably good night, and errors in the evaluation of extinction may not exceed ~0.05 magnitudes. On high extinction nights however, these errors may approach ~0.3 magnitudes.

Geographical factors may also influence the extinction law. This may be a significant factor in mountainous terrain, where wave clouds often provide direct evidence for substantial deformations in the air flow. Under these circumstances, a very clear understanding of local anomalies in the extinction law is required, and nightly variations in air flow could conceivably place severe limitations upon the usefulness of a site.

Finally, the determination of air mass usually makes use of the formula

$$\sec \phi = \frac{1}{\cos H \cos \chi \cos \delta + \sin \chi \sin \delta}$$

where χ = latitude, δ = declination, and H = hour angle. Often it is adequate to use a mean value of H to cover the period of observation, and this is certainly the procedure with programs currently employed in on-line computing at Tenerife. Under certain circumstances this procedure leads to errors however, as for instance when an extended period of observations is required, or observations at high air mass are involved (where air mass changes rapidly with hour angle). Thus an average air mass $\overline{\sec \phi}$ is required, defined by

$$\overline{\sec \phi} = \int_{H_1}^{H_2} \sec \phi \, dH \Big/ \int_{H_1}^{H_2} dH$$

where we have selected a sec ϕ law approximation for convenience. Performing the requisite integration leads to four solutions, depending upon the values taken by certain functional combinations of χ and δ. For restrictions imposed upon δ by the Tenerife flux collector, the following relation is found to be sufficient

$$\overline{\sec \phi} = \left[\frac{1}{\sqrt{(B^2-A^2)}} \ln \left| \frac{(B-A)\tan(H/2) + \sqrt{B^2-A^2}}{(B-A)\tan(H/2) - \sqrt{B^2-A^2}} \right| \right]_{H_1}^{H_2} \Big/ (H_2-H_1)$$

providing $B^2 > A^2$, where $B = \cos \chi \cos \delta$; $A = \sin \chi \sin \delta$.

1.5 The Spectracon Image Tube

The writerhas, for the last year or so, been primarily engaged in evaluating data obtained from a spectracon image tube. His observational experience with this instrument has, to say the least, been restricted. The present discussion presents only those salient features necessary to provide a basic comprehension of the system, used to obtain data presented and discussed later.

A cross-section of the spectracon is presented in figure 1.8, for which I am grateful to S. P. Worswick. The required image is focussed in the photocathode (A). Electrons are released which are then accelerated through a 40 kV potential, striking the mica window (C). This latter is thick enough (~4 μm) to withstand atmospheric pressure, but permits electrons to impinge fine grained nuclear track emulsion placed on the outer surface of the window. Image coherence during electron acceleration is maintained by the focussing solenoid (G), and by eliminating residual fields with a mu metal screen (F). Finally, power dissipation within the solenoid requires a coolant to be pumped through inlet (D), to outlet (E). Total detective quantum efficiency of the system is high (typically 6 - 8%) and this makes it particularly valuable in the measurement of faint neblosity. A second important feature (of most relevance here), is the high dynamic range achieved, permitting an accurate representation of relative intensity levels in nebulae with large relative brightness variations. The photometric capabilities of the spectracon are however less reliable.

The results thus obtained are digitised with a Joyce Loebl microdensitometer, and the data recorded on magnetic tape. The data is then processed by a contouring program, and presented as an isophotal map. The same contour program has been used to evaluate isophotal contours for model nebulae, and examples of both will be presented later.

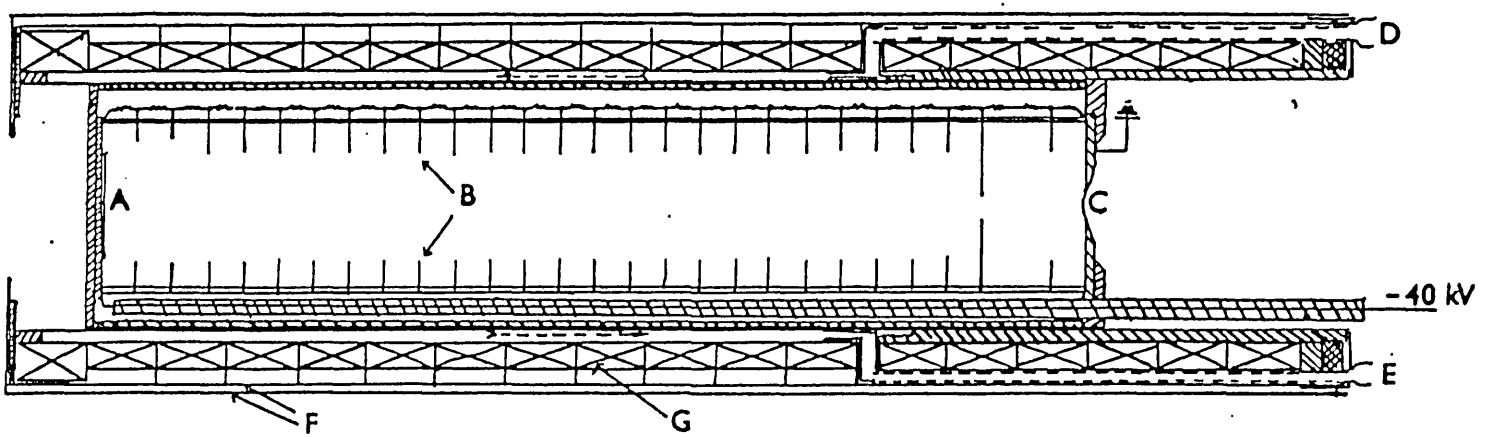

FIGURE 1.8

SPECTRACON IMAGE TUBE

1.6 Sources of Infrared Photometric Error

A full assessment of the various sources of random and systematic error prevalent in the near infrared, with scope similar to that carried out in the visible by for instance Young (1974a) remains yet to be performed. In Young's analysis, a primary source of photometric error was shown to be scintillation noise, and this accumulated as the square of the air mass. In consequence, it was demonstrated that specific air masses and observation periods were to be preferentially assigned to the evaluation of extinction. Such an analysis for the near infrared would evidently be of immense interest to workers in this field; it is not however to be found here. Rather, we consider those particular sources of photometric error which have recommended themselves to the present writer as being of particular relevance, during work with the Imperial College infrared group. These will be in general larger than those considered important in the visible. As a gauge, we may note that scintillation noise amounts to typically $\lesssim 0.01$ magnitudes in the visible and, following the recent discussion by Young (1974b), is probably similar throughout the infrared. This is less than the photometric noise limits usually considered as acceptable in the infrared, and considerably less than the probable (systematic) errors arising from uncertainties, and irregular spatial and temporal variations, in for instance extinction.

1.7 Drifting

Low frequency variations in the background signal are sometimes evident, particularly at $\lambda = 10.2$ μm. We will see how this may occur in the present section. An example of such a drift is illustrated in

figure 1.9. It is relevant to note that at that time, the telescope involved (the Tenerife 60" flux collector) had an oversized secondary, which led to the detection of radiation from around the primary mirror. This problem was subsequently corrected by a baffle at the secondary, coated however with (high emissivity) 3M paint. This arrangement is clearly open to further improvement; particularly, as we will see, if signal drift is to be reduced. The ideal arrangement (Low and Riecke 1974) is to have an undersized secondary. In that case, the detector should see the primary and secondary mirrors together with a sky background of typically low emissivity (~0.1). We consider this latter situation first in our assessment of the cause of drifts.

The presence of drifting at $\lambda \gtrsim 10$ μm alone implies a thermal origin. The existence of drifting at all indicates (with our previous statement) the existence of differences in the thermal properties of sources within the beams at the extreme chop limits. This will clearly arise if the locations of the two beam positions are asymmetrical with respect to the secondary mirror so that, for instance, the detector sees the entire secondary in one beam position, but only part of the secondary in the other.

In reality, it is unlikely (for a well aligned system) that any part of the secondary mirror is completely obscured from the detector. The beam edge is diffuse, through diffraction (see again Low and Riecke 1974) and penumbral effects. However, by assuming a sharp beam edge, we simplify the analysis and maximise the effect we are investigating.

Consider then a beam which in one extreme chop position exactly compasses the secondary mirror, and in the other is displaced off the edge of the secondary by an amount $\Delta\ell_s$. One beam therefore

FIGURE 1.9

SIGNAL DRIFT

sees an area of secondary mirror $\sim 2R_s \Delta\ell_s$ more than the other beam - and consequently more area of primary $\sim 2R_p \Delta\ell_p$, where $\Delta\ell_p \simeq \Delta\ell_s (F_p/F_s)$. F_p, F_s are the respective focal length of primary and secondary mirrors, and R_p, R_s are the corresponding mirror radii. In addition, we define the following parameters:

ε_p, ε_s = Emissivities of primary and secondary mirrors.

ΔE = Power difference at detector between extreme beam positions.

(E_{8-13}/π) = Emission.sr^{-1}.cm^{-2} from a black body at temperature T, in the 8-13 μm band.

r_o = Detector radius (defined by cooled apertures).

D_s = Distance separating secondary mirror from focal plane.

For a typical chop angle $\Delta\theta \simeq F_s . 2r_o / \{F_p (D_s - F_s)\}$, we then obtain to a reasonable approximation

$$\Delta E \simeq \frac{E_{8-13}}{\pi} \left\{ 2R_p . \Delta\ell_p . \varepsilon_p \, \pi \left\{\frac{r_o}{F_p}\right\}^2 + 2R_s . \Delta\ell_s . \varepsilon_s \, \pi \left\{\frac{r_o}{D_s}\right\}^2 \right\}$$

and taking $\varepsilon_s = \varepsilon_p$ then gives

$$\Delta E \simeq 4E_{8-13} \frac{R_p \, r_o^3}{F_s \, F_p} \varepsilon_p \left\{ 1 + \frac{R_s}{R_p} \cdot \frac{F_s}{F_p} \cdot \left\{\frac{F_p}{D_s}\right\}^2 \right\}$$

$$\simeq \phi \, E_{8-13}$$

whence the time derivative of power input

$$\frac{d \, \Delta E}{dt} \simeq \phi \frac{d \, E_{8-13}}{dT} \cdot \frac{dT}{dt}$$

for a temperature derivative dT/dt. $d\,E_{8-13}/dT$ may be evaluated from data given by Allen (1973), and is typically

$$\frac{d \, E_{8-13}}{dT} \simeq 8 \times 10^{-4} \, \sigma T^4 \text{ ergs.K}^{-1}$$

at T ≃ 300 K, with an approximately 50% variation in the constant term

for a change of 30^{o} K either side of the temperature. The determination of dT/dt is slightly more involved.

The reason for this temperature change will usually be associated with variations in local meteorological conditions. We assume the ambient temperature to have decreased, in which case the maximum rate of radiative energy loss from the surfaces of the mirrors is determined by assuming the telescope located within a black cavity at the new ambient temperature. We will call the new ambient temperature T_A, and mirror emissivity ε_m. Energy loss is then

$$\frac{dH}{dt} = \sigma \varepsilon_m (T^4 - T_A^4) \text{ ergs.cm}^{-2}.\text{s}^{-1}$$

Taking an aluminium coated mirror ($\varepsilon_m \simeq 0.02$ at $\lambda \simeq 10$ μm (Allen 1973)), T = 300 K, T_A = 290 K then gives dH/dt ≃ 0.37 B.T.U. $\text{Ft}^{-2}.\text{hr}^{-1}$. We will see that this is small compared to convective losses.

A parameter defining the turbulence of convective heat transfer is $X = L^3 \Delta t Z$, a product of the Grashof and Prandtl numbers. Applied to the mirrors, L is ~ mirror diameter, Δt is the temperature difference between mirror surface and air (at a point where temperature gradient normal to the mirror surface is negligible). Z depends upon the properties of the convecting fluid, and Δt, and can be found from textbooks on engineering thermodynamics. Convective flow is turbulent if $X > 10^9$. For L = 5 feet, Δt = 18 F and $Z \simeq 1.7 \times 10^6$, $X = 3.8 \times 10^9$, so convective processes at the mirrors are likely to be turbulent. For this case, it can be shown that

$$\frac{dH}{dt} \simeq 0.22 \, \Delta t^{4/3} \text{ B.T.U. hr}^{-1}.\text{ft}^{-2}$$

for a horizontal surface, i.e. dH/dt ≃ 10.39 B.T.U. $\text{hr}^{-1}.\text{ft}^{-2}$. For a

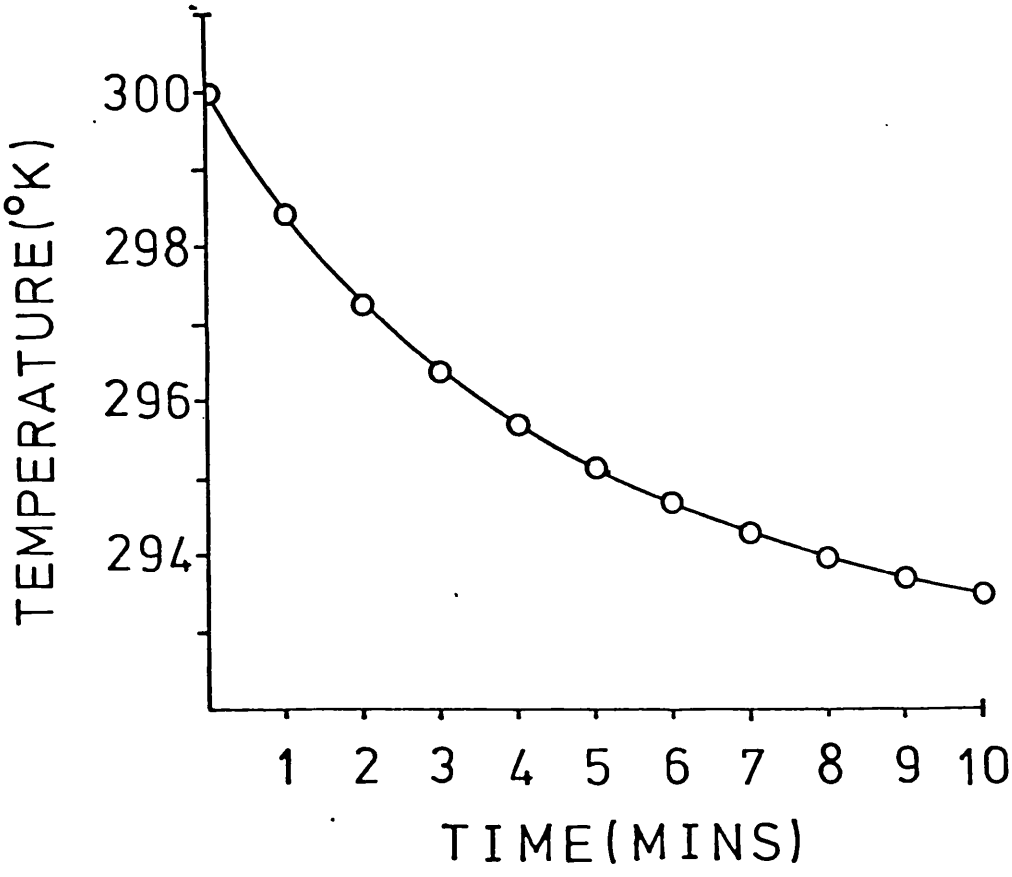

FIGURE 1.10
SCHMIDT COOLING CURVE

heavily tilted surface $dH/dt \simeq 0.19\ \Delta t^{4/3}$, giving very similar results. Assuming these relations to be reasonably applicable to the mirrors, heat is predominantly lost from the surface by convective heat transport. There are several procedures for evaluating cooling rates in such a situation. The simplest, applied here, is probably the Schmidt graphical method. As in the analysis above, the basic details are available in many books on engineering thermodynamics, and we simply present the final results. A thermal diffusivity of 2.31×10^{-5} $ft^2.hr^{-1}$ has been adopted for the mirror material. The variation of temperature with time is shown in figure 1.10. From this, it is seen that

$$\frac{dT}{dt} \simeq 1.7 \times 10^{-2}\ K\ s^{-1}$$

Taking $R_p \simeq 76$ cm, $R_s \simeq 20.3$ cm, $F_p \simeq 457$ cm, $F_s \simeq 146$ cm, $D_s = 526$ cm, and $r_o = 0.05$ cm and collecting terms, we arrive at a power depreciation rate

$$\frac{d\ \Delta E}{dt} \simeq 7.6 \times 10^{-15}\ W\ sec^{-1}$$

A 1 Jy astrophysical source would give a flux 2.83×10^{-13} W at a detector mounted on the Tenerife flux collector - or possibly, adopting a pessimistic signal attenuation, $\sim 2.8 \times 10^{-14}$ W. Since the observed drifts are typically of order 1 Jy sec^{-1} (calibrated against stellar sources), it is clear that the mirrors are incapable by themselves of explaining these drifts. Adopting however an emissivity $\varepsilon_p \simeq 1$ would indeed enable an appropriate drift rate. Such an emissivity is of course unrealistic for the primary mirror - but may be approached by the immediate surroundings of the primary (as seen from the secondary). Thus, if the beam chop is asymmetrical at the secondary, and the secondary is oversized, preferential

observation of regions adjacent to the primary in one beam position will lead to the observed drifts, if an air temperature change of 10 K occurs. Similar results ensue for the present secondary baffle. Drift rates will also be enhanced by the greater temperature depreciation rate of these high diffusivity bodies.

We have assumed up to now that the atmospheric contribution is comparatively negligible. Under good conditions this will be true. The sky has typical emissivity ~0.1, and if ~20 K cooler than the telescope fittings (this, according to Low and Riecke 1974, is fairly typical) the sky emission may be less (at the detector) than that of the telescope.

When however warm and/or humid air streams occur over the telescope, emission will increase over a time scale determined by the period of flow build up, and asymmetrical chopping will again lead to signal drift. The correlation between local humidity variation and drifts is well established in Tenerife.

At least one, and probably the principal reason for signal drifts has therefore been identified. We have already noted that the first differential of intensity variation is automatically removed in these circumstances through appropriate analysis of the photometric data. The size of the second differential is usually conjectural, however, and if weak signals are detected in the presence of drifts, they should be considered with considerable reserve until a confirmatory observation becomes available.

1.8 Spurious Signals Arising from Sky Emissivity Gradients

Dall'Oglio et al. (1973) have considered the question of

spurious signal arising from sky emissivity gradients, as a consequence of the technique of differential modulation in infrared astronomy. Their analysis involves several assumptions, which however are in certain cases of dubious validity for their treatment, and certainly require revision when applied to ground-based ($\lambda \lesssim 40$ μm) infrared photometry. We may summarise the requisite modifications as follows:

(a) A sky emissivity law $I = I_o(1 - e^{-a L \sec \phi})$ is used, where I_o is the power emitted per unit solid angle, area and optical bandwidth, a is the absorption coefficient, L the zenithal atmospheric path length and ϕ the zenith angle. We have already commented upon the applicability of such a law, and following that discussion we use an alternative expression $I = I_o(1 - e^{-\kappa \sec^{\frac{1}{2}} \phi})$.

(b) The detector-telescope system is assumed optimised; that is $\Omega S = 10^{-8}\lambda$ (λ in μms), where Ω is the sky solid angle seen by the detector, and S the telescope collecting area. Applying this to the Tenerife 60" flux collector leads to "optimum" sky beam radii of $0\overset{\prime\prime}{.}28$ at 10.2 μm and $0\overset{\prime\prime}{.}12$ at 2 μm. These are, needless to say, quite unrealistic in a practical sense; in our later comments concerning the infrared seeing disks of stars for instance, it will be found that most of the signal would be lost with such narrow beam profiles, and questions concerning the ability to guide with the required accuracies would also arise. The Imperial College group has followed a common trend in adopting a $10\overset{\prime\prime}{}$ beam diameter and we adopt this in the present analysis with corresponding mirror chop and telescope nodding amplitudes.

(c) A single chopping mode is assumed, whereby signals from one sky area are directly compared with those from an adjacent region. The signal generated by sky emission gradients is then dominated by $dI/d\phi$, and for a chop $\Delta\phi$, bandwidth $\Delta\lambda$ the corresponding atmospheric

modulated power $|\Delta W|$ is

$$|\Delta W| = \left(\frac{dI}{d\phi}\right) \Delta\phi \ \Omega \ S \ \Delta\lambda$$

For near infrared, ground-based observations, a nodding procedure is usually employed to remove this first differential term, as we have noted earlier. This leaves the second differential of sky emissivity as the primary term in $|\Delta W|$, and

$$|\Delta W| = \left(\frac{d^2 I}{d\phi^2}\right) (\Delta\phi)^2 \ \Omega \ S \ \Delta\lambda.$$

It should be further noted that setting $\Delta\phi$ equal to the absolute chop/nod amplitude maximises $|\Delta W|$. In reality, this equality is only achieved along the meridian, and at declinations $\delta \neq L$, where L is the latitude, for chopping/nodding along a north-south axis (the usual situation). At other hour angles and declinations, $|\Delta W|$ will be less than that calculated here.

(d) Dall'Oglio et al. set $\Delta\lambda = \lambda$. In reality bandwidths rarely exceed 0.5λ, and at $\lambda \lesssim 5$ μm are almost ten times smaller. We initially choose $\Delta\lambda = 0.5\lambda$. Such a large value for $\Delta\lambda$ necessitates numerical integration of the sky emission (characterised by a diluted Planck law) over the bandpass.

(e) A detector NEP ~ 10^{-13} W $Hz^{-\frac{1}{2}}$ is adopted by Dall'Oglio et al. Whilst this still represents a reasonable practical performance limit, the best detectors now achieve NEP's smaller than the background shot noise limit; ~10^{-14} W at $\lambda = 10$ μm. We adopt $|\Delta W| \simeq 10^{-14}$ W. This represents (for zero signal attenuation) a 10.2 μm magnitude $N \simeq +6.8$. Total signal attenuation of calibration sources may however approach ~2.5 magnitudes (for a discussion of this question, see Low and Riecke 1974. The Tenerife telescope is commonly less optically

efficient than the case considered by these latter authors); and the limiting chopping signal could readily be recorded as an N = +4.3 source. Since similar magnitudes are now being recorded in the literature, it behoves us to enquire whether contamination by sky background may be contributory.

From the above discussion, we find that

$$|\Delta W| = \frac{I_o \kappa}{2} e^{-\kappa \sec^{\frac{1}{2}} \phi} \sec^{\frac{1}{2}} \phi \tan \phi \left\{ -\frac{\kappa}{2} \sec^{\frac{1}{2}} \phi \tan \phi + \frac{\sec^2 \phi}{\tan \phi} + \frac{\tan \phi}{2} \right\} (\Delta\phi)^2 \Omega S \Delta\lambda \qquad \ldots (1.1)$$

After the example of Dall'Oglio et al. we plot "normalised" atmospheric modulated power ($2|\Delta W|/(\Delta\phi^2 \Omega S \Delta\lambda \kappa I_o)$) against air mass (figure 1.11). It is seen that signals close to maximum may be generated at observationally acceptable air masses. To assess the angle corresponding to maximum signal, ϕ_{max}, we set $d|\Delta W|/d\phi = 0$ and obtain

$$\frac{\kappa^2}{4} - \frac{\kappa^2}{4} \cos^2 \phi_{max} - \frac{9}{4} \kappa \cos^{\frac{1}{2}} \phi_{max} + \frac{3}{4} \kappa \cos^{5/2} \phi_{max} + \frac{15}{4} \cos \phi_{max} - \frac{1}{4} \cos^3 \phi_{max} = 0$$

after differentiation of equation 1.1, and some reduction. Deleting the highest cosine powers leads to a quadratic in $\cos^{\frac{1}{2}} \phi_{max}$, which gives

$$\cos \phi_{max} \simeq 0.21 \kappa^2 \qquad \ldots (1.2)$$

appropriate for high air masses. Typically therefore maximum signal is generated at high air mass; although for high emissivity nights maximum signal may be generated at air masses approaching those regarded

as observationally acceptable in infrared photometry. This is illustrated in figure 1.11. To assess whether a sky signal $\sim 10^{-14}$ W would be developed with the chop/nod amplitudes usually employed, we determine the minimum chop/nod amplitude $\Delta\phi_{min}$ required to generate such a signal, assuming $\phi = 60^{o}$. $\Delta\phi_{min}$ is plotted against wavelength in figure 1.11, for κ ranging from 0.1 to 1.0 in increments of 0.1. Sky temperature is taken as T = 300 K, and

$$I_o = \int_{\lambda-\Delta\lambda/2}^{\lambda+\Delta\lambda/2} \frac{c_1}{\pi \lambda^5} \frac{d\lambda}{(e^{c_2/\lambda T}-1)} \text{ erg.cm}^{-2}.\text{s}^{-1}.\text{sr}^{-1}.\text{K}^{-4}$$

$$c_1 = 3.74185 \times 10^{-5} \text{ erg.cm}^2.\text{s}^{-1}$$

$$c_2 = 1.43883$$

$\Delta\phi_{min}$ is then given by

$$\Delta\phi_{min} = \left\{ \frac{2|\Delta W|/I_o}{\kappa\, \Omega\, \psi\, S\, \Delta\, \lambda\, e^{-\kappa \sec^{\frac{1}{2}}\phi} \tan\phi \sec^{\frac{1}{2}}\phi} \right\}^{\frac{1}{2}} \text{ radians}$$

$$\psi = -\frac{\kappa}{2} \sec^{\frac{1}{2}}\phi \tan\phi + \frac{\sec^2\phi}{\tan\phi} + \frac{\tan\phi}{2}$$

It is apparent that, for a $10\hat{}''$ sky beam and removal of $dI/d\phi$ terms, very large throws ($\Delta\phi \sim 100\hat{}''$) are required to generate the required signal. For $\Delta\phi \simeq 10\hat{}''$ it follows that spurious signals ~5 magnitudes fainter than $|\Delta W| \simeq 10^{-14}$ W will be generated, and these are unlikely to represent a real problem. However, if large beams ($\simeq 20\hat{}''$) are used, then corresponding 20" chopping and mirror nodding will lead to second order differential terms approaching $\sim 10^{-14}$ W. This last situation may be encountered where observers attempt to alleviate severe seeing problems, for instance, or where measurements of extended sources are to be made. Large throws have been used for

FIGURE 1.11a. NORMALISED SKY POWER LEVELS

A. NODDING AND CHOPPING B. CHOPPING

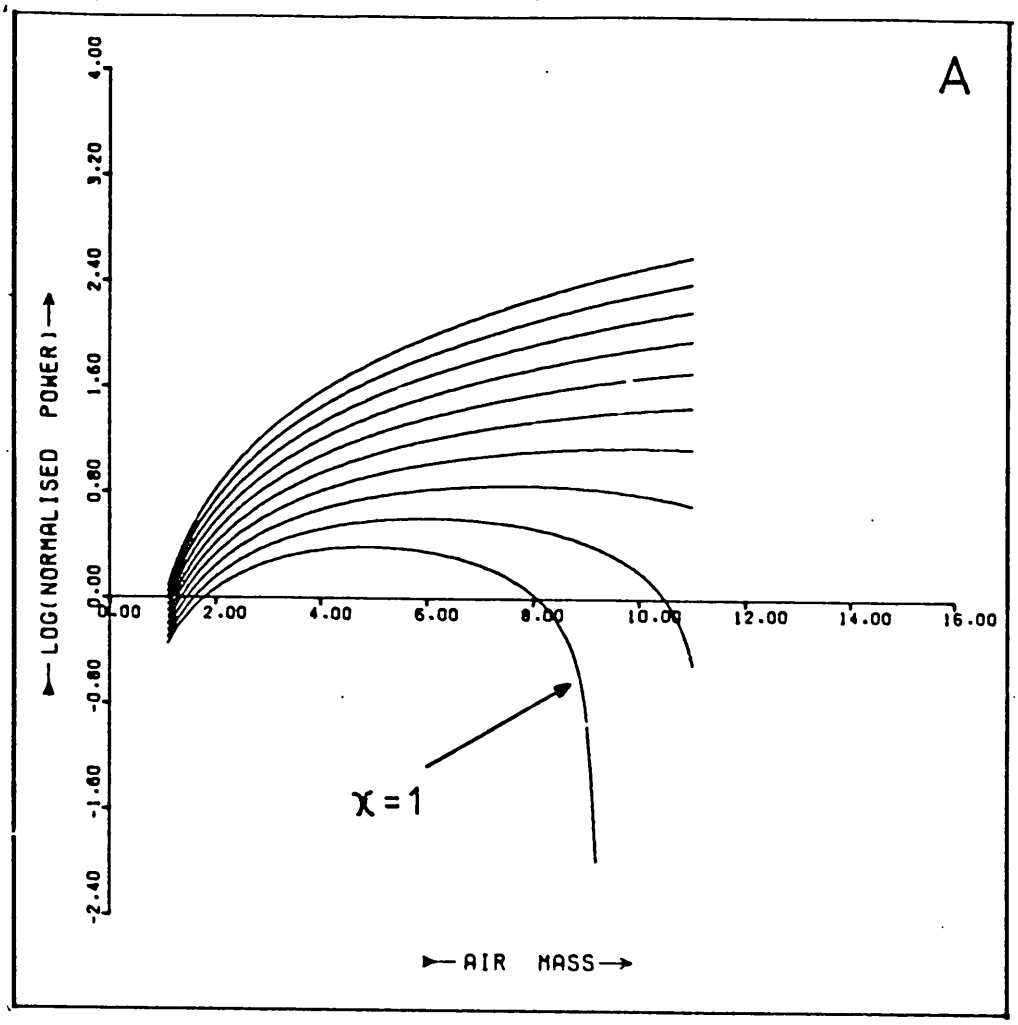

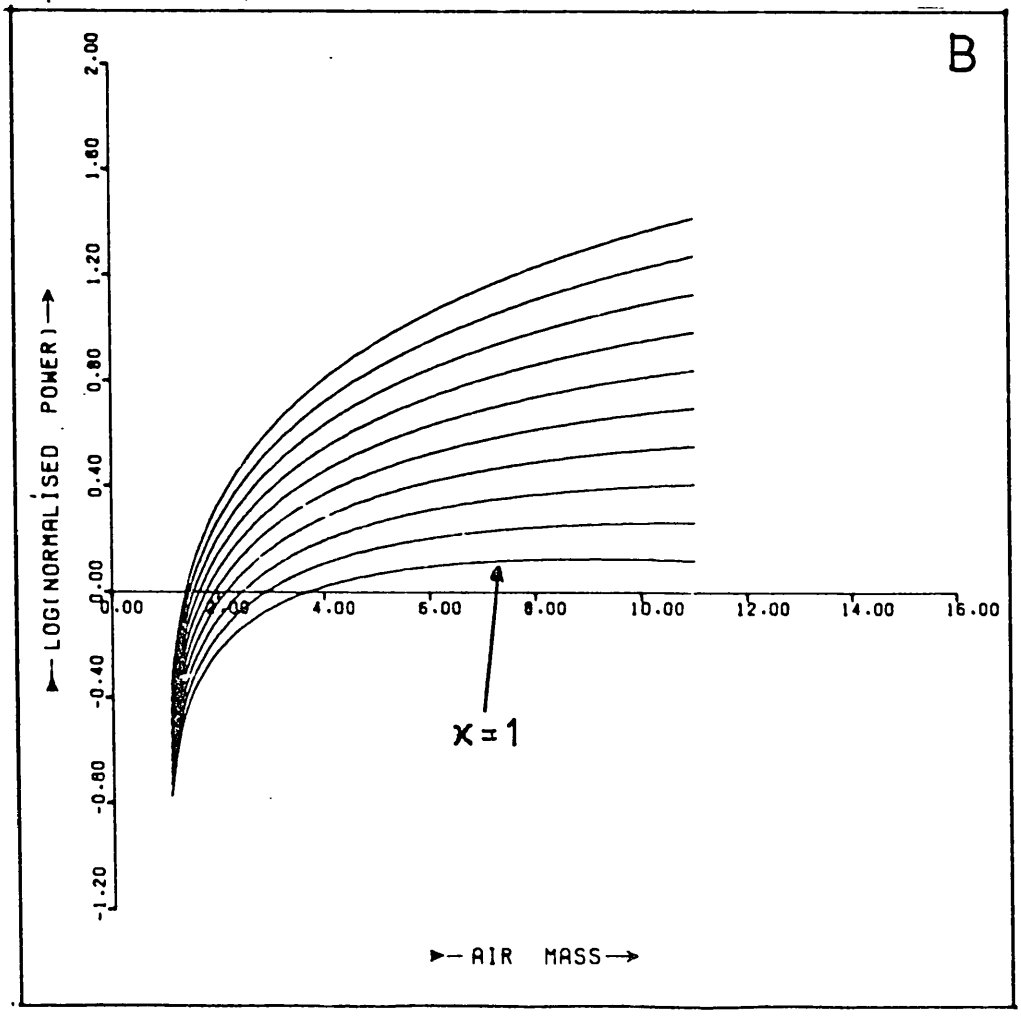

FIGURE 1.11b. LIMITING CHOP ANGLE

A. NODDING AND CHOPPING B. CHOPPING

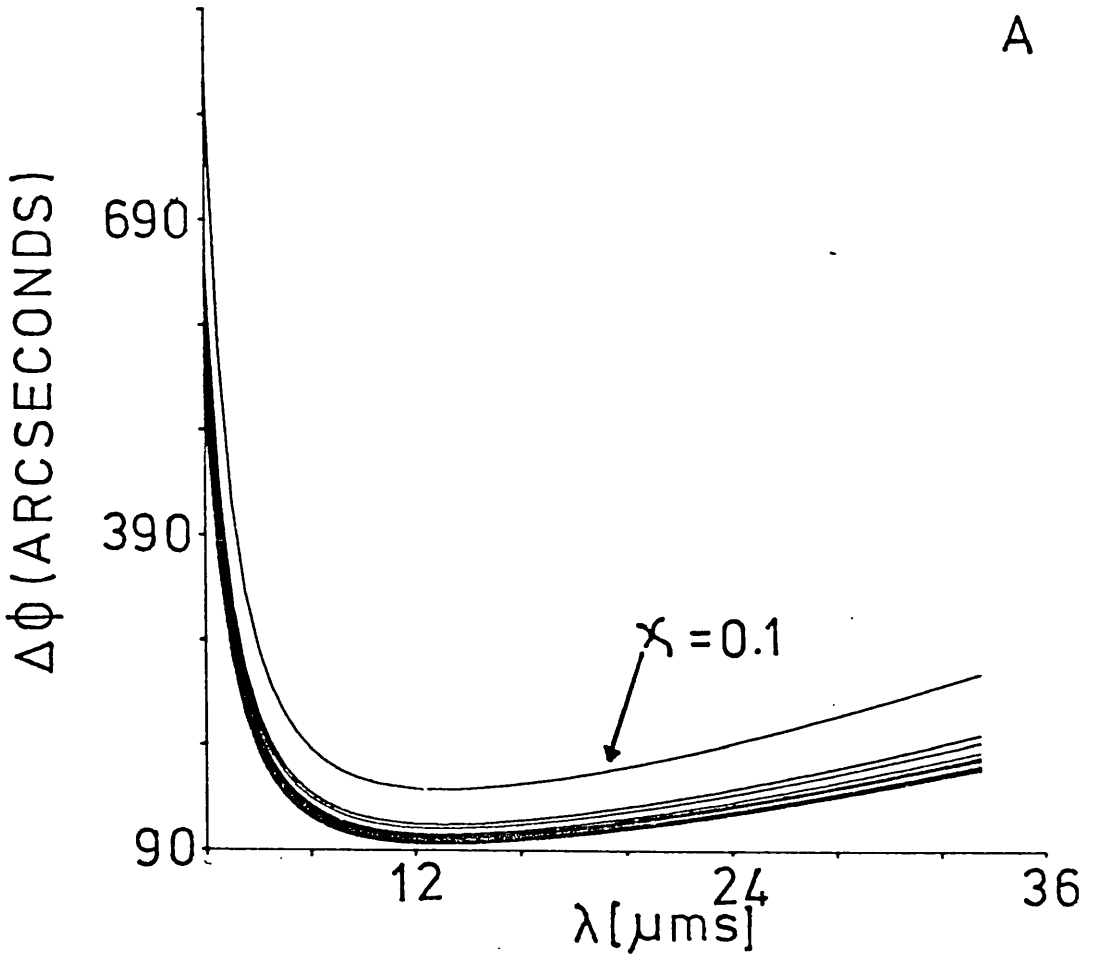

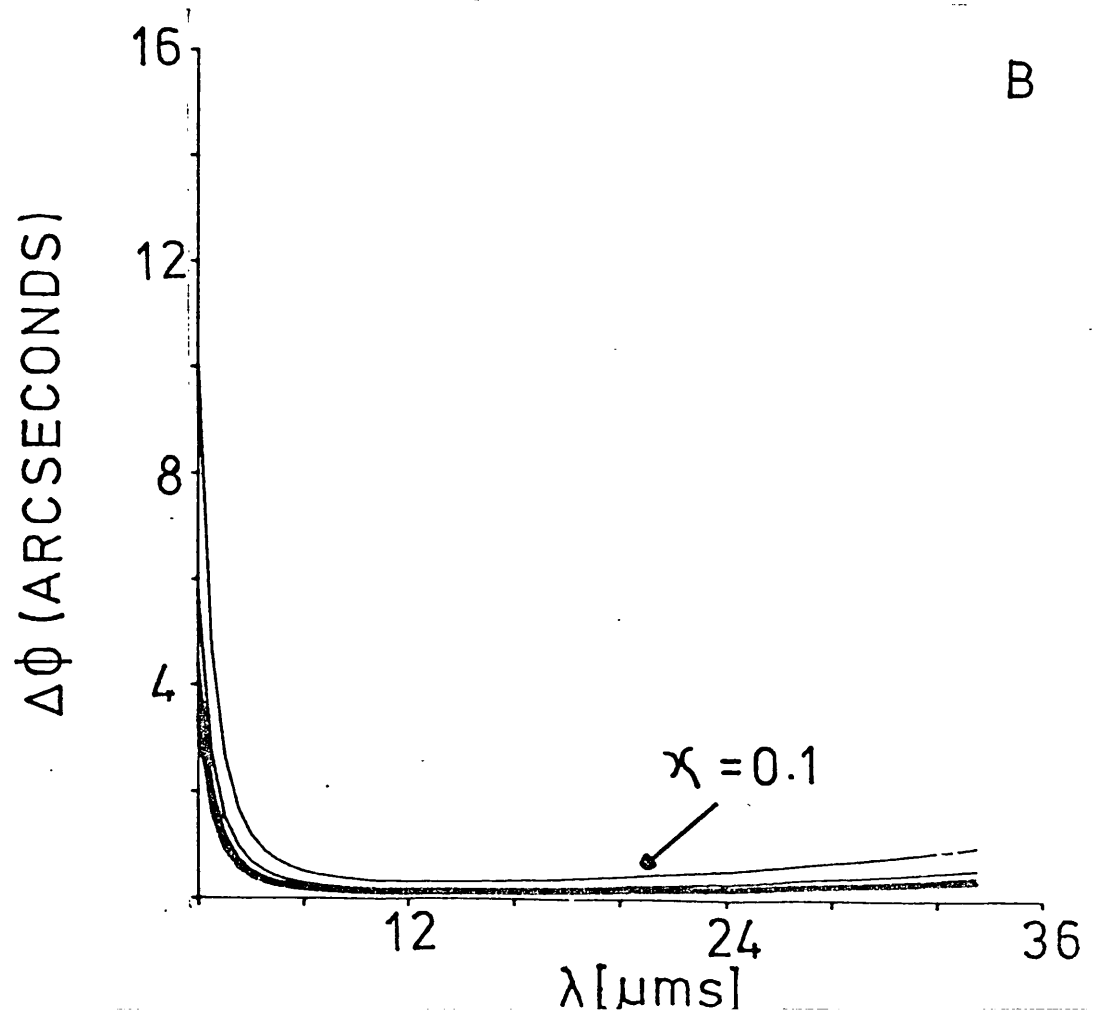

mapping purposes (to avoid the trouble of deconvolving data), and from the earlier comments it is clear that care should again be taken in the interpretation of results. For most purposes however, it is clear that the contribution of second order differential terms may be safely disregarded.

Atmospheric emission levels at 2.2 μm are ~7000 times lower than at 10.2 μm, and arise primarily from lines of OH. With narrower passbands (0.4 μm) and larger photon energy, the total photon flux incident on the detector is reduced by a factor ~3 x 10^5, and shot noise levels approach 4 x 10^{-16} W. This is similar to the best detector NEP limits, although the lower ratio of background emission signal/shot noise at 2.2 μm means that larger chop amplitudes are required than at ~10.2 μm, if spurious signals of size similar to the shot noise background are to be created. In practice, detectors currently in use are achieving typical NEP's ~2 x 10^{-15} W (corresponding to an unattenuated magnitude +13.6), and at these levels, the probability of developing spurious signals is very small indeed.

Finally, we note that for the single chopping mode

$$\Delta\phi_{min} = \frac{2|\Delta W|}{\kappa I_o \Omega S \Delta\lambda e^{-\kappa \sec^{\frac{1}{2}}\phi} \tan\phi \sec^{\frac{1}{2}}\phi} \qquad \ldots (1.4)$$

$$\cos\phi_{max} \approx \left(\frac{\kappa}{3}\right)^2$$

or, for $I = I_o(1 - e^{-\kappa \sec\phi})$ we have

$$\Delta\phi_{min} = \frac{|\Delta W|}{\kappa \tan\phi \sec\phi I_o e^{-\kappa \sec\phi} \Omega S \Delta\lambda}$$

$$\cos\phi_{max} \approx \frac{-1 + \sqrt{1+\kappa^2}}{\kappa}$$

These latter two relations being first derived by Dall'Oglio et al.

For nodding and chopping, but with an $I = I_o(1 - e^{-\kappa \sec\phi})$ sky emissivity law

$$\Delta\phi_{min} = \left\{ \frac{|\Delta W|}{I_o \kappa \sec\phi \, e^{-\kappa \sec\phi} \, \Omega S \Delta \lambda \psi} \right\}^{\frac{1}{2}}$$

$$\psi = \sec^2\phi + \tan^2\phi - \kappa \tan^2\phi \sec\phi$$

$$\cos\phi_{max} \simeq \frac{\kappa}{1.27}$$

These relations have particular fields of applicability outside ground-based near infrared work. Single beam chopping modes are for instance commonly employed in far infrared balloon work. As an indication of the impracticability of such a chop mode in the near infrared, we have plotted $\Delta\phi_{min}$, and normalised power using relation 1.4. (fig 1.11b) It is evident that substantial sky signals will develop, which would seriously vitiate the usefulness of those bands for all but the brightest sources.

To summarise, we may say that the possibility of generating sky signals from the second differential term of the zenithal variation of sky emissivity is under usual circumstances low; but for $\lambda \gtrsim 10$ μm, large apertures (~20") and/or large chopping amplitudes, spurious sources may well be generated.

1.9 Atmospheric Dispersion

The influence of atmospheric dispersion upon received signal strength is not always apprcciated. We will show that the common procedure of centring the visual image on the detector will lead to

appreciable infrared photometric errors. Atmospheric refraction is commonly represented by the form

$$R = A \tan \phi + B \tan^3 \phi \qquad \ldots (1.5)$$

where Smart (1971) gives A = 58".294, B = 0".0668 for the visible, T = 283 K, P = 30 inches Hg, although the relation becomes inadequate for zenith angles $\phi \gtrsim 75^{\circ}$. The derivation of this relation is given by Smart (1971) and we follow his terminology in extending it to the infrared.

The constants in relation (1.5) are related through

$$A = (n_{T,P,f} - 1) + B \qquad \ldots (1.6)$$

where $n_{T,P,f}$ is the atmospheric refractive index for temperatures T ($^{\circ}$C), pressure P (mm Hg) and water vapour partial pressure f (mm Hg) (Kaye and Laby 1966)

$$(n_{T,P,f} - 1) = 0.001387188\ (n_s-1)p(1+\beta_t p)/(1+\alpha T) - (a-b/\lambda_{vac}^2)f/(1+\alpha T) \qquad \ldots (1.7)$$

and $\alpha = 0.003661$, $\beta_t = (1.049 - 0.0157T)10^{-6}$, $a = 6.24 \times 10^{-8}$, $b = 0.0680 \times 10^{-8}$. We take f = 0, and extend the application through the near infrared. n_s is the refractive index of standard air (T = 15C, P = 1013250 dynes cm^{-2}, 0.03% CO_2) and can be adequately represented by the three term Cauchy equation (Kaye and Laby 1966)

$$(n_s - 1)\ 10^8 = 27259.9 + \frac{153.58}{\lambda_{vac}^2} + \frac{1.318}{\lambda_{vac}^4}$$

where $\lambda_{AIR} = \lambda_{vac}/n_{s_1}$ and units of λ are μm. Measurements at λ = 12.5 mm and 32.6 mm give $(n_s-1)\ 10^8 = 2.729 \times 10^4$ (Essen and Froome 1951; Essen 1953); in reasonable agreement with the extrapolation of the above equation.

From (1.5) and (1.6), the change in refraction ΔR due to a change of wavelength is:-

$$\Delta R = \Delta n \tan \phi + \Delta c \, \chi(\tan \phi + \tan^3 \phi)$$

where $c = \frac{n-1}{\rho_o}$; $\chi = \int_o^s \rho ds$

and ΔR is the differential refraction at wavelength λ compared with the visible. χ is the zenithal air mass, and ρ_o is air density at Earth's surface. We therefore have

$$\Delta c = \frac{\Delta n}{n_{0.55}-1} \; c_{\lambda=0.55}$$

χ is independent of wavelength, and may be determined from $\chi = B/C$. For an observatory at height h we have approximately

$$\frac{\chi_h}{\chi_o} = \frac{\int_h^\infty \rho_o(T_h) \, e^{-\frac{m_o g r}{RT_h}} dr}{\int_o^\infty \rho_o(T_o) \, e^{-\frac{m_o g r}{RT_o}} dr} = e^{-\frac{m_o g h}{RT_h}} \qquad (T_o = T_h)$$

where m_o is the mean molecular weight of air ($m_o = 28.97$), $g = 981$ cm.s^{-2}.

Using the above relations we can make a reasonable guesstimate of ΔR for any particular observatory site; although such a procedure should be avoided in favour of actual measurements at site, wherever possible.

For the Observatorio del Teide, Tenerife, we have $h \simeq 2400$ m, and pressure $P \simeq 756$ m bars. The corresponding density is $\rho = 9.36 \times 10^{-4}$ g.cm^{-3} at $T = 10^oC$. Refractive index ($f = 0$) is

$$(n-1) \simeq 20690.3 + \frac{116.6}{\lambda_{vac}^2} + \frac{0.998}{\lambda_{vac}^2}$$

from which $c_{\lambda=0.55} = 0.225$. $\chi_h = 0.749 \, \chi_o$ where we derive $\chi_o = 0.3055$

from the value of B given by Smart (1971). We therefore have

$$\Delta\hat{R''} = \alpha(A' \tan \phi + B'(\tan \phi + \tan^3 \phi))$$

$$B' = 244.4$$

$$A' = 2.063 \times 10^5$$

$$\alpha = \Delta n = \left\{396.26 - \frac{116.57}{\lambda_{vac}^2} - \frac{0.998}{\lambda_{vac}^4}\right\} 10^{-8}$$

We give below values of $\Delta\hat{R''}$ thus derived.

TABLE 1.1

ϕ/λ (μm)	1.25	1.6	2.2	3.4	5.0	10.2	22
0^o	0	0	0	0	0	0	0
10^o	0.117	0.128	0.135	0.141	0.143	0.144	0.144
20^o	0.241	0.263	0.279	0.290	0.294	0.297	0.297
30^o	0.382	0.417	0.443	0.460	0.466	0.470	0.471
40^o	0.556	0.606	0.644	0.668	0.677	0.684	0.683
50^o	0.793	0.866	0.919	0.954	0.967	0.976	0.978
60^o	1.153	1.260	1.336	1.386	1.398	1.419	1.422
70^o	1.841	2.009	2.132	2.213	2.244	2.264	2.269
80^o	3.790	4.137	4.391	4.557	4.621	4.663	4.673

It is clearly seen that for modest air masses, dispersion is adequately represented by $\Delta\hat{R''} \simeq \alpha A' \tan \phi$. In general, this is adequate for application in normal infrared photometry, where higher air masses are to be avoided. Where measurements at moderately high air masses are either desirable (c.f. determination of the extinction law) or unavoidable, however, the second order terms cannot be so readily dismissed. A specific application to an early trip led to the following relations for source intensity I as a function of dispersion

ΔR_α in right ascension, and ΔR_δ in declination:-

$$\left\{\frac{I}{I_o}\right\}_\alpha = 1 - 0.0547\ \Delta R_\alpha''$$

$$\left\{\frac{I}{I_o}\right\}_\delta = 1.367 \sin\left\{\frac{(7.5 + \Delta R_\delta)\pi}{15}\right\} - 0.367$$

These relations are fairly typical, although for the trip concerned the beam profile in right ascension was asymmetrical, leading to a reduction of the error in R.A. It is clear that errors of ~0.2 magnitudes may occur as ϕ approaches 70^o. There are two ways this error may be accounted for. The first requires an evaluation of beam profile for the trip concerned. Dispersion for the site may be determined analytically (as above), but is preferably determined empirically. Dispersion in right ascension and declination are then independently found from

$$\Delta R_\alpha = \alpha\ A'\ \sin Q$$

$$\Delta R_\delta = \alpha\ A'\ \cos Q$$

where $$\sin Q = \frac{\cos L \sin H}{\sin \phi}$$

where L is now latitude, H is the hour angle of the source. From beam parameters and dispersion, the signal correction may be determined. A better procedure however may be to maximise the source strength in the beam every time before performing high air mass photometry. Unless higher air masses are generally avoided, however, this could seriously reduce the rate at which observations are taken.

1.10 Seeing Errors

The problem of the size of astronomical seeing in the infrared has still to be fully resolved theoretically. Andriesse and Wierstra (1973) for instance, using numerical procedures, find that "under 'normal seeing' the seeing disk for a 5 m aperture would be some 30 times smaller around 10 μm than at 0.5 μm". Under these conditions, the authors note "mirror imperfections rather than seeing or diffraction may be the dominating factor for image sizes in the infrared". Providing an opposing viewpoint, Young (1974b) suggests that although the match between (constant) aperture and atmosphere is improved in going to longer wavelengths, the seeing cannot be greatly reduced. More specifically, if aperture is increased to maintain the diffraction disk invariant with wavelength, then "the r.m.s. angular blur is inversely proportional to the fifth root of the wavelength. Thus, the seeing only improves a factor of 2 in going from visible light (λ = 0.5 μm) to the thermal infrared ($\lambda \simeq$ 16 μm)". This last statement certainly appears to agree with experience. Wildey and Murray (1964) note that for the 200-inch telescope "8 - 14 μm scans across the image of Betelguese under normal seeing were flat-topped and sharp shouldered, suggesting that seeing may be better in the 8 - 14 μm region than in the visible". Low and Riecke (1974) however advance the view that "a field substantially smaller than 6 arcsec cannot be used to obtain accurate results at 10 μm on a routine basis with a 150-cm telescope" because of seeing. The 10 μm diffraction disk for a 150-cm telescope is only $3\overset{\wedge}{.}3$. In addition, "three arcsec is probably the smallest field that can be

FIGURE 1.12

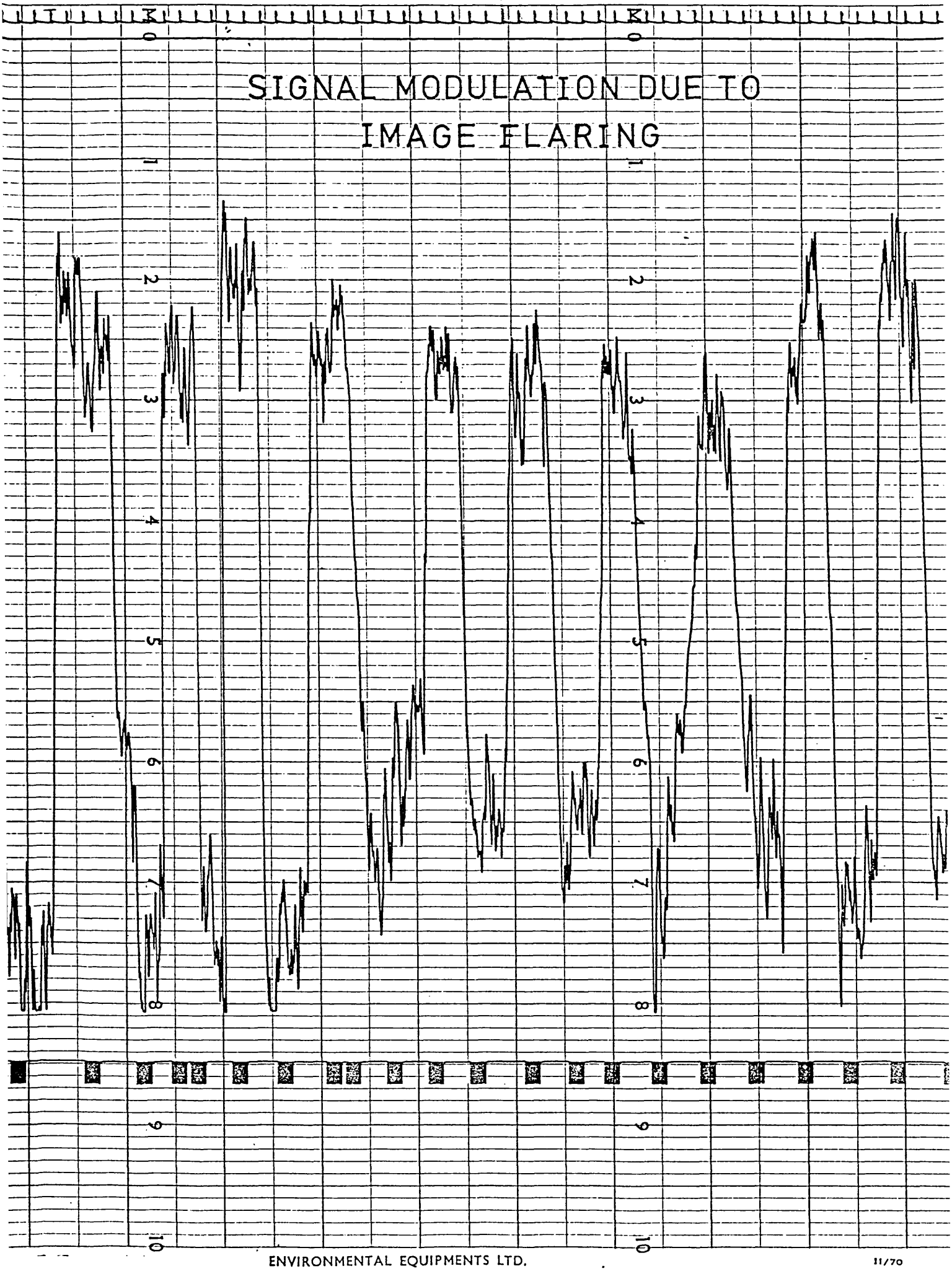
SIGNAL MODULATION DUE TO
IMAGE FLARING
ENVIRONMENTAL EQUIPMENTS LTD.
11/70

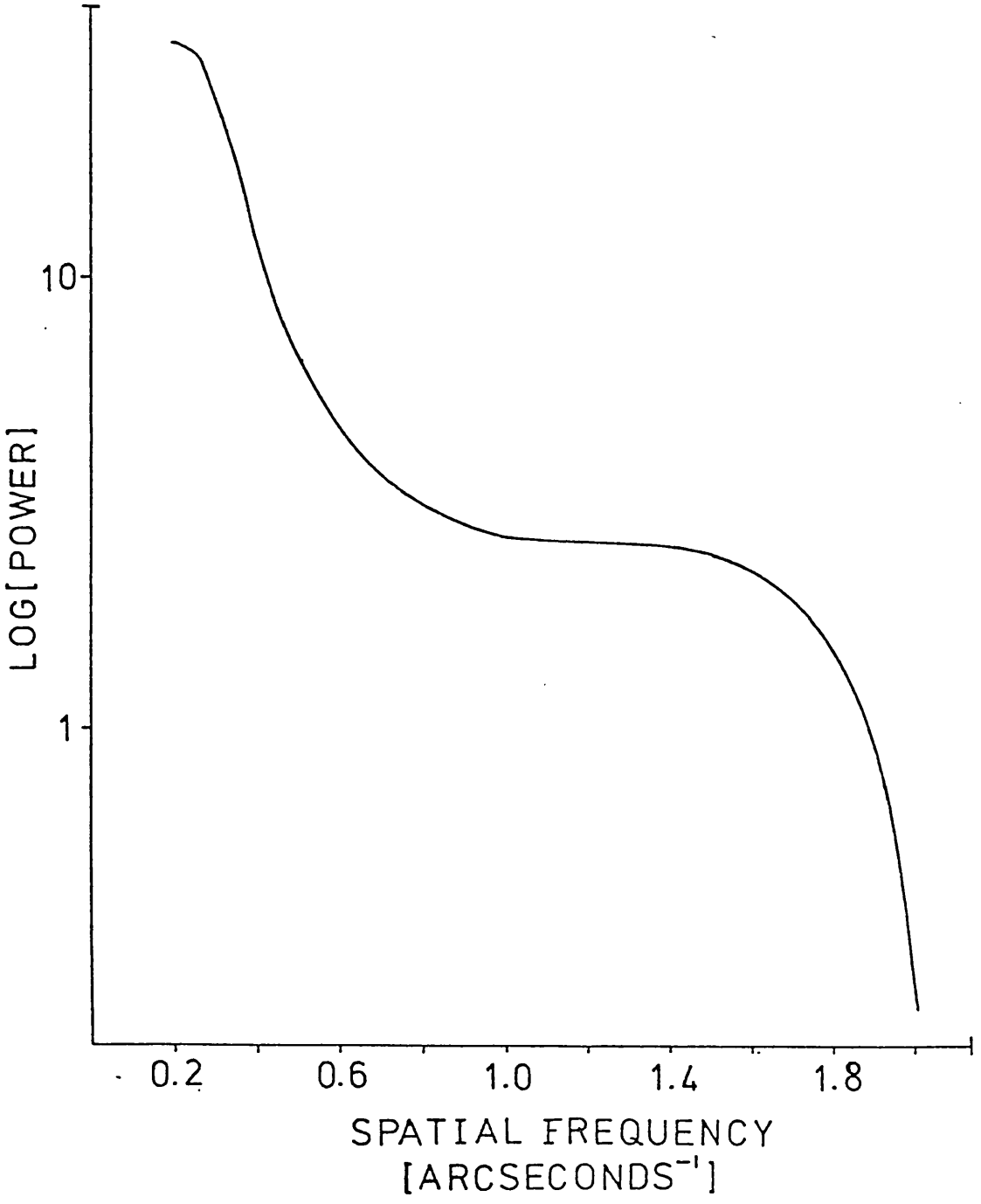

FIGURE 1.13

SPECKLE POWER SPECTRUM

used routinely on even the largest telescopes". These latter statements coincide with experience in the Imperial College group. Figure 1.12 shows results on a night with particularly poor seeing, and image flaring. A contribution from attenuation by pockets of moist air cannot be discounted for this particular case. However, on more recent trips, the adoption of larger apertures on similar nights has often eradicated this effect. It seems likely therefore that infrared seeing is comparable with that at optical wavelengths, and variable seeing may lead to systematic errors; which however may be partially alleviated with larger detector apertures. The experimental determination of infrared seeing would clearly be of considerable theoretical interest, and an infrared speckle technique being developed within the Imperial College astronomy group may provide a useful opportunity for evaluating this phenomenon.

Figure 1.13 shows preliminary results of this procedure, in the form of a point source spatial frequency power spectrum at 2.2 μm (I am grateful to R. Wade, M. J. Selby for permission to use this in advance of publication). The power contribution due to seeing is seen to be significant at spatial frequencies corresponding to ~5"; that is, comparable with the visible seeing for that night.

1.11 Clouds and Vapour Pockets

All of the near infrared windows are defined at least in part by the absorption properties of atmospheric H_2O. Thus the J, H, K bands are restricted at both short and long wave limits by steeply increasing water vapour absorption; and the same is true for the lower wavelength limit of the N band, and the long wavelength limit of

the M band. The filters used to further isolate particular bands at least partially encroach upon emission at the edges of the atmospheric windows and, with weak band emission within the windows, this leads to a correlation between extinction and atmospheric precipitable water vapour content. The presence over the sky of pockets containing variable amounts of water vapour, may then lead to irregular extinction measures. The existence of this variable extinction is not always noticeable at the time of observation, and has undoubtedly led to errors in the past. Specifically, development of wave clouds due to late evening atmospheric cooling is not uncommon at Tenerife, although these clouds are often invisible during the night. Under such circumstances, long wave ($\lambda \gtrsim 5$ μm) observations are in particular to be eschewed.

The effect of clouds is simply one extreme of this phenomenon, and perhaps the least dangerous in being usually identifiable. Fast moving streams with pockets of high humidity may lead to signal modulation of a type already illustrated in the discussion of seeing. These variations will typically occur on a time scale of ~ seconds, providing the "clouds" are composed primarily of vapour. A much more rapid variability is usually afforded by glaciated clouds. For this latter case, the primary absorption is by ice crystals, with a substantial complex term to the refractive index at $\lambda \gtrsim 2$ μm. Allied with extremely fine angular cloud structure, this leads to a distinctive noise pattern, of which a representative illustration is provided in figure 1.14. Again however, the effects of this are so easily recognised that there is usually no danger of inadvertent photometric errors. As for the weaker vapour pockets, however, diffuse glaciated pockets may be a factor in the introduction of anomalous

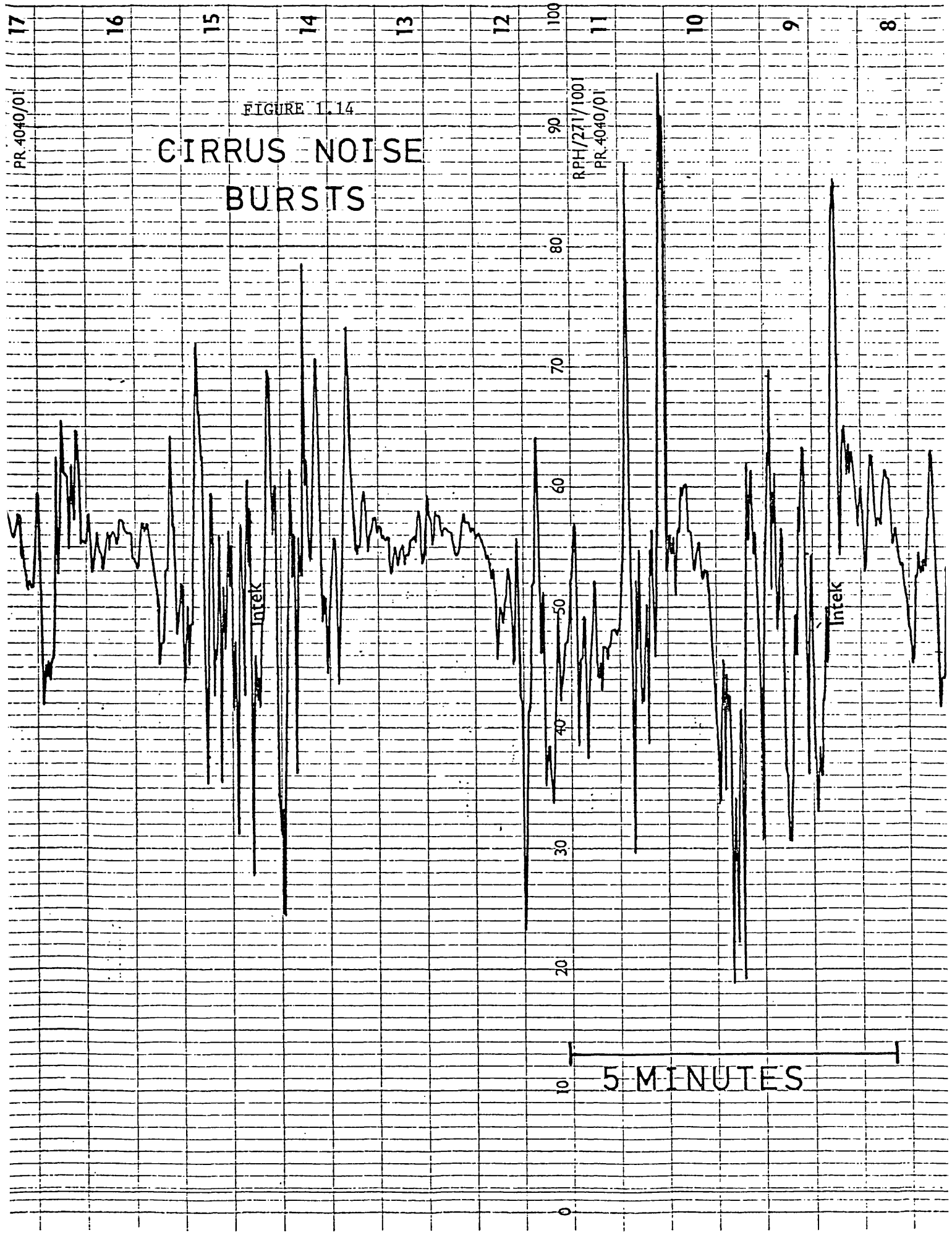

FIGURE 1.14

CIRRUS NOISE BURSTS

long wave extinction, although their presence is again usually recognisable in the late evening.

To conclude, we may say that a primary danger for photometric errors arises from variable sky extinction (both temporal and angular) due to weak pockets of H_2O. Where these are glaciated, observations at the K and shorter wavelength bands may be permissible. Where the pockets are not glaciated, then observations at all (infrared) wavelengths must be suspect, although again the shorter wave bands should be relatively less affected.

1.12 Contribution of Dust to Infrared Extinction

A problem at the Tenerife site, noted earlier, is the spasmodic contribution of air-borne dust grains to extinction. Gradual deposition of dust upon the primary mirror leads further to increases in background emission, and signal attenuation. Since this is a problem which seems likely to persist, and is present at other observing sites not far removed from desert locations, it is of interest to know whether observing in the infrared is acceptable in such conditions. Specifically, if visual extinction is high, does this also apply to infrared wavelengths?

The most obvious method of answering this question is to take the appropriate extinction measurements in dusty conditions. In the absence of these however some preliminary assessment may nevetheless be made of the likely contribution of dust to infrared extinction.

Air-borne Saharan dust has been collected in the vicinity of the Canary Islands by Parkin et al. (1972), Chester and Johnson (1971). Mineralogical analysis yields a ~20% quartz content, with the remainder

clay minerals such as kaolinite and illite. A similar deposition in Britain (Nature, 219, 112) was found to be mainly composed of quartz and feldspar, with many of the grains coated in iron oxide. The dust probably originated from a location similar, and possibly close to that responsible for extinction in Tenerife. A determination of particle size distribution showed a log-normal distribution characteristic of wind-borne aerosols (c.f. Manson 1965). Specific measurements at Harwell (personal communication) give the following values

Dust Size (a) (μm)	% Mass of Particles with Radius $\leq a$
0.21	0.016
0.42	0.39
0.84	3.00
1.68	14.40
2.5	28.2
3.4	42.1
4.2	53.0
5.25	65.1
6.30	75.6
8.40	88.0
10.50	100.0

These values, when transformed to number densities, are found to be comparable with the more restricted measurements of Chester and Johnson, and for $a > 1.68$ μm with the aerosol distribution in continental air. For smaller particle sizes the grain numbers are substantially deficient compared to a normal aerosol distribution; and we take the contribution of grains with radii <0.21 μm to be negligible.

Depending upon the thickness of the grain coating materials, and their optical properties, their contribution to total grain absorption may fall rapidly into the infrared. Under these circumstances, grain absorption at ~10 μm may well be dominated by silicate reststrahlen bands. This contribution will be particularly important when taking

spectra of astrophysical sources with similar continuum variations, and it is clearly of interest to determine the likely contribution of this atmospheric component. To do this, we assume the absorption properties of the grains in the infrared are those of quartz. The absorption coefficient is then approximated (following Kaiser 1968) by

$$Q_\lambda = \begin{cases} 4/3\ \delta_\lambda\ a & \text{for } a < \lambda/2\pi \\ 4/3\ \gamma_\lambda\ a & \text{for } \lambda/2\pi < a < 3/4\gamma_\lambda \\ 1 & \text{for } a > 3/4\gamma \end{cases}$$

where $\gamma_\lambda = \frac{4\pi k}{\lambda}$

and k is the complex term of the refractive index. If n is the real term of the refractive index, then

$$\varepsilon = n^2 - k^2$$

$$\eta = 2nk$$

$$\delta_\lambda = \frac{18\pi}{\lambda} \frac{\eta}{(\varepsilon+2)^2 + \eta^2}$$

values of n and k from Kaiser (1968) are adopted.

The total absorption per unit volume at wavelength λ is then

$$A_\lambda = \int_{a=0}^{\infty} Q_\lambda(a)\ N(a)\ da$$

where N(a) da is the number of grains per unit volume with radii between a and a+da. At visible wavelengths, absorption is increased by contaminants (iron oxide, clay minerals, etc.), and a maximum absorption is obtained by using $Q_\lambda(a) = 1$. Numerically solving for A_λ yields the result that for 2 magnitudes of visible absorption, there will be ≈0.11 magnitudes absorption at 11 μm.

It is therefore seen that total reststrahlen band absorption levels are not likely to be large. With substantial opacity from smooth continuum mantles, their effect may be further diminished, although total infrared absorption will be increased. In many cases, mantles (and entire grains) may be composed of flakes of Chlorite, Talc, and Montmorillonite (typical clay minerals), which whilst individually having typical silicate type absorption bands (Zaikowski, Knacke and Porco 1976) will in clusters possess differing optical properties; band structure may be considerably smoothed.

Although limits to reststrahlen band absorption may be reasonably assessed therefore, total absorption levels are conjectural. However, there seems little doubt that total grain extinction is comparable at infrared and optical wavelengths when absorption and scattering are accounted for; extinction will probably differ by no more than 0.4 magnitudes between 11.0 and 0.55 μm (adopting typical particle extinction curves from Wickramasinghe 1973), being larger in the visible.

To further evaluate extinction, we have acquired a sample of dust taken by Chester and Johnson between 25^{o} 24' N, 16^{o} 13' W; and 30^{o} 56' N, 13^{o} 40½' W, on the 4-5/2/73 (for which I am grateful to Dr. R. Chester), in addition to samples from the 60" flux collector mirror. Owing to lack of immediate access to an elutriator, the writer designed his own. This consisted of a glass tube ~ 1 metre in length and 1 cm bore, with outlet taps at various levels for draining off liquid containing dust particles in the requisite size ranges. Samples were then sized using a Porton graticule and travelling microscope. The dust was placed in holders, and held in place by thin mylar sheets. The holders were then placed in a mirror assembly permitting analysis with a two beam spectrometer, whilst maintaining the sample horizontal.

FIGURE 1.15

TRANSMISSION OF ATMOSPHERIC DUST SAMPLES

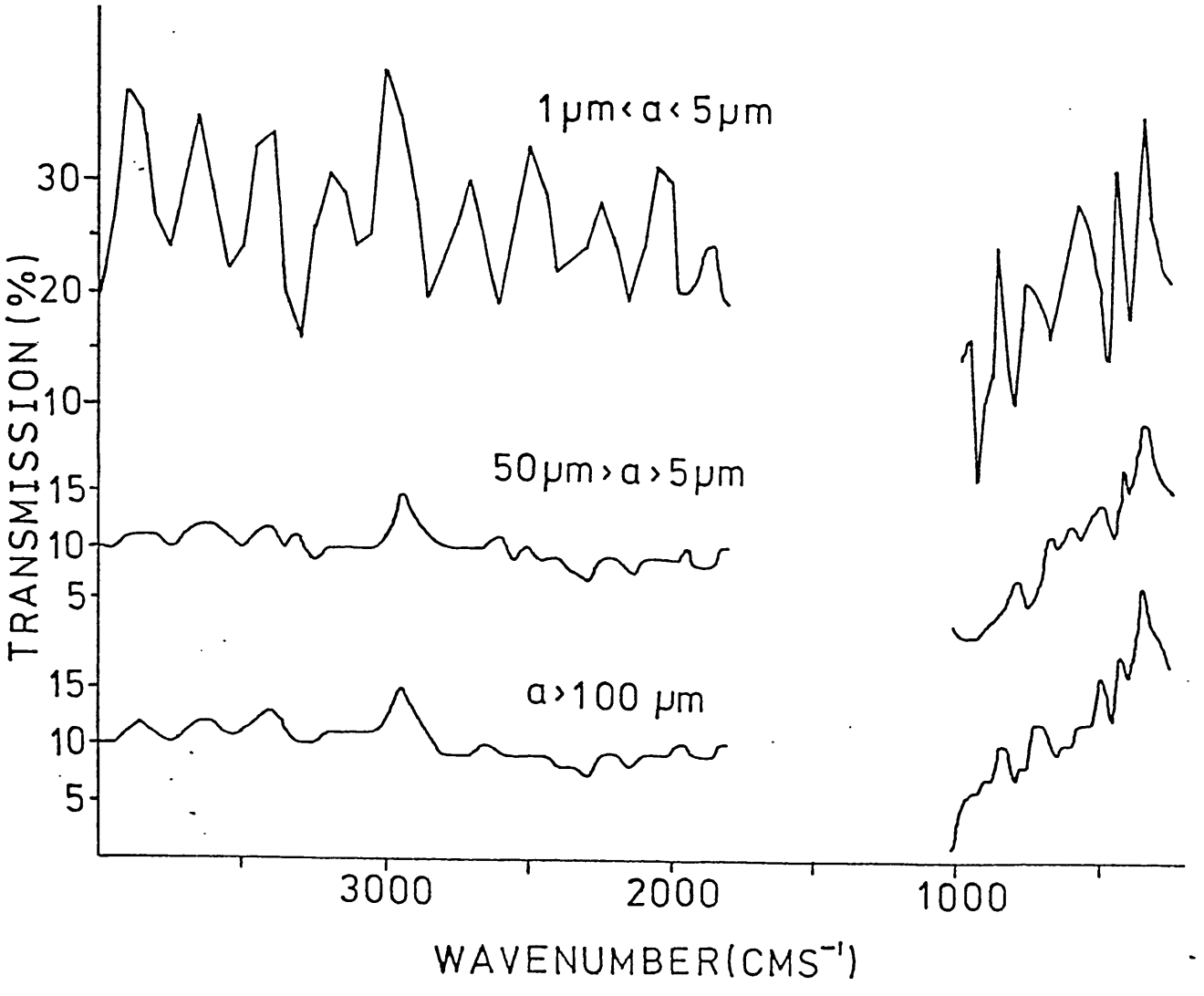

Where mylar absorption becomes large, errors in assessing grain transmission also increased, and these results are not included. The diagrams (figure 1.15) indicate relative transmission levels; absolute transmission probably differs very little, however. Semi-regular variations arise from interference within and between the mylar sheets.

The results uniformly indicate that transmission is low in the visible, and remains low through to $\lambda \sim 20$ μm. The grains involved are generally at the larger end of the size range (a restriction of the elutriation technique used), and some refinement of the procedure is required. Nevertheless, it is clear that total extinction is likely to be large in the infrared and visible, irrespective of uncertainties concerning the infrared properties of contaminants. It is probable that care should be taken when observing in the infrared under such conditions to determine the reliability of extinction.

1.13 Noise Spikes and Guiding Errors

Noise spikes may arise from inadequate cable insulation, location of cables near intermittent high power devices, and inadequate electrical contacts. These problems have a familiar place in most branches of experimental physics and require careful design, development and maintenance of the electronic components. Noise originating from power surges may be alleviated by the use of stabilised power supplies. Finally, stray radiation must be rigorously eliminated from the detector beam. Where the secondary is too large for instance, variable emission sources may lead to both drifting and spikes, and

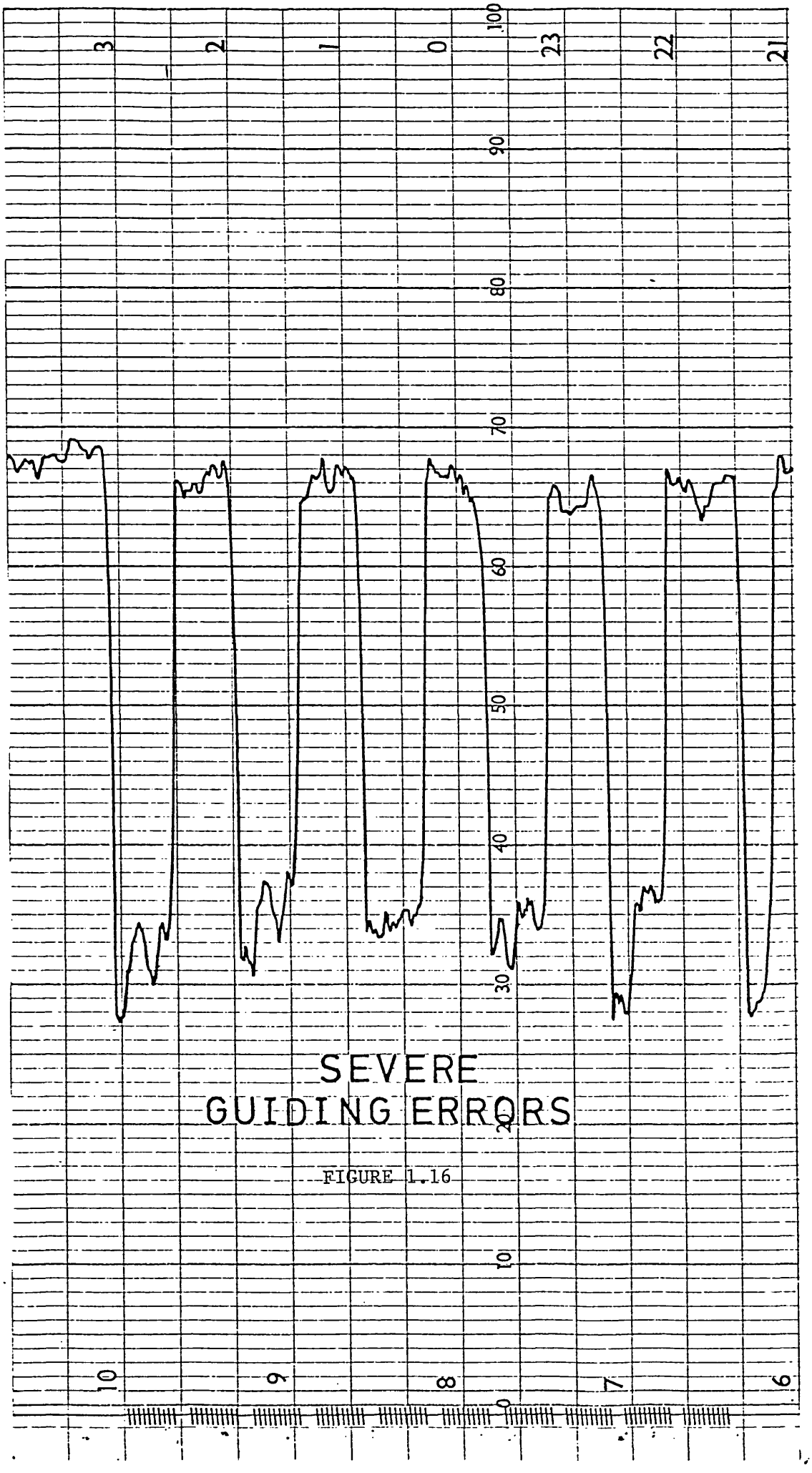

FIGURE 1.16

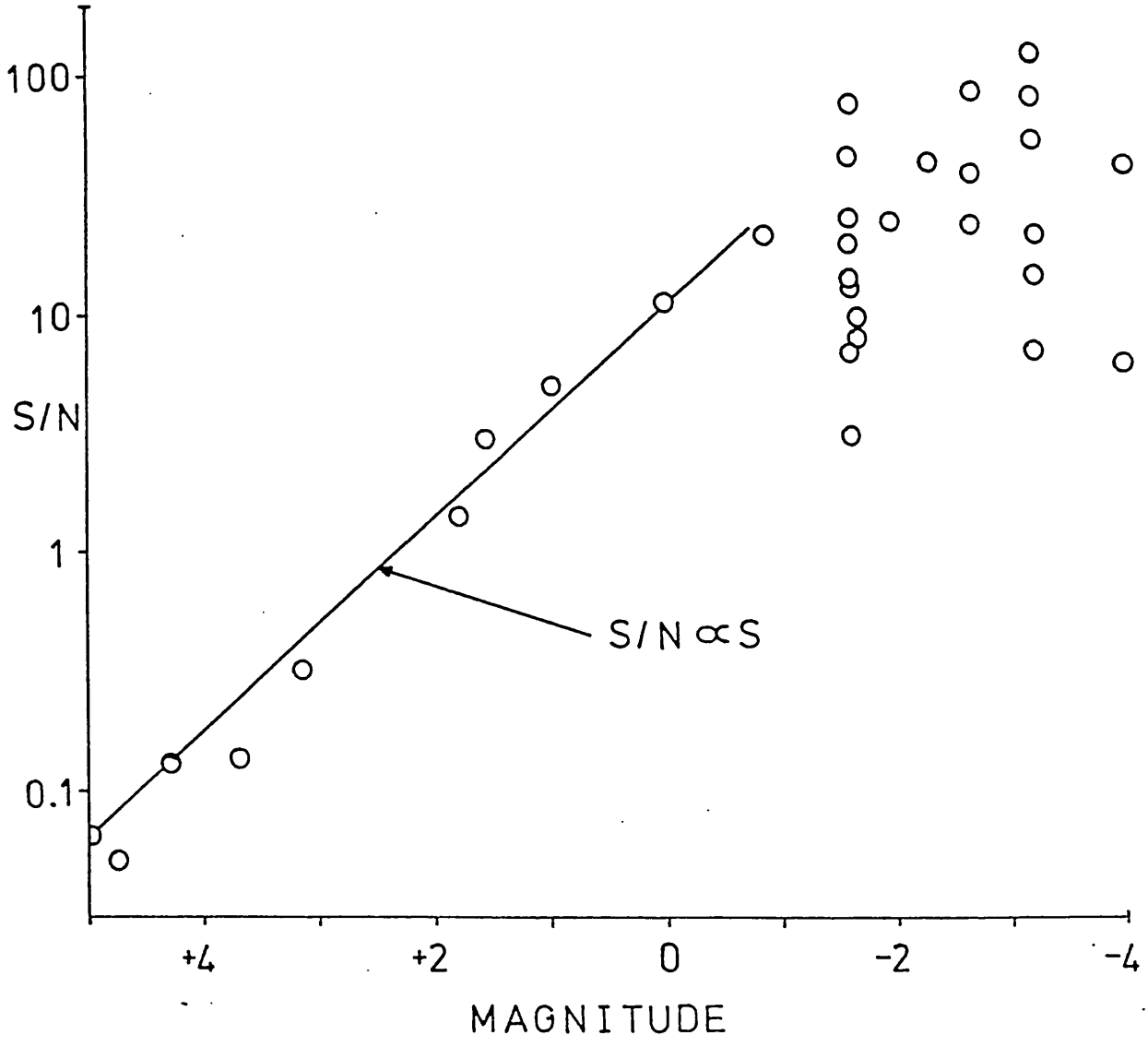

FIGURE 1.17

similar results may ensue for an inadequately shielded photometer.

"Guiding errors" represent a more insidious problem. These may arise in their more extreme form due to detector aperture radius too small compared to the seeing disk, or noncentral location of source in the detector beam. Detectivity usually falls rapidly at the beam edges, and a small error in the guiding of an asymmetrically located source may lead to severe signal changes. However, even for a small seeing disk, and location of the source at beam centre, guiding noise will still be present due to inevitable image displacement relative to the beam in the process of guiding. Usually, as we have seen, these errors may be made small; they may nevertheless be the primary source of noise during the photometry of bright sources. An extreme example of guiding error is presented in figure 1.16. It will be noted that the effect is to systematically reduce measured signal strengths, and increase the error in the result.

For weaker sources, the constant contribution of detector and background noise dominates, and signal to noise (S/N) varies as $S/N \alpha S$. Guiding errors tend to give S/N = constant. A graph illustrating this behaviour is presented in figure 1.17, from results at 4.8 μm culled over several nights.

CHAPTER 2

MASS LOSS IN BINARY SYSTEMS

2.1 Introduction

At certain stages in the evolution of close binaries, the photospheric radius of one component may expand, and exceed the Roche limit. The mass outside the Roche limit is for the most part lost to the star and may be acquired by the companion star, by interstellar space or by both. The mass loss rate is given by (Jedrzejec 1969)

$$\frac{dM}{dt} \simeq \left\{\frac{\Delta R}{R}\right\}^{n+1.5} \qquad \ldots (2.1)$$

for a star with polytropic index n, where ΔR is the excess of stellar radius R over a critical mass loss radius R_{CR} (i.e. $\Delta R = R - R_{CR}$). R_{CR} is usually indentified as the "mean" radius of the relevant Roche lobe, such that $4/3\ \pi\ R_{CR}^3$ is the volume of the lobe. Pacynski (1971) notes the expressions

$$\frac{R_{CR}}{2a} = 0.38 + 0.2 \log \frac{M_2}{M_1} \qquad 0.3 < \frac{M_2}{M_1} < 20$$

$$\frac{R_{CR}}{2a} = 0.462 \left\{\frac{M_2}{M_1+M_2}\right\}^{\frac{1}{2}} \qquad 0 < \frac{M_2}{M_1} < 0.8$$

to be accurate to within 2%, where a is the orbit semi-major axis (although for close binaries orbital ellipticity is usually considered to be small). Subscript 2 refers to the component losing mass. Jedrzejec (1969) found $\Delta R/R < 0.03$ for models given in the literature.

Equation 2.1 has been applied by Ziolkowski (1976) to β Lyrae, a system considered later, and still in the initial stage of rapid mass transfer. This initial stage occurs over the Kelvin-Helmholtz time scale

$$T_{K-H} \simeq 3.1 \times 10^{7} \left\{\frac{M}{M_{\odot}}\right\}^{2} \left\{\frac{R_{\odot}}{R}\right\}\left\{\frac{L_{\odot}}{L}\right\} \quad \text{years}$$

Subsequently, mass loss rates decrease substantially and a more quiescent phase develops, characteristic of most observed close binary systems. Mass loss may also occur for $R < R_{CR}$ if prominence activity is present.

Contact systems (W UMa variables) are less well understood, although Lucy (1968) has developed a model postulating a common convective envelope, subsequently developed by other researchers (c.f. Hazlehurst (1970), Moss and Whelan (1970)), and applied with some success by Worden and Whelan (1973) to the prototype binary. Such systems may form as a result of the substantial mass loss in semi-detached systems discussed earlier, leading to equalisation of component masses and concommitant reduction in component separation.

Evidently, mass transfer is a primary determinant of evolution in all of these systems. Its presence in many binaries is evident from Hα, CaII emission line components, from light curve distortion due to absorption of stellar continuum radiation by gas streams, and from changes of orbital period. As the limits of continuum surveillance are broadened, emission in the U.V. (c.f. Hack et al. (1974), Hack et al. (1976)) and infrared (c.f. Woolf (1973)) are revealing substantial continuum distortion due to free gaseous components within these systems. Infrared observations offer a particularly convenient mode of acquiring further understanding of mass transfer within these

systems. The present subsection presents new observations in this spectral region.

Free gaseous components may reveal themselves as continuum excesses in several ways. Three emission modes likely to be of particular significance in the infrared region are optically thin and thick free-free emission and (through associated dust grains), thermalisation of shorter wave radiation from the component stars. The detection of these excesses may be achieved by:-

(a) Determining the variation of continuum emission with phase. Any gas residing between the components of an eclipsing binary will be occulted at primary and secondary minima, leading to changes in eclipse depth. In addition, there may be phase dependent emission variations from the plasma itself, as well as distortions in the light curve arising from absorption of the stellar continua.

(b) Evaluating the trend of continuum emission with wavelength. Even if the predicted continuum is uncertain, the variation of infrared colour indices may be adequate to assess the presence of an excess. A case in point is the determination of silicate excesses in binaries by Woolf (1973), using the $[8.6] - [11.1]$ index (where $[8.6]$ represents the magnitude at $\lambda = 8.6\mu m$).

(c) A comparison of observed magnitudes with predicted magnitudes. This clearly has general applicability, but may be used to indicate a (provisional) excess if, say, only one data point were available at a particular wavelength. The method however requires confidence in the relevant physical parameters of the system.

In respect of this latter procedure, we note several expressions useful in enabling a rapid and, if correctly used, reliable evaluation of infrared magnitudes from physical parameters derived at optical wavelengths.

a. Relative Eclipse Depths

The projected ellipticity of primary and secondary components at primary and secondary eclipses as seen from Earth is the same, and in consequence the obscured area of the primary at primary eclipse is equal to the obscured area of secondary at secondary eclipse. The difference between primary and secondary eclipse depths may therefore be evaluated rapidly and with some reliability. One derivation of this quantity is shown below.

We first define the following symbols:

1. Subscripts p, s refer the quantities to primary and secondary minima.

2. Subscripts 1, 2, n (as in I_1, I_2, I_n) refer respectively to the primary, secondary and n^{th} component. I refers to observed luminosity.

3. Subscripts i, j (as in $(I_1/I_2)_i$) refer quantities to the wavelengths λ_i, λ_j.

We may therefore write

$$I_{pi} = \alpha_p I_{1i} + I_{2i} + \sum_n I_{ni}$$

$$I_{si} = I_{1i} + \alpha_s I_{2i} + \sum_n I_{ni}$$

where α_p is the fractional luminosity of the primary star eclipsed at primary minimum, and α_s is similarly defined for the secondary component at secondary minimum.

A little manipulation gives

$$\alpha_p = \left(\frac{I_p}{I_s}\right)_i \left\{\alpha_s \left(\frac{I_2}{I_1}\right)_i + \sum_n \left(\frac{I_n}{I_1}\right)_i + 1\right\} - \left(\frac{I_2}{I_1}\right)_i - \sum_n \left(\frac{I_n}{I_1}\right)_i \quad \ldots (2.2)$$

whence generally

$$\left(\frac{I_p}{I_s}\right)_j = \frac{\left\{\left(\frac{I_p}{I_s}\right)_i \left\{\alpha_s\left(\frac{I_2}{I_1}\right)_i + \sum_n \left(\frac{I_n}{I_1}\right)_i + 1\right\} - \left(\frac{I_2}{I_1}\right)_i - \left(\frac{I_2}{I_1}\right)_i\right\} + \left(\frac{I_2}{I_1}\right)_j + \sum_n \left(\frac{I_n}{I_1}\right)_j}{\alpha_s\left(\frac{I_2}{I_1}\right)_j + \sum_n \left(\frac{I_n}{I_1}\right)_j + 1} \quad \ldots (2.3)$$

and

$$\alpha_s = \left\{\left[\sum_n \left(\frac{I_n}{I_1}\right)_i \left(\frac{I_p}{I_s}\right)_i - \sum_n \left(\frac{I_n}{I_1}\right)_j \left(\frac{I_p}{I_s}\right)_j\right] + \left[\left(\frac{I_p}{I_s}\right)_i - \left(\frac{I_p}{I_s}\right)_j\right] - \left[\left(\frac{I_2}{I_1}\right)_i - \left(\frac{I_2}{I_1}\right)_j\right]\right.$$

$$\left. - \left[\sum_n \left(\frac{I_n}{I_1}\right)_i - \sum_n \left(\frac{I_n}{I_1}\right)_j\right]\right\} \Big/ \left\{\left(\frac{I_2}{I_1}\right)_j \left(\frac{I_p}{I_s}\right)_j - \left(\frac{I_p}{I_s}\right)_i \left(\frac{I_2}{I_1}\right)_i\right\} \quad \ldots (2.4)$$

For a three component system (such as βPersei) n = 1. For two component systems (c.f. U Sge), n = 0. Providing therefore (I_p/I_s) is available at two wavelengths, α_s may be evaluated, and (I_p/I_s) may thereby be determined for any other wavelength using equation 2.3.

b. Intensity at Quadrature

Intensity at quadrature may be again reliably determined for any type of system, parameters at only one wavelength being required to predict luminosities at other wavelengths. We introduce subscript Q to indicate conditions at quadrature. We then have simply

$$\frac{I_{Qj}}{I_{Qi}} = \frac{\left(\frac{I_{1j}}{I_{1i}}\right) + \left(\frac{I_{2j}}{I_{1i}}\right) + \sum_n \left(\frac{I_{nj}}{I_{1i}}\right)}{1 + \left(\frac{I_{2i}}{I_{1i}}\right) + \sum_n \left(\frac{I_{ni}}{I_{1i}}\right)} \quad \ldots (2.5)$$

Determination of Intensity Ratios

There are two obvious methods of estimating the wavelength dependence of intensity ratios. We may assume black-body behaviour for the component stars, and thence extrapolate to the infrared. Effective temperatures are available for the components of several of the systems to be discussed, and we then simply have

$$\left(\frac{I_2}{I_1}\right)_j = \frac{(e^{\frac{hc}{\lambda_j KT_1}} - 1)}{(e^{\frac{hc}{\lambda_j KT_2}} - 1)} \cdot \frac{(e^{\frac{hc}{\lambda_i KT_2}} - 1)}{(e^{\frac{hc}{\lambda_i KT_1}} - 1)} \cdot \left\{\frac{I_2}{I_1}\right\}_i$$

$$\frac{I_{1j}}{I_{1i}} = \frac{\lambda_i^3 (e^{\frac{hc}{\lambda_i KT_1}} - 1)}{\lambda_j^3 (e^{\frac{hc}{\lambda_j KT_1}} - 1)}$$

This procedure has been applied by Smyth, Dow and Napier (1975) and Jameson and Longmore (1976). It does not however have general applicability, and for binary systems with components later than M0 is to be eschewed. For such stars molecular bands play an important part in depressing the visible continuum, and recourse must be had to observed colour indices. Uncertainties in both the adopted effective temperatures and stellar temperature calibration introduce further errors and uncertainties. The discussion of Smyth et al. (1975) may be referred to in this respect. The use of observed colour indices for particular spectral types represents a second possible course of action. This assumes that binary star components have closely similar colour indices to stars which are not members of such systems, and which are in turn primarily responsible for published intrinsic indices. Accepting this, the procedure has general applicability, although

indices are not always conveniently available for all spectral classes or wavebands. Nevertheless, it is often possible to make reasonable extrapolations or interpolations of indices and where this is so, the method is probably to be employed in preference to the first. We use this latter procedure here.

The observations to be discussed were made as part of a continuing program, and for certain of the cases looked at here, more observations are yet required. The present discussion is therefore to be regarded as preliminary. A further selection of binaries has been investigated by Mr. J. Needham which, though not necessarily representative, are expected to be interesting from the viewpoint of possible infrared excesses. The specific cases investigated in this latter work are R CMa, TV Cas, δ Lib, i Boo B, TX UMa and AR Lac, and although all data has now been reduced, it has yet to be analysed. The present work describes observations of several possibly more representative binaries, with the intention of evaluating the likelihood of near infrared excesses in binaries generally. To obtain a definitive perspective from the clutch of six binaries presented here is of course to be overoptimistic. Nevertheless, some preliminary conclusions may be drawn, and these are presented at the end of this discussion.

The binaries include three prototypes (β Persei, β Lyrae and W UMa) spanning the range from semi-detached to contact systems. U Sge may also be regarded as a representative Algol type system. Also included are two systems (RR UMi, η Gem), with late type variable components which would almost certainly be losing mass even in the absence of close companions. The presence of these companions suggests the possibility of some modification to the mass loss process, with possible consequences for the infrared excesses in these stars.

η Gem has already been preliminarily investigated with this in mind (Woolf 1973). Two other systems, β Persei and β Lyrae, have also been extensively observed by Longmore and Jameson (1975), Jameson and Longmore (1976). The present results however both correct and supplement the results of these latter authors, and alternative explanations are also offered for the excesses.

2.2 β PERS

Introduction

β Persei is the prototype of a series of semi-detached binaries containing hot primaries (usually with spectral types close to AO), and later type giants filling their respective Roche lobes. The proximity of the photospheric layers of the late-type companions to their Roche limits leads to mass loss, with several observational consequences.

There have been at least two main period changes in β Persei over the last 50 years, one in 1944, by +3.5 seconds, and a change of -2.1 seconds in 1952 (Frieboes-Conde, Herczog and Høg, 1970). Ashbrook (1976) has noted a more recent change. Struve and Sahade (1957) and Sahade (1958) find Hα emission at quadrature, and proposed a corresponding plasma concentration at the L_1 Lagrangian point. This was essentially confirmed in work by Andrews (1967), who measured the phase variability of Hα emission. The period of plasma obscuration was found to be significantly longer at primary than secondary eclipse, suggesting a corresponding plasma location closer to component B (i.e. the secondary component). Although Andrews' data requires improvement, it is nevertheless possible to place preliminary limits

upon the size of the plasma, assuming exact location at the L_1 point. Specifically, if 2a is the binary separation, L the separation of the Lagrangian point from the core of the secondary, and R_1, R_2 are the radii of primary and secondary components, then at primary minimum it can be readily shown that

$$r = (p-L) \sin 2\pi\phi$$

$$L = \frac{2a\, M_2^{\frac{1}{2}}}{M_1^{\frac{1}{2}} + M_2^{\frac{1}{2}}}$$

$$p = R_2/\sin 2\pi\phi$$

where ϕ is the phase of plasma emmersion, r is plasma radius, and M_1, M_2 are the masses of components A, B. From Hill et al. (1971), $M_1/M_2 = 4.625$, $R_2 = 3.4\ R_\odot$, $R_1 = 3.0\ R_\odot$, $2a \simeq 13.9\ R_\odot$. At primary eclipse we then find

$$r = 3.4\ R_\odot - 4.41 \sin 2\pi\phi$$

and at secondary minimum

$$r = 3.0\ R_\odot - 9.49 \sin 2\pi\phi$$

From the data of Andrews, we estimate the following maximum and minimum phase values for emmersion, and corresponding limits to the plasma radius

$$\phi_{min} = 0.068 \qquad r \lesssim 1.57\ R_\odot$$

$$\phi_{max} = 0.158 \qquad r \gtrsim 0\ R_\odot$$

For secondary minimum, a lower limit is found to r by measuring the difference in phase between two distinctly depressed points on either side of eclipse, whence

$$\phi_{min} = 0.023 \qquad r \lesssim 1.63\ R_\odot$$

$$\phi_{max} = 0.039 \qquad r \gtrsim 0.70\ R_\odot$$

A subjective best fit appears to be $r \simeq 1\ R_\odot$. Again, since Hα emission is not seen in mid-eclipse, an upper limit to plasma radius can be set because of the inclination $i(\neq 90^o)$ of the system to the line of sight. Specifically

$$r \lesssim (R_1 - (2a-L) \cos i)$$

using $L = 4.4\ R_\odot$ (see above), and inclination $i = 81.^o6$ (Hutchings and Hill, 1971) then gives $r \lesssim 1.64\ R_\odot$. Note that the limits to r depend strongly upon the assumed values of i, $R_{1,2}$ and 2a, and these may be open to revision. However the range of values for r quoted here are almost certainly qualitatively correct.

Taking $r \simeq 1\ R_\odot$ we then require, assuming optical thickness to Hα, a plasma temperature $T_p \simeq 3.4 \times 10^4$ K in order to explain the observed Hα emission strength 5×10^{-10} erg.cm^{-2}.s^{-1} (Andrews 1967). The corresponding optical depth to Hα is, ignoring electron collisional excitation,

$$\tau_{H\alpha} \simeq N_2\ \alpha_{H\alpha}.2r$$

$$N_2 \simeq 10^{-14}\ N_e\ N_p \left\{\frac{10^4}{T}\right\}^{0.85} \text{cm}^{-3}$$

where N_2 is the population of hydrogen atoms with electrons in the 2s sublevel (Kaplan and Pikelner 1970). This does not include 2p → 2s

transitions (increasing N_2), or allow for 2p-3s, 2p-3d scattering. Similarly it ignores collisional excitation of 2s-2p transitions, and is therefore only broadly indicative. For $N_e = N_p$, $T = 10^4$ K, the relations then indicate that the optical depth to scattering $\tau_{H\alpha} > 1$ if $N_e \gtrsim 10^8$ cm^{-3}, where we have taken for the absorption coefficient for H_α, $\alpha_{H\alpha} \simeq 10^{-13}$. This density is a lower limit; volume emissivity for H_α is too low to account for observed H_α levels. At higher densities, the problem becomes more complicated, and must be treated with radiative transfer procedures. For the present we simply note two comments . First, the temperature 3.4×10^4 K is not too strongly dependent upon the size of the emitting plasma. A typical radius $r \simeq 2\ R_\odot$ would require $T \simeq 2.4 \times 10^4$ K. Even with this larger radius, however, which would in fact be inconsistent with the phase variability of Hα, the temperature is significantly in excess of that of the primary component. This led Sanchez, Needham, Phillips and Selby (1977) to suggest the possibility of collisional excitation of the plasma, and reference was made to various theories of mass loss, and mechanisms for radio emission, in support of this concept. A supporting argument in terms of the ability of the primary to ionise the plasma may also be presented.

Consider a sector of plasma residing between distances R_0 and R_1 of the primary star. For complete ionisation we require

$$\frac{R_1^3 - R_0^3}{R_0^3} = \frac{3}{4\pi R_0^3 N_e^2 \alpha} \frac{dN_i}{dt}$$

where α is the recombination coefficient ($\alpha \simeq 4 \times 10^{-13}$ cm^3 sec^{-1}). dN_i/dt is the total emission rate of ionising photons by the primary component.

$$\frac{dN_i}{dt} \simeq \frac{2\pi K T_*}{hc^2} \nu_c^2 e^{-\frac{h\nu_c}{KT_*}} \cdot 4\pi R_*^2$$

where T_*, R_* are stellar temperature, radius, and ν_c is the frequency of the Lyman limit ($\nu_c = 3.29 \times 10^{15}$ sec^{-1}). Adopting $T_* \simeq 10^4$ K, $R_* \simeq 3\ R_\odot$, $R_0 \simeq L = 9.5\ R_\odot$, and $R_1 - R_0 = 2\ R_\odot$ then leads to the requirement $N_e \lesssim 1.5 \times 10^9$ cm^{-3}. In reality, dN_i/dt calculated this way (i.e. assuming black body behaviour) is likely to be an upper limit in view of the observed depression of U.V. continuum in early type stars, and the value of N_e thus calculated may be an extreme upper limit. A more accurate value may be assessed using model atmospheres. It is seen however that for any appreciable optical thickness to Hα, the plasma rapidly becomes optically thick to the U.V. continuum of the B8V primary. Such a conclusion obviously has applicability for the general case; densities of order $N_e \simeq 10^{13} \rightarrow 10^{14}$ cm^{-3} are commonly regarded as necessary to explain emission and absorption properties of gas streams within such systems. Unless however they have dimensions very much smaller than the component stars, it is clear that other sources than radiative excitation by the component stars must be sought to explain the high temperatures often attributed to these gases. A case of particular interest in this respect is the model of Longmore and Jameson (1975) presented to explain a supposed variability in their long wave infrared results (i.e. at 4.8 μm and 8.6 μm) for β Persei. The model takes the form of a gas stream of cross section 2.16 $R_\odot$ x 2.87 $R_\odot$, extending in a curve between the photospheres of primary and secondary stars. The density varies from 5×10^{11} cm^{-3} at the B8 star, to 3×10^{12} cm^{-3} at the secondary. Temperature also changes from 2×10^4 K to 5×10^3 K in passing from primary to secondary. The latter temperature assumes radiative equilibrium with the secondary component, the former a modification of an initial attempt with $T = 10^4$ K for stream temperature near primary,

in order to fit the infrared observations; the temperature excess is attributed to braking of the stream near the primary. In fact, it is clear that practically the entire stream will be optically thick to ionising radiation from the star, and there is no particular reason for adopting temperatures similar to those of the component stars. It would almost certainly be necessary to invoke some degree of collisional excitation to explain gas heating which, at least in principle, supports our earlier conclusion with respect to the plasma responsible for Hα emission. There is however a serious deficiency in the model: the primary Hα emission is formed near to component A. To evaluate the consequences of this upon phase variability of Hα, for a system with inclination $i \neq 90^{o}$ would, for the given model, be complex. In any case, the model is only provisional, and an approximate treatment shows such a procedure to be unnecessary. We have assumed $i = 90^{o}$, and assessed the contributions of the various stream temperature sectors to total Hα emission, as a function of phase. This is plotted in terms of Andrews' R_{α} parameter in fig. 2.1. Several points may be made with respect to this graph:

(a) The secondary eclipse peak is broader than at primary eclipse.

(b) There is a relative phase difference of ~0.55 between the peaks.

(c) Emission between phases 0.5 and 1.0 is weaker than between 0.0 and 0.5.

The last point is interesting, since similar behaviour (previously unexplained) is actually found in Algol (Sahade 1960), and is weakly apparent in the results of Andrews (1967). Here, it arises primarily from curvature of the stream near component A. In reality, it may be a consequence of a similar plasma orientation near the internal Lagrangian point. The point (b) arises again from stream

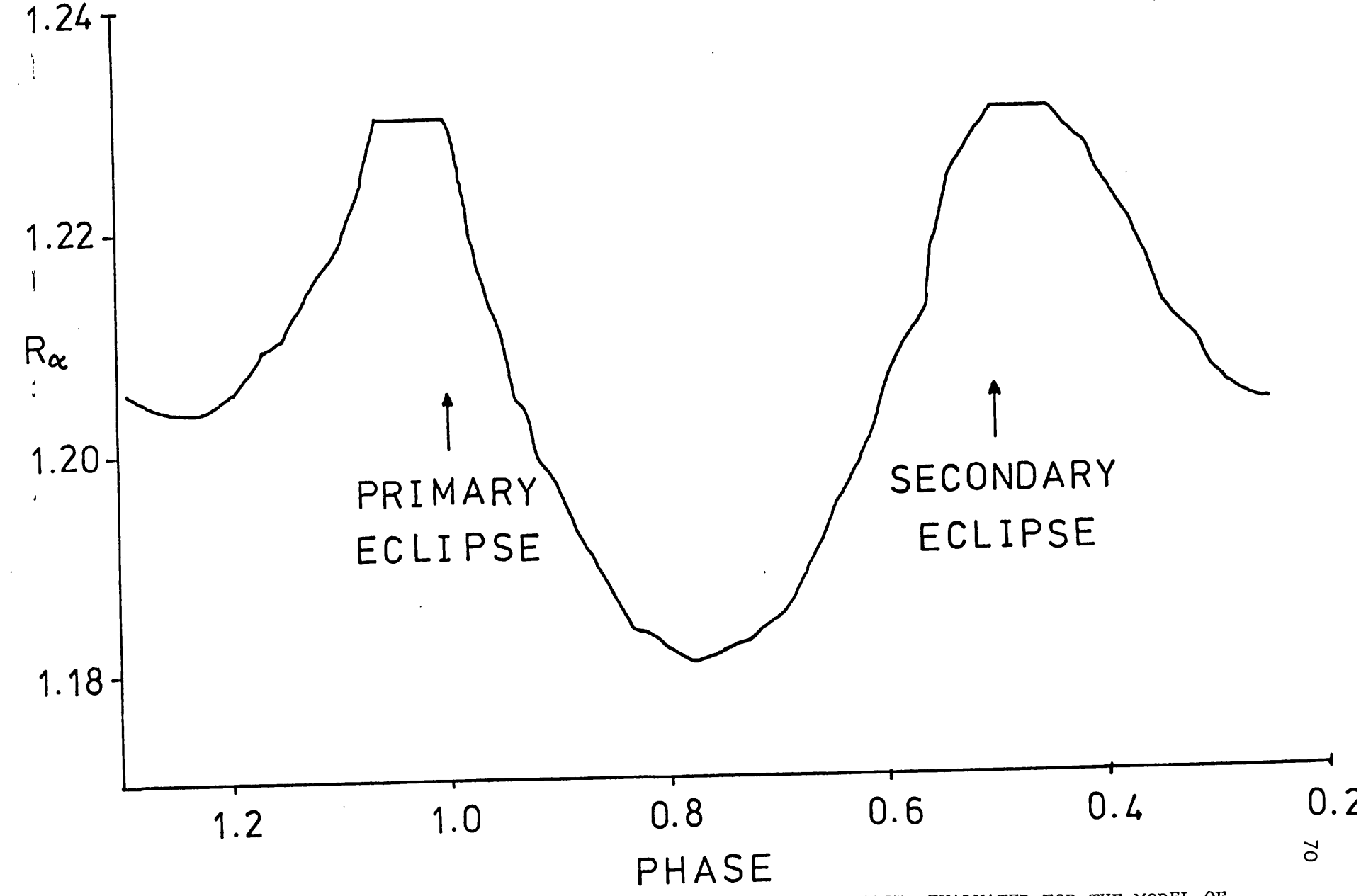

FIGURE 2.1 VARIATION OF THE ANDREWS (1967) R_α PARAMETER WITH PHASE, EVALUATED FOR THE MODEL OF LONGMORE AND JAMESON (1975)

curvature, and although a relatively small effect, seems poorly in accord with the data of Andrews. Finally, point (a), concerning peak width, represents a serious deficiency in the theory; since it represents behaviour quite at variance with the observations.

It is clear that if we are to explain the infrared variability observed by Longmore and Jameson (1975) then a new model must be evolved. However, there are also serious doubts concerning the reality of the variations these models are to be devised to explain. These were first expressed by Smyth et al. (1975), who showed the excesses at 4.8 μm first reported by Jameson, Longmore and Crawford (1973), were such as to also lead to continuum emission excesses at 2.2 μm. These latter are not observed. Further evidence of long wave excesses at 4.8 μm and 8.6 μm was published by Longmore and Jameson (1975). In all cases however (except one point at λ = 8.6 μm), the excesses have barely 2σ significance (σ is one standard deviation). The variations are also of order 0.3 magnitudes, which as Smyth et al. point out, is readily attributable to extinction at these wavelengths. In fact, a plot of the new data at 4.8 μm published in Longmore and Jameson (1975), as in Sanchez et al. (1977), shows such a considerable scatter that any claim for excess on the basis of it must warrant considerable reserve. It was for these reasons that further 4.8 μm observations were considered necessary before further modelling was attempted. Several observations at N, H and K had been made previously, although poor weather had invariably disabled attempts to obtain final confirmation of the earlier reported variability (Jameson, Longmore and Crawford (1973)). These are also presented in the next section.

Before passing on to a consideration of this infrared data, we also review some of the evidence for mass loss presented by the radio observations.

The first radio detection of β Persei was by Wade and Hjellming (1972). Subsequently, observations have shown the presence of two components; a quiescent term due to optically thin thermal emission, and radio flaring, with occasional positive spectral index indicating a non-thermal component (c.f. Hjellming et al. 1972). A recent model by Woodsworth and Hughes (1976) appears to give excellent fits to the observed radio behaviour. The model allows for optically thin free-free from gas ($N_e \lesssim 6.4 \times 10^6$ cm^{-3}, T ~ 10^4 K, radius > 5.8 a.u.) surrounding the binary, and non-thermal emission from a much smaller region "associated with the region of mass exchange", of density ≈10^8 cm^{-3}, temperature 10^6 K, and radius 0.3 a.u.

An alternative explanation for the radio flares invokes plasma oscillations at a collisionless shock front. The shock front results when a mass flow from the secondary component interacts with the stellar atmosphere of the primary. The spectrum generated is narrow, ranging from twice the minimum to twice the maximum plasma frequency, with some photon-plasmon scattering to higher frequencies. Flares then result when mass loss rate changes rapidly; variations in output emission over peroids of hours (as observed) are regarded as plausible. Woodworth and Hughes (1976) however indicate that temperature, densities and velocities of the mass stream from the secondary will be inadequate to explain observed flare emission levels.

Evidence for expansive motion associated with radio flares is presented by Clark et al. (1975), who suggested that interferometric measurements at 7850 MHz are best understood in terms of expansion at velocities between 500 - 1000 km.s^{-1} (i.e. larger than the escape velocities of the respective component stars). Hjellming et al. have also observed an intriguing variation in the level of otherwise quiescent emission strongly reminiscent of the optical primary eclipse. This can be shown to have occurred at phase ≈0.06; that is, within a

couple of hours of primary minimum. Since this last case maintained a spectral index close to zero throughout the variation, it seems possible that we were witnessing the eclipse of an optically thin spherical plasma shell, either ejected from the primary, or between primary and secondary. Certainly, the evidence of a P Cygni profile for the K line of CaII earlier that year (Bolton 1972) indicates that β Persei was shedding a considerable quantity of mass during this period.

Note however that an interpretation in terms of a plasma eclipse implies physical constraints upon the size (plasma radius $\lesssim 3\ R_\odot$) and flux ($E_\nu \simeq 5 \times 10^{-2}$ Jy at 2.7 GHz). From Allen (1973), the optically thin free-free emission from such a plasma is

$$E_\nu = 6.2 \times 10^{-16}\ g\ e^{-\frac{1.43883}{\lambda T}}\ T^{-\frac{1}{2}}\ N_e^{\,2}\ r\ \frac{4}{3}\ \pi\ \left\{\frac{r}{R_E}\right\}^2 \quad \text{Jy}$$

(T in K, N in cm^{-3})

where the Gaunt factor g is given by

$$g = 1.90 \log T + 1.26 \log \lambda - 2.64$$

where R_E (= 32 pc) is the distance from Earth, N_e electron density, λ is the wavelength of observation and T the plasma temperature.

Substituting for the known data gives

$$g_{2.7\text{GHz}}\ T^{-\frac{1}{2}}\ N_e^{\,2} = 2.07 \times 10^{19} \qquad \ldots (2.7)$$

Similarly, since the plasma was optically thin up to $\lambda = 11.1$ cms, where

$$\tau = 3.12 \times 10^{-23}\ (1 - e^{-\frac{1.43883}{\lambda T}})\ g\ T^{-\frac{1}{2}}\ \lambda^{+3}\ N_e\ N_p\ r$$

we have

$$g_{2.7GHz}\ T^{-3/2}\ N_e^{\,2} \lesssim 8.65 \times 10^{8} \qquad \ldots (2.8)$$

From (2.7) and (2.8) we then obtain

$$T \gtrsim 2.4 \times 10^{10}\ K$$

$$N_e \gtrsim 4.5 \times 10^{11}\ cm^{-3}$$

The plasma frequency is however then

$$\nu_p \sim 0.009\ N_e^{\frac{1}{2}}\ MHz \gtrsim 6\ GHz$$

Plasmas do not transmit below the plasma frequency, and this suggests a possible non-thermal origin for the emission. If the emission is thermal the plasma must be hot and dense, with emission almost certainly decreasing at $\nu < 2.7$ GHz.

It is clearly relevant to enquire whether this interesting radio behaviour is reproduced at infrared wavelengths. To determine this, we note that the stellar continuum flux $F_{*\nu}$ behaves as

$$F_{*\nu} \simeq 10^{2} \left\{\frac{2.2}{\lambda}\right\}^{2}\ Jy$$

where λ is in μms. In comparison, the quiescent radio emission rarely exceeds 0.2 Jy at 2695 MHz (c.f. Hjellming et al. 1972) whence, assuming it to be optically thin free-free

$$F_{R\nu} \lesssim 0.2 \left\{\frac{\lambda\ 10^{4}}{11.1}\right\}^{0.1}\ Jy$$

where $F_{R\nu}$ is the quiescent radio emission flux. Equating $F_{R\nu}$ and $F_{*\nu}$ gives a wavelength $\lambda \simeq 71$ μm, and there therefore seems little possibility of detecting this emission in the near infrared. It also

follows that any free-free emission excess observed at infrared wavelengths has almost certainly become optically thick by radio wavelengths. The possibility of observing flares in the infrared is a more intractable problem, since the spectral behaviour between the radio and X-ray regions (for X-ray limits see Canizares et al. 1973) is quite conjectural. Smyth et al. point out however that the excesses reported by Jameson, Longmore and Crawford appear to indicate spectral indices at variance with an interpretation in terms of non-thermal emission. Although the near infrared observation of flares cannot therefore be discounted, the excesses reported by Longmore and Jameson cannot be regarded as evidence for these. In the next section, we report further infrared observations, suggesting that β Persei is in reality well behaved at near infrared wavelengths with no phase dependent excesses.

Infrared Observations

The bulk of the new observations, at $\lambda = 4.8$ μm, have been published by Sanchez et al. (1977), to which reference should be made for further observational details. The results are again plotted in figure 2.2, with further data at J, H, K, L and N. They are calibrated with respect to α Lyrae, for which a magnitude 0.00 is adopted in all bands. In addition, we have plotted I J K L data from Johnson et al. (1966).

FIGURE 2.2a

VARIATION OF MAGNITUDE WITH PHASE FOR β PERSEI.
Δ - JOHNSON ET AL. (1966) O - PRESENT RESULTS.

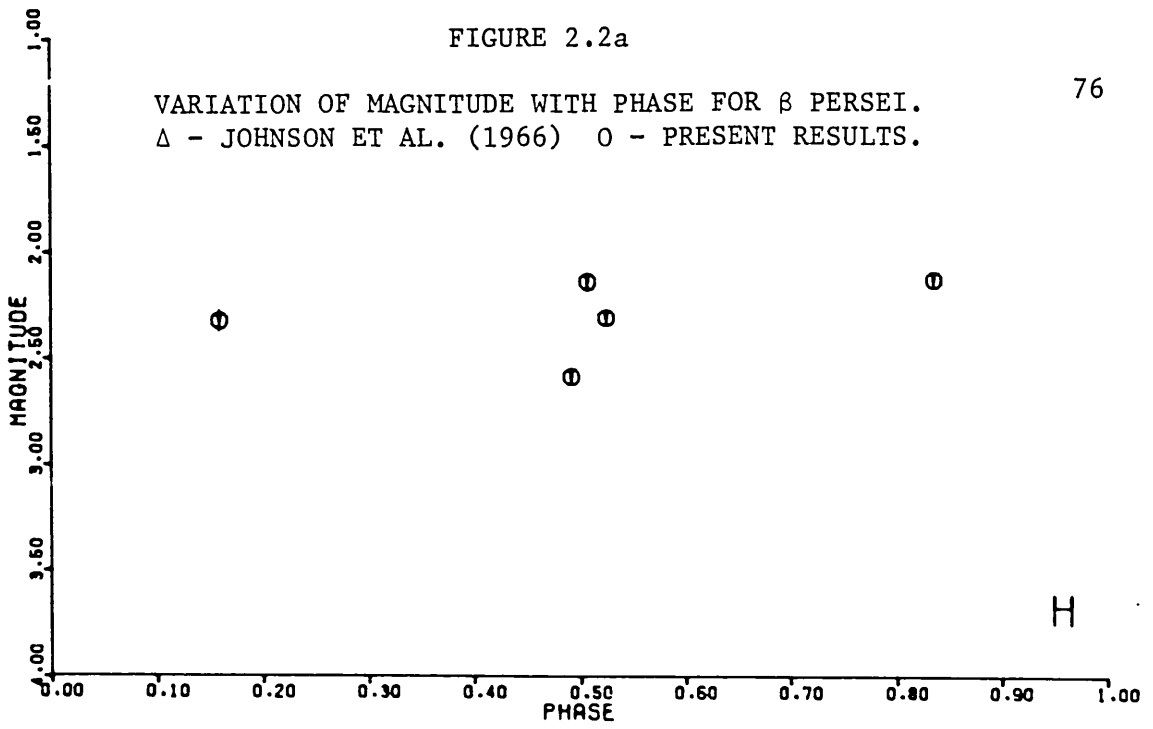

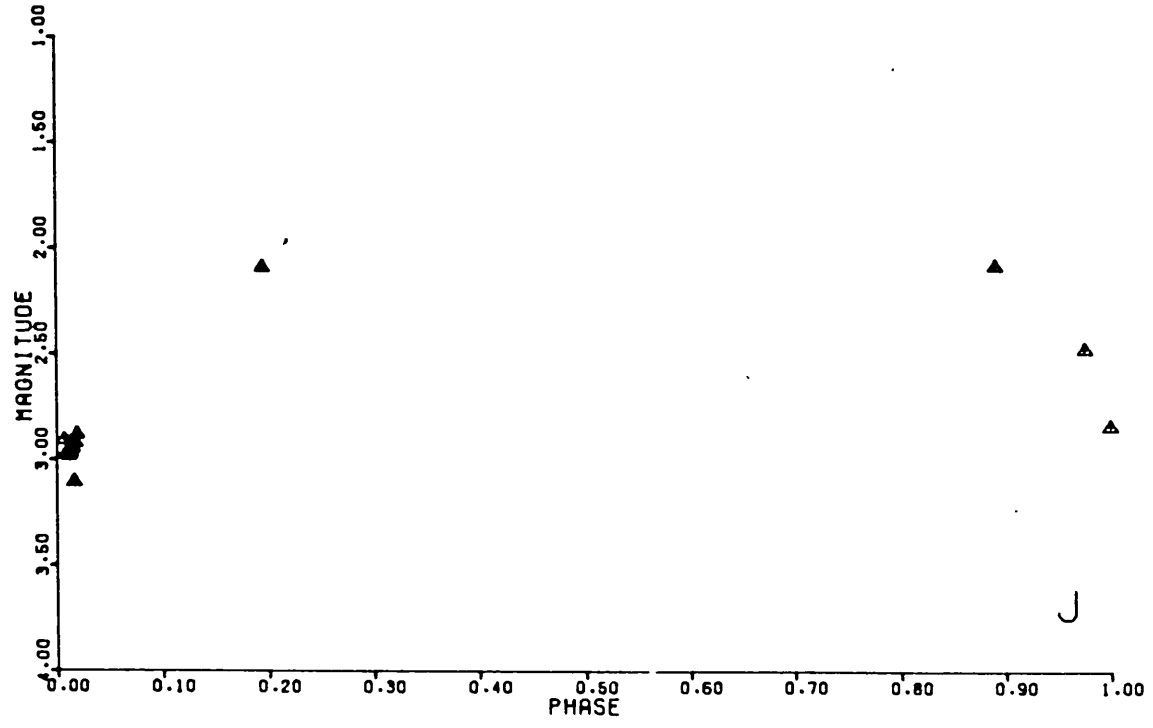

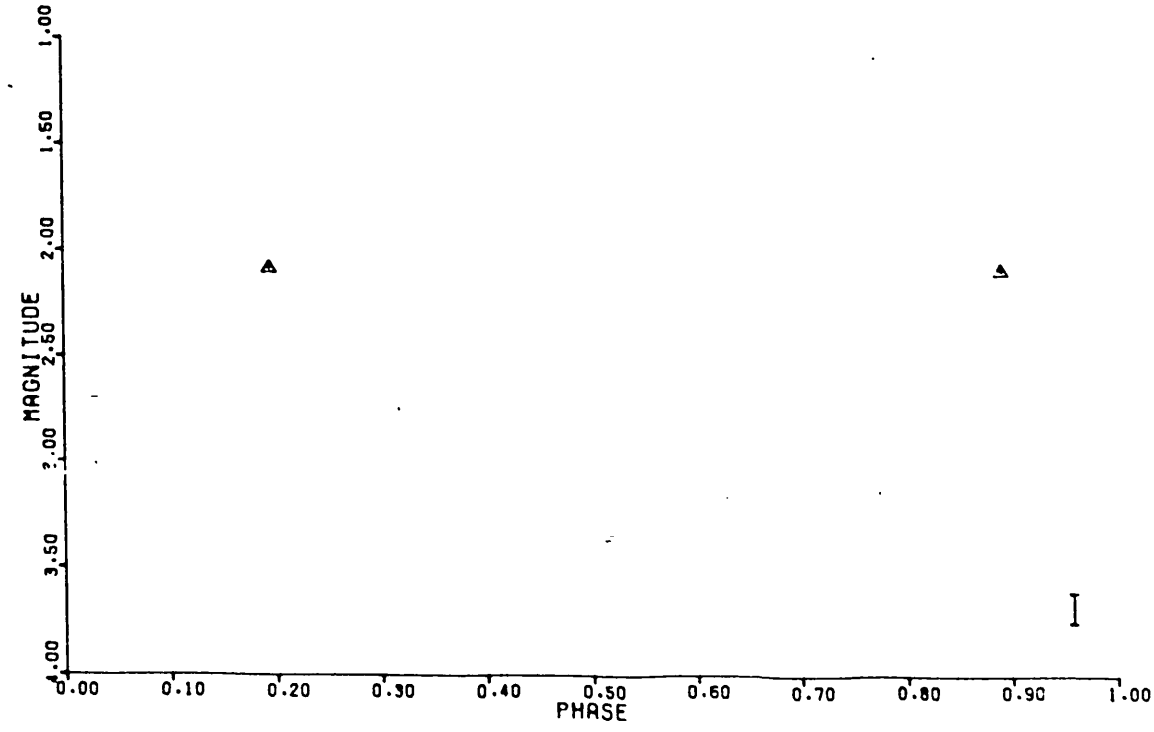

FIGURE 2.2b

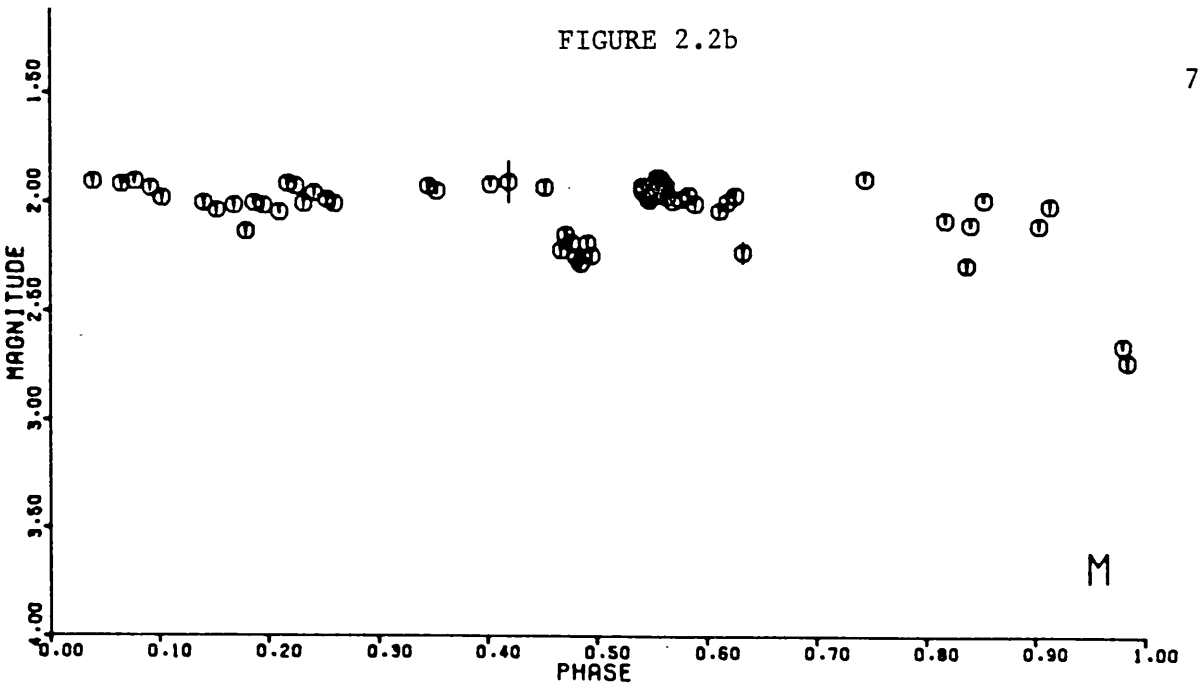
MAGNITUDE
1.50
2.00
2.50
3.00
3.50
4.00
0.00
0.10
0.20
0.30
0.40
0.50
0.60
0.70
0.80
0.90
1.00
PHASE
M

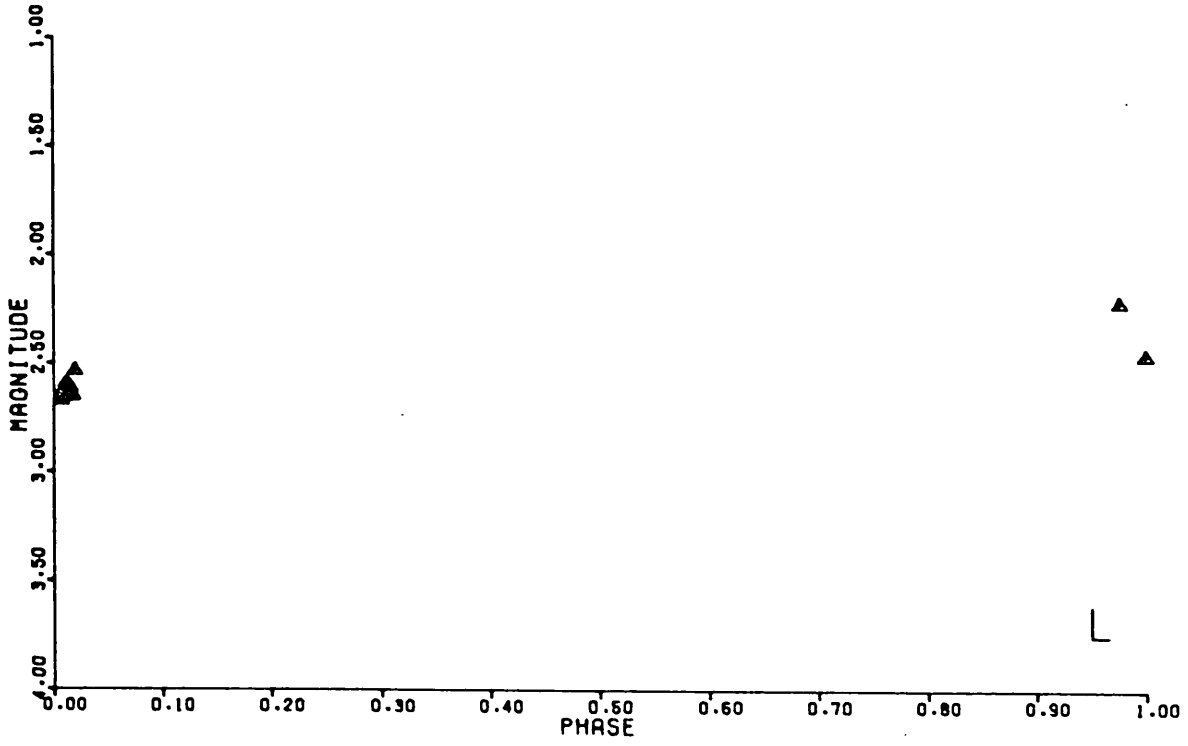
MAGNITUDE
1.00
1.50
2.00
2.50
3.00
3.50
4.00
0.00
0.10
0.20
0.30
0.40
0.50
0.60
0.70
0.80
0.90
1.00
PHASE
L

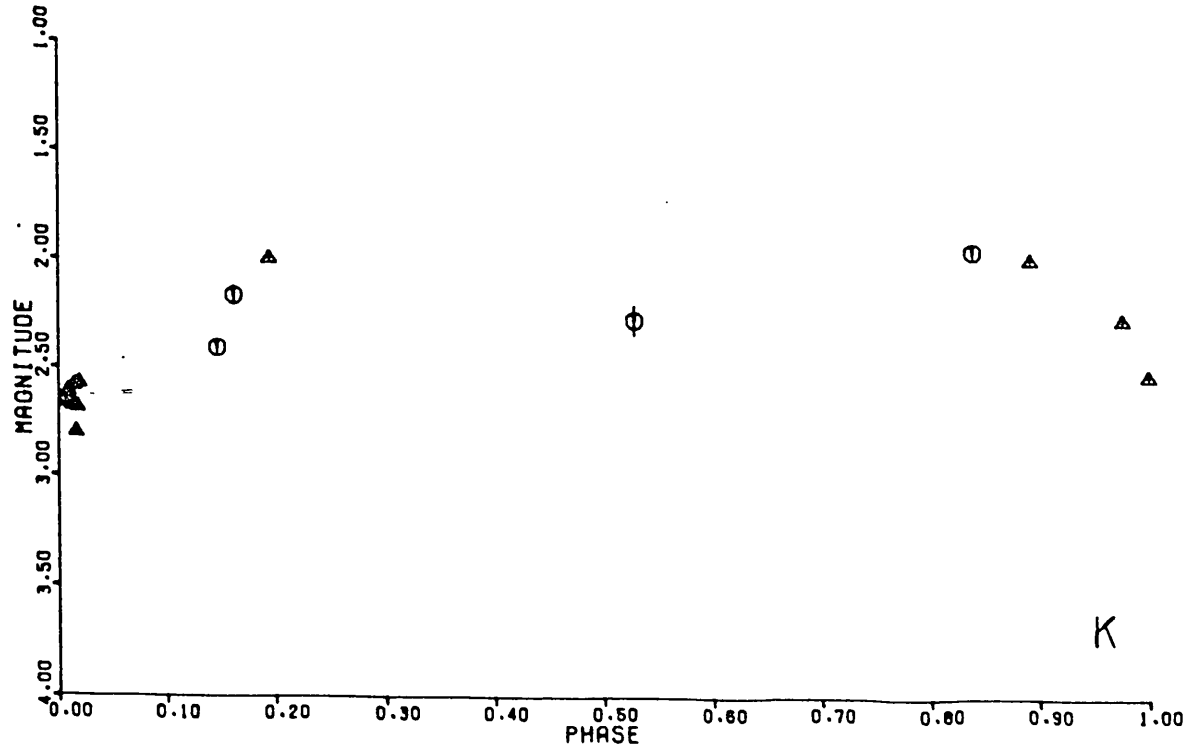
MAGNITUDE
1.00
1.50
2.00
2.50
3.00
3.50
4.00
0.00
0.10
0.20
0.30
0.40
0.50
0.60
0.70
0.80
0.90
1.00
PHASE
K

TABLE 2.1

H

JULIAN DATE 24+	PHASE	MAGNITUDE	STANDARD DEVIATION
42087.461	0.491	2.580	0.030
42088.450	0.836	2.120	0.027
42089.375	0.159	2.320	0.049
42090.373	0.507	2.130	0.041
42090.424	0.525	2.300	0.033

K

JULIAN DATE 24+	PHASE	MAGNITUDE	STANDARD DEVIATION
42086.474	0.147	2.410	0.022
42088.455	0.838	1.960	0.026
42089.386	0.163	2.170	0.043
42090.434	0.528	2.280	0.069

M

FOR RESULTS, SEE SANCHEZ ET AL. (1977)

N

JULIAN DATE 24+	PHASE	MAGNITUDE	STANDARD DEVIATION
42092.383	0.208	2.017	0.095
42092.431	0.225	2.074	0.160
42092.494	0.247	2.189	0.125

The most complete results are at M, and these show no evidence of variability with phase with amplitude $\gtrsim$0.1 magnitudes outside of eclipse. Although the eclipse data is sparse, the eclipse depths

appear consistent with predictions by Smyth et al. (1976). A similar story is revealed when the magnitudes between eclipse are plotted with respect to wavelength (fig 2.3). We have again used data by ourselves and Johnson et al. (1966). Crosses represent the predicted flux for stellar components with the following properties:

Component A

Spectral type - B8V $M_{BOL} = -0.4$

$M_V = +0.32$

Colour indices

U-V	B-V	V-R	V-I	V-J	V-K	V-L	V-M	V-N
-0.39	-0.09	-0.02	-0.12	-0.17	-0.24	-0.22*	-0.22*	-0.22*

* Extrapolated values

Component B

Spectral type - KoIII $M_{BOL} = +3.1$

$M_V = +3.29$

Colour indices

U-V	B-V	V-R	V-I	V-J	V-K	V-L	V-M	V-N
+1.93	+1.04	+0.77	+1.30	+1.71	+2.35	+2.47	+2.25	+2.28

Component C

Spectral type - A5V $M_{BOL} = +2.3$

$M_V = +2.45$

Colour indices

U-V	B-V	V-R	V-I	V-J	V-K	V-L	V-M	V-N
+0.25	+0.14	+0.16	+0.22	+0.27	+0.36	+0.40	+0.36	+0.36

The relevant data is from Hutchings and Hill (1971) and Johnson (1966). Bolometric corrections are determined from the relation $BC = -42.54 + 10 \log T_{eff} + 29000/T_{eff}$ (Allen 1973). The agreement between predicted and observed magnitudes is good, and

FIGURE 2.3

VARIATION OF MAGNITUDE WITH WAVELENGTH FOR β PERSEI.

O - JOHNSON ET AL. (1966); X - THEORETICAL EXTRAPOLATION FROM λ = 0.55 m; □ - PRESENT RESULTS

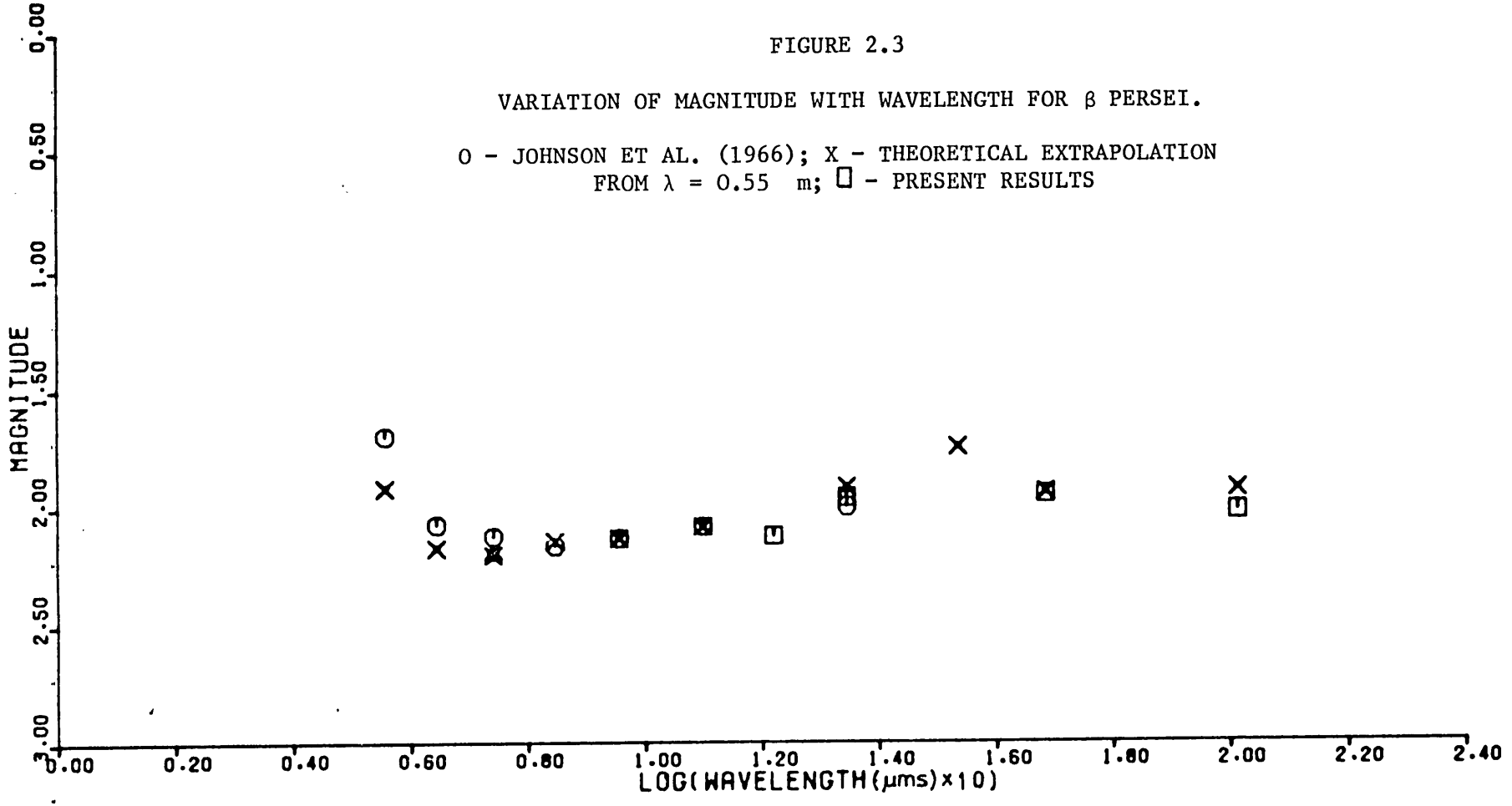

indicates no case for excess emission. It should be pointed out that the B8V component dominates emission at all wavelengths, so that uncertainties in the classification of components B and C are relatively unimportant in assessing magnitudes either at quadrature, or primary eclipse. Similar arguments apply regarding uncertainties in M_V and, because of insensitivity of indices near B8, to the indices of the B8V star. Ellipticity and reflection effects do not appear to be as large as suggested by Smyth et al. (1976) at 4.8 μm, although the photometric errors will to some extent mask these.

From the observations we have a primary eclipse depth ≈0.73 magnitudes. Smyth et al. predict a value ≈0.70 magnitudes with a small dependence upon stellar models adopted. The corresponding secondary eclipse depth predicted by Smyth et al. is 0.18 magnitudes, the present results indicating a value ≈0.26 mag. It seems clear therefore that, irrespective of any phase dependent component outside of eclipse, any emission between the stars is generally small, and probably less than 0.1 magnitudes. This enables us to place further constraints upon the Hα emitting plasma discussed earlier. A plasma with $r = 1\ R_\odot$, $T = 3.34 \times 10^4$ K would give 0.20 magnitudes excess at 4.8 μm. The probable absence of such an excess indicates that the plasma is optically thin by this wavelength. From the usual expression for free-free optical depth, the requirement $\tau(\lambda = 4.8\ \mu m) < 1$ gives $N_e < 1.9 \times 10^{12}\ cm^{-3}$ for plasma electron density.

To summarise, it is clear that although Algol is a system showing many interesting properties at radio wavelengths, and shows substantial evidence of significant mass transfer between components, there is little evidence for free gaseous mass being in any way responsible for continuum excesses ≥0.1 magnitude at near infrared wavelengths, $\lambda \lesssim 4.8$ μm.

Similarly, whilst Sanchez et al. (1977) indicate that observable excesses may nevertheless occur at 10.2 μm (and this is true also at 8.6 μm), the few 10.2 μm results presented in fig. 2.2 suggest that continuum levels again cannot be generally in excess of those expected from the stellar continua alone.

2.3 β LYR

β Lyrae is the prototype for a relatively common class of contact binaries, with light curves displaying deep secondaries and primaries, arising largely from ellipsoidal variability. Periods are generally > 1 day. Despite these common factors, the physical state of β Lyrae is almost certainly unrepresentative of its class, although Woolf (1965) has indicated that HD 30353 and ν Sgr may be similar systems, on spectroscopic grounds. This would be surprising however if the evolutionary interpretation of β Lyrae due to Ziolkowski (1976) is correct.

An early problem with this system was to account for the absence of any absorption lines ascribable to a secondary component. These would be easily visible were the main-sequence mass-luminosity law to be applicable. Indeed, recent measurements strongly suggest a "secondary" with mass several times larger than the primary component. A model of the system due to Huang (1963) is generally regarded as a turning point in our understanding of this system. In this model, the secondary is regarded as an accretion disk, generally masking the secondary component, whilst Hα emission originates from more tenuous gas occupying a spheroidal volume centred on the secondary. The disk is essentially non-emitting and the secondary minimum presumably due

largely to ellipticity of the primary, as suggested by Wilson (1971). A simple interpretation in terms of a non-emitting disk appears to be still viable, although it is now usually coupled with the possibility of a black hole secondary (c.f. Wilson 1971, Kondo et al. 1975). By "non-emitting" we mean to indicate a lack of significant optical continuum; as we will show, any such disk is possibly emitting significantly in the U.V. and infrared.

Other workers, whilst accepting a diskoidal secondary, have noted the possibility of substantial visual emission. This is true of Wilson (1974), who suggests that for a mass ratio $M_2/M_1 \simeq 5$ to 6, the luminosity of the secondary is greater than the primary by a factor two. Several contributions are considered to account for the previous belief in secondary underluminosity, including highly aspherical secondary emission characteristics, and overluminosity of the primary. This latter possibility arises from work by Stothers (1972), showing the primary to be the remaining helium core of a star which has lost most of its hydrogen rich envelope to the secondary. To explain the absence of spectral lines requires however an explanation in terms of differential rotational smearing, which is perhaps a little contrived. Huang and Brown (1976) have also investigated the constraints to be placed upon disk temperature and emissivity by the variation of secondary and primary minima with wavelength. The primary data used is that of Kondo et al. (1975), which takes the form of light curves for wavelengths between 0.332 μm and 0.143 μm. Wilson (1971) had previously suggested a non-thermal radiation source to explain the decreasing depths of primary minimum, and increasing depth of secondary minimum. Huang and Brown show that it is comparably explainable in terms of diluted black body emission at temperature T = 12,000 K.

The possible presence of hot spots is also noted, although considerably more refinement of the procedure is required before this can be taken seriously. In particular, it seems necessary to consider the consequences of limb darkening, of the kind present in Wilson's model.

There are therefore several possible interpretations of the β Lyrae system at present in vogue, involving highly oblate secondaries, or secondaries with accretion disks which may or may not be optically emitting. The possibility of an accretion disk is also supported by data (Appenzeller and Hittner 1967; Shulov 1967) which shows rapid variability of polarisation at primary minimum.

Huang (1963) has suggested "... observations of the light curve in the infrared region, where radiation emitted by the disk itself may reveal its existence." Jameson and Longmore (1976) have recently published such data. This may be characterised as follows. Increasing wavelength leads to

(a) decreasing depth of primary minimum

(b) increasing depth for secondary minimum

(c) increasing emission between eclipses

(d) increasing emission at primary and secondary minima, although at a slower rate than in (c).

Jameson and Longmore interpret this behaviour in terms of an electron scattering accretion disk, with temperature ~17,500 K. As wavelength increases, the disk optical thickness increases, and they show this to result in a reasonable quantitative explanation of changing depths at minima.

We have obtained 15 further results for this binary at J, H, K, L and M, and these are presented in table 2.2. The primary calibration star is α Lyrae which we took to have magnitude 0.00 at all bands.

TABLE 2.2

J

JULIAN DATE 24+	PHASE	MAGNITUDE	STANDARD DEVIATION
43286.730	0.101	3.440	0.002
43286.754	0.102	3.240	0.014
43294.759	0.721	3.220	0.008

H

JULIAN DATE 24+	PHASE	MAGNITUDE	STANDARD DEVIATION
43286.731	0.101	3.290	0.018
43286.752	0.102	3.070	0.005
43294.757	0.721	3.000	0.004

K

JULIAN DATE 24+	PHASE	MAGNITUDE	STANDARD DEVIATION
43286.733	0.101	3.450	0.015
43286.750	0.102	2.970	0.005
43294.755	0.721	2.890	0.034

L

JULIAN DATE 24+	PHASE	MAGNITUDE	STANDARD DEVIATION
43286.735	0.101	3.010	0.009
43286.755	0.103	2.750	0.004
43294.754	0.721	2.590	0.053

M

JULIAN DATE 24+	PHASE	MAGNITUDE	STANDARD DEVIATION
43286.737	0.101	2.880	0.021
43286.756	0.103	2.560	0.024
43294.751	0.721	2.340	0.027

The present data does not significantly improve on that of Jameson and Longmore, and it is hoped to supplement this substantially in the near future. In addition to providing these new results, however, we take this opportunity to present a re-evaluation of earlier infrared data.

The present J, K, L data is in broad agreement with the results of Jameson and Longmore. The H data is new, but provides no surprises, continuing the trends apparent at other wavelengths. Magnitudes at J, H, K, L and M near maximum light, from the present data, is plotted with respect to wavelength in fig. 2.4. Also given are measurements by Johnson et al. (1966), Jameson and Longmore (1976) (at λ = 8.6 μm), and the visual magnitude. For comparison, crosses mark the magnitudes expected of a B8Ib star (Johnson (1966)). These should be reasonably comparable with those of the B8II primary. We have taken V = +3.40 at quadrature. The observed results are shown to give a large, smoothly rising excess. Whether this is quantitatively explainable by the model of Jameson and Longmore is not clear; it is however readily explained in terms of optically thin free-free emission. To show this, we note that the excess emission (M_{B8} - M) due to free-free excess at wavelength λ is

$$(M_{B8}(\lambda) - M(\lambda)) = 2.5 \log_{10}(1 + \alpha \lambda^{2.1})$$

and $$\alpha = \frac{I_{FF1}}{I_{B8_1} \lambda_1^{2.1}} = \frac{10^{\frac{M(\lambda_2)-M(\lambda_1)}{2.5}}}{\lambda_1^{2.1} - \lambda_2^{2.1}\, 10^{\frac{M(\lambda_2)-M(\lambda_1)}{2.5}}}$$

where M_{B8} is the magnitude of the B8 component, M is the magnitude of

FIGURE 2.4

VARIATION OF MAGNITUDE NEAR QUADRATURE WITH WAVELENGTH, FOR β LYRAE.

O - JAMESON AND LONGMORE (1976); Δ - JOHNSON ET AL. (1966); □ - PRESENT RESULTS: X - B8II MAGNITUDES (JOHNSON 1966)

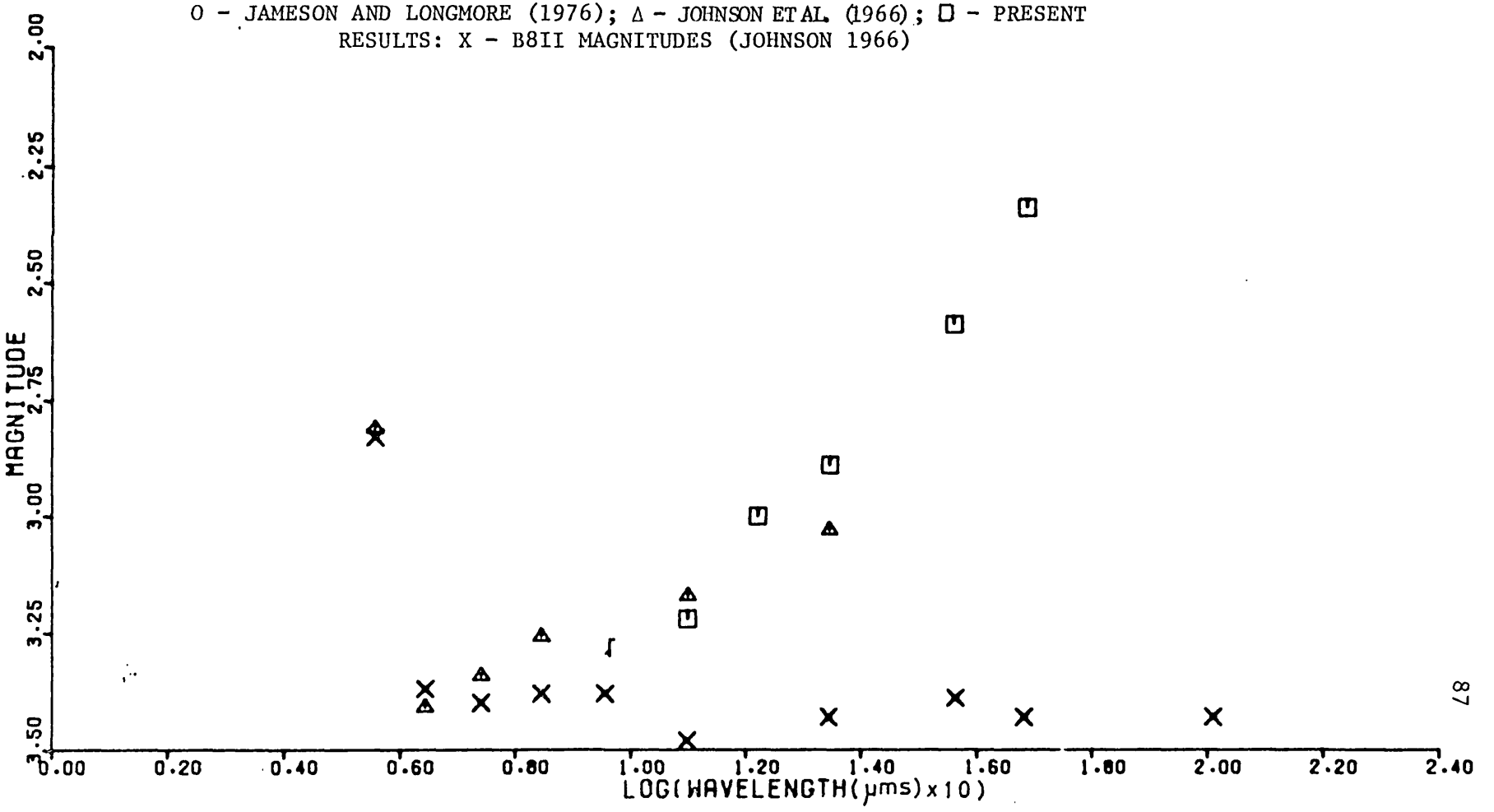

the system, and I_{FF1} is the free-free emission intensity at wavelength λ_1. The excess colour index due to free-free emission is then

$$(M(\lambda_1) - M(\lambda_2)) - (M_{B8}(\lambda_1) - M_{B8}(\lambda_2)) = 2.5 \log_{10} \left\{\frac{1 + \alpha \lambda_2^{2.1}}{1 + \alpha \lambda_1^{2.1}}\right\}$$

where $\alpha \lambda^{2.1}$ is the ratio of optically thin free-free emission to stellar continuum emission at wavelength λ. Note that we have approximated the stellar emission by the Rayleigh-Jeans law. Below we show observed indices $([H]-[X])$; the excess index $([H]-[X])_E \equiv ([H]-[X]) - ([H]-[X])_{B8}$, where $([H]-[X])_{B8}$ are the B8II intrinsic indices; $([H]-[X])_T$, the excesses expected for a fitted free-free excess, and $([H]-[X])_{TR}$, the theoretical excess reddened by $E_{B-V} = 0.065$ (Abt et al. (1962). In this latter operation, we have adopted the Van de Hulst reddening curve, which has a ratio of total to selective absorption, $R = A_V/E_{B-V} = 3.05$. This is comparable with the values $R \simeq 3.1$ derived for nearby field stars in Cygnus by Johnson (1968).

Indices at Quadrature

Index	$([H]-[X])$	$([H]-[X])_{B8}$	$([H]-[X])_E$	$([H]-[X])_T$	$([H]-[X])_{TR}$
H-V	-0.40	0.03	-0.43	-0.10	-0.28
H-J	-0.22	-0.05	-0.17	-0.06	-0.09
H-H	+0.00	0.00	0.00	+0.00	+0.00
H-K	+0.11	0.00	+0.11	+0.08	+0.08
H-L	+0.41	0.04	+0.37	+0.36	+0.37
H-M	+0.66	0.00	+0.66	+0.63	+0.64
H-8.6	+1.4	0.00	+1.4	+1.48	+1.48

Data at J, H, K, L, M is from the present work, that at 8.6 μm is an estimate from the data of Jameson and Longmore (1976). Clearly, the observed excess $([H]-[X])_E$ is very well represented throughout

the infrared by assuming optically thin free-free emission. The slightly depressed 8.6 μm result does not necessarily indicate the inception of optical thickness; the errors at this wavelength are too large to show anything but broad trends. The V and J data appear to retain a residual depression of 0.1 magnitudes. This is most probably to be ascribed to an underestimate in reddening. Hack et al. (1975) have for instance suggested a possible colour excess $E_{B-V} = 0.15$ on the basis of U.V. data, which would more than compensate for this discrepancy whilst leaving infrared data relatively unaffected. Finally it should be noted that several investigations adopt a spectral type B8.5. Alterations of this order lead to but minor changes in the calculated excess. The best fit value of α adopted is $\alpha = 0.036$. A similar procedure can be successfully carried out to determine emission excess at primary and secondary minima, assuming the B8 star and optically thin free-free to be the principal sources of continuum. The details are recorded below, and designations are as in the discussion of emission at quadrature. The data however is due primarily to Longmore and Jameson, and open to rather greater error. Despite this, the agreement of theoretical and observed curves is convincing.

Indices at Secondary Minimum

Index	$([K]-[X])$	$([K]-[X])_{B8}$	$([K]-[X])_{E}$	$([K]-[X])_{T}$	$([K]-[X])_{TR}$
K-V	-0.35	+0.03	-0.38	-0.06	-0.24
K-J	-0.05	-0.05	0.00	-0.04	-0.07
K-K	0.00	0.00	0.00	0.00	0.00
K-L	+0.15	+0.04	+0.11	+0.10	+0.11
K-M	+0.25	0.00	+0.25	+0.22	+0.23
K-8.6	~+0.35	0.00	~+0.35	+0.70	+0.70

where we have used $\alpha = 0.011$.

Indices at Primary Minimum

Index	$([K]-[X])$	$([K]-[X])_{B8}$	$([K]-[X])_{E}$	$([K]-[X])_{T}$	$([K]-[X])_{TR}$
K-V	-0.6	+0.03	-0.63	-0.24	-0.42
K-J	-0.3	-0.05	-0.25	-0.17	-0.20
K-K	0.00	0.00	0.00	0.00	0.00
K-L	+0.4	+0.04	+0.36	+0.36	+0.37
K-M	+0.7	0.00	+0.70	+0.69	+0.70
K-8.6	+1.5	0.00	+1.50	+1.64	+1.64

where, finally, $\alpha = 0.052$.

The above data gives, for the ratios of free-free emission at quadrature and primary and secondary minima the values

$$I_Q : I_P : I_S = 1 : 0.72 : 0.21$$

The close similarity between the sum of emissions at primary and secondary minima, and that at quadrature suggests that both primary and secondary components may have associated optically thin emission. The model of Flora and Hack (1975), based on the extensive data of the 1971 international observational campaign of β Lyrae, gives substantial support to such a proposition.

To summarise so far then, the β Lyrae system appears to contain a gaseous component providing an optically thin free-free emission continuum. This continuum is seen at maximum at quadratures, although is primarily absent at secondary eclipse. A little over 70% of the emission is however responsible for the reduction in depth of primary minimum. In passing, it should also be mentioned that the depths of primary and secondary minima at J are closely similar to those at V. This lends support to the concept of a wavelength independent opacity source at primary minimum, such as provided by a dark opaque disk, or a semi-opaque disk with electron scattering.

The obvious explanation of this data would be for ≳70% of the free-free emission to originate in the vicinity of the secondary. The increasing contribution of this excess at longer wavelengths leads to the increasing depth of the secondary minimum. To independently assess the emission strength responsible for the increasing depth of secondary minimum, we adopt the following procedure. First note the following definitions:

I_{1S} = Eclipsed emission at secondary minimum

I_{2S} = Uneclipsed emission at secondary minimum

I_{B8S} = B8 continuum emission at secondary minimum

I_{B8Q} = B8 continuum emission at quadrature

ΔV_S = Eclipse depth (in magnitudes) at secondary minimum.

We will take

$$\frac{I_{B8S}}{I_{B8Q}} = 2.512^{-0.40}$$

where the factor 0.40 is the secondary eclipse depth in the visible. Whence

$$\Delta V_S = 2.5 \log_{10} \left\{\frac{I_{1S} + I_{2S} + I_{B8Q}}{I_{2S} + I_{B8S}}\right\}$$

After manipulation, we have

$$\frac{I_{1S}}{I_{B8Q}} = 2.512^{\Delta V_S} \left\{\frac{I_{2S}}{I_{B8S}} \cdot \frac{I_{B8S}}{I_{B8Q}} + \frac{I_{B8S}}{I_{B8Q}}\right\} - \left\{\frac{I_{2S}}{I_{B8S}} \cdot \frac{I_{B8S}}{I_{B8Q}} + 1\right\}$$

Substituting the appropriate relation for I_{2S}/I_{B8S} obtained earlier (i.e. using $\alpha = 0.011$), we obtain the following values:

λ	ΔV_S	I_{1S}/I_{B8Q}	$\{\frac{I_Q}{I_{B8Q}} \cdot 0.72\}$
J	0.40	0.00	0.04
K	0.55	0.17	0.14
L	0.70	0.42	0.38
M	0.6		
8.6	~1.2	2.50	2.38

The fourth column records the values expected if the plasma seen at primary eclipse is totally occulted at secondary minimum. The agreement between columns three and four is impressive, particularly when the errors in determination of eclipse depths are allowed for. The eclipse depth at M is the single exception, almost certainly attributable to an error in measurement (it depends upon one measurement alone).

An important point may now be made, particularly evident in the last set of data. The emission component eclipsed by the primary exceeds the emission due to the primary itself at longer wavelengths. The trend of emission excesses however shows that the plasma remains optically thin to $\lambda = 4.8$ μm, and possibly $\lambda = 8.6$ μm. It is evident therefore that the source of emission must be hotter than the B8 primary. To place provisional limits upon the temperature we note that

$$\frac{I_{1S}}{I_{B8S}} = \{\frac{I_{1S}}{I_Q}\}\{\frac{I_Q}{I_{B8Q}}\}\{\frac{I_{B8Q}}{I_{B8S}}\}$$

$$= (0.72) \cdot (0.036\ \lambda^{2.1})(2.512^{+0.40})$$

$$= 3.75 \times 10^{-2}\ \lambda^{2.1}$$

where λ is in μms, and we have again taken secondary minimum in the

visible to arise from ellipticity of the primary. Wilson's model suggests a possibly smaller ellipticity, leading to $I_{B8Q}/I_{B8S} \simeq 1.25$. The results are not materially altered by using this latter value, however.

When $T_o = T_*$, where T_o is the plasma temperature, we expect $I_{1S}/I_{B8S} \simeq 1$ when the optical depth $\tau \simeq 1$*. According to the above equation, we should therefore have $\tau \simeq 1$ at $\lambda \simeq 4.78$ μms. That the plasma does not become optically thick at this wavelength indicates that the plasma temperature must be larger than T_*. At the wavelength λ_{TH} when $\tau = 1$, $I_{1S}/I_{B8S} = 0.63\ B(\lambda_{TH}, T_o)/B(\lambda_{TH}, T_*)$, where $B(\lambda,T)$ is the Planck function. In the Rayleigh-Jeans limit

$$\frac{T_o}{T_*} \simeq 5.95 \times 10^{-2}\ \lambda_{TH}^{2.1}$$

whence for $T_* \simeq 1.075 \times 10^4$ K (Wilson 1974) we obtain the following plasma temperatures T_o for corresponding wavelength limits λ_{TH}:

λ_{TH}(μm)	T_o(K)
8.6	5.87×10^4 K
10.2	8.39×10^4 K
20.0	3.45×10^5 K

The present results indicate $T_* << T_o \gtrsim 5.9 \times 10^4$ K although, as we have noted, the accuracy of the 8.6 μm results clearly requires improvement. It is clear however that near infrared observations should afford an opportunity for unambiguously assessing the temperature of the optically thin plasma. The presence of an emission excess at primary minimum would also imply a plasma temperature greater than that of the primary, if the plasma were directly between Earth and the (otherwise) unobscured primary photosphere. The concentration of

---

* Taking equality of projected areas of primary star and plasma.

emission at the secondary component however suggests an intimate relation with the postulated (semi-) opaque disk, and emission may therefore be projected against a cooler surface.

At longer wavelengths there is distinct evidence for the onset of optical thickness. Jameson and Longmore (1976) obtain an upper limit magnitude +1.5 at λ = 18 μm, and Gehrz, Hackwell and Jones (1974) give a λ = 19.5 μm measure of +1.62. The former limit is at quadrature, the latter probably close to quadrature. Both these values are considerably fainter than would be expected if optically thin free-free were present, and taken at face value suggest a value λ_{TH} only little greater than 8.6 μm. This is even clearer at radio wavelengths. Wade and Hjellming (1972) obtain a typical flux 0.015 Jy at λ = 3.7 cms. The infrared optically thin free-free observed at quadrature on the other hand has a strength

$$F_{\nu FF} \simeq 50.0 \left\{\frac{\lambda}{2.2}\right\}^{0.1} \text{ Jy} \qquad (\lambda \text{ in μms})$$

so that at λ = 3.7 cms, the strength would be 132 Jy - 8.8×10^3 times in excess of observations. The flux at 2695 MHz is however $\lesssim$0.005 Jy, and this suggests the possibility that the radio emission is simply the long wave tail of the optically thick plasma. For this to be the case requires optical thickness to develop at 489 μms. Accepting that the 20 μm results are in error, the implied plasma temperature would then be $\simeq 2.8 \times 10^8$ K. This is not so unrealistically high as to preclude consideration, and further results at 20 μms are to be awaited with interest.

It is interesting to see how the above interpretation couples with data at other wavelengths. Hα emission appears to originate

from an extended volume, encompassing the binary. Apart from particular anomalous readings, Batten and Sahade (1973) found total Hα emission to be broadly phase invariant. In the ultra-violet, an analysis of spectra taken by the Copernicus U.V. satellite between ~1100 and 1400 Å by Hack et al. (1974, 1975, 1976) shows a rapidly rising U.V. excess continuum at $\lambda \lesssim 1150$ Å, and a proliferation of displaced, and broadened emission lines. The lines of NV, λλ 1238 and 1242, indicate considerable excitation, and these and other lines show P Cygni profiles, corresponding to expansion at ~150 $km.s^{-1}$. Again, phase effects are relatively weak, but distinct, showing attenuation of line heights at secondary minimum. Line areas are less strongly affected than line heights, and this is interpreted as indicating occultation of a rapidly rotating accretion disk; the lower velocity layers (contributing to the central zones of lines) being preferentially occulted at mid-eclipse. It is clear therefore that the U.V. data provides qualitative support for a scenario in which very hot gas is located near the secondary. The degree of concentration is perhaps less severe, however, for the plasma responsible for the emission lines.

Kondo et al. (1975, 1976) have provided U.V. light curves from OAO II over an adjacent wavelength régime (1380 Å - 3330 Å). Secondary minimum is shown to deepen and primary minimum becomes shallower as wavelength increases, in behaviour reminiscent of the infrared light curves. Although specific criticisms have been levelled by Wilson (1971) these have been indirectly answered by Kondo et al. (1975). Whatever the final evaluation of the curves may be, it seems certain that they are at least qualitatively significant. A single anomalous curve at λ 1910 Å, showing significantly decreased primary and secondary eclipse depths, may be attributable to particularly strong line emission.

Underhill and Fahey (1973) have found similar behaviour in another star. The precise nature of the "excess" U.V. emission found by Kondo et al. is not entirely clear, and could presumably be due to smeared out line emission (a very strong possibility in view of the work by Hack et al.), non-thermal continuum emission (Wilson 1971) or even black-body emission (Huang and Brown 1976). The additional suggestion of Kondo et al. (1975) that significant thermal continuum from a hot circumbinary gas may contribute is difficult to understand, however, in view of its apparent absence in the optical continuum.

To conclude, we may say that the new infrared results both supplement (H band) and confirm the recently published results of Jameson and Longmore (1976), so far as they go. Further results, particularly at longer wavelengths, are required. A steeply rising excess may almost certainly be ascribed to optically thin free-free emission, primarily located in the vicinity of the secondary component. The gas is shown to be considerably hotter than the primary, and is possibly responsible for similar results in the U.V. light curves. Although it may give rise to certain U.V. emission lines these, like Hα, appear to be less spatially localised. The plasma responsible for these lines is, like that responsible for the infrared excess, almost certainly at high temperature.

2.4 W UMa

As Kopal (1959) has indicated, β Lyrae systems in many ways represent a simple extension of the semi-detached Algol type systems, the primary difference being that the components in β Lyrae systems are systematically closer than in Algol type systems. W UMa stars

represent a still more extreme development, with both components in contact at the L_1 point. Lucy (1968) has developed a model for such systems in which the component stars have a common convective envelope. Application of this model to W UMa by Worden and Whelan (1973) leads to reasonably satisfactory results, and in particular enables an explanation of the peculiar mass luminosity law for this system ($L \alpha M^{0.8}$).

Herczog (1969) has noted that the great majority of W UMa systems are undergoing period changes of a few tenths of a second, possibly in short jumps leading to immediate increases and decreases in period, although the overall trend is for steadily increasing periods. In addition, Struve and Horak (1950), and Worden and Whelan (1973) have both noted CaII K line emission, and Kuhi (1964) has apparently observed a flare. In this latter respect W UMa is probably again not unique (Huruhata, 1952; Eggen, 1948).

These latter observations suggest an active system, and W UMa was observed in the infrared in the partial hope of detecting excess emission components. Observations were acquired at J, H, K, L, M and N. They are presented in table 2.3, and plotted in figure 2.5. The primary calibration star was μ UMa (see discussion on RR UMi for magnitudes adopted).

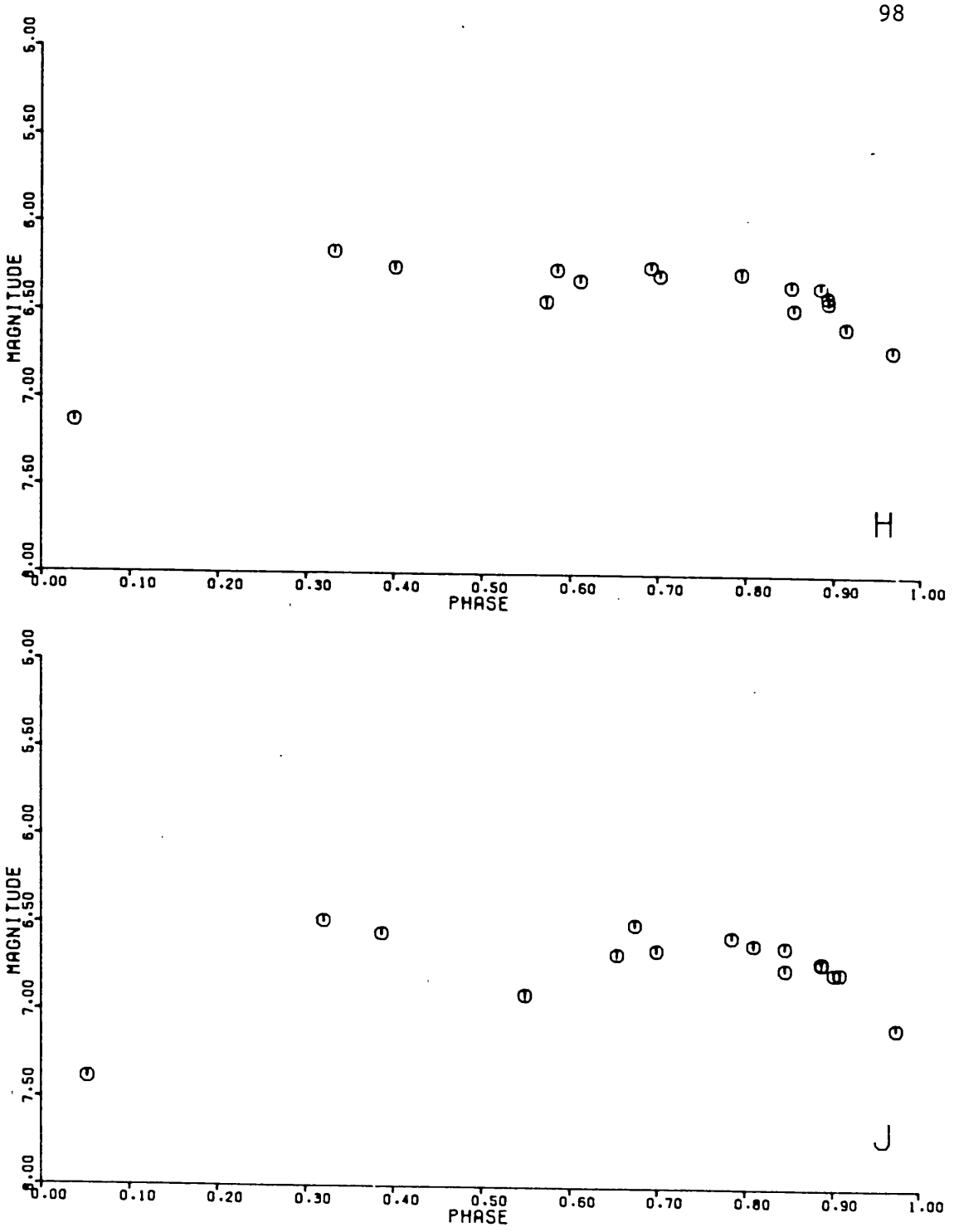

FIGURE 2.5a

VARIATION OF MAGNITUDE WITH PHASE FOR W UMa

FIGURE 2.5b

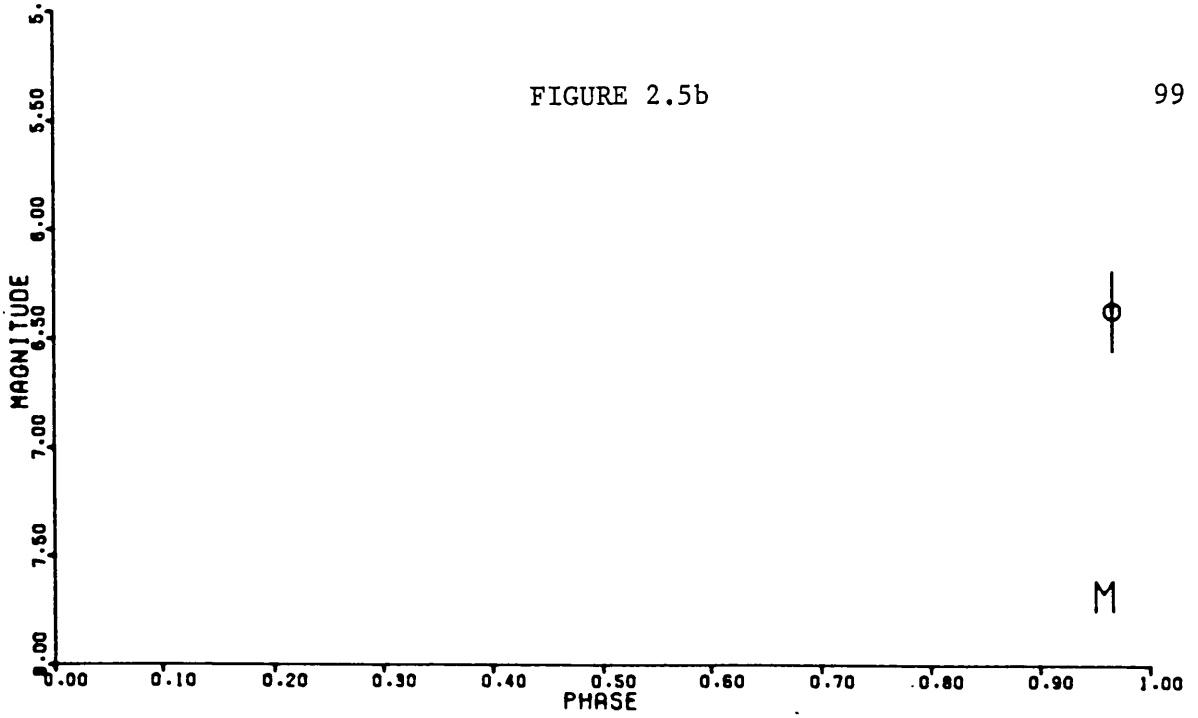
MAGNITUDE
5.00
5.50
6.00
6.50
7.00
7.50
8.00
0.00
0.10
0.20
0.30
0.40
0.50
0.60
0.70
0.80
0.90
1.00
PHASE
M

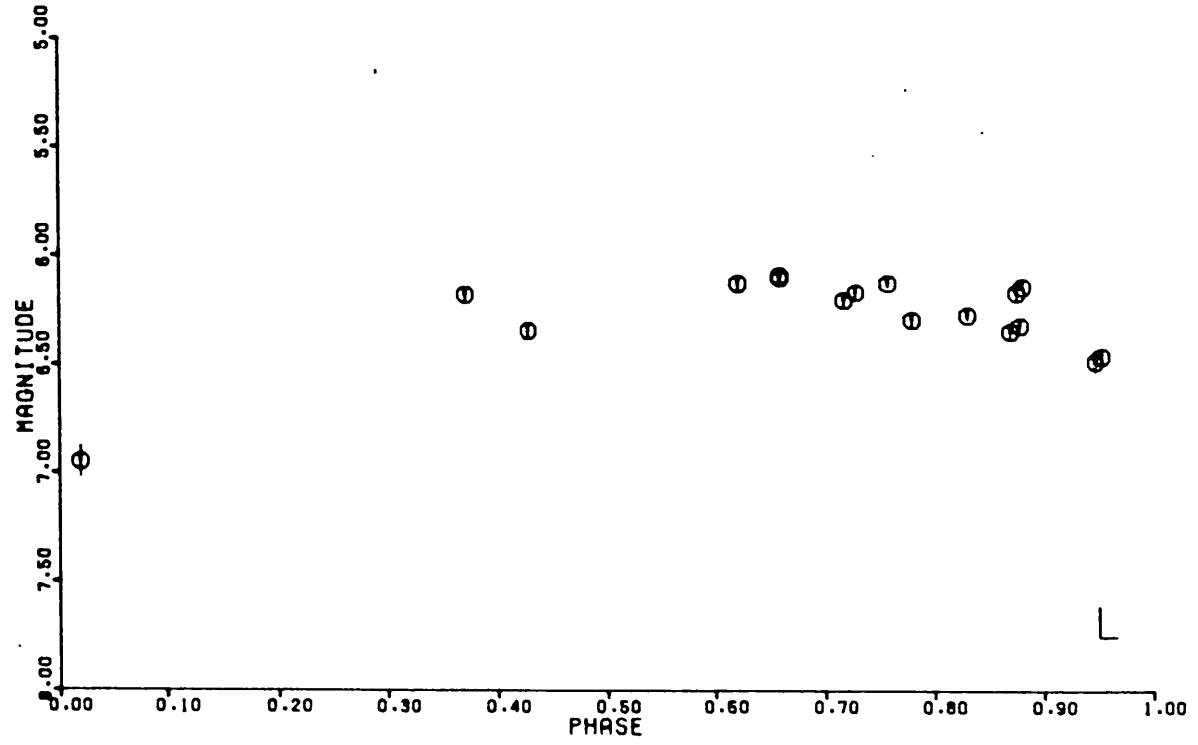
MAGNITUDE
5.00
5.50
6.00
6.50
7.00
7.50
8.00
0.00
0.10
0.20
0.30
0.40
0.50
0.60
0.70
0.80
0.90
1.00
PHASE
L

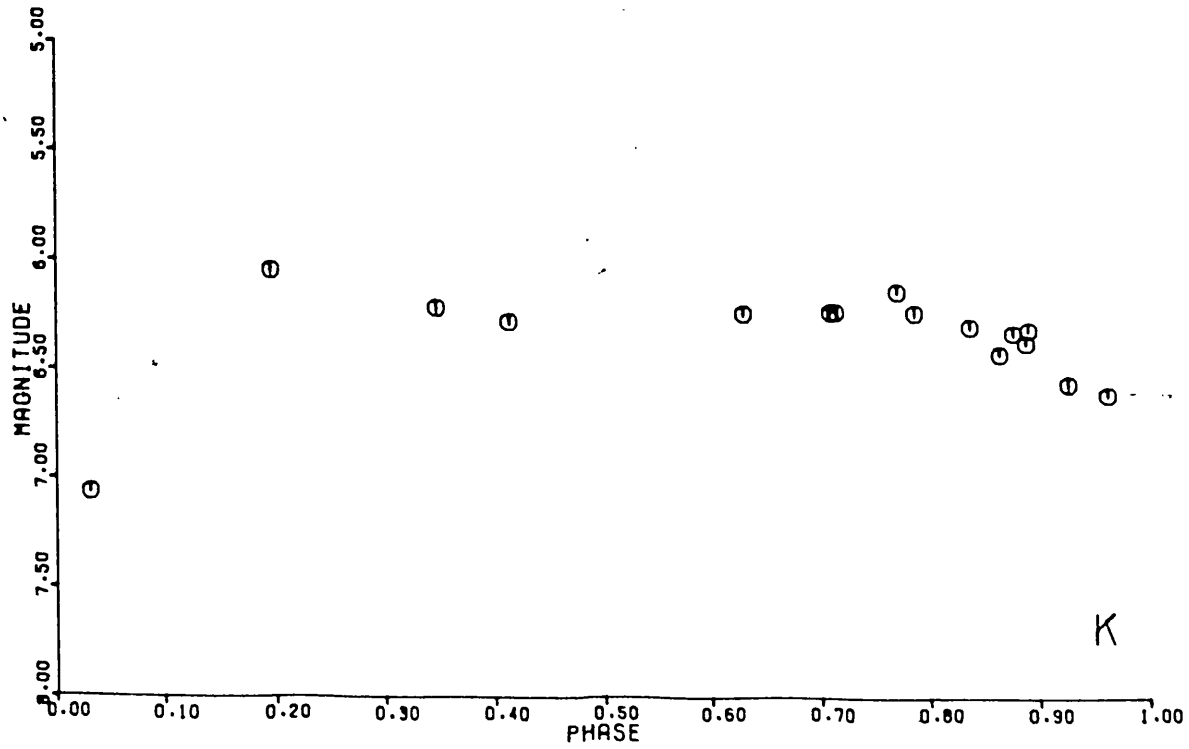
MAGNITUDE
5.00
5.50
6.00
6.50
7.00
7.50
8.00
0.00
0.10
0.20
0.30
0.40
0.50
0.60
0.70
0.80
0.90
1.00
PHASE
K

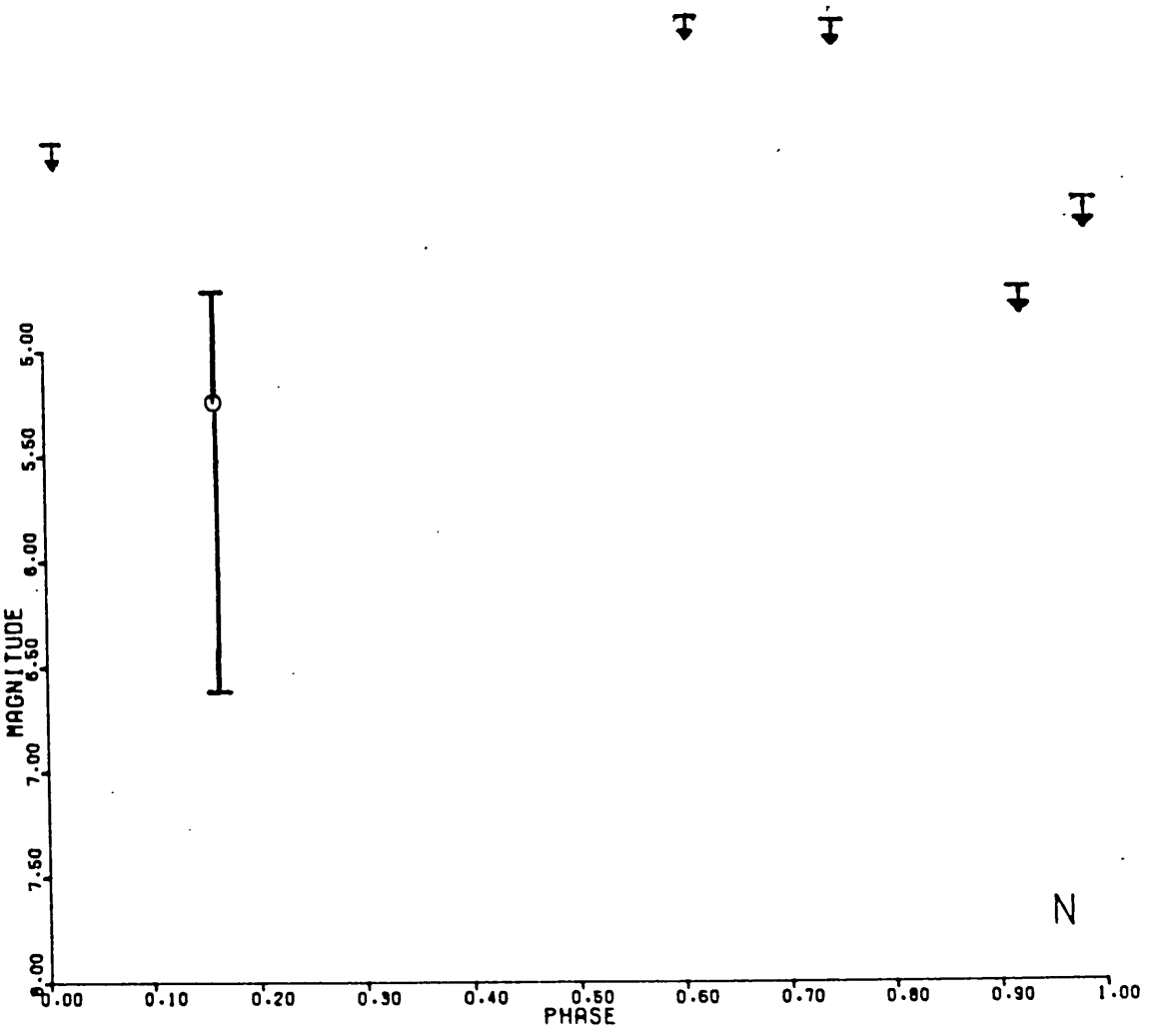
MAGNITUDE
5.00
5.50
6.00
6.50
7.00
7.50
8.00
0.00
0.10
0.20
0.30
0.40
0.50
0.60
0.70
0.80
0.90
1.00
PHASE
N

FIGURE 2.5c

TABLE 2.3

J

JULIAN DATE 24+	PHASE	MAGNITUDE	STANDARD DEVIATION
43295.411	0.785	6.567	0.007
43295.450	0.902	6.772	0.015
43295.474	0.974	7.083	0.003
43298.434	0.846	6.623	0.008
43298.455	0.909	6.769	0.032
43299.423	0.810	6.611	0.018
43299.449	0.888	6.709	0.015
43159.641	0.846	6.748	0.007
43159.710	0.053	7.386	0.009
42850.518	0.321	6.486	0.010
42850.540	0.387	6.557	0.010
42850.629	0.653	6.668	0.019
42850.636	0.674	6.500	0.012
42850.707	0.887	6.713	0.031
42853.597	0.549	6.903	0.028
43300.387	0.700	6.644	0.013

H

JULIAN DATE 24+	PHASE	MAGNITUDE	STANDARD DEVIATION
43295.678	0.585	6.260	0.014
43295.447	0.893	6.404	0.009
43295.472	0.968	6.708	0.005
43298.436	0.852	6.344	0.008
43298.450	0.894	6.433	0.019
43299.418	0.795	6.275	0.021
43299.448	0.885	6.350	0.011
43159.644	0.855	6.477	0.005
43159.705	0.038	7.136	0.009
43300.388	0.703	6.290	0.006
42850.522	0.333	6.165	0.011
42850.545	0.402	6.251	0.019
42850.615	0.611	6.319	0.011
42850.642	0.692	6.243	0.010
42850.716	0.914	6.579	0.017
42853.605	0.573	6.440	0.027

K

JULIAN DATE 24+	PHASE	MAGNITUDE	STANDARD DEVIATION
43295.406	0.770	6.149	0.009
43295.446	0.890	6.321	0.005
43295.470	0.962	6.619	0.008
43298.431	0.837	6.306	0.011
43298.448	0.888	6.382	0.007
43299.415	0.786	6.246	0.017
43299.445	0.876	6.336	0.016
43159.647	0.864	6.432	0.005
43159.703	0.032	7.066	0.009
43300.390	0.709	6.242	0.018
42850.527	0.348	6.224	0.027
42850.549	0.414	6.288	0.016
42850.621	0.629	6.250	0.015
42850.649	0.713	6.242	0.014
42850.720	0.926	6.569	0.039
42853.613	0.197	6.052	0.020

L

JULIAN DATE 24+	PHASE	MAGNITUDE	STANDARD DEVIATION
43295.402	0.758	6.125	0.017
43295.443	0.881	6.141	0.012
43295.467	0.953	6.460	0.022
43298.429	0.831	6.272	0.020
43298.445	0.879	6.321	0.027
43299.413	0.780	6.294	0.031
43299.443	0.870	6.346	0.032
43159.651	0.876	6.169	0.030
43159.699	0.020	6.950	0.071
43300.393	0.718	6.203	0.030
42850.535	0.372	6.180	0.030
42850.554	0.429	6.345	0.033
42850.631	0.659	6.097	0.038
42850.631	0.659	6.097	0.038
42850.654	0.728	6.167	0.030
42850.727	0.947	6.484	0.048
42853.621	0.621	6.127	0.038

M

JULIAN DATE 24+	PHASE	MAGNITUDE	STANDARD DEVIATION
43159.681	0.966	6.370	0.184

N

JULIAN DATE 24+	PHASE	MAGNITUDE	STANDARD DEVIATION
42091.715	0.983	>4.310	
42092.591	0.609	>3.440	
42154.498	0.161	5.240	$^{+1.72}_{-0.64}$
42157.421	0.922	>4.720	
42158.452	0.012	>4.020	
42160.365	0.746	>3.460	

The variation of continuum with wavelength is presented in fig. 2.6, in which crosses again represent the predicted flux. Two cases are represented:

(a) Primary Spectral Type F8

Secondary Spectral Type F7

$L_p/L_S = 3.98$ (Kopal and Shapley 1956)

(b) Primary Spectral Type G0

Secondary Spectral Type G0

$L_p/L_S = 3.98$ (Strohmeier 1972)

where L_p, L_S are the respective bolometric luminosities of primary and secondary components. Worden and Whelan (1973) indicate a lower luminosity ratio, $L_p/L_S \simeq 1.41$, but this will not seriously change the values for the predicted magnitudes. These predicted values are in turn extrapolated from a maximum visual magnitude V = +7.5 (Breinhorst 1971). No correction for reddening has been applied, but this is unlikely to exceed 0.1 magnitudes at V (Worden and Whelan 1973). We see that the spectrum is probably normal, the observed magnitudes residing close to the extrapolated magnitudes. Perhaps surprisingly, there is no excess emission at $\lambda \lesssim 4.8$ μm. 10.2 μm values give 3σ upper limits (σ representing one standard deviation) to the flux,

FIGURE 2.6

VARIATION OF MAGNITUDE NEAR QUADRATURE
WITH WAVELENGTH, FOR W UMa

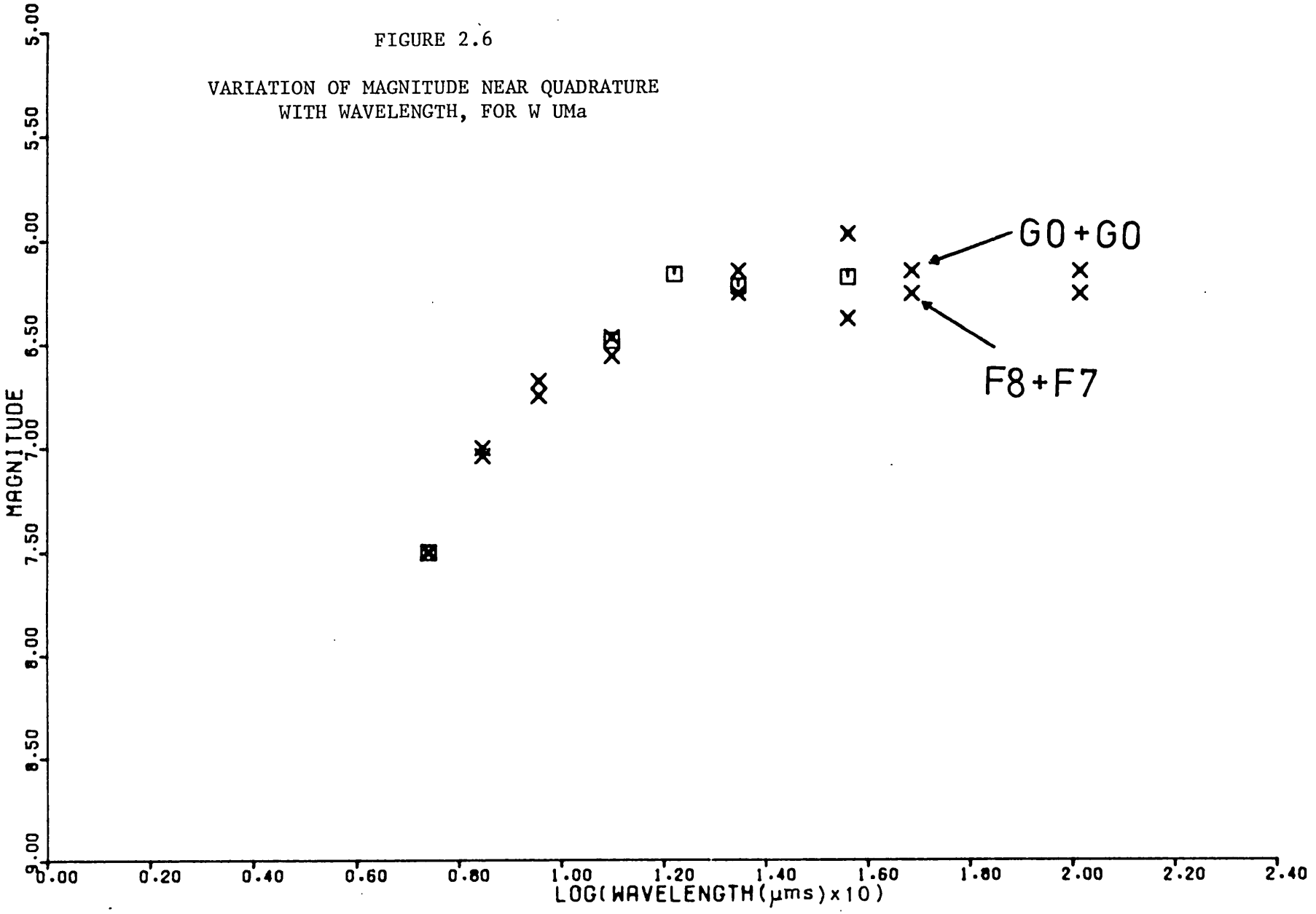

although these represent too great a brightness to provide sensible physical constraints upon any gaseous component to the system. Phase was determined from Cester et al. (1976) using

MIN = J.D. 2441004.39769 + 0.33363696 E

The period of the binary had recently changed, and this represents the most recent evaluation. Comparison with more recent timings of minima at JD 2442838 (Baldinelli and Ghedini, 1976) indicates O-C residuals of ≈0.002 J.D., corresponding to a discrepancy in phase of ≈0.006; acceptable for present purposes. The primary eclipse depth appears invariant with wavelength, within errors. This is to be expected for component stars of similar temperature, providing reflection effects do not change too considerably into the infrared.

Unfortunately, a paucity of results near secondary minimum prevents proper evaluation of any changes there, although the light curve appears preliminarily to be abnormally flattened (see for comparison the B, V curves in Rigterink, 1972), and the single result close to phase 0.5 suggests a possible reduced depth for secondary minimum. More results are to be obtained, and these will hopefully clarify the situation at these phases. These however appear to be the only indication of significant abnormality.

2.5 U SGE

U Sge is a totally eclipsing semi-detached binary of the Algol type. The respective spectral types of primary and secondary components have been given as B7III + K1III (Sahade 1960, Hoffleit 1964, Strohmeier 1972); B7V and G2III (Naftilon 1976); B9 + gG2 (Kukarkin

et al. 1968, Kopal 1959, Glasby 1968, Strohmeier 1972, Allen 1973). Finally, Hall (1974) notes a spectral type B7V-IV for the primary. Following the more recent work, we shall adopt a spectral type B7V for the primary, and later evaluate the results in terms of a G2III and K1III secondary. The orbital period is slightly fluctuating (Jacchia 1941, Tchudovitchev 1939, 1943) and the velocity curve of the primary shows a strong rotational effect (Struve 1949) suggesting rapid axial rotation.

As for many other Algol-type systems (c.f. Sahade 1960, Huang 1973), U Sge also possesses a circumprimary gaseous disk. Earlier data indicated a general relation between ring velocity V and orbital period P, $V^3 \alpha P^{-1}$ (Struve 1950), a functional form which could be understood in terms of particle dynamics (Huang and Struve 1956), providing gravitational forces alone dominated motion. More recent data (Batten 1973) indicates however that $V^{4.6} \alpha P^{-1}$, and this implies a less elegant interpretation in terms of the Huang-Struve model (Huang 1973). Huang (1973) has suggested that grain condensation within the rings may lead to observable infrared emission, providing temperatures are low enough. For high temperatures, free-free emission may be more relevant. We have at present insufficient data to assess the relative importance of these processes. Although current estimates of disk temperatures tend to be high, comparable with those of the primary components (c.f. Gunther 1959), their validity is not unquestioned (Batten 1973). Consider then two situations as they relate to a typical disk, with density $N_e = 2.10^{11}$ cm^{-3}, mass $M = 2.10^{-11} M_\odot$, and radius $R_D = 0.6a$ (Batten 1973), where a is the binary semi-major axis. An homogeneous disk of this kind has ratio of shell thickness to diameter

$$\Gamma = \frac{\dot{M}}{2\,\pi\, R_D^{\,3}\, N_e\, M_H} \simeq 0.26$$

where we have taken $a \simeq 10\ R_\odot$. The optically thin free-free emission from the disk is

$$F_{\nu FF} = 7.79 \times 10^{-38}(10.6 + 1.9 \log T_e - 1.26 \log \nu)\ \frac{e^{-\frac{1.43883}{\lambda T}}}{T_e^{\frac{1}{2}}}\ \frac{N_e\, M}{M_H}$$

$$\text{erg.s}^{-1}.\text{Hz}^{-1}$$

and in the infrared, the stellar flux is adequately represented by

$$F_{\nu BB} = 4\,\pi\, R_*^{\,2} \cdot \frac{2\,\pi\, K\, T_*}{\lambda^2} \quad \text{erg.s}^{-1}.\text{Hz}^{-1}$$

Dividing the last two expressions then gives

$$\frac{F_{\nu FF}}{F_{\nu BB}} = 4.27\ \frac{\lambda^2\, e^{-\frac{1.43883}{\lambda T}}}{R_*^{\,2}\, T_*\, T_e^{\frac{1}{2}}}\ N_e\, M\ (10.6 + 1.9 \log T - 1.26 \log \nu)$$

Taking $T_* = T_e = 10^4$ K, $\lambda = 4.8$ μm and $R_* = 4\ R_\odot$, we then obtain

$$\frac{F_{\nu FF}}{F_{\nu BB}} \simeq 6.2 \cdot 10^{-2}$$

Alternatively, consider dust formation in the disk. In equilibrium with the stellar radiation field dust acquires a temperature T_g, at a radius R, given through

$$\frac{R}{R_*} = \left\{\frac{T_*}{T_g}\right\}^2 \left\{\frac{\bar{Q}_{abs}\,(T_*)}{4\,\bar{Q}_{em}(T_g)}\right\}^{\frac{1}{2}}$$

where $\bar{Q}_{abs}$, $\bar{Q}_{em}$, are respectively the Planck mean absorption and emission coefficients. From work by Gilman (1974) on grains considered to be

astrophysically likely, we note that for silicate grains with temperature $T_g < T_*$, $Q_{abs} > Q_{em}$. Since we expect $T_g \lesssim 10^3$ K (silicates are relatively unrefractory), it is clear that the formation zone must be substantially outside the binary for a reasonably warm primary star. Similar difficulties apply to graphite and iron grains. Specifically we may write $\bar{Q}_{abs} \propto T^{1.9}$, for the latter materials, whence

$$\frac{R}{R_*} \simeq \frac{1}{2}\left\{\frac{T_*}{T_g}\right\}^{2.95}$$

Although graphite grains are more refractory than silicate (or iron) grains, it again requires an anomalously cool primary before R/R_* becomes less than the typical binary dimensions.

It seems therefore unlikely that dust is a serious constituent of cool gaseous matter within Algol systems. There is however a strong possibility that systems with gaseous disks, such as U Sge, support a substantial "excess" optically thin free-free continuum. With this in mind, we have obtained a series of infrared observations of the system U Sge at J, H, K, L and M. The primary calibration star is ν Her, for which we adopt

I = +3.78; H = +3.23; J = +3.51; K = +3.20; L = +3.19; M = +3.25.

The results are presented in table 2.4. Phases were determined using the relation

MIN = J.D. 2442275.4572 + 3.380618 E

The period is from Kukarkin et al. (1970) and the epoch of initial minimum from Pohl and Kizilirmak (1975). The O-C residuals between the initial minimum of Kukarkin et al., and Pohl and Kizilirmak

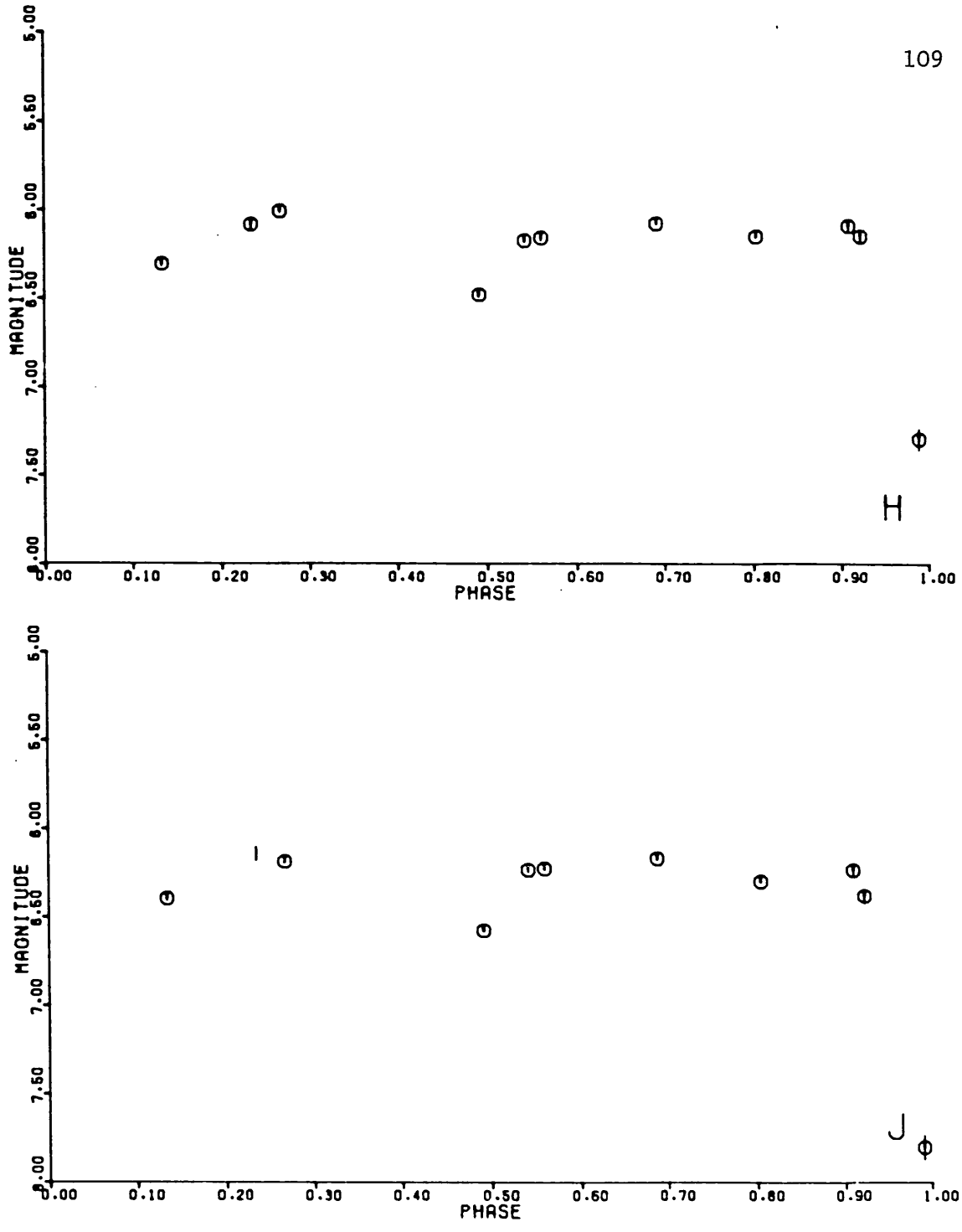

FIGURE 2.7a

VARIATION OF MAGNITUDE WITH PHASE FOR U SGE

FIGURE 2.7b

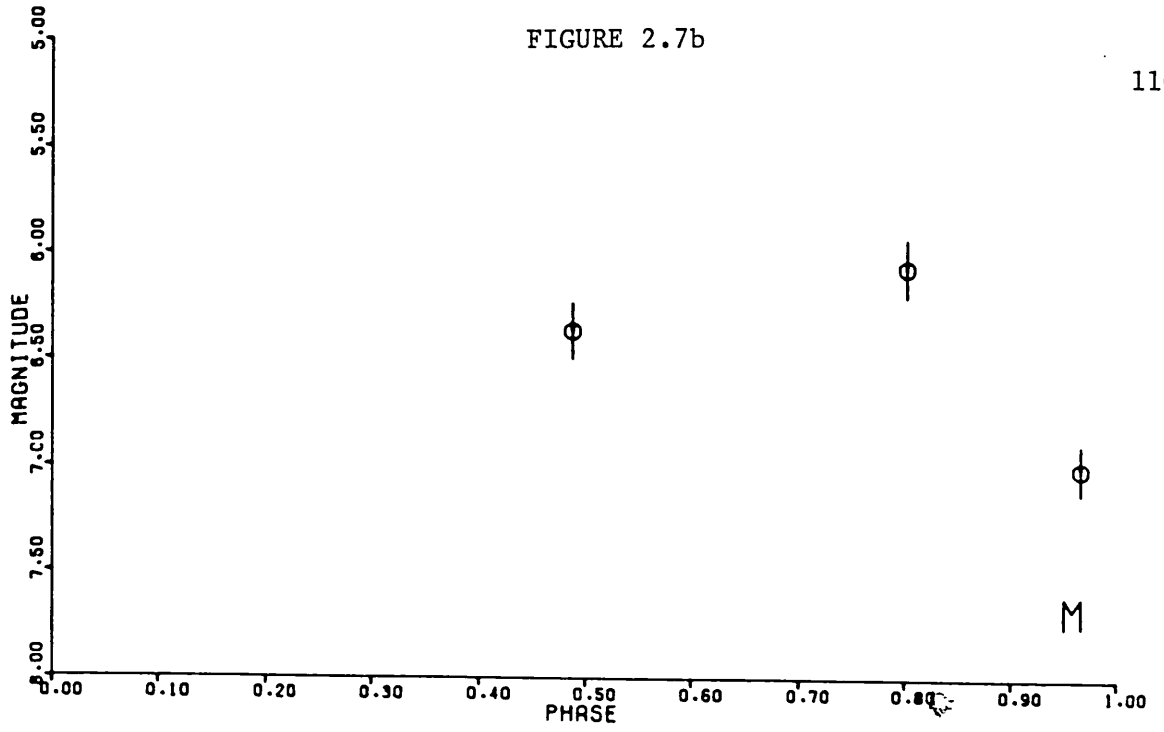
MAGNITUDE
5.00
5.50
6.00
6.50
7.00
7.50
8.00
0.00
0.10
0.20
0.30
0.40
0.50
0.60
0.70
0.80
0.90
1.00
PHASE
M

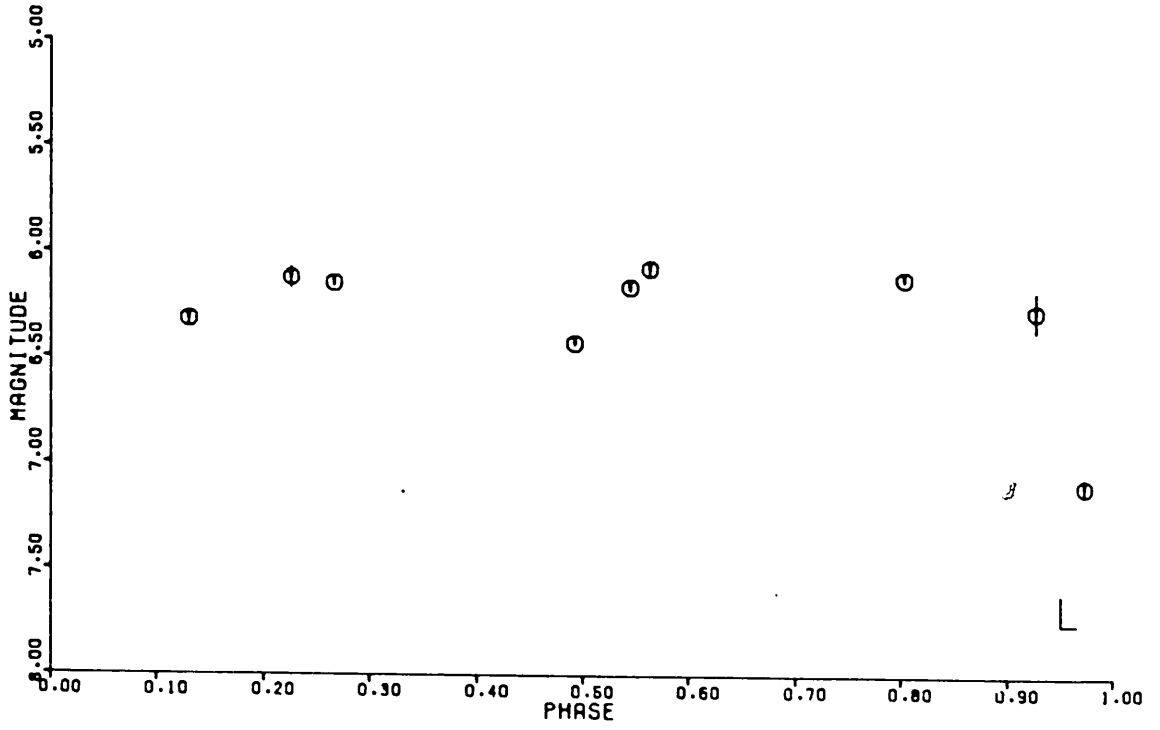
MAGNITUDE
5.00
5.50
6.00
6.50
7.00
7.50
8.00
0.00
0.10
0.20
0.30
0.40
0.50
0.60
0.70
0.80
0.90
1.00
PHASE
L

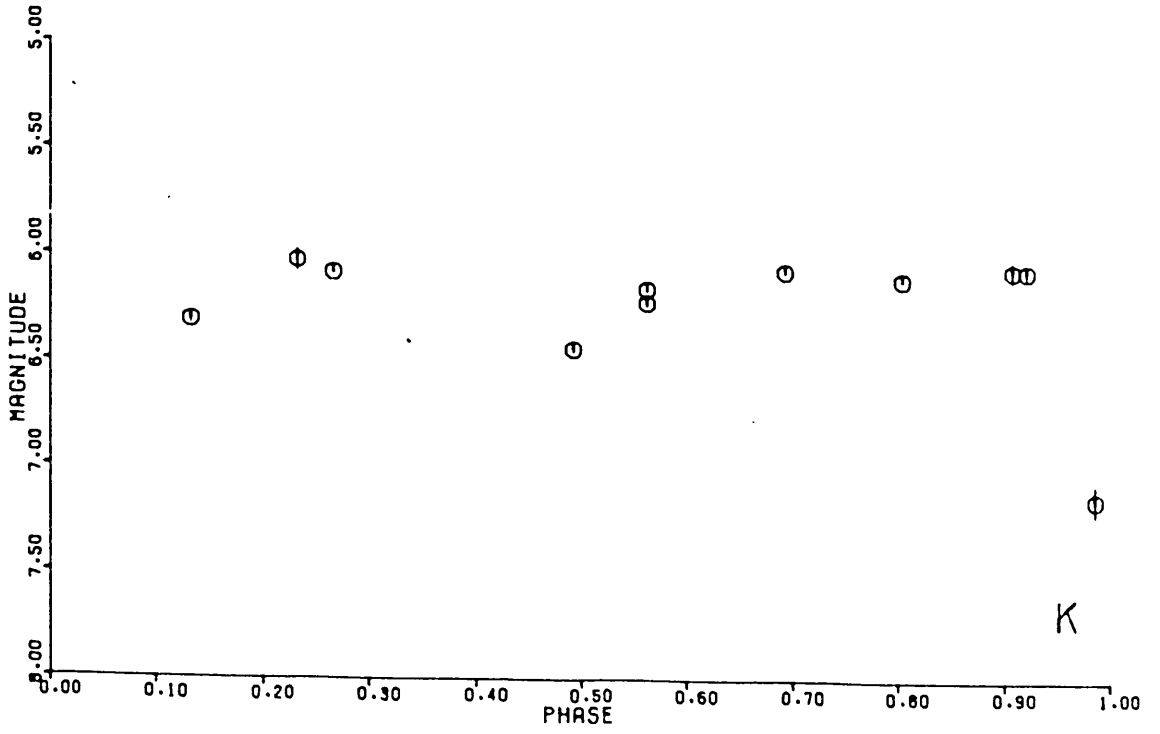
MAGNITUDE
5.00
5.50
6.00
6.50
7.00
7.50
8.00
0.00
0.10
0.20
0.30
0.40
0.50
0.60
0.70
0.80
0.90
1.00
PHASE
K

FIGURE 2.8

VARIATION OF MAGNITUDE NEAR QUADRATURE
WITH WAVELENGTH, FOR U Sge

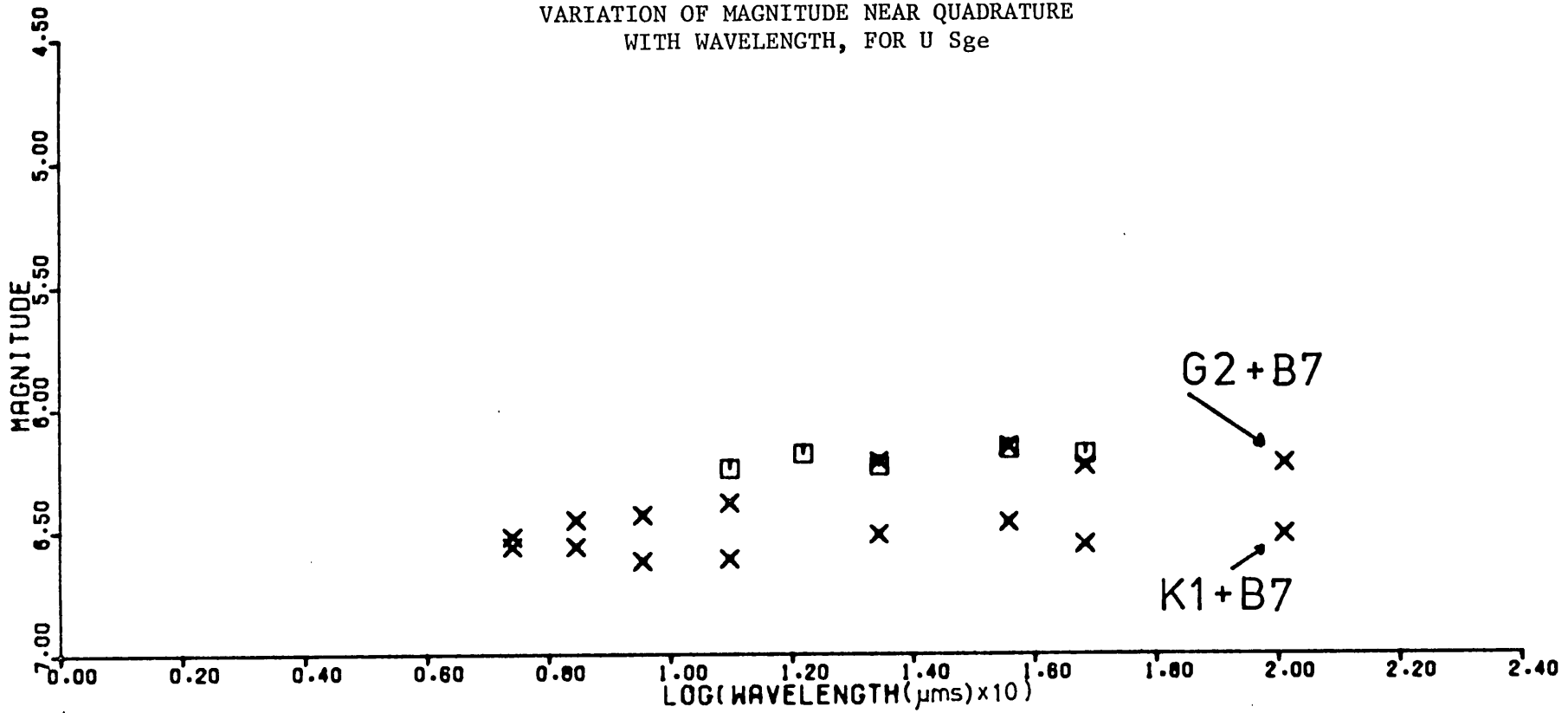

are only J.D. -0.0045 (J.D. 2429111.3228). The data plotted with respect to phase is given in fig. 2.7.

TABLE 2.4

J

JULIAN DATE 24+	PHASE	MAGNITUDE	STANDARD DEVIATION
43294.686	0.492	6.580	0.003
43298.728	0.687	6.170	0.007
43295.743	0.805	6.300	0.004
43300.690	0.268	6.190	0.005
42998.606	0.910	6.235	0.035
42998.649	0.923	6.381	0.042
43005.640	0.991	7.801	0.069
43006.468	0.236	6.146	0.040
43007.502	0.542	6.237	0.012
43007.564	0.560	6.229	0.008
43009.505	0.134	6.398	0.012

H

JULIAN DATE 24+	PHASE	MAGNITUDE	STANDARD DEVIATION
43294.686	0.492	6.480	0.014
43295.740	0.804	6.150	0.007
43298.740	0.691	6.080	0.002
43300.688	0.267	6.010	0.007
42998.600	0.908	6.093	0.033
42998.646	0.922	6.152	0.037
43005.632	0.989	7.294	0.061
43006.463	0.234	6.084	0.030
43007.504	0.542	6.175	0.010
43007.567	0.561	6.160	0.017
43009.502	0.133	6.308	0.012

K

JULIAN DATE 24+	PHASE	MAGNITUDE	STANDARD DEVIATION
43294.686	0.492	6.450	0.011
43295.739	0.803	6.120	0.001
43298.742	0.692	6.080	0.004
43300.686	0.267	6.090	0.003
42998.593	0.906	6.074	0.044
42998.639	0.920	6.077	0.028
43005.622	0.986	7.150	0.070
43006.458	0.233	6.034	0.050
43007.570	0.562	6.229	0.012
43007.570	0.562	6.165	0.007
43009.499	0.132	6.315	0.017

L

JULIAN DATE 24+	PHASE	MAGNITUDE	STANDARD DEVIATION
43294.686	0.492	6.430	0.010
43295.737	0.803	6.120	0.009
43300.685	0.266	6.150	0.015
42998.660	0.926	6.272	0.095
43005.579	0.973	7.098	0.040
43006.435	0.226	6.125	0.050
43007.511	0.544	6.164	0.017
43007.574	0.563	6.076	0.029
43009.491	0.130	6.322	0.036

M

JULIAN DATE 24+	PHASE	MAGNITUDE	STANDARD DEVIATION
43294.671	0.487	6.360	0.132
43295.735	0.802	6.060	0.137
43005.555	0.966	7.003	0.118

We have again assessed the wavelength dependence of magnitude at quadrature. For the various spectral types to be considered we adopt the following colour indices:

Sp.T.	V-R	V-I	V-J	V-K	V-L	V-M	V-N
B7V	-0.04	-0.17	-0.25	-0.35	-0.34	-0.35*	-0.35*
K1III	+0.81	+1.37	+1.80	+2.48	+2.61	+2.36	+2.48
G2III	+0.68*	+1.16*	+1.48*	+2.00*	+2.10*	+1.95*	+1.98*

*Extrapolated values

The respective bolometric luminosities of primary and secondary components are usually given as -1.4, +1.2, following the work of Kopal and Shapley (1956). These in turn are derived from

$$M_{BOL\ 1,2} = M_{\odot} - 5 \log R_{1,2} - 10 \log(T_{1,2}/T_{\odot})$$

where the mean radius $R_{1,2}$ of primary and secondary components are determined from photometric data. Kopal and Shapley give $R_1 = 4.1\ R_{\odot}$, $R_2 = 5.4\ R_{\odot}$. The temperatures are found from the adopted spectral types,

and an appropriate temperature calibration. This latter has since been improved, and is used to determine temperatures for the new spectral types considered here. In addition, we use a revised solar bolometric absolute magnitude $M_{BOL} = +4.75$, and temperature $T_{\odot} = 5770$ K (Allen 1973). The following luminosities are thereby determined:

Sp.T.	M_{BOL}	M_V	T(K)
B7V	-2.01	-1.10	13,500[1]
G2III	+1.09	+1.09	5,770[2]
K1III	+2.09	+2.49	4,580[2]

[1] Schild et al. (1971) [2] Johnson (1966)

where bolometric corrections are derived from the given temperatures, and an appropriate relation from Allen (1973). The photographic magnitudes of U Sge are +6.47 (quadrature), +9.15 (Primary) and +6.57 (Secondary). These may be approximately converted to B magnitudes through the relation $B \simeq M_{pg} + 0.11$ (Allen 1973). For a K1III + B7V system, the corresponding visual magnitude at quadrature is then V = +6.56, and for a G2III + B7V system, V = +6.52. For comparison, Allen (1973) records V = +6.4, and Hoffleit gives V = +6.5.

The extrapolated luminosity at quadrature is presented in fig. 2.8 for the two cases considered here, in addition to the observed magnitudes. The crosses (representing the theoretical extrapolations) are all below the observed values. The upper set of crosses represents a G2III + B7V system, the lower a K1III + B7V system. Clearly, the G2III + B7V indices agree well with observed values. This by itself cannot however be used to distinguish the relevance of this particular combination of spectral types. The work of Fitzgerald (1968) shows U Sge to reside close to the interface of regions possessing differing interstellar extinction . For a distance 0.5 kpc these rates are

$0.1 < E_{B-V} < 0.2$, and $0.2 < E_{B-V} < 0.3$. The (reddened) modulus for a G2III + B7V system would be $m_v - M_V = 6.52 - (-1.24) \simeq 7.76$, corresponding to a distance $R < 356$ pc. There is little variation in upper limit distance for the adopted spectral types, although these are larger than the value determined by Allen (1973) ($R < 250$ pc) using the luminosities of Kopal and Shapley (1956).

It seems likely therefore that $E_{B-V} \gtrsim 0.036$, $A_V \gtrsim 0.11$. If the secondary does have spectral type G2III, then the residuals between extrapolated and observed infrared magnitudes indicate that reddening must be small, and comparable with the lowest possible value consistent with Fitzgerald's (1968) data.

There are however reasons for believing a G2III classification to be more appropriate for the secondary. From the data in fig. 2.7 we evaluate the following magnitude differences $(m_p - m_s)$ between primary and secondary minima:

λ	$(m_p-m_s)_{T1}$	$(m_p-m_s)_{T2}$	m_p-m_s
B	2.58	2.58	2.58
J	0.94	1.10	1.22
K	0.62	0.60	0.70
L	0.58	0.52	0.67
M	0.64	0.64	0.64

There are several sources of possible error in these values. In addition to the usual photometric errors, there are errors arising from the use of values close to, but not precisely at primary and secondary minima. For the B value, there is also an error arising from the difference in $(m_p - m_s)$ between 0.44 μm (the effective wavelength of the B-band) and 0.425 μm (effective wavelength for photographic magnitudes, whose value is the one quoted here). Accepting for the present that the values $m_p - m_s$ presented above are however representative,

we may use the theory described earlier to evaluate $m_p - m_s$ at, say, J, K and L, given the values at B and M. The values thus determined for a G2III + B7V system are presented in the column labelled $(m_p - m_s)_{T1}$. We take $V_2 - V_1 = +2.29$ for the difference between primary and secondary visual magnitudes (from the earlier discussion), and thereby obtain $\alpha_s \simeq 0.90$; reasonably consistent with expectation from the relative mean radii. The predicted values $(m_s - m_p)$ however disagree significantly with the observed values, a problem which is not appreciably evaded by taking a larger $V_2 - V_1 = +3.0$ (column $(m_s - m_p)_{T2}$). The latter difference in luminosities leads also to a quite unrealistic value $\alpha_s \simeq +0.13$. The situation for a K1III + B7V combination deteriorates beyond even this however, since the earlier adopted component luminosities now lead to $\alpha_s = -0.12$ (for data at B and M) or $\alpha_s = -0.16$ (for data at J and M).

It seems likely that these discrepancies are to be attributed to errors in the data, for the B7V + G2III classification, and considerably more photometric work is required to determine the levels of primary and secondary minima. From the value of α_s alone, however, it seems clear that the value $(m_p - m_s)$ at M would have to be considerably (and unreasonably) discrepant for a description in terms of a K1III + B7V system to be viable. There are therefore three preliminary conclusions to be drawn from this work. First, the secondary is almost certainly close to spectral type G2III (this is relatively unaffected by uncertainties in the spectral type of the primary component). Second, on the basis of the latter identification, we may say that reddening is probably very small, considering the location of the binary near the Galactic plane. Finally, both the trend of the data with wavelength, and the possibility of explaining it in terms of a

G2III + B7V system, preclude the liklihood of excesses between minima. Although there is no evidence of phase dependent components of excess emission, it must be conceded that the number of results presented here does not preclude the possibility of short term excesses over limited ranges of phase.

Accepting the most likely interpretation of the data however (i.e. zero excess), if U Sge is representative of Algol systems with gaseous rings, it seems possible that the electron density and/or mass, and/or temperature of the "typical disk" used earlier are serious overestimates. A cautionary note must however be introduced. Kruzewski (1967) finds that gaseous disks are unlikely to form in U Sge, using particle dynamics. Batten (1973) interprets this as an indication of the irrelevance of particle dynamics to disk formation. Batten also however interprets Kruzewski's results as indicating likely instability in disks formed within this and other similar systems. In support of this, he cites the transience of disk emission features in U Sge and other systems (McNamara 1951). In view of this frequent absence of disk emission features for the particular system under investigation, it would clearly be rash to make any broad assertions concerning disk emission either in this system, and other systems generally. We may only say that U Sge appears usually to behave "normally", with no indication of strong excess, and that this must place severe constraints upon the mass of any residual ionised gas within the system. Taken in combination with the results of β Persei, the other Algol system investigated in this chapter, there must therefore be serious doubts that mass transfer in semi-detached systems is sufficient to enable detection at near infrared wavelengths.

2.6 η GEM

η Gem is a spectroscopic binary of period 2983 days (Hoffleit 1964). McLaughlin and Van Dijke (1943) have also proposed that it is an eclipsing variable, although Woolf (1973) suggests that variability arises primarily from ellipticity of the component stars. Deutsch (1960) notes that a nearby G0 III-IV companion at a projected distance of only ~1", may show evidence for circumstellar lines from the circumbinary envelope. The large expansion velocity of this envelope (~26 $km.s^{-1}$) indicated by the results of McLaughlin and Van Dijke "... suggests the very credible inference that mass ejection proceeds more vigorously in the presence of a relatively close companion". Kukarkin et al. (1958) record the primary minimum as

MIN = J.D. 2429355 + 2984E

(the period differs marginally from that of Hoffleit). One component is also a variable of type SRb (Kukarkin et al. 1958) with minimum

MIN = J.D. 2429368.2 + 233.4E

Hoffleit gives the range of variation in visual magnitude as +3.1 - +3.9. We present in table 2.5 some early data obtained for the binary, with appropriate phase of intrinsic and ellipsoidal variability. The primary calibration star is β Gem, for which the following magnitudes were adopted:

H = -1.02; K = -1.09; N = -1.24

TABLE 2.5

H

JULIAN DATE 24+	PHASE 1*	PHASE 2*	MAGNITUDE	STANDARD DEVIATION
2090.4118	0.51	0.268	-1.23	0.01

K

JULIAN DATE 24+	PHASE 1*	PHASE 2*	MAGNITUDE	STANDARD DEVIATION
2090.4222	0.51	0.268	-1.56	0.01

N

JULIAN DATE 24+	PHASE 1*	PHASE 2*	MAGNITUDE	STANDARD DEVIATION
2091.4764	0.51	0.268	-1.87	0.03
2359.6785	0.66	0.358	-1.92	0.11

* PHASE 1: SRb VARIABILITY
  PHASE 2: ELLIPSOIDAL VARIABILITY

The data is also plotted with respect to wavelength in fig. 2.9, in addition to data from Woolf (1973); Gillett, Merrill and Stein (1971); Johnson et al. (1966); and Gehrz and Woolf (1971). The crosses indicate intrinsic magnitudes for an M3III star (Johnson 1966) with magnitude -1.5 at K. None of the infrared data, saving that of Johnson et al. and the new data presented here, has an associated record of the time of observation. Nevertheless, the observations (again excepting Johnson et al.) agree to within a few hundredths of a magnitude at K. The results of Johnson et al. are fainter by ~0.2

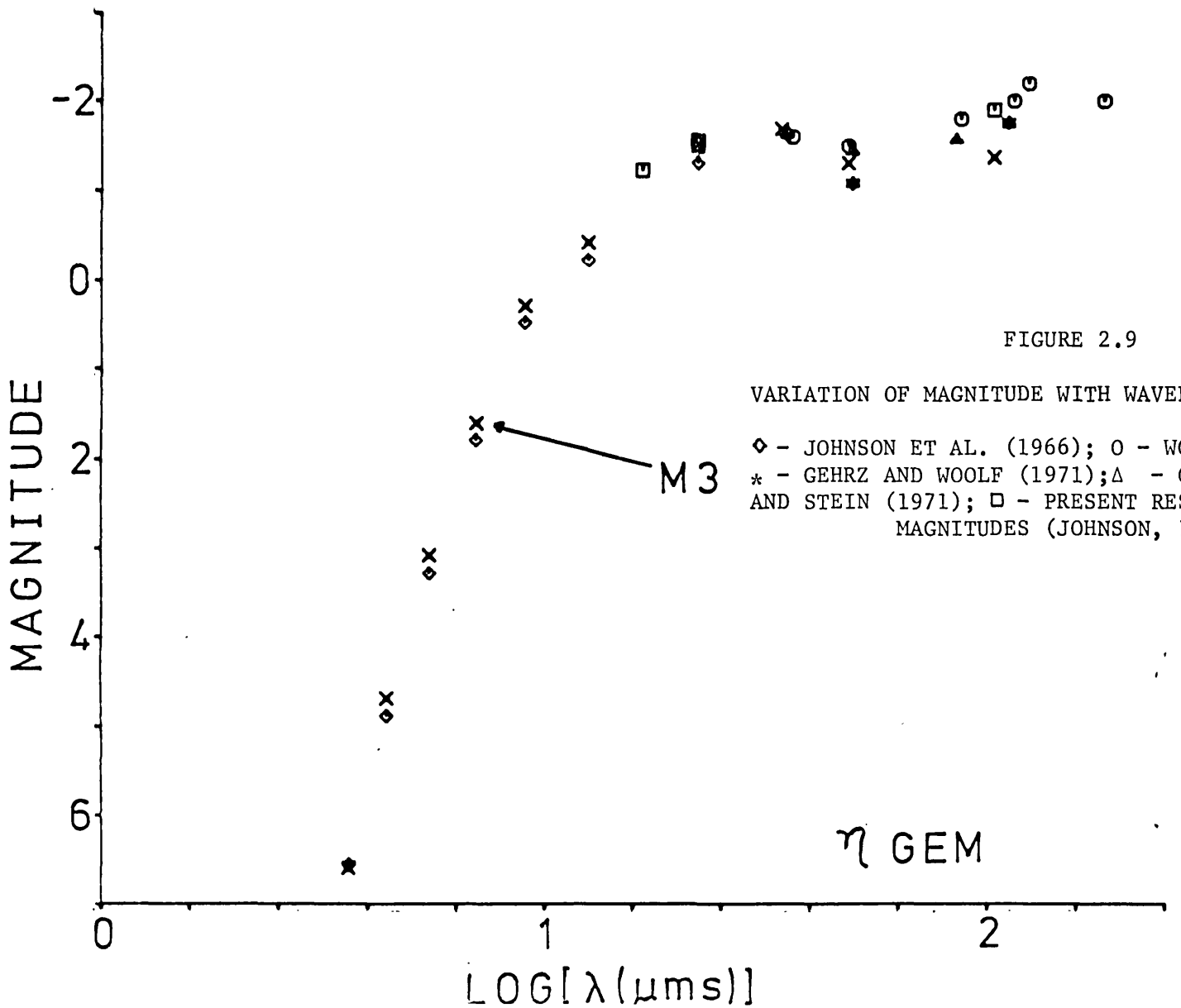

FIGURE 2.9

VARIATION OF MAGNITUDE WITH WAVELENGTH, FOR η GEM

◇ - JOHNSON ET AL. (1966); O - WOOLF (1973); * - GEHRZ AND WOOLF (1971); Δ - GILLETT, MERRILL AND STEIN (1971); □ - PRESENT RESULTS; X - M3 III MAGNITUDES (JOHNSON, 1966)

magnitudes at this wavelength, and retain this difference with respect to the extrapolated M3III magnitudes, down to B. This appears to arise because of data acquisition within the phase range 0.003 to 0.04 of the primary minimum of ellipsoidal variability. When this is allowed for, it is seen that η Gem is a remarkably well behaved binary up to L. The present H data fills a previous observational gap, but the K data agrees well with other observations. Beyond L the scatter in the results is larger, presumably arising from problems in estimating extinction. The present 10.2 μm data however fits in close with Woolf's, providing further support for a small excess emission. Woolf assessed this excess in terms of the ([8.6]-[11.3]) index, as ≃0.3 magnitudes. The extrapolation of M3III intrinsic colours to 10.2 μm indicates a possibly greater excess of ≃0.5 magnitudes. This is rather larger than would normally be expected for a star of this class and, despite Woolf's pessimism, may possibly indicate enhanced mass flow due to the nearby companion star.

2.7 RR UMi

Relatively little is known concerning RR Ursae Minoris. What is known however suggests a possibly interesting object in the same sense as η Gem.

It is, first, a spectroscopic binary of period 750 days (Bidelman 1954) with maximum visual magnitude +4.69 (Hoffleit 1964). The photovisual variation of +6.2 - +6.5 (Kukarkin et al. 1958) arises from semi-regular variability with period of ~40 days (this period is not well established) of the g M5 component. Joy and Wilson (1948) note CaII emission to the red and violet side of the absorption lines (red

emission being about twice as strong as violet), but do not appear to have detected a central chromospheric reversal.

Infrared observations commenced in 1974 for this object, and the catalogue of observations is presented in table 2.6. The primary calibration star was μ UMa, for which we adopted the following magnitudes:

H = -0.68; K = -0.82; L = -0.95; N = -0.93.

TABLE 2.6

H

JULIAN DATE 24+	PHASE	MAGNITUDE	STANDARD DEVIATION
42086.797	0.066	-0.960	0.021
42087.781	0.064	-1.060	0.021
42089.804	0.062	-0.660	0.019
42153.482	0.023	-1.200	0.010
42159.552	0.031	-0.600	0.011

K

JULIAN DATE 24+	PHASE	MAGNITUDE	STANDARD DEVIATION
42087.799	0.064	-1.100	0.053
42089.818	0.062	-0.790	0.029
42153.490	0.023	-1.240	0.003
42086.804	0.066	-1.220	0.015
42159.555	0.031	-0.810	0.006

L

JULIAN DATE 24+	PHASE	MAGNITUDE	STANDARD DEVIATION
42153.501	0.023	-1.350	0.010

N

JULIAN DATE 24+	PHASE	MAGNITUDE	STANDARD DEVIATION
42091.659	0.059	-1.310	0.070
42156.494	0.027	-1.450	0.040
42157.588	0.029	-1.310	0.020
42158.490	0.030	-0.460	0.020
42161.603	0.034	-1.170	0.020
42163.615	0.037	-1.390	0.020

A variability of ~0.7 magnitudes is to be noted at all wavelengths. This is similarly reflected in the 3 sets of I, J, K observations, and 2 sets of J, K, L observations recorded by Johnson et al. Plots with respect to phase assuming 40 day, and 750 day variability (figs. 2.10, 2.11) show no systematic trends. The range of variability is however considerably in excess of the likely error in these results. In both figures, the epoch of initial minimum is arbitrary.

In figure 2.12, H, K, N, and H, K, L, N data, each representing sets of closely spaced observations, are plotted with respect to wavelength. U, B, V, R, I, J, K, L magnitudes* from Johnson et al. (1966) are also given, as well as intrinsic magnitudes for an M5III star (Johnson 1966) fitted to the V magnitude of Johnson et al. No distance is recorded for this binary. Assuming however a typical M5III absolute magnitude $M_V \simeq -0.8$ (Allen 1973) we obtain a (reddened) modulus $m_V - M_V \simeq +5.39$. This places it barely 120 pc from Earth, and since reddening is $\lesssim 0.3$ mags.kpc^{-1} (Fitzgerald 1968) within this region of sky we can consider the reddening of RR UMi to be small.

Perusal of figure 2.12 shows the extrapolated M5III magnitudes to be significantly brighter than the corresponding observed short wave infrared magnitudes, although the N data lies very close to the extrapolated result. This behaviour almost certainly indicates the need for a more refined spectral classification. Colour indices change rapidly with spectral type for M5 and later, and an alteration by a few tenths of a spectral class may lead to considerable changes to predicted infrared magnitudes.

With this in mind, we note that the observed (V-K) index of Johnson et al. (1966), V-K = 5.54, corresponds in fact to a star of

* These results are mean values.

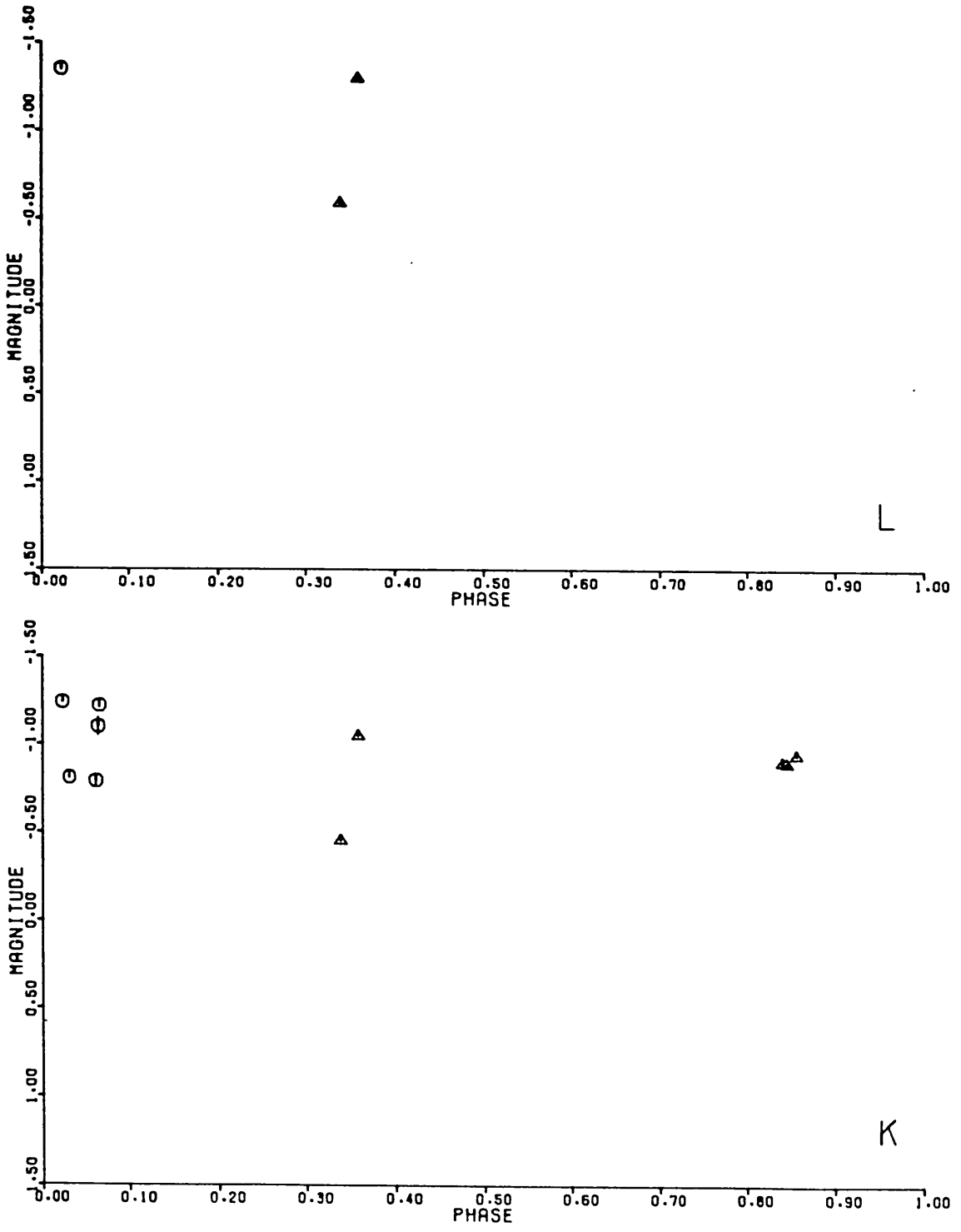

FIGURE 2.10

VARIATION OF MAGNITUDE WITH PHASE OF SPECTROSCOPIC BINARY, FOR RR UMi

Δ - JOHNSON ET AL. (1966); O - PRESENT RESULTS

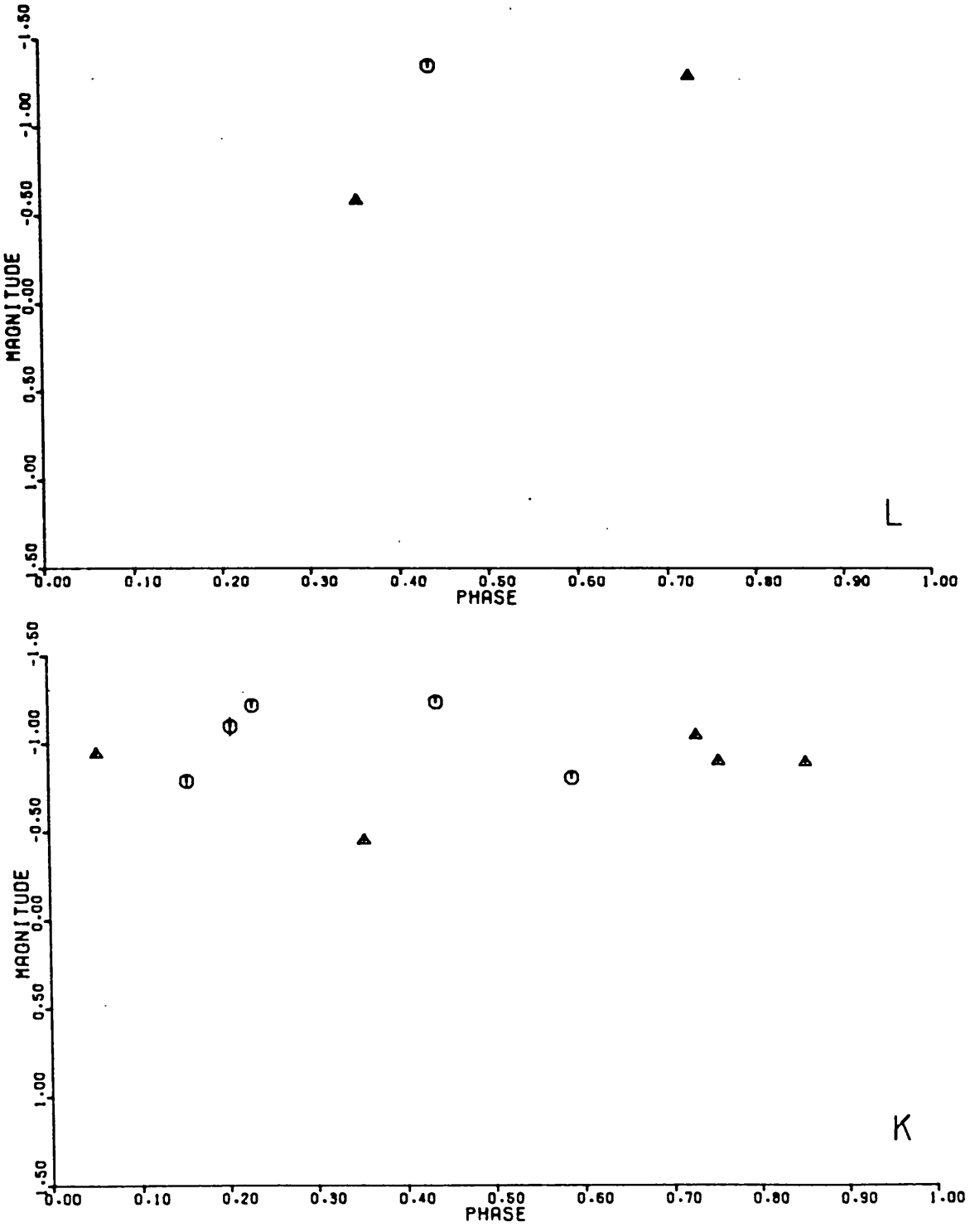

FIGURE 2.11

VARIATION OF MAGNITUDE WITH PHASE OF SRb VARIABLE, FOR RR UMi

Δ - JOHNSON ET AL. (1966); O - PRESENT RESULTS

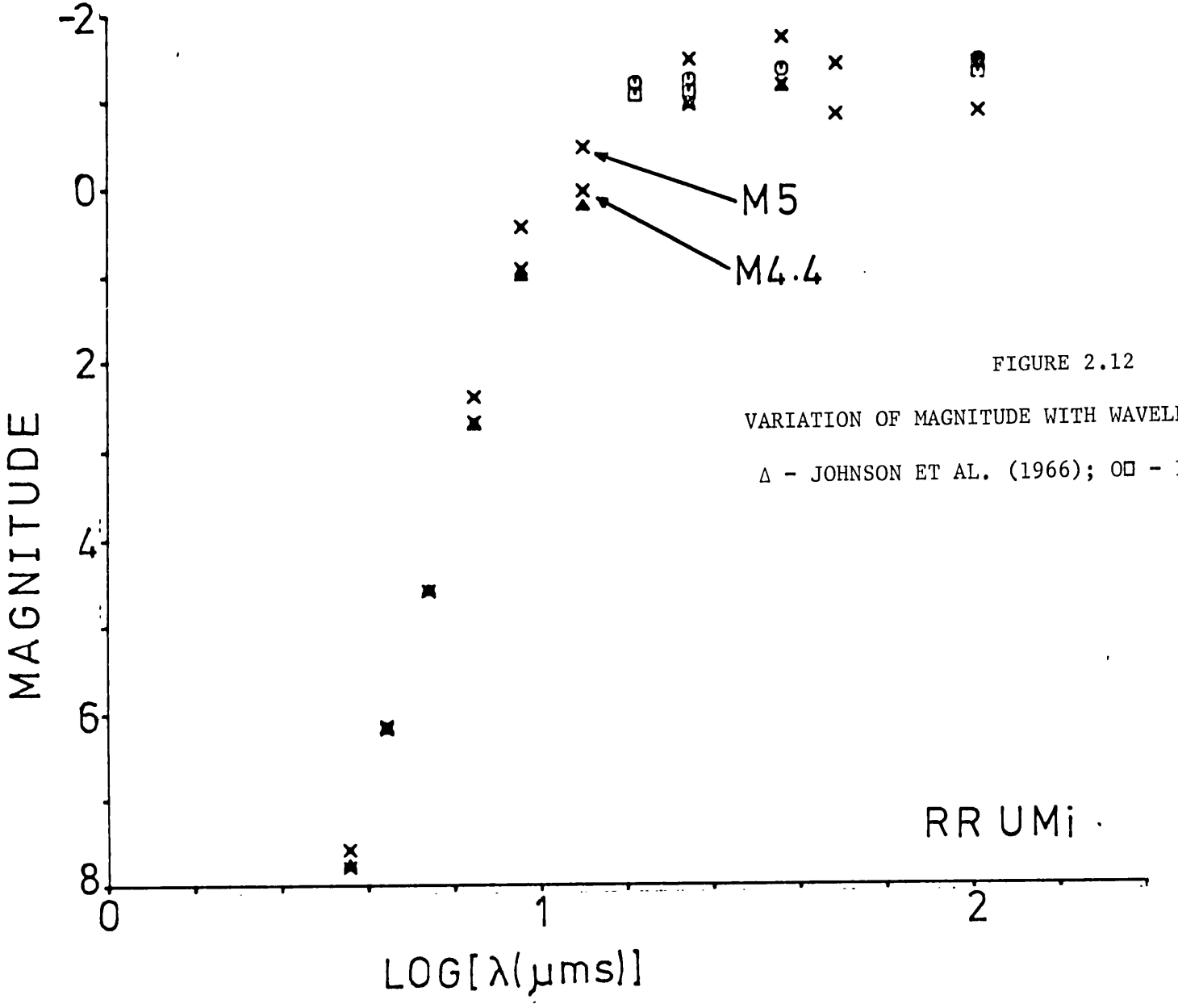

FIGURE 2.12

VARIATION OF MAGNITUDE WITH WAVELENGTH FOR RR UMi

Δ - JOHNSON ET AL. (1966); O□ - PRESENT RESULTS

spectral type ~ M 4.4, for which other colours would be approximately:

V-N = +5.45; V-M = +5.42; V-L = +5.76; V-J = +4.55

V-I = +3.66; V-R = +1.90; B-V = +1.58; U-V = +3.20

The indices provide an excellent fit to observed Johnson short wave magnitudes, and are correspondingly plotted in fig. 2.12, fitted as for the M5III results to a magnitude V = +4.59. The observed (K-N) indices presented here, (K-N) ≃ +0.21, are however ~ +0.30 magnitudes in excess of that expected for an M 4.4 III star, suggesting a corresponding continuum emission excess of this order. Should this be confirmed, it is if anything rather small for a star of this class. It must therefore be concluded that, despite the apparent presence of displaced calcium emission components, the formation of dust does not appear to be particularly prolific near RR UMi, and there are therefore no grounds for supposing enhanced mass loss arising from the presence of a companion star. Apart from this, it is not possible to make any firm generalisations since, as Woolf points out, companion stars may inhibit dust formation (through grain sublimation), as they enhance mass flow.

2.8 Conclusions

If we are to draw any conclusions from the above discussion, it is that Algol systems appear likely to show little sign of near infrared excesses. The residual gas within a typical system appears to be too small for detection. As usual with any rule, there are almost certainly exceptions. Particularly promising candidates in this last respect may be those binaries displaying distortion of light

curves attributed to absorption by gaseous streams (c.f. Walter 1973). Other systems displaying particularly strong emission from circumprimary gaseous rings may also display excesses, although U Sge did not.

As binary separations decrease, so mass loss/transfer may become more extreme. This certainly appears to be the case with β Lyrae, although the system may in many respects be unique. Observations of other β Lyrae systems are required, and particular note should perhaps be made of HD 30353 and ν Sgr in this respect (Woolf 1973). The β Lyrae system itself appears to contain a very hot, optically thin, free-free emitting plasma close to the location of the secondary component, and further observations at longer wavelengths are required to determine the spectrum turn-off point corresponding to optical thickness. Finally, for W UMa, although transfer of mass and energy is occurring through the inner Lagrangian point, this is probably taking place within an optically thick common convective envelope. The presence of flares may cause transient increases in infrared flux, but in the quiescent state W UMa appears to behave normally in the infrared, with no evidence of emission excesses.

Finally, the two systems with SRb variable components (η Gem and RR UMi) both appear to show small excesses, which in neither case is particularly anomalous. It appears likely therefore that normal mass loss for these variables is relatively unaffected by close companions.

CHAPTER 3

THE INTERPRETATION OF OBSERVED NEBULAR STRUCTURES

3.1 Introduction

We will be concerned in this chapter to interpret the observed emission structures of nebulae in terms of corresponding physical structures. There have been various attempts to do this in the past. One of the earliest is due to Curtis (1918), who suggested that planetary nebulae may be oblate spheroidal structures. In attempting to fit this model to the observations however, he was forced to introduce arbitrary increases of density at strategic points within the shells; and for one case (NGC 6720) concluded that the available evidence was best supported by supposing NGC 6720 to be a toroid. This represents what may be termed the empirical approach. We will later find that, particularly with more modern techniques at our disposal, a careful analysis of the available data can impose powerful constraints upon the physical structures of nebulae. With more restricted data, these constraints are loosened and structural descriptions of nebulae become ad hoc; as reflected in the proliferation of models for single nebulae.

Theoretical models cannot replace an empirical approach, but may provide a useful adjunct to the interpretation of observed structures, possibly leading to new lines of observational attack. Theoretical and empirical approaches may therefore be considered as complementary, and we will illustrate the application of both these methods in the following section. Much of the work has been published

in Hicks, Phillips and Reay (1976), Phillips and Reay (1977), and Phillips, Reay and Worswick (1977). For the illustration of empirical methods, we will only summarise the basic procedures; it is intended that direct reference should be made to the relevant published papers for a more complete discussion.

For the initial theoretical discussion in this section, Phillips and Reay (1977) may again be consulted. In this case however we have chosen to expand certain aspects of this discussion, and recast the framework of the argument. The discussion is therefore given in complete form, and no reference to the earlier publication is necessary.

3.2 Theories of Nebular Structure

The theoretical investigation of the formation of non-spherical nebular structures is a time dependent hydrodynamic problem. Previous treatments have however tended to eschew this line of approach in its more rigorous form, presumably because of its complexity, and opted for a simpler discussion of the primary mechanisms involved, and their broad consequences. In this respect the present work is no exception. We are concerned to understand the basic causes of shell shape and, making some plausible assumptions concerning density structure, temperature, etc. within the shells, to evaluate the morphological types that may ensue. Simulated emission maps of certain of the models are then compared with representative nebulae, in a critical final assessment of the proposed mechanisms. Earlier attempts to explain shell structure have invoked magnetic fields, ejection by rotating stars, and the effect of uniform internal pressure upon slightly distorted shells. Of these, magnetic processes have received most attention(see for instance Woyk, 1968; Gurzadyan, 1969) although the discussion by

Menzel (1968) (who finds fields effective only for plasma temperatures $\lesssim$1 K) appears to seriously question their actual effectiveness in these circumstances. An apparent trend for nebulae to be orientated non-randomly with respect to the galactic plane (Cudworth, 1975; Melnick and Harwit, 1975; Grinin and Zvereva, 1968) may however reflect at least some influence upon shell shapes due to the galactic magnetic field.

Most recently, Kirkpatrick (1976) has considered the development of shells under the influence of a continuous accelerative process (of the kind produced by ablation of the inner surface) and concludes that prolate forms may develop, although this result is dependent upon the assumptions employed. Louise (1973) has discussed a model involving the ejection of a nebular envelope from a spherical rotating star. Although the contribution of gravity is discussed qualitatively the analytical treatment is confined to cases where the gravitational retardation is negligible, whence nebulae acquire oblate spheroidal shapes.

The present discussion is in some respects intended as a correction, and advance upon the investigation by Louise. We again consider the ejection by a rotating star, which is now however oblate, and consider both gravity and radiation pressure at an analytical level. We shall assume that mass is ejected from the central star with sufficient energy to escape. Possible modes for this ejection process are summarised by Salpeter (1971) and more recent work on ejection through pulsational instability is given by Härm and Schwarzschild (1975), Kutter and Sparks (1974) and Smith and Rose (1972). It will be noted that this ejection mode almost certainly requires some Mira-like star as progenitor, having as they do low escape velocities ($\sim$30 km.s^{-1}).

In contrast, the presently observed central stars have escape velocities some two orders of magnitude greater, and to acquire observed nebular terminal velocities of ~20 $km.s^{-1}$ would require ejection velocities to be unrealistically close (within ~0.02%) to the escape velocities. This ejection mode differs from certain other treatments, which presume a transfer of entropy from the nebula to the radiation field, and a consequent steady mass loss at a rate below escape velocity (c.f. Finzi and Wolf, 1970, 1971; Faulkener, 1970). A problem with this latter mechanism however is that there appear to be no obvious evolutionary tracks to the supposed progenitors (i.e. the present central stars) (Osterbrock, 1974). To acquire the distinctive shapes of planetary nebulae, other processes must also be invoked; possibly Kirkpatrick's mechanism, or magneto-dynamic mass redistribution.

In a similar vein Paczynski (1971), whilst accepting Mira variables as progenitors, suggests that the weak, presumably radiatively-driven, mass loss characteristic of these stars may be the ultimate cause of planetary nebulae.

The characteristics of mass emission from M-type stars have been conveniently summarised by Wilson (1960), and these need few amendments. Specifically, it is found that mass is emitted at a unique velocity which appears to be invariant with distance from the star, and below the stellar escape velocity (suggesting that the mass flow is powered by the radiation field). The mass loss rate dM/dt for Miras has been found more recently (Gehrz and Woolf, 1971) to be $\simeq 2 \times 10^{-6}$ $M_{\odot}.yr^{-1}$. We do not believe this continuously-driven mass flow to be a likely origin of planetary nebula shells, however, for the following reasons.

If mass flow from Miras is similar to other M-type stars, a lower limit velocity $V_{ML} \simeq 5$ km.s^{-1} may be adopted.

A corresponding lower limit to the mass loss rate $(dM/dt)_{ML}$ for the period of shell emission may then be obtained from

$$\left(\frac{dM}{dt}\right)_{ML} = 4 \pi r_n^2 V_{ML} \cdot n_e \cdot \varepsilon \cdot M_H \quad \ldots (3.1)$$

where M_H is the hydrogen atom mass, r_n the nebular radius, n_e electron density, and ε the filling factor.

Values of $(dM/dt)_{ML}$ are given in table 3.1. The nebulae are those selected by Phillips and Reay (1977) from Allen (1973). The data is now taken from Kaler (1970)(n_e and ε) and Cahn and Kaler (1971) (r_n) however. It is seen that although typically $(dM/dt)_{ML}$ are smaller than the values quoted by Phillips and Reay, they are still significantly above the requirements of Paczynski ($(dM/dt)_{ML} \simeq 2 \times 10^{-6}$ $M_\odot.yr^{-1}$). Only very serious revision of nebular parameters would enable agreement, to a degree which at this stage appears unacceptable. It seems therefore rather unlikely that this mechanism can really account for observed nebulae.

If we turn to a purely explosive model on the other hand, and assume that any acceleration or deceleration of the shells occurs only in the initial stages of expansion, then we would expect nebula shape to reflect the variation in radial velocity over the shell surface; ellipsoid-like shells should for instance be generally matched by a corresponding velocity ellipsoid. Wilson (1958) has remarked that the observational evidence for this is very strong, and Weedman (1968) has subsequently noted that generally

$$r_n = S \cdot V_n + P \quad \ldots (3.2)$$

TABLE 3.1

MINIMUM MASS LOSS RATES FOR SELECTED PLANETARY NEBULAE

Nebula	r (pc)	n_e	ε	$(dM/dt)_{ML}$
NGC 2392	0.118	9.59×10^3	0.14	2.95×10^{-5}
3242	0.091	3.23×10^3	0.22	9.30×10^{-6}
6210	0.080	6.55×10^3	1.00	6.62×10^{-5}
6543	0.071	7.99×10^3	0.30	1.91×10^{-5}
6572	0.055	9.46×10^3	1.00	4.52×10^{-5}
6720	0.125	9.90×10^2	0.32	7.82×10^{-6}
6853	0.271	4.2×10^2	0.40	1.95×10^{-5}
7009	0.094	6.13×10^3	0.30	2.57×10^{-5}
7027	0.055	1.47×10^4	1.00	7.03×10^{-5}
7662	0.082	4.69×10^3	0.90	4.48×10^{-5}

where S and P are constants, and r_n, V_n are the nebular radius and velocity. Typically $P \simeq 0.3\ r_n$: the fact that $P > 0$, suggesting some influence upon shell motions for a finite period after ejection. In this respect it will be noted that values of P are similar to (although rather smaller than) the value determined by Cahn and Kaler (1971) for r_{th} ($\simeq$0.04 pc), where r_{th} is the radius for which a shell becomes optically thin.

Consider then a segment of nebular shell of thickness dr, subtending solid angle $d\Omega$ at distance $r(\beta)$ from the central star. The radial component of nebular acceleration may then be written

$$m\frac{d\underset{\sim}{r}(\beta)}{dt^2} = -\frac{GmM_*\underset{\sim}{r}(\beta)}{r^3(\beta)} + \frac{L_*d\Omega\underset{\sim}{r}(\beta)(1-e^{-\tau(\beta)})}{4\pi r(\beta)c} - d\Omega(\nabla(P_g+P_R).\underset{\sim}{r})\ .\ \underset{\sim}{r}\ .\ dr \qquad \ldots (3.3)$$

where M_*, L_* are the stellar mass and luminosity respectively, β is the angle between the stellar equatorial plane and radius vector $\underset{\sim}{r}(\beta)$, $\tau(\beta)$ is the shell optical depth, and P_g, P_R are respectively gas and Lyman α photon pressures. When a spherical shell is involved, this corresponds to the general equation of motion, and making this assumption a very similar equation is investigated in the final chapter. Generally however, for the third term on the right hand side $\underset{\sim}{\nabla} \neq (d/dr)\hat{\underset{\sim}{r}}$ and some non-radial mass redistribution will occur. The contribution of this third term is neither clear nor analytically trivial, although initially it will be relatively small due to low U.V. radiant flux, plasma temperatures, and subsequent adiabatic cooling. Its contribution will be considered qualitatively later. The first two terms in the equation represent the respective contributions of gravitational braking and Lyman continuum (Ly_c) radiation pressure. We consider first the development of the shell under the influence of the first term. The

less certain contribution of Ly_c pressure to the shell shape will be investigated separately.

A first point to note is that we will be dealing with terminal configurations alone. Louise (1973) has argued that some nebular shells may be wholly or partially in the process of collapsing back towards the star so that there could be cases where terminal shell shapes are not appropriate. In fact, such nebulae are most unlikely to the observed, even though they probably occur. This may be readily seen by noting that

$$\frac{\Delta V}{V_{esc}} = -\frac{1}{2} \cdot \frac{R_*}{r_n}$$

for a shell brought to a standstill in the gravitational field. ΔV is the difference between the ejection velocity and the escape velocity V_{esc}. For a nebular radius $r_n \simeq 10^{17}$ cm (below which the structure of very few planetaries has been resolved) and stellar radius $R_* \simeq 200\ R_\odot$, we obtain $\Delta V/V_{esc} \simeq 7 \times 10^{-5}$ which, for $V_{esc} \simeq 35$ km.s^{-1} gives $\Delta V \simeq 2.45$ m.s^{-1}. So, unless ejection velocities are exceptionally close to the escape velocity, it is unlikely that gravitationally unstable structures of this kind will be observed.

Consider now the ejection of an element of shell perpendicular to the surface of a rotating star. The situation is illustrated in figure 3.1. Following the commonly accepted discussion of Jeans (1928), the photospheric layers are taken to follow the equipotential surface so that

$$\frac{G\,M_*}{R(\theta)} - \frac{R_*^2(\theta)\ \omega^2(\theta)\ \sin^2\theta}{2}$$

is constant, where $R(\theta)$, $\omega(\theta)$ are the radius, angular velocity of the

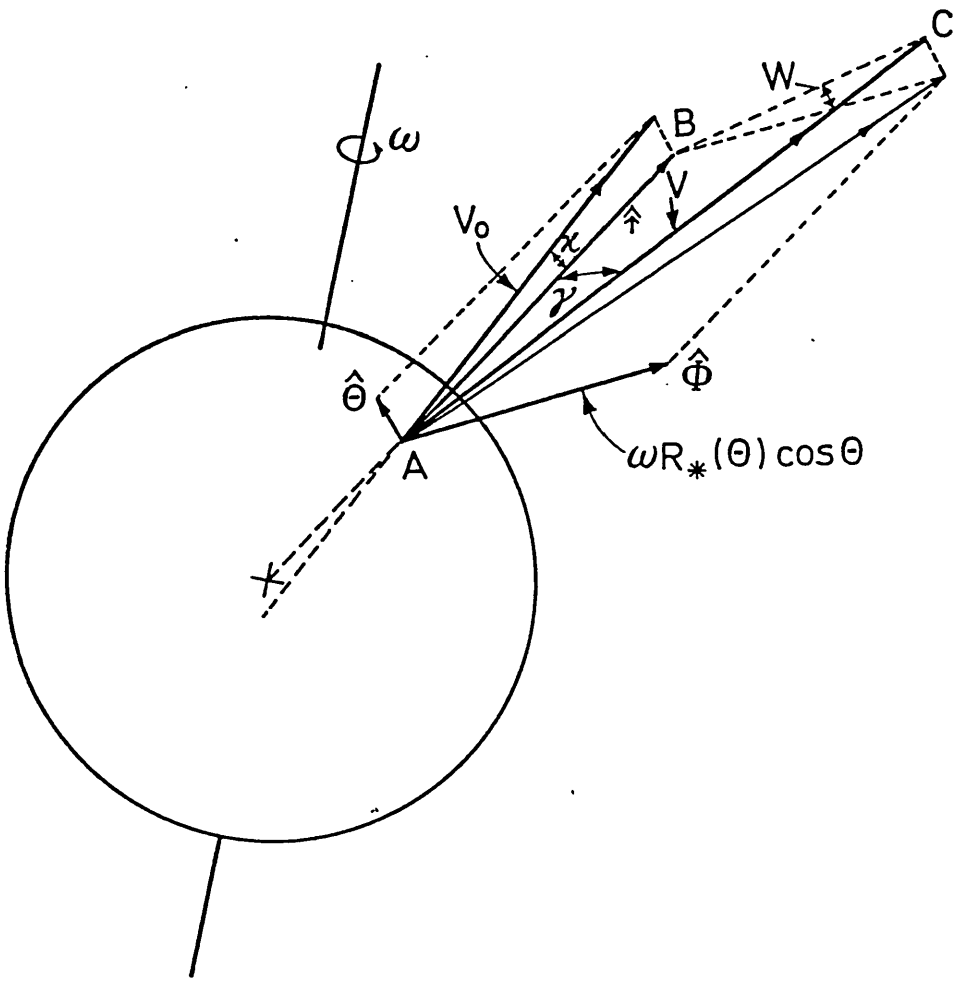

FIGURE 3.1

GEOMETRY OF MASS EJECTION FROM A ROTATING STAR

surface layers at stellar latitude θ. It follows that to a reasonable approximation the stellar surface layers have a figure

$$R_*(\theta) = R(0)\left\{1 - \frac{\omega^2 R_*^3(0) \sin\theta}{2 G M_*}\right\} \qquad \ldots (3.4)$$

providing that $\omega^2 R^2(\theta)/V_{esc}^2(\theta) \ll 1$, where $V_{esc}(\theta)$ is the escape velocity

$$V_{esc}(\theta) = \left\{\frac{2 G M_*}{R_*(\theta)}\right\}^{\frac{1}{2}} \qquad \ldots (3.5)$$

When $\omega^2(\theta) R_*^2(\theta)/V_{esc}^2(\theta) \to 1$, higher order terms in the expression for $R(\theta)$ begin to acquire importance, involving the moments of inertia about the polar and equatorial axes. For red giants however we anticipate $\omega^2 R_*^2(\theta)/V_{esc}^2(\theta) \lesssim 0.01$, and the equation should be reasonably representative of most red giants. This of course excludes the question of whether $\omega = \omega(\theta)$, a point we will cover later. For the present we let ω = constant.

The mass element has ejection velocity V_o, and is taken to be ejected perpendicularly to the photospheric layers, whence

$$\underset{\sim}{V} = \hat{\underset{\sim}{r}}\, V_o \cos\kappa + \hat{\underset{\sim}{\theta}}\, V_o \sin\kappa + \hat{\underset{\sim}{\phi}}\, \omega R_*(\theta) \cos\theta,$$

i.e.
$$V^2 = V_o^2 + \omega^2 R_*^2(\theta) \cos^2\theta \qquad \ldots (3.6)$$

where $\hat{r}$, $\hat{\theta}$ and $\hat{\phi}$ are spherical unit vectors, κ is the angular deviation of $\underset{\sim}{V}_o$ from $\underset{\sim}{r}$, and

$$\kappa = \tan^{-1}(V_{esc}^2(\theta)/(V_{esc}^2(\theta)\cos\theta - 2 R_*^2(\theta)\,\omega^2 \cos^2\theta)) - \theta \quad \ldots (3.7)$$

It will be seen that $\underset{\sim}{V}$ is inclined at angle γ to $\hat{\underset{\sim}{r}}$ within the plane ABC, defined by these two vectors, where

$$\gamma = \tan^{-1}\left[\omega\, R_*(\theta)\, \cos\theta / V_o \cos\kappa \cos W\right] \qquad \ldots (3.8)$$

where ABC is in turn tilted at angle W to the plane containing $\hat{\underset{\sim}{r}}$, $\hat{\underset{\sim}{\phi}}$, and

$$W = \tan^{-1}\left[V_o \sin\kappa / \omega\, R_*(\theta) \cos\theta\right] \qquad \ldots (3.9)$$

Within the plane ABC the mass element will traverse a hyperbolic orbit of eccentricity

$$\varepsilon = \left\{1 + \frac{4\left[V_o^2 + \omega^2 R_*^2(\theta)\cos^2\theta - V_{esc}^2\right]\left[V_o^2 \sin^2\kappa + \omega^2 R_*^2(\theta)\cos^2\theta\right]}{V_{esc}^4}\right\}^{\frac{1}{2}}$$

Again, from the properties of hyperbolic orbits

$$R = \frac{a\,(\varepsilon^2 - 1)}{1 + \varepsilon \cos\phi} \qquad \ldots (3.10)$$

So for $R = \infty$ we may define a terminal angle

$$\phi_\infty = \cos^{-1}\left\{-\frac{1}{\varepsilon}\right\} \qquad \ldots (3.11)$$

and an initial angle ϕ_o

$$\phi_o = \cos^{-1}\left\{\frac{a\,(\varepsilon^2 - 1)}{R_*\varepsilon} - \frac{1}{\varepsilon}\right\} \qquad \ldots (3.12)$$

At infinity therefore the mass element subtends a terminal angle χ to the direction of the initial radius vector $R(\theta)$,

$$\chi = \phi_\infty - \phi_o \qquad \ldots (3.13)$$

Alternatively, the terminal angle between radius vector and stellar equatorial plane is

$$\beta = \tan^{-1}\left\{\frac{\sin\chi\sin W\cos\theta+\cos\chi\sin\theta}{(\sin^2\chi\cos^2 W+\cos^2\chi\cos^2\theta+\sin^2\chi\sin^2 W\sin^2\theta-2\sin\chi\sin W\sin\theta.\cos\chi.\cos\theta)^{\frac{1}{2}}}\right\} \qquad ...(3.14)$$

and terminal velocity is

$$V_T^2(\beta) = \omega^2 R_*^2(\theta)\cos^2\theta + V_o^2 - V_{esc}^2 \qquad ...(3.15)$$

In the absence of appreciable radiative acceleration, equations 3.6 to 3.15 enable the determination of a terminal velocity surface. Particular examples of these surfaces for constant α, $V_{escp} = 35$ km.sec^{-1} (the polar escape velocity) are given in figure 3.2. For $\omega^2 R^2(0)/V_{escp}^2 \to 0$ it can be readily shown that these, to a good approximation, asymptotically approach the form

$$r_t(\beta) = r_t(\pi/2)(1 + (\alpha^2-1)\cos^2\beta)^{\frac{1}{2}} \qquad ...(3.16)$$

where α is the ratio between the terminal nebular axis in the stellar equatorial plane, and the nebular axis in the polar direction

$$\alpha^2 = (1 + 2\omega^2 R_*^2(0)/(V_o^2-V_{escp}^2)) \qquad ...(3.17)$$

For two shells (subscripted 1 and 2) ejected simultaneously with differing velocities, we also have

$$r_1(0) = r_2(0)(\alpha_1/\alpha_2)\left\{\frac{\alpha_2^2-1}{\alpha_1^2-1}\right\}^{\frac{1}{2}} \qquad ...(3.18)$$

Given then a shell of finite thickness acquired primarily through velocity dispersion within the shell, the value α of the outer surface is related through this last equation to that of the inner surface. We will return to this point later.

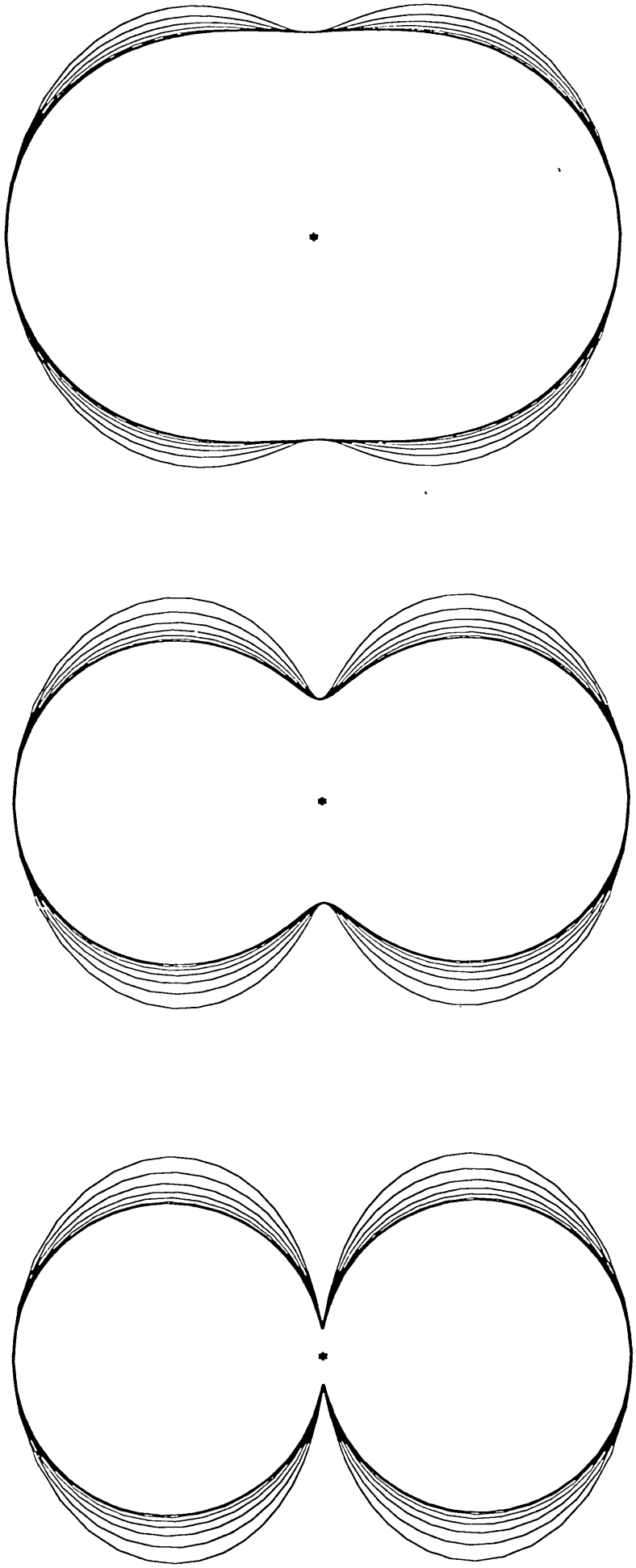

FIGURE 3.2

TERMINAL NEBULAR SHAPES. $\omega R_{\star}(0)$ = 17.5 km.sec^{-1} FOR OUTER CONTOUR, DECREASING BY 2.5 km.sec^{-1} FOR SUCCESSIVE INNER CONTOURS. V_{escp} = 35 km.sec^{-1}.

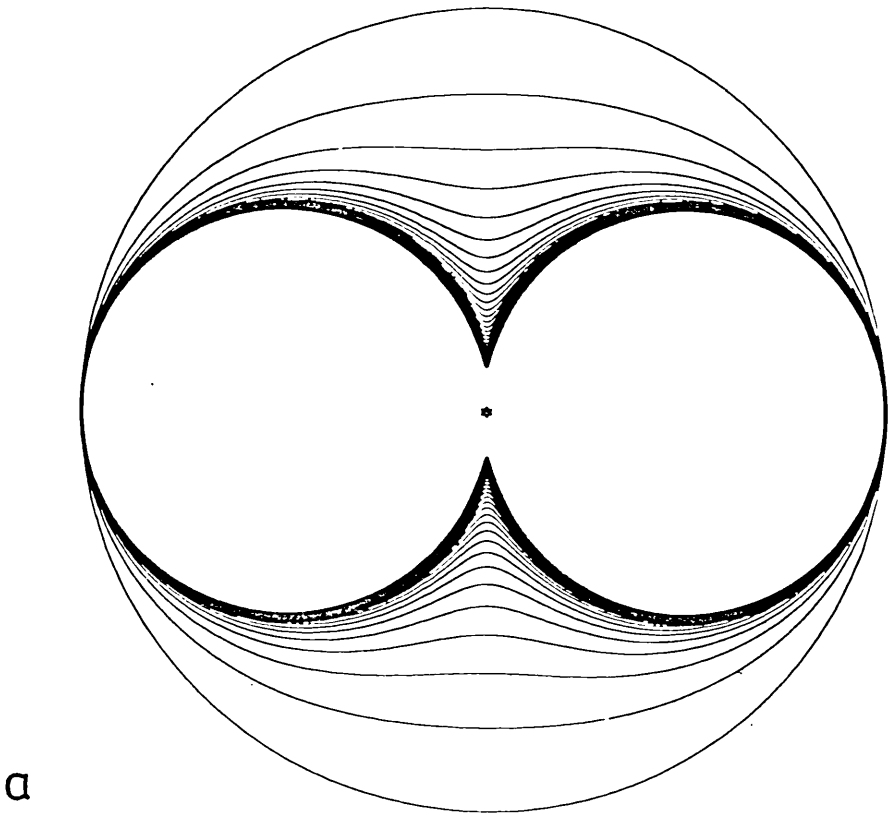

a

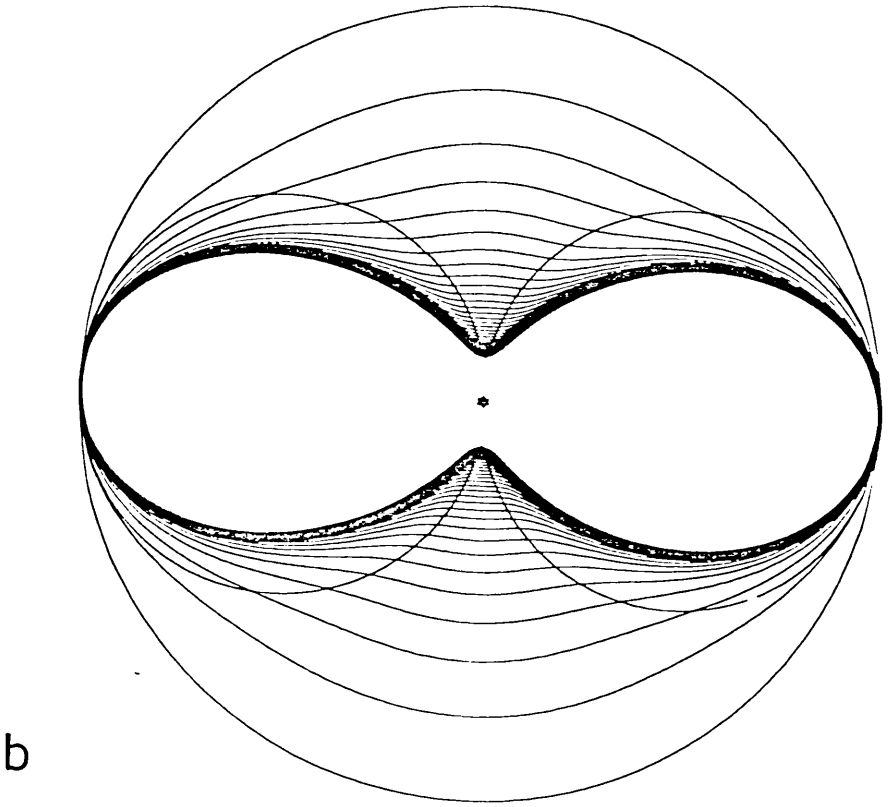

b

FIGURE 3.3

TERMINAL NEBULAR SHAPES AFTER GRAVITATIONAL BRAKING

a. $\omega \neq \omega(\theta)$. b. $\omega = \omega_o(1-0.8 \sin^2\theta)$

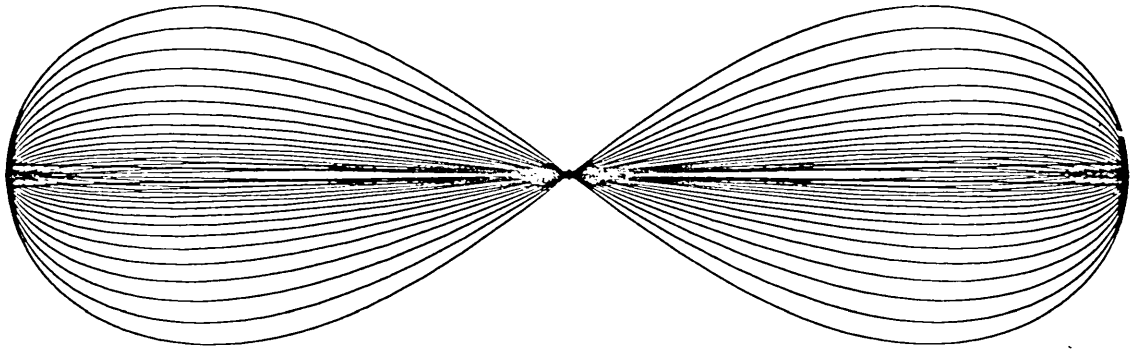

FIGURE 3.4

TOROIDAL SHELL PROFILES

Before doing so, however, it should also be noted that the asymptotic form (equation 3.16) for terminal nebular radius is convenient in allowing the determination of a wide range of representative hydrogenic isophotal contour maps for comparison with observed nebulae, thereby allowing some assessment of the suggested physical mechanism. This will also be done later. An illustration of the range of relevant shapes is presented in figures 3.3a and 3.4.

Clearly, within the context of explosive mass ejection, there are several possible means of removing mass to infinity, irrespective of any subsequent evolution of shell. We shall represent these in terms of three extreme ejection modes. In the first, ejection mode A, we take mass to be ejected with a range of velocities at a single time. Subsequent shell thickness is primarily determined through the initial velocity dispersion within this mass. For ejection mode B, mass is ejected at a single velocity, but over an extended temporal period. This is superficially similar to the situation apparently pertaining in many Miras and red giants, although as we have noted, mass loss rates in these stars appear to be inadequate to explain the shell densities and velocities actually observed in planetaries. Finally, for mode C we assume instantaneous ejection at a single velocity. This is taken to give rise to a shell in which thermal and (primarily) Ly_{α} radiative pressures are dominant in the acquisition of finite shell thickness, and within which density is constant. Since $dM(\theta)/d\Omega$, the mass ejected per unit solid angle at angle θ in the absence of appreciable rotation, is taken to be roughly constant, the shell thickness for mode C ejection will be inversely proportional to the mean shell radius. For thermal expansion alone expansion might be expected to be at sonic velocities and, given roughly constant nebular

temperature, then a uniform expansion around mean shell radius may be more appropriate. As we shall see however, the morphological forms of the model nebulae are surprisingly stable against assumptions concerning the shell density structure, and the proposed shell ejection modes are almost certainly adequate in representing the range of nebular forms to be expected of explosive mass ejection.

The appropriate density radial dependencies are readily determined. For mode C, as we have noted,

$$\rho(r) = \text{constant} \qquad \ldots(3.19)$$

and for mode B ejection

$$\rho(r) = \rho_I \ (\beta=0) \left\{\frac{r_I^{\,3}(\beta=0)}{r_I(\beta)\ r^2(\beta)}\right\} \qquad \ldots(3.20)$$

where subscript I refers to conditions on the inner surface of the shell. For mode A ejection a little more development is required.

We define a mass emission function $\eta(V_o)$, where $\eta(V_o)\Delta V_o$ is the mass ejected possessing velocities between V_o and $V_o+\Delta V_o$. For the present we let $\eta(V_o) = 0$ for $V_o > V_2$, $V_o < V_1$ $(V_2 > V_1)$, and $\eta(V_o) = 1$ for all other velocities. This is generalised later. For an element of shell of area A (at time $t_s = 0$), and radius $r_t(\beta)$ at time t_s, the value is

$$V = \Delta V_t \ . \ t_s \ . \ A \ . \left\{\frac{r_t}{R_*}\right\}^2 \qquad \ldots(3.21)$$

where ΔV_t is the shell terminal velocity dispersion corresponding to an initial velocity range ΔV_o. Consequently, if $\eta(V_t)$ is the terminal mass function

$$\rho(V_t) = \frac{\eta(V_t).\Delta V_t}{V} \qquad \ldots(3.22)$$

and since

$$\eta(V_t)\Delta V_t = \eta(V_o)\Delta V_o \qquad \ldots(3.23)$$

then

$$\rho(V_t) = \frac{\eta(V_o)\Delta V_t}{V} \cdot \frac{V_t}{V_o} \qquad \ldots(3.24)$$

whence taking $r_t = V_t.t_s$ and noting that

$$r_t = ((V_o^2 - V_{esc}^2) + 2\omega^2 R_*^2 \cos^2\beta)^{\frac{1}{2}} t_s \qquad \ldots(3.25)$$

we can obtain the form

$$\rho^2(r_t) = \rho_1^2 \left\{\frac{r_1}{r_t}\right\}^2 \left\{\left(\frac{r_1}{t_s}\right)^2 + V_{esc}^2\right\} \Big/ \left\{\left(\frac{r_t}{t_s}\right)^2 + V_{esc}^2 - 2\omega^2 R_*^2 \cos^2\beta\right\} \qquad \ldots(3.26)$$

where ρ_1 is the density at the inner shell surface at $\beta = \pi/2$, and r_1 is the corresponding shell radius.

More generally if

$$\eta(V_o) = Q\, V_o^{\mu} \qquad \ldots(3.27)$$

then

$$\frac{\rho(r_o)}{\rho_1} = \left\{\frac{r_o}{r_1}\right\}\left\{\left[\left(\frac{r_t}{t_s}\right)^2 + V_{esc}^2 - 2\omega^2 R_*^2 \cos^2\beta\right] \Big/ \left[\left(\frac{r_1}{t_s}\right)^2 + V_{esc}^2\right]\right\}^{\left(\frac{\mu-1}{2}\right)} \qquad \ldots)3.28)$$

To a rather good approximation however, unless μ is considerably different from zero, or shell thickness large, the term in parentheses is close to 1, and setting $\mu = 0$ (as for the models) will give a

reasonable idea of the range of possible models. This range is illustrated in figures 3.5 to 3.8, where we have presented cross-sections (with contours of equal density) for selected model nebulae (roughly 1/3 of the cross-sections actually computed). These cross-sections cover two main categories: "toroidal" and "non-toroidal". The toroidal nebulae are simply those cases where the mass ejection velocity V_o, in combination with rotational terms, permits ejection from the equatorial regions of the star alone; a situation also investigated by Louise (1973). The restriction upon ejection is then such that mass does not escape if β is greater than some limit β_{LIM}

$$\beta_{LIM} = \cos^{-1} \left(\frac{1}{1-\alpha^2}\right)^{\frac{1}{2}}$$

where α is now imaginary if defined through

$$\alpha^2 - 1 = \frac{2\omega^2 R_*^2}{V_o^2 - V_{escp}^2}$$

Saving this restriction upon β, the equations for the toroidal nebulae are the same as those for non-toroidal nebulae, although the equations must now be normalised with respect to the radius of the inner shell surface in the stellar equatorial plane.

Normalised density is then

$$\rho^2(r_t) = \frac{1}{r_t^2} \left\{ \frac{t_s^{-2} + V_{esc}^2 - 2\omega^2 R_*^2}{(r_t/t_s)^2 + V_{esc}^2 - 2\omega^2 R_*^2 \cos^2\beta} \right\}$$

Several of these models were then selected for contouring at three elevations to the line of sight ($\beta = 0^o$, 45^o and 90^o). The primary responsibility for these was taken by Dr. N. K. Reay, who

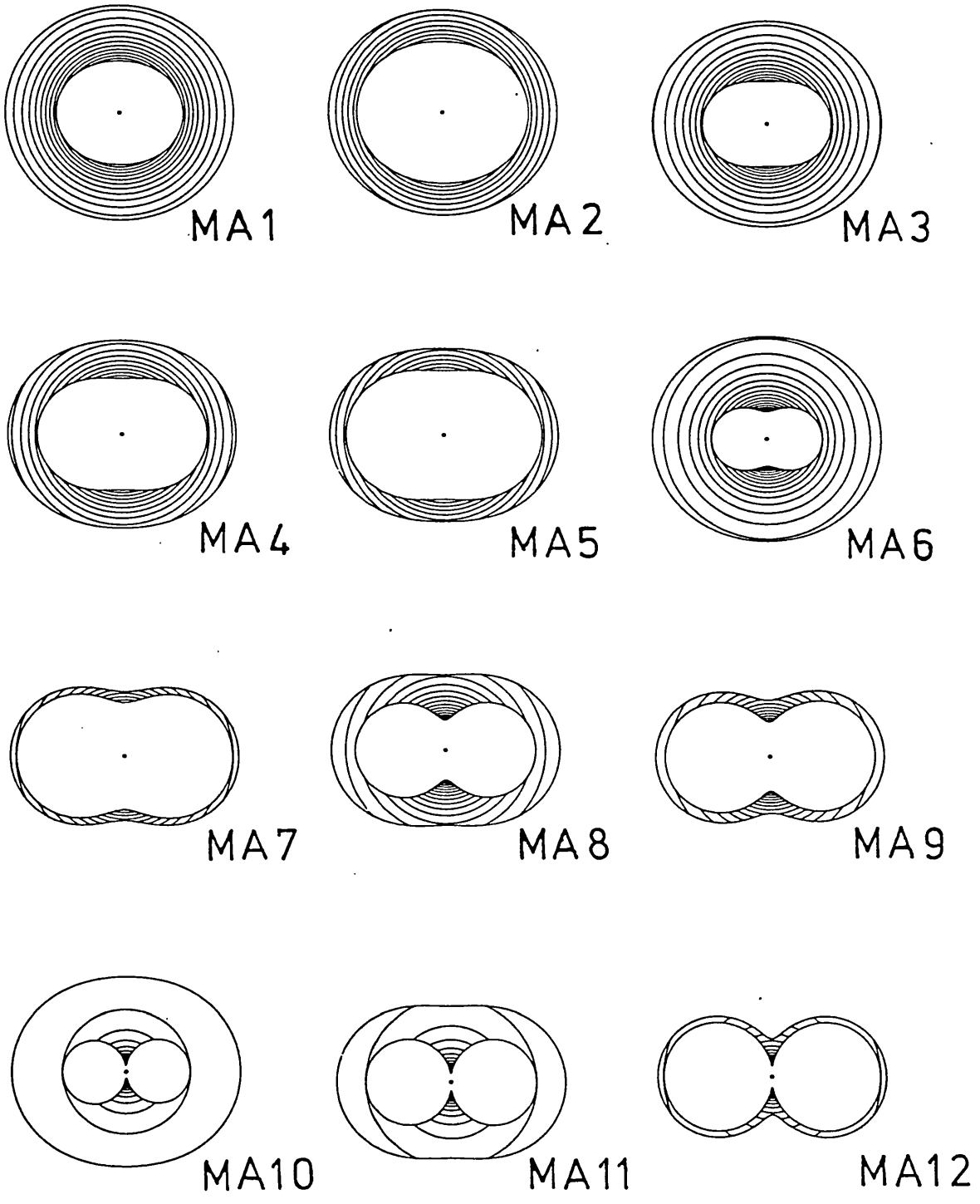

FIGURE 3.5

NEBULAR CROSS SECTIONS : MODEL A

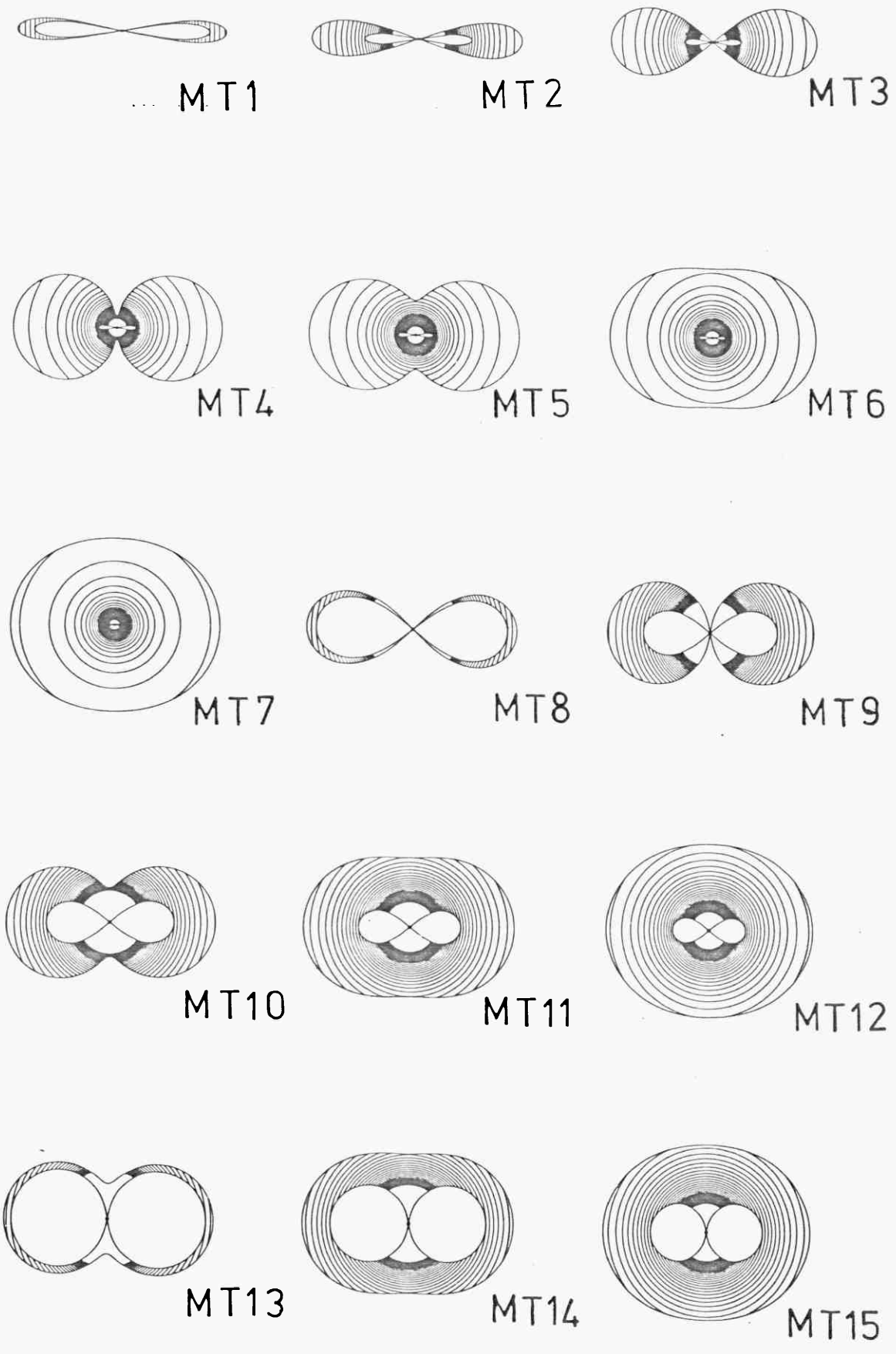

FIGURE 3.6

NEBULAR CROSS SECTIONS : MODEL A

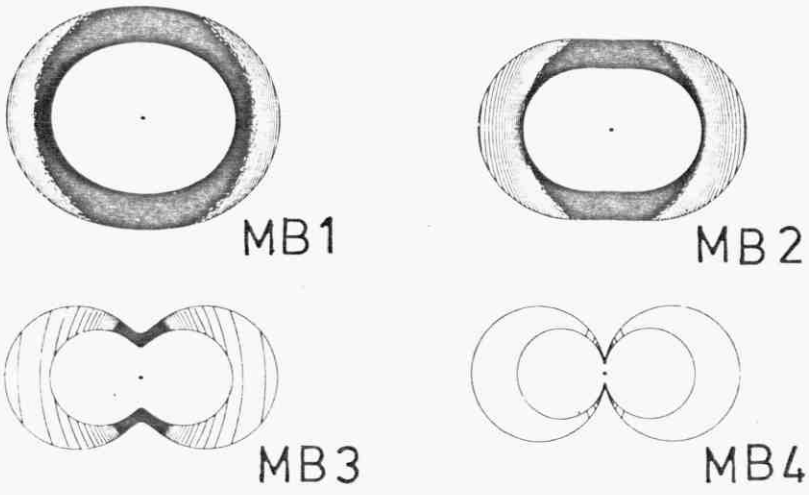

FIGURE 3.7

NEBULAR CROSS SECTIONS : MODEL B

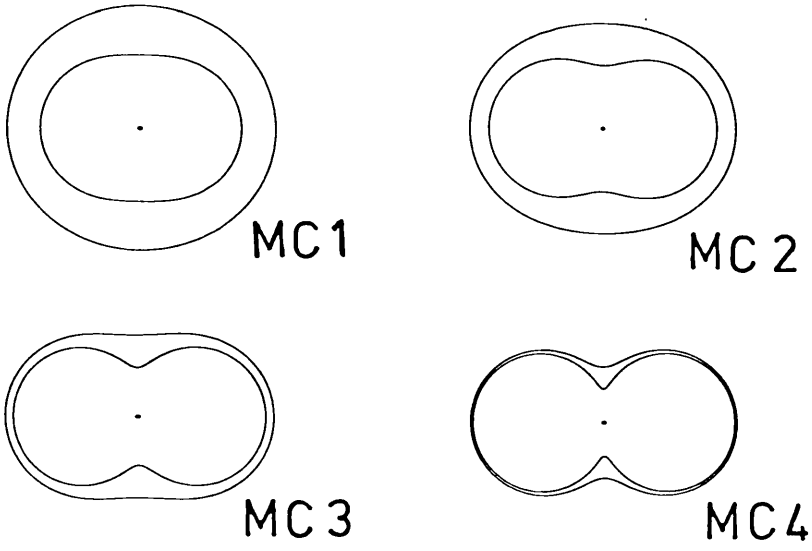

FIGURE 3.8

NEBULAR CROSS-SECTIONS : MODEL C

modified an already extant contouring programme for the purpose. The contoured maps are presented in figures 3.9 to 3.12. The procedure involved computing the density at a number of points along the line of sight through the nebula. These were then squared and summed, giving a value of the emission measure along that line. After computing similar values for a grid matrix across the projected nebular area, and convolving with a circular aperture to simulate seeing, an isophotal emission contour map is produced.

The primary assumptions here are that temperature is constant throughout the nebula (so emission is proportional to the emission measure $\int Ne^2 dL$), and the nebula is optically thin. Where these approximations hold (the procedure will be particularly valid for radio free-free, and Balmer emission line maps), the simulated maps should represent a realistic comparison with observed nebulae.

Before proceeding to discuss these emission maps in any detail, however, we will revert to a consideration of some of the factors which may be responsible for appreciable modifications of the model structures.

A first possibility is that stellar angular velocity ω may be latitude dependent. The observational evidence pertaining to this is by no means clear. A discussion of this and related evidence is provided by Huang and Struve (1960). The only star for which we have unambiguous evidence concerning rotation is the sun, for which

$$\omega(\theta) = \omega(0)(1 - A \sin^2\theta)$$

where A is a constant (Allen 1973). It seems unlikely that A will be less for red giants than for the sun. As an extreme example of the contribution to shell shape for which differential rotation may be responsible, we have determined a range of terminal contours corresponding

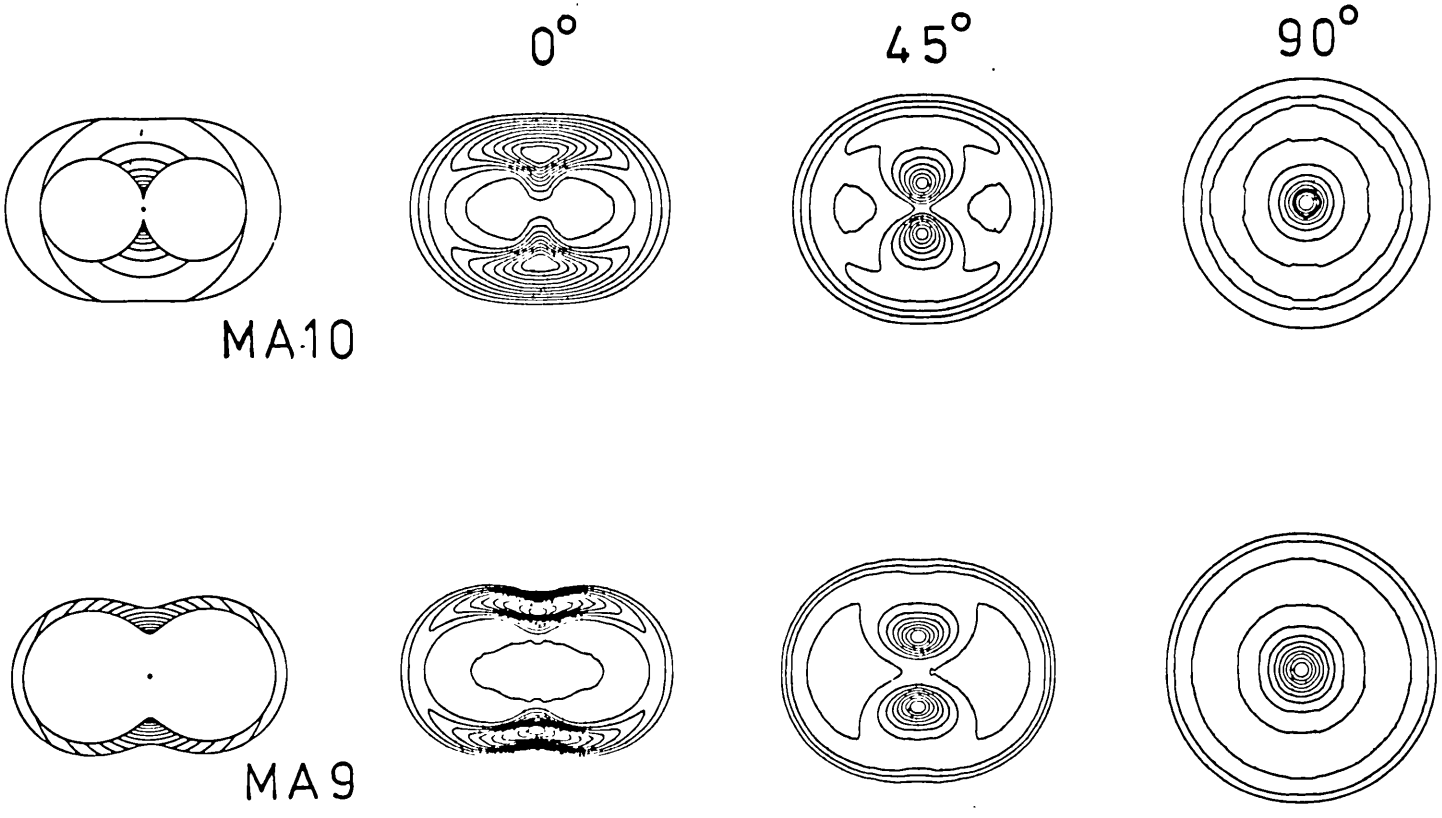

FIGURE 3.9a

CONTOUR MAPS FOR MODEL A NEBULAE

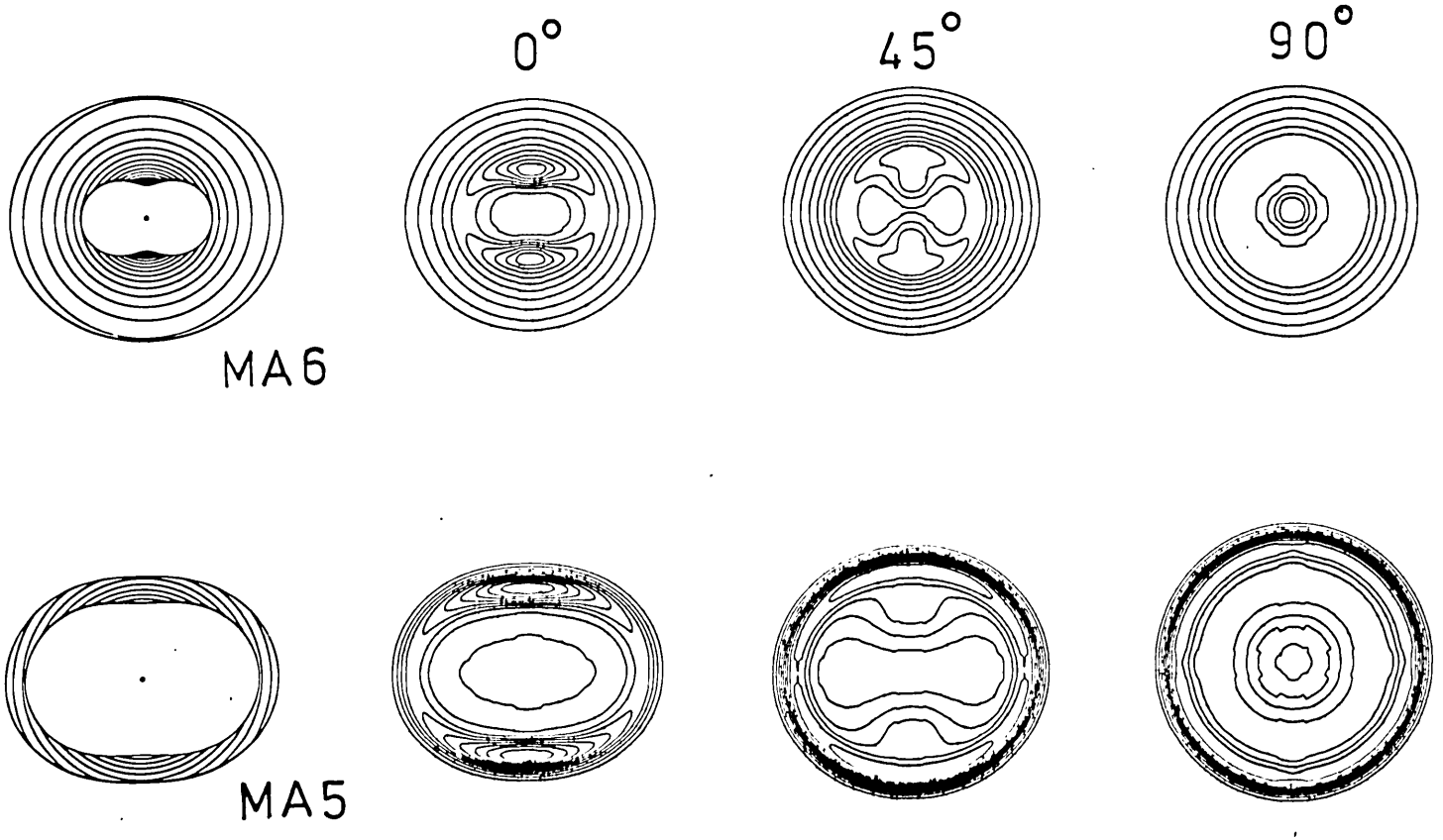

FIGURE 3.9b

CONTOUR MAPS OF MODEL A NEBULAE

FIGURE 3.10

SIMULATED EMISSION MAPS. MODEL A NEBULAE

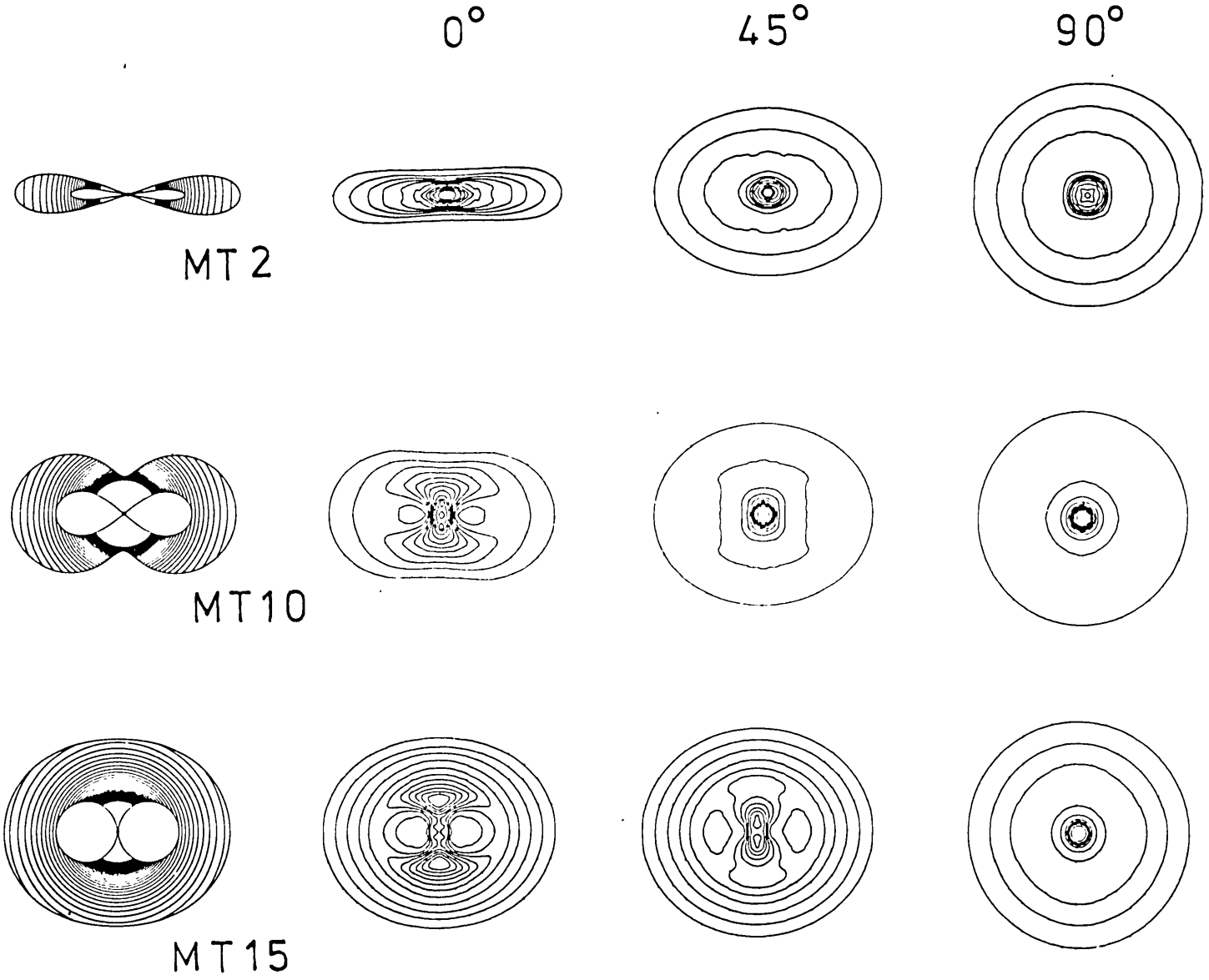

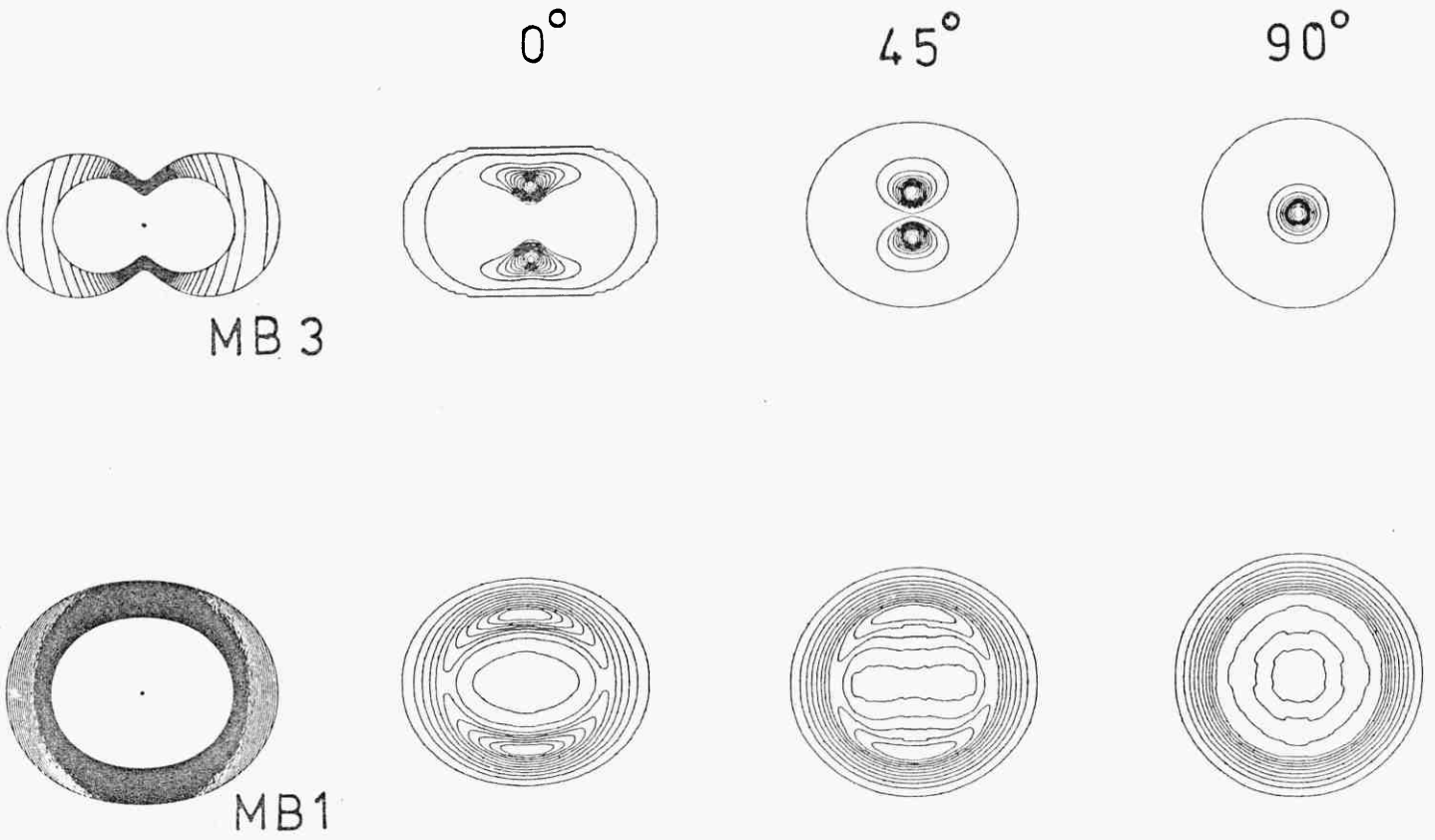

FIGURE 3.11

SIMULATED EMISSION MAPS : MODEL B NEBULAE

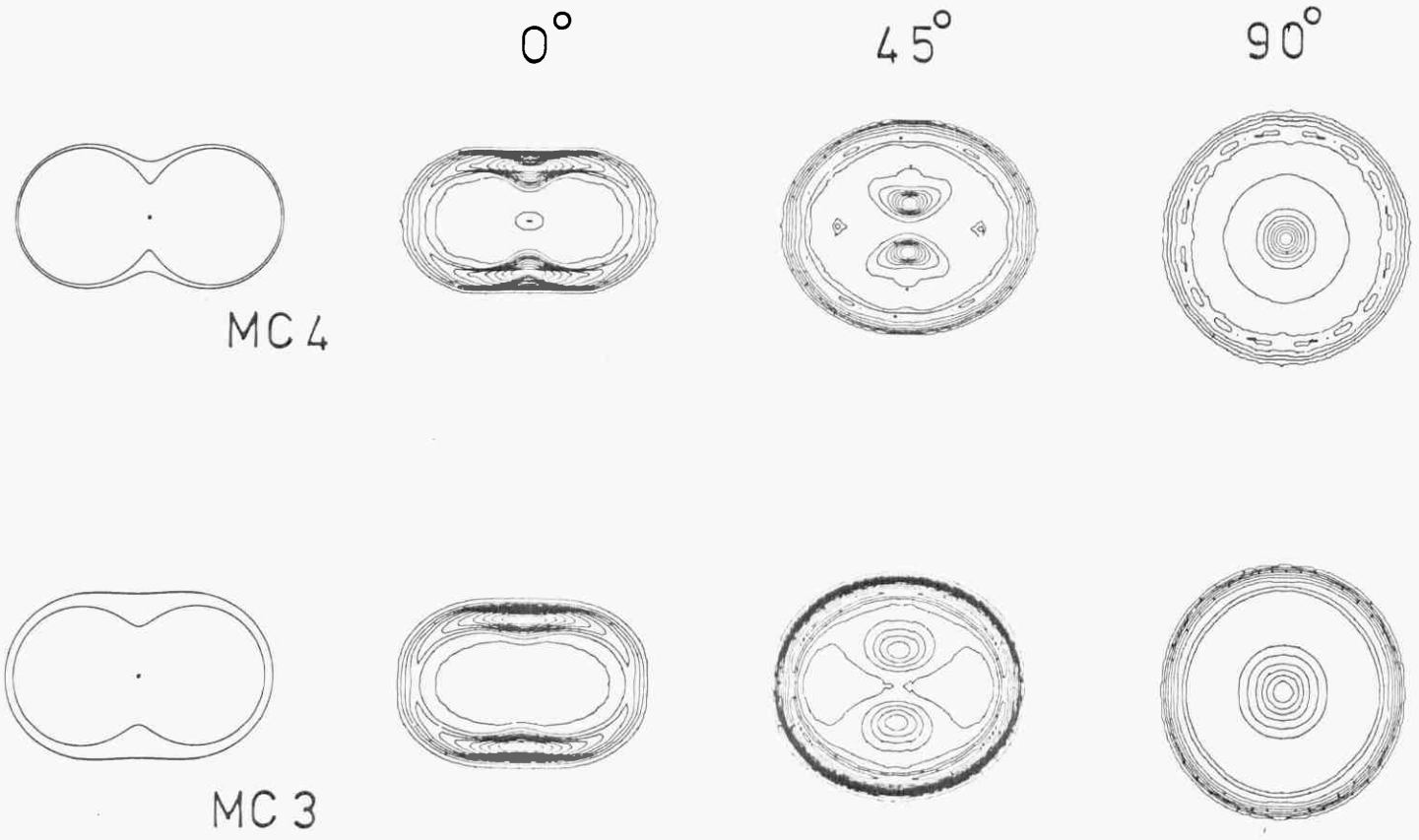

FIGURE 3.12

SIMULATED EMISSION MAPS : MODEL C NEBULAE

to A = 0.8. These are presented in figure 3.3b, and are to be compared with the contours in figure 3.3a (corresponding to A = 0). It is seen, as we would anticipate, that differential rotation will cause "extension" of the nebular shapes. There is however no serious development of new morphological forms aside from this.

A second factor which may appreciably modify relative intensity levels is the effect of mass redistribution. Up to this point, we have taken the terminal mass per unit solid angle $(dM/d\Omega)_\beta$ to be constant, and equal to the value appropriate for ejection from a non-rotating star ($(dM/d\Omega)_\theta$). Providing $\omega^2 R_*^2/V_{esc}^2 \lesssim 0.02$ this is reasonable. For larger values of $\omega R_*/V_{esc}$ however some qualifications are required.

Consider a non-rotating star ejecting mass between θ and $\theta+d\theta$. These angular limits define a thin walled cone with apex at the stellar centre, and axis coincident with the stellar polar axis. The solid angle subtended at the stellar centre is $2\pi\cos\theta\, d\theta$, and mass emitted between these angular limits is $2\pi\cos\theta\, d\theta (dM/d\Omega)_\theta$. θ is the stellar latitude. Mass ejected from a rotating star will however acquire a terminal angle $\beta \neq \theta$, and for mass ejected between latitudes θ, $\theta+d\theta$ we have corresponding terminal values β, $\beta+d\beta$. A terminal mass per unit solid angle $(dM/d\Omega)_\beta$ is then defined by

$$\left(\frac{dM}{d\Omega}\right)_\beta 2\pi\cos\beta\, d\beta = \left(\frac{dM}{d\Omega}\right)_\theta 2\pi\cos\theta\, d\theta$$

hence we can define a mass concentration parameter ϕ through

$$\phi = \frac{(dM/d\Omega)_\beta}{(dM/d\Omega)_\theta} = \frac{\cos\theta}{\cos\beta}\cdot\frac{d\theta}{d\beta} \qquad \ldots(3.29)$$

An interesting application of this is the Louise model (Louise 1973). Before we can proceed however it should be noted that the

equations we require relating terminal angle θ to the radial variation of the shell are not correctly stated by Louise. The problem arises from a confusion of terminal angle β with stellar latitude of ejection, on the part of Louise. To determine the correct relation for the particular model, we note after Louise that

$$\frac{X^2 + Y^2}{V^2 + \omega^2 R_*^2} + \frac{Z^2}{V^2} = 1$$

where X, Y, Z are Cartesian components of mass ejection velocity, V is the velocity of ejection normal to the (spherical) stellar surface, and $\omega R_* \cos\theta$ is the rotational velocity, again at the point of ejection. The Z axis is coincident with the stellar pole. As Louise points out, this is the equation of an oblate spheroid. The intersection of the surface in a plane containing the X-Z axis is therefore an ellipse, and we let major axis length = b, minor axis length = a (α = b/a). Reverting to spherical coordinates then

$$r^2 \left\{ \frac{\sin^2\beta}{a^2} + \frac{\cos^2\beta}{b^2} \right\} = 1$$

and

$$r = a \left\{1 + \frac{1-\alpha^2}{\alpha^2} \cos^2\beta\right\}^{-\frac{1}{2}} \qquad \ldots(3.30)$$

and since Louise only allows for density changes resulting from increasing terminal shell radius, the shell density is

$$n = n_o \left\{1 + \frac{1-\alpha^2}{\alpha^2} \cos^2\beta\right\}^{+1} \qquad \ldots(3.31)$$

This differs from the corresponding Louise equation in the acquisition of a term α^2, and the exclusion of a term for surface tilt which is not relevant for shells of finite thickness. The equation

implies higher shell densities near the pole ($\theta = 90^o$). However, we also have

$$\tan^2\beta = \frac{V^2\sin^2\theta}{V^2\cos^2\theta+\omega^2R^2\cos^2\theta} = \alpha^{-2}\tan^2\theta \qquad ...(3.32)$$

whence

$$\frac{d\theta}{d\beta} = \alpha^{+1}\frac{\cos^2\theta}{\cos^2\beta} \qquad ...(3.33)$$

Also from 3.32 we have

$$\cos^2\theta = \left\{\alpha^{+2}\left\{\frac{1}{\cos^2\beta} - 1\right\} + 1\right\}^{-1} \qquad ...(3.34)$$

So from 3.29, 3.33 and 3.34 we obtain

$$\phi = \frac{\alpha^{-2}}{\left(1 + \cos^2\beta\left(\frac{1-\alpha^2}{\alpha^2}\right)\right)^{3/2}} \qquad ...(3.35)$$

and

$$\left(\frac{dM}{d\Omega}\right)_\beta = \left(\frac{dM}{d\Omega}\right)_{\beta=90^o}\frac{1}{\left(1 + \cos^2\beta\left(\frac{1-\alpha^2}{\alpha^2}\right)\right)^{3/2}} \qquad ...(3.36)$$

from 3.30 and 3.36

$$n = n_o\left\{1 + \frac{1-\alpha^2}{\alpha^2}\cos^2\beta\right\}^{-\frac{1}{2}} \qquad ...(3.37)$$

and in consequence, density increases towards the equatorial plane in proportion to the radius. Clearly then there are serious modifications required of the Louise model, even in its present unrealistic form.

The variation of ϕ with β for various angular velocities, for the new models presented earlier in this section, but with $\alpha = 1.5$,

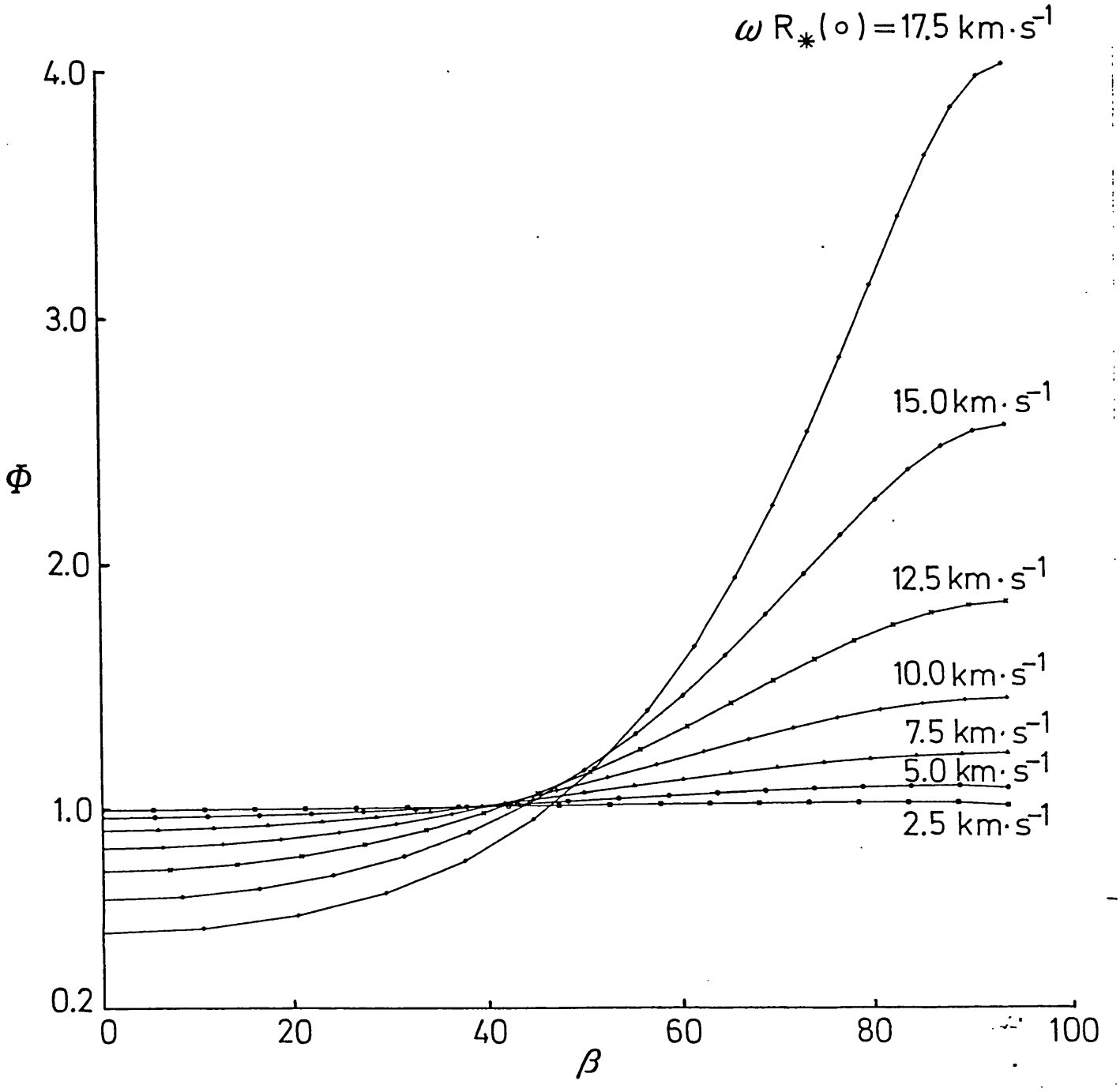

FIGURE 3.13

VARIATION OF MASS CONCENTRATION COEFFICIENT WITH β

V_{escp} = 35 km.s^{-1}. α = 1.5

V_{escp} = 35 km.s^{-1} is shown in figure 3.13. It is seen that relatively appreciable variations of ϕ for quite small variations in $\omega^2 R_*^2/V_{escp}^2$ are possible; and these are particularly important for the maps, since emission varies as ϕ^2.

To summarise the mechanisms which may modify the basic emission forms given in figures 3.9 to 3.12, we may note that mass may be concentrated towards the poles (figure 3.13). Appreciable stellar radiation will tend to "squash" the shell equatorially, and differential rotation to extend it, in the manner shown in figures 3.2 and 3.3. Finally, the intensity structures will depend upon $\eta(V_o)$. All these factors may be accounted for in discussion of individual cases, and do not detract from the validity of the models presented in figures 3.9 to 3.12 in describing the basic forms of nebular envelopes. They may however be among the least important determinants of shell shape, and we now discuss several further mechanisms which may critically influence nebular form.

3.3 Radiation Pressure

The rôle of radiation pressure in determining nebular shapes is not very clear, although various studies indicate that the dynamic effect cannot be ignored (Finzi and Wolf, 1970; Mathews, 1966; Hunter and Sofia, 1971). We will here be concerned primarily with the consequences of nebular acceleration due to the capture of Lyman continuum (Ly_c) radiation, where the capture may arise through atomic ionisation, or absorption by dust grains. In either case, forward momentum is directly transferred from the radiation field to the gaseous shell. The study will also be broadly applicable where a stellar wind

is the driving force. The dynamical consequences of Ly_α and gas pressures, which may well be extremely important, will be mentioned later. It is first however convenient to outline the possible evolution of the central star from a postulated red giant progenitor, to evaluate the early importance of radiative acceleration. An early collapse of the central star to form a very hot nucleus might for instance severely reduce the relevance of gravitational braking in determining shell shape, as we have so far envisaged it. In fact, the observational evidence supports a rapid but by no means instantaneous evolution of central star ionising flux (Seaton 1966), and this is qualitatively supported by the theoretical work of Harm and Schwarzschild (1975). For this latter treatment, it is clear that the evolutionary path from red giant to present day nucleus is probably initially quite slow, and over the typical period of ~10 years required to establish a gravitationally braked shell profile the acceleration due to radiation will be small. During these initial stages of expansion however, the high shell density and low stellar temperature ($T_* < 10^4$ K) mean that the shell is optically thick to Ly_c and the efficiency of momentum transfer for the radiation field to the nebular shell is high

$$\frac{dV_n}{dt} \simeq \frac{E_{Ly_c}}{M_n\, c}$$

where E_{Ly_c} is the total Lyman continuum flux, M_n is the mass of the nebular shell, and c is the velocity of light. As the star evolves, bolometric luminosity actually decreases, but increasing T_* causes E_{Ly_c} to increase until between 3000 and 6000 years from ejection, when $\log T_* > 4.5$, The nebular material is now tenuous and fully ionised. The envelope becomes increasingly transparent and the

efficiency of the radiative process decreases, the acceleration declines and an asymptotic shell velocity is approached.

This is a simplified scenario, but may be adopted to give some conception of the likely changes in shell shape resulting from radiative acceleration. We assume the accelerated shell has constant mass M_n (ablation is taken in this respect to be relatively unimportant). We also take the Ly_c luminosity E_{Ly_c} to be roughly constant over the period for which radiative acceleration is most influential. Finally, we take E_{Ly_c}/M_n to represent the ratio of incident energy to mass over all parts of the shell; that is, $\phi = 1$.

The shell acceleration is then given by

$$\frac{dV_n}{dt} = \left\{\frac{E_{Ly_c}}{M_n\, c}\right\} (1 - e^{-\tau(\beta)}) \qquad \ldots(3.38)$$

where $\tau(\beta)$ is the shell optical depth at angle β to the stellar equatorial plane. This can be reasonably approximated as

$$\tau(\beta) = \left\{\frac{r_{th}}{r}\right\}^2 \qquad \ldots(3.39)$$

where r is the shell radius, r_{th} is the shell radius at which $\tau(\beta) = 1$. For purely gaseous nebulae, this corresponds to the stage where

$$\left\{\frac{M_n\, g\, f}{m_H\, 4\pi r_{th}^2 \Delta r}\right\} \Delta r = 1$$

where shell thickness is Δr, r is mean shell radius, f is the fractional ionisation, m_H the hydrogen atom mass, and g is the hydrogen atom cross-section at the Lyman limit. The evaluation of r_{th} is considerably complicated by the presence of dust with appreciable albedo, however (Petrosian and Dana, 1975). Substituting for $\tau(\beta)$ in 3.38 and

integrating gives

$$V_r^2(\beta) - V_{r_o}^2(\beta) = \frac{2\,E_{Ly_c}\,r_{th}}{M_n\,c}\left\{\frac{1}{2}\int_{\tau_o}^{\tau}(1-e^{-\tau})\,\frac{d\tau}{\tau^{1.5}}\right\}$$

which, on integrating by parts, and performing appropriate substitutions for τ, gives after some reduction

$$V_r^2(\beta) - V_{r_o}^2(\beta) = \frac{2\,E_{Ly_c}\,r_{th}}{M_n\,c\,\sqrt{\tau_o}}\left\{\frac{r}{r_o}(1-e^{-\tau}) - (1-e^{-\tau_o}) + \sqrt{\pi\tau_o}(\mathrm{erf}(\sqrt{\tau_o}) - \mathrm{erf}(\sqrt{\tau}))\right\}$$

In the limit $r/r_o \to \infty$, then $\tau \to 0$, erf $\sqrt{\tau} \to 0$ and

$$V_\infty^2(\beta) = V_{r_o}^2(\beta) + \frac{2\,E_{Ly_c}\,r_{th}}{M_n\,c\,\sqrt{\tau_o}}\left\{\sqrt{\pi\tau_o}\,\mathrm{erf}(\sqrt{\tau_o}) - (1-e^{-\tau_o})\right\}$$

for expansion from an initially optically thick shell ($\tau_o \gg 1$) we then have

$$V_\infty^2(\beta) = V_{r_o}^2(\beta) + \frac{2\,E_{Ly_c}\,r_{th}}{M_n\,c}\sqrt{\pi}$$

For optically thin shells, we return to equation 3.38, and noting that

$$V_r^2(\beta) - V_{r_o}^2(\beta) = \frac{2\,E_{Ly_c}\,c}{M_n\,c}\int_{\tau_o}^{\tau}\tau\,dr$$

substituting again for r, and integrating gives

$$V_r^2(\beta) - V_{r_o}^2(\beta) = \frac{2\,E_{Ly_c}\,r_{th}\,\tau_o^{0.5}}{M_n\,c}\left\{1 - \frac{r_o}{r}\right\}$$

Generally therefore

$$V_\infty^2(\beta) - V_{r_o}^2(\beta) = \frac{2\, E_{Ly_c}\, r_{th}}{M_n\, c}\,\delta \qquad \ldots(3.40)$$

where $\delta = \tau_o^{0.5}$ for optically thin shells, and $\sqrt{\pi}$ for optically thick shells, τ_o being the optical depth at initial radius r_o. Needless to say, the analysis above permits the evaluation of intermediate shell configurations ($r/r_o > 1$). For the present however we restrict the analysis to considering those cases for which $r/r_o >> 1$.

A comparison of equation 3.40 with equation 3.15 reveals that for shells optically thick at $r = r_o$, radiative acceleration leads to identical terminal shapes to those in figure 3.3; although for a given ejection velocity V_o, the terminal axial ratios will be systematically smaller.

For significant optically thin absorption the changes are more serious. For all the ejection models considered here

$$\tau_o(\beta) \propto r_m^{-2}(\beta)$$

where r_m is the mean shell radius. If α is the axial ratio before radiative acceleration, and α_∞ is the terminal axial ratio, then for the normalised terminal radius we obtain

$$r_\infty^2 = (1 + (\alpha^2-1)\cos^2\beta + (\alpha^2-\alpha_\infty^2)/((\alpha_\infty^2-\alpha^{-1})(1 + (\alpha^2-1)\cos^2\beta)^{\frac{1}{2}}))/$$

$$(1 + (\alpha^2-\alpha_\infty^2)/(\alpha_\infty^2-\alpha^{-1}))$$

Terminal shapes for several initial values of α are presented in figure 3.14. We also have

$$\frac{E_{Ly_c}\, r_{th}\, \tau_o^{\frac{1}{2}}(\beta)}{M_n\, c} = \frac{\omega^2\, R_*^2(\alpha^2-\alpha_\infty^2)}{((\alpha^2-1)(\alpha_\infty^2-\alpha^{-1}))}$$

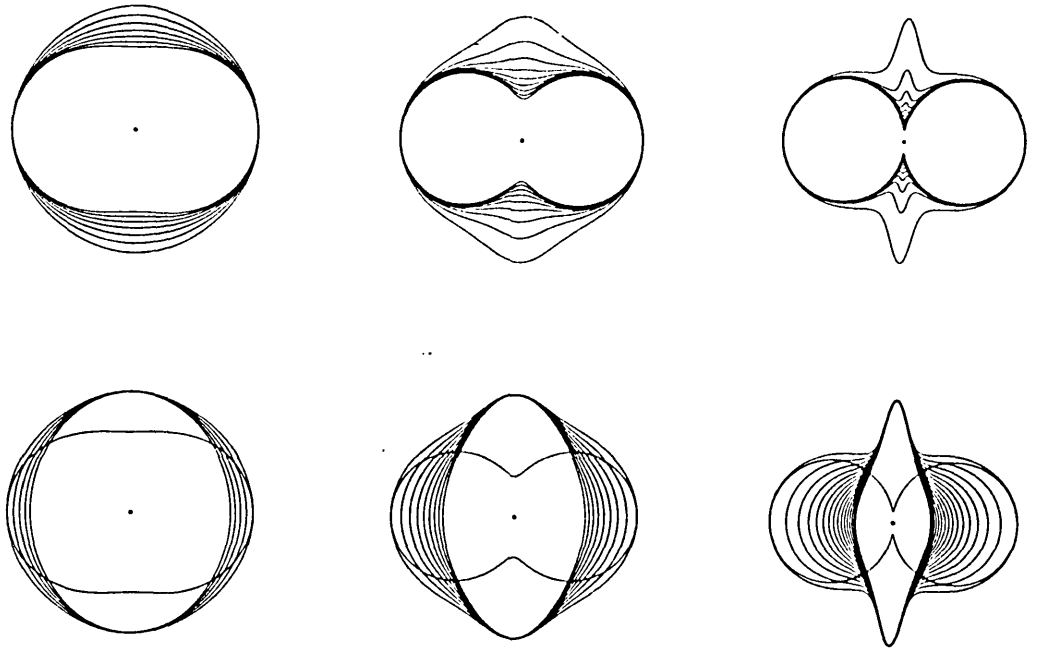

FIGURE 3.14

NEBULAR SHAPES RESULTING FROM RADIATIVE ACCELERATION OF GRAVITATIONALLY BRAKED SHELLS. INNER CONTOUR REPRESENTS INITIAL SHAPE

since the left hand side cannot be less than zero, it follows immediately that

$$\alpha_{\infty L} = \alpha^{-\frac{1}{2}}$$

where $\alpha_{\infty L}$ is the limiting value that the terminal axial ratio may acquire. It is possible therefore to have $\alpha_{\infty L} < 1$ (excepting of course when $\alpha = 1$). Where initial axial ratios are modest, therefore, prolate spheroidal forms may be acquired; forms that have been suggested previously on empirical grounds (Weedman, 1968). If however the primary shell acceleration occurs during the optically thick stage (and there is suggestive evidence for this (Weedman, 1968)) it is arguable that optically thin configurations will be unlikely to be common. In the future discussion, we will nevertheless find evidence for such structures: although as secondary distortion of oblate spheroidal shells. There appears to be little evidence that primary shell structure need be explained in terms other than we would expect if shells were simply gravitationally braked, and radiatively accelerated while optically thick. In an anticipatory discussion in a previous section however we have already found that novae shells are almost certainly explainable in terms of optically thin radiative expansion.

To assess the relevance of Ly_c acceleration we note that if

$$V_L^2 = \frac{2\, E_{Ly_c}\, r_{th}\, \pi^{\frac{1}{2}}}{M_n\, c}$$

then the maximum possible terminal axial ratio is

$$\alpha_{\infty u}^2 = 1 + \frac{2\, \omega^2\, R_*^2}{V_L^2}$$

for $E_{Ly_c} = 2.3 \times 10^{19}$ W (typical of a star with $R_* = 1R_\odot$, $T_* = 50{,}000$ K),

$M_n = 0.05\ M_\odot$, $r_{th} \simeq 0.1$ pc and $\omega R_* = 5$ km.s^{-1} we obtain $\alpha_{\infty u} \simeq 1.5$. Clearly these parameters could be varied. Doubling the stellar temperature for instance produces more than an order of magnitude increase in E_{Ly_c}. The basic point to note is that radiative acceleration is likely to be quite influential, and is an important discriminant against envelopes with large axial ratios.

Finally, for purely gaseous nebulae Ly_α scattering seems likely to be a dominant accelerative factor (Kovach, 1971) where nebulae are optically thick to Ly_c. For expansion of nebulae which are optically thin to Ly_c, Ly_α densities would be much lower. Recent infrared observations (c.f. Cohen and Barlow, 1974) have also shown that many if not all planetary nebulae contain some proportion of dust, for which case the importance of Ly_α as an accelerative mechanism could again be greatly reduced (Kovach, 1971; Ferch and Salpeter, 1975). If for simplicity we follow Kirkpatrick in considering the shells as containing a uniform pressure Ly_α photon (or particulate) gas, it seems clear that for the models discussed here, there will be an equatorial distension of the kind determined for differential stellar rotation. In short, the result is likely again to be a modification of the original gravitationally braked structures illustrated in figure 3.3, but no serious development of new nebular forms. Clearly though, the problem of structural modifications due to Ly_α and gaseous pressure needs to be considered within the framework of a more rigorous discussion.

3.4 Interaction of Nebulae and the Interstellar Medium

The possibility of some distortion of nebular envelopes arising

from motion through the interstellar medium has been considered previously by Gurzadyan (1969) and Smith (1976), although with equivocal results. The question is clearly of interest; besides its relevance in a general discussion of the origin of nebular structures, the rôle of shell distortion in the statistics of nebular orientation is for instance quite conjectural (Melnick and Harwit, 1975; Cudworth 1975). In the present discussion we assess the relevance of this mechanism for general shell development, and suggest from available photographs cases where such shell distortion may be occurring.

To estimate the probability of observing shell retardation it is necessary to determine a representative parameter for this which can be readily related to the other determinative quantities. A snow-plough model of shell retardation is considered to this end. In this model, a spherically symmetric shell of gas is ejected from a central star with velocity V_{exp}, density $\rho_n(t)$ into a medium of density ρ_o. The central star moves through this medium with velocity $\underset{\sim}{V}_s$. For convenience we assume $|\underset{\sim}{V}_s| > V_{exp}$ (in fact, the typical case for planetary nebulae). It follows that if an element of shell surface with projected area A(t) in the direction of stellar motion $\underset{\sim}{V}_s$, moves a component of distance S(t) along the axis defined by $\underset{\sim}{V}_s$, its velocity dS/dt is given through conservation of momentum by

$$\frac{dS}{dt} = \frac{M_o|\underset{\sim}{V}_o|}{(M_o+\overline{A}\rho_o S(t))} \qquad \ldots(3.41a)$$

$$|\underset{\sim}{V}_o| = |(\underset{\sim}{V}_s\cdot\underset{\sim}{V}_{exp})\cdot\underset{\sim}{V}_s/|\underset{\sim}{V}_s|^2 + \underset{\sim}{V}_s| \qquad \ldots(3.41b)$$

where $\overline{A}$ is the time averaged value of projected area A(t). It is more convenient for the present to let $\overline{A} = \int_o^t A(t)dt/\int_o^t dt \simeq A(t)/3$; a

reasonable approximation providing shell retardation is small. If we further let $\underset{\sim}{V}_{exp}/|\underset{\sim}{V}_{exp}| = \underset{\sim}{V}_s/|\underset{\sim}{V}_s|$ and take as a representative value $A(t)/M_o \simeq \pi R^2(t)/\{4 \pi R^3(t) \rho_n(t)/3\}$, where $R(t) = |\underset{\sim}{V}_{exp}|t$; then we obtain through integration of 3.41a, for $S(t) = (1-\alpha) R(t) + |\underset{\sim}{V}_s|t$, the relation

$$\alpha = \left\{\left\{\left\{1 + \frac{S_o(t)}{R(t)}\right\} + \frac{4 \rho_n(t)}{\rho_o}\right\} - \left\{\frac{8 \rho_n(t)}{\rho_o}\left\{\frac{S_o(t)}{R_o(t)} + 1\right\} + 16\left\{\frac{\rho_n(t)}{\rho_o}\right\}^2\right\}^{\frac{1}{2}}\right\} \qquad ...(3.42)$$

where $S_o(t) = |\underset{\sim}{V}_s|t$, i.e. $S_o(t)/R(t) = |\underset{\sim}{V}_s|/|\underset{\sim}{V}_{exp}|$. It is seen that α, which is the fractional retardation in radius, can in this way be related to just two dimensionless variables; $u = (S_o(t)/R(t))$, and $w = (\rho_o/\rho_n(t))$. This relationship is illustrated in figure 3.15.

For typical planetary nebulae, the velocity ellipsoid (Delhaye, 1965) suggests a velocity dispersion $V_s \simeq 60$ km.s^{-1} relative to the surrounding medium, and since typically $V_{exp} \simeq 20$ km.s^{-1}, we are most concerned with the curves having $u \simeq 3$. Cudworth (1974) has more recently found similar values of V_s for Greig's (1971, 1972) class C planetaries, but a rather lower value ($V_s \simeq 40$ km.s^{-1}) for class B.

Since for observed nebulae $\rho_n \simeq 10^3$ cm^{-3}, it is clear that even for relatively large values of u, shell retardation (and distortion) will not be observable for interstellar densities $w \lesssim 10^{-3}$, $\rho_o \lesssim 1$ cm^{-3}. Since the intercloud medium has a typical density very much less than this ($\rho_o \simeq 0.1$ cm^{-3}, Allen 1973), planetary nebulae can be expected to show little observable retardation or distortion outside of interstellar clouds; the essential conclusion of Smith (1976).

Although the defining parameters for interstellar clouds remain questionable in detail, the evidence from colour excess measurements can

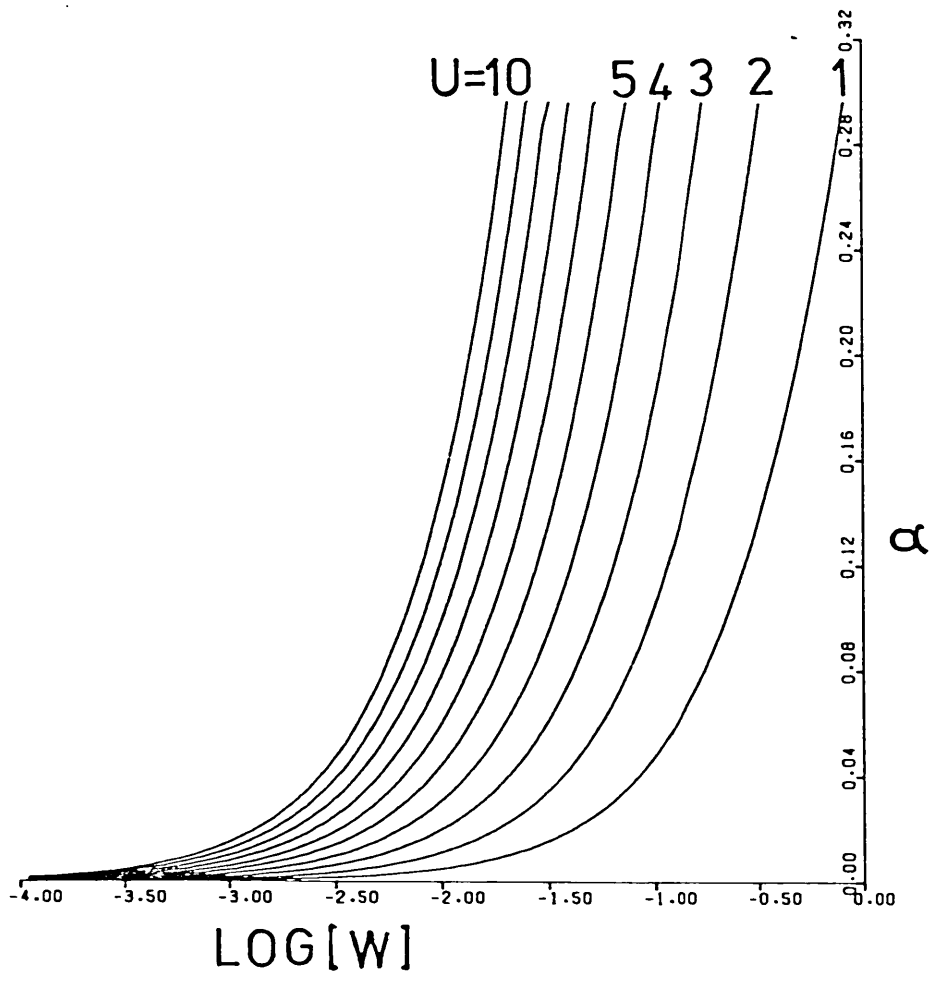

FIGURE 3.15

SHELL RETARDATION PARAMETERS

usually be well represented by a two cloud model (c.f. Spitzer 1968, Scheffler 1966, 1967). We adopt Scheffler's parameters; for small clouds he finds a typical diameter $\langle D_s \rangle \simeq 3$pc, frequency $\langle \nu_s \rangle \simeq 5$ Kpc^{-1}, and (from Mezger 1972) gaseous density $n_s \simeq 48$ cm^{-3}. For large clouds the parameters are $\langle D_L \rangle \simeq 70$ pc, $\langle \nu_L \rangle \simeq 0.5$ Kpc^{-1}, and, again from Mezger, we obtain $\langle n_L \rangle \simeq 12.7$ cm^{-3}. Figure 3.15 shows that observable shell distortion is plausible for both kinds of clouds. Given this situation, it is of interest to determine the probability of observing such retardation.

If α, β are the respective exponential scale heights for the number density variation of planetary nebulae and interstellar clouds above the galactic plane; ε_{CSO}, ε_{CLO} are the fractional volumes of interstellar space occupied by small and large clouds at height Z = 0 above the galactic plane; and n_{p_o} is the number density of planetary nebulae, also at Z = 0, then the fraction f of planetary nebulae within interstellar clouds is

$$f = \frac{\int_o^\infty (\varepsilon_{CSO}+\varepsilon_{CLO}) \cdot n_{p_o} e^{-Z\{1/\alpha+1/\beta\}} dZ}{\int_o^\infty n_{p_o} e^{-Z/\alpha} dZ}$$

$$= \frac{\varepsilon_{CSO} + \varepsilon_{CLO}}{(1+\alpha/\beta)}$$

Paranego and Van der Kamp have found $\beta \simeq 0.10$ Kpc (Dufay 1968) and Cahn and Kaler (1971) give $\alpha \simeq 0.09$ Kpc. If we use Scheffler's cloud frequencies as typical for height Z = 0 (in fact an underestimate), then we have $\varepsilon_{CSO} \simeq 0.010$, and $\varepsilon_{CLO} \simeq 0.047$, giving $f \simeq 0.03$. Thus some 40 of the planetary nebulae catalogued by Perek and Kohoutek (1967), for instance, may show some evidence of shell retardation, of which about 7, existing in higher density clouds, could display the more extreme forms of shell distortion.

Gurzadyan (1969) has already pointed to NGC6888, A16 and NGC7139 as possible objects within the category of retarded nebulae, selecting them primarily because of asymmetrical shell brightness; compression of shell material on the side facing the direction of motion is presumed to occur.

The catalogue of Perek and Kohoutek (1967) has been used to identify further possible nebulae falling within this category. Although many possibilities were found, 219+31°1 (A31), 153+22°1 (A16), 68-0°1 (M1-75), 238+34°1 (A33), 272+12°1 (NGC3132), 197+17°1 (NGC2392) and 38+2°1 (YM16) were all noted as showing particularly distinctive deformations, or a particularly prominent displacement of the central star with respect to the main nebular mass. The last four cases allowed independent assessments of α_M, and these are given in table 3.2, where $\alpha_M = (R_2-R_1)/R_2$, and R_1, R_2 are the radii of the (presumed) leading and trailing nebular edges along an axis containing the velocity vector of the central star, the axis of nebular symmetry. Defined this way, the measured value α_M is equivalent to α defined earlier, providing $|V_s/V_{exp}| > 1$.

The nebula 38+2°1 did not show a readily identifiable central star, and for this case α_M was assessed by drawing an axis through the greatest nebular length perpendicular to the axis of symmetry, and identifying the intersection of the axes as a preliminary position for the central star. At the least, this gives a measure of the deformation, and α_M obtained on this basis would in fact be expected to be a lower limit to α if $|V_s/V_{exp}| > 1$. With this in mind the values of α_M suggest that all cases in table 3.2 probably reside in exceptionally dense regions of the interstellar medium, unless they have particularly anomalous u values.

TABLE 3.2

RETARDATION IN SELECTED PLANETARY NEBULAE

PEREK AND KOHOUTEK (1967) DESIGNATION	α_M
272 + 12°1	0.132 ± 0.004
197 + 17°1	0.241 ± 0.005
238 + 34°1	0.161 ± 0.006
38 + 2°1	0.21

Evidently, more observational data on these and similar nebulae would be of interest; for instance, many of these nebulae must, on the present hypothesis, be within particularly dense regions of the interstellar medium, and where the nebular shells are optically thin this would lead to the formation of a low intensity halo where the interstellar medium is ionised. NGC 2392 and NGC 6543 should be noted in this respect, and other examples are known (Kaler 1974), although in many cases it seems likely that observed halos are a consequence of secondary ejection processes (Kaler 1974), nebular splitting due to the build-up of internal Ly_{α} pressure (Gurzadyan 1970), or even a consequence of certain structural forms (see later).

3.5 Ejection from Binary Systems

In a later discussion, we will indicate some evidence for supposing that certain nebulae are spheroidal structures with three orthogonal axes of differing lengths. It is however difficult to conceive how any of the previous mechanisms would lead to such a result. One possibility which may however deserve consideration is that shell ejection occurs from an ellipsoidal, tidally deformed giant component of a binary system. Such a possibility may not be as contrived as it first appears; the nucleus of NGC 3132 is almost certainly a binary for instance, with a hot blue component ionising the nebula, and an A2V star dominating the optical continuum from the nucleus (Mendez, 1975). In addition, we have already noted the propensity of close binary systems to be involved in mass transfer, and a particular case of interest (in view of our earlier comments concerning escape velocities) would be the ejection of mass from the late type components in Algol

systems. Evidence for mass loss in β Persei is well established, and we have specifically noted that the primary may well have been observed in the process of ejecting a shell; that the system as a whole is highly active; and that the secondary suffers considerable mass loss to both primary component and, probably, interstellar space.

3.6 The Observed Structure of Nebulae

We now indicate how observed nebulae generally may be explainable in terms of the preceding models. We will be satisfied here simply to draw attention to broad correlations between observed and theoretical emission structures, illustrated with references to particular nebulae. A more complete discussion of these specific cases is reserved for later.

3.7 Bipolar Nebulae

In bipolar nebulae the principal nebular intensity is concentrated within two "bars", one each on either side of the central star and most often at the ends of the nebular minor axis. These constitute a large fraction of known planetary nebulae, and can be well represented by models with axial ratios ≈1.5 (e.g. see figure 3.9). An example of this type is NGC 7027. In figure 3.16 we present the radio map (Scott, 1973), models based on the foregoing theory, and a strictly ellipsoidal model. The latter model was first discussed by Hicks et al. (1976) and although the two show similar bipolar structures, the new models are significantly better at accounting for the squarer shape of NGC 7027. In particular, note that apart from relatively minor

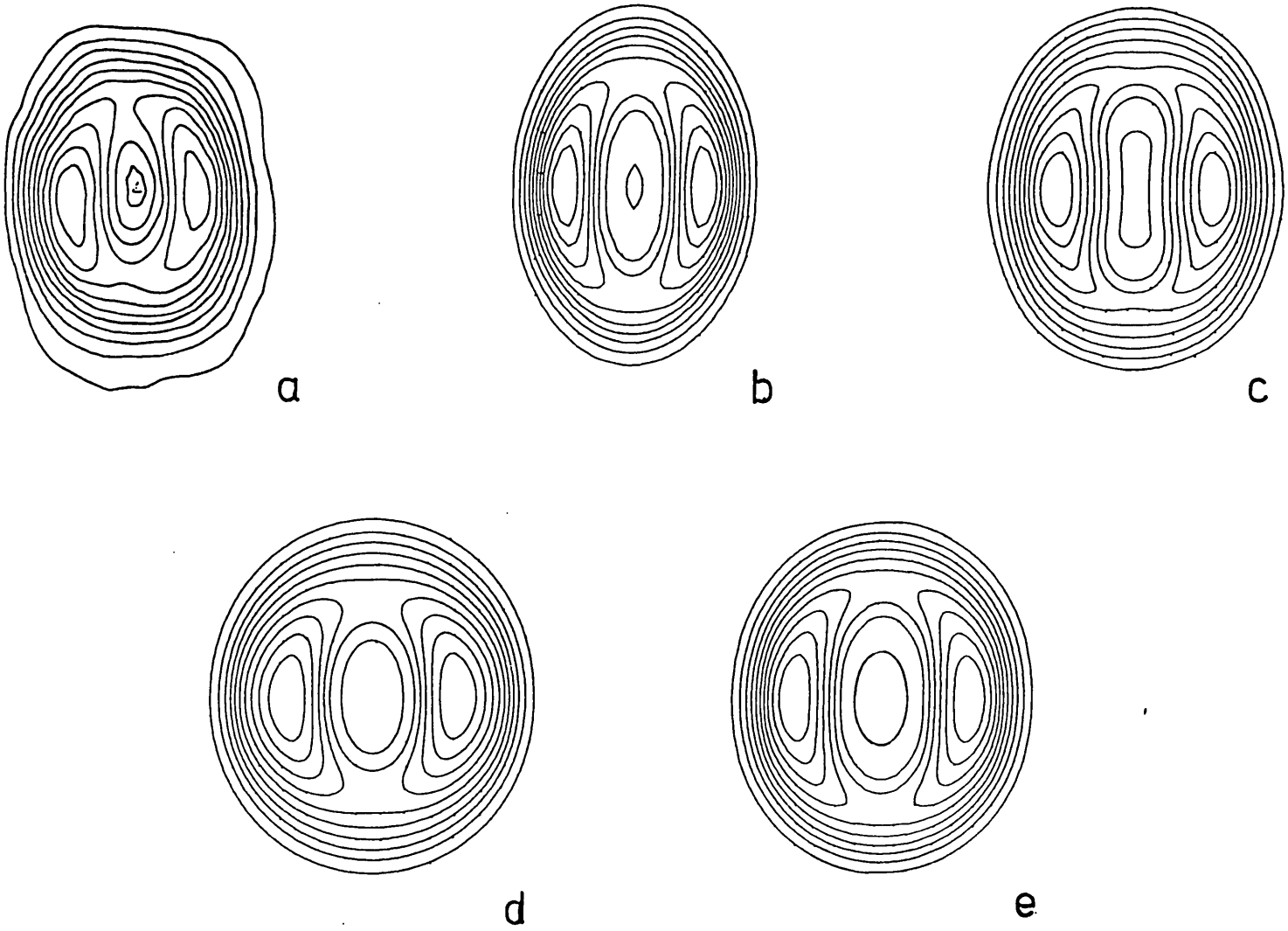

FIGURE 3.16 NGC 7027. a. 5 GHz RADIO MAP FROM SCOTT (1973). b. ELLIPSOIDAL MODEL FROM HICKS ET AL. (1976). c. MODEL C EJECTION MODEL. d. MODEL B EJECTION MODEL. e. MODEL A EJECTION MODEL. SEE PHILLIPS AND REAY (1977) FOR MODEL PARAMETERS

differences, all three ejection modes enable reasonable representations of this nebula. This illustrates forcibly the point made, earlier in the chapter, that the morphological characteristics of model nebulae are relatively insensitive to the large differences in density structure that characterise the various ejection modes. The observational constraints indicated by Hicks et al. (1976) favouring a closed shell configuration in preference to the Scott model, are also applicable to the new models. We will look at these arguments later.

More generally, Hromov and Kohoutek (1968) describe a morphological sequence strongly dominated by the bipolar structure, of which they identify two basic kinds: a structure in which the "bars" are straight, and a structure in which the intensity bars are slightly curved. In terms of the theory presented here this is seen as a natural consequence of a structural development from nebulae with $\alpha \lesssim 1.5$ (which have straight sides) to nebulae with lower values of α, for which the curvature at the minor axis increases. We believe that the forms of the outer envelopes identified by Hromov and Kohoutek are more probably indicative of ionisation than density structure, and therefore outside the scope of this paper.

Another point to note here is that the strength of the bipolarity, as indicated by the variation of relative intensities between the ends of the major and minor axes, is observed to vary widely. For instance, nebula A 66 has a higher degree of bipolarity than A 70. This can be understood in terms of a variation in the mass concentration factor between nebulae, and since intensity is roughly proportional to the square of the electron density, a relatively small variation in ϕ will suffice to cause quite large modifications to the emission structures of nebulae.

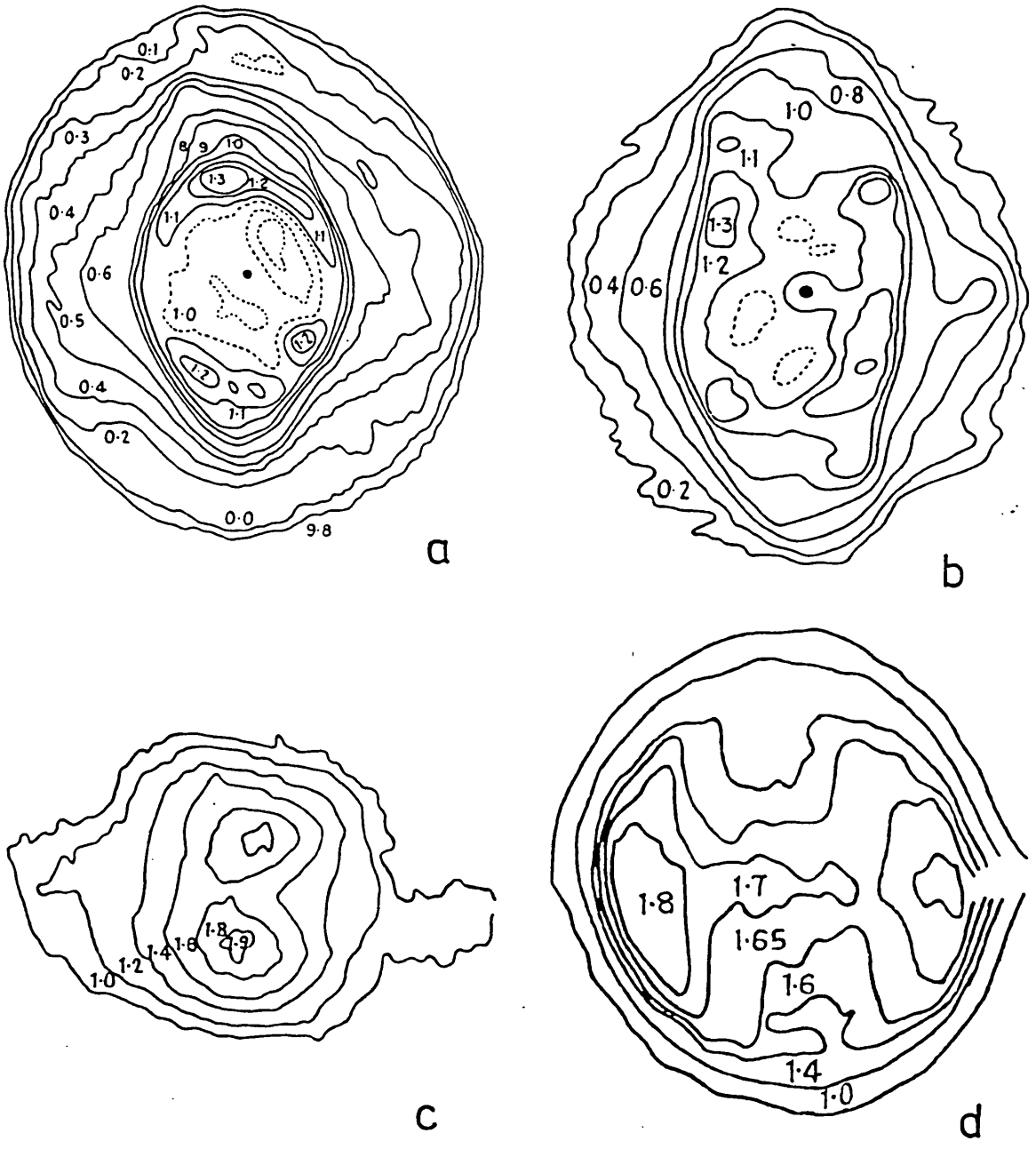

FIGURE 3.17

MISCELLANEOUS ISOPHOTAL MAPS OF PLANETARY NEBULAE, ADAPTED FROM ALLER (1956)

a. NGC 3242 IN WHITE LIGHT. b. NGC 7009 IN Hα. c. NGC 2440 IN Hβ
d. IC 418 IN Hβ

Axial ratios $\alpha > 1.5$ will tend to produce hour-glass (elevation $\beta = 0$, see figure 3.6) or diskoidal structures ($\beta = 90^{o}$) depending upon the nebular elevation. At intermediate elevations however a strong bipolarity is evidenced whereby two high intensity roughly circular regions are enclosed by a lower intensity halo. An example of this, similar to Models MB 3 (figure 3.11) or MA 9 (figure 3.9) viewed at $\beta = 45^{o}$ is NGC 2440. Figure 3.17 shows for comparison an isophotal map (Aller, 1956) of this object produced from an H_{β} exposure. The same figure shows an isophotal map of IC 418, and we note that the characteristic central anvil shape is well reproduced by Model MT 15 (figure 3.17) when viewed at an elevation of $\beta = 45^{o}$. Care should be exercised in comparing IC 418 and NGC 2440 directly with the theoretical models, however; the contour levels reproduced in figure 3.17 are set at logarithmic intervals, whereas the model contours are at linear intervals.

3.8 Ring Nebulae

It is clear that as α approaches 1, the emission contours of the model nebulae will become circular, and for shells this will lead to ring-like emission structures. In this respect the models closely approach the usual interpretation for these structures (c.f. Gurzadyan 1969), for which a certain amount of central gaseous filling is also usually required to explain intensity levels. As α increases, and $1.5 \gtrsim \alpha \gtrsim 1$, a certain amount of bipolarity arises and this is also observed in nebulae commonly classified as rings - the borderline between bipolar and ring nebulae being a matter of subjective assessment. Illustrative of this are perhaps the most well known ring nebulae,

NGC 6720 and NGC 7293. Both of these show appreciable bipolarity, and they have been explained in terms of spheroids and (more recently and popularly) as tilted toroids and rings (Minkowski and Aller, 1954; Warner and Rubin, 1975; Hua and Louise, 1970; Louise, 1974; Minkowski and Osterbrock, 1960). NGC 6720 has further been explained in terms of a tilted "barrel" (Proisy, 1974) and cylinder (George et al. 1974), and the label "The Helix" for NGC 7293 indicates another qualitative assessment of the structure on the basis of broad-band photographs. This multiplicity of models is at least partially a consequence of the independent analyses of restricted observational material. We may also however be dealing with structures that are in fact less simple than the emission structures appear to superficially indicate. In our later discussion of NGC 6720, this will be found to be not unlikely. For the present we consider these nebulae simply as indicative of a particular morphological class. Taken as such, it is clearly seen that the hydrogenic emission structure may be reasonably represented in terms of particular models (a representative electronograph, and comparative models are presented in figure 3.18) and the emission ratio between peak ring brightness and the brightness of the central hole, $\simeq$ 3:1, is readily obtained. NGC 7293 has a similar overall shape and ring/hole intensity ratio (Gurzadyan, 1969), and may be similarly modelled. A certain crowding of the bipolar contours in the models indicates however that for these particular cases, a more uniform shell density may be appropriate. To the extent that they are broadly consistent with the hydrogenic isophotal maps of NGC 6720 and NGC 7293, it is seen that intermediate structures having axial ratios neither too large to lead to extreme bipolarity ($\alpha > 1.5$, say), nor so low as to produce sample rings ($\alpha = 1$), reasonably explain this particular morphological type.

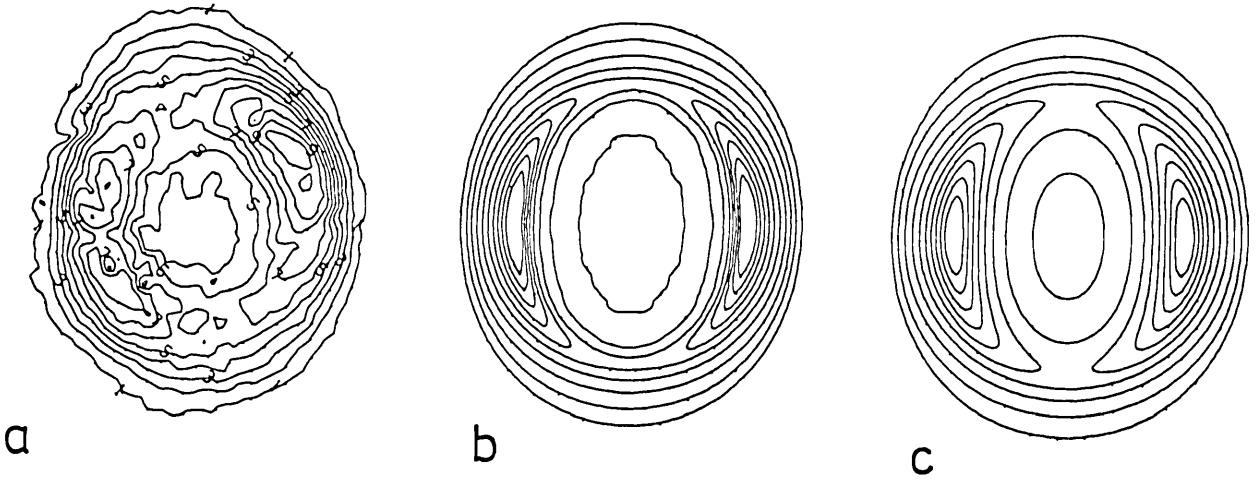

FIGURE 3.18

NGC 6720

a. Hβ ISOPHOTAL CONTOUR MAP. b. MODEL B CONTOURS. c. MODEL B CONTOURS WITH INTERNAL FILLING

3.9 Hour Glass Shapes

Perusal of the models illustrated in figure 3.5 appears to show a disproportionate number of hour glass models, when regard is had to their actual frequency. This is of course of little consequence; the models are chosen for illustration purely to indicate the varieties of structure which may develop, with little regard taken of their actual liklihood of occurrence. Nevertheless, a little thought suggests that hour glass structures are almost certainly less frequently observed than we might anticipate. There are however several possible reasons for this. First, it will be noted that hour glass configurations are most readily seen at elevations near $\beta \simeq 0^{o}$; away from this elevation, the hour glass structure is rapidly replaced by a strong bipolarity. Another reason is that for many hour glass formations gas density near the star will be very much greater than that of more distant neblosity. As a result, because of the restricted dynamic range of photographic plates there would in the past have been a bias for recording only the inner, brighter nebular structure at the expense of the possibly more characteristic hour glass structure. NGC 650-1 is a case in point. Only when the outer nebular envelope was specifically investigated by taking long exposure photographs was the intrinsic hour glass configuration revealed. In addition, we should note that the nature of the ejecting process itself may tend to preclude the formation of nebulae with high axial ratios, if higher ejection velocities are preferred.

We also note that $d\alpha/dV_o$, the variation of terminal axial ratio with ejection velocity, is a function of V_o

$$\frac{d\alpha}{dV_o} \simeq \frac{2V_o\,\omega^2\,R_*^2(0)}{(V_o^2 - V_{escp}^2)} \quad ; \quad \frac{\omega^2\,R^2(0)}{V_{escp}^2} << 1$$

For small ($V_o^2 - V_{escp}^2$) therefore (corresponding to large α), α varies rapidly with V_o. In the case $\omega R_* = 10$ km.s^{-1}, $V_{esc} = 35$ km.s^{-1} for instance, for axial ratios $2 \lesssim \alpha \lesssim \infty$ the ejection velocity must be within a range ~1 km.s^{-1}, whereas for $2 \lesssim \alpha \lesssim 1.3$ the corresponding velocity range is ~3 km.s^{-1}. Thus if shell ejections are equally frequent at all velocities below some fixed limit, say $V_o < 40$ km.s^{-1}, we would expect roughly three times more ellipsoidal type shapes than hour glass configurations. Finally, we should mention perhaps the most important discriminant of all; the effect of radiation pressure in reducing α, already discussed in an earlier section.

There is therefore a large catalogue of discriminatory mechanisms against hour glass shapes, which illustrates the difficulties which must be overcome before an adequate treatment of nebular statistics becomes feasible.

Despite this strong bias against observing hour glass structures, there are several clear examples in the literature, certain of which are illustrated by Phillips and Reay (1977). NGC 650-1 has already been mentioned. Another almost classic example is NGC 2474-5, previously described by Minkowski and Aller (1954) as evidence for peculiar ejection processes; a natural position to adopt in view of the observed configuration. A comparison of the observed structures with model MA 8 shows a strong resemblance, where the two bright regions correspond in this model to the minor axis lobes on the inner surface. The greatly increased brightness of these lobes is a direct consequence of their spatial proximity to the central star and, more important, the increased density in these parts of the shell. Although the internal arcs formed by the rest of the shell are rather less circular than in the model, it is possible to understand this

variation in terms of the stellar rotational effect illustrated in figure 3.2.

Other distinctive examples of hour glass structures reminiscent of models are NGC 2346, Henize 30 (NGC 2899), NGC 650-1, NGC 6772, NGC 6537 and MH_{α} 362. LK H_{α} 208 also shows this characteristic structure, although this nebula would not usually be classified as a planetary nebula; the central star is almost certainly very young.

3.10 Diskoids and Other Nebulae Types

A third common morphological category is the "diskoid", in which surface brightness is either uniform, or falls from the nebular centre outwards. It is not possible to define a unique structural form for this type of nebula; both toroidal and non-toroidal structures appear capable of emulating this behaviour, and it is not therefore surprising that this constitutes an important nebular grouping (c.f. Westerlund and Henize, 1967). Some reservations concerning the toroidal models should however be expressed at this point. It is noted that despite most of the mass residing some way from the central star, the intensity at elevation $\beta \simeq 90^{\circ}$ rises monotonically towards the central star. This is a consequence of the thin compressed wedges of gas near the central star. There are several questions concerning the likelihood of these persisting; it seems probable that radiation pressure will disrupt them, and thermal expansion attenuate them. Where this does not occur, they are almost certain to be optically thick. Either way, we would anticipate central emission to be greatly reduced; whether enough however to lead to emission toroids is unclear; there is certainly very little observational evidence that such structures are required.

A perusal of two particular cases of the diskoid category, NGC 3042 and NGC 7009 (Aller, 1956) indicates some interesting secondary characteristics worth noting; namely, the peculiar distortion of the internal isophotes along the minor axis. This is a distinctive sign of optically thin radiative acceleration (see figure 3.14) and may possibly be taken as evidence that radiation pressure has a significant influence upon nebular shapes.

Finally, a closer look at the simulated emission maps of several of our models (c.f. figures 3.10 and 3.12) reveals that many display a strong central concentration of emission, surrounded by a weak and sometimes extensive halo, leading in some cases to peripheral brightening and the development of a weak secondary ring. This is highly reminiscent of the halo found round many nebulae which have previously been ascribed to multiple ejections (Kaler, 1974), shell splitting due to internal Ly_α pressure (Gurzadyan, 1969) and ionisation of the interstellar medium (c.f. Kaler, 1974). It appears that a further explanation may now be given in terms of the structural forms adopted by shells under the circumstances investigated by this paper.

3.11 The Structure of Nebulae Deduced from Observations

A theoretical approach may enable a fresh understanding of planetary nebulae generally. A more satisfactory approach for individual nebulae however is to determine structural constraints using observations. In the following sections we give three examples of the applications of this method: NGC 7027; NGC 6720 and NGC 6543.

3.12 NGC 6543

A full consideration of this nebula is given in Phillips, Reay and Worswick (1977), and we give here only a brief account of the method employed to deduce the structure, and the main conclusion of this investigation.

NGC 6543 is particularly interesting since, aside from NGC 7293, it is the only other nebula for which a helical structure appears to have been suggested. Such a structure would be quite inexplainable in terms, for instance, of the mode of shell formation outlined in the previous section. It may however be explainable in terms of magnetodynamic mass redistribution. In view of the small lifetime attributed by Munch (1968) to the helical filaments of his model, it seems likely that we must further postulate an extant magnetic field frozen into the plasma. To propose a helical structure is therefore to pose serious questions concerning the modes of nebular structural development. On these grounds, it was considered relevant to reinvestigate the evidence upon which the helical interpretation was based.

An immediate point to be made is that a helical structure is by no means unambiguously indicated by the data presented by Munch. Rather, it seems that, as elsewhere for NGC 7293, the interpretation may have been biassed by a subjective interpretation of broad band photographic data. The fresh radial velocity data presented by Munch is extremely complex, and it is suggested by Phillips et al. (1977) that this in fact reflects chaotic small scale condensations, similar to that almost certainly present in most other nebulae, and specifically indicated by Dopita and Gibbons (1975) for NGC 6543 using other data. With this interpretation, and assuming a linear

dependency of expansion velocity with radius, provisional structures were determined for the nebula.

At this stage, further observational evidence was introduced. Electronographs of the nebula had been acquired for various forbidden and permitted lines. Isophotal contour maps of these were presented, and showed two distinct trends. The forbidden line maps (excluding [OIII]) showed a very strong bipolarity orientated along p.a. ~160°. For the H, H_e and [OIII] maps however, the bipolarity was contracted, weaker, and rotated in position angle. In addition, the axis of symmetry for the internal isophotes was distinctly rotated with respect to the outer isophotes. An obvious test then of the model deduced from the radial velocity data was whether it could reasonably simulate these quite peculiar features of the hydrogenic maps, as well as the structural change in passing from hydrogenic to (low excitation) forbidden line maps. The answer turned out to be in the affirmative, providing the model had parameters reasonably similar to those indicated in table 3.3. Of particular interest is the fact that the internal twist of the hydrogenic isophotes cannot be reproduced for a density radial exponent $\alpha(\rho \propto r^{-\alpha})$ equal to 0 or 2; but is well reproduced for $\rho \propto r^{-1}$. Similarly, the twist disappeared unless all three axes had differing lengths, as indicated by the radial velocity data, and if any axis was along, or perpendicular to the line of sight. Finally, it was noted that for density $\rho \propto r^{-2}$, the simulated isophotes always led to a nebula considerably more foreshortened than observed.

Forbidden line maps were simulated tolerably well by increasing the size of the central hole. The evidence for three axes of differing lengths appears therefore to be strong, and this has serious

TABLE 3.3

SUGGESTED STRUCTURAL PARAMETERS FOR NGC 6543

DEFINING EQUATION FOR SHELL (CARTESIAN COORDINATES)	$\frac{x^2}{a^2} + \frac{y^2}{b^2} + \frac{z^2}{c^2} = 1$ AXES $a \geq b \geq c$
NEBULAR DIMENSIONS	OUTER SURFACE: $a = 18\hat{''}0$; $b = 8\hat{''}85$; $c = 4\hat{''}4$ INNER SURFACE (HYDROGEN MAPS): $a = b = c = 3\hat{''}$ INNER SURFACE (FORBIDDEN LINE MAPS): $a = b = c = 5\hat{''}$
DENSITY VARIATION	$\rho \propto (x^2 + y^2 + z^2)^{-\frac{1}{2}}$
NEBULAR ORIENTATION	$\theta_a = 30^\circ$ = ANGLE SUBTENDED BY AXIS "a" TO LINE OF SIGHT $\phi_b = 55^\circ$ = ANGLE SUBTENDED BY AXIS "b" TO LINE OF SIGHT ($\theta = 0^\circ$)

consequences for an understanding of the formation of this nebula. We have already indicated one possible way in which this could arise (i.e. ejection from one component of a binary system). A contributory factor may well however be nebular shearing arising from the passage of the nebula through an interstellar cloud. This is discussed in rather more detail in a speculative section of the paper by Phillips, Reay and Worswick (1977). The supporting evidence may be summarised as follows.

(a) Observed compression of radio, Hα, HeI and [OIII] maps along a direction of motion corresponding to the proper motion vector.

(b) Intensity and spatial asymmetry of forbidden line maps indicating compression and retardation, again in the direction of motion.

(c) A radio tail with requisite orientation and length.

(d) The probable proximity of the velocity vector with the physical major axis of the nebula.

(e) An extended, roughly circular low intensity halo with density comparable to interstellar clouds.

(f) A nebular shape and density distribution consistent with that expected for a plausible shearing mechanism.

In total then, NGC 6543 appears to be a very interesting object, worthy of more attention.

3.13 NGC 7027

Details of the investigation of this nebula have again been published, by Hicks, Phillips and Reay (1976). We again summarise the principal arguments:

(a) The emission structure in [OIII] is found to be essentially the same as in Hβ. For this and other reasons it is suggested that spectral profiles of [OIII] lines are indicative of behaviour in the main nebular mass.

(b) The spectral line profiles are shown to possess two components, the red component being weaker than the blue at all points sampled in the nebula.

(c) The most likely source of this line asymmetry is shown to be dust; arguments are presented for believing the asymmetry to be unlikely to be due to variations in temperature or density.

(d) The Scott (1973) model is rejected as incapable of explaining double components away from the minor axis, although by a suitable contrivance the line asymmetry near nebular centre may be explainable in terms of dust absorption.

(e) An appropriate ellipsoidal model is shown to explain both the trend of line asymmetry, and the emission contours of the radio map, if the dust responsible for the asymmetry resides within the nebular shell.

(f) It is suggested that, because the grains would otherwise have to be anomalously large ($\gtrsim 5$ μm), they are more likely to be co-spatial with the gaseous material of the shell, than within the cavity defined by the inner shell surface.

There are several further points made in Hicks et al. (1976) concerning, for instance, the likely mass of dust grains in the nebula, which are not however of direct relevance here. It is sufficient to point out that the acquisition of further spectral line and electronographic data enabled a reassessment of nebular structure, where there was previous ambiguity arising from the radio map alone. The final

comment (f) does however require some extension and qualification although this does not seriously affect the arguments concerning structure.

We have already indicated evidence for supposing much of typical nebular expansion to be at roughly constant velocity. If this is the case then the expansion period would be $t \sim R/V$, where R is the present nebular radius, V the expansion velocity. Certain other investigations (c.f. Kahn, 1968) propose a roughly uniform acceleration from small velocities, however, for which case $t \sim 2r/V$, $dV/dt \simeq V^2/2r$. For NGC 7027 we have specifically $V \simeq 21.4$ km.s^{-1}, $t \simeq 10^4$ years, $dV/dt \simeq 10^{-5}$ cm.sec^{-2} (both the latter values for uniform acceleration). If grains are within a vacuum inside the inner shell surface, it is most likely that this is so because their terminal velocity is less than the shell velocity (for shell expansion having $dV/dt = 0$), or because their acceleration is less than the shell acceleration. For grains in a vacuum the terminal grain velocity W is given by (Spitzer, 1968)

$$W^2 = \frac{3\, L_* \, \overline{Q}_{PR}}{8\pi c \, r_o \, a \, \rho_{gr}}$$

where r_o is the radius of grain release, ρ_{gr} is the grain density, $\overline{Q}_{PR}$ is the radiation pressure scattering efficiency and L_* the stellar luminosity. If we set W less than or equal to the present expansion velocity of the nebula, a minimum estimate of grain radius "a" is achieved by letting r_o equal to the present nebular radius (0.07 p.c.). After Becklin et al. (1973) we set $L_* = 2.5 \times 10^4\ L_\odot$. This results in the requirement $a \geq 4.5$ μm if grains are not to be blown into the nebular shell. Similarly, for grain acceleration we have

$$\frac{dW}{dt} = \frac{3\ L\ \bar{Q}_{PR}}{16\pi c\ r_o^{\ 2}\ a\ \rho_{gr}}$$

Setting dW/dt equal to or less than the earlier suggested acceleration of the nebular shell then gives $a \gtrsim 4.7$ μm; essentially the same result as before.

In both cases we assumed $\bar{Q}_{PR} \simeq 1$, to be expected if the grains have strong U.V. absorption bands (suggested by the work of Becklin et at., 1973); and reside in a high temperature radiation field; the case for NGC 7027. This is certainly true of the astrophysically likely condensates investigated by Gilman (1974); the only deviations from $\bar{Q}_{PR} \simeq 1$ (for smaller grains) being such as to make $\bar{Q}_{PR}/a \simeq$ constant at its maximum value.

If the grains are neutral, and gaseous density in the cavity is ρ, then terminal velocity (Gilman, 1969) is alternatively

$$V_T = \left\{\frac{L_* \bar{Q}_{PR}}{4\pi c\ \rho\ r_o^{\ 2}}\right\}^{\frac{1}{2}}$$

whence

$$\frac{V_T}{W} = \left\{\frac{a\ \rho_{gr}}{r_o\ \rho}\right\}^{\frac{1}{2}}$$

For a rather high gaseous density $\rho \simeq 10^3\ m_H$, and $\rho_{gr} \simeq 3$ gm.cm^{-3}, $r_o = 0.07$ pc. we obtain

$$\frac{V_T}{W} = 92.5\ a^{\frac{1}{2}}$$

so $V_T/W < 1$ for small grains ($a \lesssim 1$ μm) - for which however W is so large that the grains are still blown into the shell. If the grains have appreciable charge, however, then coupling to the plasma will be much stronger, and in these circumstances small grains may well be held

in the cavity region - the requisite qualification to comment (f). It is however for all that unlikely that this is the actual situation; the infrared map of Becklin et al. for instance would be unlikely to be so reminiscent of the radio map were the grains primarily concentrated within the shell cavity.

3.14 NGC 6720

New information for this nebula has been published most recently by Reay and Worswick (1977), and Atherton et al. (1977). I am grateful to the latter authors for allowing me access to pre-publication data. In this last paper, one of the model nebulae discussed earlier is indicated as offering perhaps the most reasonable explanation of the available data. It will be shown however that without qualification this model does not explain certain (low excitation) forbidden line maps, and that no other published model appears capable of explaining the data in total.

The available models of this nebula appear to be as follows:

1. Toroidal (Minkowski and Aller, 1954; Hua and Louise, 1970)
2. Barrel (Proisy, 1974)
3. Cylinder (George et al., 1974)
4. Oblate spheroid (Phillips and Reay, 1977; Louise, 1974)
5. Prolate spheroid

The data of Atherton et al. clearly shows substantial splitting ($\sim$50 km.s^{-1}) of central line profiles, and this is reasonably explained by the authors in terms of intervening shells, presumably responsible also for the central [OIII] and hydrogenic emission in the maps of Reay and Worswick (1977). The count numbers of the central lines

indicate that they almost certainly arise from the bright, central shell (as opposed to the halo that this nebula possesses). It is primarily on these grounds that a spheroidal model is considered most appropriate. Certainly, a simple toroidal model would fail to meet these requirements. A more critical test of toroidal, barrel and cylinder models however is that they all require a substantial variation in the median Doppler velocity across the nebula, and this Atherton et al. show to be absent to any significant degree.

Of the available models, this leaves only oblate and prolate spheroidal structures as possible explanations of the observed nebula. In view of the trend of radial velocities, we must have for a prolate spheroid the major axis, and for an oblate spheroid, the minor axis, roughly in the plane of the sky. This however has consequences for the intensity ratio of ring to central hole. To see this, note that a cross section through the nebula along a direction defined by the emission map minor axis, and perpendicular to the plane of the sky, would for a prolate model yield a circular shell profile. For an oblate model, a similar profile would ensue for a cross section along the major axis of the emission structure. For a shell with circular cross section in which the seeing disk is smaller than the shell thickness, we readily obtain for the intensity ratio A_1 of shell to central hole

$$A_1 \simeq \left\{\frac{\phi_1 - 1}{\phi_1 + 1}\right\}^{-\frac{1}{2}}$$

where ϕ_1 is the ratio of the radii of outer and inner shell surfaces. Similarly, for a shell very much thinner than the seeing disk diameter, the appropriate ratio is

$$A_2 \simeq (2\phi_2)^{\frac{1}{2}}$$

where ϕ_2 is the ratio of shell radius to seeing disk diameter (providing ϕ_2 is reasonably large; say $\phi_2 \gtrsim 4$).

In table 3.4 we present appropriate values of A_1 and A_2 for selected emission maps from Reay and Worswick; making (for A_1) reasonable assumptions for shell thickness. It should be noted that values A_2 determined for the oblate model are almost certainly inapplicable in view of the absence of concentrated emission structure along the nebular major axis.

It is seen that whilst the intensity ratios are reasonably well accounted for in most cases, this is not true for the [NII], [OI] maps. Indeed, for these latter cases the central hole intensity is not significantly above sky background, and it seems likely that we are indeed looking through a zone of zero emission. An oblate spheroidal nebula with major axes in the plane of the sky would almost certainly account for this change in ring/hole intensity ratio, on passing from high to low excitation lines. It would not however explain the observed bipolarity. Preliminary modelling has shown that appropriate oblate spheroidal structures with minor axes tilted by up to 25° do not reproduce the bipolarity; by which stage they are also beginning to seriously conflict with the requirements of the radial velocity data, indicating low nebular inclination.

A possible explanation would be that shell density and/or mass differs along all three of the nebular axes, in a situation reminiscent of NGC 6543. It would be remarkable however if the shearing mechanism proferred for the structure of NGC 6543 were to apply also to NGC 6720, and it would seem preferable to seek some other mechanism (c.f. ejection from a binary component) were this possibility to be confirmed.

TABLE 3.4

OBSERVED AND THEORETICAL INTENSITY RATIOS FOR NGC 6720

MAP	PROLATE MODEL			OBLATE MODEL		
	OBSERVED INTENSITY RATIO	A_1	A_2	OBSERVED INTENSITY RATIO	A_1	A_2
[OIII]	3.0	2.8	4.2	1.6	2.0	4.2
[OII]	7.5	4.1	4.6	3.0	2.2	4.8
[OI]	>15	5.9	4.6	>5	1.9	4.8
Hα	3.0	3.0	4.3	1.6	2.1	4.3
[N_eIII]	3.8	2.6	4.2	2.0	2.5	4.2
[NII]	>15	3.7	4.6	>6	2.2	4.8
[SII]	5.0	3.5	4.5	2.0	3.0	4.8

For an alternative, and more likely explanation however, it should be noted that the forbidden line emission appears to principally arise from non-uniform filamentary structure, clearly seen in the best photographs of NGC 6720. This non-regularity almost certainly occurs both radially and over the surface of the nebula, and is probably responsible for the severe asymmetry and unevenness in the bipolarity. For an oblate nebula, the area of shell covering the central hole is only a fraction of that contributing to the emission peaks, and an extremely fragmentary emission structure could lead with relatively little contrivance to a situation where few filaments were projected against the central zone of the emission maps.

Thus, it is clear that where filamentary structure is reasonably uniform, and below the level of photographic resolution, a naive comparison with model isophotes is reasonably acceptable. This is not necessarily true however when the filaments are resolved, and/or non-uniformly distributed within the nebular mass, and particular care is then required to avoid spurious conclusions.

3.15 Conclusions

We have demonstrated that a theoretical approach assuming ejection from a red giant progenitor, enables us to account of the shapes of most planetary nebulae. An earlier application of this approach to novae (assuming of course a different progenitor) also produced good agreement with observation, and gives some confidence in the applicability of these mechanisms when discussing shell structures in general.

An alternative approach to evaluating shell structure is to apply observational constraints. This latter procedure was also demonstrated for three nebulae. Whilst the investigation was by no means exhaustive, it was shown that the number of tenable models may be drastically reduced if care is taken both in obtaining sufficient high quality data, and in interpreting this data.

CHAPTER 4

MASS LOSS IN NOVAE AND GLOBULAR CLUSTERS

4.1 Mass Loss from Novae

Problems relating to mass emission from novae have been considered in two papers: Phillips and Selby (1977), and Phillips and Reay (1977). Reference should be made to these papers for more detailed discussion of aspects summarised here.

Observationally, novae light curves are characterised by a steep rise to primary maximum. This appears to coincide with a rapid expansion of the effective photosphere, which achieves a maximum radius $\simeq 10^2 R_\odot$. During this expansion, the spectrum is characterised by a low velocity system of strong absorption lines with weaker emission components (the "pre-maximum spectrum"), although this transforms rapidly to a system indicating a considerably greater velocity of expansion (the "principal spectrum"). The transformation has been interpreted as being a consequence of rapidly increasing radiative acceleration of the ejected nova shell, near primary maximum (McCrea 1937, Mustel 1957). The visual luminosity subsequently declines ("early decline"), in most cases interrupted between 3.5 to 6 magnitudes below maximum visual luminosity by a "transition zone", in which the luminosity may oscillate semi-periodically, or perform a steep dive, recovering gradually in brightness until the final luminosity decline. The morphology of light curves and spectral variation has been ably discussed in many previous accounts, and reference may in particular be made to, for instance, McLaughlin (1939), Gaposhkin (1957). The final

decline eventually terminates with the establishing of constant luminosity, and spectrum indicating white dwarf characteristics. The observation that many of these remnants also appear to be members of binary systems has influenced the discussion of nova formation. The companion of the post-nova remnant appears usually to be a larger, cooler star, and Kraft (1962) and subsequently Starrfield et al. (1972) have suggested that mass transferred from the cool star through the inner Lagrangian point is accreted by the white dwarf companion. The compression and basal temperature of the accreted envelope rises as its mass increases, until hydrogen burning reactions start and thermonuclear runaway occurs.

The shells ejected by novae, though having relatively low mass ($\sim 10^{-7}$ $M_\odot$) compared to, say those of planetary nebulae, are not infrequently observed with appreciable angular size, often long after the central star has become incapable of ionising them itself. This arises due to the rapid decline in recombination rate $\alpha_r N_e N_i$ (where α_r is the recombination coefficient), due to decreasing density. Eventually a cold plasma may be formed which is still appreciably ionised, but capable of only weak emission. Such shells must eventually disintegrate when their densities approach that of the surrounding medium (c.f. Gurzadyan 1969), through the establishing of Rayleigh-Taylor instabilities.

Although there is considerable observational and physical understanding of these objects then, there are still broad gaps to be filled. It has only recently been recognised for instance that the decline in visual luminosity does not necessarily indicate a concommitant change in bolometric luminosity, but for Nova Serpentis at least resulted from a redistribution of continuum energy output, with a primary increase in U.V. flux (Gallagher and Code 1974). The physical

reasons for this redistribution appear however quite obscure. Nova Serpentis was also interesting for indicating further continuum changes, the most significant being an increase in infrared flux in the transition zone, with a corresponding decline in visual luminosity. The coincidence of visual decline and infrared excess led to an obvious explanation involving the formation of dust in the nebular shell, which it was in turn suggested caused short wave energy absorption and long wave re-emission. This idea has been subsequently developed by Clayton and Wickramasinghe (1976). It seems clear that similar explanations are relevant for many earlier examples of this type, and in particular the prototype DQ Her. The variation of the transition zone light curve of this latter nova appears to be particularly suggestive of a dispersing dust cloud, and coincidental continuum reddening led to the early proposal of such a mechanism (McLaughlin 1960).

Transition zone oscillations are less readily understood, although the early proposal of Grotrian (1937) involving variable mass loss rates has received nominal acceptance. Basically, it is proposed that variations in mass loss rate of a semi-regular nature develop (for reasons which are not properly considered), causing variations in the effective photospheric level, and thereby photospheric temperature. The photosphere is not therefore in hydrostatic equilibrium.

Even if the surface was in large scale hydrostatic equilibrium, the absence of a Balmer jump in the continuum is taken to indicate small scale chaotic motion (Mustel 1951). Nevertheless, a stable photospheric surface during stages of the post maximum decline is not inconsistent with the available data, and this possibility has stimulated an alternative exploratory discussion of transition zone oscillations (Phillips and Selby 1977).

This arises from the realisation that the luminosities of many novae almost certainly exceed the Eddington limit

$$L_o = \frac{4 \pi c G m}{\chi_o}$$

where m is the nova mass, and χ_o the opacity of the photospheric layers. As $\chi_o \rightarrow \chi_{TH}$, the Thomson opacity, then $L_o \rightarrow L_{CRIT}$, the maximum luminosity permitted before mass loss is inevitable. This luminosity corresponds to a bolometric magnitude M_{CRIT}, where numerically (Finzi 1973)

$$M_{CRIT} = -6.8 - 2.5 \log_{10} \left\{\frac{m}{m_\odot}\right\}$$

Where novae mass values have proved determinable, it appears that $m/m_\odot \lesssim 1$. A comparison with observed visual absolute magnitudes shows that in the immediate post maximum phase of decline, the outer layers of a nova must necessarily be forced outwards. If however bolometric luminosity M_{BOL} declines, there almost certainly comes a stage when $M_{BOL} \leq M_{CRIT}$, and the photospheric layers achieve temporary hydrostatic equilibrium. This stage is identified as the point of transition zone inception. Subsequent luminosity decline leads to the removal of hydrostatic support for the surface layers followed by collapse; the degree of collapse being in large part dependent upon the ratio of gas to total pressure (β) when $M_{BOL} = M_{CRIT}$. This is restrained by gas pressure, and oscillations may develop with frequency varying with both β, and changing mean radius. For a general discussion and later specific analysis, Phillips and Selby assumed radial variability of period P given by (Sterne 1937)

$$P = \frac{2\pi}{\sigma}$$

$$\sigma^2 = \frac{1}{3}(3j + q)(3j + q + 3)\left\{\frac{\Gamma G m}{R^3}\right\} \quad ; \quad j = 0, 1, 2 \ldots$$

$$q = \left\{\frac{3(3\Gamma - 4)}{\Gamma}\right\}^{\frac{1}{2}}$$

where R is the mean radius, Γ the ratio of specific heats. Further relations for Γ and β are given by Phillips and Selby (1977). From these it ensues that the transition zone nova radius is typically $R \sim 20\ R_\odot$ (and therefore would typically enclose the binary system). A more specific application to V603 Aql further indicates that, for that case at least (assuming the oscillations to be transient), the variation in radius over the entire transition zone must have been small. Similarly, bolometric luminosity must have declined less than the visual luminosity, and temperature probably decreased by less than 30%.

For the discussion of mass loss however the point of more specific interest in the above discussion is that the outflowing envelope must separate from the photospheric layers at a time very near the observed development of transition zone behaviour; assuming our present interpretation to be correct.

Observations show that the main shell typically acquires an equatorial toroid, polar jet configuration. Whilst this has only been photographed as a distinctive spatial structure in the case of DQ Her, there is considerable spectroscopic evidence that this is a common structural characteristic of many novae envelopes. In particular, the nebula from nova V603 Aql appears to have been fortuitously orientated so that the polar jet was directed towards Earth. In consequence, the observed nebula was almost exactly circular.

Such a peculiar structure represents an interpretative

challenge, which has been taken up by Warner (1972), who suggested non-radial stellar pulsations, and Mustel and Boyarchuck (1970), who indicated possible magnetodynamic processes. Hutchings (1972) has suggested an interaction between the expanding nebula and the secondary component of the DQ Her system, and Sparks and Starrfield (1973) invoked interactions between the expanding shells and pre-novae circumstellar rings. The suggestion of Hutchings (1972) has been criticised by Sparks and Starrfield (1973), although there appears to be a degree of contrivance about most of the explanations. Phillips and Reay (1977) investigated an alternative idea, in which it was suggested that the initial, low velocity line system represented an ejected shell which had been gravitationally braked, and acquired in consequence a high axial ratio. Subsequent radiative acceleration arising from a rapid increase in Ly_c flux, then resulted in preferential acceleration of those regions of nebula nearest the nova. In consequence, it was shown that the observed form of the nebular shell in DQ Her is readily acquired. Phillips and Reay (1977) should be consulted both for a direct comparison between model and observation, and details of the mechanism. This represents a specific application of a more general discussion of nebular development. It appears likely that nova rotational velocity at shell ejection was close to $\sim 10^2$ km.s^{-1}, and that at least one of the envelopes ejected had an axial ratio ~10 preceding radiative acceleration. This low rotational velocity is in contradistinction to post-novae rotational velocities of $\sim 10^3$ km.s^{-1}, and may indicate photospheric expansion by at least x10 (to ~1 $R_\odot$) before ejection of the primary shells.

4.2 Mass Loss in Globular Clusters

Theoretical studies, ranging from early work by Oort and van Herk (1959) to more recent work by for instance Taylor and Wood (1975) have consistently shown that an appreciable amount of free gaseous mass is to be expected within globular clusters. Whilst the actual amounts indicated have declined drastically from the estimate of 3×10^5 $M_\odot$ due to Oort and van Herk, to $\sim 10^2$ $M_\odot$ in Taylor and Wood (both values refer to M3), observations have similarly kept pace by defining limits for ionised and neutral hydrogen significantly below the theoretical values. See for instance Smith, Hesser and Shawl (1976), and earlier references in Taylor and Wood (1975). On the other hand, the explicit assumption in these calculations, that ~ 0.2 $M_\odot$ is lost in passing from red giant branch to horizontal branch, seems theoretically and observationally inescapable. Evidently then, current observations enable severe tests of present evolutionary theory for globular clusters. We will extend the discussion in a later section.

The mass may be lost gradually as the stars progress along the red giant branch. There is considerable precedent for this behaviour in disk population red giants, and the apparent observation of mass loss of order 2×10^{-9} $M_\odot.yr^{-1}$ in certain globular cluster red giants (Cohen 1976) suggests that much of the mass must indeed be lost through this mechanism. The latter reference also indicates that mass loss velocities may be larger than those characteristic of disk stars, taking values ~ 45 $km.s^{-1}$; greater that is than the cluster escape velocities. This evidently provides a plausible basis for understanding the low gaseous mass concentrations of these clusters. On the other hand, at least some stars must go through the planetary

nebula phase (viz. the progenitor of Psl), and it is difficult to see how this result could be regarded as anomalous, both on physical and (see later) statistical grounds (we will find that if it is anomalous, the actual observation of it would be inexplicable). It therefore seems necessary to conclude that both explosive and non-explosive mass loss processes are probably important in the evolution of globular cluster stars. This evolution might be rapidly speeded up were, say, stellar collisions to lead to atypically massive member stars, however, and the possibility that this or other interesting processes might be occurring in the concentrated cores of certain clusters led to a search for infrared emission in these regions. The possible presence of dust clouds in M13 suggested by Roberts (1960) on the basis of non-random structure, also suggested the possibility that certain clusters may have interesting behaviour in the infrared. More recently Kanagy and Wyatt (1975) have taken a fresh look at M13 and M15, and find extinctions of $A_V \sim 0.7$ magnitudes for a large patch in M13 based on microphotometric work, if the patch is located at the distance of cluster centre.

For a patch location at the near side of the cluster, the extinction would fall to ~0.3 magnitudes, whereas if on the far side, the cloud would be virtually opaque. These authors estimate a mass of only a few times 10^{-3} $M_\odot$ for the relevant patch. Similar results are noted for an apparent obscuring patch in M15.

4.3 Infrared Observations of Globular Clusters

The core of M15 was observed at 10.2 μm in October 1972, using a 4.2 K copper doped germanium photoconductor. The beam diameter was 10 arcseconds, and a 10 arcsecond sky nod was employed. This

resulted in the apparent detection of a source of magnitude N = +1.6 to a 3.3 σ level of significance. For more complete details of this measurement, attention is directed to Macgregor, Phillips and Selby (1973). This result has stimulated further observational work (Cohen and Fawley 1974) and theoretical discussion (c.f. Caloi and Panagia 1974). Further attempts were subsequently made both to improve the signal to noise of the specific result, and determine its relevance to globular clusters in general. Some results of this program, taken during the period 1973-1974 with the Tenerife 60 inch flux collector, are presented below. The results were all calibrated using C.I.T. standards, and quoted errors are one standard deviation.

Observations took the forms of normal photometry and continuous scans in declination. The photometric mode has been described earlier. Scans were taken by moving the telescope through the cluster cores at a rate 1.5 arcseconds.sec^{-1}, and signals were sampled once per second with a time constant 0.3 second. Beam size was in all cases 10 arcseconds. The scans were subsequently summed following least squares removal of low spatial frequency drifts, and convolution with the reversed response function to a point source to optimise detection. The result of this procedure for a strong point source is shown in figure 4.1. Details of both photometry and scans are given in table 4.1. Upper limits refer to the signal required for 3σ detection, and scan areas are centred on the cluster cores.

Four clusters were measured: M2; M80; M92 and M15. M80 is of particular interest for being the possible site of an early nova (personal communication, Professor B. V. Kukarkin), and M92 is very similar to M15 in the degree of central stellar concentration. M2 is representative of a broader class of globulars with less central stellar

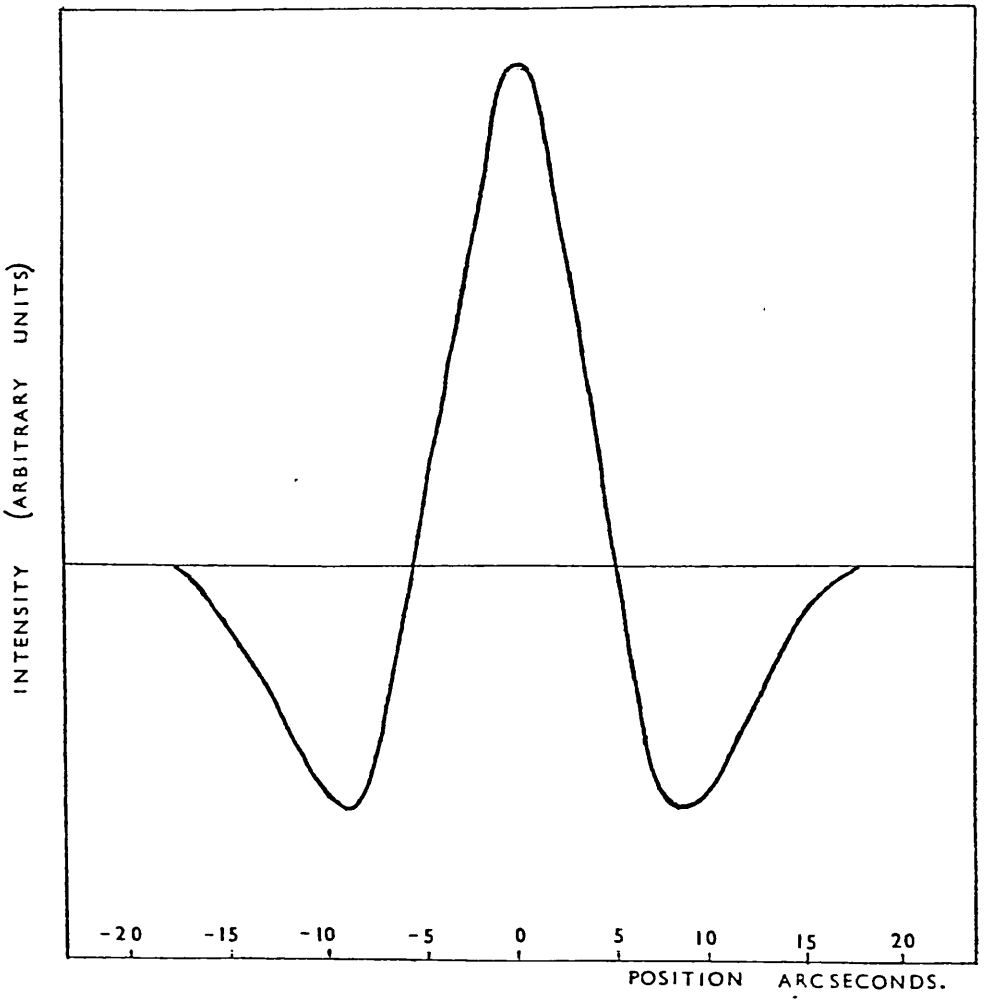

FIGURE 4.1

FILTERED RESPONSE TO SCAN-OF STRONG POINT SOURCE

TABLE 4.1

CLUSTER	DISTANCE* KPC	MODULUS*	CONCENT-RATION +	DATE OF OBSERVATION	OBSERVING MODE	WAVE-LENGTH (λ μm)	AREA SCANNED (δ x α)	CORE MAGNITUDE AT λ
NGC 6093 ≡M80	9.7	14.93	II	21-22/8/73	PHOTOMETRY	5.0	-	>+2.16
	-	-		26-27/8/74	SCANS	10.2	120" x 10"	>+2.15
NGC 6341	14.34	7.4	IV	7-8/8/73	PHOTOMETRY	10.2	-	>+3.09
	-	-		22-23/8/73	PHOTOMETRY	5.0	-	+4.97 (2.4σ)
NGC 7078 ≡M15	14.95	9.8	IV	5-6/8/73	PHOTOMETRY	10.2	-	+4.29 (3σ)
	-	-		21-22/8/73	PHOTOMETRY	5.0	-	>+4.48
	-	-		21-22/8/73	SCANS	5.0	60" x 0"	>+3.17
	-	-		21-22/8/74	SCANS	10.2	105" x 0"	>-0.11
	-	-		22-23/8/74	SCANS	10.2	90" x 20"	+1.53 (3σ)
				23-24/8/74	MATRIX PHOTOMETRY ABOUT CORE	10.2	40" x 40"	>+2.33
				25-26/8/74	SCANS	10.2	120" x 30"	>+2.14
NGC 7089 ≡M2	15.25	11.2	II	6-7/8/73	PHOTOMETRY	10.2	-	>+3.70
	-	-		22-23/8/73	PHOTOMETRY	5.0	-	>+5.12
	-	-		26-27/8/74	SCANS	10.2	120" x 0"	>+2.15

* KUKARKIN (1974)

+ARP (1965)

concentration. Yet again however, no photometric detection above 3σ was found in any of the clusters. Although limits in M80 and M2 were not particularly faint, it is clear that no central source comparable in brightness to that earlier reported in M15 can be present. The 4.8 μm signal for M92 will similarly require improvement in statistical significance before it can be accepted as indicating a central source. M15 yet again shows a signal at 3σ level, however, although for a much reduced signal strength. There are only two explanations for this which stand up to any degree of examination:

(a) the source is variable;

(b) it is located near the edge of the beam.

Although locational accuracy was estimated to be better than 2 arcseconds, it may just be possible that uncertainties in this could account for the suggested diminuation of source strength, if the source were located near the edge of the beam. This is probably the most conservative position to adopt at present, although there is no particular unliklihood in variability for a source which is already sufficiently peculiar to have been detected at all at these wavelengths (see later discussion). Indeed, Grindlay and Liller (1977) have recently published results suggesting a significantly variable central source of Hα emission for this cluster.

Detection levels for the scans were much lower than for the photometry. A typical scan of length 80 arcseconds (taking one minute of time to complete) is, in respect of detectivity, equivalent to about

three seconds of photometry. The advantage of scanning comes with the delineation of strong off-centre point sources, or strong extended sources with low spatial variability. In one of two series of scans at 10.2 μm, an apparent source of emission was detected with strength N = +1.53. The convolved scan profile is given in figure 4.2. A comparison with figure 4.1 suggests that the responsible source is possibly point-like, although more likely extended.

Despite these confirmatory observations, it was felt that several improvements in signal detection capabilities were required before further work could usefully proceed. First, an improvement in detector sensitivity was desirable; and American work suggested that this would soon be available to U.K. groups. Sources having $N \gtrsim +2$ were approaching uncomfortably close to the limits of detection, and improvements in this limit required lengthy observation periods. There was, further, no possibility of observational feedback; particularly crucial for globular cluster work, where observation periods of 3 to 4 hours per object were not uncommon. An on-line computer would solve this, and of course greatly facilitate the optimisation of weak signal strengths. The situation in regard to both detectors and computing facilities is now improved to the level where further observations are plausible.

To conclude, we may say that current observations suggest a strong, possibly variable 10.2 μm source in M15 to a reasonably high level of significance. Further observations are however still required. There appears to be no reason to suspect that this is a common feature of globular clusters in general.

FIGURE 4.2 SCANS THROUGH CORE OF M15, ACQUIRED 22-23/8/74. ERROR BARS INDICATE $\pm 1\sigma$. POSITION IS WITH RESPECT TO OPTICAL CENTRE; ERROR BAR C INDICATES POSITIONAL UNCERTAINTY

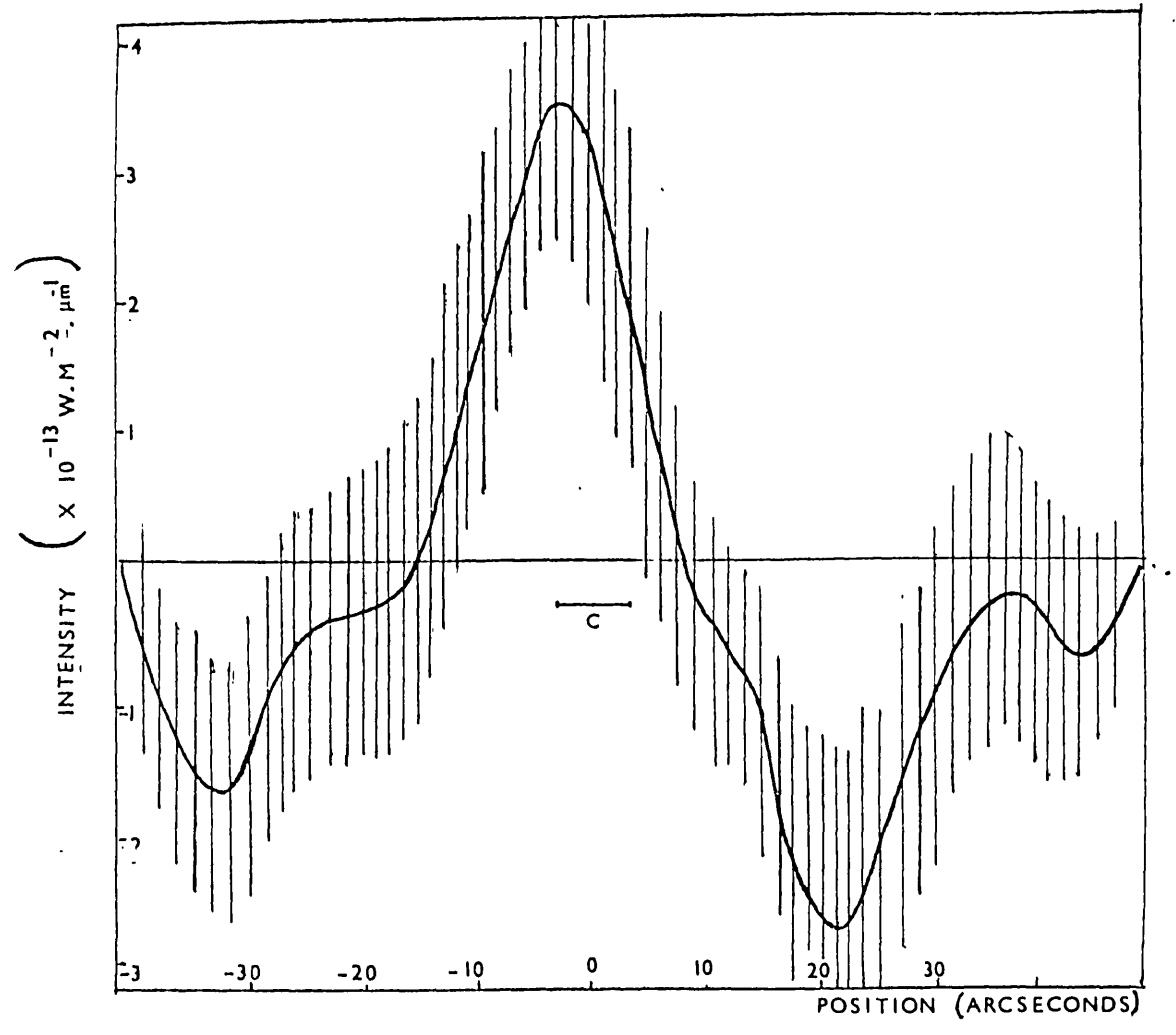

4.4 Mechanisms for Infrared Emission in Globular Clusters

There are several conventional sources of infrared emission which may contribute to the observed source in M15. Few however seem capable of satisfactorily explaining the entire flux. MacGregor et al. argued that the central stellar flux would not exceed N = +8.5, assuming the core luminosity function to be similar to that of M3; more recently, Newell et al. (1976) have shown the blue spectrum of the cluster to vary little between regions centred on, and a little away from the core, supporting the concept that the core population is reasonably similar to the rest of the cluster. Grasdalen (1974) has further shown that this is probably also true for other clusters, for which infrared-optical colour indices were found to be closely invariant with distance from cluster centre. The question was reviewed again by Caloi and Panagia (1974), who came to a similar conclusion using rather different arguments.

An uncertainty in the original estimate of MacGregor et al. was the importance of TiO absorption in depressing the visible continuum. Globular clusters generally, and extremely metal deficient clusters such as M15 in particular would perhaps be expected to have reduced TiO absorption levels. In fact, subsequent work by Glass and Feast (1973) has indicated that TiO absorption in globular clusters is very similar to that of population I stars. These uncertainties may now be short circuited to some extent by the work of Grasdalen, however (with appropriate qualifications concerning its applicability to the core of M15, not measured by Grasdalen). Typically we have V-K $\simeq$ +2.2, with little dispersion. From King (1966) we have V = +9.90 as the visual magnitude of the 11.16 arcsecond diameter central region; a correction A_V = 0.42 having been applied for reddening (Arp 1965). It follows

that K ≃ +7.7, and the N band magnitude is unlikely to be brighter than this by more than ~0.1 magnitudes (i.e. N ≃ +7.6). Hansen and Hesser (1975) have apparently detected M15 at K, although with some error; their value is consistent with that calculated above. Clearly then, even appreciable Mira-like excesses for these stars would not explain the observed source strength.

MacGregor et al. (1973) also argued against a substantial central dust cloud, non-localised with respect to the individual stars, and Caloi and Panagia (1974) concur with this. The most likely source of infrared emission seemed then to require an object, or objects which were either very cool and luminous, or which supported a massive excess at 10.2 μm. MacGregor et al. suggested that an NML Cyg type object might be present because of its comparable intrinsic luminosity to the infrared source in M15, and its faintness at optical wavelengths. Because of the spectral type of the underlying star in NML Cyg (M6 Ia, Johnson 1966b) this would make it anomalously cool and bright. It is still not clear that this possibility can be entirely dismissed, although the recent limit of M ≳ +4.8 at 4.7 μm (Hansen and Hesser 1975) suggests that a silicate-type excess may be present, leading to a closer resemblence to NML Tauri type stars.

Another possibility is that the central source is a planetary nebula. A substantial amount of evidence (c.f. Woolf 1969; Cohen and Barlow 1974) has shown that these objects have typically large values of (V-N). Since one planetary nebula is already known to be present in M15 (Ps1; sufficiently far from the core however not to have contaminated our results (MacGregor et al. (1973)), the suggestion of Caloi and Panagia that such an object could explain the M15 source clearly carries some weight, and has stimulated work attempting an optical

detection. Peterson (1976) and Leroy et al. (1976) have found a small region of enhanced central emission; and the former author has interpreted this as a possible centrally located planetary. Presumably however this enhanced emission is that noted recently by Newell et al. (1976) and Bahcall et al. (1975) and attributed by them to a high density of core stars. This latter hypothesis requires a severe departure from an isothermal model, found to be reasonably applicable for other clusters, and a central massive component is invoked. The consequent theoretical trend of cluster surface brightness with radius has only qualified success in explaining the results, however. The spectral data of Newell et al. mentioned earlier, whilst also supporting an explanation in terms of enhanced stellar density, probably requires extension to visible-red wavelengths (and thereby to the strong nebular emission lines of Hα, [OIII]) before a decisive test of the planetary nebula hypothesis can be made in these terms. It is however clear from the work of Newell et al. that the central region of enhanced emission is appreciably extended, with a size ~3". At a distance 10.5 kpc for M15 (Arp 1965), this corresponds to 0.15 pc, and if a planetary nebula, would almost certainly be optically thin (Cahn and Kaler 1971). This conflicts with the suggestion of Caloi and Panagia (1974), who invoke a very young nebula in order to explain the 10.2 μm results. This latter proposal is however not a requisite of their analysis; a reasonable change in a parameter such as grain radius readily enables an extension of the argument to larger nebular radii. There are however several further doubts which must be levelled at any explanation in terms of a central planetary nebula.

First there is a statistical query. We will later find that the expected planetary nebula detection rate does not climb rapidly with increasing survey detection limit.

If we therefore propose a core planetary nebula in M15, this would represent probably the intrinsic limit to the number of planetary nebulae in a survey such as Peterson's, with visual magnitude greater than or equal to the M15 core brightness, M_{CORE}. Irrespective then of arguments concerning the probability of observing a nebula in the core, we may question the probability of observing the only two observable nebulae in one cluster. For a sample of 43 clusters, as in Peterson's survey, for instance, the mean probability η of detecting a planetary nebula down to M_{CORE} would be $\eta \simeq 2.33 \times 10^{-2}$, and the probability of finding two nebulae in one cluster is, by Poisson statistics

$$P = \frac{e^{-\eta}\,\eta^2}{2} = 1.13 \times 10^{-3}$$

or for all 43 clusters, the chances are ~20:1 against. This of course is not to dismiss the possibility. It would however strongly suggest the necessity of anomalous conditions in the core of M15.

A second objection would arise from the required level of infrared excess. As for Ps1 (O'Dell et al. 1964), it seems probable that any central planetary nebula would be metal deficient. Under these conditions, dust condensation would be expected to be less prolific than for galactic nebulae; thermalisation of short wave stellar radiation by dust is almost certainly the primary mechanism for generating excesses. In figure 4.3 we present a histogram showing the variation of planetary nebula numbers with (V-N), for galactic nebulae. The V magnitudes corrected for reddening are from Cahn and Kaler (1971). Their radii range from 0.023 pc (this lower limit being particularly

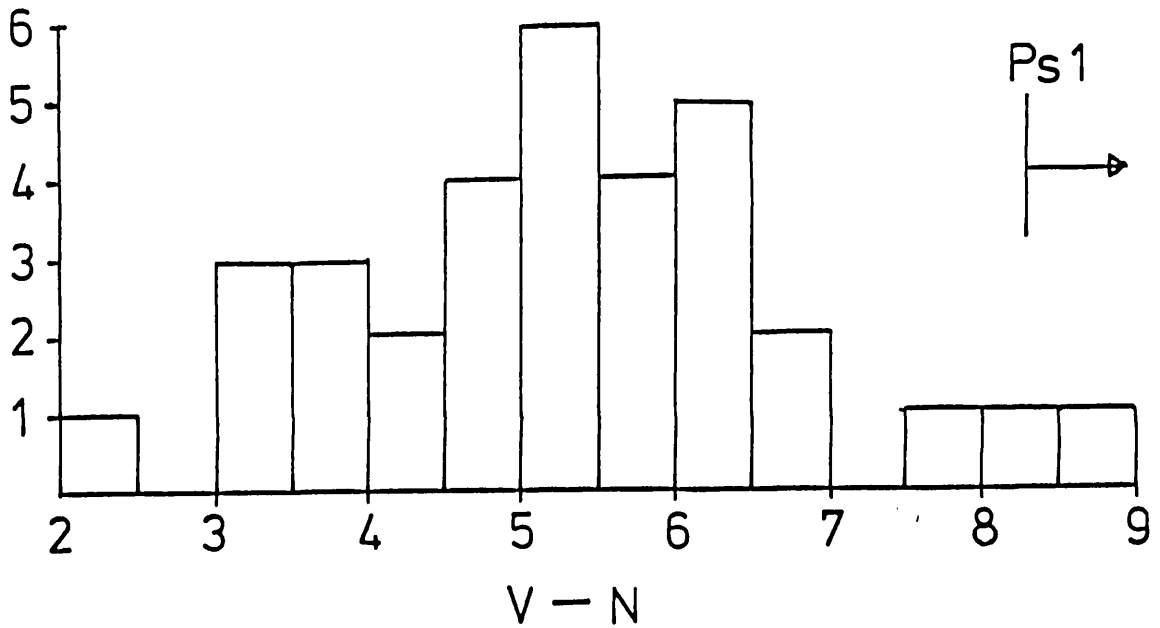

FIGURE 4.3

(V-N) DISTRIBUTION OF PLANETARY NEBULAE

uncertain) to 0.474 pc; most of them almost certainly being optically thin. They correspond to those nebulae for which infrared data is available from Cohen and Barlow (1974). Even if a central planetary nebula in M15 contributed the entire visual core flux, it is clear that (V-N) would have to be ≃ +8.3, giving it one of the largest infrared excesses on record. This, in view of our previous comments concerning dust content would be a distinctly peculiar result.

Although, therefore, the concept of a central planetary nebula cannot be necessarily dismissed on the basis of earlier data, there are substantial reservations to be attached to such an hypothesis. We will, in the next section, present new data which appears to finally dispose of an explanation of the infrared emission in terms of either a central planetary nebula, or any hydrogenic plasma.

To anticipate this result, the core enhancement is almost certainly due to stellar concentration (although see Grindlay and Liller (1977), who suggest a possible ~10% Hα excess in the core). If a central massive object is invoked to explain this, such as a black hole, then various other possibilities for explaining an excess become more likely, such as non-thermal emission. The presence of a massive, collapsed object appears to be reasonably acceptable on theoretical grounds (see for instance Bahcall and Ostriker 1975, and references therein) and the concept is made attractive by the detection of a weak X-ray source within an error box incorporating the cluster core. The evidence therefore appears to be strong that exotic processes may be operating in the core of M15, and in these circumstances it seems not improbable that an explanation of the observed 10.2 μm emission will have to be found in similar terms.

4.5 The Emission Enhancement in the Core of M15

As a test of the possibility that the enhancement of core emission in M15 is due to a planetary nebula, we have secured electronographs with narrow band filters centred on Hα and λ 6700 Å continuum.

These electronographs have been ratiod, and Hα, λ 6700 and ratio maps are presented in figure 4.4. Before proceeding to discuss these, we discuss some earlier work in the field.

Although adopting a rather different procedure (i.e. assessing the infilling of the Hα absorption line profile by emission), Smith et al. also used Hα emission to test the presence of a central plasma. The method however is open to considerable uncertainties (such as the correct equivalent width to adopt for stellar Hα absorption), and for strongly localised emission, less sensitive than the procedure employed here. It is for instance quite consistent with their data to suppose a second planetary nebula, similar to Ps1, to reside somewhere in the vicinity of the core; although the presence of a brighter nebula can almost certainly be precluded.

After acquiring our observations, Grindlay and Liller published further photometry, in which ratios of Hα to R band emission were measured from small regions ($4\hat{}''$ - $21\hat{}''$ diameter) at the cluster cores, and larger regions ($40\hat{}''$ - $52\hat{}''$ diameter), again centred on the cores. Significant differences were apparently detected between these two ratios for several clusters, including M15, and interpreted as plasma emission at the cores. However, the results of two independent sets of ratios for M15 with a 16 Å Hα filter bandwidth were contradictory; one showing an excess of ~(13±2)%, the other an essentially zero excess, ~(3±2)%. This may indicate a real variability, as Grindlay and Liller suggest. Considerable caution should be exercised however before

FIGURE 4.4a M15 IN CONTINUUM λ 6700 Å. CONTOURS ARE EQUISPACED BETWEEN LARGEST AND SMALLEST INTENSITY LEVELS

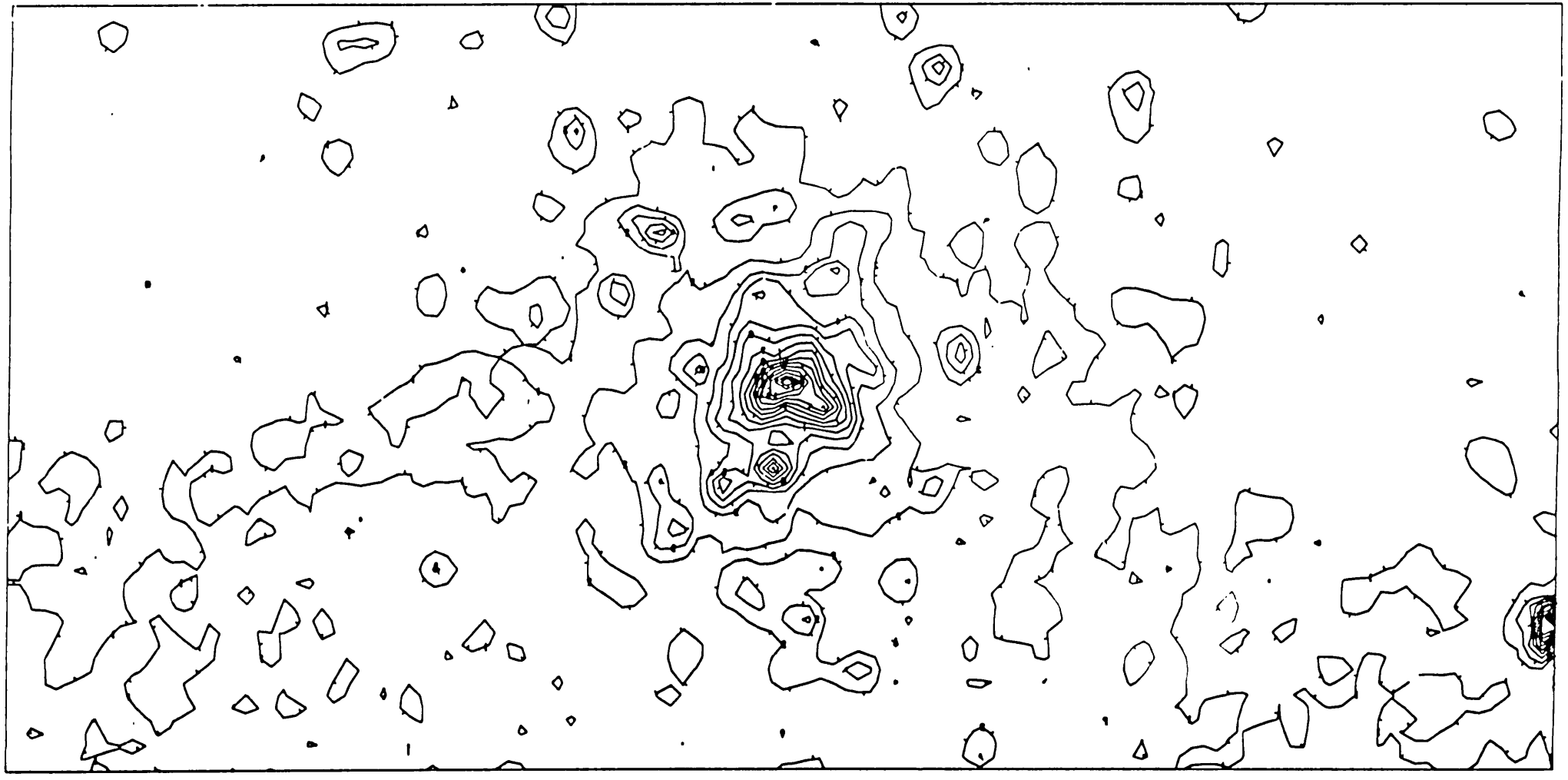

10 ARCSEC

FIGURE 4.4b M15 IN Hα. CONTOURS ARE EQUI-SPACED BETWEEN LARGEST AND SMALLEST INTENSITY LEVELS

CORE OF M15 + Ps 1. RATIO Hα/λ 6700 Å.
EQUISPACED CONTOURS. PEAK RATIO (CONTOUR 15) = 6.1

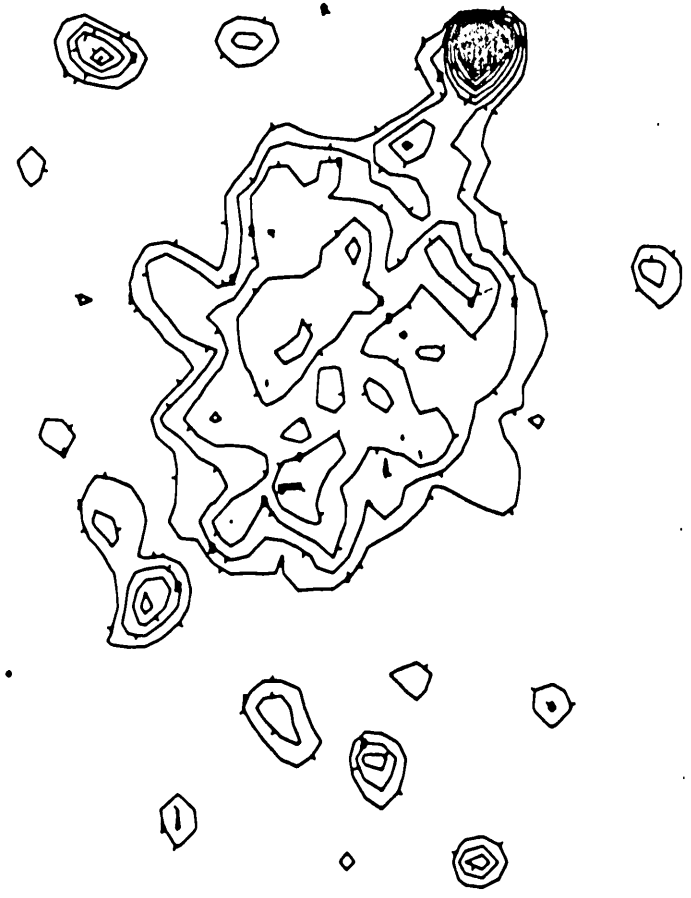

10 ARCSEC

FIGURE 4.4d

RATIO MAP OF Hα/λ 6700 CONTINUUM. CORE OF M15. THE STEEP GRADIENTS AT THE EDGE OF THE CENTRAL EMISSION ZONE IN THIS MAP, AND FIGURE 4.4c, ARE A CONSEQUENCE OF THE REDUCTION PROCEDURE. CONTOUR 15 CORRESPONDS TO A RATIO 2.45.

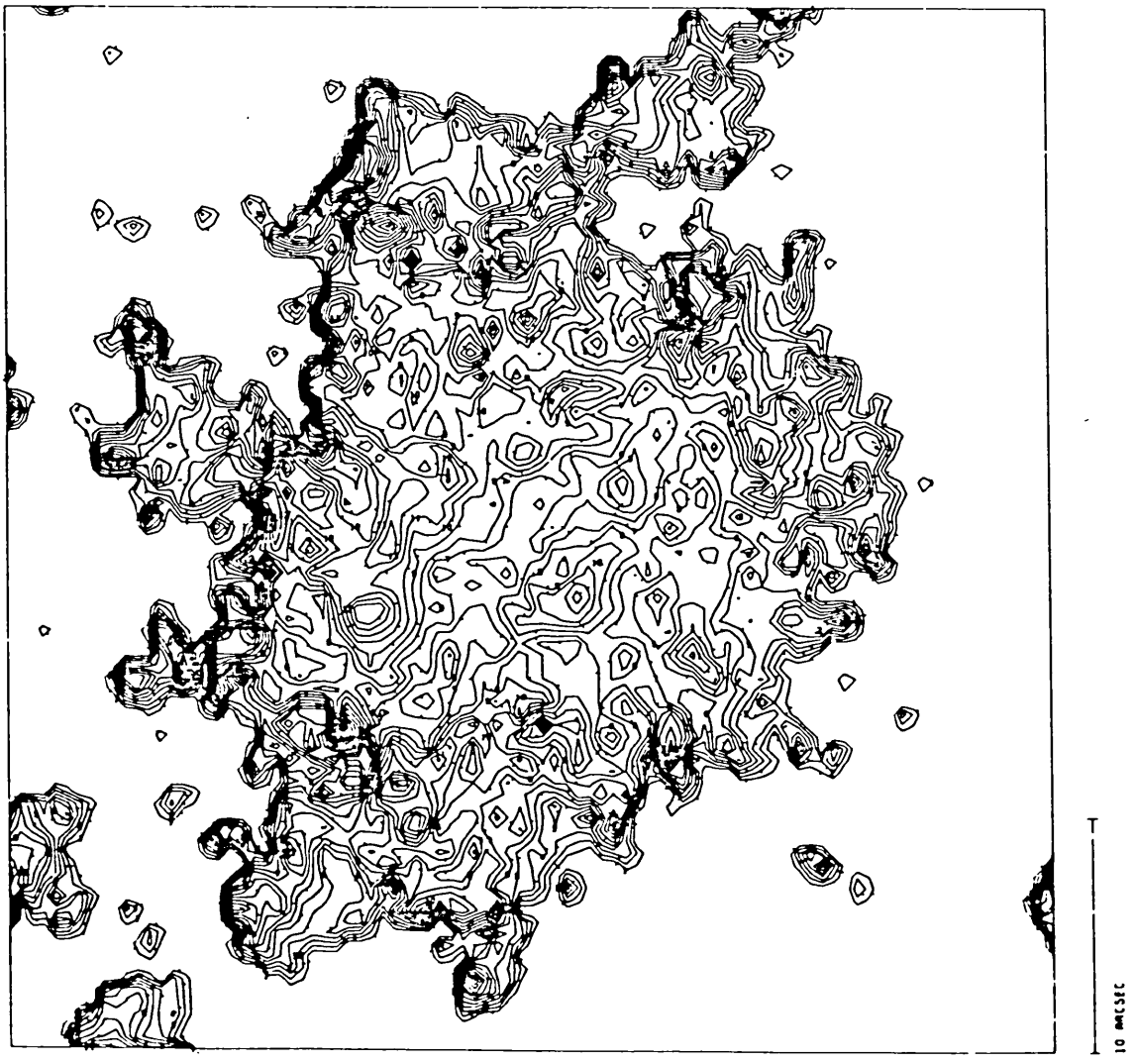

accepting this position. In particular, each of the above results derives from the ratioing of four independent measurements. It is clear that a procedure involving a reduction in the number of independent measurements is to be preferred.

For the present results, we have presented two ratio maps of the core region (figure 4.4). The first ratio map shows the core with Ps1. The planetary nebula dominates, leaving the core-region relatively ill defined. For the second ratio map we have excluded Ps1. Relative variations in intensity by a factor ~1.5 are seen within a radius ~30$\hat{}$" of the core; rather larger than would be expected from variations in the temperature of the constituent stars. As a measure of this latter quantity, it will be noted that blue horizontal branch (and early type foreground) stars have a continuum variability given in the Rayleigh-Jeans limit by $F_\lambda \alpha \lambda^{-4}$. For late-type stars with temperature T_R, the continuum variation in the Wien limit is $F_\lambda \alpha \lambda^{-5}\ e^{-1.44/\lambda T_R}$. Between two wavelengths $\lambda_1 < \lambda_2$, relative continuum levels will then vary as $Rg = (\lambda_1/\lambda_2)\exp\{1.44\{\frac{1}{\lambda_1}-\frac{1}{\lambda_2}\}/T_R\}$. Since the latest spectral type present in galactic globular clusters in ~M4, we may set T_R ~ 3000 K to obtain a maximum ratio variability $Rg \simeq 1.14$ for the case under consideration. In fact, as we have noted, the observed rate of ratio variability is very much greater than this, and must be presumably ascribed to variation in the depth of the Hα line in late type giants. Further analysis of the data is at present being undertaken. Two important points may however be made with the data as it stands. Variations of the Hα/continuum ratio over the core region of this (and other clusters not discussed here) are large, and probably dominated by the behaviour of single bright late-type giants. The presence of similar variations in the ratios of Grindlay and Liller

are therefore not to be unexpected. Whether late giants can account for the entire variability observed by these latter authors will require a clear understanding of the sensitivity of core U-B, B-V indices with Hα line depth (Grindlay and Liller argue for small stellar differentiation in M15 on the basis of U-B, B-V indices). From the present evidence, the presence of core Hα emission from an interstellar plasma would appear to require stronger backing before it can be accepted.

Secondly, if a substantial fraction of the excess core emission were due to planetary nebula, large Hα/λ 6700 emission ratios would be expected at the centre of the maps. There is no evidence for this. The hypothesis of Peterson in this regard may therefore be dismissed.

4.6 Limits to the Incidence of Planetary Nebulae in Globular Clusters

In the previous section, it was shown that any excess infrared emission from the core of M15 is almost certainly not attributable to a planetary nebula. This introduces however an interesting and broader question as to whether the observed incidence, or some future program of observations, may be used to place constraints on the relevance of the planetary nebula stage as a mass loss mode.

The rate of formation of planetary nebulae dN/dt may be defined in terms of the evolution in the bolometric turn-off luminosity at the main sequence $(d \log_{2.512} L/dt)_{MS}$ and the number of stars per unit bolometric magnitude range $(dN/d \log_{2.512} L)_{MS}$ at the turn-off point, through

$$\frac{dN}{dt} = \left\{\frac{dN}{d\ \log_{2.512} L}\right\}_{t=T-T',MS} \left\{\frac{d\ \log_{2.512} L}{dt}\right\}_{t=T-T',MS}$$

$$= \left\{5\ \psi \frac{d\ M_V}{d\ M_{BOL}}\right\}_{t=T-T',MS} \left\{\frac{d\ \log_{2.512} L}{dt}\right\}_{t=T-T',MS} \qquad \ldots (4.1)$$

where T is present cluster age, and T' the evolutionary time between main sequence turn-off and planetary nebula formation. T' is taken to be comparable with the evolutionary time for initial main-sequence to red giant tip; ψ is the initial main sequence luminosity function, and subscript "M.S." indicates initial main sequence.

An evolutionary parameter more readily available than $(d\ \log_{2.512} L/dt)_{MS}$ is the corresponding value at the Schonberg-Chandrasekhar limit, subscripted SC, defining the location of core hydrogen exhaustion, and inception of the red-giant branch. Sandage (1957b) originally determined

$$t = \left\{\frac{L_\odot}{L_{SC}}\right\}\left\{\frac{M_{SC}}{M_\odot}\right\} 1.1 \times 10^{10} \text{ yrs}$$

for cluster age t, assuming homologous evolution to a 12% hydrogen exhaustion limit. Whilst this relation is still commonly quoted, it is discrepant with more recent relations by, for instance, Iben and Rood (1970 a,b), who obtain

$$\log t \simeq 10.42 - 1.1 \log \frac{L_{SC}}{L_\odot} + 0.59\ (0.3 - Y) - 0.14\ (\log Z + 3) \qquad \ldots (4.2)$$

where Y, Z are the fractional abundances of helium, and heavier atoms respectively. For M3, $\log Z \simeq -3$, and $Y \simeq 0.3$ (Sandage 1970), within fairly small errors, so that typically

$$t \simeq 2.63 \times 10^{10} \left\{\frac{L_\odot}{L_{SC}}\right\}^{1.1}$$

This has specific applicability for t between ~1.2 x 10^{10} and ~1.6 x 10^{10} years, but in fact is reasonably appropriate down to at least t ≃ 6 x 10^{9} years. The data of Demarque et al. (1971) for Y = 0.25, log Z = −3 can be represented to reasonable accuracy by

$$t \simeq 2.37 \times 10^{10} \left\{\frac{L_\odot}{L_{SC}}\right\}^{1.1} \qquad t > T_1 = 8 \times 10^{9} \text{ years} \qquad \ldots (4.3)$$

$$t \simeq 8 \times 10^{10} \left\{\frac{L_\odot}{L_{SC}}\right\}^{2.6} \qquad t < T_1 \qquad \ldots (4.4)$$

Comparison with the Iben-Rood equation shows small, but not serious differences in L_{SC} for a cluster age t = 10^{10} years. The trend of results for Demarque et al. suggests a scaling down of t as Y increases, and some decrease in T_1 – although for a change Y → 0.3 the alterations will be small. For a given L_{SC}, and Y, reducing Z leads to increasing t (a feature first noted by Simoda and Iben 1968), although for the specific clusters in which Z is particularly small, such as M15 and M92, Y is correspondingly larger, tending to counteract this behaviour. Nevertheless, for M15 and M92, the main sequence turn-off is brighter than for M3 (Sandage 1970) although their ages are comparable. As equation (4.2) indicates, however, the constant terms in equations (4.3), (4.4) are not unduly sensitive to even large variations of log Z .

To cover some of the uncertainties we shall use both expressions 4.3 and 4.4 over the time period of interest; serious deviation of typical clusters from the consequent range of values for dN/dt will almost certainly indicate a revision of present evolutionary theory or, more likely, a restriction upon the planetary nebula mode of mass loss. We will call expressions 4.3 and 4.4 respectively case 1 and case 2, and a little manipulation gives the corresponding relations

CASE 1 $$\frac{d \log_{2.512} L_{SC}}{dt} = -4.16 \times 10^{-11} \left\{\frac{L_{SC}}{L_\odot}\right\}^{1.1} \text{ magnitudes.yr}^{-1} \quad \ldots (4.5)$$

CASE 2 $$\frac{d \log_{2.512} L_{SC}}{dt} = -5.22 \times 10^{-12} \left\{\frac{L_{SC}}{L_\odot}\right\}^{2.6} \text{ magnitudes.yr}^{-1} \quad \ldots (4.6)$$

At the main sequence, these rates are typically increased by an approximate factor $\Omega \simeq 1.25$.

For clusters generally $T \simeq (1.0 \pm 0.4) \times 10^{10}$ years (Schwarzschild 1970), and T' is therefore probably reasonably bracketted by 6×10^9 years $< T' < 1.4 \times 10^{10}$ years. For M3, $L_{SC}/L_\odot \simeq 1.96$, and we can therefore take $T_{M3} \simeq 1.1 \times 10^{10}$ years. For other estimates of T_{M3}, and a discussion of the uncertainties in the parameter, see for instance Sandage (1970).

Using current evolutionary models (c.f. Iben and Rood 1970a; Demarque et al. 1971) and data from Sandage (1957a) with the relation

$$\psi_{M3}(M_{BOL}) = \xi_{M3}\,(M_{BOL}=6).\left\{\frac{\psi(M_{BOL})}{\psi(M_{BOL}=6)}\right\}$$

where ψ is the Salpeter initial luminosity function, $\xi_{M3}(M_{BOL})$ the bolometric luminosity function for M3, we obtain for case 1:-

$$\frac{dN}{dt} = 5.6 \times 10^{-14} \rightarrow 2.4 \times 10^{-13} \text{ sec}^{-1}$$

and for case 2

$$\frac{dN}{dt} = 6.3 \times 10^{-14} \rightarrow 3.5 \times 10^{-13} \text{ sec}^{-1}$$

$\frac{dN}{dt}$ is therefore not strongly model-dependent, and we adopt $5.6 \times 10^{-14} \leq dN/dt \leq 3.5 \times 10^{-13}$. Notice that we have taken $\psi_{M3}(M_{BOL})$ as reasonably typical of other clusters. In fact M3 is probably

richer than the average, and using $\psi_{M3}(M_{BOL})$ will give an upper limit dN/dt. The observed luminosity functions of M13 and M92 suggest $\xi/\xi_{M3} < 1$, for instance, and the number of blue horizontal branch stars are respectively comparable (~522) and substantially less than (~154) the number in M3 (~511) (Taylor and Wood 1975). Even the exceptionally rich clusters ω Cen and 47 Tuc appear to have respective blue horizontal branch memberships of only 2066 and 930, suggesting values of dN/dt not substantially outside the bracket suggested for typical clusters.

Rather more specifically

$$\left(\frac{dN}{dt}\right)_{t=T-T'} \simeq \frac{N_{HB}}{\tau_{HB}}$$

where N_{H3} is the total number of horizontal branch stars, and τ_{HB} is the time spent on the horizontal branch. The uncertainties in N_{HB} and τ_{HB} have been discussed by Taylor and Wood, and it seems clear that τ_{HB} in particular may yet be open to substantial revision. Taking $\tau_{HB} \approx 10^8$ years however, and $N_{HB} = 511$, gives $dN/dt \approx 1.6 \times 10^{-13}$ for M3.

Determining dN/dt from the rate of main-sequence turn-off we obtain $dN/dt \approx 6.2 \times 10^{-14}$ sec^{-1} (case 1), 9.6×10^{-14} sec^{-1} (case 2).

It is clear that the agreement between the main sequence turn-off, and horizontal branch estimates of dN/dt is reasonably good, and the limits to dN/dt determined earlier for clusters generally are almost certainly of reasonable reliability.

It is now necessary to determine the observability of nebulae in clusters. We shall be assuming that galactic planetary nebulae are reasonably representative of those likely to occur in globular clusters.

The only nebula observed in a globular cluster, Psl, is in fact under-luminous for its size, although whether this is to be expected generally is conjectural. Many "sub-luminous" galactic planetary nebulae undoubtedly exist, although are less readily recognised as such. We simply remark that should such behaviour prove the rule, the calculated incidence of planetary nebulae would again represent an upper limit.

For the physical argument concerning the expected evolution of the observed flux we will follow Seaton (1966). Seaton recognised three main phases of nebular expansion: an initial optically thick stage; an intermediate optically thin stage; and finally a stage where the nebula again becomes optically thick. These correspond to stages where the nebula is (a) initially very dense, and the stellar ionising flux is low (though evolving rapidly as ~ the square of the nebular radius); (b) the nebula is much more tenuous (through expansion) and stellar luminosity is peaking; and finally (c) the nebula, though less dense than in (b), is irradiated by a decreasing central star ionising flux.

We define monochromatic surface brightness through

$$S_\lambda = \frac{F r_g^2}{\pi(r_I + r_s)^2} \qquad \ldots (4.7)$$

where

r_g = distance of planetary nebula from Earth (pc)

r_s = equivalent seeing disk radius at position of globular cluster. This term also includes instrumental image degradation (pc)

r_I = radius of ionised volume of planetary nebula (pc)

r_p = physical radius of nebula (pc)

F = observed flux

For Hβ emission we have

$$F = F_{H\beta} = \frac{h \nu_\beta N_e^2 \alpha(H\beta)}{4 \pi r_g^2} \cdot \frac{4}{3} \pi r_I^3 \qquad \ldots (4.8)$$

For an optically thin nebula, $r_I = r_p$, where r_p is the physical radius of the nebular envelope. For the final optically thick stage however

$$r_I \propto \frac{Q_1^{1/3}}{N_e^{2/3}}$$

where Q_1 is a parameter defined by Seaton. Seaton finds $Q_1 \propto t^{-6}$, $N_e \propto t^{-3}$, so that

$$r_I \simeq \text{constant} = r_2 \qquad \ldots (4.9)$$

The physical dimensions of the ionised region are roughly constant. Seaton believes $r_2 \simeq 0.6$ pc. We follow the more recent discussion of Cahn and Kaler (1971), and let $r_2 = 0.4$ pc. Similarly, we may define a radius of transition from the initial optically thick régime, to optically thin expansion, $r_1 \simeq 0.04$ pc (again using the data of Cahn and Kaler). A final radius limit to define is the terminal radius, or radius of shell disruption. There are various contributory factors to shell fragmentation, of which the following are most obvious.

(a) Hydrodynamic instabilities arising from interaction with gas inside a globular cluster. The condition for this is that (Gurzadyan 1969)

$$r_p \gtrsim \left\{\frac{4}{3} \frac{\rho_o}{m_o}\right\}^{-1/3}$$

where ρ_o is the density of the surrounding medium, and m_o is shell mass. Effectively, this states that when planetary nebula density is comparable with interstellar density, serious deformation of nebular shape may be

anticipated. Values for the total mass of interstellar matter are unknown for clusters; only upper limits are available. These suggest (c.f. Smith et al. 1976) that the total mass of ionised gas is small, and probably less than ~4 $M_\odot$. For a typical cluster, this corresponds to a smeared out density ~0.04 cm^{-3}, and for a typical planetary, such a density would be reached at radius $r_p \simeq 2.0$ pc.

(b) Passage through the galactic plane. This will completely sweep clusters of available gas, through interaction with interstellar clouds within the galactic plane. Since however the typical period out of the plane is ~10^8 years for globular clusters, this represents a limitation primarily on interstellar gas density within the clusters, and only indirectly through mechanism (a) does it constitute a restriction on nebular radius; except of course for those very few clusters which have very recently (within the past ~10^5 years) passed through the plane.

(c) Distortion and fragmentation by the gravitational field of the cluster. Assuming fragmentation by mechanism (a) has not already occurred, shell development may be primarily determined by acceleration within the potential field of the cluster, for appreciable shell sizes. Since cluster radii are typically ~10 pc, a nebula would possibly be expected to start fragmenting, and/or becoming heavily distorted, by $r_p \gtrsim 3$ pc.

(d) Intershell Collisions. If the upper limit nebula formation rate $dN/dt = 3.5 \times 10^{-13}$ sec^{-1} is adopted, a nebula forms every $\sim 9 \times 10^4$ years. This permits shells to grow to $r_p \sim 1.9$ pc before a new planetary nebula develops (taking an expansion velocity of ~20 $km.s^{-1}$). Typically therefore, the shells of previous planetary nebulae will be greatly attenuated during the expansion of any new

shell, and will probably be primarily important as contributors to the smeared out, interstellar gas density within clusters.

From this discussion, then, we may set a limiting nebular radius of probably $r_p = 2$ pc $= r_3$ which, although uncertain, will not in fact be a significant variable in the determination of nebular incidence.

Returning to equation 4.8, we note that for $r_2 < r_p < r_3$, $F_{H\beta} \propto N_e^2 \propto r_p^{-6}$. Whence

$$S_{\beta 3} = \frac{F_{H\beta}(r_2)}{\pi(r_2+r_s)^2} \left\{\frac{r_2}{r_p}\right\}^6 \cdot r_g^2 \qquad \ldots(4.10)$$

Similarly for $r_1 < r_p < r_2$, $F_{H\beta} \propto N_e^2 r_p^3 \propto r_p^{-3}$, whence

$$S_{\beta 2} = F_{H\beta}(r_1) \left\{\frac{r_1}{r_p}\right\}^3 \frac{r_g^2}{\pi(r_p+r_s)^2} \qquad \ldots(4.11)$$

Finally, for $r_p < r_1$

$$S_{\beta 1} = F_{H\beta}(r_1) \left\{\frac{r_1}{r_p}\right\}^{\alpha} \frac{r_g^2}{\pi(r_I+r_s)^2}, \qquad \ldots(4.12)$$

The relation between r_I and r_p is again not critically important. Since

$$r_I \propto N_e^{-2/3} L^{1/3}$$

then taking* $N_e \propto r_p^{-3}$, $L \propto r_I^2$ (based on observational evidence) gives $r_I \propto r_p^6$; or $r_I \simeq r_1(r_p/r_1)^6$. From 4.8 and 4.10 we also have

$$S_{\beta 3} = \frac{r_2^3 r_1^3}{\pi(r_2+r_s)^2} \frac{F_{H\beta}(r_1)}{r_p^6} r_g^2 \qquad \ldots(4.13)$$

If then V_{10} is the absolute magnitude of the nebulae at radius

---

* $N_e(r_p)$ may decrease less rapidly with increasing r_p if, as Seaton (1966) suggests, the neutral hydrogen is in a thin compressed shell in pressure equilibrium with the ionised zone.

$r_p = r_I = r_1$, we may write for the observed surface brightness (visual magnitudes.arcsec^{-2})

$$r_p < r_1 \quad M_{V_1} = V_{10} + 2.5 \log_{10} \left\{ \left(\frac{r_p}{r_1}\right)^{\alpha} \frac{\phi^2 \pi (r_1 (r_p/r_1)^6 + r_s)^2}{100} \right\} + \Delta M \quad \text{magnitudes.arcsec}^{-2} \qquad \ldots(4.14)$$

$$r_2 > r_p > r_1 \quad M_{V_2} = V_{10} + 2.5 \log_{10} \left\{ \left(\frac{r_p}{r_1}\right)^{3} \frac{\pi \phi^2 (r_p + r_s)^2}{100} \right\} + \Delta M \quad \text{magnitudes.arcsec}^{-2} \qquad \ldots(4.15)$$

$$r_3 > r_p > r_2 \quad M_{V_3} = V_{10} + 2.5 \log \left\{ \left(\frac{r_p^{\,2}}{r_1\, r_2}\right)^{3} \frac{\pi \phi^2 (r_2 + r_s)^2}{100} \right\} + \Delta M \quad \text{magnitudes.arcsec}^{-2} \qquad \ldots(4.16)$$

where for instance

$$R_2 = \frac{r_2}{r_g} \phi$$

R_2 is the equivalent angular radius to r_2 (in arcseconds), and $\phi = 2.06 \times 10^5$. ΔM is the reddening correction. Notice that whilst surveys are advantageously carried out in Hβ, say, the present analysis will give limits corresponding to an equivalent visual magnitude, related to Hβ flux through (O'Dell 1962)

$$M_V = -2.5 \log F_{H\beta} + 15.77 \text{ magnitudes}$$

($F_{H\beta}$ in ergs.cm^{-2})

We now have the equations necessary to determine an appropriate relationship between the number of observable planetaries, and the equivalent visual surface brightness limit of any survey. Note that

$$\frac{dN}{dr_p} = \frac{dN}{dt} \cdot \frac{dt}{dr_p} = \frac{1}{V_{exp}} \cdot \frac{dN}{dt} \qquad \ldots(4.17)$$

= number of planetaries per unit range of radius

whence

$$N_{LIM} = \frac{r_p - r_1}{V_{exp}} \frac{dN}{dt} + \frac{\beta\, r_1}{V_{exp}} \frac{dN}{dt}$$

$$= \frac{dN}{dt} \frac{1}{V_{exp}} \{r_p + r_1(\beta-1)\} \qquad (r_p > r_1) \qquad \ldots(4.18)$$

= Total number of planetaries having radius less than r_p

and $$N_{LIM} = \frac{\beta\, r_p}{V_{exp}} \frac{dN}{dt} \qquad (r_p < r_1) \qquad \ldots(4.19)$$

where β is a constant allowing for variable V_{exp}.

From 4.18

$$r_p = \frac{N_{LIM}\, V_{exp}}{dN/dt} - r_1(\beta-1) \qquad \ldots(4.20)$$

Substituting into equation 4.16 and re-organising then gives, for a survey with limiting magnitude $M_{V_{LIM}}$

$$N_{LIM} = \frac{dN/dt}{V_{exp}} \left\{ 10^{\frac{M_{V_{LIM}} - V_{10} - \Delta M}{15}} (r_1\, r_2)^{\frac{1}{2}} \right.$$
$$\left. \left\{ \frac{100}{\pi\phi^2 (r_2+r_s)^2} \right\}^{1/6} + r_1(\beta-1) \right\} \qquad \ldots(4.21)$$

for $M_{V_{LIM2}} \leq M_{V_{LIM}} \leq M_{V_{LIM3}}$

where

$$M_{V_{LIM2}} = V_{10} + 2.5 \log \left\{ \left(\frac{r_2}{r_1}\right)^3 \frac{\pi\phi^2}{100} (r_2+r_s)^2 \right\} + \Delta M$$

$$M_{V_{LIM3}} = V_{10} + 2.5 \log \left\{ \left(\frac{r_3^2}{r_1 r_2} \right)^3 \frac{\pi\phi^2}{100} (r_2+r_s)^2 \right\} + \Delta M$$

The last three equations are equivalent to the statement $r_3 \geq r_p \geq r_2$. For $r_p > r_3$, $N_{LIM} = N_{LIM}\ (r_p = r_3)$. For $r_1 < r_p < r_2$, corresponding to $M_{V_{LIM1}} < M_{V_{LIM}} < M_{V_{LIM2}}$ where

$$M_{V_{LIM1}} = V_{10} + 2.5 \log_{10} \left\{ \frac{\pi\phi^2 (r_1+r_s)^2}{100} \right\} + \Delta M$$

then

$$r_p^3 (r_p+r_s)^2 = \frac{r_1^3\ 10^{\frac{M_{V_{LIM}} - V_{10} - \Delta M}{2.5}}\ 100}{\pi\phi^2} \qquad \ldots(4.22)$$

This is soluble numerically for r_p, which may then be substituted into 4.20 to obtain N_{LIM}. Very approximate equations for rapid evaluation of N_{LIM} (accurate to better than 23%) are

$$N_{LIM} = \frac{dN/dt}{V_{exp}} \left(\left\{ \frac{r_{10}^3\ 10^{\frac{M_{V_{LIM}} - V_{10} - \Delta M}{2.5}}\ 100}{1.9\ r_s^2\ \pi\ \phi^2} \right\}^{1/3} + r_{10}(\beta-1) \right) \qquad (r_p < r_s)$$

$$N_{LIM} = \frac{dN/dt}{V_{exp}} \left(\left\{ \frac{r_{10}^3\ 10^{\frac{M_{V_{LIM}} - V_{10} - \Delta M}{2.5}}\ 100}{1.9\ \pi\ \phi^2} \right\}^{1/5} + r_{10}(\beta-1) \right) \qquad (r_p > r_s)$$

where the condition $r_p > r_s$ is equivalent to the requirement

$$M_{V_{LIM}} \geq V_{10} + 2.5 \log_{10} \left\{ \left(\frac{r_s}{r_1} \right)^3 \frac{\pi\phi^2 (2r_s)^2}{100} \right\} + \Delta M$$

The factor 1.9 in these equations has been introduced to reduce overall maximum error.

For the specific calculations mentioned later however we have chosen to determine r_p numerically.

The final radial range $r_p < r_1$ requires

$$r_p^{\alpha}(r_1(r_p/r_1)^6 + r_s)^2 = \frac{r_1^{\alpha}\, 10^{\frac{M_{V_{LIM}} - V_{10} - \Delta M}{2.5}}\, 100}{\pi\, \phi^2}$$

whence, using values of α, β determined later, this gives

$$N_{LIM} = \frac{dN/dt}{V_{exp}}\, r_1 \left(\left\{ \frac{10^{\frac{M_{V_{LIM}} - V_{10} - \Delta M}{2.5}}\, 100}{\pi\, \phi^2\, r_1^2} \right\}^{\frac{1}{2}} - \frac{r_s}{r_1} \right)^{1/6} \qquad \ldots(4.23)$$

Various terms have been used in the analysis which yet require definition. We let $V_{10} = -4.9$, consistent with the data of Cahn and Kaler (1971). The parameters α and β, determining the first optically thick stage of expansion are less certain. If stellar luminosity and temperature are constant, then nebular luminosity would also be invariant with respect to r_p. This follows by noting that the ionising flux $L \propto N_e^2\, r_I^3$, and $F_\beta \propto N_e^2\, \alpha_\beta\, r_I^3$. Since however L almost certainly increases with r_I, it is almost certainly the case that $\alpha < 0$. On the other hand, from the data of Weedman (1968) a slower initial expansion rate is suspected, and $\beta > 1$. The trends of α and β are therefore compensatory, and the effect in relatively complete galactic surveys of planetary nebulae appears to be such that $N(r_p < 2r_1) \simeq N(2r_1 < r_p < 4r_1)$ (the factor 2 compensating for uncertainties in the estimated radius of optically thick nebulae; see Cahn and Kaler (1971) for details). It seems likely therefore that no great distortion in N_{LIM} should result by taking $\beta = 1$, $\alpha = 0$.

We are now at the stage where expected numbers of planetary nebulae, N_{LIM}, may be determined for representative surveys of limiting equivalent magnitude $M_{V_{LIM}}$ arcsec^{-2}. There are two obvious ways of carrying out such a survey. The first is to perform a deep survey of a particular cluster to a large value $M_{V_{LIM}}$. This is feasible however only so far as overcrowding by faint cluster members will permit the detection of anomalous enhancement of emission. The alternative is to attempt a survey with more modest limiting magnitude $M_{V_{LIM}}$, but to measure several clusters. This in principle is Peterson's intention in observing 43 globular clusters accessible to the 24 inch Cassegrain telescope at Capilla Peak, New Mexico. As we have already noted, the only significant detection appeared to be of the nebula in M15, Ps1. Ps1 has a photovisual magnitude +14.9, although Peterson apparently missed the M15 core emission in this first survey (Peterson 1973), which he later found (Peterson 1976) to be ~3 to 4 magnitudes fainter in Hα.

The survey appears therefore to have $15 \lesssim M_{V_{LIM}} \lesssim 19$, assuming $\pi(R_s+R_I)^2 = 1$ arcsec^{-2}. Peterson also quotes a survey magnitude limit of +15 (Peterson 1976) which, if applicable to Hα, corresponds to $M_{V_{LIM}} \simeq +16.2$ for a 50 Å bandwidth and 1 arcsecond seeing ($R_s = 0.5''$ in the limit $R_p \to 0''$). For optimum surface brightness and $R_s = 2''$ however, $M_{V_{LIM}} \simeq +19.3$. There is therefore some uncertainty in survey detection limits from present evidence, and we adopt $+16.2 < M_{V_{LIM}} < +19.3$.

Ideally, for a direct comparison with Peterson's survey, N_{LIM} should be determined for those clusters observed by Peterson; at the time of writing, this information is not however available. By determining N_{LIM} for a heterogeneous collection of globulars, however (say all the clusters listed by Arp (1965) with available reddening

values and distances), we can obtain a value broadly comparable with Peterson's survey (assuming this had comparable heterogeneity). Because of its lack of specificity, it would also act as a baseline for the initial assessment of future surveys. The results are presented in figure 4.5. The ordinate is in units of planetary nebulae/cluster, and the result of Peterson's survey is noted by a horizontal bar, indicating the degree of uncertainty arising from the absence of an appropriate mean seeing disk radius.

Several points may be made in respect of this graph:

(a) Surveys of the kind undertaken by Peterson enable constraints to be placed upon the nature of stellar evolution in clusters.

(b) The current detection of only one planetary nebula (Ps1) in a globular cluster is consistent with expectations from stellar evolutionary theory, providing a reasonably high proportion of stars pass through the planetary nebula stage subsequent to the horizontal branch. A higher sample of nebular detection is required to determine the mean value of N_{LIM} per cluster with any accuracy however.

(c) There are quite a few planetary nebulae remaining to be found, and the effort to detect them is probably worthwhile. A hundred cluster survey to limits ~4 magnitudes fainter than achieved by Peterson could possibly result in ~30 new discoveries, although this is likely to be an upper limit.

We have made separate determinations of planetary nebulae numbers for the relatively nearby rich cluster ω Cen, assuming the high nebular formation rate implied by the horizontal branch membership. The graph (figure 4.6) suggests that very deep surveys are required for several such clusters before further nebulae are likely to be discovered.

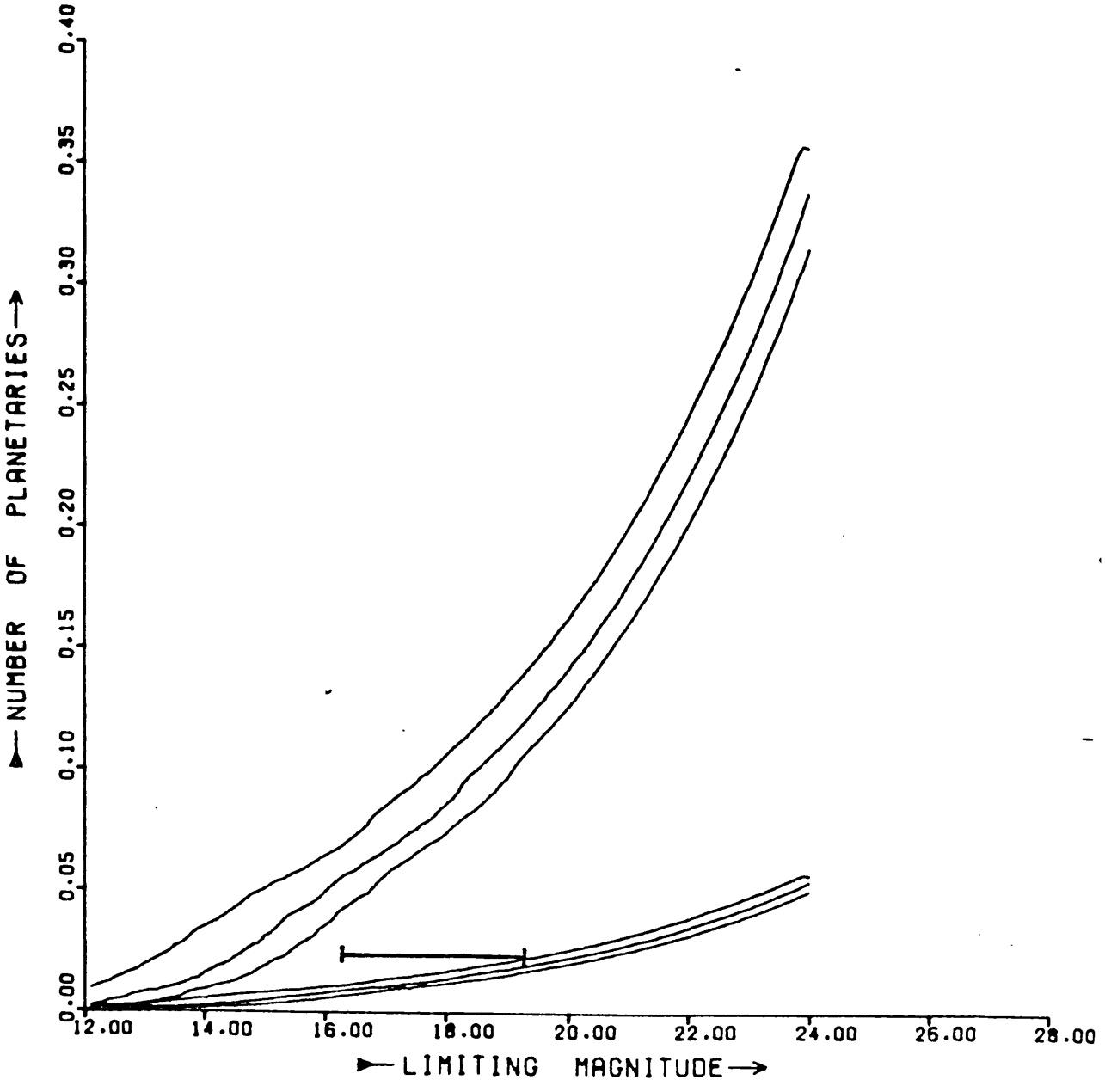

FIGURE 4.5

PLANETARY NEBULA DETECTION RATE PER CLUSTER, VERSUS VISUAL SURFACE BRIGHTNESS (MAGNITUDES ARCSECOND^{-2}). BAR INDICATES PROVISIONAL LIMITS RESULTING FROM PETERSON'S SURVEY. SEEING FOR TWO SETS OF CURVES IS 1" (UPPER CURVE FOR EACH CASE), INCREMENTING BY 1" FOR SUCCESSIVE ADJACENT CURVES

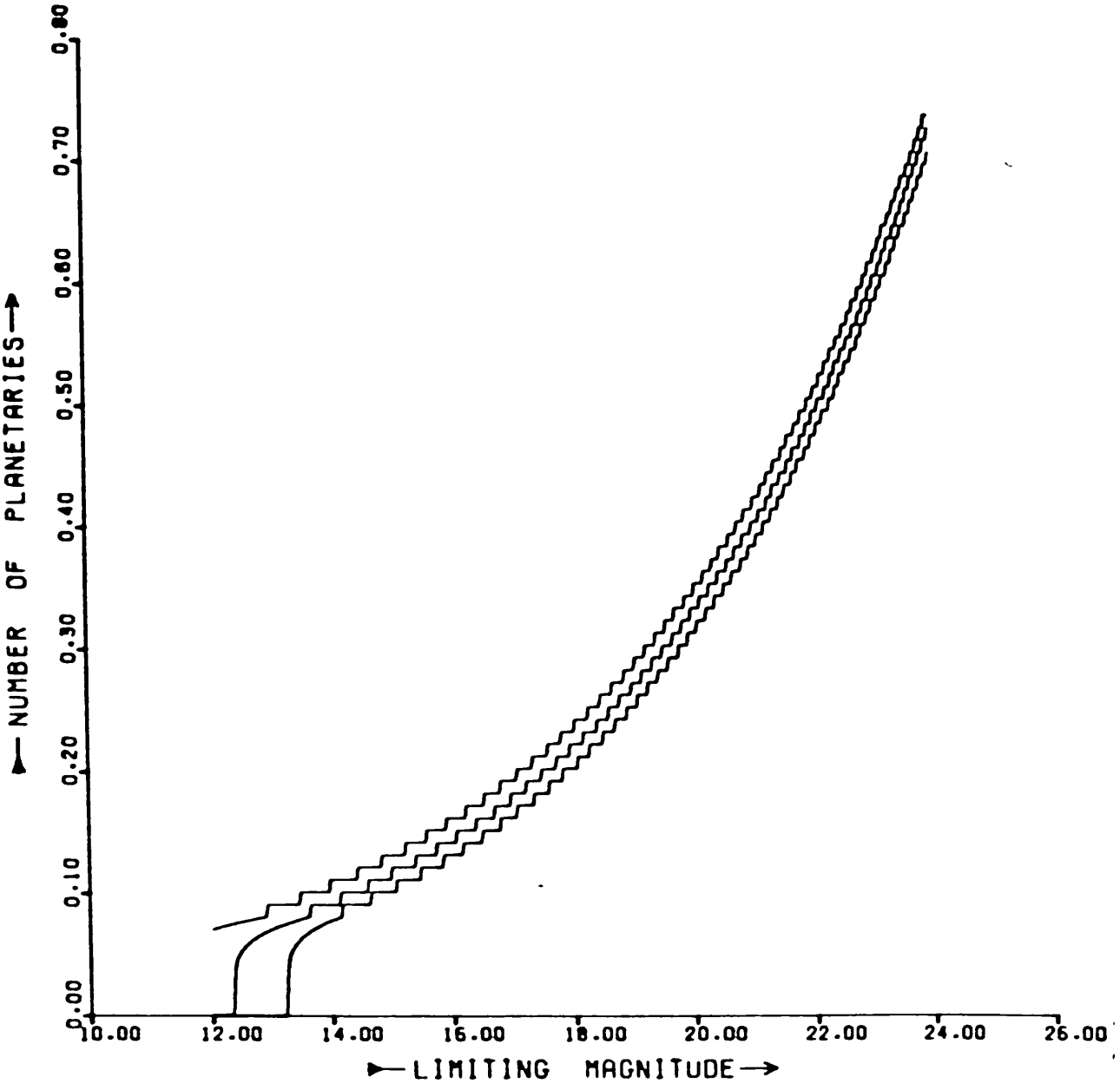

FIGURE 4.6

NEBULAR DETECTION RATE FOR ω CEN

We end by noting that a most effective procedure for such surveys may be monochromatic electronography. This represents a highly accessible mode of registering extended emission, with high dynamic range. Nebulae may then be detectable as typically semi-ellipsoidal enhancements upon the background of stellar continuum. Confirmation of the nature of these enhancements may follow through ratioing Hα and continuum electronographs. This latter procedure may be optimised by introducing procedures for the removal of most of the stellar background continuum. We are investigating the core regions of several clusters with this technique.

CHAPTER 5

MASS LOSS IN LATE TYPE STARS

5.1 Abstract

An extended analysis of various questions relating to conditions of grain formation, growth and acceleration in stellar atmsopheres is provided. Deficiencies are noted in earlier mass loss models; evaluations of mass loss rates; and model critiques. Numerical analysis of the appropriate differential equations of supersonic flow has been performed for a wide range of models, involving red giants, supergiants, dwarfs, and Mira variables, and for grain materials iron, olivine and graphite. Although supersonic solutions were not found in red giants, supergiants and dwarfs, solutions were obtained for Miras which strongly resemble observed flow properties. The results differ from certain earlier work, partly because of a more thorough discussion of constraints upon conditions prevalent in the condensation zone. Ways by which the mechanism might be made applicable to stellar types other than Miras are also briefly considered. One possibility is that alternative grain materials, or even composite grains, are present. Partly to evaluate this possibility, the optical circumstellar absorption in late type stars is investigated. The extensive photometric data of Johnson et al. (1966), Johnson et al. (1967) and Lee (1970) are further reduced. Evidence for anomalous variable extinction is noted in red supergiants, similar to that expected from iron core/silicate mantle grains. It is demonstrated that such absorption curves are capable of explaining observed infrared excesses, for

appreciable supergiant visible extinction. Evidence for appreciable supergiant circumstellar visual extinction is noted. Anomalies found by Humphreys et al. in Carina supergiants, and ascribed to photometric error, are explained. The likely presence of substantial visual extinction in Carbon and IRC stars is noted. The possibility of extinction in red giants is investigated. Absorption similar to that responsible for the variable anomalous supergiant extinction is found. Earlier evidence favouring substantial optical circumstellar extinction in such stars is noted, and it is found that such extinction may be a plausible consequence of observed mass loss rates in these stars if grains are the responsible opacity source.

5.2 Summary of Observational Evidence

That mass is lost to space by red giants and supergiants has been known for about twenty years, although the mechanisms lying behind this mass loss remain controversial. We give here a brief historical resumé, and detail some primary observational consequences of such flows.

The first evidence of gaseous outflow from late-type stars was noted by Adams and MacCormack (1935), who found secondary zero volt absorption cores displaced by ~5 $km.s^{-1}$ to the blue. Since this velocity was very much less than photospheric escape velocity, it was presumed by early investigators that any observed flow must be one phase of a circulatory cycle, with no net loss of mass from the star.

This interpretation was radically revised in 1956, when Deutsch (1956) demonstrated that atypical low excitation displaced cores in the spectrum of a G0 II-III star, α^2 Herculis, almost certainly arose from an extensive envelope surrounding the late type companion, the M2 II-III

star α^1 Herculis. Displaced absorption cores in late type stars have subsequently been uniformly attributed to low velocity mass outflow to infinity (or more accurately, to the shock-front interface with the interstellar medium).

The primary characteristics of this mass flow were rapidly established, and the summary by Deutsch (1960) requires few emmendations. We summarise some of the more relevant points:

(a) The displaced cores are exceptionally narrow, implying low excitation, constant outflow velocity and a rapid flow initiation. In some cases acceleration of the flow is evident in the gradient of line displacement with ionisation potential (Deutsch quotes certain late type variables having $\Delta V/\Delta I \simeq 1 \rightarrow 3$ km.sec^{-1}.e.v.$^{-1}$). In general however, the evidence (from for instance spectral lines such as FeI, $\lambda\lambda$ 4046, 4064 and 4072) suggests that the flow has essentially acquired its terminal velocity by the "top of the reversing layer", in agreement with the implied sense of the displaced core profiles. Figure 5.1 shows examples of AlI λ3961.5, TiI λ3981.8 from Weyman (1962) for α ORI, indicating a deep displaced core superimposed upon a broad shallow absorption line from the "reversing layer". This will be compared with model profiles later.

(b) Mass loss is evident in late type stars brighter than luminosity class III, and later than M0. Earlier (Deutsch, 1960) and more recent data (Sanner, 1976) supports a simple functional relationship $dM/dt = -k_o L_*$, where dM/dt is the time derivative of mass loss, and L_* the stellar bolometric luminosity. k_o is a constant.

(c) Outflow velocities in giant stars have a maximum value of ~30 km.s^{-1} at M0, falling to <10 km.s^{-1} by M6. Specific data points are plotted in figure 5.2 (adapted from Deutsch 1960). Also shown

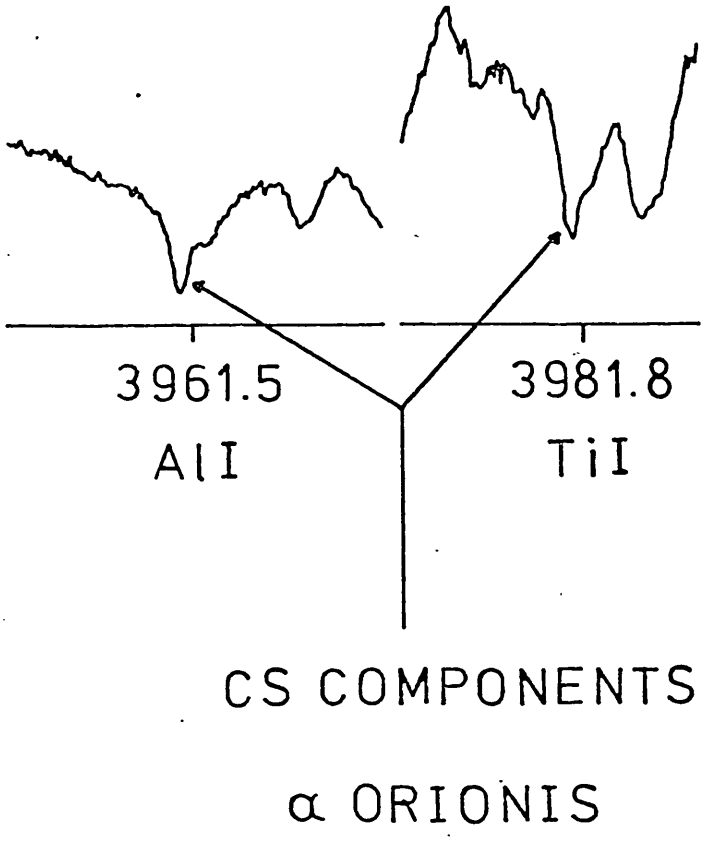

FIGURE 5.1

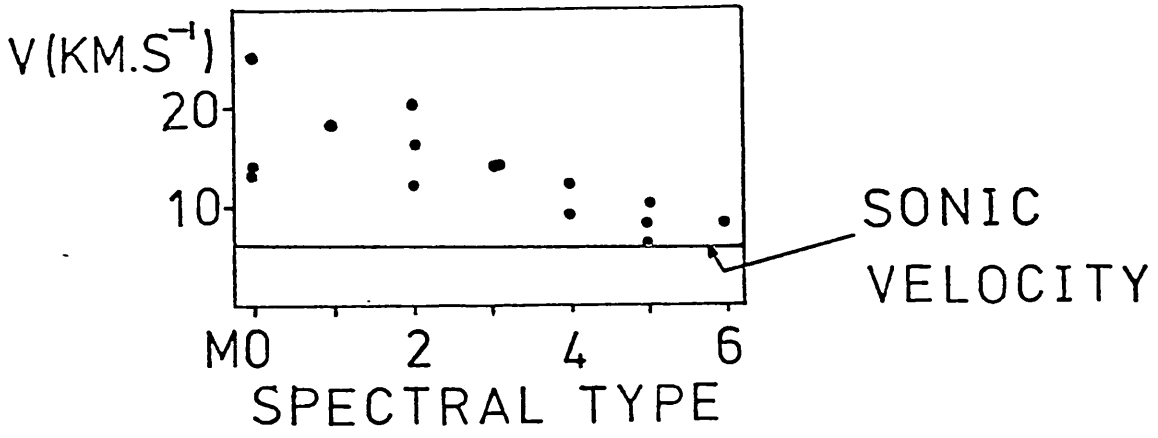

FIGURE 5.2

is the photospheric sonic velocity corresponding to the effective temperatures T_* of the stars, derived from the calibration of Dyck, Lockwood and Capps (1974). For all spectral types the observed velocities exceed the sonic velocity, and since the gas outflow is certainly much cooler than T_*, we may adduce that, at least up to M6, the outflows are supersonic. The mass outflow velocities for luminosity classes I and II also fall within the same range.

(d) Early work (c.f. Weymann 1962[9]) has shown that the fully developed flows are essentially HI regions, within which nearly all the metal atoms are singly ionised. The possibility of some double ionisation is referred to later.

(e) Appropriate mass loss rates are still debatable, for reasons we will discuss more fully later, but it seems clear that the momentum transfer from radiation field to mass flow is relatively efficient, whether through resonance lines or broad-band absorption - if we assume radiation to be the primary power source for the mass loss. Specifically, the momentum carried by the radiation field is L_*/c. If this is entirely transferred to the outflowing envelope, a mass loss

$$\left\{\frac{dM}{dt}\right\}_{LIM} = \frac{L_*}{V_{gas}\, c}$$

is supportable, and for a typical value $V_{gas} = 10^6$ cm.s^{-1} we obtain

$$\log \left\{\frac{dM}{dt}\right\}_{LIM} = -6.8 - 0.4\ M_{BOL}$$

This may be compared with Sanner's (1976) estimate

$$\log \left\{\frac{dM}{dt}\right\}_{S} = -10 - 0.5\ M_{BOL}$$

We may then define an efficiency

$$\eta = \frac{\left\{\frac{dM}{dt}\right\}_S}{\left\{\frac{dM}{dt}\right\}_{LIM}} = 10^{-(3.2+0.1\ M_{BOL})}$$

Typically, $\eta < 10^{-3}$. Sanner's estimates of dM/dt are however lower than most evaluations, and if for a star j we define a mean of various mass loss estimates i through

$$\overline{(dM/dt)}_j = 10^{\frac{1}{n}\sum_{i=1}^{n} \log(\frac{dM}{dt})_{i,j}}$$

we obtain for the collation of values from Bernat (1977) the values shown in table 5.1.

TABLE 5.1

RADIATIVE TRANSFER EFFICIENCIES

STAR	M_{BOL}*	$(dM/dt)_{LIM}$	η^1	η^2	η^3
αOri	-7.2	1.20×10^{-4}	1.03×10^{-2}	2.07×10^{-2}	2.8×10^{-1}
αSco	-7.2	1.20×10^{-4}	4.64×10^{-3}	7.33×10^{-3}	1.8×10^{-2}
αHer	-5.7	3.02×10^{-5}	3.87×10^{-3}	8.68×10^{-3}	2.2×10^{-2}
μCep	-8.1	2.75×10^{-4}	1.12×10^{-2}	3.82×10^{-2}	1.53

1. Efficiency for all results, excluding Bernat.
2. Efficiency for all results.
3. Efficiency for Bernat
* SANNER (1976)

TABLE BASED ON MASS LOSS RATES FROM DEUTSCH (1956), WEYMANN (1962), GEHRZ AND WOOLF (1971), REIMERS (1975), SANNER (1976).

This averaging technique is chosen to avoid undue weighting by Bernat's larger than average values of dM/dt. Independently, we also

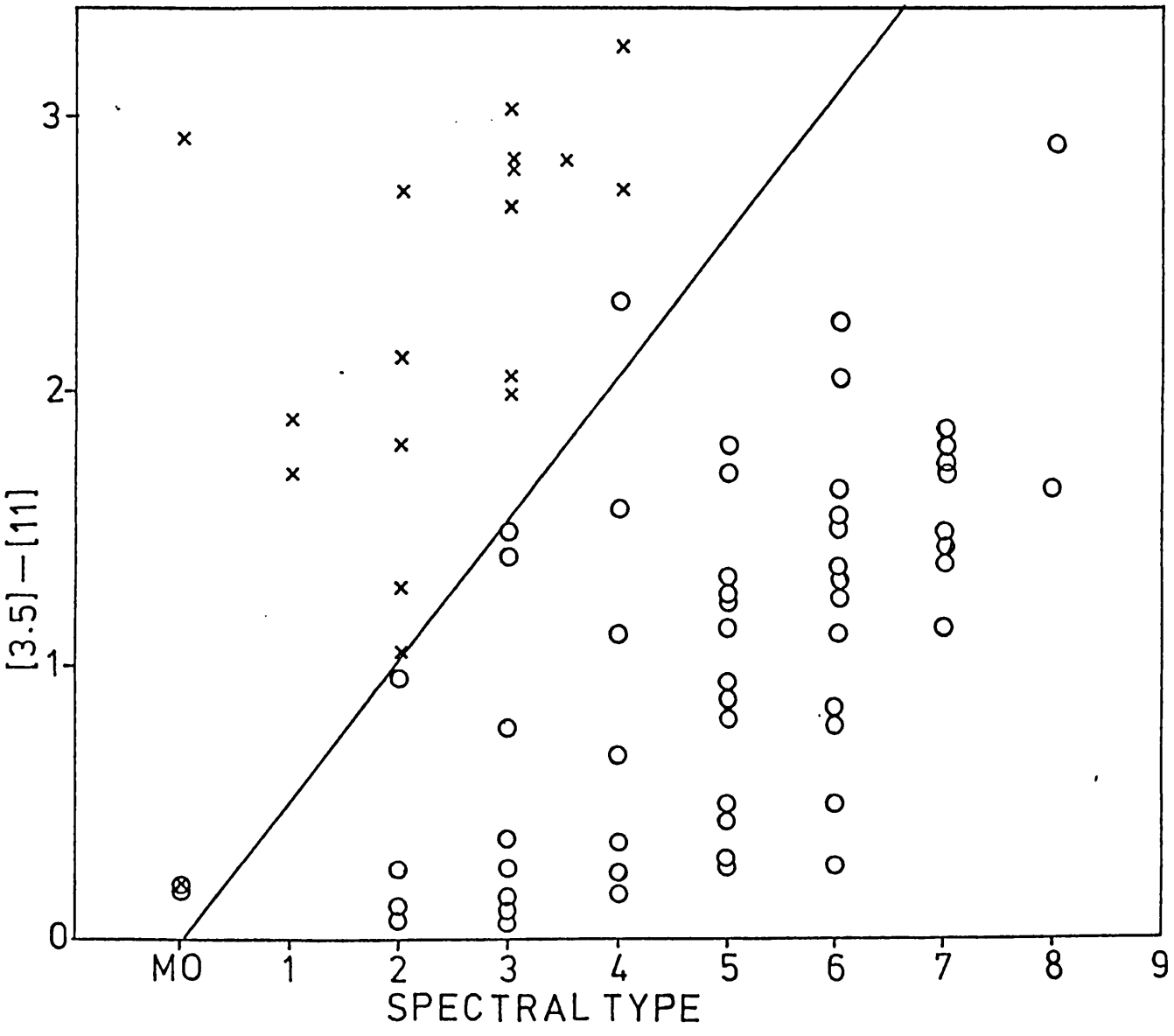

FIGURE 5.3

O - GIANTS X - SUPERGIANTS

give η for values of $\overline{(dM/dt)}$ excluding Bernat's results, and finally for Bernat's results alone. In the latter case, it is clear that if such large mass loss rates are acceptable, then serious constraints are placed upon both the ejecting mechanism and, as Bernat indicates, the evolutionary time scale of the respective stars.

A final observation of relevance, not available to Deutsch in 1960, is the presence of infrared continuum excesses in most stars later than M0, and brighter than luminosity class III. These excesses are usually attributed to thermal radiation by circumstellar dust grains. For red giants at least, the O/C ratio is marginally greater than 1 (specifically Spinrad and Vardya (1966) find O/C = 1.05 for M giants, 1.04 for a mild S star; the ratio decreases from M through to S and C stars (Fujita 1965)) and in these circumstances there is a slight excess of free oxygen (the oxygen being predominantly tied up as CO). For this case Gilman (1969) finds silicates to be one of the more likely condensates, and this appears to be borne out by the nature of the excesses. These often show a rather narrow band emission centred upon ~10 μm, reminiscent of the strong reststrahlen band emission originating from the vibrational bands of SiO. This is occasionally supplemented by secondary emission at longer wavelengths (c.f. Woolf 1973), or more rarely by broader band emission dominating the entire infrared from ~1 μm to >20 μm, and possibly even giving rise to veiling (masking of the optical stellar continuum by extraneous sources of continuum emission in certain high mass loss supergiants (c.f. Humphreys, 1974)).

As a measure of the silicate absorption, we have plotted the [3.5]-[11] index (in this designation [X] will again be understood to refer to the magnitude at X μm) versus spectral type for various late-

type giants and supergiants (figure 5.3). Notice that the index [3.5]-[11] is typically several times larger for supergiants than giants. This can be understood if similar grain condensation efficiencies are involved in all cases. Consider in this respect a giant and a supergiant star with similar spectral types (and therefore effective temperatures).

Both stellar continuum flux $I_{\nu *}$ and mass loss rate dM/dt are then roughly proportional to r_*^2, where r_* is stellar radius. If grain sizes, velocities and condensation efficiencies are broadly the same, the canonical grain emission source function $S_\nu(r/r_*)$ is invariant, and total grain thermal emission at frequency ν, $I_{\nu g} = \int_V S_\nu(r/r_*)dV \propto r_*^3$. Whence $I_{\nu g}/I_{\nu *} \propto r_*$. It follows that $(I_{\nu g}/I_{\nu *})_{sg}/(I_{\nu g}/I_{\nu *})_g \simeq (r_{sg}/r_g)$, where subscript sg stands for supergiant, and g for giant. Whence $([3.5]-[11])_{sg} - ([3.5]-[11])_g \simeq 2.5 \log (r_{sg}/r_g) \simeq 2$ magnitudes, as observed. A second trend is for the index to increase with later spectral types, and this matches at least qualitatively a similar trend for mass loss rates, insofar as the evidence is at present interpreted. This probable condensation of grains in the mass outflow (and there seems to be no other source so capable of explaining the infrared excesses) has naturally led to a reconsideration of the rôle of grains in the actual mechanism of mass loss; a rôle originally regarded as negligible by Weymann (1962a). It is to this problem that the continuing discussion will be primarily addressed.

5.3 Mass Loss Mechanisms in Late Type Stars

For the present purposes available mass loss mechanisms may

be divided into two classes; those which do and do not involve the radiation field as a mode of momentum transfer. The latter include

(a) Coronal Expansion: a mechanism first discussed generally by Parker (see particularly Parker 1960), this involves evaporation from a Corona at sufficiently high temperature for thermal velocities to exceed escape velocity. Weymann has certain reservations concerning the mechanism, primarily the absence of a large enough Hα emission from an extended HII region. A primary cause of coronal heating may be collisional excitation arising from degradation of shock waves emanating from the photospheric zone. However, these shock waves may themselves be a direct mode of mass transport.

(b) Shock Waves. The possibility of shock waves propagating to infinity is not new. One of its more recent applications has been to late type variables. Gehrz and Woolf (1970) have specifically attributed mass loss in RV Tauri stars to this mechanism on the basis of exceptional mass loss rates, and previously postulated large amplitude atmospheric shock waves. These latter had induced Christy to speculate upon possible mass loss (Christy 1966) before evidence of the excesses was available. A more recent treatment of mass loss through shock waves is due to Slutz (1976).

(c) Other mechanisms. Various other mechanisms proposed include the possibility of a transfer of energy of ionisation to provide outward radial motion (Hoyle 1956) and more recently, the outward propulsion of coronal layers by means of Alfven waves (Belcher and Olbert 1975).

Turning to mechanisms more directly relating to the radiation field, we find an area of considerable general confusion, and since

many of these mechanisms are closely related (in principle) to the main thrust of this chapter, some space will be devoted to trying to clarify the relative merits of certain of these mechanisms.

If we could rely on early work (specifically Weymann's (1962a) discussion) we would find most processes involving transfer of entropy from radiation field to some outer envelope inadequate. Since Weymann's thesis has proven influential, and is still quoted as a source by which competing theories may be dismissed (c.f. Kwok 1975; Maciel 1976; Kutter 1970), it is obviously relevant to review the validity of these arguments.

The more important mechanisms appear to involve momentum transfer through

(a) Molecular absorption,

(b) Grain extinction,

(c) Ly_{α} scattering,

(d) Absorption by atoms.

Extending the range to earlier stellar types we can complete the list by including electron scattering, and various U.V. resonance lines (beside Ly_{α}).

Rubbra and Cowling (1959) have argued against general atomic opacity leading to significant mass outflow by itself and these arguments still appear to be viable. On the other hand, Weymann's objections to a grain scattering mechanism have been ably answered by Gilman (1972), so that various early theories ignoring grain-gas coupling (c.f. Wickramasinghe et al. 1966; Wickramasinghe 1972) now require serious revision. Two of the most recent discussions of mass loss, by Salpeter (1974 a,b) and Kwok (1975), indicate the necessary direction any full analysis of mass loss must now take.

Weymann also considered momentum transfer through molecular absorption to be unlikely to lead to mass loss, and this may yet prove to be the case. In this respect, it should however be noted that Maciel (1976, 1977) has constructed models involving mass loss along precisely these lines. In a careful treatment, band absorption from OH and H_2O are considered, as well as the dominant opacity source, CO. The flow is considered as starting with a velocity ~0.64 x sonic velocity, however, and a question then arises as to how this steady state condition is to be achieved. In the case of grains for instance, we might expect initial grain condensation to lead to some increase in atmospheric scale height (in the way proposed by Fix and Alexander (1974)), leading to radial expansion and the introduction of fresh material into the condensation zone. Under equilibrium conditions

$$n_i = n_1 \, e^{-\Delta G_i / kT}$$

where n_i is the number density of grain clusters containing i atoms, n_1 is the number density of single atoms/molecules, and ΔG_i is the Gibbs free energy of formation of a cluster of i atoms, given by

$$\Delta G_i = 4 \pi r^2 \sigma_s - \frac{4}{3} \pi r^3 \frac{kT}{V_m} \ln \left(\frac{p}{p_{SAT}}\right)$$

where σ_s is the surface energy, r grain radius, V_m is molecular volume, and p_{SAT} the saturation vapour pressure. The number of nuclei per unit mass is then

$$\frac{n_i}{\rho} = \frac{n_1}{\rho} \, e^{-\frac{\Delta G_i}{kT}} = \frac{n_1 \, kT}{\mu \, m_H \, P} \, e^{-\frac{4 \pi r^2 \sigma_s}{kT}} \, e^{\frac{4 \pi r^3}{3 V_m} \ln \left(\frac{p}{p_{SAT}}\right)}$$

Reorganising, we obtain

$$\frac{n_i}{\rho} = \left\{\frac{n_1\, kT}{\mu\, m_H}\; e^{-\frac{4\pi r^2 \sigma_s}{kT}}\right\} p^{-1} \left\{\frac{p}{p_{SAT}}\right\}^{\frac{4\pi r^3}{3V_m}}$$

$$\simeq \frac{X_i}{A_T\, m_H}\; e^{-\frac{4\pi r^2 \sigma_s}{kT}} \left(\frac{p}{p_{SAT}}\right)^{\frac{4\pi r^3}{3V_m}}$$

for low fractional condensation. X_i is the fractional cosmic mass abundance.

For grains larger than the critical radius for grain growth (see for instance Wickramasinghe 1967), for which $4\pi r^3/3V_m >> 1$, n_i/ρ is therefore sensitive to p/p_{SAT}. If conditions in the condensation zone consequently lead to a reduction in p/p_{SAT}, fewer stable condensation nuclei per unit mass will develop. The possibility of grain growth to larger sizes then becomes possible. For the specific case of silicates, the drag per unit gaseous mass $dF_{DRAG}/dM \propto Q_{PR}/a \simeq$ constant for $a < 10^{-6}$ cm. For $a > 10^{-6}$ cm however $dF_{DRAG}/dM \propto a^{1.75}$ (see later) and the development of grains larger than $\sim 10^{-6}$ cm will lead to further atmospheric expansion, and further mass flow through thermal relaxation. Finally, initial flow conditions in the condensation zone are acquired such that flow to supersonic velocities becomes feasible.

This of course is a very simple scenario to illustrate what is in fact a complex time dependent problem. If however it is presumed that initial flow conditions are acquired through relaxation of the stellar atmosphere in such a manner, then for initial flow velocities which are a substantial fraction of the initial sonic velocity one would expect that

$$\frac{L_* \bar{\kappa}_{gr}}{4\pi r^2 c} \simeq \frac{G M_*}{r^2}$$

i.e.
$$L_* \simeq \frac{4 \pi c G M_*}{\bar{\kappa}_{gr}}$$

where $\bar{\kappa}_{gr}$ is the mean atmospheric opacity per unit mass due to grains M_* in the stellar mass. In fact, for grains we will find that initial velocities only a fraction of those used by Maciel are required. Nevertheless, putting

$$n_{gr} = \frac{X}{\frac{4}{3} \pi a^3 \rho_{gr}} = \text{number of grains per unit mass}$$

we obtain
$$\bar{\kappa}_{gr} \simeq \frac{3 X \bar{Q}_{PR}}{4 a \rho_{gr}}$$

for efficient grain condensation, where $\bar{Q}_{PR}$ is the radiation pressure efficiency factor, a is grain radius and ρ_{gr} grain density. We use abundances from Allen (1973), and from Gilman (1974)

$$\bar{Q}_{PR} \simeq 1.18 \times 10^{-4} \left\{\frac{a T_*}{3 \times 10^{-3}}\right\}^{2.75} \qquad 3 \times 10^{-5} > a > 10^{-6}$$

for silicate grains. Taking $\rho_{gr} \simeq 2.6$ gm.cm^{-3}, and $a \simeq 0.3$ μm (the optimum)

$$\bar{\kappa}_{gr} = \begin{cases} 18.0 & (T_* = 3000 \text{ K}) \\ 5.9 & (T_* = 2000 \text{ K}) \end{cases}$$

whence for $M_* = 1 M_\odot$

$$\frac{L_*}{L_\odot} \simeq \begin{cases} 730 & (T_* = 3000 \text{ K}) \\ 2230 & (T_* = 2000 \text{ K}) \end{cases}$$

Stars more luminous than these limits may therefore be capable of providing flows which may approach supersonic velocities. Evidently,

most giants and supergiants meet this criterion (c.f. Allen 1973) which is in any case, as we have mentioned, in excess of the actual requirements for initial gas flow containing grains.

The situation with Maciel's (1976, 1977) model is however quite the reverse. For the particular case considered we find (from his figure 2, Maciel 1977) initial number densities for CO and H of $n_{CO} \simeq 2.3 \times 10^{5}$, $n_{H} \simeq 2.6 \times 10^{8}$, whence $X_{CO} \simeq 1.8 \times 10^{-2}$. From Tsuji (1966), for the important 2.3 μm band, and T = 2100 K, we find $\kappa_{\nu} \simeq 4.8 \times 10^{-22}$ cm^{-2} for molecular opacity: a maximum value at this temperature, and a value which decreases very slowly with decreasing temperature. Taking this value as typical for the entire continuum (in fact the band width is only ~0.3 μm), a maximum mean opacity may be defined

$$\bar{\kappa}_{CO} = \frac{X_{CO}\,\kappa_{\nu}}{M_{CO}}$$

M_{CO} is the molecular mass. A similar argument as used for the grains then leads to the requirement that

$$L_{*} \gtrsim 7.1 \times 10^{4}\ L_{\odot}$$

if the initial drag force of the molecules is to just compensate for gravitational deceleration. This is an extreme value for late-type supergiant luminosities, and because of the approximations the actual limit will be considerably larger. It should also be noted that Maciel's Mira model has a value of radius ($R \simeq 10^{3}\ R_{\odot}$) leading to exceptionally low photospheric escape velocities for this class of star, and the high luminosity adopted ($L_{*} \simeq 1.4 \times 10^{4}\ L_{\odot}$) leads to conditions particularly favourable to the model discussed. The temperature (T_{*} = 2000 K) is also advantageously chosen to give peak

emission near the 2.3 μm CO vibrational band, and substantial emission in the stronger 4.6 μm band. If the mechanism operates generally, it is likely to be contributory, providing a final boost to supersonic velocities.

Finally, we remark upon the feasibility of mass ejection through Ly_α scattering. This has been discussed by Wilson (1960) and Weymann (1962a). Specifically, when total momentum carried by mass loss is equated to the momentum carried by Ly_α, as by Weymann (1962a), the luminous fluxes considerably exceed acceptable limits set by other spectral line data. A rather different argument by Wilson (1960) equates energy loss from the star through Ly_α with the work required to accelerate an envelope, but arrives at essentially the same result.

It should first be remarked that Ly_α will be multiply scattered through the expanding envelope, and any treatment of the problem then requires the solution of radiative transfer equations. In stating this, we immediately conflict with Wilson, who explicitly regarded Ly_α photons as effectively removed from the accelerative mechanism after a single scattering. Implicitly, this is also the position of Weymann. Consider then a thin shell of gas embedded in an envelope. From the general solution of the equation of radiative transfer we have for a stationary envelope

$$\frac{d\rho_\nu}{dr} = \frac{3\,\rho(r)\;\;\kappa_\nu\,L_\nu}{4\,\pi\,r^2\,c}$$

where κ_ν is the opacity per unit mass and frequency at frequency ν, ρ_ν is the radiation density, $(L_\nu/4\,\pi\,r^2) = J_\nu$ is incident luminous flux per unit area and c is the velocity of light. This is equivalent

to a pressure difference across the shell

$$dp_\nu = \frac{d\rho_\nu}{3} = \frac{J_\nu}{c} (\rho\ (r)\ \kappa_\nu\ dr)$$

Evidently $\rho\ \kappa_\nu dr = \tau_\nu$, the optical depth, and $dp_\nu = J\ \tau_\nu/c$. Letting $\tau_\nu = 1$ then corresponds to the position where most photons are singly scattered, or absorbed, and we obtain for the net pressure upon the shell a value J_ν/c; the value used by Wilson and Weymann. If however $\tau_\nu > 1$, the net pressure is $>J_\nu/c$ and the radiation field imparts more momentum to the shell than is in fact carried by the radiation flow. This is conceptually surprising, and the reason why the previous analyses arrived at differing results.

On one level this can be understood as a consequence of retardation in the energy flow because of multiple scattering. Across any surface within the envelope the luminous flux is L_ν. If optical scattering depth within the envelope is increased, the photons passing through the surface must emanate from a shorter mean free distance away, and to maintain flux then requires $d\rho_\nu/dr$ and consequently dp_ν/dr to be increased. The increase in ρ_ν over that of an unretarded field permits in these circumstances, dp_ν to exceed J_ν/c over specific elements of shell thickness.

On a more profound level, the radiative acceleration arises from differences in the momentum transfer coupling between adjacent envelope layers. This results in an accumulating back pressure which, in total, amounts to $V_T\ dM/dt/4\ \pi\ R_*^2$, where V_T here is the terminal gas velocity. For a typical red giant of spectral class M5, $V_T \simeq 10^6$ cm.s^{-1}, $dM/dt \simeq 10^{-7}$ M yr^{-1}, and $R_* \simeq 100\ R_\odot$, whence $P_{back} \simeq 10^{-2}$ dynes.cm^{-2}; readily accommodated by red giant atmospheres, for which $p_{gas} \simeq 10^3$ dynes.cm^{-2} near the stellar photosphere (c.f.

Allen 1973). For a red supergiant, μ Cep, using $R_* = 1030\ R_\odot$ (Sanner 1976), and $dM/dt = 4.2 \times 10^{-4}\ M_\odot\ yr^{-1}$ (Bernat 1977); (probably an upper limit, as we will note later) we obtain $P_{back} \simeq 0.4$ dynes.cm^{-2}, a value which can again be accommodated tolerably well by the outer atmospheric layers.

It should be noted however that the Ly_α photons will be trapped within an accelerating gas flow, which leads to photon red-shifting and eventual escape. The probable consequence of this, the main photon sink, is to increase $d\rho_\upsilon/dr$. The velocity gradient is therefore both a consequence of, and a contributor to, the steep energy density gradient within the shell. As Weymann points out, the prime Ly_α density is indeed confined to a thin fringe at the base of the flow (the primary acceleration zone) but this is now seen as a consequence of, rather than an argument against, an extremely plausible hypothesis. Whether internal shell coupling is, in the final analysis, adequate to promote observed envelope velocities must be the subject of a full scale analysis however.

Wilson further points out that Ly_α regions may also be variably distributed across the stellar photospheres and this may lead to anisotropic mass emission; a by no means easy object to attain with broad band absorption mechanisms unless other processes (such as magnetic guiding) are invoked. The apparent evidence favouring anisotropic envelopes around certain M stars (see Bernat and Lambert (1976) for spectral line data, and Dyck et al. (1971) for evidence from infrared polarisation measures) is therefore probably to be regarded as support for this and similar mechanisms.

To summarise, we may say that there appear to be a series of non-explosive models for mass loss which may be capable of explaining

the broad features of observed mass flow, and which do not directly involve the stellar radiation field. Of those theories invoking radiative acceleration, two may superficially be capable of providing primary mechanisms for mass loss (Ly_α scattering, and radiation scattering by grains). It seems unlikely that general atomic/molecular opacity sources provide more than a supporting rôle.

5.4 Equations of Motion for Isothermal and Adiabatic Flow

The equations of mass and momentum conservation of a spherically symmetric gaseous outflow may be respectively written, following Weymann (1961) as

$$\frac{1}{r^2}\ \frac{d}{dr}\ (r^2\ \rho\ V_r) = 0 \qquad \ldots\ (5.1)$$

$$\frac{d}{dr}\ \left(\frac{V_r^2}{2}\right) = -\frac{1}{\rho}\frac{dP}{dr} - \frac{G\ M_*}{r^2}\ (1 - \omega(r)) \qquad \ldots\ (5.2)$$

where V_r is radial gas velocity, ρ gaseous density, P is pressure and r radial distance from the stellar core. The generalisation to include the gravitational reduction term $(1 - \omega(r))$ follows recent conventions, and is to allow for radiative force terms. Equations similar to the above were first discussed by Marlborough and René Roy (1970), who derived the isothermal equation of motion

$$\left(V - \frac{kT}{\mu m_H} \cdot \frac{1}{V}\right)\ dV + \left(\frac{1}{r}\left\{G\ M_* - \frac{1}{4\pi c}\int_0^\infty \kappa_\nu(r)\ L_\nu(r)\ d\nu\right\} - \frac{2kT}{\mu m_H}\right)\frac{dr}{r} = 0$$

where κ_ν is the opacity per unit mass of accelerated material, μ the mean atomic weight, T the gas temperature, and $L_\nu(r)$ is the stellar

continuum flux at frequency ν and radial distance r. This has been subsequently investigated by Salpeter (1974b). Marlborough and René Roy noted that for $V = (\frac{kT}{\mu m_H})^{\frac{1}{2}}$, the sonic point condition, we require

$$G M_* > \frac{1}{4\pi c} \int_o^\infty \kappa_\nu L_\nu \, d\nu$$

and for specifically early type stars where the primary atmospheric opacity source is electron scattering we obtain the corresponding requirement

$$L_* < \frac{4 \pi c G M}{\kappa_e} \qquad \ldots (5.3)$$

for supersonic flow. If luminosity exceeds this limit, then supersonic flow is not permissible. For possibly more realistic adiabatic flows, this condition is still applicable.

For the present problem we let

$$\omega(r) = \left(\frac{G M_*}{r^2}\right)^{-1} \left\{ \int_o^\infty \frac{L_\nu (\kappa_{mol\nu} + \kappa_{g\nu}) \, d\nu}{4 \pi r^2 c} - \frac{1}{2} \frac{dV_\phi^2}{dr} \right\} \qquad \ldots (5.4)$$

$$\text{i.e.} \quad \omega(r) = \left(\frac{G M_*}{r^2}\right)^{-1} \left\{ \frac{L_*}{4 \pi r^2 c} (\bar{\kappa}_{MOL} + \bar{\kappa}_g) - \frac{1}{2} \frac{dV_\phi^2}{dr} \right\} \qquad \ldots (5.5)$$

where $\bar{\kappa}_{MOL}$ is the Planck mean coefficient for molecular absorption, per unit mass, and $\bar{\kappa}_g$ is the same parameter for grains. In the numerical computation we also take luminosity to be attenuated to a first approximation as

$$L_* = L_*(r) = L_*(\infty) \exp \left(- \int_{r_*}^{r} \pi a^2 \bar{Q}_a(a(r), T_*) \, n_{gr}(r) \, dr \right)$$

where $\bar{Q}_a$ is the Planck mean absorption coefficient, n_{gr} the grain number density. Notice that here and later, we follow common precedent by

taking the mean stellar effective temperature seen by the grain as invariant, although it will slightly vary with distance from the star. dV_ϕ^2/dr determines the rate of change of azimuthal momentum per unit mass. For simple expansion of a rotating gas in which azimuthal drag terms are small

$$V_\phi = V_{\phi I} \left\{\frac{r_I}{r}\right\} \qquad \ldots (5.6)$$

whence

$$\frac{\frac{1}{2}\frac{dV_\phi^2}{dr}}{\frac{GM}{r^2}} = \frac{-\, r_I^2\, V_{\phi I}^2}{G\, M\, r} = -\,2 \left\{\frac{V_{\phi I}}{V_{escI}}\right\}^2 \left(\frac{r_I}{r}\right) \qquad \ldots (5.7)$$

where V_{escI} is escape velocity, and subscript "I" refers quantities to the base of the mass flow. This assumes that mass is ejected from a star spinning with latitude independent rotational velocity and a spherical surface. This is quite unrealistic. However, for relatively gentle change of stellar rotational velocity with latitude θ, and rapid acceleration and adiabatic cooling of gas outflow, non-radial mass motion will be expected to introduce second order contributions only. We will deal with finite rotational velocity examples as special cases, in the hope of obtaining some understanding of how terminal velocity varies with V_ϕ, and thereby θ. For the most part, we assume $V_\phi = 0$, probably reasonable for most red giants. Another assumption is that azimuthal drag terms due to grain motion may be ignored. We will discuss this later.

For mean molecular opacity we follow Auman (1969) and Alexander and Johnson (1972), by letting $\bar{\kappa}_{MOL} = 0.005$, and for grain "opacity" per unit mass we have

$$\bar{\kappa}_{gr} = \pi\, a^2\, \bar{Q}_{PR} \left(\frac{n_{gr}}{\rho}\right) \qquad \ldots (5.8)$$

where n_{gr} is the number of grains per unit volume. Following Kwok (1975) we may let

$$\frac{n_{gr}}{\rho} = \frac{3\ X\ f}{4\ \pi\ a^3\ \mu\ \rho_{gr}} \left\{\frac{V_r}{V_r + V_d}\right\} \qquad \ldots\ (5.9)$$

where V_d is the grain drift velocity with respect to the gas, X the fractional abundance of grain material by mass, and

$$f = f_o \left\{\frac{a}{a_o}\right\}^3 \qquad \ldots(5.10)$$

is the fraction of grain material condensed, where suffix "o" refers to sonic point conditions.

The modification of equation 5.2 to cover adiabatic cases now follows. We may write

$$\frac{d}{dr}\ (P\ \rho^{-\gamma}) = 0 \qquad \ldots(5.11)$$

$$\frac{d}{dr}\ (T\ \rho^{1-\gamma}) = 0 \qquad \ldots(5.12)$$

whence

$$\frac{dP}{dr} = c_s^{\,2}\ \frac{d\rho}{dr} \qquad \ldots(5.13)$$

where $c_s = (\gamma kT/\mu m_H)^{\frac{1}{2}}$ is the adiabatic sound velocity. Also from (5.1)

$$\frac{d\rho}{dr} = -\left\{\frac{2\rho}{r} + \frac{\rho}{V_r}\ \frac{dV_r}{dr}\right\} \qquad \ldots(5.14)$$

Substituting 5.14, 5.1 and 5.13 into 5.2 gives

$$\frac{dV_r}{dr} = \frac{V_r}{(V_r^{\,2} - c_s^{\,2})} \left\{\frac{2c_s^{\,2}}{r} - \frac{G\ M_*}{r^2}\ (1 - \omega(r))\right\} \qquad \ldots(5.15)$$

For real solutions we require

$$\omega(r_o) = 1 - \frac{2\, c_{so}^{\,2}\, r_o}{G\, M_*} \qquad \ldots(5.16)$$

An interesting consequence now follows. From 5.1 and 5.12 we note that

$$T = T_c \left\{ \frac{V_{rc}\, r_c^{\,2}}{V_r\, r^2} \right\}^{\gamma-1}$$

whence

$$c_{so}^{\,2} = c_{sc}^{\,2} \left\{ \frac{V_{rc}\, r_c^{\,2}}{V_{ro}\, r_o^{\,2}} \right\}^{\gamma-1} \qquad \ldots(5.17)$$

where subscript c refers to conditions at the radius of grain condensation. This latter quantity will represent one boundary of our numerical solutions. Since $V_{ro} = c_{so}$

$$c_{so}^{\,1+\gamma}\, r_o^{\,2(\gamma-1)} = c_{sc}^{\,2} (V_{rc}\, r_c^{\,2})^{\gamma-1} \qquad \ldots(5.18)$$

For $\omega(r_o)$ to be uniquely determined from initial conditions (c_{sc}, V_{rc} and r_c) requires

$$\frac{1+\gamma}{2(\gamma-1)} = 2 \qquad \text{i.e. } \gamma = \frac{5}{3}$$

Since we will numerically integrate equation 5.15 outward from condensation radius r_c, using $\gamma = 5/3$, $\omega(r_o)$ is then given by

$$\omega(r_o) = 1 - \frac{2\, c_{sc}^{\,3/2} (V_{rc}\, r_c^{\,2})^{\frac{1}{2}}}{G\, M_*} \qquad \ldots(5.19)$$

This in turn enables accurate provisional values of f_o to be determined. Letting $\bar{\kappa}_{MOL} + \bar{\kappa}_{gr} \simeq \bar{\kappa}_{gr}$ we have from 5.5, 5.8, 5.9 and 5.10

$$f_o \simeq \frac{4\ a_o\ \mu\ \rho_{gr}\ (c_{so} + V_{do})\ 4\ \pi\ c\ G\ M_*\ \omega(r_o)}{3\ X\ c_{so}\ \overline{Q}_{PR}\ L_*} \qquad \ldots(5.20)$$

For c_{so} we note that, providing acceleration is rapid and $r_c \simeq r_o$

$$c_{so}^{\ 2} \simeq c_{sc}^{\ 2} \left(\frac{V_{rc}}{V_{ro}}\right)^{\gamma-1}$$

that is

$$c_{so} \simeq (c_{sc}^{\ 3}\ V_{rc})^{\frac{1}{4}} \qquad \ldots(5.21)$$

The equations of grain drift have been determined by Gilman (1972) and Kwok, and we may write

$$V_d = (0.5((4k_p^{\ 2} + V_T^{\ 4})^{\frac{1}{2}} - V_T^{\ 2}))^{\frac{1}{2}} \qquad \ldots(5.22)$$

where

$$V_T = \frac{3}{4}\left\{\frac{3kT}{m_H}\right\}^{\frac{1}{2}} \qquad \ldots(5.23a)$$

and

$$k_p = \frac{\overline{Q}_{PR}\ L_*}{4\ \pi\ c\ \alpha\ \rho\ r^2} \qquad \ldots(5.23b)$$

For completely inelastic collisions a proportion $\cos^2\theta'$ of incident momentum in a grain/atom collision gives radial drag, the residue providing rotational terms, where θ' is the angle between the radial vector connecting impact site to grain centre and the direction of grain motion. Integrated over all incident particles this gives an effective $\alpha = 0.5$. This value is used here. For elastic collisions fractional input drag momentum reduces to $2\cos^2\theta'$, and $\alpha = 1$. Kwok has used $\alpha = 0.75$, implying intermediate elasticity collisions. Although the value of α is rather conjectural therefore, it cannot vary over a very wide range, and the qualitative sense of the results should remain unaffected.

For sonic point conditions the denominator term of k_p, $\rho_o r_o^2$, is approximated by

$$\rho_o r_o^2 = \frac{\rho_c r_c^2 V_{rc}}{c_{so}} \qquad \ldots(5.24)$$

Equations 5.19 through to 5.24 enable trial values of f_o to be determined for initial assumed values of sonic point grain radius c_o, and mass loss rate

$$\frac{dM}{dt} = 4 \pi \rho r^2 V_r \qquad \ldots(5.25)$$

This is found to be useful both for the numerical solution of gas flow, and the choosing of appropriate models for consideration through the requirements $V_c \leq c_{sc}$, $f_o \leq 1$. The determination of grain drift velocity in the radial direction follows from the requirement

$$F_{DRAG} = F_{RAD}$$

where, in Kwok's terminology F_{RAD} is the radiative force on the grain, and F_{DRAG} the retarding force due to motion relative to the gas. The relation implicitly assumes that F_{RAD} is very much greater than gravitational deceleration of the grains. For azimuthal grain motion we may follow a similar procedure, where for the equation of motion in vacuo we have

$$\frac{d\, mr^2 \dot{\phi}}{dt} = - \frac{L_*}{4 \pi c^2} \overline{Q}_{PR} \pi a^2 \phi$$

This is the Poynting-Robertson drag. In fact, there are other terms arising from the finite stellar size, which will not however be considered in the present approximation. Differentiated, it gives

$$m \frac{dV_\phi}{dt} = - \frac{V_\phi L_* \overline{Q}_{PR} \pi a^2}{4 \pi c^2 r^2} - \frac{V_\phi m}{r} \frac{dr}{dt} \qquad \ldots(5.26)$$

The first term resulting from abberation. The second term accounts for the conservation of angular momentum. If there were no abberational drag term the grains and gas would be azimuthally comoving, irrespective of radial distance, or any relative motion in the radial direction, and equations of grain growth, grain acceleration would remain unaltered. This would represent an extremely convenient simplification of the analysis. To assess how realistic this would be we let

$$F_{RAD} = \frac{V_\phi L_* \overline{Q}_{PR} \pi a^2}{4 \pi c^2 r^2}$$

and

$$F_{DRAG} = \alpha \pi a^2 \rho V_d (V_r^2 + V_d^2)^{\frac{1}{2}} \qquad \ldots(5.27)$$

The equation for F_{DRAG} is due to Kwok, and is in turn a slight generalisation of the relation due to Gilman (1972). V_T is the thermal velocity, given by equation 5.23a. Equating the two leads to an equation for V_d identical in form to equation (5.22), but with

$$k_\phi = \frac{L_* \overline{Q}_{PR} V_\phi}{4 \pi c^2 r^2 \alpha \rho} \qquad \ldots(5.28)$$

whence

$$\frac{V_{d\phi}^2}{V_d^2} \simeq \frac{k_\phi}{k_r} = \frac{V_\phi}{c}$$

for significant azimuthal grain drift (the case of interest). Alternatively

$$\left(\frac{V_{d\phi}}{V_\phi}\right)^2 = \frac{V_d^2}{cV_\phi}$$

whence for $V_d \lesssim 20$ km.s^{-1}, $V_\phi \simeq 10$ km.s^{-1}, $V_\phi/V_{d\phi} \simeq 10^2$. It is therefore a tolerable assumption under many circumstances to assume gas and grains to be azimuthally comoving - a condition that breaks down when V_d is particularly large, or V_ϕ small. In the latter circumstance, where $(V_\phi/V_{esc})^2 << 1$, the mass outflow in any case approximates to the case of zero rotation.

Finally, it should be mentioned that further azimuthal and radial accelerative terms of order

$$\frac{dV_r}{dt} = - \theta \frac{3 e B_o r_*^3}{4 \pi \rho_{gr} c a^3 r^2} \qquad ...(5.29)$$

$$\frac{d^2\theta}{dt^2} = \frac{3 e B_o r_*^3 V_r}{4 \pi \rho_{gr} c a^3 r^4} \qquad ...(5.30)$$

must be allowed for a significant (dipole) magnetic field (Maciel 1973). Although we have assumed negligible field strength B_o at the stellar surface in the present analysis, Maciel's work suggests that some care to incorporate such effects may be necessary. This latter author specifically follows the example of earlier workers in the field however in not investigating dynamical coupling of gas and grains (the grains are assumed to move through an hydrostatic isothermal atmosphere of scale height $2r_*$).

A final consequence of these equations may be noted.

In the subsonic regime we require the condition

$$\frac{2 c_s^2}{r} < \frac{G M_*}{r^2} (1 - \omega(r)) \qquad ...(5.31)$$

if $dV/dr > 0$.

Substituting for c_s leads to a subsonic gas temperature restriction

$$T_s \lesssim \frac{G M_* \mu m_H}{2 \gamma k r_*} \qquad \ldots(5.32)$$

where we have let $r \simeq r_*$. This corresponds to the requirement

$$c_s \lesssim 0.5 V_{esc} \qquad \ldots(5.33)$$

or, for an isothermal stellar atmosphere in hydrostatic equilibrium, for which

$$\rho(r) = \rho_o e^{-\frac{r-r_*}{h}} \qquad \ldots(5.34)$$

$$h = \frac{r_*^2 kT}{G M_* \mu m_H} = 2 r_* \frac{c_{SI}^2}{V_{esc}^2}$$

and c_{SI} is the isothermal sound velocity, it corresponds to the limit $h \lesssim r_*$. Of more specific interest, it defines temperature limits for any chromospheric zone accelerating adiabatically and supersonically to infinity, providing that in the process there are no significant energy processes involving, say, a change in the state of ionisation for certain atomic species.

For that case, it is necessary to revise the equations of motion in the manner prescribed by Weymann(1960) and Stanyvkovich (1958). We will in any case find that for flows in which grains provide a primary accelerative force, it is almost certainly necessary to define condensation zones having an initial temperature less than the stellar effective temperature, and therefore in the cooler regions of the essentially neutral atmospheres of late type stars.

5.5 Grain Growth

Three physical processes are considered as relevant to grain growth; accretion, sputtering and sublimation. Sublimation and sputtering are respectively important in the early and terminal stages of grain acceleration. We shall discuss these factors individually. Despite important work by for instance Donn et al. (1968), Salpeter (1974a) on grain nucleation, the discussion involves such uncertainties (see for instance Salpeter 1974a) that the results are almost certainly best taken as qualitative. There are for instance considerable uncertainties concerning the feasibility of silicate condensation. Fix (1971) has speculated upon this, noting of Al_2 Si O_5 and Mg Si O_3 that "We know nothing about the gas phases of these compounds; they have never been observed in the laboratory and very possibly do not exist in nature. They are certainly not likely to be abundant in a stellar atmosphere. Even should they be present, nucleation theory predicts that the high volume per molecule in the solid state for these materials would act as a serious barrier to nucleation. Spontaneous nucleation of Al_2 Si O_5 or Mg Si O_3, then, seems unlikely."

Salpeter (1974a) develops a similar line of argument, finding that the development of stable polysilicate molecules may require relatively substantial supercooling. The uncertainties are again large however. Fix and Salpeter argue that silicates may actually condense only as mantles to some more refractory material, such as certain oxides and titanates, although we will later find that certain less refractory materials (such as iron) may act as plausible nuclei.

For the present however we note that the most important mechanism of grain growth is probably homogeneous nucleation (as opposed to ion nucleation, Salpeter 1974a), for which case the

equations outlined in section 5.3 are applicable. The free energy ΔG of atom clusters above a critical size begins to decrease with increasing radius, leading to increasing stability. The critical energy obtained from Wickramasinghe (1967) is

$$\Delta G^{*} = \frac{16\ \pi\ \sigma_s^3}{3(kT/V_m)^2\ \ln^2(p/p_{SAT})} \qquad ...(5.35)$$

It is these stable clusters we will be primarily concerned with. A fuller discussion of this topic is provided by for instance Hoyle and Wickramasinghe (1962), Fix (1969), Faktor and Garrett (1974) and other references mentioned earlier. A discussion of the thermal balance of the proto-grains is given later. They will be found to lead to severe constraints upon the physical state of the gas in the condensation zone, as well as the range of available mass-loss models.

Given the protograins, subsequent accretion will lead to a mass increment rate

$$\frac{dM}{dt} = \pi\ a^2\ V_d\ X\ \rho\ \beta\ (1 - f(r)) \qquad ...(5.36)$$

where β is a sticking factor, X is the fractional abundance (by mass) of accreting material. The rate of radial growth is thereby

$$\frac{da}{dt} = \frac{V_d\ X\ \rho\ \beta}{4\ \rho_{gr}}\ (1 - f(r)) \qquad ...(5.37)$$

Following Kwok we replace V_d by $(V_d^2+V_T^2)^{\frac{1}{2}}$, to cover grain growth at both subsonic and supersonic grain velocities, to obtain

$$\frac{da}{dr} = \frac{\beta\ X\ \rho\ (V_T^2+V_d^2)^{\frac{1}{2}}}{4\ \rho_{gr}\ (V_r+V_d)}\ (1 - f(r)) \qquad ...(5.38)$$

5.6 Grain Sublimation

The mass loss from an evaporating grain is given by (Langmuir 1913)

$$\frac{dM}{dt} = \left(\frac{A_T\, m_H}{2\pi\, kT}\right)^{\frac{1}{2}} p_{VAP} \cdot 4\,\pi\, a^2$$

where, since $dM/da = 4\,\pi\, a^2\, \rho_{gr}$

$$\frac{da}{dt} = -\frac{1}{\rho_{gr}}\left\{\frac{A_T\, m_H}{2\pi\, kT}\right\}^{\frac{1}{2}} p_{VAP}$$

or, in the frame of reference of the central star

$$\frac{da}{dr} = -\frac{1}{\rho_{gr}} \frac{p_{VAP}}{(V_d+V_r)} \left\{\frac{A_T\, m_H}{2\pi\, kT}\right\}^{\frac{1}{2}} \qquad \ldots(5.39)$$

p_{VAP} is the saturation vapour pressure, which at the low pressures appropriate to this problem is given by the Clausius-Clapeyron relation

$$\log_{10} p_{VAP} = -\frac{A}{T_{gr}} + B \qquad \ldots(5.40)$$

A and B are constants, T_{gr} is temperature. Values of A and B (to give p_{VAP} in dynes.cm^{-2}) are given in table 5.2 for graphite, iron and fused quartz. Data is from Centolanzi and Chapman (1966), Rosebury (1965), Dushman and Lafferty (1962), and Lee (1972).

Equation 5.40 is in fact slightly temperature dependent, and higher order terms are, strictly, necessary. In practice, it is not always possible to obtain even A or B for materials of interest, and higher order data is certainly not readily available for the condensates to be studied here. The equation should however be reasonably accurate for the range of vapour pressures of relevance to the present problem.

TABLE 5.2

ADOPTED VAPOUR PRESSURE CONSTANTS

TERM	IRON	GRAPHITE	FUSED QUARTZ
A	2.0×10^4	4.0×10^4	2.49×10^4
B	12.56	15.85	14.02

5.7 Grain Sputtering

Equations from Wickramasinghe (1972) based on the compilation of Kaminsky (1965) are used. The sputtering yield is defined as the mean number of atoms/molecules lost by a grain per collision. The yield is, for various régimes of incident particle energy, given by

$$S(E) = 0 \qquad E < E_T$$

$$S(E) = S_o(E-E_T)/(E_A-E_T) \qquad E_T < E < E_A$$

$$= S_o \qquad E_A < E < 10\ E_B$$

$$= S_o(10E_B/E) \qquad E > 10\ E_B$$

where

$$E_T = S_A(M+m)^2/4Mm$$

$$E_A = S_B(M+m)/M$$

$$E_B = S_C\ m/M$$

$$S_o = S_D\ m(M+1)/(M+m)$$

where m and M are the respective atomic weights of incident and target atoms. S_A, S_B, S_C and S_D are constants which, for the three primary materials being discussed, are given in table 5.3. The data is derived from information summarised by Wickramasinghe (1972).

TABLE 5.3

SPUTTERING CONSTANTS

TERM	IRON	GRAPHITE	SILICATE
S_A	1.73×10^{-3}	7.10×10^{-3}	3.34×10^{-3}
S_B	2.21	0.339	0.820
S_C	195	4.584	30.90
S_D	0.03	0.01	0.01

For the grain environments we will be considering, thermal energies are <1.7 eV (corresponding to T < 20,000 K) and sputtering is unimportant. Sputtering becomes relevant when

$$\left(\frac{10^{12}}{1.602}\right) \frac{A_{TM}\, m_H\, V_d^2}{2} \gtrsim 25 \text{ eV}$$

where A_{TM} is the atomic weight of the heaviest species considered important, and m_H is the hydrogen atom mass. Taking $A_{TM} \simeq 200$ gives a limit to drift velocity

$$V_d \simeq 4.9 \text{ km.s}^{-1}$$

Significant sputtering occurs for drift velocities two to three times higher, when the more abundant species become involved. Even for initial gas temperature $T_c \simeq T_*$, $V_d \sim 5$ km.s^{-1} is supersonic for the models we will consider, and in reality the gas temperature at this value of drift velocity will be substantially less than T_c. We may therefore write to a good approximation, the relation for mean sputtering rate per incident hydrogen atom

FIGURE 5.4a

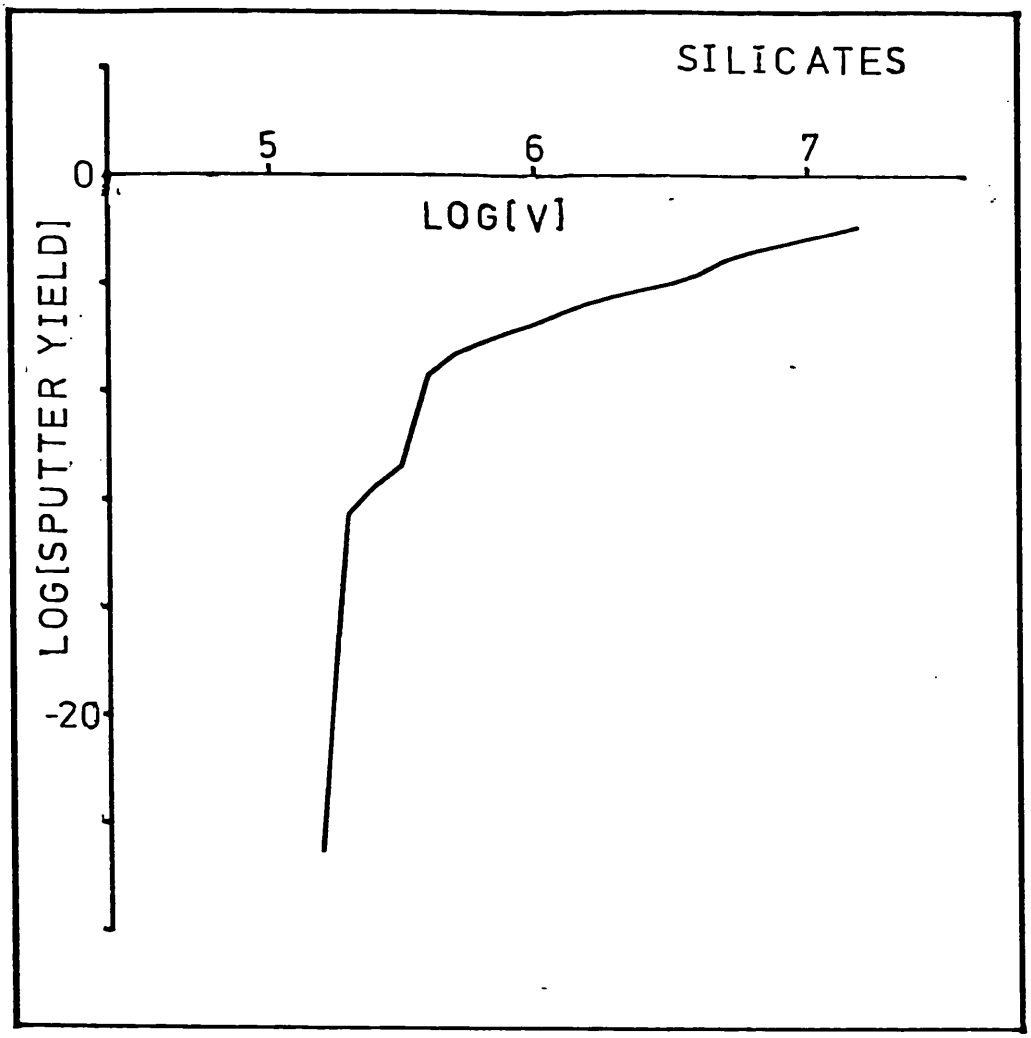
SILICATES
5
6
7
0
LOG[V]
LOG[SPUTTER YIELD]
-20

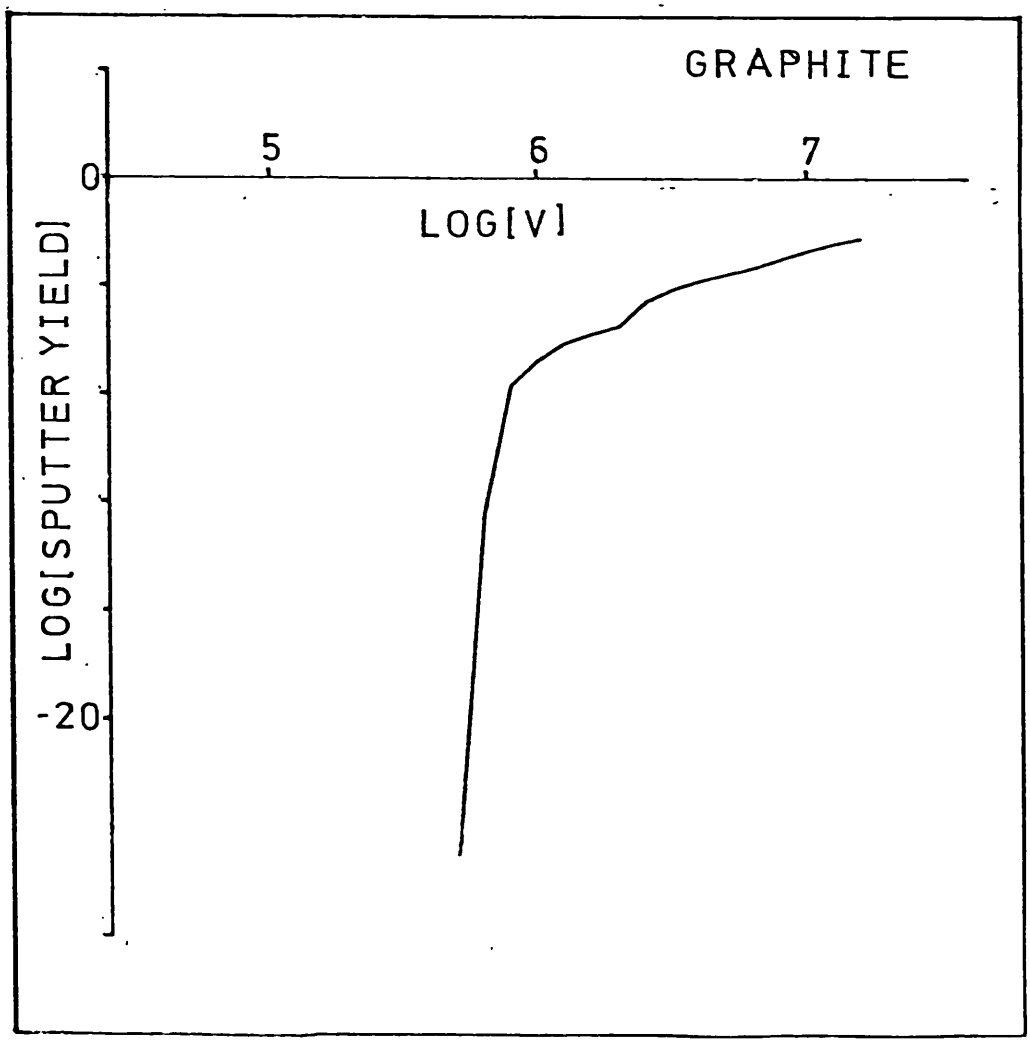
GRAPHITE
5
6
7
0
LOG[V]
LOG[SPUTTER YIELD]
-20

FIGURE 5.4b

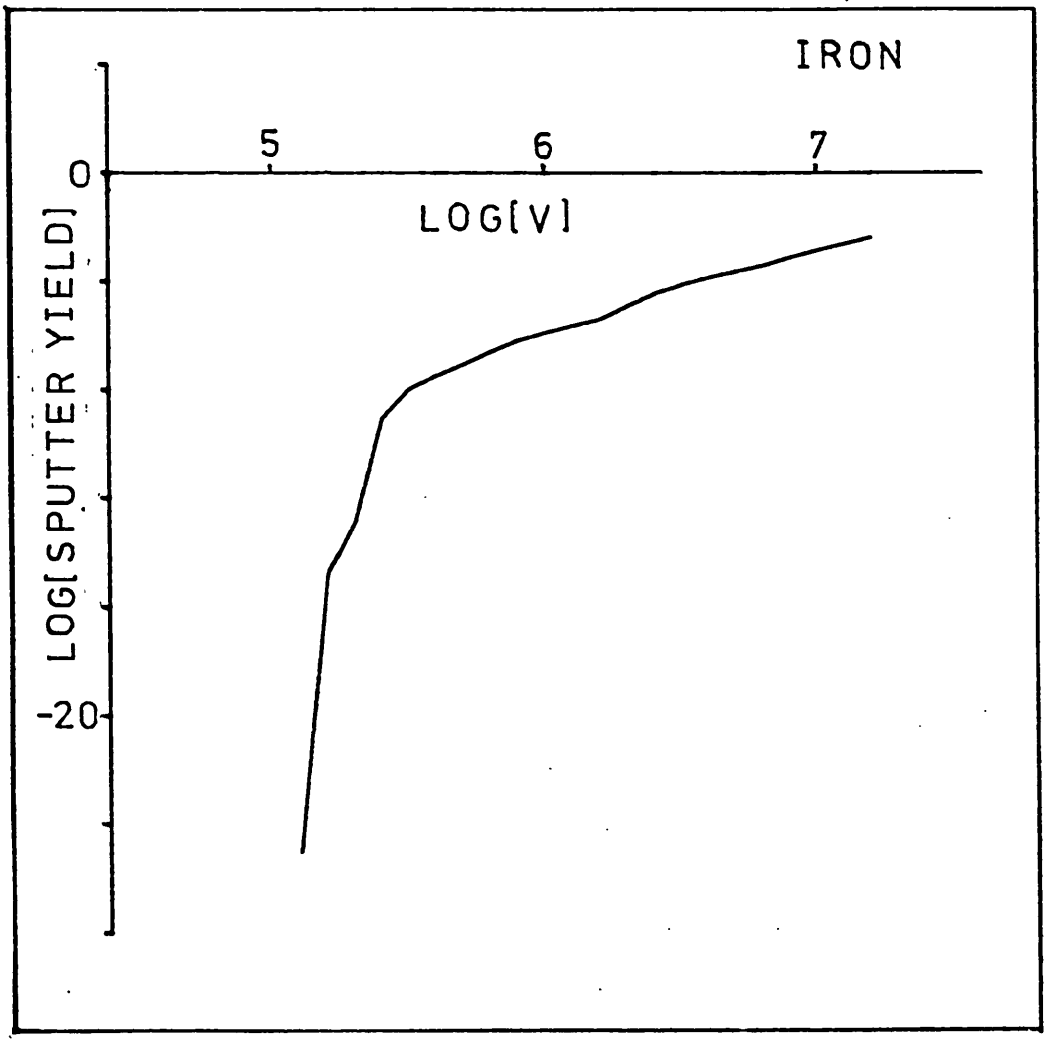

$$\overline{S}(V_d) = \xi \sum_i \frac{S\ (E(A_{Ti}))\ X_i}{A_{Ti}}$$

$$E(A_{Ti}) = \frac{1}{2}\ m_H\ A_{Ti}\ V_d^{\ 2}$$

where the summation i is over the various atomic species, and ξ is the mean atomic weight per hydrogen atom. In figure 5.4 we show the relation between $\overline{S}(V_d)$ and V_d for grains composed of graphite, iron and silicate. These graphs may be conveniently summarised by the expressions

$$\overline{S} = 10^{S1}\ V_d^{\ S2} \qquad \log V_d > C \qquad \ldots(5.41a)$$

$$\overline{S} = 10^{S3}\ V_d^{\ S4} \qquad D < \log V_d < C \qquad \ldots(5.41b)$$

$$\overline{S} = 0.0 \qquad \log V_d < D \qquad \ldots(5.41c)$$

The constants S1 → S4, C and D are given in table 5.4 for the three grain materials. For these calculations, 82 values of A_i, X_i were used, from the compilation of Allen (1973).

TABLE 5.4

SPUTTERING PARAMETERS

TERM	IRON	GRAPHITE	SILICATES
S1	-25.48	-21.60	-26.63
S2	3.25	2.70	3.50
S3	-111.05	-39.24	-54.7
S4	18.5	5.4	8.0
C	5.45	6.35	5.55
D	5.15	5.85	5.25

We have assumed all species with abundances listed by Allen to be available for sputtering; there is no assumption concerning species removed from sputtering by condensation. In this respect the values of $S(V_d)$ are upper limits although in fact the removal of elements through grain condensation causes, for the materials considered here, negligible modifications of the above relations. To complete the argument however, we note that for the fractional condensation f_j of species j, the modified sputtering rate $S'(V_d)$ is

$$S'(V_d) = S(V_d) - \xi \sum_j \frac{S_j\ E(A_j)\ f_j\ X_j}{A_j}$$

5.8 General Equation of Grain Growth

Combining equations 5.40, 5.39, 5.38 and 5.43, the rate of grain growth is given by

$$\frac{da}{dr} = \beta \frac{X\ \rho(V_T^2+V_d^2)^{\frac{1}{2}}}{4\rho_{gr}(V_r+V_d)} (1 - f(r)) - \frac{10^{A-B/T}}{\rho_{gr}(V_d+V_r)} \left\{\frac{A_T\ m_H}{2\pi\ kT}\right\}^{\frac{1}{2}} - \frac{A_T\ \rho\ \overline{S}}{\xi\ m_H\ 4\rho_g} \frac{V_d}{(V_d+V_r)}$$

...(5.49)

We therefore now have two coupled equations, 5.15 and 5.49, numerically integrable using Runge-Kutta procedures. Before this is possible however we require relations for various further grain parameters, and a procedure for determining appropriate boundary conditions for the gaseous flow.

For the grain materials we are considering, the cosmic mass abundances (relative to hydrogen) and atomic/molecular weights from

the compilation of Allen (1973) are adopted. The abundance for olivine is a maximum, and assumes all the available magnesium is used. This is permissible if ≥6% of the oxygen atoms are not in the form of (primarily) CO, and ≥40% of silicon atoms are available. For red giants/supergiants, this is probably a reasonable expectation. Nevertheless, actual abundances of condensible matter may be rather less than quoted here, and models with atomic/molecular deficiencies are also considered. Note that the absolute cosmic abundances are obtained by dividing the values in table 5.5 by $\xi(=1.36)$, the mean atomic weight per hydrogen atom. For the mean atomic weight, μ, a value $\mu = 1.26$ was used. Both these latter values are again from Allen (1973). Finally, we give the mean grain densities adopted. There is some variability in the values assigned to terrestrial condensates. The values here are adapted from the Handbook of Chemistry and Physics, 55th Edition, 1974.

TABLE 5.5

CONDENSATE	MOLECULAR/ATOMIC WEIGHT	MASS ABUNDANCE	GRAIN DENSITY ($gm.cm^{-3}$)
Fe	55.847	2.24×10^{-3}	7.87
C	12.011	3.98×10^{-3}	2.3
Mg_2SiO_4	140.694	1.87×10^{-3}	3.2

5.9 Grain Optics

Grain scattering and absorption parameters may be determined from the data compilations of Gilman (1974) and Wickramasinghe (1973). These are reduced for analytical convenience to approximate relations. The parameters of particular interest are $\overline{Q}_{PR}(a,T)$; the Planck mean

radiative pressure efficiency factor; $\overline{Q}_a(a,T)$, the Planck mean absorption coefficient, relevant in determining grain temperature, and finally $Q_{abs}(\lambda^{-1} = 1.8\ \mu m^{-1})$; the optical absorption coefficient at $\lambda^{-1} = 1.8\ \mu m^{-1}$. We shall take multiple scattering to be small ($\tau_{SCA} \lesssim 1$).

For $\overline{Q}_{PR}$, the following expressions are adequate for iron, graphite, and magnesium silicate

$$\overline{Q}_{PR} = QA\ (\frac{aT}{30})^{QB} \qquad \frac{aT}{3000} < A2$$

$$\overline{Q}_{PR} = QC\ (\frac{aT}{30})^{QD} \qquad A2 < \frac{aT}{3000} < A1$$

$$\overline{Q}_{PR} = QE\ (\frac{aT}{30})^{QF} \qquad A1 < \frac{aT}{3000} \qquad (a \text{ in } \mu ms)$$

The constants QA → QF, A1 and A2 for "a" in μms are detailed in table 5.6, and adopted from the data in figures 1, 2 and 4, and table 2 of Gilman (1974). Gilman has noted that

$$\overline{Q}_{PR}(T,a) = \overline{Q}_{PR}\ (3000\ K,\ aT/3000)$$

for 2000 K < T < 4000 K and $Q_{PR} < 0.05$ to within 1% for olivine, 3% for graphite and 10% for iron.

TABLE 5.6

RADIATION PRESSURE EFFICIENCY FACTOR

TERM	IRON*	GRAPHITE*	OLIVINE*
QA	1.82×10^{-2}	3.8×10^{-2}	1.18×10^{-4}
QB	1.00	1.00	1.00
QC	1.82×10^{-2}	3.8×10^{-2}	1.18×10^{-4}
QD	1.6	1.4	2.75
QE	1.9	1.9	1.5
QF	0.0	0.0	0.0
A2	10^{-2}	10^{-2}	10^{-2}
A1	10^{-1}	10^{-1}	0.3

* "a" in μms

For iron and graphite $\overline{Q}_{PR}$ is a simple increasing function of T over a wide range of temperatures, a consequence of the absence of significant optical and near infrared absorption bands. For olivine, the form of $\overline{Q}_{PR}$ is quite different, dominated at low temperatures by strong reststrahlen bands at $\lambda \simeq 10$ μm, arising from the formation of phonons, and for higher temperatures by strong U.V. exciton bands. In consequence, the gradient of $\overline{Q}_{PR}$ against temperature reverses rapidly near T ≃ 4000 K. Similar arguments apply for $\overline{Q}_a$ (a,T). Gilman has further noted that $\overline{Q}_{PR}$ is almost entirely determined by these two bands, and in this respect the data for $\overline{Q}_a$ and $\overline{Q}_{PR}$ will be broadly applicable to silicates in general.

For $\overline{Q}_a$ the following equation appears to be adequate

$$\overline{Q}_a = QAA\ T^{QAB}\ (10^5 a)^{QAC}$$

applicable for $a \lesssim 5 \times 10^{-5}$ cms, 300 K < T ≲ 4000 K. Values of constant terms are given in table 5.7.

TABLE 5.7

PLANCK MEAN ABSORPTION COEFFICIENT PARAMETERS

TERM	IRON	GRAPHITE	OLIVINE
QAA	1.32×10^{-7}	1.74×10^{-7}	9.1×10^{2}
QAB	1.88	1.92	-1.95
QAC	-1.2	+1.0	+1.0

The relationship is primarily important for determining grain temperature T_{gr}. Its breakdown near ~300 K is responsible for an underestimate in T_{gr} for $T_{gr} \lesssim 300$ K. Although this will lead to corresponding under-

estimates in grain sublimation rates, the circumstances in which these temperatures are met (i.e. in which grain growth and sputtering rates are many orders of magnitude greater than sublimation rates) are such as to render this virtually irrelevant.

Finally, from data provided by Wickramasinghe (1973) we have prepared figure 5.5, representing the variation of Q_{abs} ($\lambda^{-1} = 1.8\ \mu m^{-1}$) with grain radius a for iron. The graphs are approximated analytically by the expressions

$$Q_{abs} = Q1\ a^{Q2} \qquad a < AA$$

$$Q_{abs} = Q3\ a^{Q4} \qquad AB > a > AA$$

$$Q_{abs} = Q5\ a^{Q6} \qquad a > AB$$

constants Q1 → Q5, AA and AB being given in table 5.8.

TABLE 5.8

OPTICAL ABSORPTION CONSTANTS

TERM	IRON*	GRAPHITE*
Q1	6.05	10.5
Q2	1.00	1.00
Q3	95.9	55.1
Q4	1.6	1.36
Q5	0.65	0.93
Q6	-0.29	-0.24
AA	10^{-2} μm	10^{-2} μm
AB	8×10^{-2} μm	8×10^{-2} μm

* CONSTANTS ARE FOR "a" IN μm.

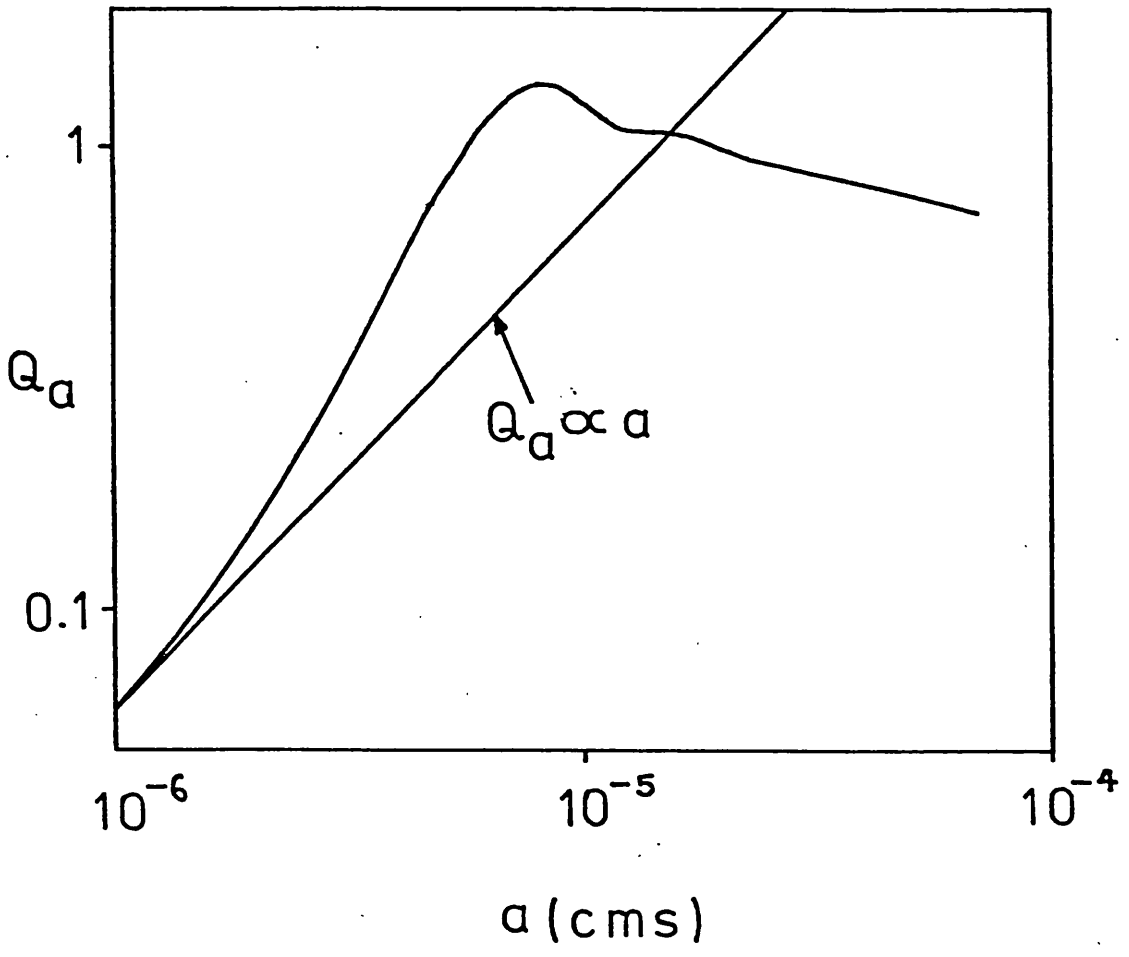

FIGURE 5.5

VARIATION OF IRON ABSORPTION COEFFICIENT WITH GRAIN RADIUS AT $\lambda = 0.56$ μm

5.10 Grain Radiative Equilibrium

For a grain in thermal equilibrium with the radiation field we may write

$$\frac{\pi a^2 L_* \overline{Q}_a \quad (a,T_*)}{4\pi r^2} = 4 \pi a^2 \overline{Q}_{em}(a,T_g) \sigma T_g^4$$

or, taking $L_* = 4 \pi r_*^2 \sigma T_*^4$

$$\left(\frac{r_*}{r}\right)^2 = 4 \left\{\frac{\overline{Q}_{em}(a,T_g)}{\overline{Q}_a \quad (a,T_*)}\right\} \left\{\frac{T_g}{T_*}\right\}^4$$

for $T_g \gtrsim 300$ K, T_g, $T_* < 4000$ K, the dependence of $\overline{Q}_{em}$, $\overline{Q}_{abs}$ upon "a" is the same, and we have

$$T_g = T_* \left\{\frac{1}{2} \frac{r_*}{r}\right\}^{\frac{2}{4+QAB}} \qquad \ldots(5.50)$$

5.11 The Grain Condensation Zone

From the previous subsection, the temperature of a grain whose thermal balance is determined by the stellar radiation field alone is given closely by

$$T_c = \frac{T_*}{2^{\beta_T}} ; \quad \beta_T = 2/(4+QAB)$$

We have assumed $r_c = r_*$. This is of course an approximation; the extent to which it represents a reasonable approximation may be assessed in the following manner. If we approximate the stellar atmosphere by an isothermal hydrostatic model (this is a poor, but not excessively discrepant description) then we may write for atmospheric pressure P_{AT}

$$P_{AT} \approx 300 \frac{G M_*}{r_*^2} e^{-\frac{(r-r_*) G M_* \mu m_H}{r_*^2 kT_{AT}}}$$

and define

$$T_2 = \frac{A_T}{B_T - \text{Log } P_{AT}}$$

where T_2 is the temperature for saturation of the condensate at (total) gas pressure P_{AT}.

The value of r for which $T_2 = T_{gr}$ may then be determined numerically. This gives the maximum radius for grain condensation. The results for graphite and olivine are similar. A typical graph is shown in figure 5.6. It is seen that maximum condensation zone radius is indeed very little greater than the stellar radius, and to a good approximation (so far as this argument is valid) we may say $r_c \approx r_*$. This is expected to remain the case wherever $h/r_* << 1$, where h is the atmospheric scale height. For this isothermal hydrostatic approximation, $h/r_* \approx 2c_{sc}^2/V_{esc}^2$. Since we will later be finding that grains are unlikely to condense in atmospheres where T_{AT} greatly exceeds T_c, it is perhaps relevant to note that the radius of grain condensation should be changed to $r_2 = (r_1 T_{AT2}/T_{AT1} + r_*(1 - T_{AT2}/T_{AT1}))$ from r_1 for a change in atmospheric temperature from T_{AT1} to T_{AT2}. Insertion of trial values will (as we would expect) show r_2 to differ insignificantly from r_1, insofar as its similarity to r_* is concerned.

For iron grains, the situation is more problematic and at least superficially it seems that formation in stellar atmospheres is precluded. This is seen most clearly by plotting T_2 and T_{gr}, as in figure 5.7, where it is seen that T_{gr} at all values r exceeds the corresponding value T_2. Also plotted is a corresponding value T_3

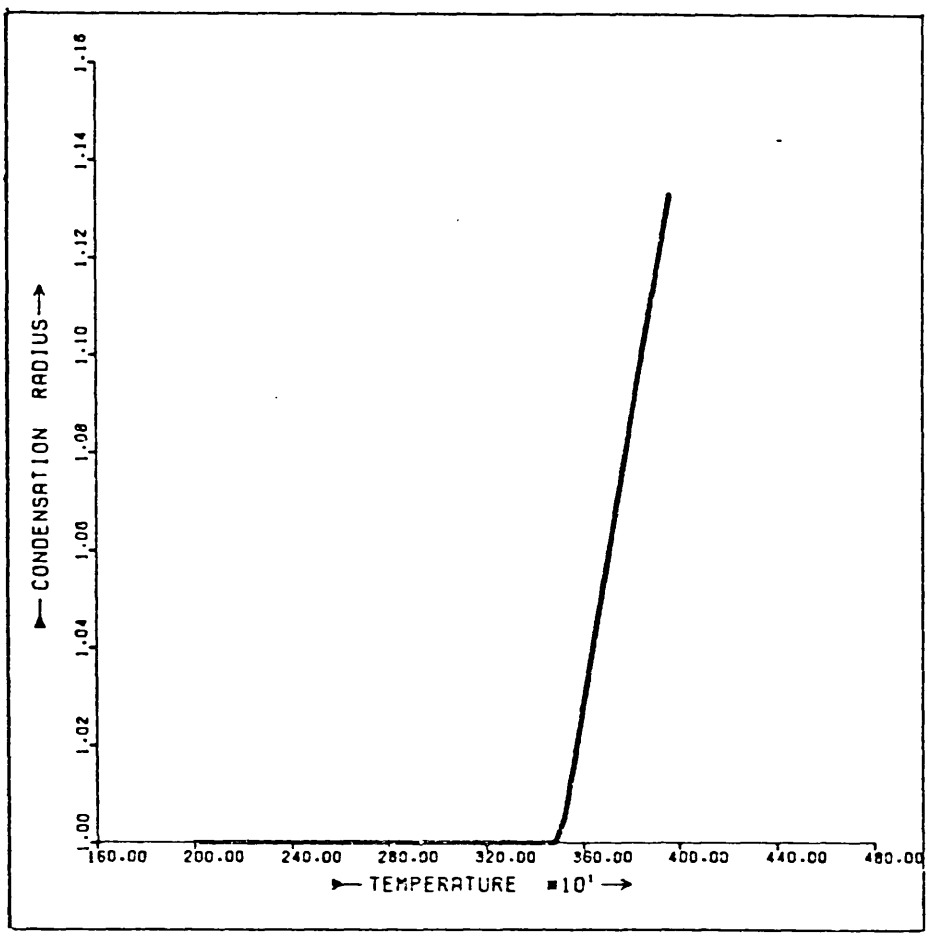

FIGURE 5.6

VARIATION OF SILICATE GRAIN CONDENSATION RADIUS (UNITS OF R_*) WITH STELLAR TEMPERATURE

FIGURE 5.7a

VARIATION OF GRAIN TEMPERATURE PARAMETERS WITH DISTANCE FROM STAR
$R_* = 10^2\ R_\odot$; $T_* = 3000$ K

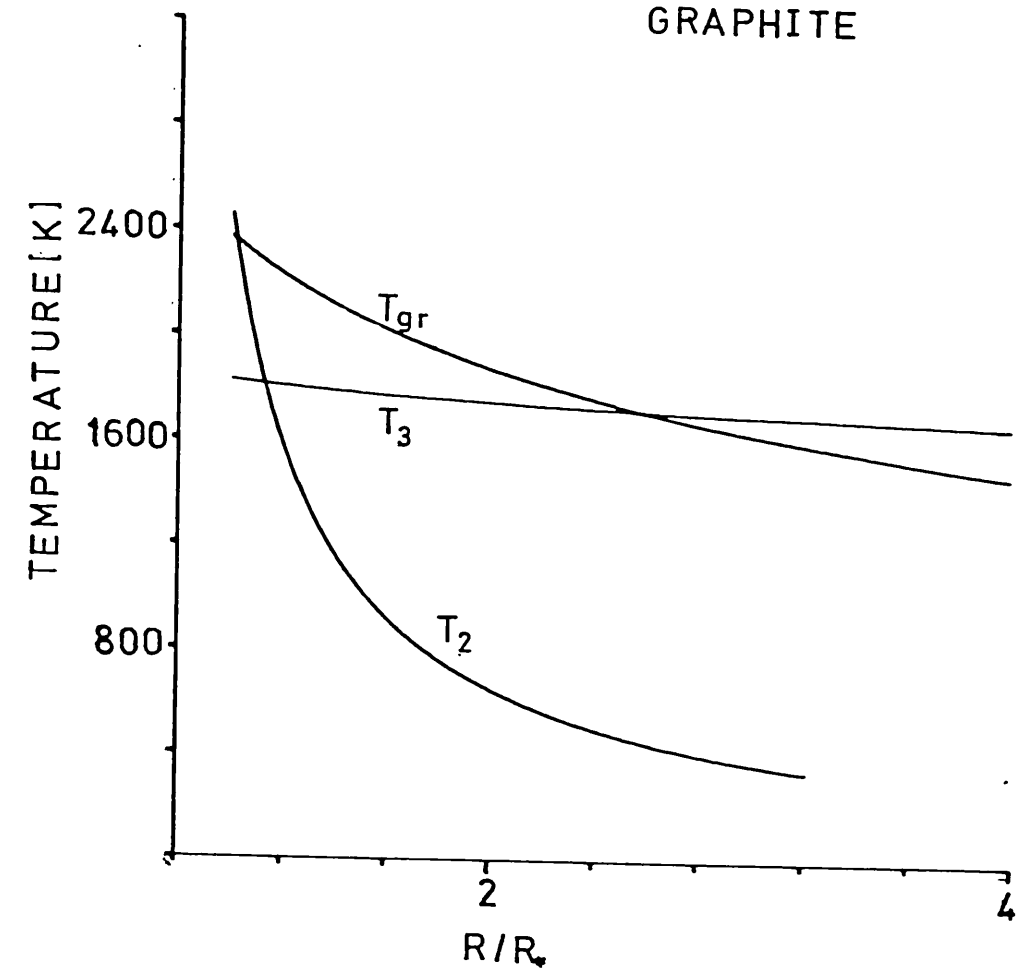

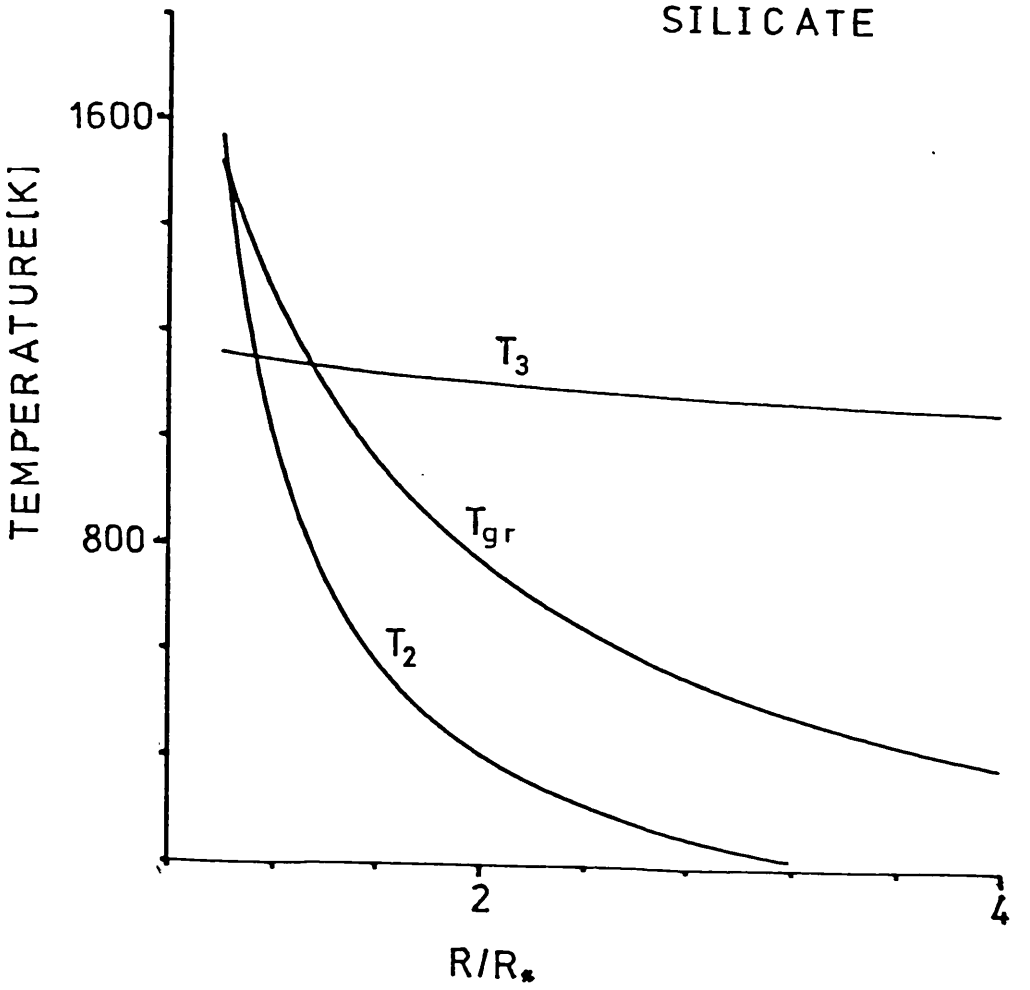

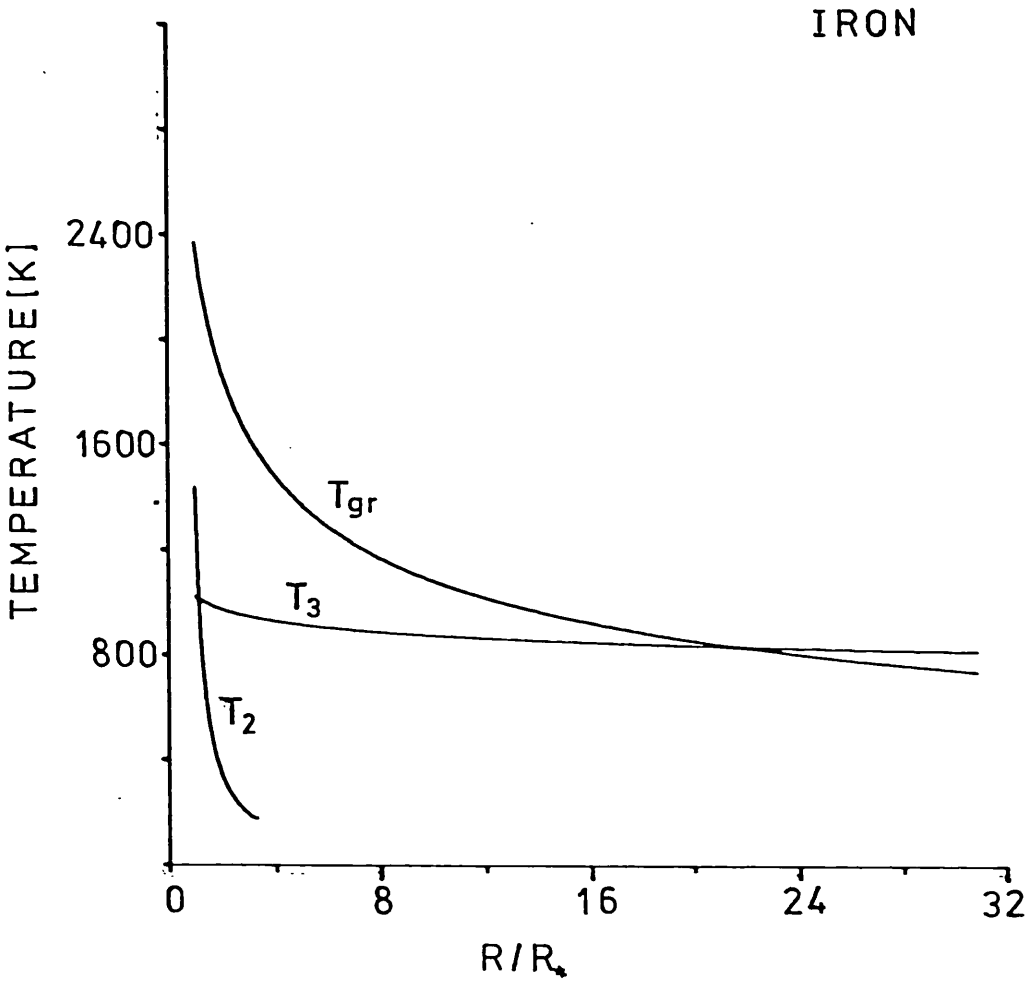

FIGURE 5.7b

VARIATION OF GRAIN TEMPERATURE PARAMETERS WITH DISTANCE FROM STAR
$R_* = 10^2\ R_\odot$; $T_* = 3000$ K

appropriate for the pressure in an adiabatic flow

$$P = \frac{\rho_*^{\gamma-1} kT_{r*}}{\rho^{\gamma} \mu m_H}$$

T_{r*}, ρ_* being the values of flow temperature, density at the stellar surface. We have used $T_{r*} = T_*$, and ρ is determined from equation 5.48, assuming a uniform gas velocity $V_r = 10^6$ cm.s^{-1}. It is evident that iron grains may condense further out in the flow, perhaps forming mantles around more refractory grains. We shall return to this question later.

Returning to equation 5.51 we note that the parameters (A_T, B_T) have values $(2.0 \times 10^4, 16.99)$, $(4.0 \times 10^4, 19.36)$ and $(2.49 \times 10^4, 18.93)$ for iron, graphite and silicates respectively. We have assumed here that the total possible material required for condensation is available, and that abundances are similar to those given by Allen (1973). It has already been noted that this would be optimistic. The consequence of assuming a lower fractional mass of potential condensate is for a larger value of total pressure P, however, which will only serve to underline the point to be made. For effective temperatures $T_* = 3000$ K we thereby obtain total required condensation zone pressures

IRON	$T_c = 2370$ K	$P_{TOT} \simeq 3.28 \times 10^8$ dynes.cm^{-2}
GRAPHITE	$T_c = 2370$ K	$P_{TOT} \simeq 2.58 \times 10^2$ dynes.cm^{-2}
SILICATE	$T_c = 1520$ K	$P_{TOT} \simeq 3.54 \times 10^2$ dynes.cm^{-2}

For comparison, we note the representative values of atmospheric optical depth τ, and temperatures T_{AT} corresponding to similar gaseous pressures:-

MODEL	C/O	Log g	T_{AT} (K)	τ	P_{TOT}
J22	5.0	0.0	3709.3	3.981	2.437×10^2
J21	5.0	2.0	2543.2	0.063	2.540×10^2
J10	0.6	0.0	3559.3	3.362	2.442×10^2
J9	0.6	2.0	2412.9	0.020	2.352×10^2

The data is from Johnson (1974). All models here have $T_* = 3000$ K. Note for comparison that for class III stars log g ≃ 1.4, and for class I, log g ≃ 0.2. Evidently, for class III stars, or thereabouts, there should be no problems in forming graphite and silicate grains, although iron grains would appear to be impossible to form (note that the pressure ascribed to iron grains above is outside the range of applicability of equation 5.51 - it is given here to indicate a very high value). For supergiants, on the other hand, the relevant conditions seem unlikely to be available, at least in terms of the figures above. Care should be taken however in such interpretations. Johnson's models involve many assumptions, which are freely admitted; the most obvious (in the present context) being perhaps that of hydrodynamic stability. Earlier (c.f. Alexander and Johnson 1972) and contemporary models by other workers differ in details, and for certain of these grain formation does seem to be plausible in both giants and supergiants, providing grains and gas are thermally decoupled*, and $T_{AT} > T_{gr}$. All of the atmospheric models appear to preclude any source of grain energy input considerably greater than radiative inputs. For all cases, the range of possible grain temperatures, corresponding to the available range of atmospheric pressures above P_c, is small, and it is therefore possible to say that

* Or poorly coupled (see later).

for condensation in hydrostatic model atmospheres, T_{gr} cannot greatly exceed T_c. Further, for most models investigated having $T_* \gtrsim 2500$ K, the minimal atmospheric temperature $T_{AT\ MIN}$ so exceeds the maximum permissible grain temperature $T_{gr\ MAX}$, that setting $T_{gr\ MAX} = T_{AT\ MIN}$ leads to atmospheric pressures considerably in excess of these models. It seems in short that available atmospheric models for the warmer late type stars typically require $T_{AT} > T_{gr} \simeq T_c$ within the condensation zone.

Whilst discussion involving current stellar atmospheric models yields interesting results, it is nevertheless clear that the uncertainties are sufficiently broad that too much specific confidence in these conclusions would be misplaced. The conclusion capable of being considered with some generality is that $T_{gr} \lesssim T_c$, and we will adopt this position in selecting models of mass loss.

As to whether T_{gr} can be significantly less than T_c requires an analysis of thermal balance involving radiative absorption/emission, and atomic/molecular collisions with grains. No assumptions will be made concerning condensation zone conditions outside of the requirement that the gas is saturated, or supersaturated with respect to the appropriate condensate, and that its temperature is consistent with the grain temperature $T_{gr} \lesssim T_c$.

5.12 Thermal Balance of Grains with Respect to Stellar Atmospheres, and Radiative Fields

The problem of thermal balance for grains, incorporating grain/gas coupling, has been approached by for instance Spitzer (1968) and Greenberg (1968) in discussing the interstellar environment, and HII

regions. Both these authors conclude that it may in these circumstances be neglected. Its application to stellar atmospheres appears to have been discussed implicitly, sometimes suggesting results for which however no explicit supporting analysis is presented (c.f. Krishna Swamy 1970).

Considering first grain/gas interactions alone, we note that the incident energy to a grain is strongly dependent upon the atomic and ionic species involved. Neglecting for the moment all questions of grain charge, and assuming energy equipartition among the various incident particles, the incident energy for a mass M and relative number abundance (to hydrogen) Y_H, as a fraction of that due to hydrogen is $Y_H(m_H/M)^{\frac{1}{2}} \simeq 4.3 \times 10^{-2}$ for helium. Other species are even less effective. For an ionised atmosphere the primary energy input may be due to electrons (and, it should be noted, this is also the case for an HII region; a possible deficiency in Greenberg's analysis, where incident protons alone appear to be considered). For late type stars, the stellar atmospheres are however expected to be essentially neutral; for an M0III star for instance, at the atmospheric level where $P_{AT} \simeq 2.0 \times 10^3$ dynes.cm^{-2} (close to the photosphere), we have $P_{AT}/P_e \simeq 10^5$, and for an M5III star where $P_{AT} \simeq 7.9 \times 10^2$ dynes.cm^{-2}, $P_{AT}/P_e \simeq 2.5 \times 10^5$, where P_e is electron pressure. For the former case, relative heat input due to electrons compared to hydrogen atoms is $\sim 4.3 \times 10^{-4}$; comparatively negligible. We may therefore to a good approximation consider hydrogen atoms alone as providing a significant energy input vector. The flux of hydrogen atoms upon a spherical grain is

$$\frac{dN}{dt} = 4 \pi a^2 u_x \frac{\rho}{\xi m_H} \qquad \ldots(5.52)$$

Power input is then given by

$$\overline{P} = \left\langle \frac{dN}{dt} E_p \right\rangle \qquad \ldots(5.53)$$

$$= \frac{2 \pi a^2 \rho}{\xi} \langle u^2 u_x \rangle \qquad \ldots(5.54)$$

where E_p is particle energy, and u is velocity. Adopting a Cartesian framework, with velocity component u_x normal to grain surface, and orthogonal components u_y, u_z then gives for a Maxwellian distribution of particle velocities

$$\langle u^2 u_x \rangle = \left\{\frac{m}{2\pi kT}\right\}^{\frac{3}{2}} \left\{ \int_0^\infty u_x^3 \, e^{\frac{-mu}{2kT}x^2} \, du_x \int_{-\infty}^{+\infty} e^{-\frac{mu_y^2}{2kT}} \, du_y \int_{-\infty}^{+\infty} e^{\frac{-mu}{2kT}z^2} \, du_z \right.$$

$$+ \int_0^\infty u_x \, e^{-\frac{mu_x^2}{2kT}} \int_{-\infty}^{+\infty} u_y^2 \, e^{-\frac{mu_y^2}{2kT}} \, du_y \int_{-\infty}^{+\infty} e^{-\frac{mu_z^2}{2kT}} \, du_z$$

$$\left. + \int_0^\infty u_x \, e^{-\frac{mu_x^2}{2kT}} \int_{-\infty}^{+\infty} e^{-\frac{mu_y^2}{2kT}} \, du_y \int_{-\infty}^{+\infty} u_z^2 \, e^{-\frac{mu_z^2}{2kT}} \, du_z \right\}$$

Note that negative values of u_x are excluded. The evaluation of the integrals is standard, and gives

$$\langle u^2 u_x \rangle = \frac{4kT}{m} \left\{\frac{kT}{2\pi m}\right\}^{\frac{1}{2}} \qquad \ldots(5.55)$$

It is perhaps of interest to note that, despite the absence of negative values for u_x, half the incident energy budget is provided by velocity components normal to the grain surface. This arises because, for similar kinetic energies, particles with higher values of u_x strike the grain proportionately more often. The same distortion of the input energy spectrum will not apply for re-emitted atoms however, and the

mean emitted particle energy for thermalised atoms is probably more closely related to $\langle u_{gr}^2 \rangle$ (u_{gr} being the velocity of emission). That is, for a Maxwellian spectrum, mean output energy flux is $5/4\ kT_{gr}\mathcal{F}$, where $\mathcal{F}$ is the input particle flux. Clearly, there are several uncertainties here, which will cause small changes in the energy terms. If however we write the energy balance equation in the form

$$\frac{5}{4} k\ (T\chi_1 - T_{gr}\chi_2)\ 4\pi^2 \left\{\frac{kT}{2\pi m_H}\right\}^{\frac{1}{2}} \frac{\rho}{\xi m_H} + \frac{L_* \overline{Q}_a(a,T_*)}{4\ \pi\ r}\ \pi\ a^2$$

$$= 4\ \pi\ a^2\ \overline{Q}_{em}(a,T_{gr})\ \sigma\ T_{gr}^4$$

then for low elasticity grain-gas collisions the energy transfer functions $\chi_{1,2} \simeq 1$. For the present models we in fact set $\chi_1 = \chi_2 = 1$. This will limit condensation zones to (in the main) sub-photospheric temperatures. Chromospheric models of the grain condensation zones require $\chi_1/\chi_2 < 1$.

Letting $\rho = P_{\mu m_H}/kT$, $L_* = 4\ \pi\ r_*^2\ \sigma\ T_*^4$ then gives

$$5k(T - T_{gr}) \frac{P}{kT} \frac{\mu}{\xi} \left(\frac{kT}{2\pi m_H}\right)^{\frac{1}{2}} + \left(\frac{r_*}{r}\right)^2 \sigma\ T_*^4\ \overline{Q}_a(a,T_*) = 4\ \overline{Q}_{em}(a,T_{gr})\ \sigma\ T_{gr}^4$$

Finally, we note that for the grain condensation zone we require

$$P = \frac{P_X\ A_T}{X\mu}$$

where P_X is the partial pressure of the atomic species with abundance X which is condensing to form grains. Since $P_X = 10^{B-A/T_{gr}}\ Z$, where Z is the supersaturation ratio ($Z \geq 1$) then

$$\frac{5\ kZ}{\sigma(2\pi k m_H)^{\frac{1}{2}}\xi} \frac{A_T}{X} \frac{10^{B-A/T_{gr}}}{T^{\frac{1}{2}}} (T - T_{gr}) = 4\ \overline{Q}_{em}(T_{gr},a)\ T_{gr}^4 - \overline{Q}_a(T_*,a)\ T_*^4$$

Finally we substitute for $\overline{Q}_{em}$, $\overline{Q}_a$ to obtain

$$\frac{5\ kZ}{\sigma(2\pi km_H)^{\frac{1}{2}}\xi}\ \frac{A_T}{X}\ \frac{10^{B-A/T_{gr}}}{T^{\frac{1}{2}}}\ (T - T_{gr}) = QAA\ (10^5 a)^{QAC}\ (4\ T_{gr}^{2/\beta_T} - T_*^{2/\beta_T})$$

or

$$\frac{W\ 10^{B-A/T_{gr}}\ (T - T_{gr})\ Z}{T^{\frac{1}{2}}} = a^{QAC}\ (4\ T_{gr}^{2/\beta_T} - T_*^{2/\beta_T}) \qquad ...(5.56)$$

where constant W is 6.0×10^{13}, 5.56×10^{13}, and 2.68×10^5 for respective grain materials iron, graphite and olivine. A cursory examination suggests that for large T_{gr}, the term $10^{B-A/T_{gr}}$ will be large, and to match the right hand side we require $T \simeq T_{gr}$. The corollary for small T_{gr} is however that grain and gas temperature may be quite different.

Numerical solutions of equation 5.56 have been performed for Z = 1,100 for all three grain materials. In figure 5.8 we have plotted log P versus log T, and T_{gr} versus T.

These curves represent the necessary pressure - temperature relation for any grain condensation zone, for the given assumptions, irrespective of any question of model atmospheres. Several points will be noted:

(a) Grain temperature and gas temperature are very closely coupled for $T_{gr} > T_c$.

(b) Grain and gas temperatures remain coupled to below T_c, until a specific grain temperature T_{CRIT} at which rapid decoupling occurs.

(c) The depression of T_{gr} below T_c may be substantial, being most for iron, least for graphite.

The results for iron are particularly intriguing. Its possible survival near a warm stellar surface (not likely if gaseous cooling were not operative) is a direct consequence of its high vapour pressure* for a given grain temperature, compared to say graphite. The more refractory a material, the greater its ability to survive in a low pressure environment at higher temperatures; but a concommitant result is that the maximum temperature depression possible ($T_c - T_{CRIT}$)

* as well as the trend in grain opacity with temperature.

FIGURE 5.8a

PRESSURE VERSUS GAS TEMPERATURE IN THE CONDENSATION ZONE

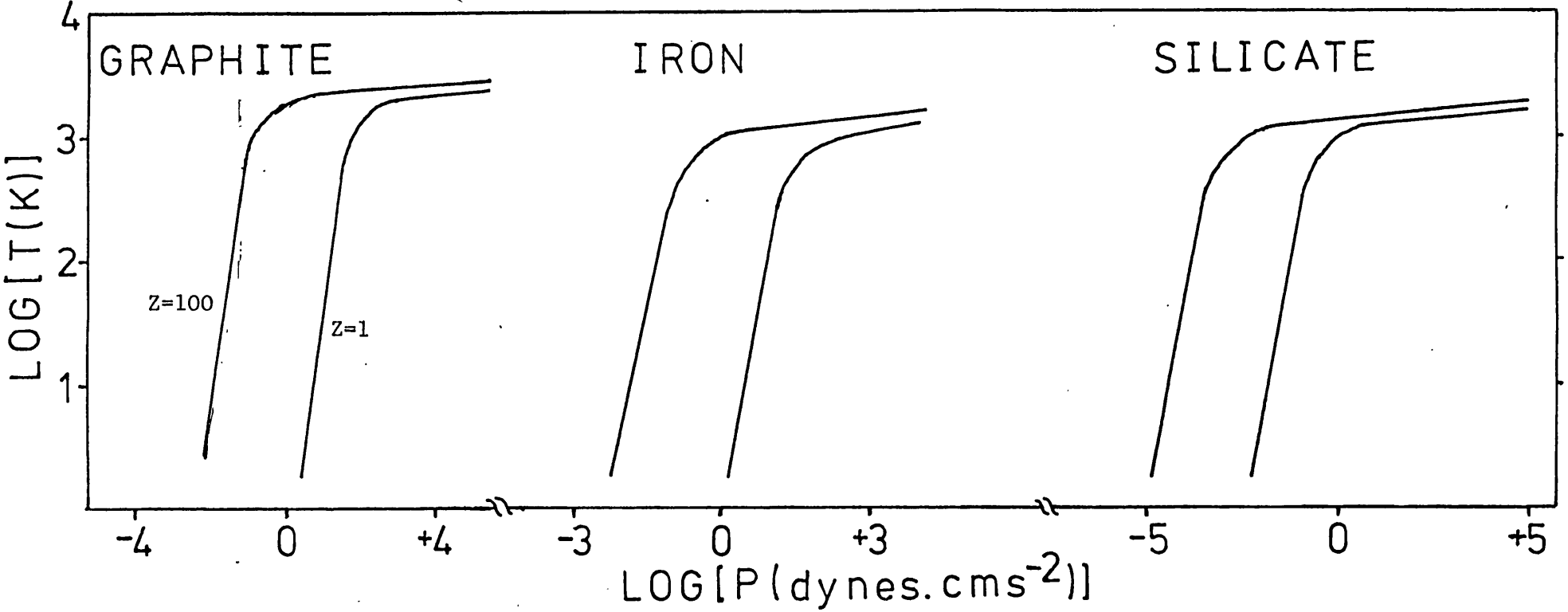

FIGURE 5.8b

GAS TEMPERATURE VERSUS GRAIN TEMPERATURE IN THE CONDENSATION ZONE

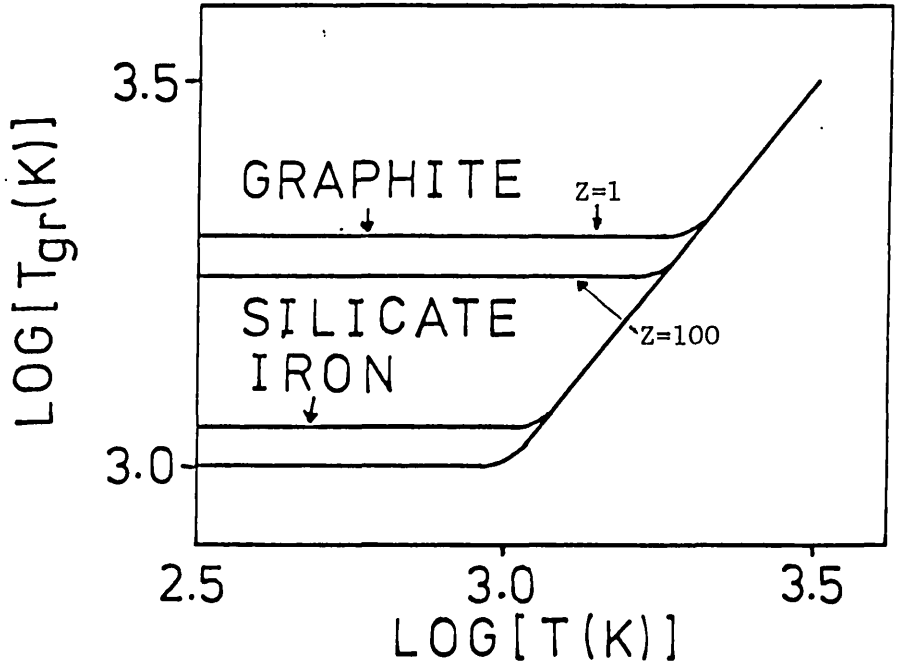

decreases. In consequence, although iron grains may form near stars, their dispersal to the interstellar medium is more problematic. Any attempt to escape the environment of the condensation zone will be found in practice to lead to the rapid acquisition of radiative temperatures, a massive increase in sublimation rate, and total evaporation of the grain. A possible solution to this problem will be discussed later.

The equation 5.56 may be written in the form

$$T - T^{\frac{1}{2}} \left(4\ T_{gr}^{2/\beta_T} - T_*^{2/\beta_T}\right) a^{QAC} \frac{10^{\frac{A}{T_{gr}} - B}}{W\ Z} - T_{gr} = 0$$

a quadratic in $T^{\frac{1}{2}}$ which gives

$$T^{\frac{1}{2}} = \frac{-b \pm \sqrt{b^2 - 4c}}{2} \qquad \ldots(5.57a)$$

$$b = -\left(4\ T_{gr}^{2/\beta_T} - T_*^{2/\beta_T}\right) \frac{10^{\frac{A}{T_{gr}} - B}}{W\ Z}\ a^{QAC} \qquad \ldots(5.57b)$$

$$c = -T_{gr} \qquad \ldots(5.57c)$$

Only the root $(-b+(b^2-4c)^{\frac{1}{2}})/2$ has physical relevance. If we let

$$T = \alpha_T\ T_{gr} \qquad \ldots(5.58)$$

and substitute into 5.57a we obtain

$$\frac{1 - \alpha_T}{\alpha_T^{\frac{1}{2}}} = \omega_T$$

$$\omega_T = 4\ \gamma_T^{-\frac{1}{2}}\ T_c^{2/\beta_T - \frac{1}{2}} \left\{1 - \gamma_T^{2/\beta_T}\right\} C_1\ 10^{\frac{A}{\gamma_T T_c}} \qquad \ldots(5.59)$$

where $T_c = \frac{T_*}{2}$ $\qquad$ $C_1 = \frac{a^{QAC}\ 10^{-B}}{W\ Z}$ $\qquad$ $\gamma_T = \frac{T_{gr}}{T_c}$

whence

$$\alpha_T^{\frac{1}{2}} = -\frac{\omega_T + \sqrt{\omega_T^2+4}}{2} \qquad \ldots(5.60)$$

Thus, given γ_T, a measure of the depression of grain temperature below radiative equilibrium values, the difference between grain and gas temperatures is readily evaluated.

Whilst this relation will be found useful when selecting viable mass loss models, it will also be found necessary to have a relatively efficient procedure for determining γ_T. The relation

$$\gamma_T = \frac{A}{T_c\left(\log\frac{\omega_T}{4} - \log\left(\frac{1-\gamma_T^{2/\beta_T}}{\gamma_T^{\frac{1}{2}}}\right) - \left(\frac{2}{\beta_T} - \frac{1}{2}\right)\log T_c - \log C_1\right)} \qquad \ldots(5.61)$$

is found to give rapid iterative solutions. The extension of this analysis to cover grains moving through any gaseous environment is now required.

5.13 Thermal Balance of Grains Outside Condensation Zone

At thermal velocities the analysis is similar to that for the condensation zone; interactions with hydrogen atoms alone gives an adequate description. The mean flux of hydrogen atoms is

$$\mathcal{F} = \frac{\pi a^2 \rho}{\xi m_H} V_c \qquad \ldots(5.62)$$

$$V_c = 4\left\{\frac{kT}{2\pi m_H}\right\}^{\frac{1}{2}} \qquad \ldots(5.63)$$

at drift velocities $V_d > V_c$, the mean atomic flux is

$$\mathcal{F} = \frac{\pi a^2 V_d \rho}{\mu m_H} \qquad \ldots(5.64)$$

where μ is the mean atomic weight. Combining 5.62 and 5.64 we take for the general flux

$$\mathcal{F} = \frac{\pi a^2 \rho}{\mu m_H} \left\{ V_d^2 + \frac{\mu^2 V_c^2}{\xi^2} \right\}^{\frac{1}{2}}$$

At subsonic grain velocities hydrogen atoms dominate the energy input, as we have noted. At supersonic velocities heavier atoms become significant, and to a reasonable approximation we may write for the rate of energy input due to collisions with atoms

$$\frac{dE}{dt} = \frac{\pi a^2 \rho}{2} \left(V_d^2 + \frac{V_c^2}{\mu} \right) \left(V_d^2 + \frac{V_c^2 \mu^2}{\xi^2} \right)^{\frac{1}{2}}$$

where we assume the entire kinetic energy is converted into phonons. Arguably, χ_1 may be smaller than ~1 for large V_d, but this would not significantly alter the results. Grain temperature is found to be primarily determined by the stellar radiation field in these circumstances. Energy losses through sputtering are taken to be relatively small. The total energy balance equation is then

$$\chi_1 \frac{\pi a^2 \rho}{2} \left(V_d^2 + \frac{V_c^2}{\mu} \right) \left(V_d^2 + \frac{V_c^2 \mu^2}{\xi^2} \right)^{\frac{1}{2}} + \frac{L_* \overline{Q}_a (T_*)}{4 \pi r^2} \pi a^2$$

$$- \frac{5}{4} \frac{\pi a^2 \rho \chi_2}{\mu m_H} \left(V_d^2 + \frac{V_c^2 \mu^2}{\xi^2} \right)^{\frac{1}{2}} k T_{gr} = 4 \pi a^2 \overline{Q}_{em}(T_{gr}) \sigma T_{gr}^4$$

or

$$4 \overline{Q}_{em}(T_{gr}) T_{gr}^4 + \frac{5}{4} \frac{\rho \chi_2}{\mu m_H \sigma} \left(V_d^2 + \frac{V_c^2 \mu^2}{\xi^2} \right)^{\frac{1}{2}} k T_{gr}$$

$$- \left\{ \frac{\rho}{2} \chi_1 \frac{(V_d^2 + V_c^2/\mu)(V_d^2 + V_c^2 \frac{\mu^2}{\xi^2})^{\frac{1}{2}}}{\sigma} + \overline{Q}_a(T_*) T_*^4 \left\{ \frac{r_*}{r} \right\}^2 \right\} = 0$$

This equation is analytically insoluble for $\overline{Q}_a \neq \overline{Q}_{em}$ (i.e. for small grains). For the particular case $\overline{Q}_a = \overline{Q}_{em}$ however (applicable for warm iron and graphite grains ($T_{gr} \gtrsim 300$ K) if $a \gtrsim 1$ μm, and silicate grains with $a \gtrsim 10$ μm, $T_{gr} \gtrsim 100$ K) the equation takes the form of a quartic in T_{gr}, and is therefore open to specific solution. The result is of interest, although in the present context unlikely to be relevant. We simply quote the result

$$T_{gr} = -\frac{\sqrt{y}}{2} + \frac{1}{2}\sqrt{\frac{2c_2}{\sqrt{y}} - y}$$

$$y = \sqrt[3]{\frac{c_2^2}{2} + \sqrt{\frac{c_2^4}{4} + \frac{64}{27}d^3}} - \sqrt[3]{\sqrt{\frac{c_2^4}{4} + \frac{64}{27}d^3} - \frac{c_2^2}{2}}$$

$$d = \frac{1}{4\overline{Q}_e}\left\{\frac{\rho}{2}\frac{(V_d^2 + V_c^2/\mu)}{\sigma}\left(V_d^2 + \frac{V_c^2\mu^2}{\xi^2}\right)^{\frac{1}{2}} + \overline{Q}_a(T_*)\,T_*^4\left(\frac{r_*}{r}\right)^2\right\}$$

$$c_2 = \frac{5}{4}\frac{\chi}{4\overline{Q}_e(T_{gr})}\frac{\rho}{\mu\, m_H\,\sigma}\left\{V_d^2 + \frac{V_c^2\mu^2}{\xi^2}\right\}k$$

More generally, we use the relation

$$T_{gr}^{2/\beta_T} = \left\{\frac{\rho}{2}\left\{V_d^2 + \frac{V_c^2}{\mu}\right\}\left\{V_d^2 + \frac{V_c^2\mu^2}{\xi^2}\right\}^{\frac{1}{2}} + T_*^{2/\beta_T}\sigma\left\{\frac{r_*}{r}\right\}^2 QAA(10^5\,a)^{QAC} - \frac{5}{4}\frac{\rho}{\mu\, m_H}\left\{V_d^2 + \frac{V_c^2\mu^2}{\xi^2}\right\}^{\frac{1}{2}} k\, T_{gr}\right\}\frac{1}{QAA(10^5 a)^{QAC}\,4\sigma} \quad \ldots(5.65)$$

where we have again let $\chi_{1,2} = 1$. This is not soluble iteratively, and is extremely unstable at higher stellar temperatures, leading to unrealistically large positive and negative values for T_{gr}^{2/β_T} for initial estimates of T_{gr} differing by no more than ~1% either way of the true value. This in itself is a useful characteristic, and is used to estimate T_{gr} with reasonable accuracy and efficiency.

5.14 Radius of Flow Inception

Evidence summarised by Deutsch (1960) appears to indicate that the outflowing envelope consists of a neutral hydrogen zone in which the metal ions are singly ionised. Absorption cores corresponding to these ions have similar displacements, excepting the H and K lines of Ca II, which appear in some cases to give discrepant expansion velocities. Possible merging with adjacent lines has been suggested by way of an explanation, although the possibility that the H and K lines originate from a different region of flow cannot be dismissed. The extent of the outflowing envelope as defined by the region leading to H and K absorption lines remains controversial. Deutsch appears uncertain whether other levels of ionisation are present in the envelope (besides Ca I, Ca II). We will find that this is probably unlikely.

If Ca is predominantly singly ionised and the mass flow originates close to the stellar surface, it seems clear that the H and K lines must also originate from a similar spatial zone. This interpretation is challenged by Bernat (1977) and Weymann (1962b), who argue for a flow developing at a substantial distance from the parent star. This position however is open to reservations.

The earliest suggestion that flow, and the H and K lines begin well above the stellar photosphere appears to be due to Weymann (1962b). There are several points of uncertainty in Weymann's analysis. First of these is the estimation of Ca ion column densities. For this purpose he uses a mean value of hydrogen column density (primarily determined using lines other than the H and K lines of calcium), and then derives an appropriate Ca column density using an assumed abundance. There are two aspects worth noting here: (a) the calcium

abundance relative to hydrogen used by Weymann may be quite inapplicable to the case in hand, and in fact is less by ~30% than modern estimates of the cosmic abundance (c.f. Allen 1973). This latter method also gives column densities at variance with those derived from the H and K lines, which are themselves however open to considerable uncertainty; (b) The derivation of the inner radius of flow using these calcium atom column densities relies upon an extremely approximate model, based upon radiative transfer procedures outlined by Jeffries and Pottasch (1959), to determine limits for the infrared triplet lines of Ca II. Taking both these aspects into account, it is clear that little accuracy can be realistically claimed for the resulting estimate of inner flow radius. This is unfortunate, since estimates of mass loss depend critically upon the combined estimates of hydrogen column density, and inner flow radius. It is however clear that, if Ca column densities are estimated from the H and K lines alone, the range of uncertainty is probably sufficient for us to adduce a flow origin at the stellar surface. The primary reason for this uncertainty lies in the fact that the H and K lines lie on the flat portion of the curve of growth, and small errors in the determination of the equivalent width lead to large uncertainties in the number of ions integrated along the line of sight. Deutsch (1956) and Weymann (1962b) for instance obtain values for this column density differing by a factor of 20 for α Her, mostly due to this effect. This is compounded in α Ori by Weymann's use of Wrubel's curve of growth analysis, appropriate for plane-parallel geometry.

The systematic error resulting from this has apparently been corrected by Bernat (1977) in a more recent analysis of the problem. No analytical details of the generalisation to spherically symmetric

geometry are however provided. The result of this correction appears to be to decrease Weymann's estimate of Ca column densities by a factor ~4. It is at least partly for this reason that Bernat finally concludes that the radius of flow inception is typically very large indeed, and in consequence arrives at mass loss rates considerably in excess of previous estimates.

Despite the considerable sophistication of Bernat's method, the weaknesses are fundamental, and demonstrated most clearly by a consideration of the discussion of α Ori.

The first estimate of flow inner radius, R_{FI}, is in Bernat and Lambert (1975), where Weymann's infrared triplet method is used to determine $R_{FI} \simeq 40\ R_*$. The Ca column depth as determined by Weymann is used (corrected, as mentioned, for the assumption of plane parallelism). There is otherwise no discussion of errors arising from H and K line curve of growth analysis. In a later paper (Bernat and Lambert 1976) this inner flow radius is increased yet further, to $R_{FI} \simeq 100\ R_*$, presumably to give agreement with K I spectral line measurements of the extended shell of α Ori. There is however no supporting evidence that such an increase is necessary, and the consequent model in any case gives a poor representation of the spatial variations of the K I line profile. There are therefore two steps to the final value of R_{FI}, both of which are open to alternative analysis. It is important to keep this in mind, since certain mass loss models involving radiative acceleration of grains lead to physical conclusions at variance with the assumption of Bernat (1977), Bernat and Lambert (1975, 1976), and Weymann (1962b). It seems likely that models invoking Ly_α pressure, and acceleration due to molecular opacity, will lead to a similar conflict.

If the hypothesis of large R_{FI} should prove to be justified however, it seems likely that the only reasonable explanation would be to suppose a massive chromosphere (for which the H and K lines would be in emission). Mass flow from the edge of the chromosphere could proceed through the grain acceleration mechanism, even possibly for a large grain-gas temperature difference (i.e. $\chi_2/\chi_1 << 1$), and the lower gravitational potential may increase the feasibility of the mass loss process. These are attractive features, and future discussions may well fruitfully take these into account. Such large chromospheres would almost certainly lead to substantial Hα emission however, for which there is little evidence (Weymann 1962a). Taking this, and the dubious necessity of requiring a large R_{FI} at all into account, we will for the present work adopt an internal radius of flow near the stellar surface.

5.15 Inception of the Ca II Zone

The presence of an inner zone of the envelope for which calcium was in the doubly ionised state might superficially be used to explain a Ca II zone detached from the central star. In fact, we will find this to be rather implausible for Ca II and other metal ions for the following reasons.

The determination of ionic concentration throughout an adiabatically expanding envelope is a problem requiring radiative transfer procedures. The results of such procedures are of course critically open to the large uncertainties in our present understanding of envelope conditions. We shall use a simple procedure and model to gain a rough idea of the sizes of zone appropriate for various metal ions.

Consider a flow with uniform velocity V extending to the stellar surface. Subscript * will as usual indicate conditions pertaining to the stellar surface. For a hydrogenic atom ionised W_A times the recombination coefficient for species i is approximately

$$\alpha_i \simeq 3 \times 10^{-10} W_{Ai}^2 T^{3/4} \qquad ...(5.66)$$

For adiabatic expansion

$$T = T_{*g} \left\{\frac{\rho_*}{\rho}\right\}^{\gamma-1} = T_{*g} \left\{\frac{r_*}{r}\right\}^{2(\gamma-1)}$$

where T_{*g} is gas temperature at $r = r_*$.

The total number of recombinations for a volume of radius r_c (assuming spherical symmetry) is then

$$\eta_i = \int_{r=r_*}^{r_e} 4 \pi r^2 \, dr \, n^2{}_i \, \alpha_i \, \phi_{ei} \qquad ...(5.67)$$

n_i is the number density of the appropriate ion, ϕ_{ei} the number of electrons per ion.

$$n_i = \frac{X_i \rho_*}{A_{T_i} m_H} \left\{\frac{r_*}{r}\right\}^2 \qquad ...(5.68)$$

X_i is the mass abundance of the ion, which we take equal to the cosmic abundance of the atom (i.e. within the zone corresponding to that particular ion, we take fractional ionisation to be large). Collecting the various expressions we have

$$\eta_i = 4 \pi W_{Ai}^2 \left\{\frac{X \rho_* r_*^2}{A_i m_H}\right\}^2 \frac{3\times10^{-10}}{T_{*g}^{0.75}} \frac{\phi_{ei}}{r_*^{1.5(\gamma-1)}} \int_{r_*}^{r_e} r^{1.5\gamma-3.5} \, dr$$

where the lower bound adopted for the integral ($r=r_*$) is reasonably appropriate, since no species with significant abundance seems likely to be doubly ionised away from the stellar surface.

A lower limit to the radius r_e of this zone is then obtained by equating η_i (summed over all ions) to the total number of ionising photons emitted between frequencies $\chi_{j-1}{}^I/h$ and $\chi_j{}^I/h$, where h is the Planck constant, and j is the state of ionisation of the ion with largest potential $\chi_{j-1}{}^I$. The number of photons is given by

$$N_{\lambda_1-\lambda_2} \simeq \frac{N_{o-\infty}}{2.404} \left\{\kappa_1{}^2 e^{-\kappa_1} - \kappa_2{}^2 e^{-\kappa_2}\right\} 4\pi r_*{}^2$$

$$N_{o-\infty} = 1.5204 \times 10^{11} T^3 \text{ photons.cm}^{-2}.\text{s}^{-1}.\text{K}^3.$$

Because internal zones have a higher photon flux (corresponding to radiation with $\nu > \chi_j{}^I/h$), the flux of photons with $\chi_j{}^I/h > \nu > \chi_j{}^I/h$ will be rather larger than otherwise in the zone under consideration, and the use of the value $N_{\lambda_1-\lambda_2}$ as determined above leads to a lower limit $\ln r_e/r_*$. Because of the steepness of the Planck curve in the Wien limit however, the modifications due to this are small.

For equilibrium we have

$$\sum_i 4\pi \phi_{ei} \left\{\frac{X_i \, dM/dt}{A_{Ti} \, m_H \, 4\pi V}\right\}^2 \frac{3\times10^{-10}}{T_{*g}{}^{0.75}} \frac{1}{r_*} \ln \frac{r_e}{r_*} \cdot W_{Ai}{}^2$$

$$= \frac{1.5204 \times 10^{11} T_*{}^3}{2.404} (\kappa_2{}^2 e^{-\kappa_2} - \kappa_1{}^2 e^{-\kappa_1}) 4\pi r_*{}^2$$

where we have taken $\gamma = 5/3$, and $\kappa = 1.43883/\lambda T$, whence

$$\ln \frac{r_e}{r_*} = \frac{9.3 \times 10^{-26} T_*{}^3 T_{*g}{}^{0.75} (\kappa_2{}^2 e^{-\kappa_2} - \kappa_1{}^2 e^{-\kappa_1}) r_*{}^3 V^2}{(dM/dt)^2 \sum_i \frac{\phi_{ei} X_i{}^2 W_{Ai}{}^2}{A_{Ti}{}^2}} \quad \ldots(5.69)$$

where we define

$$\phi_{ei} = \sum_K \frac{X_K}{X_i} \cdot W_{AK} \cdot \frac{A_{Ti}}{A_{TK}} \quad \ldots(5.70)$$

and the summation is over all ions with ionisation potentials less than that for ion i, for which cosmic abundances are significant.

TABLE 5.9

IONISATION ZONE RADII

ION	$\ln r_e/r_*$	ION	$\ln r_e/r_*$
Ca III	9.48×10^{-9}	Mg II	7.14
C II	7.37×10^{-8}	Mn II	3.57×10^{2}
S II	2.65×10^{-5}	Cr II	3.83×10^{3}
Si II	1.15×10^{-1}	Ca II	4.68×10^{4}
Fe II	0.66	Al II	2.02×10^{5}
		Na II	1.87×10^{7}

In table 5.9 we give $\ln r_e/r_*$ derived from the above expressions, using $R_* = 100\ R_\odot$, $dM/dt = 5 \times 10^{-8}\ M_\odot.yr^{-1}$, values characteristic of red giants. We have also used $T_{*g} = T_*$. More generally, since

$$\ln \frac{r_e}{r_*} \propto \frac{r_*^3}{(dM/dt)^2} \propto r_*^{-1} \qquad (T_* \text{ constant})$$

it is clear that supergiants will lead to qualitatively similar results. We have ignored $\kappa_1^2\ e^{-\kappa_1}$, since this will lead to increases in $\ln r_e/r_*$ by a factor ~2 or 3 at most, and for most cases much less. We note the following points of particular interest:

(i) The metal ions are all singly ionised. This couples with similar conclusions from the observations.

(ii) Ca exists in a singly ionised state throughout the envelope. Ca III is strongly confined to the photospheric region.

(iii) The radius of the ionisation zone is strongly related to the ionisation potential of the ion. This is a consequence of the rapidity with which the U.V. blackbody curve decreases with decreasing wavelength.

(iv) The size of the region of ionisation is, for the same reasons given in (iii), extremely sensitive to the temperature of the radiation field. To achieve a Ca III zone for instance, which is characteristically ~10 r_* in radius, would require a particularly delicate contrivance of mass loss rate and U.V. temperature. It is the implausibility of this which must be regarded as a prime argument against the uniform application of such an hypothesis.

Several qualifications are worth making. The first is that any appreciable initial acceleration will lead to such rapid gaseous cooling near the star, that an initial gas temperature very much less than T_* may be appropriate. This will indeed be found to be the case for expansion arising from radiative pressure upon grains. The consequence of this is to reduce the radii of zones containing the ions. For instance, if $T_{*g} = 10^{-3}\ T_*$, values of $\ln r_e/r_*$ are reduced by a factor ~178. We also note that a radius for the base of the flow $>> r_*$ will lead to an increase in $\ln r_e/r_*$. It seems rather more plausible however that the flow near the stellar surface will be rather slower than at larger radial distances, and gas densities correspondingly higher. This will lead to further contraction of the zones of ionisation. "Dynamical ionisation" is also important: at large distances from the star, the recombination rate is so low that the zones of ionisation for such ions as Ca II extend effectively to infinity. Finally, the uncertainties in relevant U.V. stellar fluxes should be noted, although as for other cases, it seems unlikely that the qualitative sense of the results will be unduly affected.

5.16 Spectral Line Profiles

To evaluate line profiles for the calculated mass outflow, the following procedure is adopted. For simplicity, we assume ground state transitions, low scattering and that the relevant atomic species is almost entirely in the ground state. This latter will be true for most if not all the singly ionised metals in the prevalent temperature regimes; ground state partition functions will be closely similar to the ground state statistical weights (Bolton 1970). For purposes of argument we assume a rest wavelength $\lambda_{oo}=0.39$ μm; the absorption with respect to $\Delta\lambda/\lambda$ will be almost independent of this assumption.

The total optical depth of an element of column, i, of 1 cm^2 cross-sectional area and length dr_i is then

$$d\tau_{\nu i} = \left\{\frac{N_o}{N}\right\}_i \frac{X\,\rho_i\,dr_i}{A_T\,m_H}\;\phi_i(\nu)$$

where N = total number of absorbing atoms

N_o = total number of ground state absorbing atoms

$\phi_i(\nu_R)$ = Voigt function in frame co-moving with element i

where $$\phi(\nu_R) = \frac{1}{\pi^{\frac{1}{2}}\,\Delta\nu_D}\;H(a,b)$$

$$a = \frac{\Delta\nu_L}{2\Delta\nu_D}$$

$$b = \frac{\nu_R-\nu_{OO}}{\Delta\nu_D}$$

and $$H(a,b) = \frac{a}{\pi}\int_{-\infty}^{+\infty}\frac{\exp(-y^2)\,dy}{(b-y)^2+a^2}$$

$\Delta\nu_L$ is the natural line width $\Delta\nu_L = \gamma_{CL}/2\pi$, and γ_{CL} is the classical damping constant. Numerically, $\gamma_{CL} = 0.2223\,\lambda_{OO}^{-2}$ (Allen 1973) whence

$$\Delta\nu_L = 3.93 \times 10^{-23}\ \nu_{00}^{\ 2}\ \text{Hz}$$

ν_{00} is the rest frequency in the frame co-moving with the fluid, and

$$\Delta\nu_D = \frac{2\nu_{00}}{c}\left[\ln 2\left(\frac{2K\ T_i}{A_T\ m_H} + V^2_{TURBi}\right)\right]^{\frac{1}{2}} \qquad \ldots(5.71)$$

where V_{TURBi}, included here for generality, is the most probable turbulent velocity. We will set $V_{TURBi} = 0$. To a good approximation

$$\phi(\nu) = \phi(\nu_R = \nu(1 - V_r/c))$$

In the actual numerical summation, the values used for T_i and ρ_i will be those corresponding to radial distance $r_i + \Delta r_i$, for an element i between r_i, $r_i + \Delta r_i$. In general, Δr_i will be such that the velocity dispersion ΔV_i across the element, due to radial acceleration, will be less than 2.5% of the radial velocity at r_i. Δr_i may however approach 10% of r_i, and an appropriate density and temperature average is required to determine $d\tau_i$. To this end, we note that for a general function $f(r) = r^{-\alpha}$, we may write for the average value

$$\bar{f}(r_1) = \int_{r_1-\Delta r}^{r_1} r^{-\alpha}\, dr \Big/ \int_{r_1-\Delta r}^{r_1} dr$$

$$= \frac{-1}{1-\alpha}\left\{(r_1-\Delta r)^{1-\alpha} - r_1^{\,1-\alpha}\right\}\Big/\Delta r \qquad (\alpha > 1)$$

whence since $T \propto r^{-2(\gamma-1)} = r^{-4/3}$, and $\rho \propto r^{-2}$

$$\bar{T}_{gas}(r_1) = T_{gas}(r_1)\left\{\frac{3}{\Delta r}\left\{(r_1-\Delta r) - \frac{(r_1-\Delta r)^{4/3}}{r_1^{\,1/3}}\right\}\right\}^{-1}$$

and $$\bar{\rho}(r_1) = \rho(r_1)\,\frac{r_1}{r_1-\Delta r}$$

For the emergent stellar flux in the vicinity of the line we then have

$$F_\nu = F_{*\nu}\, e^{-\tau_\nu} \simeq F_{*\nu}(1 - \tau_\nu),\ \tau_\nu << 1$$

where $F_{*\nu}$ is the stellar flux at frequency ν before absorption. To illustrate the relevant line shapes, the latter function has been used with $F_{*\nu} = 2$, and τ_ν arbitrarily normalised to 0.5.

5.17 Selection of Mass Loss Models

For a reasonable series of input parameters for stellar temperature, radius, mass loss rates, etc., there is only a small probability that the model will be viable. This result is primarily a consequence of the restrictions upon physical conditions in the condensation zone. In this respect, reservations must be expressed regarding the uniqueness of Kwok's solutions. In Kwok's analysis it is arbitrarily assumed that sonic point temperature is the same as the stellar effective temperature. Extrapolating the gaseous flow from the sonic point, back to the condensation zone radius, it is clear that adiabatic compression will lead to condensation zone temperatures many times those of the stellar effective temperature, for only moderate gaseous pressures. Unless the grain/gas energy transfer factors $\chi_{1,2}$ are exceptionally small, the grains would then sublimate before achieving sonic velocities. His adoption also of a drag parameter $\alpha = 0.75$ however (see section 5.4) suggests the assumption of substantial inelasticity in grain/atom collisions, and therefore of reasonably large values $\chi_{1,2}$. Kwok also discusses condensation zone radii in terms of isothermal atmospheres with

temperatures the same as the stellar effective temperatures, and opacities consistent with both observation and other model atmospheres. The analysis is therefore internally inconsistent. It is also unfortunate that the method of determining condensation zone radius apparently submitted for publication by Gehrz and Woolf, remains yet to be published. This latter paper is reported to show that the radiation field, and not the gas, is the primary determinant of grain temperature. It is not clear that this is a necessary conclusion of the present analysis.

The range of models selected involves permutations of the following variables.

(a) Stellar Models

Representative models for red supergiants, giants, long period variables (Miras), and red dwarfs were used. The latter category was included at least partly because of the observation of a possible 11 μm excess in the M2V star Lal1 21185 (Gehrz and Woolf 1971) which would be quite unexpected if the relation $dM/dt \propto L_*$ were extrapolated down from giants and supergiants. Unfortunately, M dwarfs are typically faint, and this appears to have restricted observations of other dwarfs to the nearer infrared.

The masses, temperatures and luminosities are representative values based on the compilation of data by Allen (1973). The mass loss rates straddle the range of values considered appropriate in earlier work (c.f. Gehrz and Woolf 1971, Sanner 1976, Weymann 1962a) although all models were re-run for mass loss rates 100 times larger, to incorporate the values considered appropriate by Bernat (1977). For stellar spectral classes with no previously quoted mass loss rates, the range of values was deduced by extrapolation from stellar models

for which mass loss rates were available, assuming a proportionality to stellar luminosity. The models are itemised in table 5.10.

TABLE 5.10

STELLAR MODELS

STELLAR TYPE	MASS ($M_\odot$)	LUMINOSITY ($L_\odot$)	TEMPERATURE (K)	dM/dt* ($M_\odot.yr^{-1}$)
SUPERGIANT	25	10^5	3000	$5x10^{-7}$, 10^{-7}, 10^{-6}
"	"	10^6	3000	$5x10^{-6}$, 10^{-6}, 10^{-5}
"	"	10^5	3500	$5x10^{-7}$, 10^{-7}, 10^{-6}
"	"	10^6	3500	$5x10^{-6}$, 10^{-6}, 10^{-5}
GIANT	10	$7x10^3$	2000	$5x10^{-8}$, 10^{-7}, $5x10^{-7}$
"	"	$4x10^3$	2500	$5x10^{-8}$, 10^{-8}, 10^{-7}, $5x10^{-7}$
"	"	$2x10^3$	3000	$5x10^{-8}$, 10^{-8}, 10^{-7}, $5x10^{-7}$
"	"	10^3	3500	$5x10^{-9}$, 10^{-9}, 10^{-8}
MIRA	1	10^4	2000	10^{-6}, $5x10^{-6}$, 10^{-5}
"	"	"	2500	"
"	"	"	3000	"
DWARF	0.3	10^{-2}	2500	10^{-14}, $5x10^{-14}$, 10^{-13}
"	"	"	3000	"

* Mass Loss Rates 10^2 larger were also investigated

(b) Two values of the abundance parameter X were used, one corresponding to the normal cosmic abundance, X_{cos}, and a comparative value $X_{cos}/50$.

(c) The grain materials iron, graphite and olivine were investigated.

(d) Two values of supersaturation ratio, Z = 8 and Z = 16 were used.

(e) Fifteen values of sonic point grain radius were used ranging from 10^{-7} cms, increasing by increments of $10^{0.2}$.

(f) Five values of condensation zone gas temperature were introduced, decreasing from 0.9 T_c in increments of 0.1 T_c, and 32 values of grain temperature ranging from 0.975 T_c downwards in increments of 0.025 T_c. Grain and gas temperature are of course coupled. Two differing procedures, outlined in section 5.12, must however be used to cover a reasonable range of gas and grain temperatures.

The variables defined in (b) to (f) represent a selection thought to be reasonably comprehensive on the basis of modelling experience with a greater range of parameter values. Experience, for instance, with a supersaturation ratio Z = 1 indicated that the range of stellar models having supersonic mass flows would not be appreciably increased, and indeed no appropriate models with this value of Z were obtained; grain sublimation becoming critical when gaseous expansion leads to grain/gas decoupling.

The modelling procedure itself involved three stages. In the first, model testing program, models were assessed as to whether $f_o \leq 1$, $C_{sc} \cdot 2 \times 10^{-3} \leq V_{rc} \leq C_{sc}$. The former requirement is self evident, the lower limit of the latter a consequence of modelling experience. The equations used to determine f_o have been noted earlier. Successful models were then assessed in a trial modelling procedure, with numerical integration to the sonic point. For a successful model, input sonic point fractional condensation, and grain radius has to closely equal values determined from the integration. Input sonic point grain radius was varied iteratively to optimise models, and input values of condensation-zone temperature, supersaturation ratio were also varied depending upon feedback from the results. Successful models were then integrated to ~100 r_* and plotted, with microfilm output.

The results may be summarised as follows. Extensive trials have shown that subsonic to supersonic flow would be impossible to achieve in red supergiants, giants and dwarfs, if gaseous drag by grains were the primary mass loss mode. There are two primary reasons for this. For graphite and silicate grains, the gaseous drag is inadequate to drive flows to supersonic velocities; for iron, a further problem arises in that the slightest decoupling from the gas leads to rapid increases in grain temperature, and to sublimation. This last problem also occurred for certain models involving graphite and silicate grains, although overall its effect is less important for these latter materials.

Certain Mira models were however successful. Details are given in table 5.11 and plots are presented in figure 5.9. All models are for silicate grains.

TABLE 5.11

SUPERSONIC MASS FLOW MODELS

Model	T_* (K)	L_* ($L_\odot$)	M_* ($M_\odot$)	dM/dt ($M_\odot.yr^{-1}$)	Z	$(T/T_{gr})_c$	a_o (μm)	$2(\frac{V_{\phi I}}{V_{escI}})^2$	Xcos/X
1	$2.5x10^3$	10^4	1.0	$5.0x10^{-6}$	13	0.915	0.334	0.0	1.0
2	$2.5x10^3$	10^4	1.0	$5.0x10^{-6}$	16	0.912	0.377	0.0	1.0
3	$2.5x10^3$	10^4	1.0	$1.0x10^{-5}$	16	0.911	0.208	0.0	1.0
4	$2.5x10^3$	10^4	1.0	$1.0x10^{-5}$	20	0.910	0.325	0.0	1.0
5	$2.5x10^3$	10^4	1.0	$5.0x10^{-6}$	16	0.915	0.592	0.2	1.0
6	$2.5x10^3$	10^4	1.0	$5.0x10^{-6}$	13	0.915	0.455	0.2	1.0
7	$2.5x10^3$	10^4	1.0	$5.0x10^{-6}$	16	0.915	0.535	0.1	1.0

Velocity of outflow is uniformly less than 40 $km.s^{-1}$, a primary consequence of grain sputtering which in turn restricts grain drift velocity. Line profiles possess a greater variability, but are most

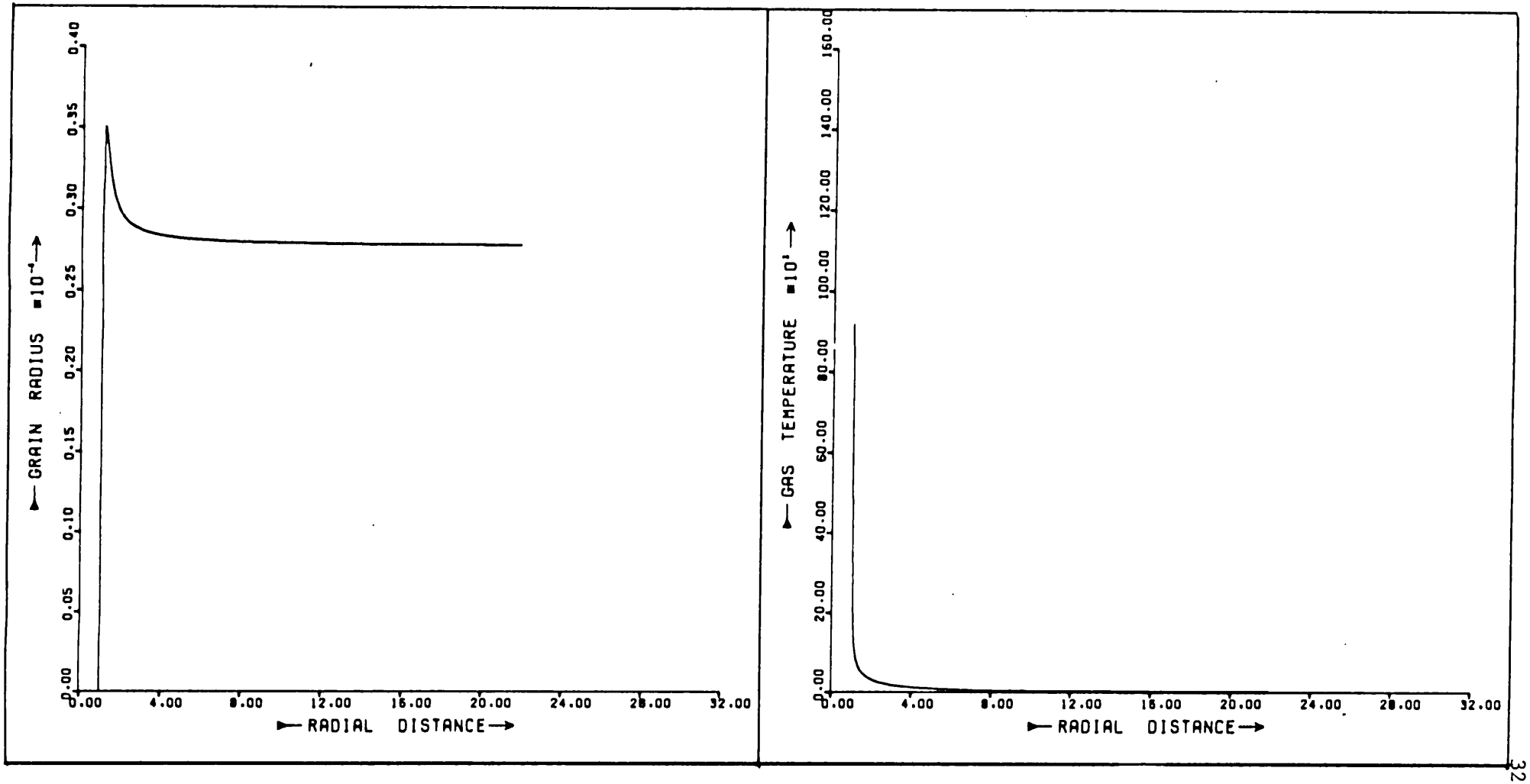

FIGURE 5.9a

MIRA SUPERSONIC MASS FLOW MODEL 1

FIGURE 5.9b MIRA SUPERSONIC MASS FLOW MODEL 1

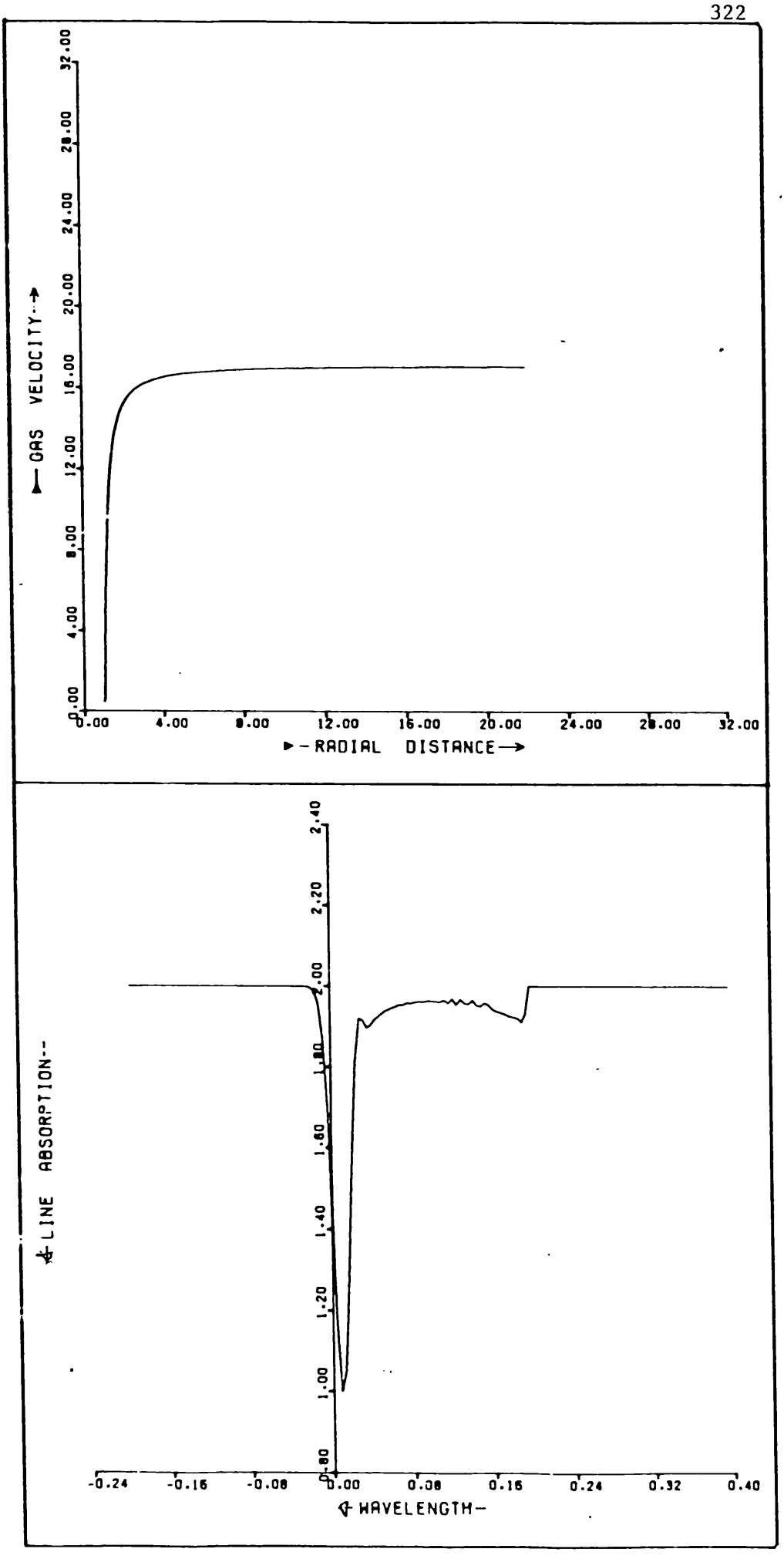

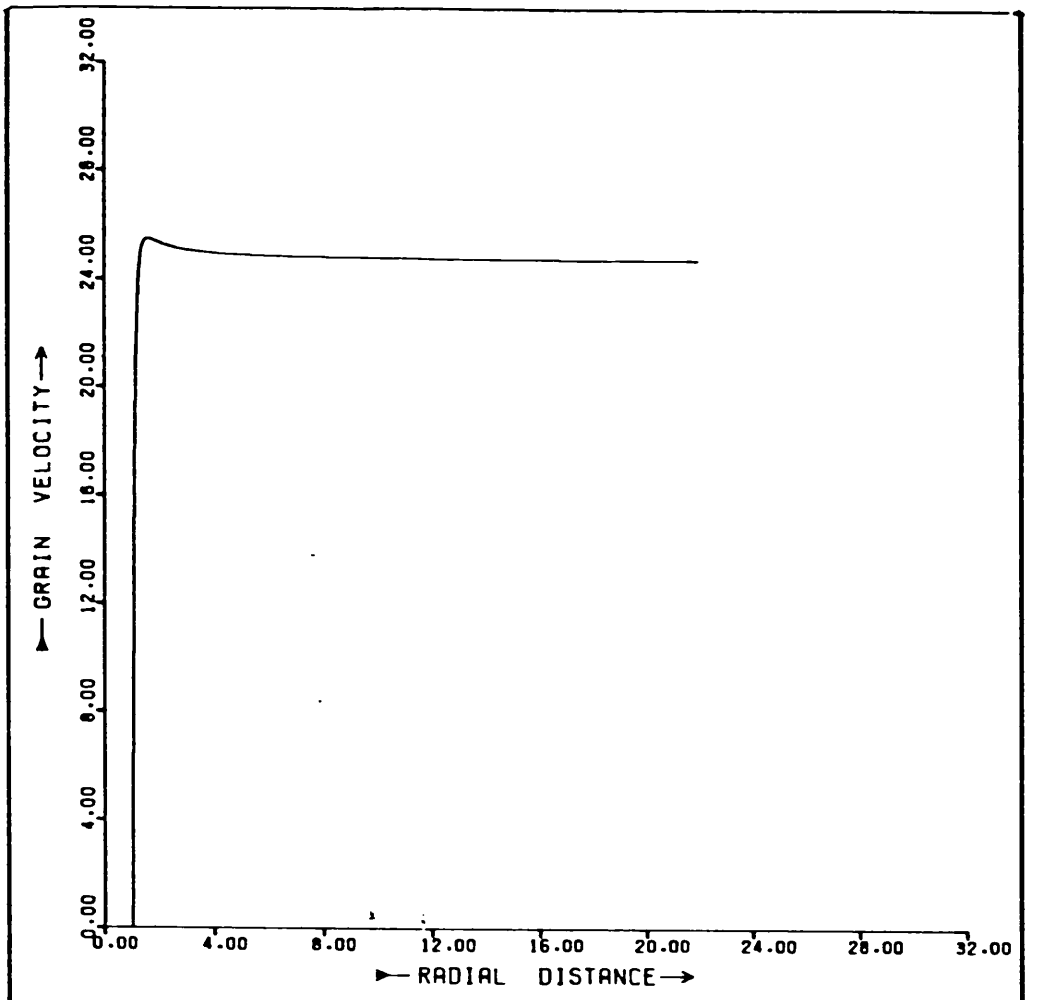
GRAIN VELOCITY
0.00
4.00
8.00
12.00
16.00
20.00
24.00
28.00
32.00
0.00
4.00
8.00
12.00
16.00
20.00
24.00
28.00
32.00
RADIAL DISTANCE

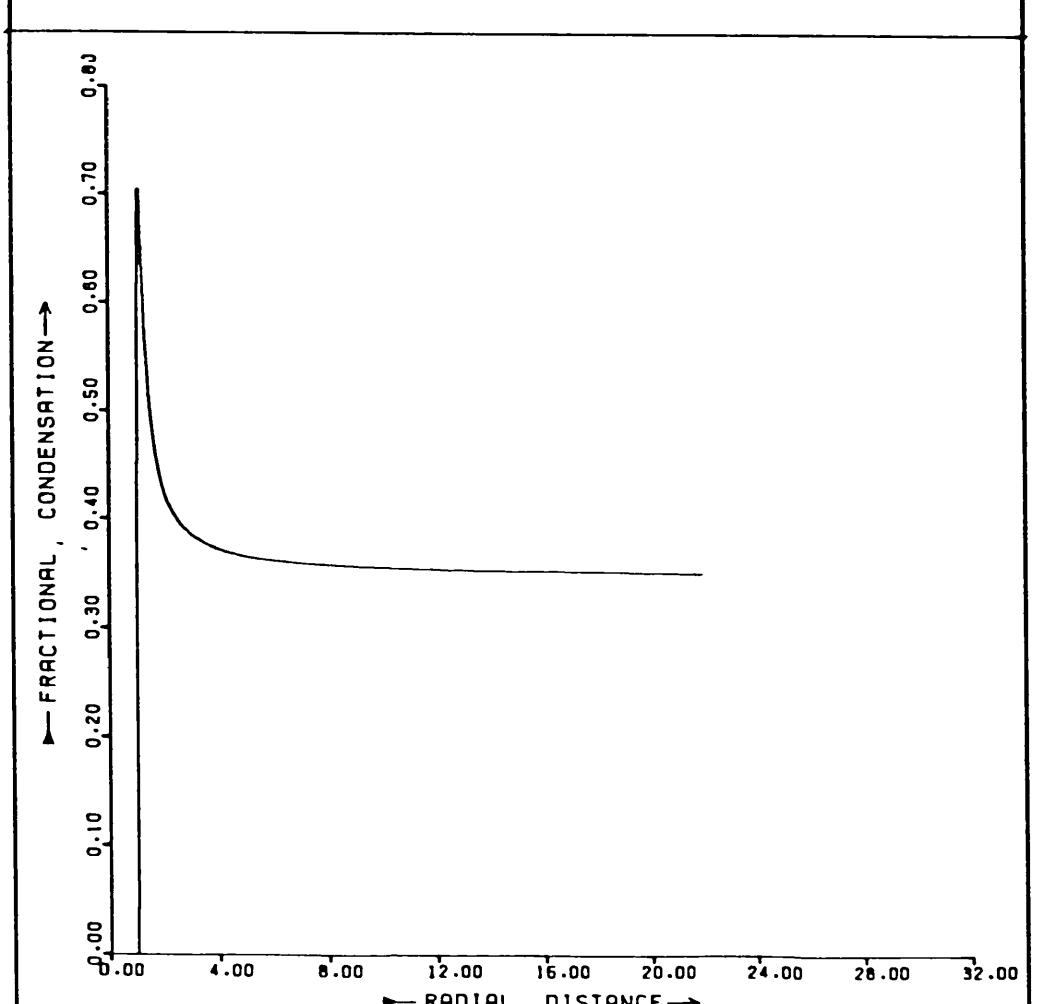
FRACTIONAL CONDENSATION
0.00
0.10
0.20
0.30
0.40
0.50
0.60
0.70
0.80
0.00
4.00
8.00
12.00
16.00
20.00
24.00
28.00
32.00
RADIAL DISTANCE

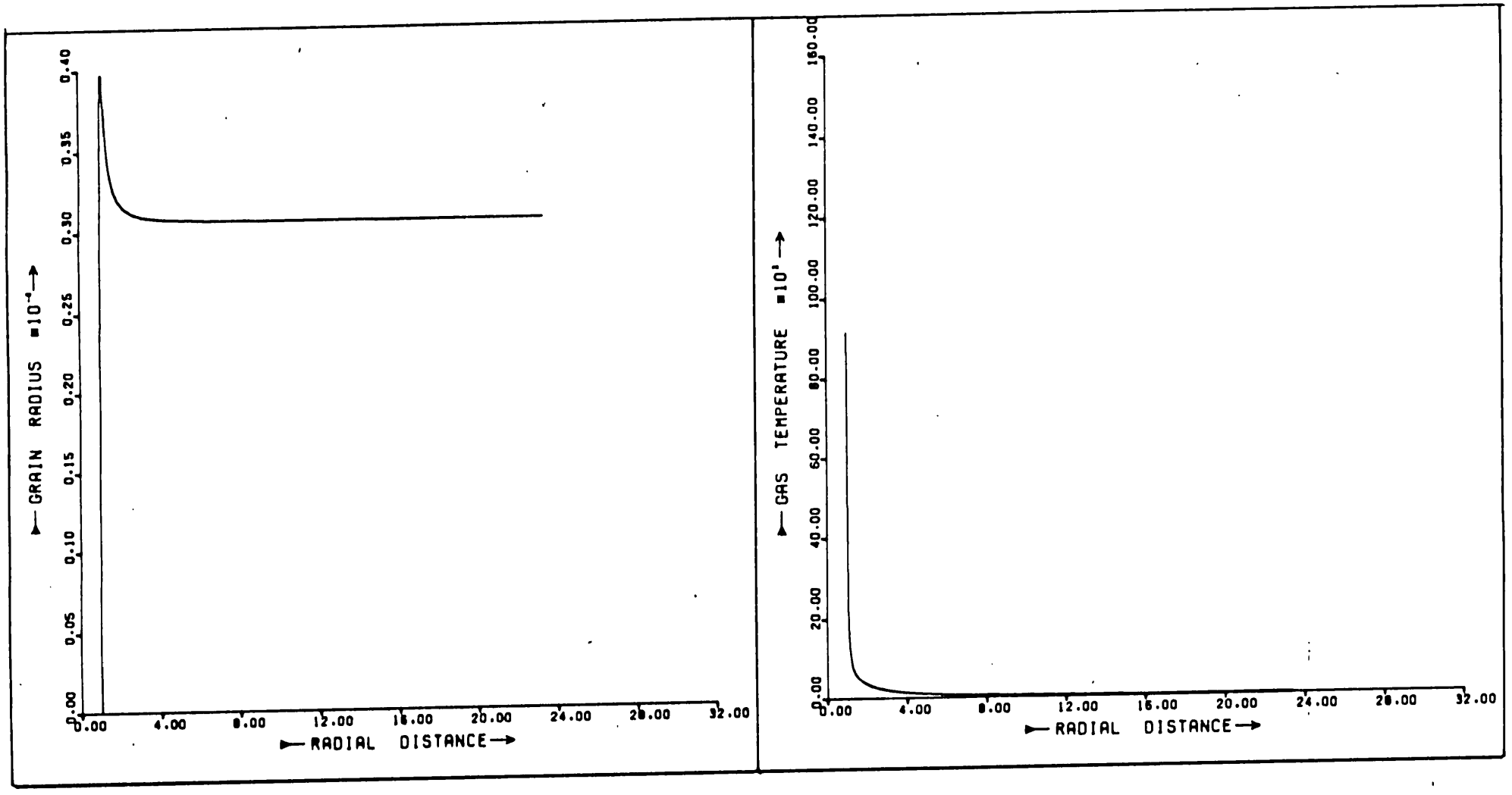

FIGURE 5.9d MIRA SUPERSONIC MASS FLOW MODEL 2

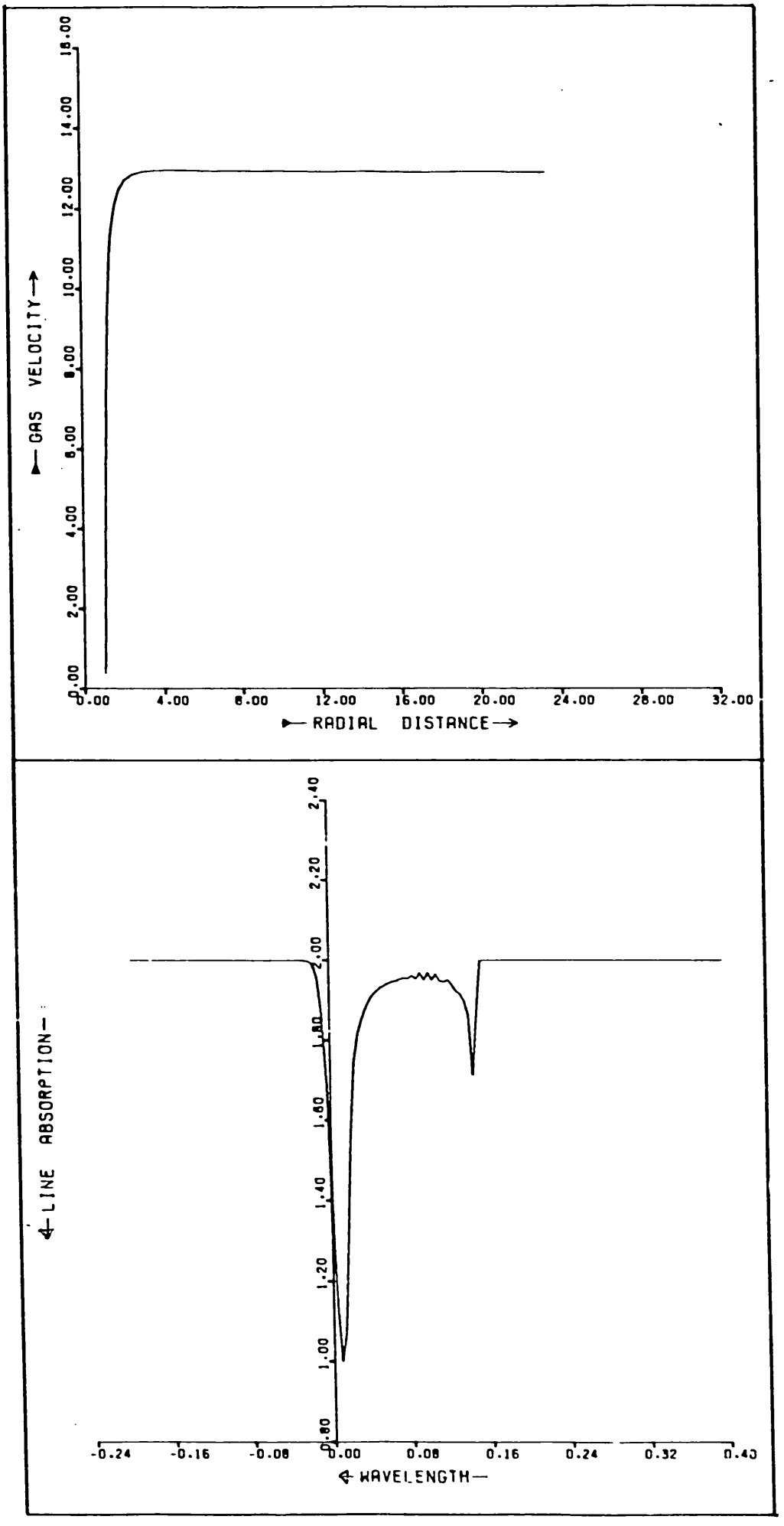
GAS VELOCITY
0.00
2.00
4.00
6.00
8.00
10.00
12.00
14.00
16.00
0.00
4.00
8.00
12.00
16.00
20.00
24.00
28.00
32.00
RADIAL DISTANCE
LINE ABSORPTION
0.80
1.00
1.20
1.40
1.60
1.80
2.00
2.20
2.40
-0.24
-0.16
-0.08
0.00
0.08
0.16
0.24
0.32
0.40
WAVELENGTH

FIGURE 5.9f MIRA SUPERSONIC MASS FLOW MODEL 2

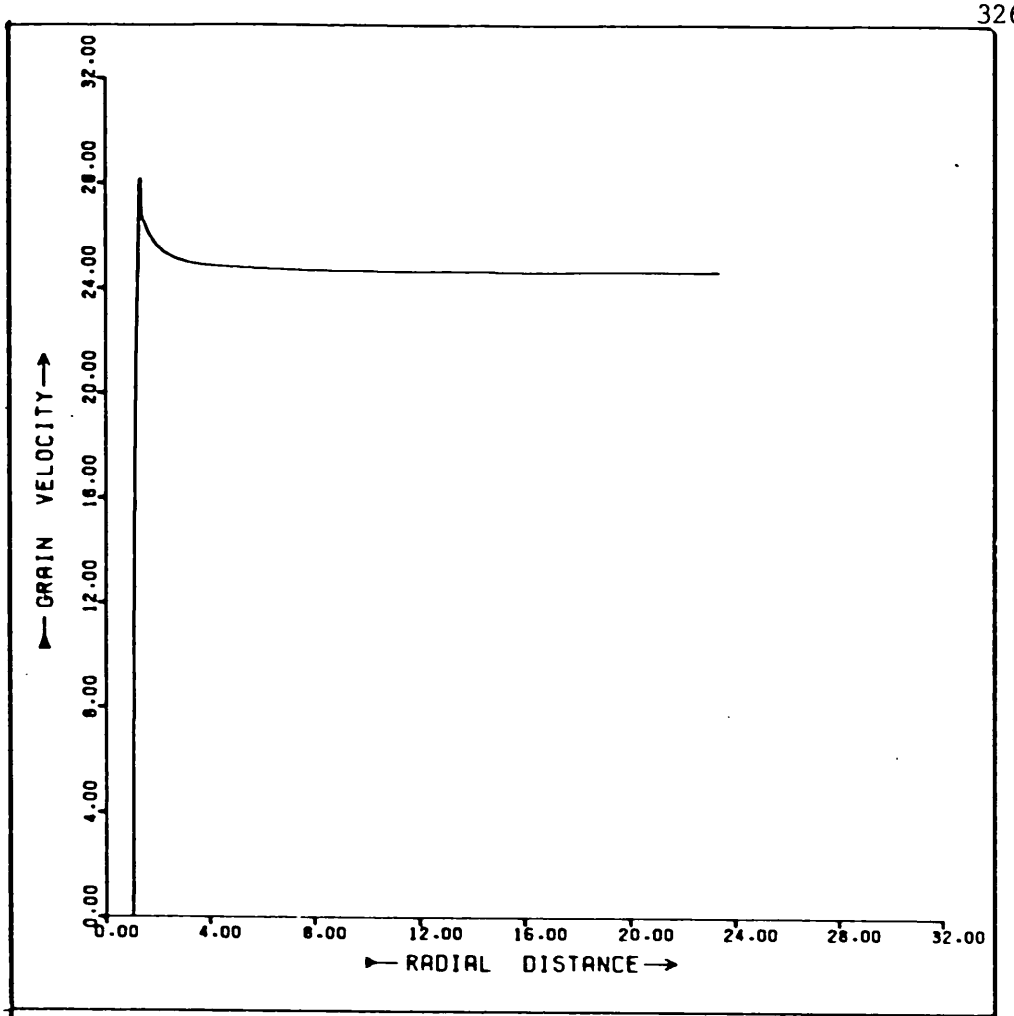

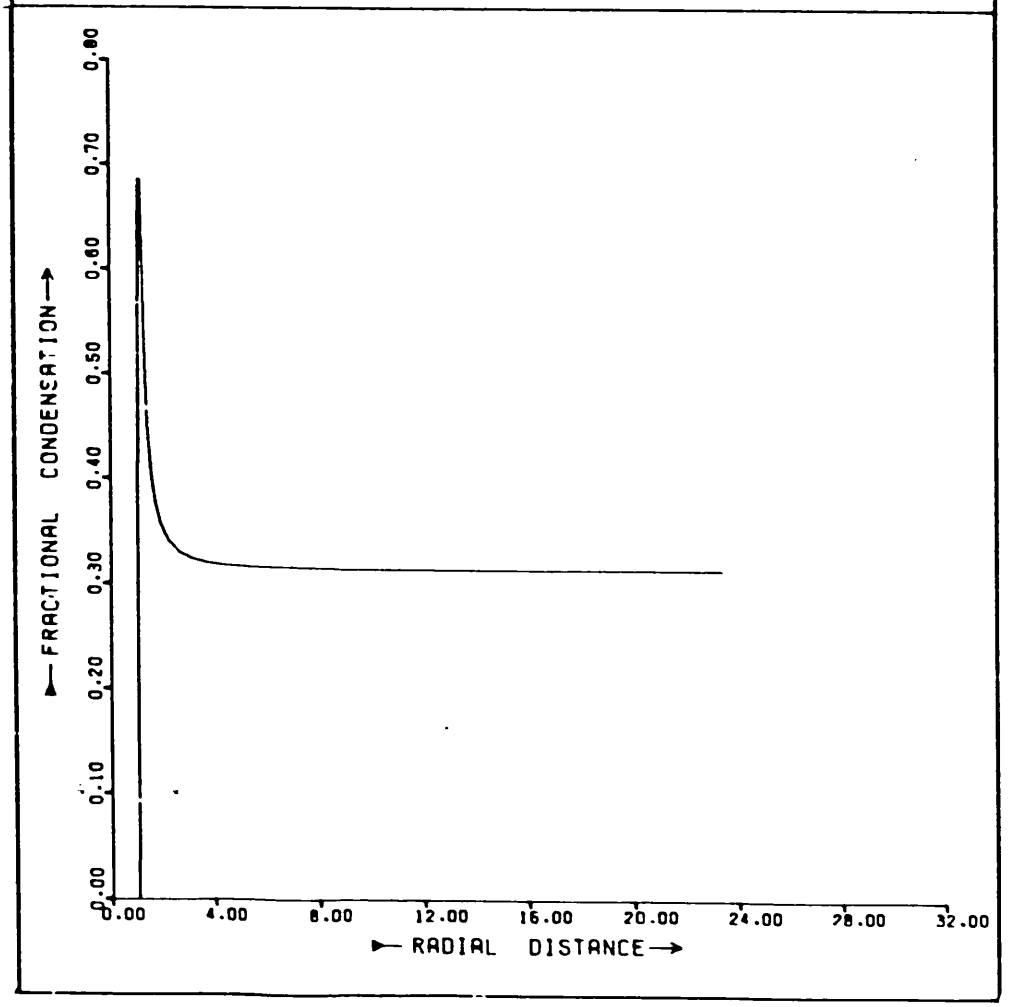

FIGURE 5.9g MIRA SUPERSONIC MASS FLOW MODEL 3

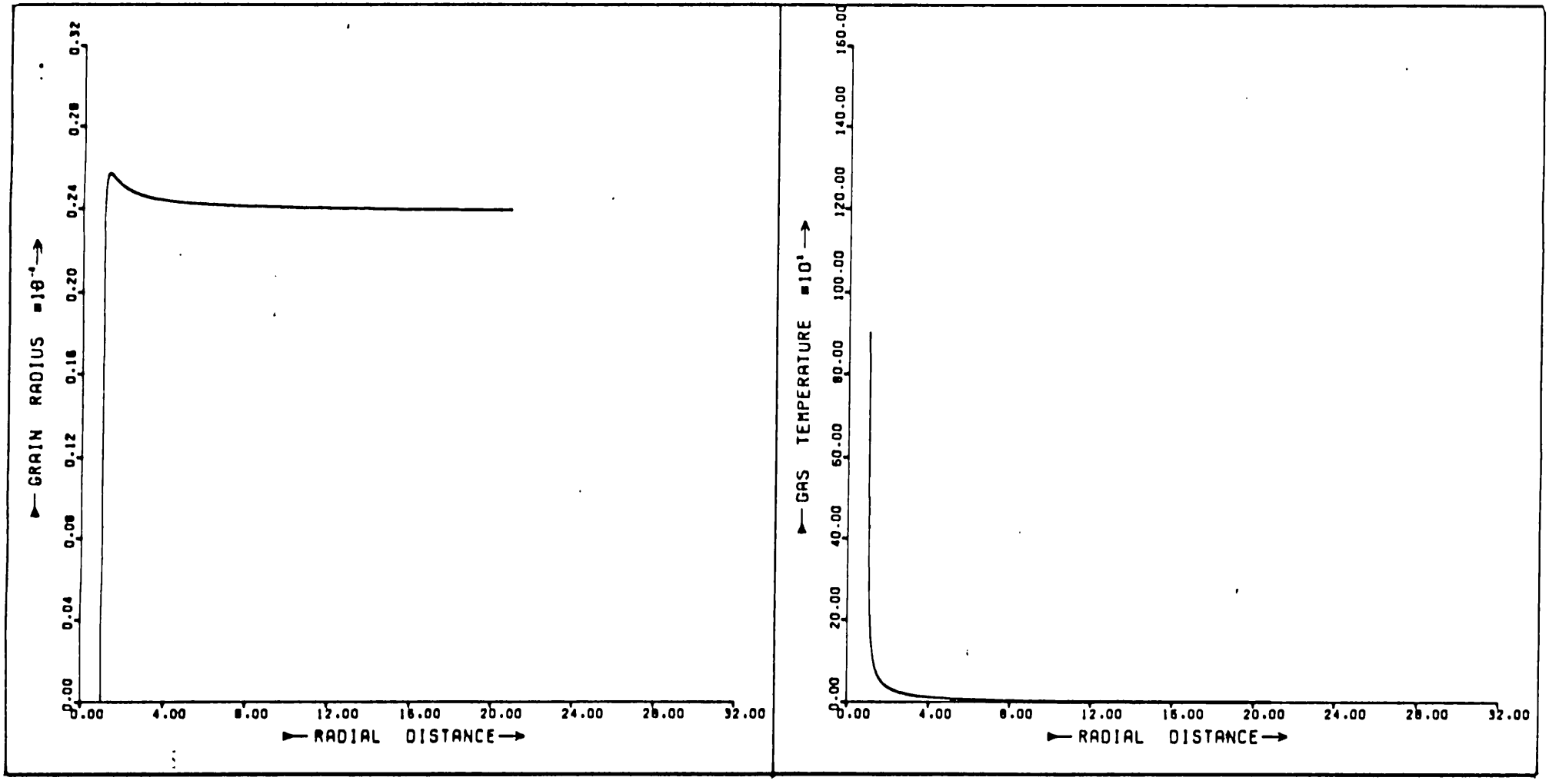

FIGURE 5.9h MIRA SUPERSONIC MASS FLOW MODEL 3

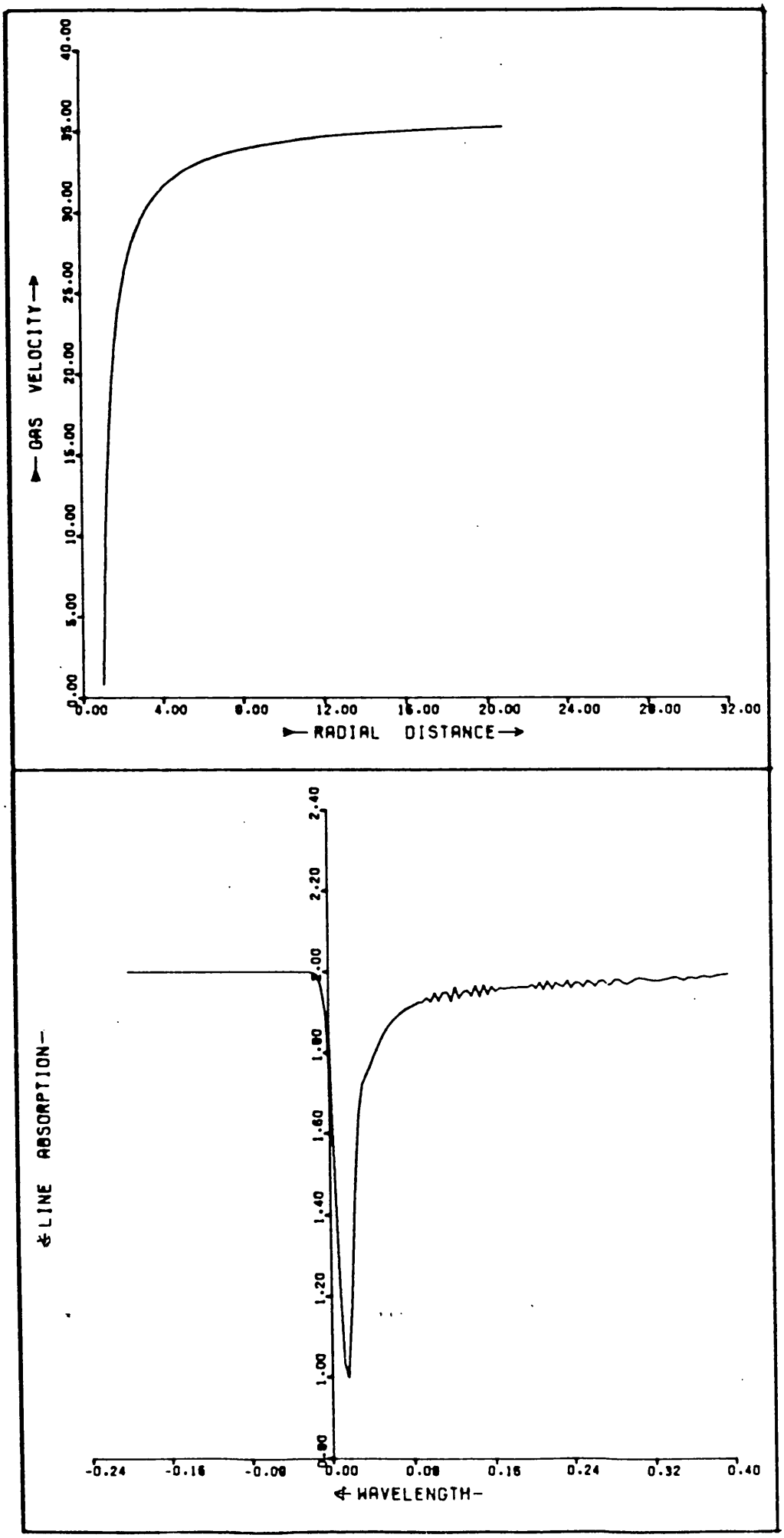

FIGURE 5.9i MIRA SUPERSONIC MASS FLOW MODEL 3

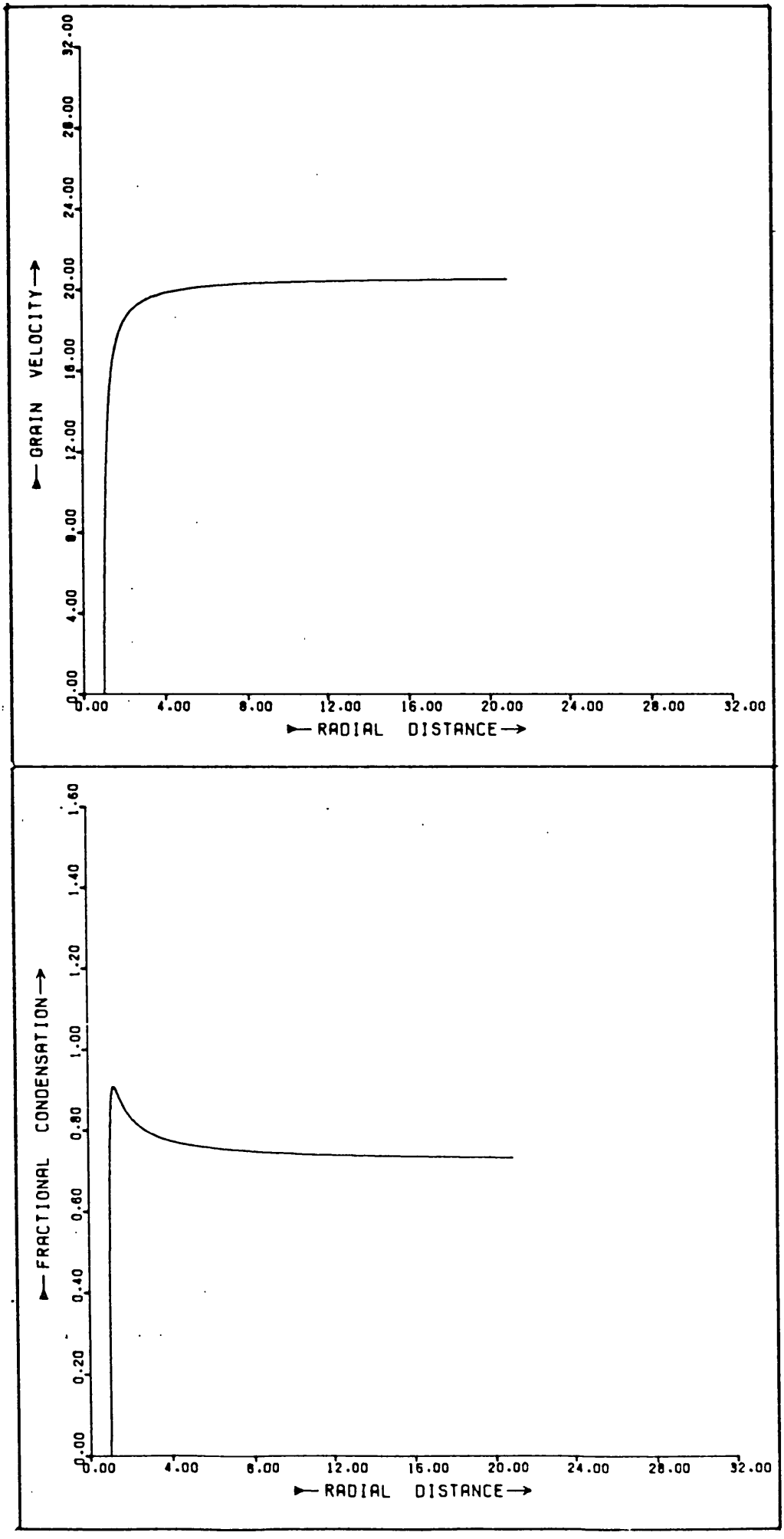

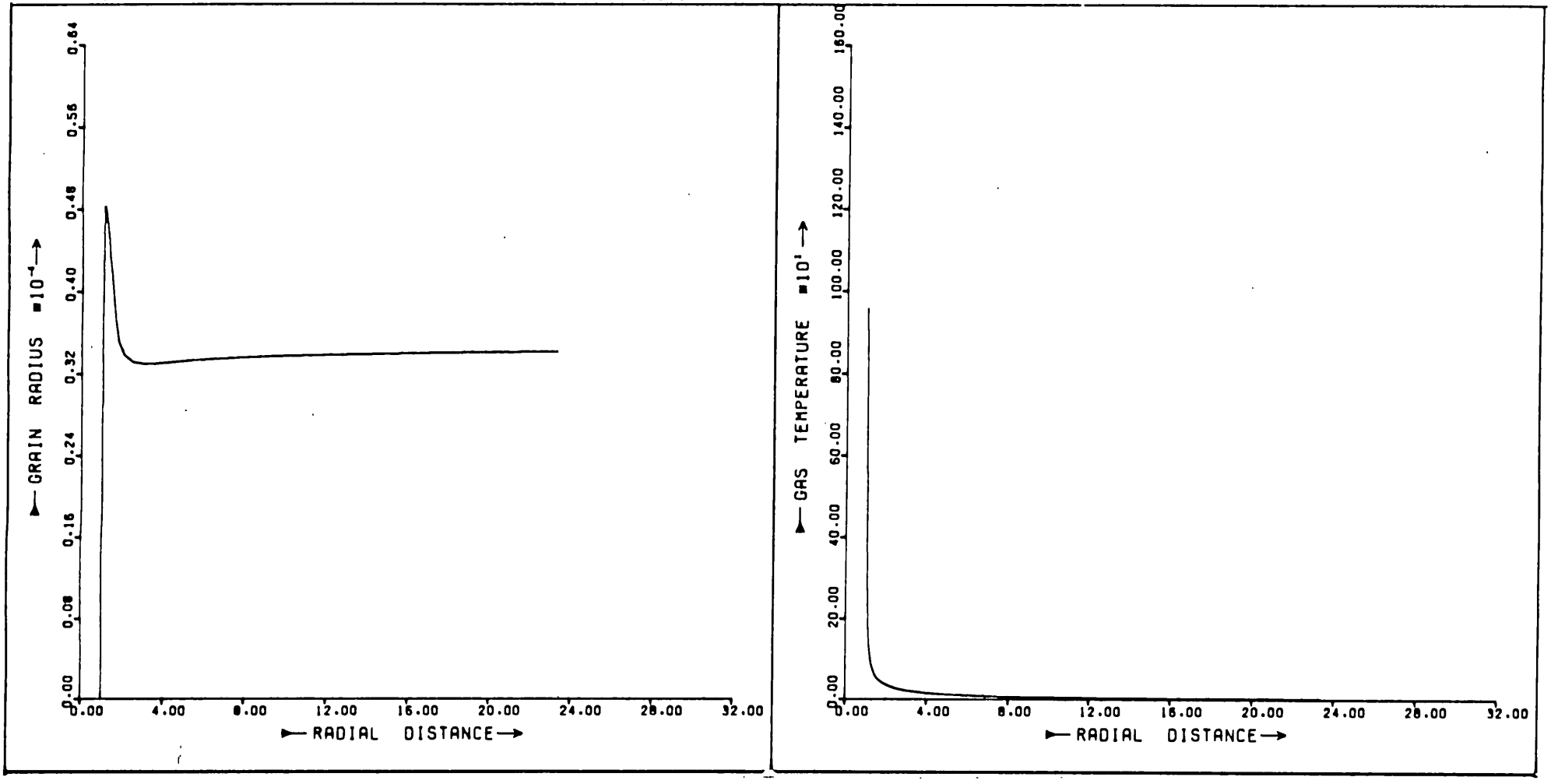

FIGURE 5.9j MIRA SUPERSONIC MASS FLOW MODEL 4

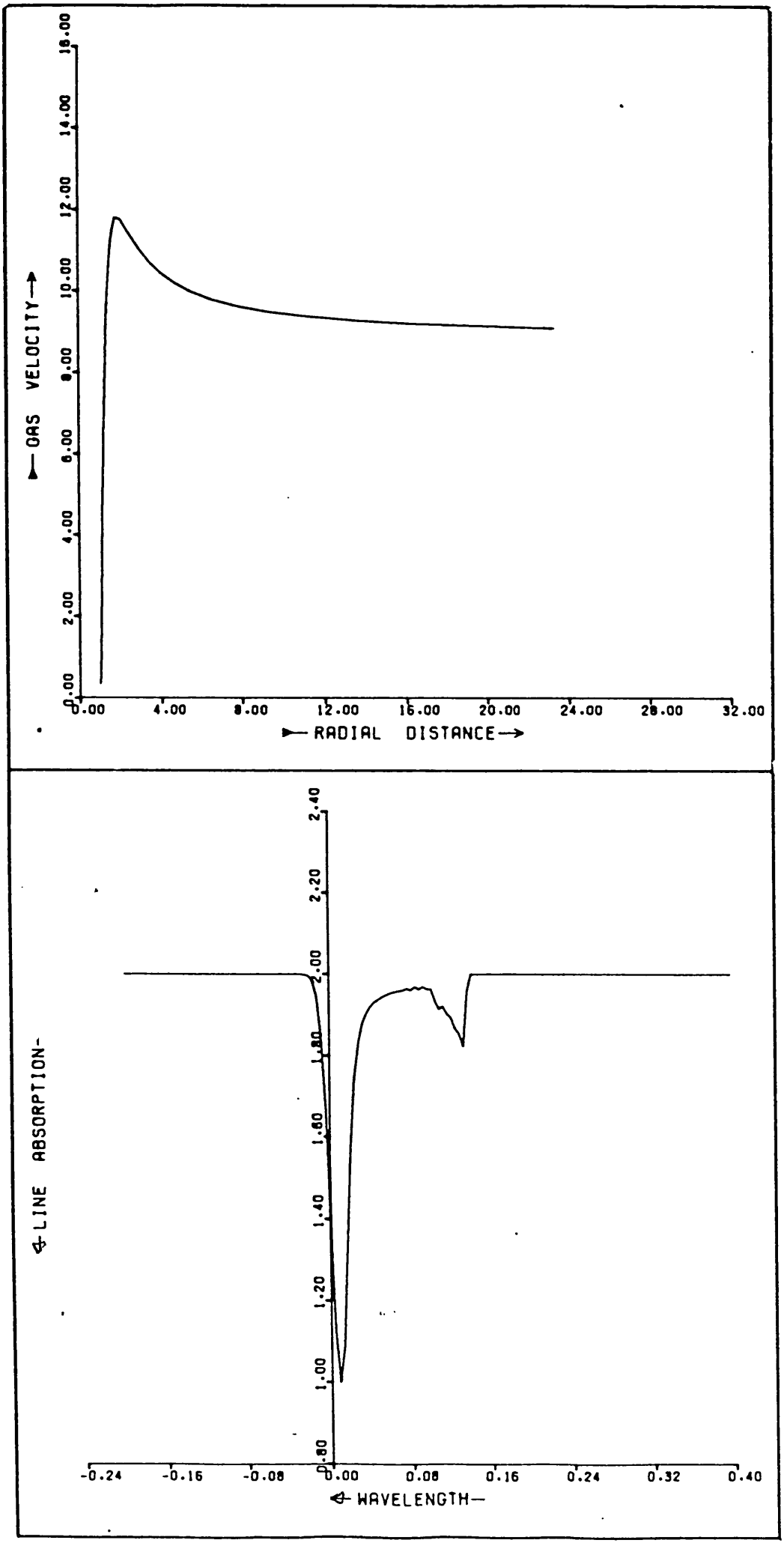
GAS VELOCITY
0.00
2.00
4.00
6.00
8.00
10.00
12.00
14.00
16.00
0.00
4.00
8.00
12.00
16.00
20.00
24.00
28.00
32.00
RADIAL DISTANCE
LINE ABSORPTION
0.80
1.00
1.20
1.40
1.60
1.80
2.00
2.20
2.40
-0.24
-0.16
-0.08
0.00
0.08
0.16
0.24
0.32
0.40
WAVELENGTH

FIGURE 5.91 MIRA SUPERSONIC MASS FLOW MODEL 4

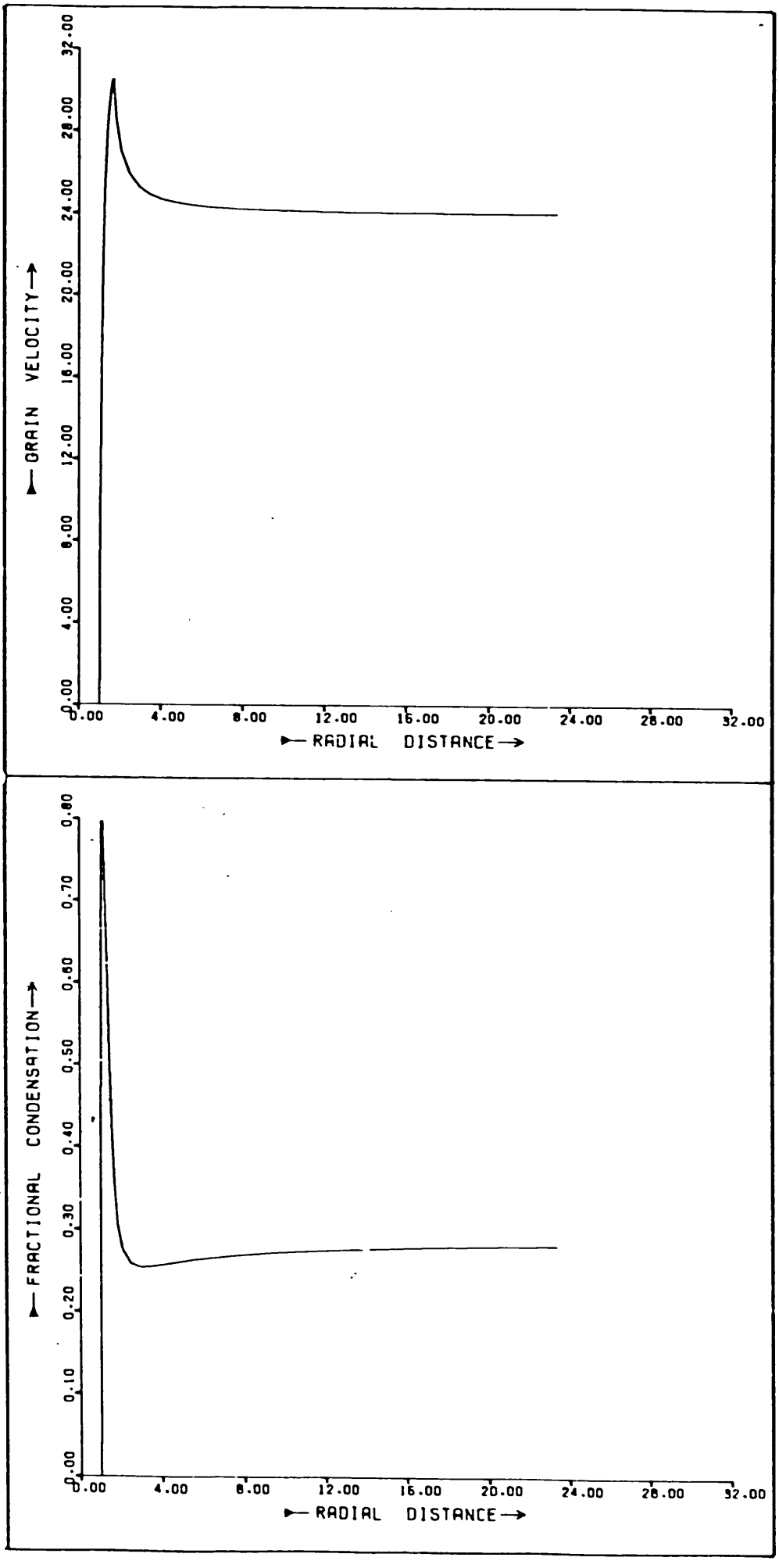

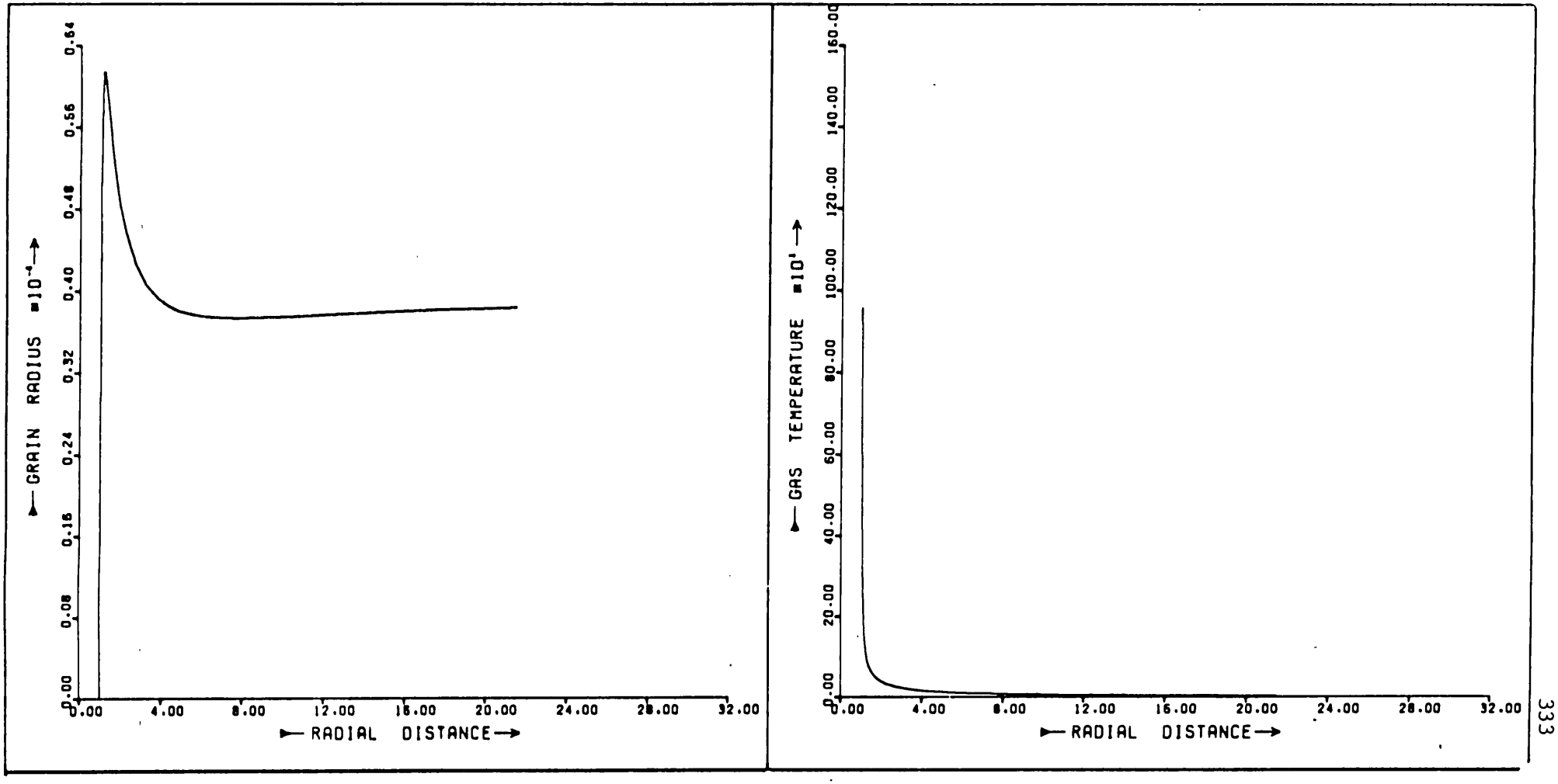

FIGURE 5.9m MIRA SUPERSONIC MASS FLOW MODEL 5

FIGURE 5.9n MIRA SUPERSONIC MASS FLOW MODEL 5

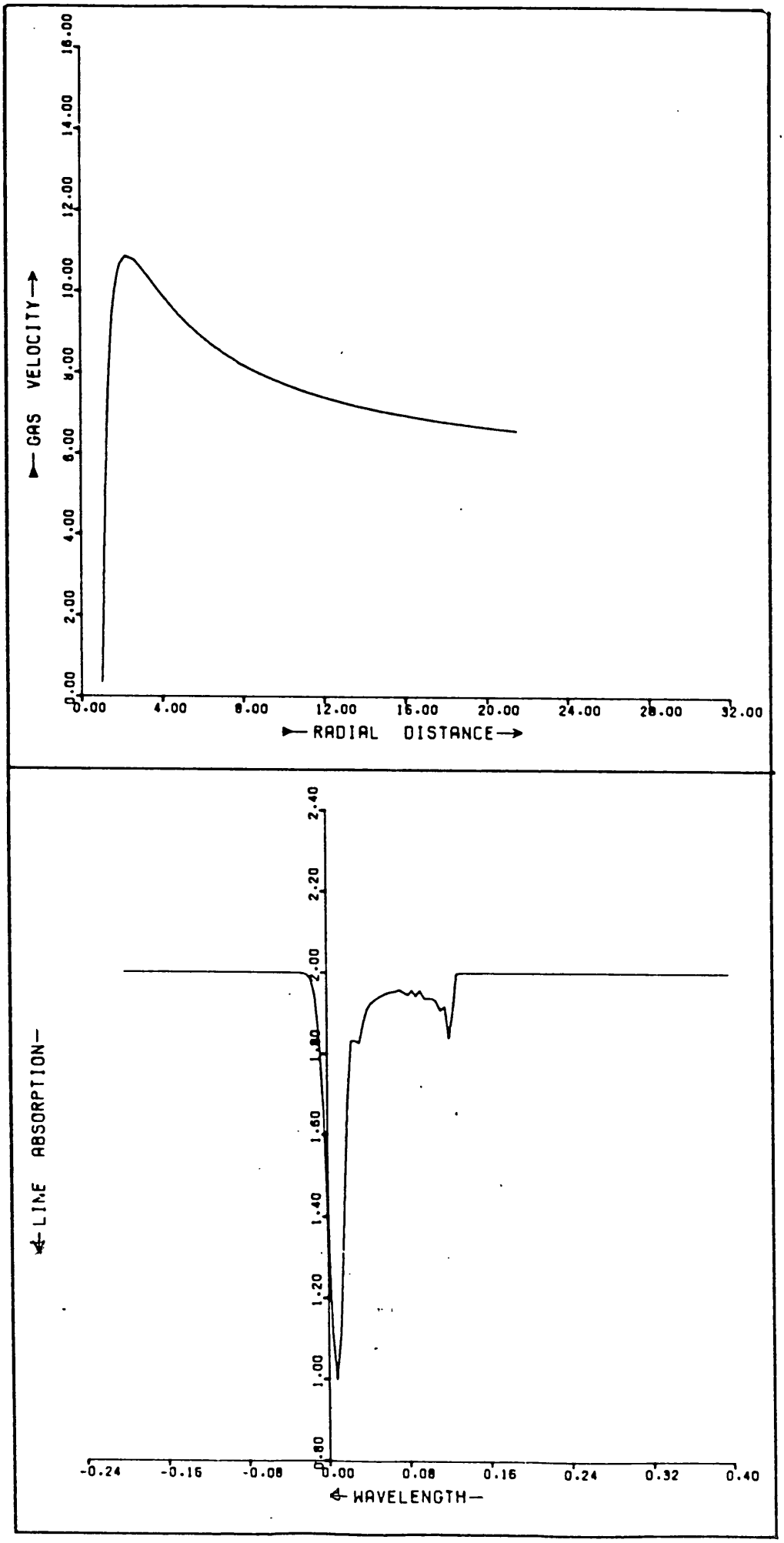

FIGURE 5.9o MIRA SUPERSONIC MASS FLOW MODEL 5

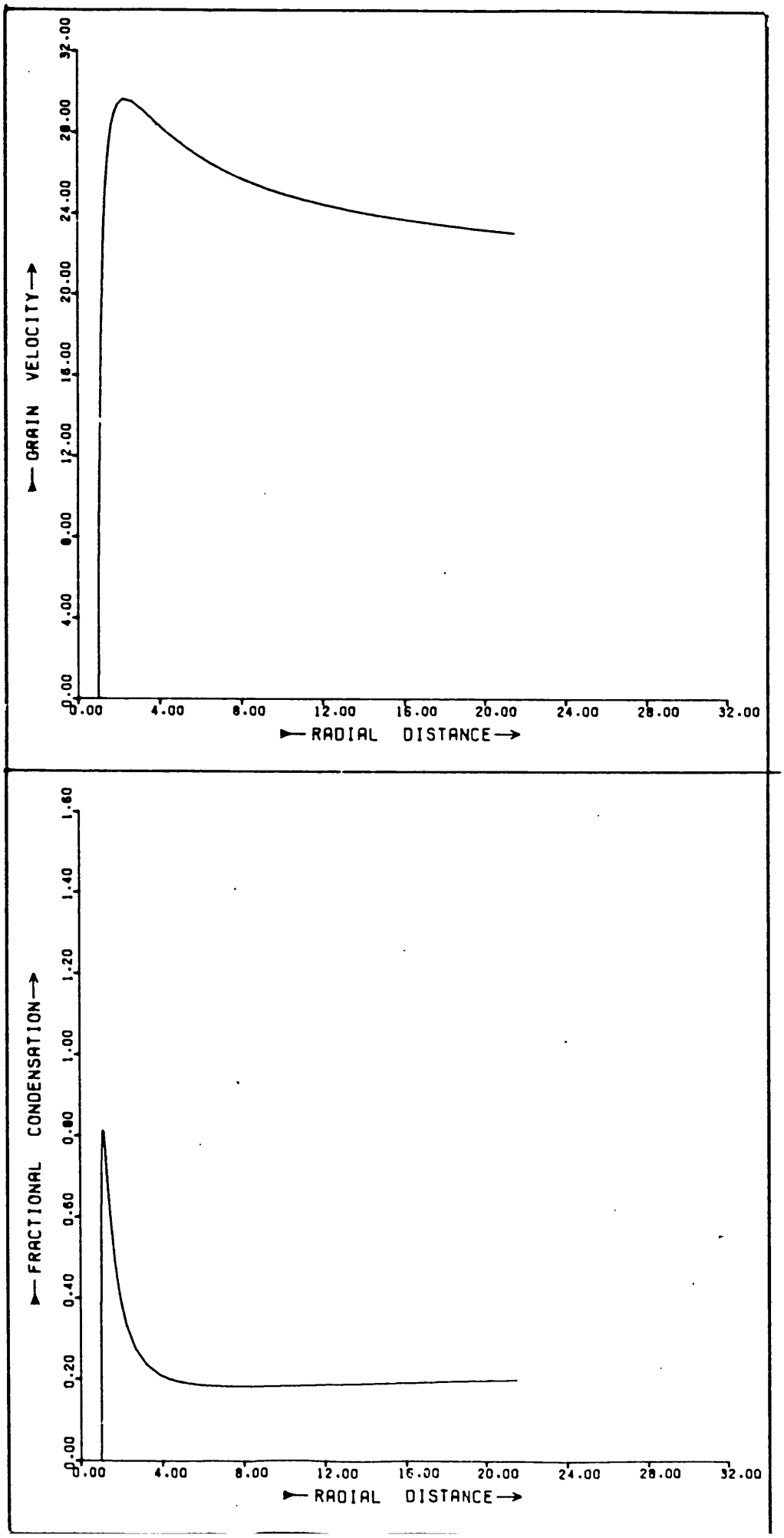

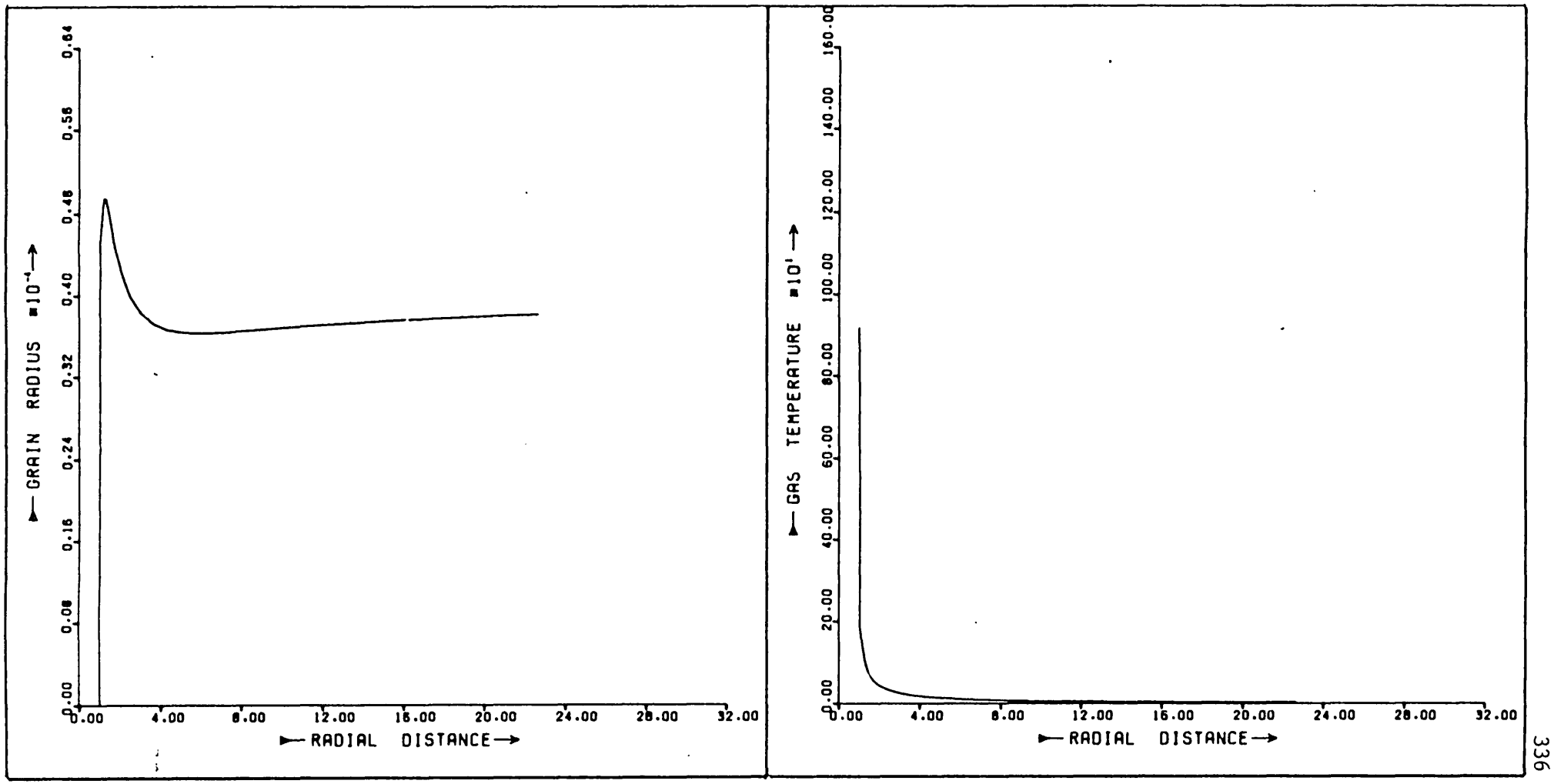

FIGURE 5.9p MIRA SUPERSONIC MASS FLOW MODEL 6

FIGURE 5.9q MIRA SUPERSONIC MASS FLOW MODEL 6

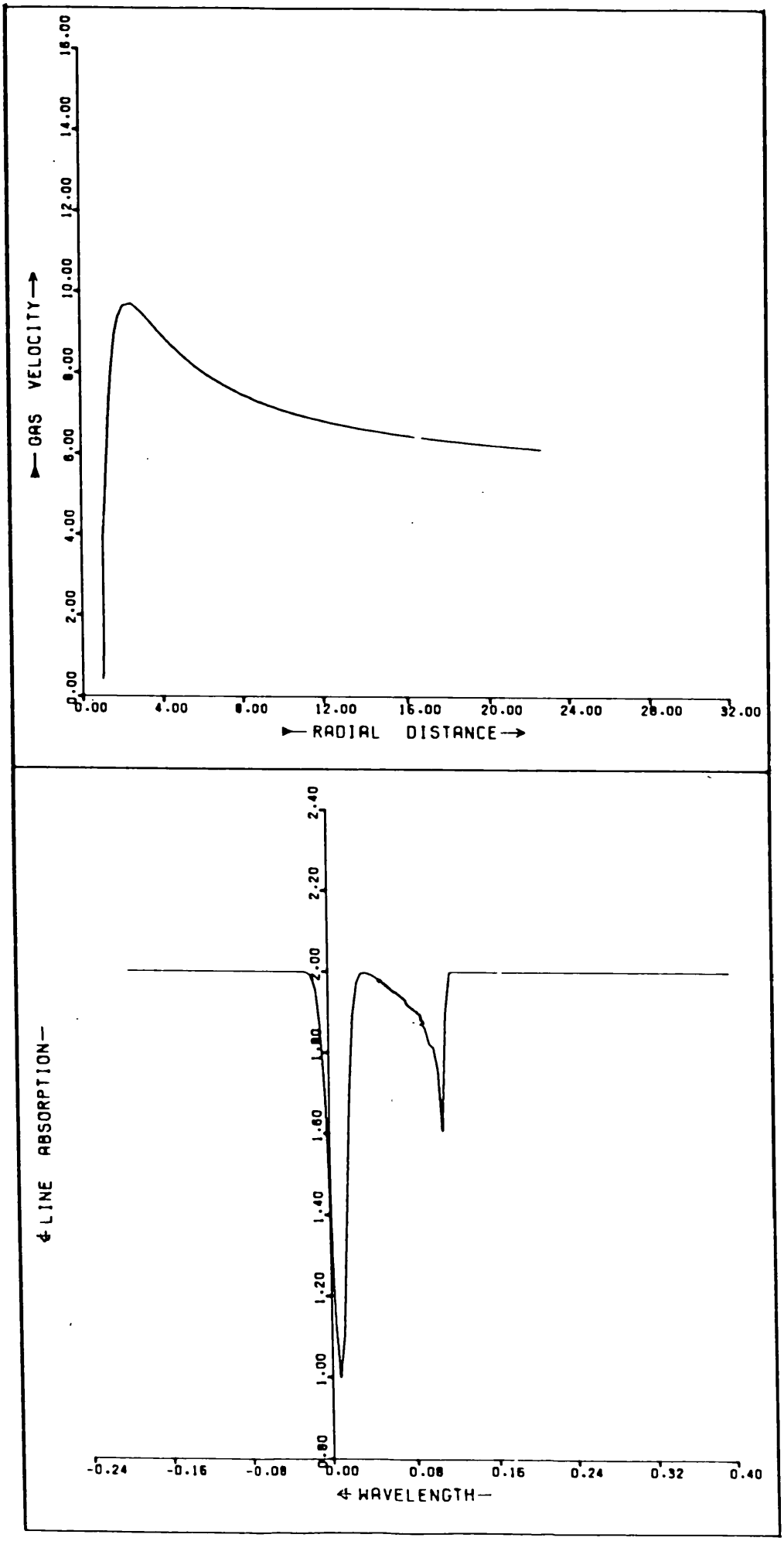

FIGURE 5.9r MIRA SUPERSONIC MASS FLOW MODEL 6

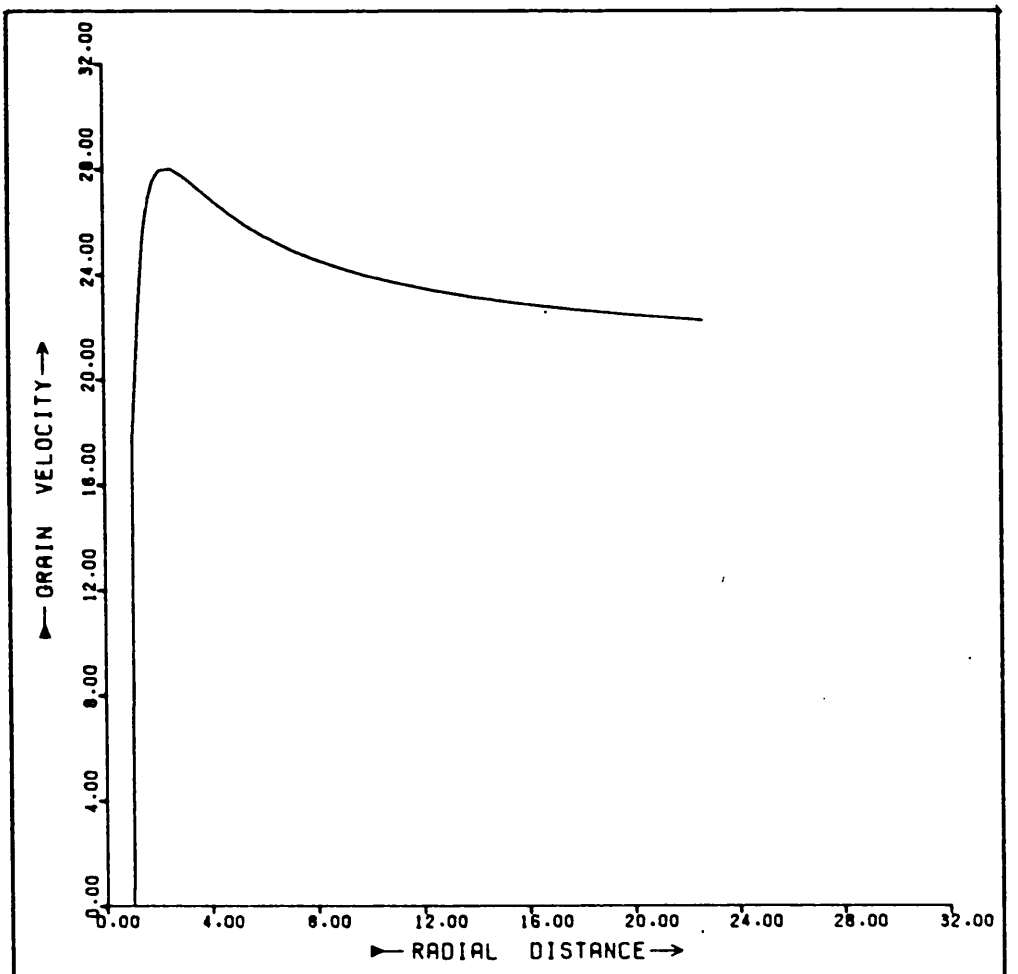

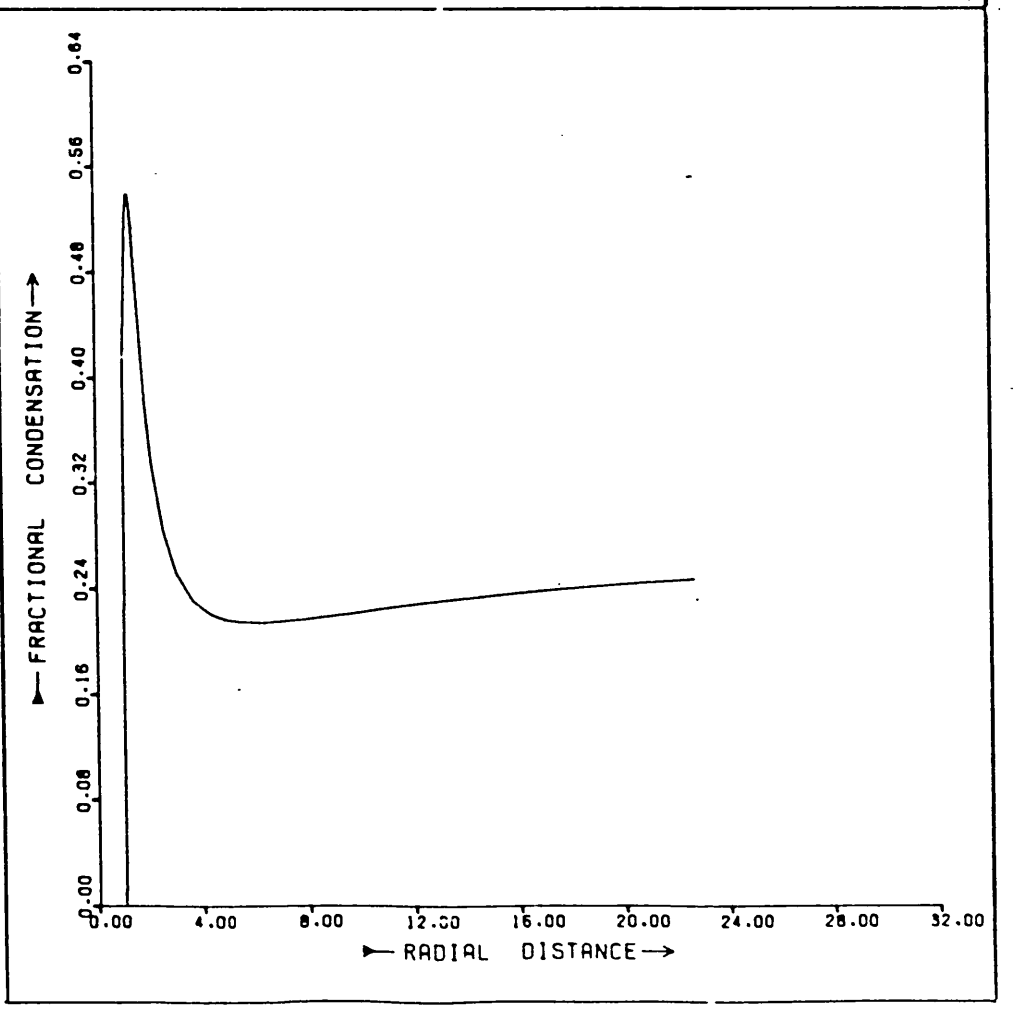

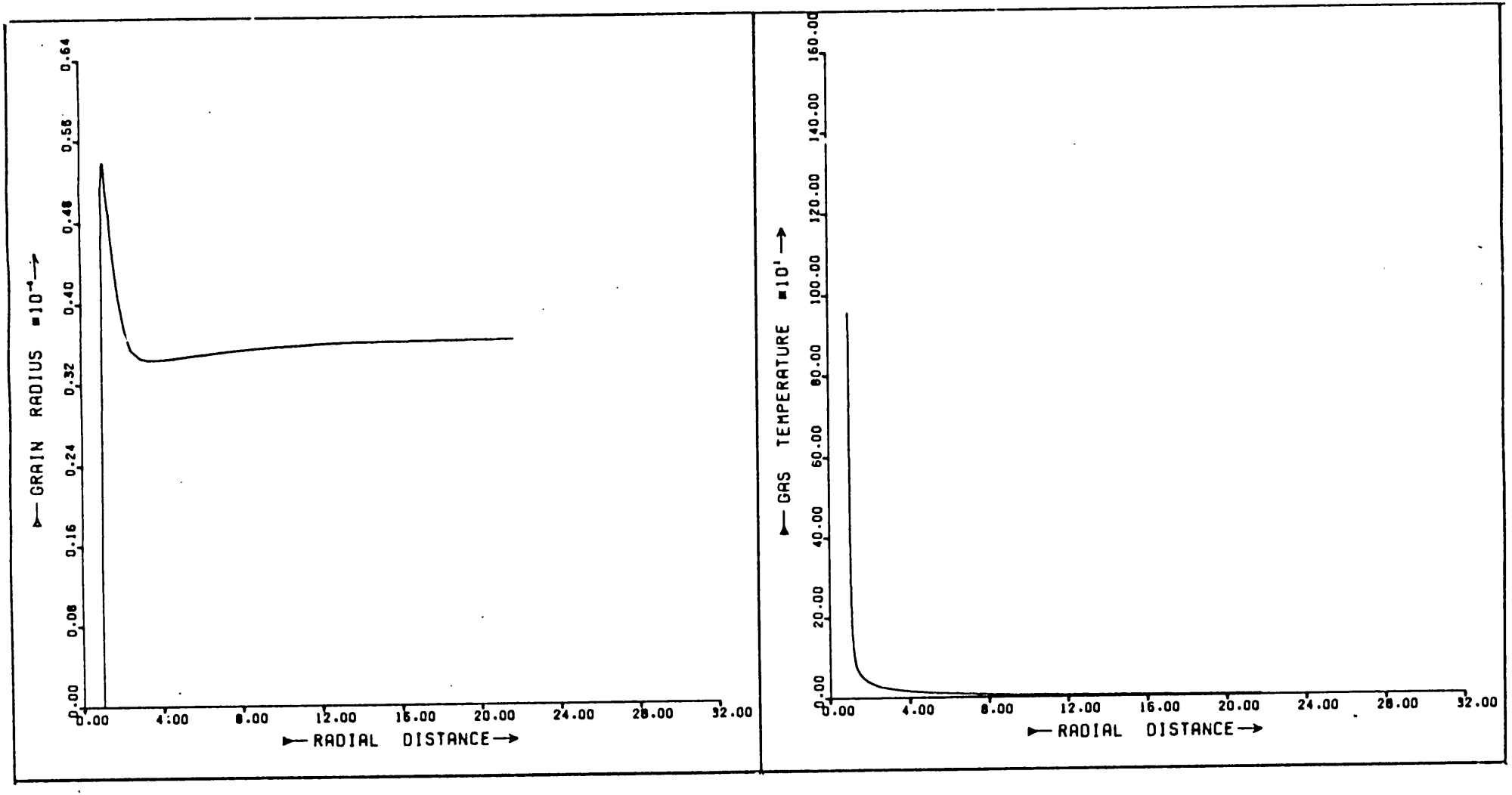

FIGURE 5.9s MIRA SUPERSONIC MASS FLOW MODEL 7

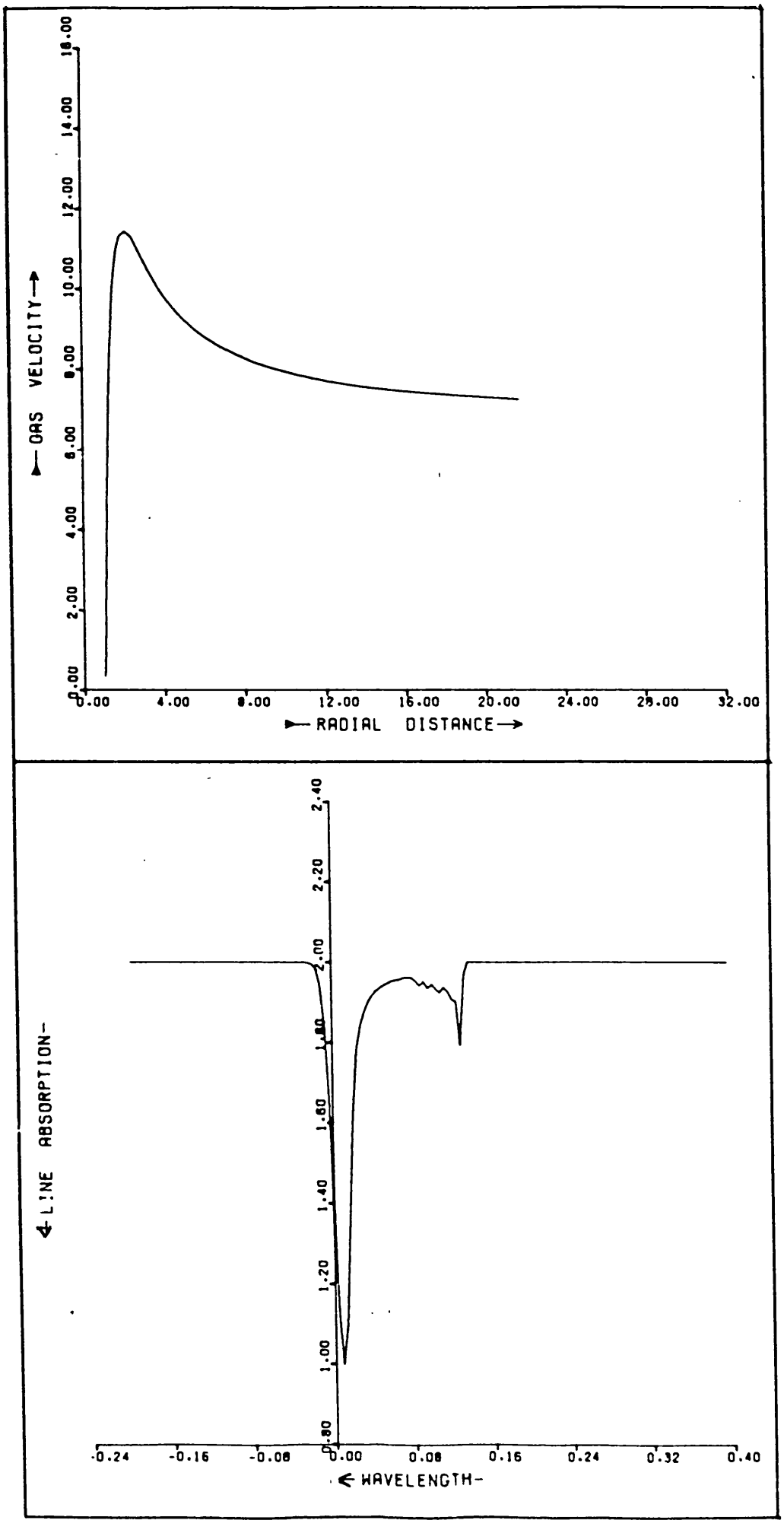
GAS VELOCITY
0.00
2.00
4.00
6.00
8.00
10.00
12.00
14.00
16.00
0.00
4.00
8.00
12.00
16.00
20.00
24.00
28.00
32.00
RADIAL DISTANCE
LINE ABSORPTION
0.80
1.00
1.20
1.40
1.60
1.80
2.00
2.20
2.40
-0.24
-0.16
-0.08
0.00
0.08
0.16
0.24
0.32
0.40
WAVELENGTH

FIGURE 5.9u MIRA SUPERSONIC MASS FLOW MODEL 7 341

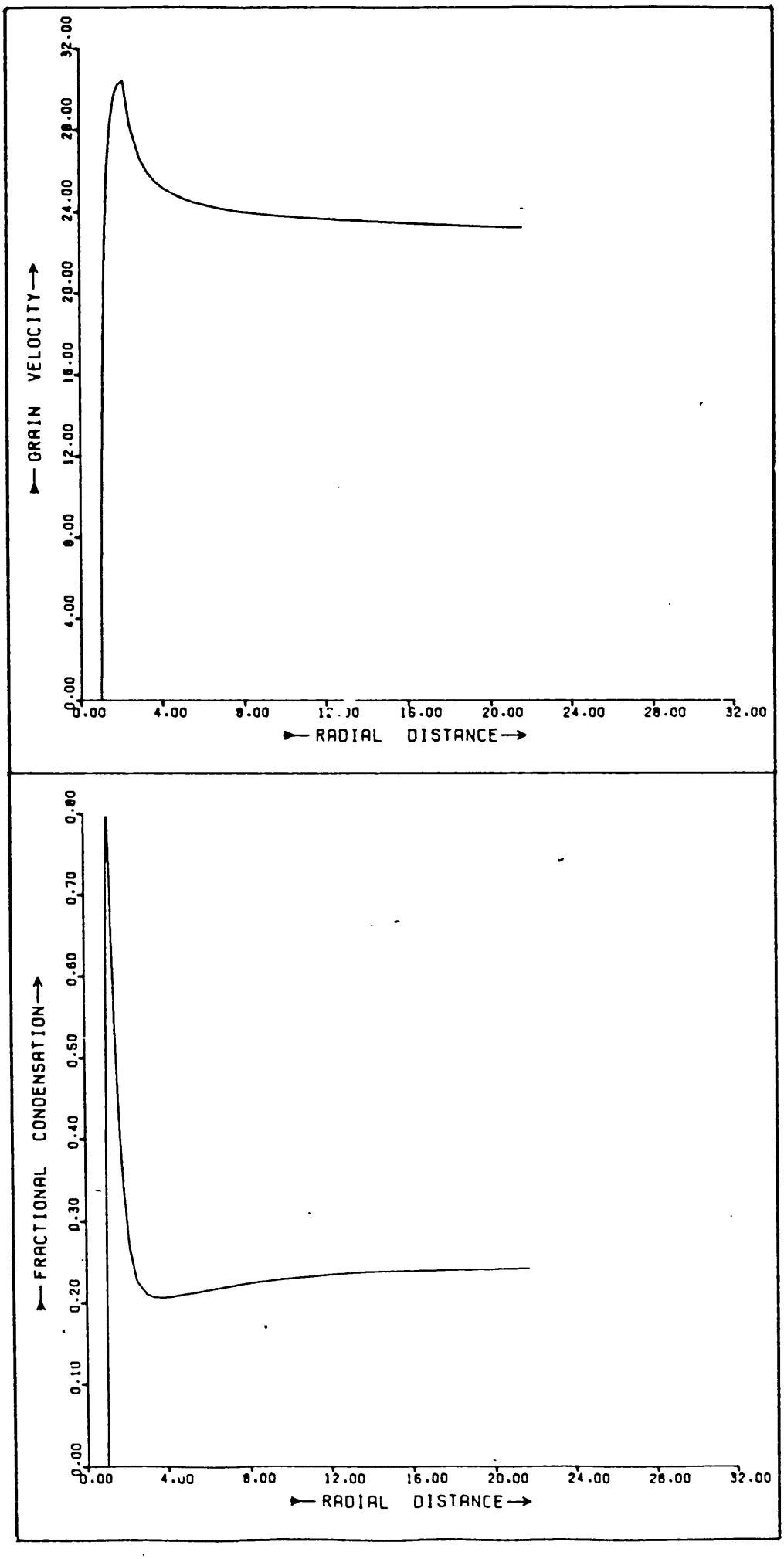

typically categorised by a deep zero velocity absorption, and shallower core displaced to the blue; the latter feature reminiscent of the sharp displaced core in figure 5.1.

Rotational terms appear to lead to lower velocity mass flows (at least for the cases considered here), and there seems little doubt that a variation of rotational velocity with stellar latitude may well lead to a corresponding variability in terminal mass flow velocities. Such a mechanism for anisotropic mass ejection may be added to those already considered, in the attempt to explain the structure of planetary nebulae.

The rapid establishment of a stable outflow velocity, and development of low envelope temperatures through adiabatic cooling, agree well with flow properties deduced from observation.

Finally, fractional increments in gas velocity and grain radius were less than 2.5%, and in radius less than 10%. These step lengths permitted accuracies out to 100 r_* of better than 1% in the derived parameters.

5.18 Final Comments on Mass Loss Models

We have seen that under certain circumstances, supersonic mass loss from late type stars is possible if radiative acceleration of grains is the primary cause of mass flow. The conditions for this mass flow appear to be most readily satisfied in cool, Mira type stars. The ability of this mechanism to explain mass flow in late type stars generally may however require some alterations in boundary conditions. For instance, although a very provisional assessment of $\chi_{1,2}$ (the grain/gas energy transfer factors) is determinable from adsorption

data for cool grains, it is conjectural for grain/gas temperatures appropriate to the present problem. A value $\chi_1/\chi_2 << 1$ may require a concommitant increase in condensation zone temperatures however, and chromospheric grain growth and acceleration would then merit serious consideration. Note in this respect that if chromospheric temperatures approach or exceed $\sim 10^5$K, changes of gas internal energy due to atomic recombination become important. A change in grain structure and/or composition may also be relevant.

We have already noted the difficulty in trying to remove iron grains from the vicinity of the condensation zone, without a consequent serious depreciation in grain size arising from sublimation. One mode of removing iron grains may occur if they were to form the cores of composite iron-silicate grains. This would also facilitate silicate condensation, which may otherwise prove a problem; although depending on the C/O ratio, the silicate may be in a state of high supersaturation.

Unfortunately, the available numerical data does not allow an immediate attack upon the question of the relevance of composite grains. The variation of $\overline{Q}_{PR}$ with total grain size and relative core/mantle radii still requires determination, for instance. This is not by itself of particular difficulty, and Professor Wickramasinghe has kindly provided programs which will with modifications enable the determination of such parameters. Before proceeding upon such a course of action however it is of interest to determine what other evidence there is to support the existence of composite grains. Or, less specifically, if there is any information at all (aside from the infrared evidence of silicate excesses at $\lambda \sim 10$ μm) to indicate the nature of circumstellar grains. One obvious course of action for instance would be to investigate the evidence for any grain absorption leading to anomalous optical continuum in late type stars. In the

following we will review available evidence concerning this.

5.19 Optical Continuum Absorption in Late Type Stars

There is considerable circumstantial evidence to suggest possible significant optical absorption by circumstellar dust grains in certain late type stars. Some of the most relevant information comes, for example, from stellar associations such as h and χ Persei, where we can be fairly certain that the stars are at a similar distance, and subject to a uniform interstellar reddening law. In this case however, certain supergiants are unaccountably bluer than cluster members with similar spectral types and luminosities (Johnson and Mendoza V. 1966; Lee 1970). Other evidence comes, for instance, from another galactic cluster, NGC 2264 , investigated by Strom et al. (1972), where careful investigation revealed many stars having attenuated optical continua (with complementary infrared excesses), and even one case of possible neutral absorption (i.e. similar attenuation at all wavelengths), only to be explained by very large circumstellar grains. A similar situation may also be relevant to Cyg OB2, investigated initially by Reddish et al. (1966), although an alternative and no less interesting possibility of generalised internal absorption arising from gaseous residue within the cluster may be appropriate (Voelcker and Elsasser 1973). In this last respect, it does seem clear that anomalous reddening within clusters is at least in part a consequence of the youth of the component stars, and possibly the presence of remnants of the star forming material, rather than an evolutionary consequence of stellar ageing.

There is also evidence however for possible reddening in field red giants and (more obviously) supergiants. Lee (1970) for instance suggests that a possible discrepancy in the difference ΔMv between Ib and Iab type stars when compared to theoretical expectations may be accounted for "if the highest luminosity class I stars were in dustier regions and more highly reddened". He seeks to explain this in terms of association between class I stars and interstellar material, but concludes that "... it is doubtful that this can account for all of the discordance ...". It should be mentioned that the luminosity difference between Ib and Iab, Ia stars is quite considerable, and the infrared excesses reflect this.

A relation between size of infrared excess and degree of circumstellar optical absorption has been demonstrated in other stars. Humphreys et al. (1971) for instance suggest that such a situation applies for certain G-type supergiants, and excellent work by Gilra (1973) has almost certainly correctly identified the strong U.V. continuum attenuation in certain carbon rich late type stars with the condensation of SiC; since convincingly linked to a corresponding characteristic excess infrared continuum (Cohen and Treffers 1974). The present author has sought to explain the U.V. continuum deficiency in these stars in rather different terms. The U.V. absorption has a rapid onset, naturally explained in terms of molecular band absorption. A rather similar effect may be achieved however if multiple scattering rapidly increases with decreasing wavelength, in a manner to be expected for a rapidly increasing grain scattering cross section, $Q_{SCA}(\lambda)$ (as possessed by for instance small graphite grains). The output flux is determined by the solution of the appropriate transfer equations for an optically thick shell. Whilst this mechanism is

introduced as an interesting alternative solution to the problem, the observations of Cohen and Treffers are persuasive that Gilra's explanation is probably correct. Broad band infrared emission noted by Dyck, Lockwood and Capps (1974) in certain very late type giants may indeed be due to graphite however, and it is intriguing to note that the degree of infrared excess in several of these stars having similar spectral types is correlated (with some qualifications) to the size of the [V]-[I.R.] colour indices, in the sense of decreasing visual luminosity corresponding to increased infrared excess (although there is some scatter due to uncertainties in the spectral classification of these stars).

A similar correlation between infrared and optical deviations from black body behaviour is demonstrated, using different data, for carbon stars as well. The evidence for IRC and carbon stars is presented in more detail in Appendix 1. Apart from arguments which are primarily statistical, however, such as Lees', a most likely way to identify any circumstellar reddening component would be for circumstellar reddening laws to differ appreciably from interstellar reddening laws, although even here, for supergiants, the typically massive interstellar extinction resulting from their large distances, and propensity for lying close to the galactic plane, will tend to obscure any but the most substantial and anomalous circumstellar components. Typically however, if we were to deredden stars possessing anomalous reddening using an extinction curve derived from observations of early type stars, we would expect to correspondingly obtain rather anomalous colour indices compared to, say, "intrinsic" values. (It should be pointed out that the method of obtaining "intrinsic" colour indices (c.f. Johnson 1966) is such as to weight the results towards

those appropriate for stars with little circumstellar reddening; and from the intrinsic scatter of the infrared excesses alone, it seems not unlikely that circumstellar absorption is open to similar variability within the spectral/luminosity classes).

The only direct application of this procedure to late-type stars using recent data appears to be due to Humphreys, Strecker and Ney (1972). If generally $A_V(E(X-V))$ is the estimated visual absorption from the excess in the index $[X]-[V]$, then Humphreys et al. (1972) find $\Delta = \{A_V(E(V-I)) - A_V(E(B-V))\}$ to be an increasing function of spectral type. The specific results for M supergiants in Carina, differ depending upon whether Lee's or Johnson's (1966) intrinsic colours are used; but the trends are similar. By M4, $\Delta = +1.09$ for Johnson's data, and $\Delta = +0.79$ for Lee's. In contrast, the parameter $\{A_V(E(V-L)) - A_V(E(B-V))\}$ shows no trend with spectral type. Humphreys et al. suggest a systematic error in the I measurements of Johnson and Lee. This would be rather surprising however, and an alternative possibility will be suggested later.

Another aspect of the continuum behaviour of late type giants and supergiants of particular interest is the increasing discrepancy between the observed visible continua and extrapolation of an appropriate blackbody curve from infrared wavelengths. Whilst stellar continua normally do show departures from simple blackbody behaviour, which may be quite substantial in the U.V. the deviations from the Planck law for late type stars in the visible are quite exceptional.

The discrepancy is usually attributed to TiO absorption, after the example of Smak (1966), although in supergiants atomic absorption is also important (Fay and Johnson 1973). The TiO bands become of increasing importance with advancing spectral type and occupy a

substantial portion of the visible - ultraviolet spectrum of these stars (see for instance Kopp et al. 1974, and in particular Pearse and Gaydon 1976, for details concerning known bandheads). The contribution of TiO bands is undoubtedly considerable. When actual measurements of band TiO absorption are made however, results often indicate values falling considerably short of explaining the discrepancy between a black body extrapolation and the actual continuum. Kubiak (1966) for instance finds for reductions in the strength of the V band continuum due to band absorption alone values of A_V = -0.21 mag, -0.42 mag and -0.61 mag for particular stars of respective spectral types M2III, M4III, and M5III. Smak (1966) for comparison notes total continuum depressions of -0.45 mag, -1.1 mags, and -1.6 mags for stars of the same classes. Gabovits and Opik (1935) similarly obtain results 40% less than those required to explain continuum depression. Dobronravin (1950) also suggests that for a change in stellar effective temperature from 3000 K to 2500 K for late type giants, there is a corresponding change in the colour index due to continuous absorption, of 1.05 mags, whereas increased band strength accounts for only a 0.29 mag change in this value.

The uncertainties are large, and the evidence that a broad continuum absorption is necessary to explain the available observations not decisive. The presence of significant continuum absorption would on the other hand not only be interesting per se, but have serious consequences for, for instance, stellar atmospheric modelling. The possibility that dust may contribute an absorption continuum will be investigated in the following discussion. For the moment, we simply note that the size of absorption continuum suggested by Dobronravin is an entirely plausible consequence of circumstellar absorption by

dust, given the mass loss rates apparently applicable for these stars (see next section). In the later discussions the terms of reference will be broadened in an attempt to identify the characteristics of circumstellar absorption from the observational material.

5.20 Continuum Absorption in Late Type Stars

It is first necessary to determine if the likely condensates of oxygen rich late type stars could explain the continuum absorption which appears to be suggested in evidence presented in the last section.

For grains moving outwards from a star with constant velocity V_{gr} ($= V_d + V_r$), and for a radius of flow inception r_I, the total envelope absorption optical depth is

$$\tau_{\nu abs} \simeq \int_{r_I}^{\infty} X\, f(r)\, \rho(r)\, \kappa_{\nu ga}(r)\, dr \simeq \frac{\kappa_{\nu ga}\, dM/dt\, X}{4\, \pi\, r_I\, V_{gr}}$$

where $\kappa_{\nu ga}$ is the absorption per unit mass of grain material, X is the fractional abundance of the condensate, and f(r) is the fractional condensation (for the purposes of the present argument f(r) = 1). $\kappa_{\nu ga}$ is then determined from

$$\kappa_{\nu ga} = \frac{3}{4\, a\, \rho_{gr}}\, Q_{abs\nu}$$

For iron we use $\rho_{gr} = 7.87$ gm.cm^{-3}, and from Wickramasinghe (1973) we have for small grains

$$Q_{abs\nu} \simeq Q_o\, a$$

where Q_o has respective values 3.9×10^2, 2.1×10^3 and 5.8×10^4 for the wavelengths λ = 2.2 μm, 1.04 μm and 0.56 μm.

These values are reasonably accurate providing $a < 10^{-6}$ cms. For $10^{-6} \lesssim a \lesssim 1.5 \times 10^{-5}$ the values are lower limits, whereas for $a \gtrsim 1.5$ μm they are upper limits (see figure 5.5). In terms of realistic circumstellar grain sizes, the absorption coefficients are likely to be lower limits. For small grains we then obtain for the visible

$$\tau_o = 8.94 \times 10^8 \, dM/dt \, \{\frac{r_\odot}{r_I}\}$$

where dM/dt is in solar masses per year.

We have assumed $V_{gr} \simeq 10^6$ cm.s^{-1}. Letting $r_I \simeq 10\, r_*$, $r_*/r_\odot \simeq 10^2$, and $dM/dt \simeq 5 \times 10^{-7}\, M_\odot.yr^{-1}$ gives $\tau_o \simeq 0.45$. If the iron grains form nearer the stellar surface and initial flow velocities are smaller (both these are plausible, if not likely), then τ_o will be even larger. Similarly, since $dM/dt \propto L_*$, τ_o scales roughly as r_* within a given spectral class. Thus τ_o is roughly ten times larger for supergiants, and a hundred to a thousand times less in dwarfs. It is clear that even for relatively pessimistic assumptions concerning fractional condensation, circumstellar grains represent an appreciable potential source of optical extinction. There are other considerations of relevance, however.

Typical infrared excesses for late type stars represent an appreciable fraction of the total radiant energy output, which can only partly be derived from U.V. absorption bands. To illustrate the problem we have determined the wavelength ranges $0 - \lambda_V$, $\lambda_{IR-\infty}$ over which the energy removed would correspond to a given infrared excess. The excess here is taken to be a broad band emission of width $\Delta\lambda = 3.0$ μm centred on $\lambda = 10.5$ μm; reasonably representative of the primary infrared excess continua of many late type stars. The results

FIGURE 5.10

VARIATION OF BROAD BAND ABSORPTION LIMITS WITH SILICATE (10.5 μm) EXCESS

$T_* = 3000$ K

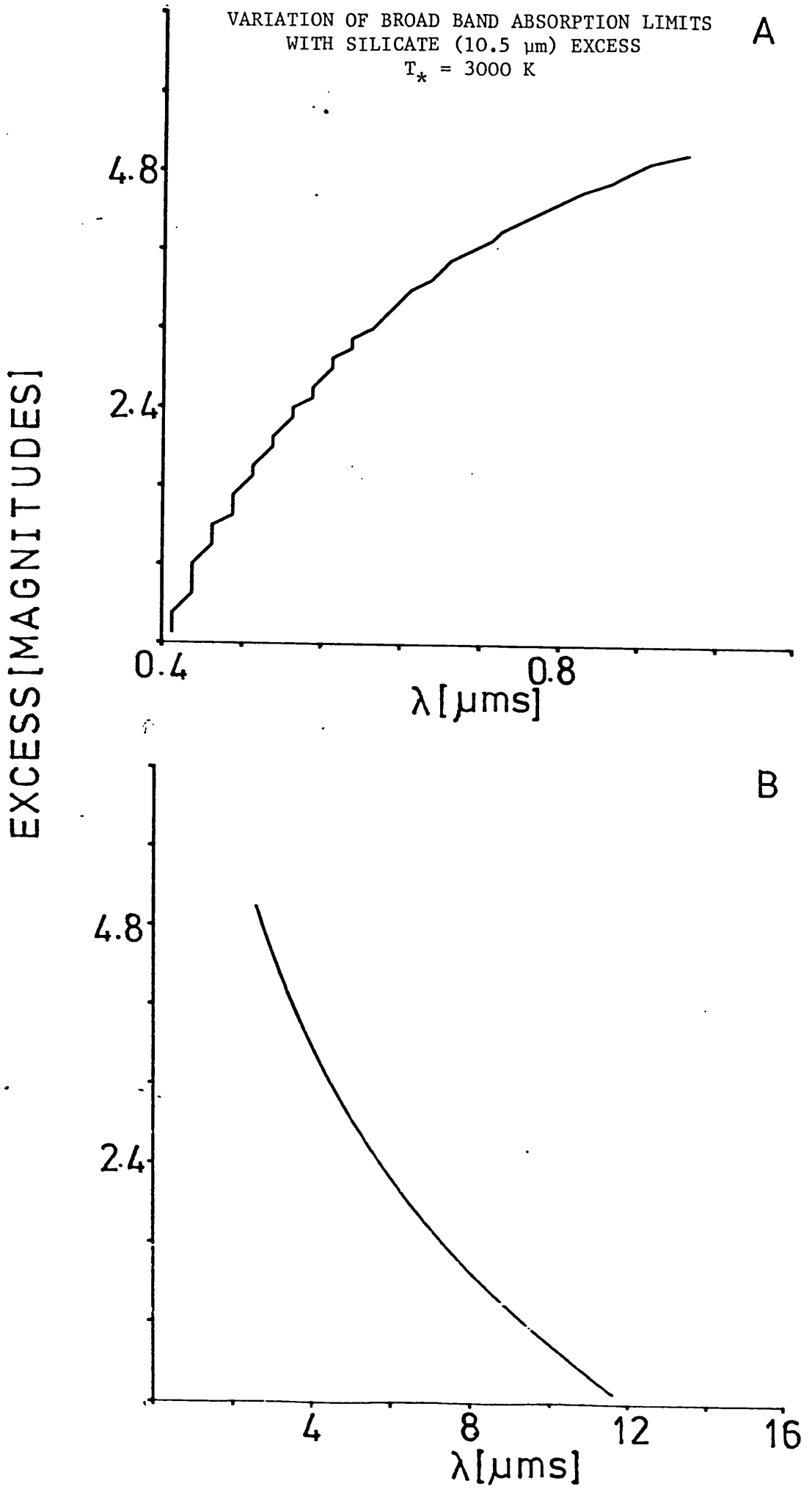

are illustrated in figure 5.10. It is seen that to support an excess reasonably similar to those observed (c.f. figure 5.3) a considerable fraction of the observable optical/infrared continua of these stars must be removed. It follows that we cannot assume that the reststrahlen bands are produced by pure silicate grains with a zero complex term to the refractive index between the primary absorption bands. On the other hand, a much smaller total absorption near the peak of the stellar continuum would remove the necessity of appreciable optical absorption. To explain observed infrared excesses and have appreciable continuum absorption at optical wavelengths, requires severe constraints upon the optical properties of any single grain type. Before proceeding to further delineate these characteristics however, it is instructive to identify the reasons why iron by itself is inadequate to explain circumstellar absorption.

5.21 Iron Continuum Absorption

5.21a Near Infrared, Optical Absorption

Dyck et al. (1974) have published new observations of certain late type giants/Miras to spectral type M9 using the 2 μm Infrared Survey of Neugebauer and Leighton (1969), to identify some of the later type members. Using this and other data, it has been possible to redetermine the colour temperature - effective temperature relation. We use these effective temperatures to determine black body functions, which are taken to be characteristic of the continuum energy distribution of the appropriate stars (excluding molecular band, and dust continuum absorption). This assumption will be reasonably validated by the ensuing results.

TABLE 5.12

STELLAR EFFECTIVE TEMPERATURES

SPECTRAL TYPE	T_{COL}	T_*	SPECTRAL TYPE	T_{COL}	T_*
M0	3425	3690	M6	2925	3100
M1	3360	3600	M7	2689	2800
M2	3300	3550	M8	2456	2520
M3	3225	3450	M9	2110	2100
M4	3150	3360	M10	1717	1630
M5	3040	3230			

The effective temperatures used are given in table 5.12, derived from figure 4, and the relation $T_* = 1.21\ T_{COL} - 451$ (T_* = effective temperature; T_{COL} = colour temperature) of Dyck et al. (1974). The corresponding curves of the flux ratios $F_{1.04}/F_{TOT}$, $F_{2.2}/F_{TOT}$, and $F_{0.55}/F_{TOT}$ are given in figure 5.11 (the upper curves in all cases), where $F_{1.04}/F_{TOT}$ is the flux at 1.04 μm divided by the total flux. The comparative results are again those of Dyck et al., circles representing normal giants, and crosses IRC stars and Mira variables.

To evaluate the modification of these curves due to variable quantities of circumstellar material, the following model was adopted.

Gas flow is assumed to emanate from the photospheric layers and maintain constant velocity.

Grain drift velocity V_d was taken to be small, so that $V_{gr} \simeq V_r$, and grains are fully developed at $r \simeq r_*$. The data of Deutsch (1960) is used to adduce a relation between gas velocity and spectral type

$$V_r = 20\ e^{-0.185Sp}\ km.s^{-1}$$

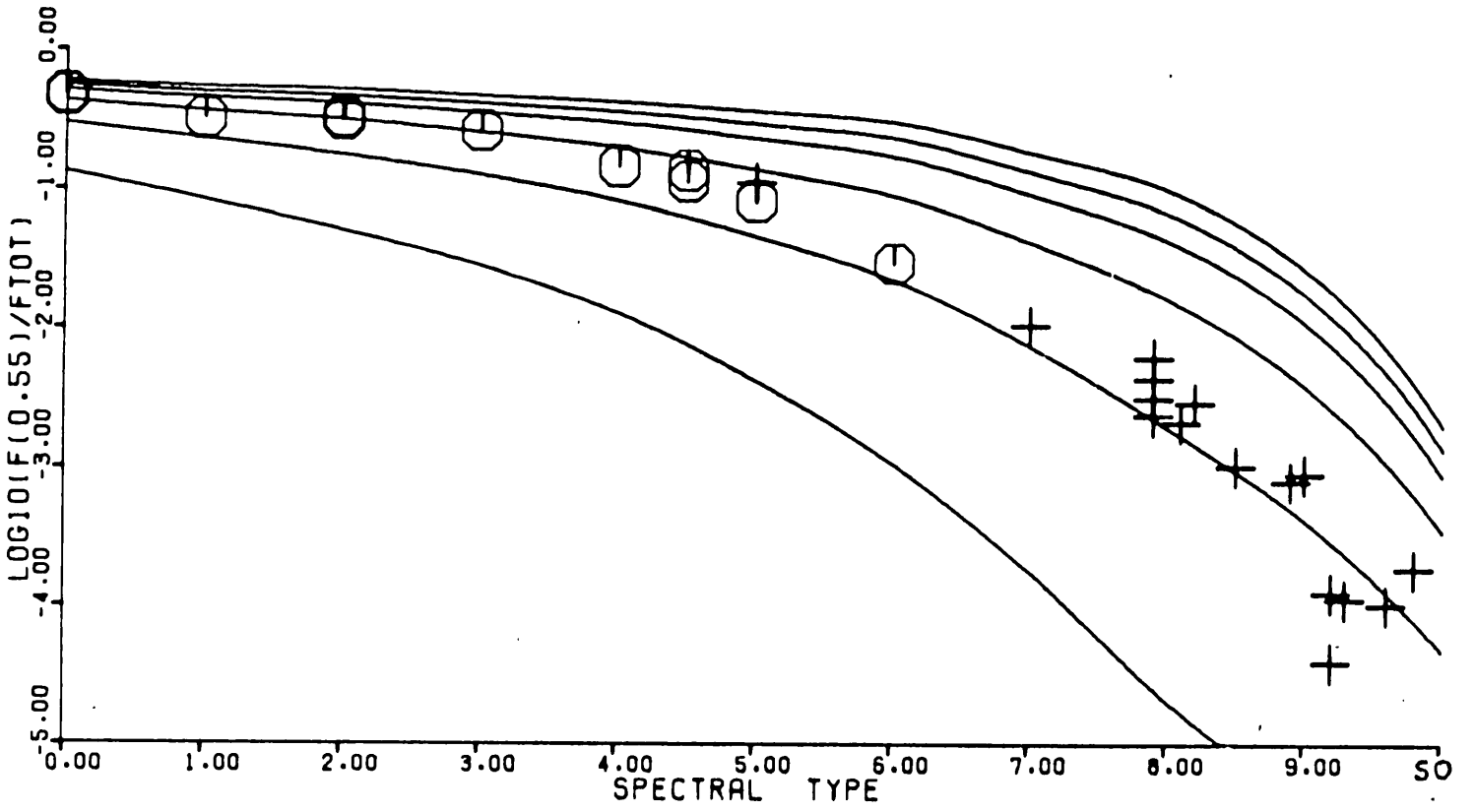

FIGURE 5.11a

IRON ABSORPTION CURVES COMPARED WITH RED GIANT (O) AND MIRA (+) DATA

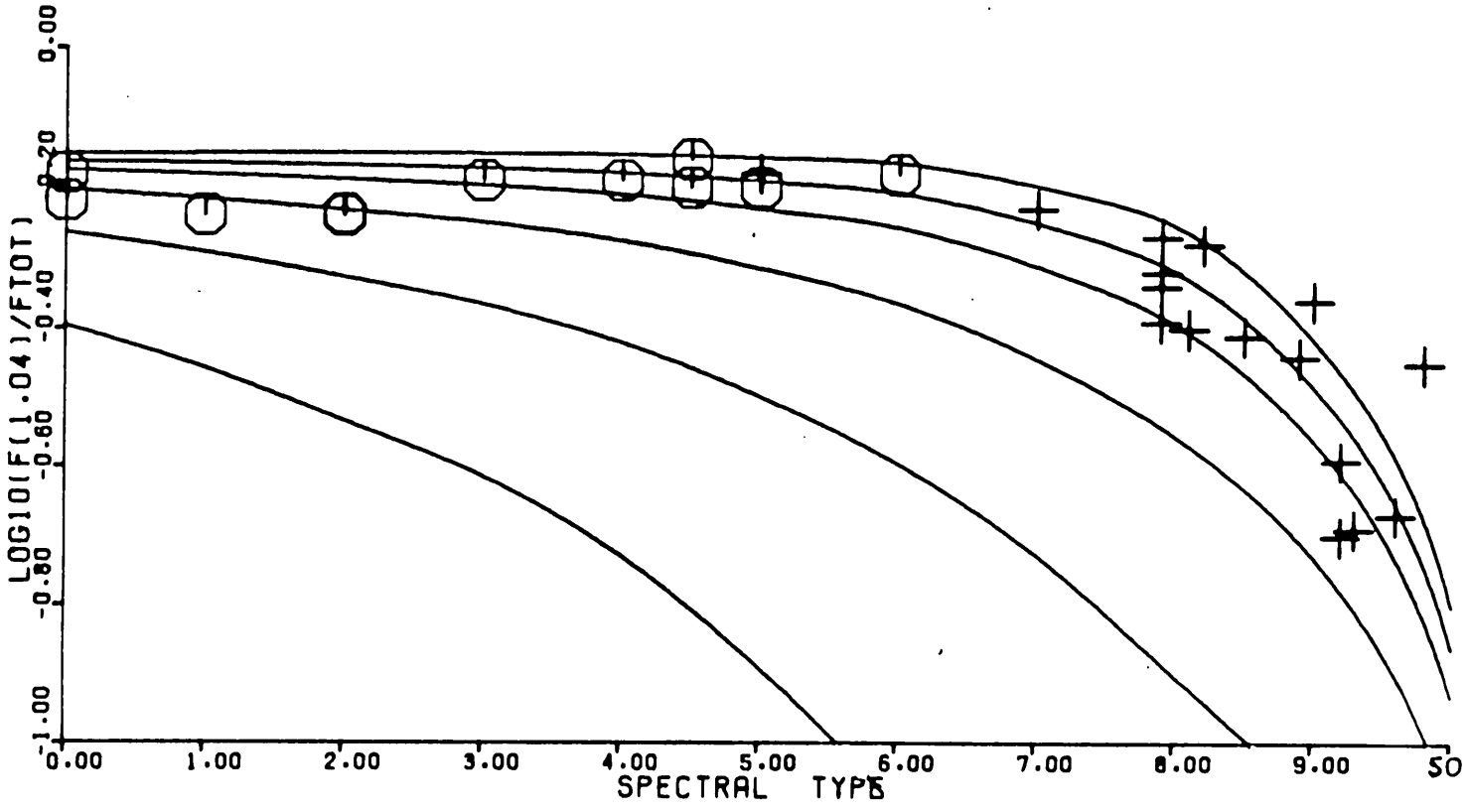

FIGURE 5.11b

IRON ABSORPTION CURVES COMPARED WITH RED GIANT (O) AND MIRA (+) DATA

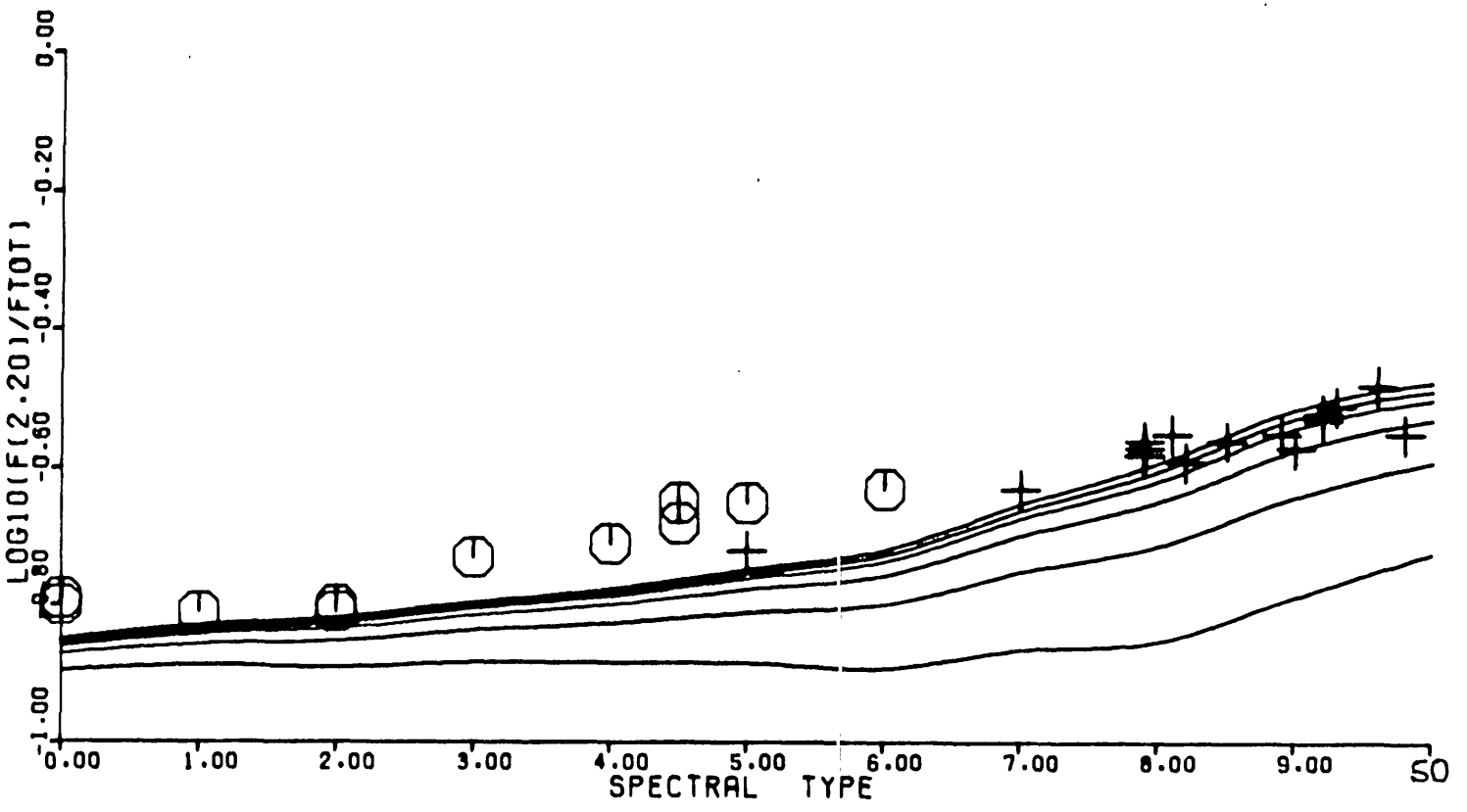

FIGURE 5.11c

IRON ABSORPTION CURVES COMPARED WITH RED GIANT (O) AND MIRA (+) DATA

where Sp is the spectral class (c.f. Sp = 5 for M5 stars). For mass loss rate we use

$$\frac{dM}{dt} = 5 \times 10^{-7} \cdot 2.512^{3+M_{BOL}} \; M_{\odot}.yr^{-1}$$

and assume thereby a straightforward extrapolation to very late types of the mass loss relation for earlier M type stars. M_{BOL} is the bolometric magnitude. Values for M_{BOL} are adapted from Allen (1973) and given in table 5.13. Finally, mass absorption coefficients are as given in the previous section.

TABLE 5.13

BOLOMETRIC MAGNITUDE FOR GIANTS*

SPECTRAL CLASS	M_{BOL}	SPECTRAL CLASS	M_{BOL}
M0	-2.00	M6	-3.30
M1	-2.20	M7	-3.80
M2	-2.35	M8	-4.30
M3	-2.50	M9	-4.80
M4	-2.70	S0	-5.30
M5	-3.00		

* THE TREND IS BASED ON THAT FOR MIRAS

Because of the low albedo of iron grains, multiple scattering is not unduly important over the range of spectral types of particular interest (the earlier M types); its effect however will be to cause the curves in figure 5.11 to represent increasingly significant lower limits to total absorption as very late spectral types are approached. The resulting curves are shown in figure 5.11 (this time, the lowest curve in each case). Intermediate curves represent varying degrees of

absorption, corresponding to fractional grain condensations $f = 10^{1-0.333i}$, i = 1 to 4 in increments of 1.

Taking the data in figure 5.11 as a whole, we may make the following points:

(i) Iron grains are potentially more than capable of explaining visible continuum depressions; this of course repeats the conclusion of the last section.

(ii) The trend of results at 0.55 μm is well represented by the theoretical curve.

(iii) The data at 1.04 μm, 2.2 μm, relatively less affected by TiO absorption than that at 0.55 μm, are remarkably well represented by the black body curves. In particular, there is no way of explaining absorption at 0.55 μm and the trend of results at 1.04 μm and 2.2 μm, in terms of any material such as iron (or graphite), or TiO opacity law such as Yamashita's (1962), having relatively slowly decreasing absorption coefficient with increasing wavelength. The absorption at visible wavelengths must, again, fall precipitously in the near red. This is the decisive result of this subsection.

5.21b Infrared Emission and Optical Absorption

The total emission from circumstellar iron grains is taken to be

$$E_G(\lambda) = \int_{r_c}^{\infty} 4\pi r^2 n(r) \cdot 4\pi a^2 Q_{em}(\lambda,a) \cdot E(\lambda,T_{gr})\, dr \qquad \ldots(5.72)$$

where we let

$$n(r) = n_c\left\{\frac{r_c}{r}\right\}^{\beta_n} = \text{number density of iron grains} \qquad \ldots(5.73)$$

Equation (5.72) is reasonably applicable providing A_V is small, grain albedo is low, and continuum excesses are restricted to the infrared.

"a", the grain radius, is assumed constant. Visual absorption is

$$A_V = 1.086 \int_{r_c}^{\infty} \pi a^2 Q_{abs}(\lambda_V)\, n_c \left(\frac{r_c}{r}\right)^{\beta_n} dr$$

$$= \frac{\pi a^2 Q_{abs}(\lambda_V)\, n_c\, r_c \cdot 1.086}{\beta_n - 1} \qquad (\beta_n > 1) \qquad \ldots(5.74)$$

and from the star, there is an emission component

$$E_*(\lambda) = 4 \pi r_*^2 E(\lambda, T_*)\, e^{-\tau(\lambda)} \qquad \ldots(5.75)$$

From 5.72 and 5.73

$$E_G(\lambda) = 16 \pi (\pi a^2 n_c)\, Q_{em}(\lambda)\, r_c^{\beta_n} \int_{r_c}^{\infty} \frac{E(\lambda, T_{gr})}{r^{\beta_n - 2}} dr$$

Excluding $\pi a^2 n_c$ using equation 5.74, and letting $Q(\lambda) = Q_n \lambda^{-\alpha_n}$ then gives

$$\frac{E_G(\lambda)}{A_V} = \frac{16 \pi (\beta_n - 1)}{1.086} \left(\frac{\lambda_V}{\lambda}\right)^{\alpha_n} r_c^{\beta_n - 1} \int_{r_c}^{\infty} \frac{E(\lambda, T_{gr})}{r^{\beta_n - 2}} dr$$

For iron $\alpha_n \simeq 2.33$, $T_{gr}(r) \simeq T_*/(2\frac{r}{r_*})^{0.34}$ and we use $\beta_n \simeq 2$. The integral is evaluated numerically, taking step lengths $\Delta r = 0.1\, r$. In this way, an appropriate terminal radius r_{TER} is rapidly achieved. Using the Wien relation $T_{gr} = 0.29/\lambda_{max}$, if λ_{TER} is the longest wavelength of interest, then

$$r_{TER} \simeq \frac{r_*}{2} \left\{\frac{T_*\, \lambda_{TER}}{0.29}\right\}^{1/0.34}$$

Figure 5.12 presents an example of the continuum behaviour of a star with circumstellar iron grains. It is clear that for any appreciable absorption, the infrared continuum is unacceptably raised and distorted. Total excess energy output is also significantly larger than typically observed. Any single grain type with strong visual absorption characteristics

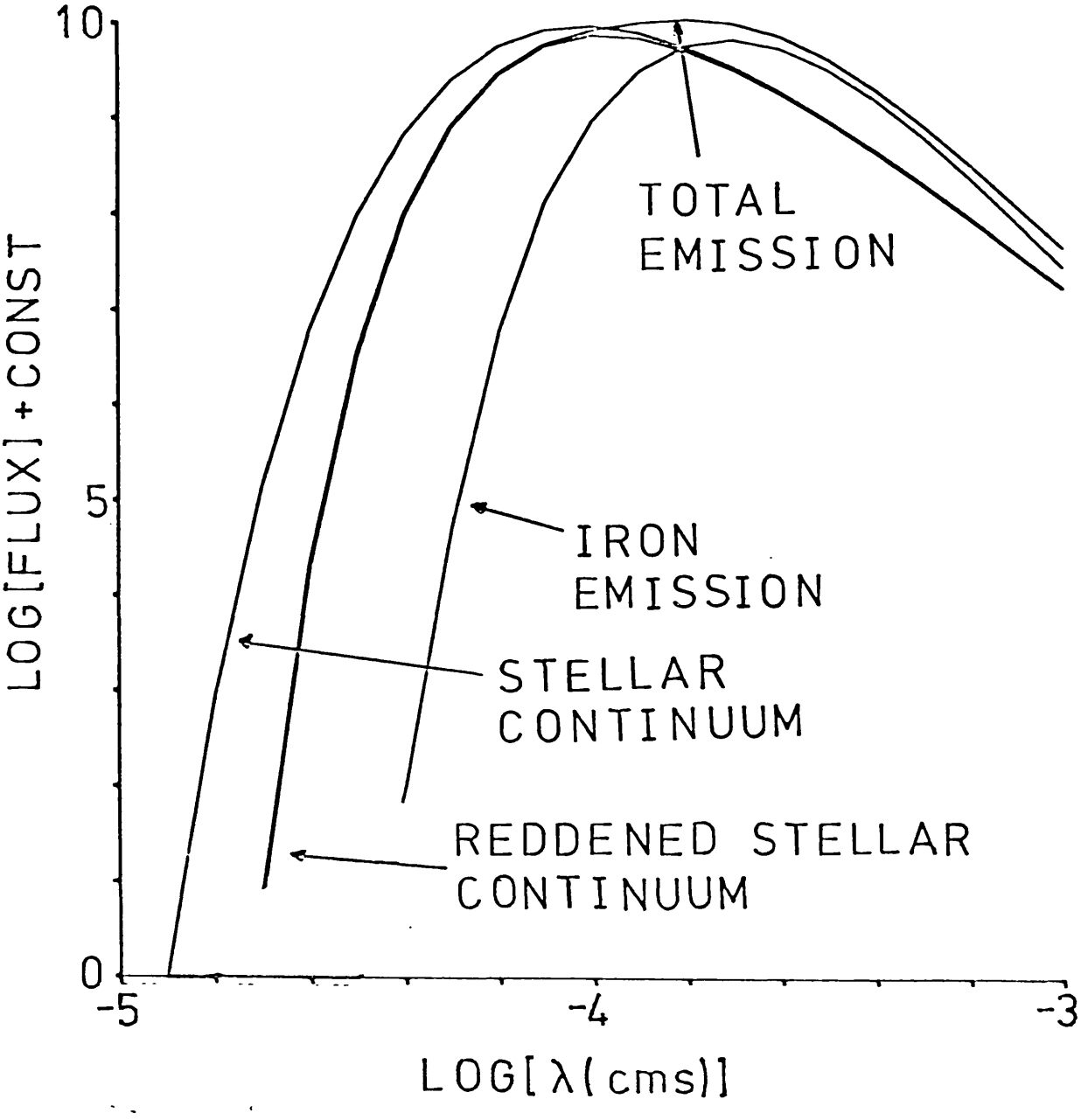

FIGURE 5.12

STELLAR CONTINUUM AND CIRCUMSTELLAR IRON GRAIN EMISSION. $A_V = 1.0$, $T_* = 3000$ K. THE INNER RADIUS LIMIT OF THE CIRCUMSTELLAR DUST SHELL $r_c = 12r_*$. THE LONG WAVE CONTINUUM DISTORTION, WHICH IS INSENSITIVE TO r_c, DIFFERS APPRECIABLY FROM OBSERVED CONTINUA.

must therefore have an absorbidity/emmissivity falling more rapidly than iron in the far red/near infrared; a conclusion in sympathy with the results of earlier sections.

5.22 The Observed Continua of Late-Type Stars

Three primary sources have been used to determine mean (reddened) continua of red giants and supergiants. The data for giants is from the UBVRIJKL photometry of Johnson, Mitchell, Iriate and Wiesnewski (1966) (herafter called J1), and the eight colour narrow band photometry of Johnson, Mitchell and Latham (1967) (J2). The latter catalogue gives photometry extending from the red (0.63 μm) to U.V. (0.33 μm), and therefore complements the infrared measures of J1. The data for supergiants was taken from Lee (1970) (L1). Only stars having spectral types between M0 and S0, and present in both J1 and J2 were used. Otherwise the data was treated similarly for both giants and supergiants.

The initial procedure is to separate data by luminosity and spectral class, and within each category average the colour indices, irrespective of reddening. The result is a series of average indices I_{XY}^{jk} for wavebands X, Y corresponding to spectral class j, luminosity class k

$$I_{XY}^{jk} = \frac{1}{n_{jk}} \sum_{i=1}^{n_{jk}} I_{XY}^{ijk}$$

where n_{jk} is the number of independent measurements in the luminosity/spectral class jk. For giants this is a normal procedure (c.f. Johnson 1966) to determine mean intrinsic indices, since reddening is generally taken to be small. For supergiants this operation differs from normal procedures because of the substantially increased interstellar reddening.

These indices are dependent upon the absolute energy standard used, usually defined such that its magnitude at all wavelengths is zero. J1 and J2 provide appropriate data to construct a composite standard covering their entire data. We shall first illustrate the departure of this mean (red giant) data from appropriate black body extrapolations.

TABLE 5.14

RED GIANT COLOUR INDICES

SPECTRAL TYPE	n_{jk}	33-K	35-K	U-K	37-K	40-K	B-K	45-K	52-K	V-K	58-K	63-K	R-K	I-K	J-K
M0III	11	7.63	7.19	7.33	7.25	6.59	5.41	4.92	4.28	3.84	3.49	3.03	2.59	1.62	0.98
M1III	4	7.95	7.48	7.57	7.52	6.84	5.63	5.19	4.43	4.01	3.65	3.15	2.67	1.64	1.02
M2III	8	8.03	7.57	7.67	7.59	6.95	5.76	5.18	4.57	4.16	3.81	3.30	2.80	1.68	1.04
M3III	11	8.51	8.02	8.12	7.99	7.39	6.28	5.82	5.04	4.66	4.36	3.78	3.29	1.83	1.10
M4III	2	9.15	8.53	8.58	8.39	7.77	6.84	6.41	5.55	5.22	4.97	4.29	3.48	1.92	1.12
M5III	2	9.89	9.05	5.91	8.83	8.03	7.45	7.16	6.19	5.82	5.69	4.87	3.86	2.05	1.20

The data is presented in table 5.14, together with the number of stars (n_{jk}) used to determine the average. For comparison with standard black body indices, however, it is convenient to revise this data to correspond to a new 10^4 K black body standard. To determine the appropriate modifications we note that

$$I_{XY} = -2.5 \log \left\{\frac{I_{X,T_*}}{I_{Y,T_*}} \cdot \frac{S_Y}{S_X}\right\}$$

$$= -2.5\left\{\log \left\{\frac{I_{X,T_*}}{I_{Y,T_*}} \cdot \frac{I_{Y,10^4K}}{I_{X,10^4K}}\right\}\right.$$

$$\left. + \log \left\{\frac{I_{X,10^4K}}{I_{Y,10^4K}} \cdot \frac{S_Y}{S_X}\right\}\right\}$$

$$= I'_{XY} - 2.5 \log \left\{\frac{I_{X,10^4K}}{I_{Y,10^4K}} \cdot \frac{S_Y}{S_X}\right\}$$

where S_X, S_Y are the intensities of the old standard.

I'_{XY} is the new index, giving the magnitude difference between spectral bands X and Y, and I_{XY} is the measured index. The requisite corrections to the spectral indices I_{XY} ($I_{COR} = 2.5 \log \left(\frac{I_{X,10^4K}}{I_{Y,10^4K}} \cdot \frac{S_Y}{S_X}\right)$) are given separately in table 5.15. Comparative indices for the black body curves are determined from

$$I^{BB}_{XY} = -2.5 \log \left\{\frac{B(\lambda=X,T_*)}{B(\lambda=Y,T_*)} \cdot \frac{B(\lambda=Y,10^4K}{B(\lambda=X,10^4K)}\right\}$$

where $B(\lambda,T)$ is the Planck function, and T_* is the stellar effective temperature. The values derived by Dyck et al. and given in table 5.10 are again used.

TABLE 5.15

INDEX	JOHNSON ET AL. (1966, 1967)*	10^4K B.B.*	$I'_{XY}-I_{XY}$
33-K	85.38	157.4	0.664
35-K	90.00	151.0	0.562
36-K	111.5	147.4	0.302
37-K	129.2	143.5	0.114
40-K	198.2	131.0	-0.450
44-K	184.6	114.0	-0.523
45-K	161.8	109.9	-0.420
52-K	108.2	83.97	-0.371
55-K	100.5	74.57	-0.324
58-K	85.13	66.22	-0.273
63-K	63.85	54.41	-0.174
R-K	45.13	41.58	-0.089
I-K	21.28	20.43	-0.044
J-K	8.72	7.21	-0.206
K-K	1.00	1.00	0.000

*Intensities relative to K

The revised data is first presented for each spectral type up to M5 as a straight plot of respective black body and stellar magnitude versus wavelength (the K result being arbitrarily set as zero) (figure 5.13). Filled circles represent the results of wide band photometry, unfilled circles are narrower band results from J2. The distinct and increasing deviation of the continuum results with decreasing wavelength and advancing spectral type will be noted. A U.V. depression occurs in the vicinity of the Balmer discontinuity at 0.3646 μm. The trend of the data with wavelength is evocative of the anticipated trends if a dust continuum source similar to iron were significant, and the substantial increase in the departure from

FIGURE 5.13a

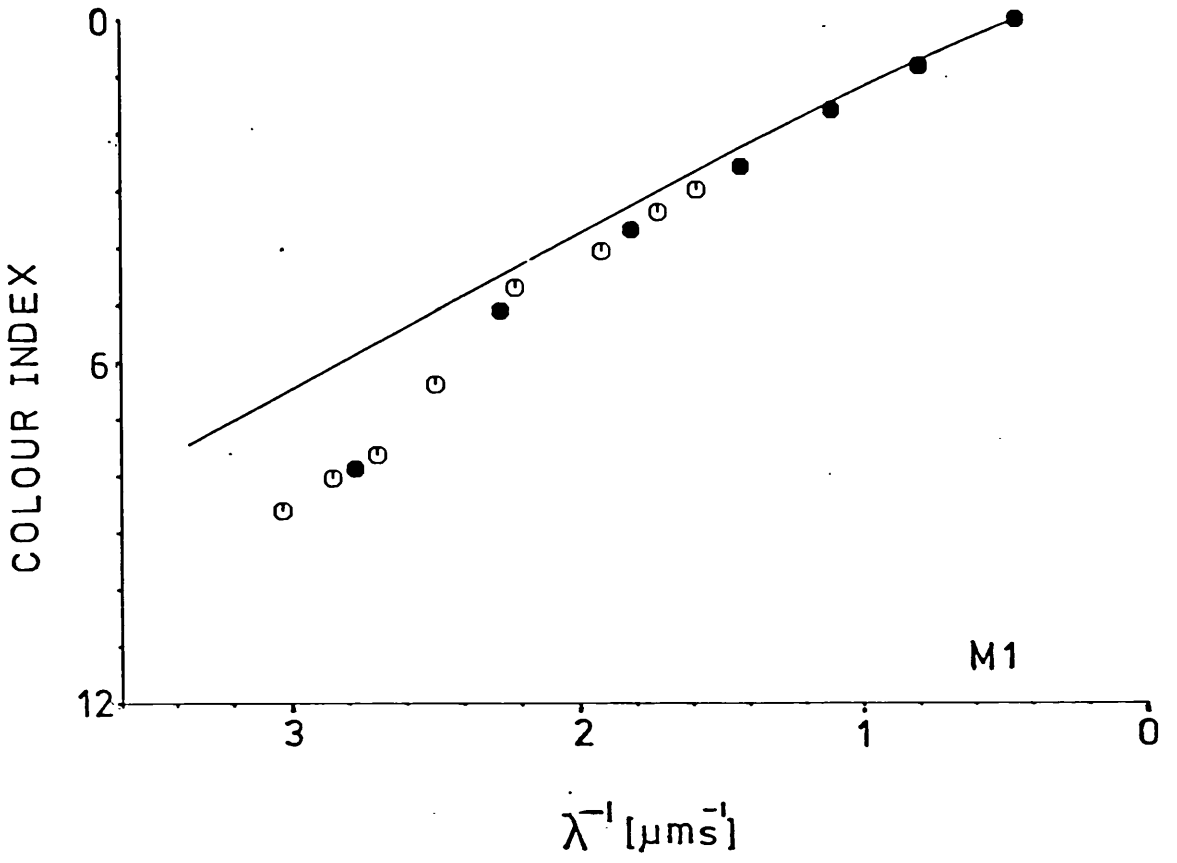
0
6
12
COLOUR INDEX
M1
3
2
1
0
λ⁻¹ [μms⁻¹]

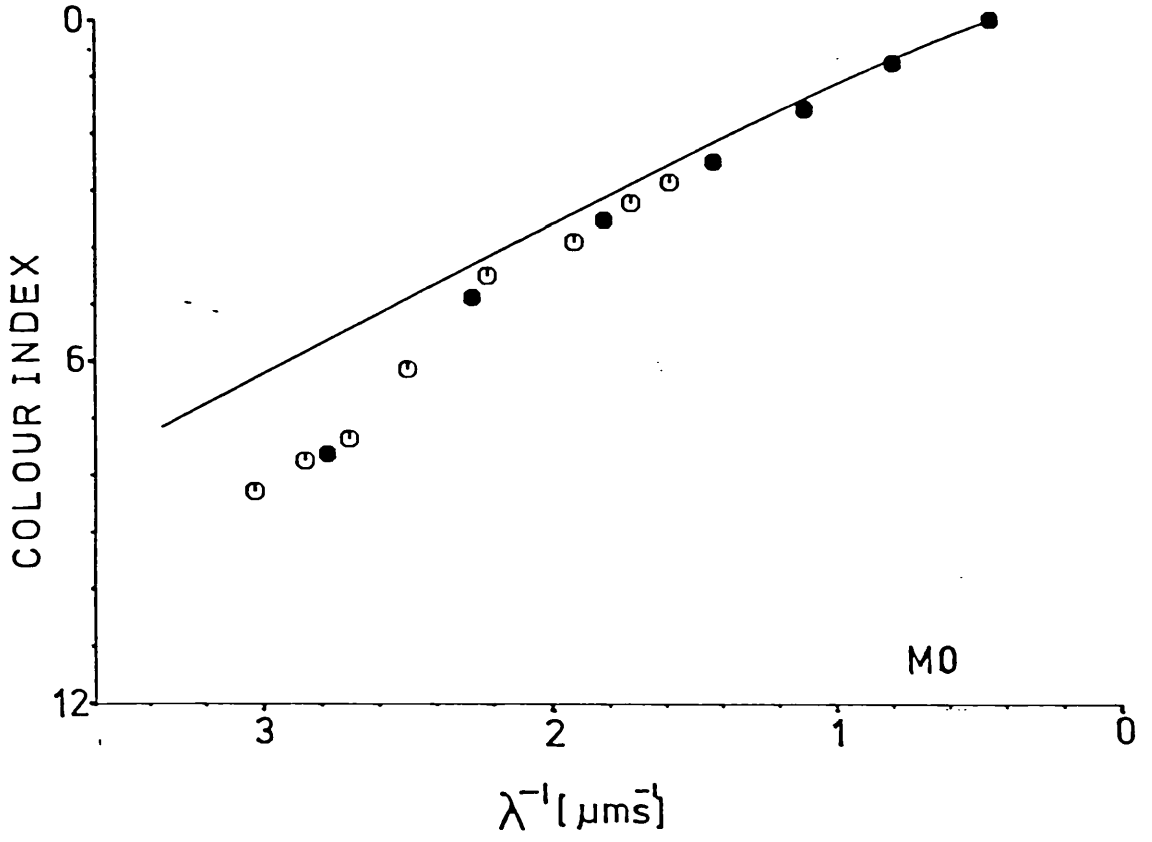
0
6
12
COLOUR INDEX
M0
3
2
1
0
λ⁻¹ [μms⁻¹]

FIGURE 5.13b

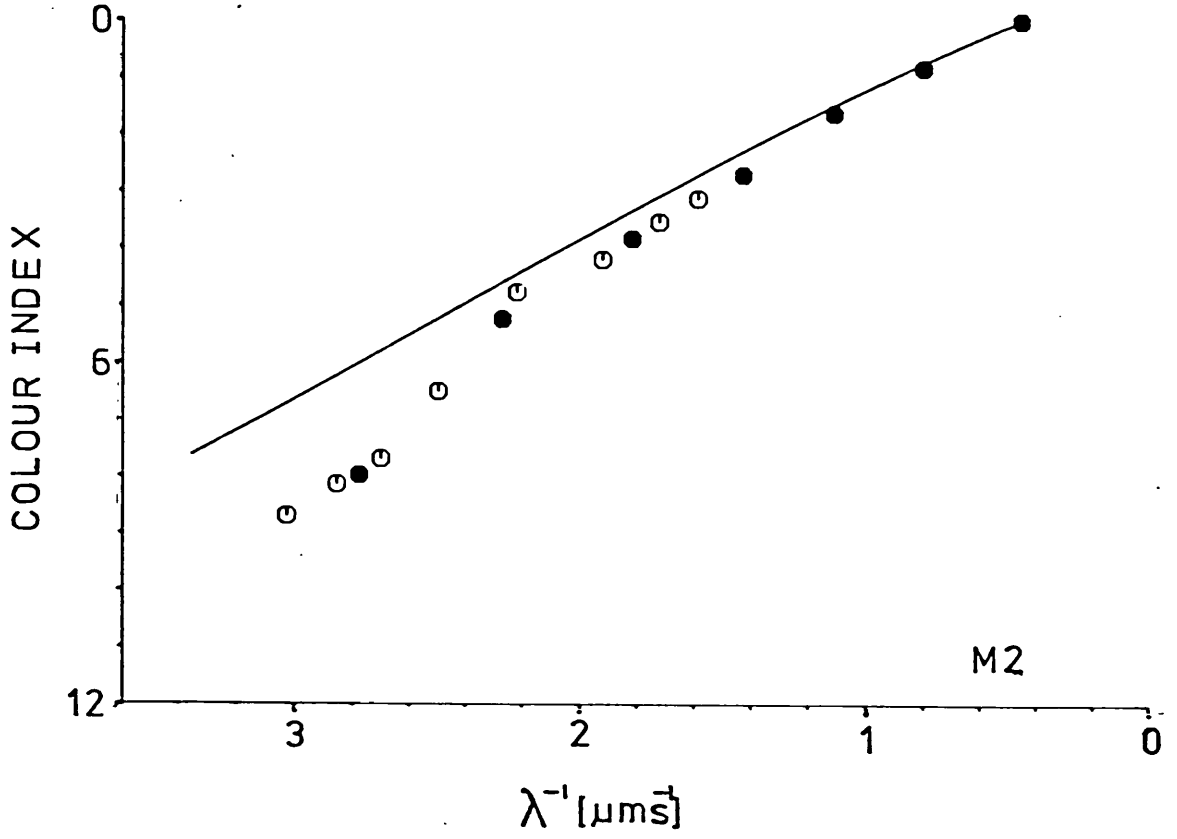
0
6
12
COLOUR INDEX
M2
3
2
1
0
λ⁻¹ [μms⁻¹]

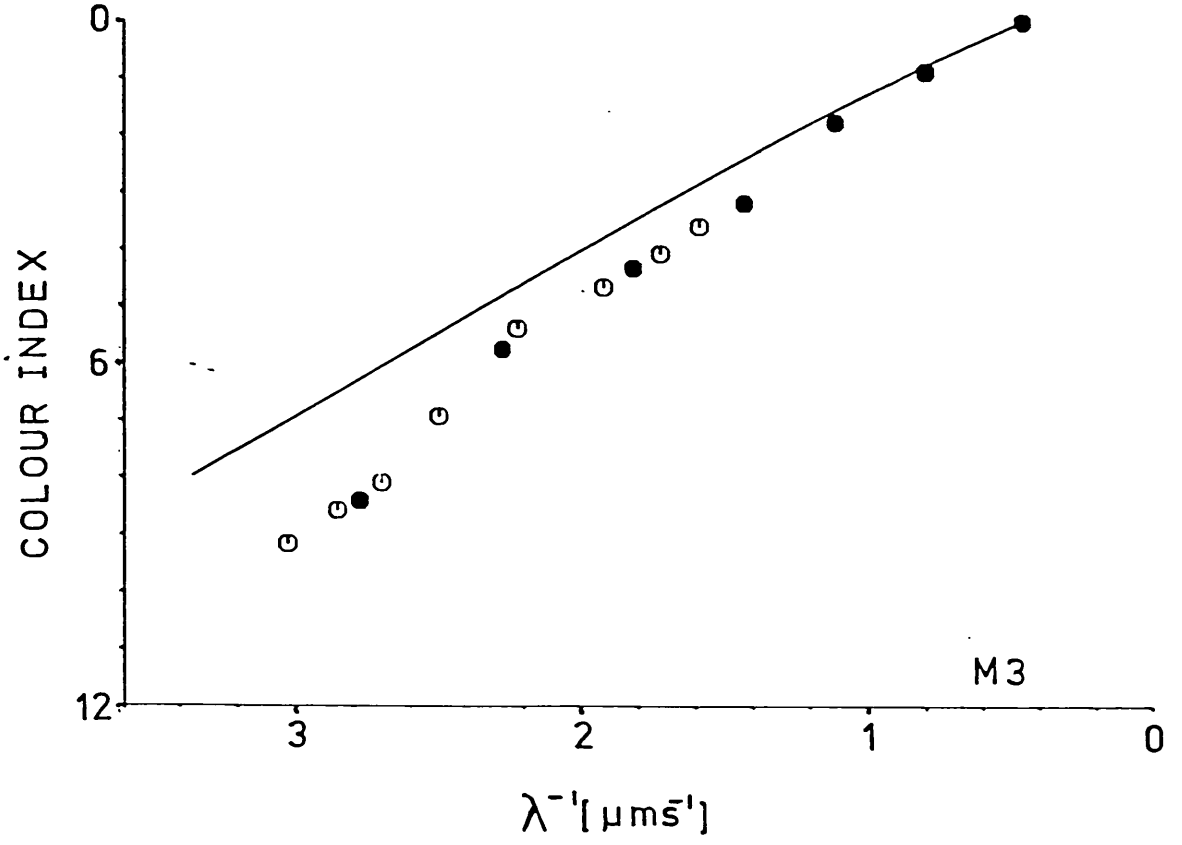
0
6
12
COLOUR INDEX
M3
3
2
1
0
λ⁻¹ [μms⁻¹]

FIGURE 5.13c

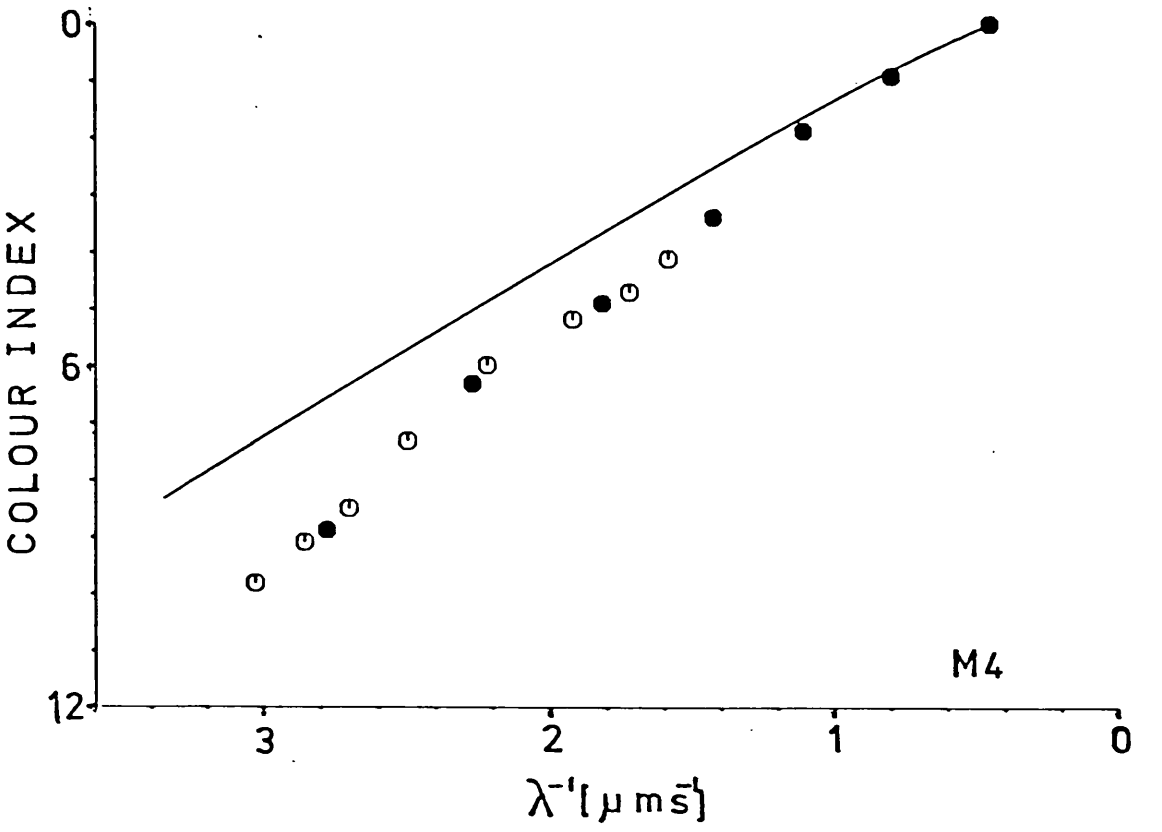
0
6
12
COLOUR INDEX
M4
3
2
1
0
λ⁻¹[μms⁻¹]

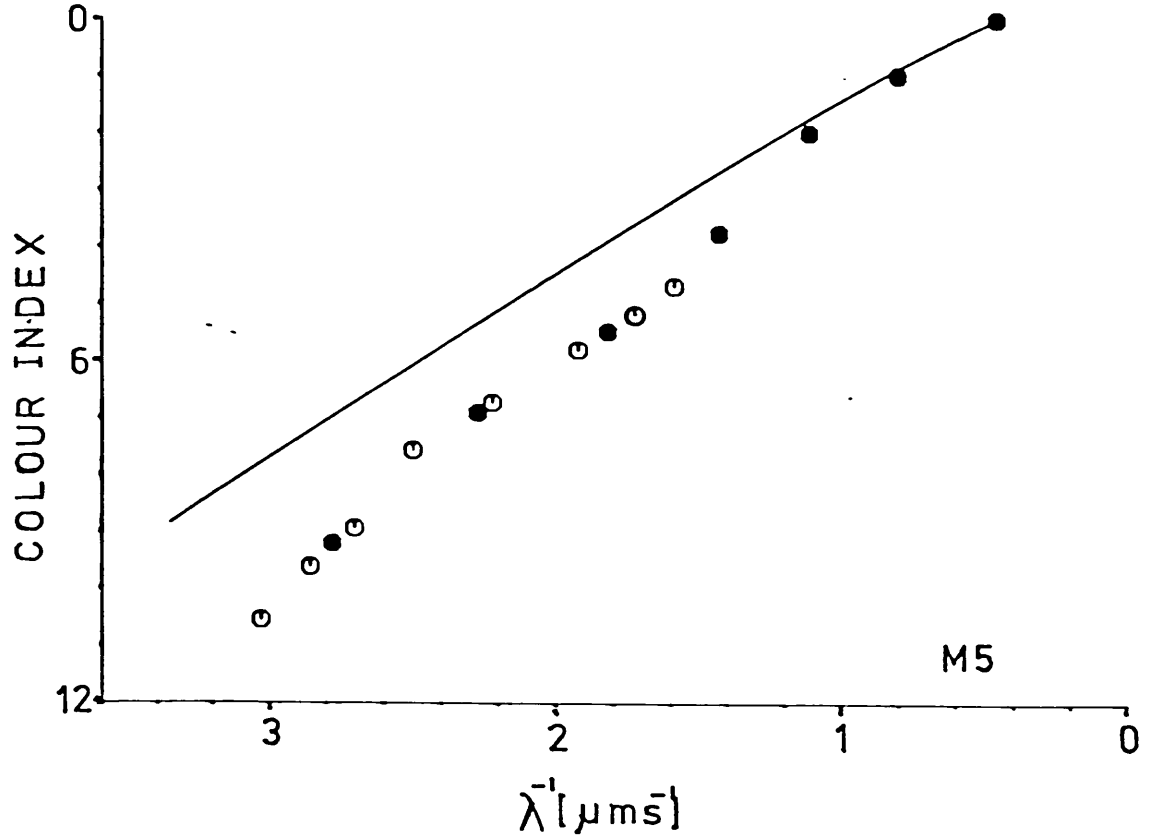
0
6
12
COLOUR INDEX
M5
3
2
1
0
λ⁻¹[μms⁻¹]

black body behaviour at about M4-M5 also correlates with the substantial establishment of mass loss in these spectral types (Deutsch 1960). These trends are seen more clearly if the difference between the black body extrapolations and stellar continua are plotted separately, as in figure 5.14, where we have also fitted the data with a comparative function

$$\mathfrak{n}_{XY} = \mathfrak{n}_{XY,\ MO} + \mathfrak{n}_{XY,\ IRON}$$

normalised so that the curve fits first and last data points. $\mathfrak{n}_{XY,\ MO}$ is the deviation of index I_{XY} from the black body index I_{XY}^{BB} for MO stars, where under any circumstances circumstellar absorption is expected to be small. $\mathfrak{n}_{XY,\ IRON}$ is absorption due to iron, a contribution which is varied to meet the conditions of normalisation. It is clear that the curves match observations only tolerably well. In particular, there is a very sharp increase in absorption between 0.6 μm and 0.7 μm.* It should be noted that increasing stellar luminosity with spectral type will not affect the median distance of later spectral types enough for us to attribute any significant absorption continuum to the interstellar medium.

Atomic line blanketting of Fay and Johnson (1973), as applied to α Ori, would lead to a roughly linear increase in magnitude discrepancies with λ^{-1}. TiO opacity has been considered by Yamashita (1962), Fujita (1970), Tsuji (1969) and most recently by Tsuji (1971), Collins and Fay (1974), and Mould (1976). Yamashita finds opacity $\propto \lambda^{-2.5}$, from $\lambda \sim 0.3$ μm to $\lambda > 1$ μm. Tsuji (1971) uses a Voight-analogue-Elsasser band model due to Golden (1969), to find an opacity maximum between $\lambda \sim 0.6$ μm and $\lambda \sim 0.7$ μm, but declining rapidly towards longer and shorter wavelengths (for $T = 2100$ K). The results of Collins and Fay (1974) and Mould (1976) are broadly similar.

---

* confirming the results of Dyck, Lockwood and Capps (1974)

FIGURE 5.14

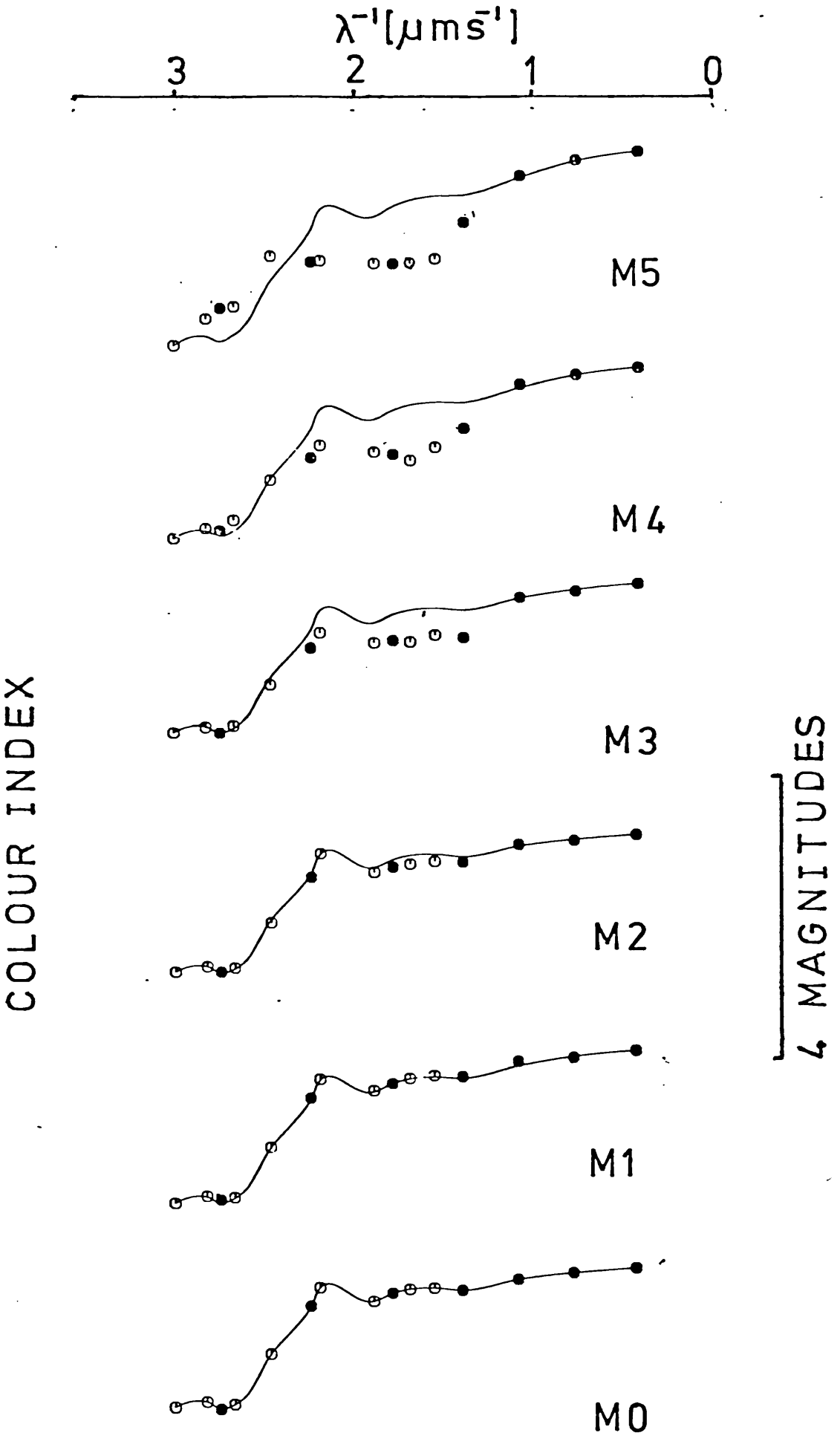

Whether more sophisticated procedures for assessing opacities, and full atmospheric modelling will explain the observed departures from a simple black body continuum relation remains to be seen. The results of Tsuji (1971), Collins and Fay (1974), and Mould (1976) in particular suggest that TiO absorption cannot yet be dismissed as a primary opacity source, although the general agreement with present results is only tolerably good.

The requirement that the discrepancies be explained in terms of a single grain type places severe constraints upon the available candidates, although the observed continuum deviations are in satisfactory agreement with the requisite constraints determined earlier. Few grains developing from a single condensate material seem likely to fill this rôle. A single composite grain seems likely to require a siliceous component to explain the wavelength variability of infrared excesses. In terms of C/O ratio, elemental abundance, and requisite visual absorption properties, iron is another primary choice for a component material - although many other less abundant condensates (c.f. other metals) will possess similar absorption properties, and may be regarded in preference.

The only published data for iron core, silicate mantle grains appears to be due to Wickramasinghe (1973). Selected curves of the scattering and extinction coefficients taken from this reference are presented in figure 5.15. The absorption coefficient is the difference between these curves, and is seen to be typically large at visual wavelengths, but to decline rapidly towards the infrared. As we have already noted, the presence of such grains may greatly alleviate certain problems associated with grain sublimation, and silicate nucleation.

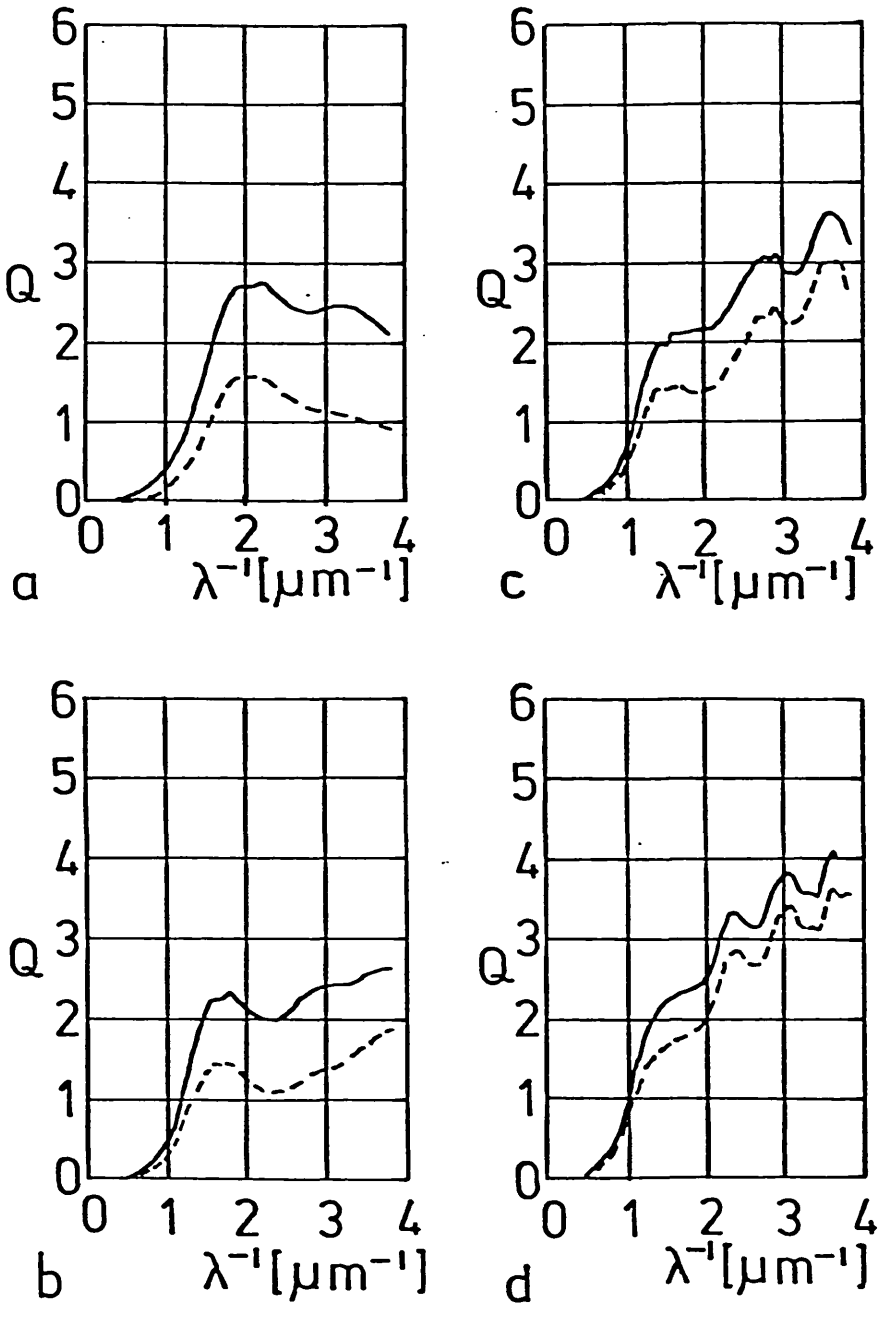

FIGURE 5.15

OPTICAL PROPERTIES OF SILICATE MANTLE - IRON CORE GRAINS. LOWER DASHED CURVES, Q_{SCA}. UPPER SOLID CURVES, Q_{EXT}. a. r_m/r_c = 1.5; b. r_m/r_c = 2.0; c. r_m/r_c = 2.5; d. r_m/r_c = 3.0 r_c = 0.06 μm

The curves in figure 5.15 are for a core radius $r_{CORE} = 0.06$ μm. It is apparent that an increasing value of r_{MANTLE}/r_{CORE} leads to an increasingly sharp absorption depreciation rate in the far red. The observed results for giants, and in particular supergiants (see later) probably imply $r_{MANTLE}/r_{CORE} \gtrsim 2$. Reducing the core radius further leads to a reduction in the wavelength of significant absorption inception, and for $r_{CORE} = 0.03$ μm this occurs at $\lambda \simeq 0.4$ μm. The grains must therefore have $r_{MANTLE} \gtrsim 0.1$ μm, $r_{CORE} \simeq 0.05$ μm. An additional point of interest from the data of Wickramasinghe is that the rapidity of the absorption cut-on depends fairly sensitively upon mantle refraction index; an ice mantle ($m \simeq 1.3$) being in this respect far less effective than a silicate mantle ($m \simeq 1.6$, the illustrated case).

To assess supergiant extinction, the data of Lee (1970) has been averaged in accordance with the procedures outlined earlier. This is presented in table 5.16. Reddening is determined by subtracting intrinsic indices (Lee 1970). We will designate total extinction by $A^{j,k}_{X-Y}$, following the example of the colour indices, where j, k are again the spectral, luminosity class. An evaluation of the circumstellar component was then made by subtracting an interstellar component a^{IS}_{X-Y}:

$$A^{j,k,cs}_{X-Y} = A^{j,k}_{X-Y} - Z^{j,k}\, a^{IS}_{X-Y}$$

where $Z^{j,k}$ is such that some fixed index ($A^{j,k,cs}_{X-Y}$) has a constant value (in practice, values $A^{j,k,cs}_{U-L} = 0.5$, 1 magnitude were tried). The results for luminosity class I stars of various spectral types are shown in figure 5.16. The Johnson (1968) Cygnus curve has been adopted for a^{IS}_{X-Y}.

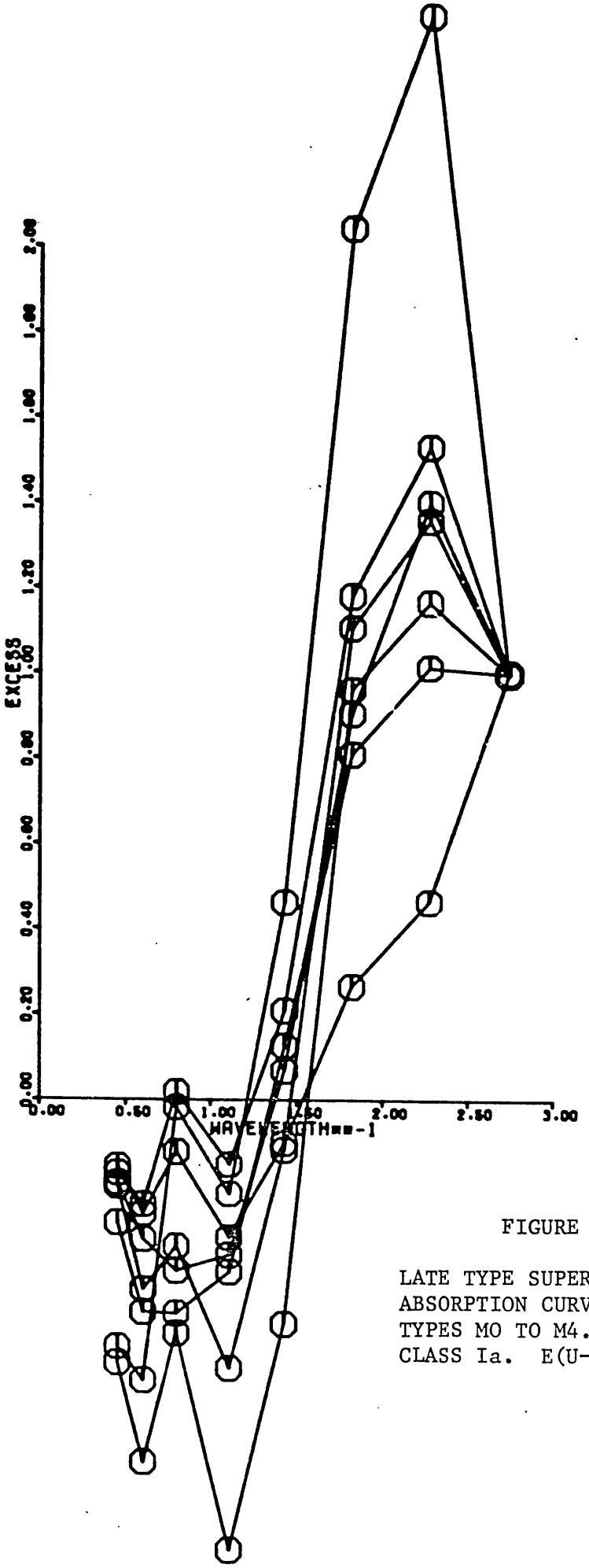

FIGURE 5.16a

LATE TYPE SUPERGIANT RESIDUAL ABSORPTION CURVES. SPECTRAL TYPES M0 TO M4. LUMINOSITY CLASS Ia. E(U-L) = 0.5.

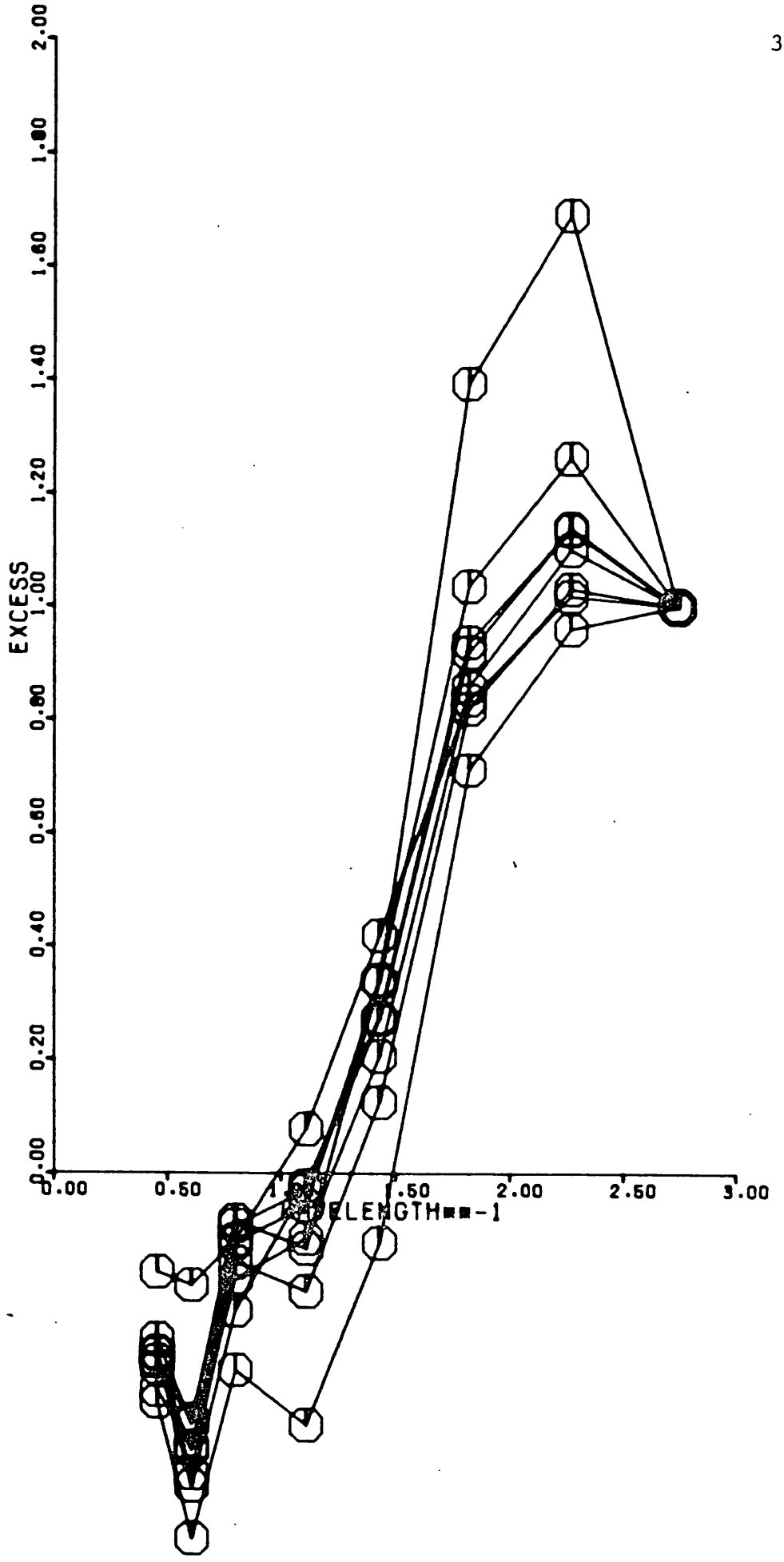

FIGURE 5.16b

LUMINOSITY CLASS Ib+Iab. E(U-L) = 0.5

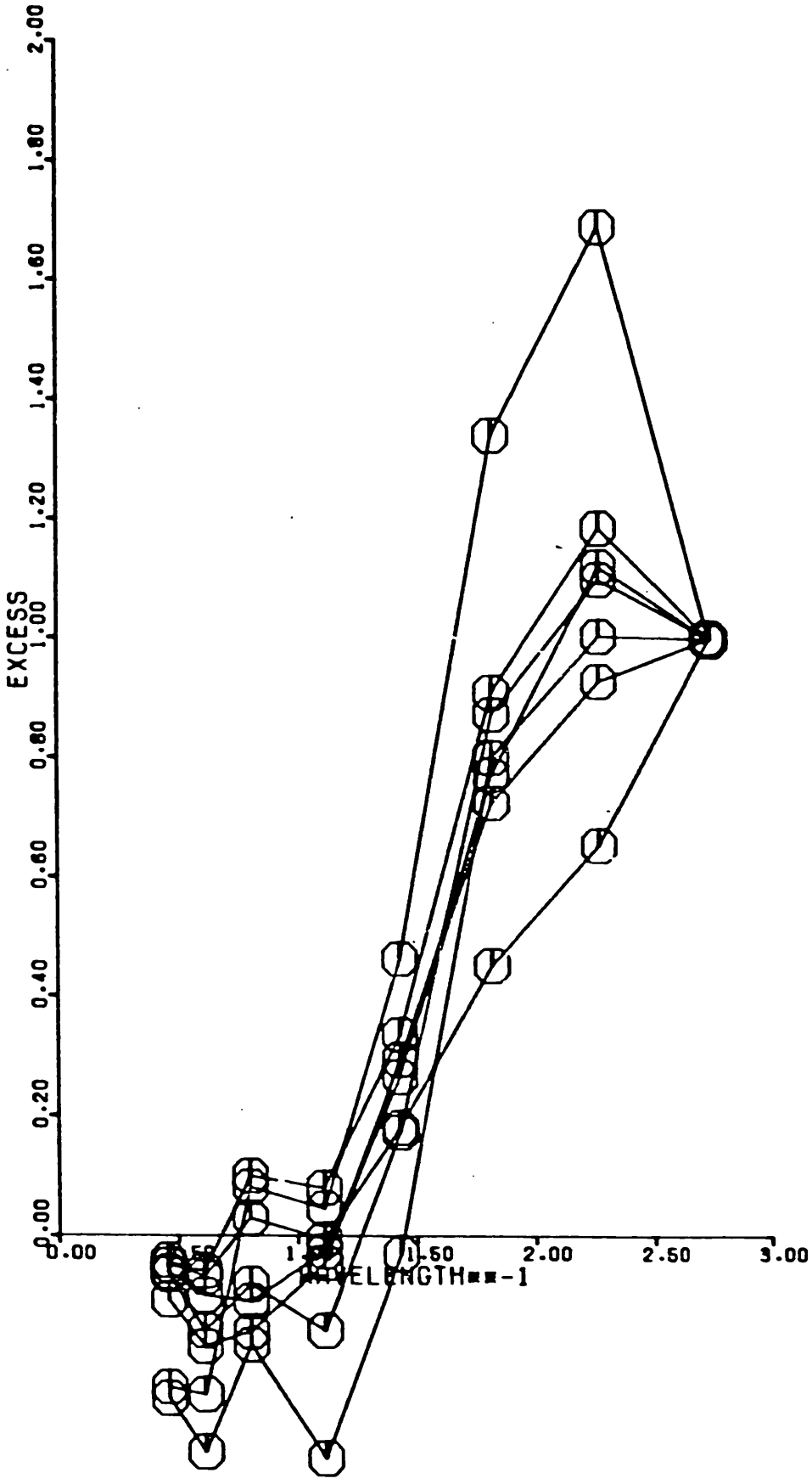

FIGURE 5.16c

LUMINOSITY CLASS Ia E(U-L) = 1.0

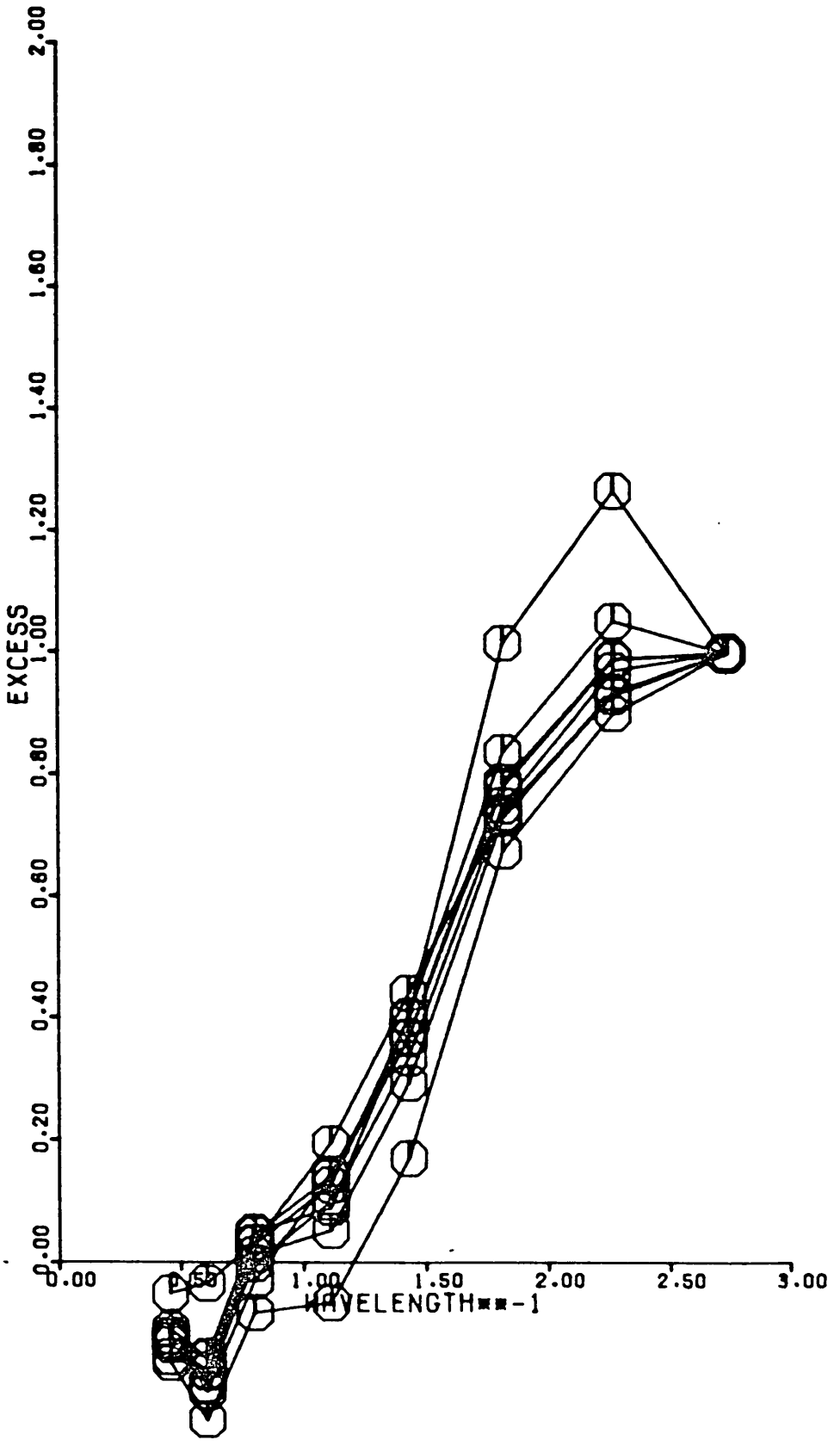

FIGURE 5.16d

LUMINOSITY CLASS Ib+Iab E(U-L) = 1.0

TABLE 5.16

SUPERGIANT REDDENED COLOUR INDICES

SPECTRAL TYPE	LUMINOSITY CLASS	n_{jk}	U-L	$\frac{B-L}{U-L}$	$\frac{V-L}{U-L}$	$\frac{R-L}{U-L}$	$\frac{I-L}{U-L}$	$\frac{J-L}{U-L}$	$\frac{H-L}{U-L}$	$\frac{K-L}{U-L}$
M4	I	2	13.77	0.854	0.681	0.433	0.260	0.168	0.077	0.040
M3.5	Ia	3	15.73	0.828	0.631	0.408	0.239	0.153	0.071	0.035
M3.5	Ib+Iab	4	12.90	0.816	0.620	0.411	0.247	0.155	0.067	0.035
M3.5	I	7	14.12	0.822	0.625	0.409	0.245	0.154	0.069	0.035
M3.0	Ia	2	13.50	0.826	0.626	0.408	0.241	0.156	0.076	0.042
M3.0	Ib+Iab	4	12.79	0.838	0.636	0.423	0.257	0.164	0.074	0.037
M3.0	I	6	13.03	0.834	0.633	0.419	0.252	0.162	0.075	0.039
M2.5	Ia	1	13.13	0.826	0.619	0.414	0.257	0.168	0.083	0.043
M2.5	Ib+Iab	2	11.42	0.806	0.606	0.409	0.255	0.155	0.063	0.032
M2.5	I	3	11.99	0.813	0.611	0.410	0.256	0.160	0.070	0.037
M2.0	Ia	3	12.39	0.799	0.593	0.401	0.243	0.152	0.071	0.037
M2.0	Ib+Iab	12	12.05	0.798	0.593	0.399	0.249	0.159	0.068	0.035
M2.0	I	15	12.12	0.798	0.593	0.399	0.248	0.158	0.068	0.035
M1.5	Ia	1	13.90	0.814	0.597	0.403	0.251	0.151	0.080	0.043
M1.5	Ib+Iab	9	11.70	0.804	0.595	0.403	0.253	0.157	0.064	0.032
M1.5	I	10	11.92	0.806	0.596	0.403	0.253	0.157	0.066	0.034
M1.0	Ia	1	10.49	0.764	0.550	0.382	0.234	0.153	0.063	0.034
M1.0	Ib+Iab	5	11.55	0.795	0.581	0.394	0.248	0.152	0.059	0.028
M1.0	I	6	11.37	0.790	0.576	0.391	0.246	0.152	0.059	0.029
M0.5	Ib+Iab	1	9.61	0.780	0.566	0.391	0.248	0.152	0.061	0.028
M0.0	Ia	1	14.33	0.853	0.630	0.416	0.259	0.165	0.068	0.031
M0.0	Ib+Iab	3	11.49	0.795	0.580	0.396	0.254	0.158	0.063	0.030
M0.0	I	4	12.20	0.811	0.594	0.402	0.256	0.161	0.065	0.030

Despite procedural distortions in the curves (it seems likely for instance that $A_{U-L}^{j,k,cs} > 1$ magnitude for the brighter stars), it is clear that absorption may decrease with increasing wavelength much more slowly to the R band than is the case for interstellar absorption. Between R and I however the decline in absorption is precipitous.

Similar results are obtained using the van de Hulst curve no. 15 (van de Hulst 1949), and Johnson (1968) Perseus reddening curve. There is therefore very strong evidence of an anomalous, variable reddening component in late type supergiants, with features reminiscent of opacity sources in M4, M5 type giants, and the postulated properties required of grains with significant optical absorption. If it is assumed that the reduction in extinction present for certain spectral classes, in passing from B to U bands is purely a consequence of the procedure employed, it is evident that certain M4I stars have anomalous components A_V in excess of 2 magnitudes. More typically, the absorption has a value $A_V \simeq 1$ magnitude, and is therefore comparable to excess extinction levels noted by Lee (1970). The consequences of this would be wide ranging. Such behaviour for instance explains the results obtained when Humphreys et al. (1972) attempted to deredden the Carina supergiant data. The expected relation between A_V, and a 10.5 μm silicate excess with 3 μm bandwidth may also be assessed. Using the relations

$$A_{\lambda}^{j,k,cs} = 0.58\, Z^{j,k}\, (\lambda^{-2} - 1.56) \qquad 1.56 < \lambda^{-2} < 3.3$$

$$A_{\lambda}^{j,k,cs} = Z^{j,k}\, (0.086\, (\lambda^{-2} - 3.3) + 1) \qquad \lambda^{-2} \gtrsim 3.3$$

$$A_{\lambda}^{j,k,cs} = 0 \qquad \lambda^{-2} \leq 0.7$$

(λ in μms)

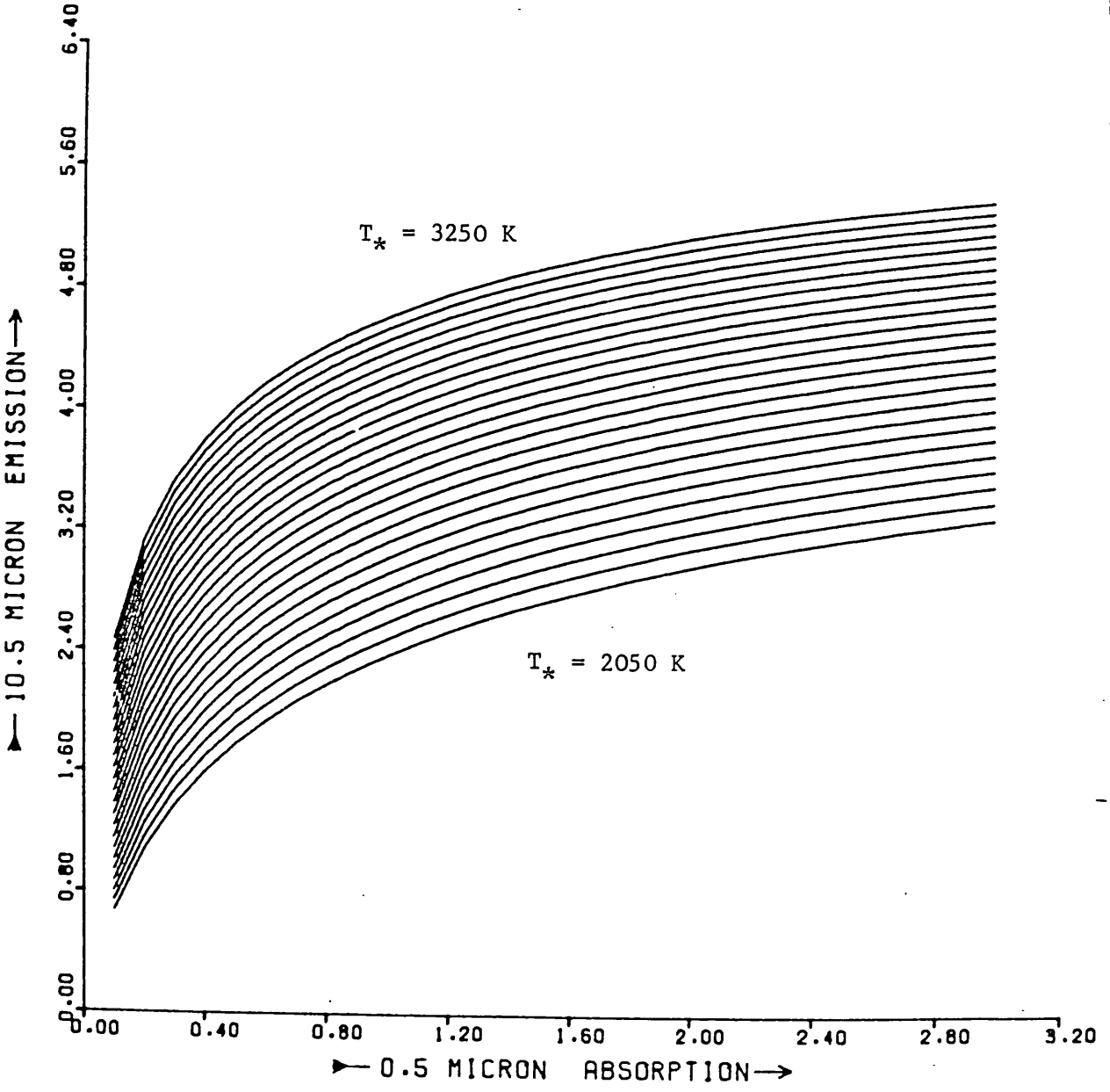

FIGURE 5.17

10.5 μm SILICATE EMISSION RESULTING FROM
TYPICAL SUPERGIANT ANOMALOUS EXTINCTION

based on figure 5.16, the graph in figure 5.17 is determined. $Z^{j,k}$ is a constant for a particular j,k. It is seen that for a modest infrared excess of the kind observed in giants and supergiants (figure 5.3), optical absorption acquires the values typically present in the form of anomalous extinction.

Finally, the possibility of variable anomalous extinction in supergiant stars is not only of relevance to stellar atmospheric modelling, but may have repercussions upon derivative data. An obvious example would be in our understanding of interstellar absorption over large distances determined from supergiant reddening data, and our consequent understanding of local galactic structure. It is a clear consequence of circumstellar reddening in these stars that the sun should appear to be uniquely placed in an interstellar "hole", with extinction rising rapidly in the immediate vicinity and in practically all directions, thereto varying much less over larger distances. This behaviour corresponds closely to the observed situation (Lee 1970).

5.23 Preliminary Conclusions Regarding Optical Continuum Absorption in Late Type Stars

We have shown that red supergiants possess a variable component of optical extinction which is both strong and anomalous. This extinction also appears to be present in giants later than M4. Such extinction would introduce errors when assessing intrinsic supergiant continua by applying standard dereddening procedures, and may also be responsible for distortions in the derived spatial properties of interstellar reddening. Whilst molecular opacity may be responsible, a plausible absorption source is shown to be composite iron/silicate

grains. Such grains would give the observed infrared excesses, optical absorption levels, and wavelength variability of absorption. They would also be plausible in terms of the observed O/C ratio, abundances, and mass loss rates. Their future investigation may enable the solution of problems connected with mass loss in red supergiants/giants, and silicate condensation.

APPENDIX 1

OPTICAL ABSORPTION IN IRC AND CARBON STARS

Evidence indicating the possibility of appreciable visible circumstellar absorption in certain IRC stars (very late type M giants) and carbon stars is noted.

A graph of the flux ratios $F_{0.78}/F_{1.04}$ versus $F_{10.2}/F_{2.2}$ for M9 stars alone (reducing thereby the uncertainties introduced by spectral classes) is given in figure A1.1, from data in Dyck et al. (1974). Optical band absorption is weakly correlated with increasing infrared excesses, and this can be reasonably explained in terms of extinction by circumstellar dust. The most obvious alternative is to suppose a relation between molecular absorption and the prevalence of dust (assuming of course that dust is responsible for the I.R. excesses). The trend in $F_{10.2}/F_{2.2}$ is clearly a consequence of infrared excesses, whose prevalence and size appear to rapidly develop between M8 and SO (see figure 2 of Dyck et al. 1974 illustrating the behaviour of the excess continua).

A similar result for carbon stars follows using the U band data of Mendoza and Johnson (1965), and infrared data of Gillet et al. (1971). Gilra (1973), using the same data, has plotted M - [8.4] against U-B to obtain a correlation which, he suggests, could be explained in terms of an increasing C_3 absorption dip at 4.9 μm. In fact, this appears to be untenable. To demonstrate this, we first present a slightly differing plot from Gilra's (figure A1.2), illustrating [11] - L versus U-L, which again indicates particularly

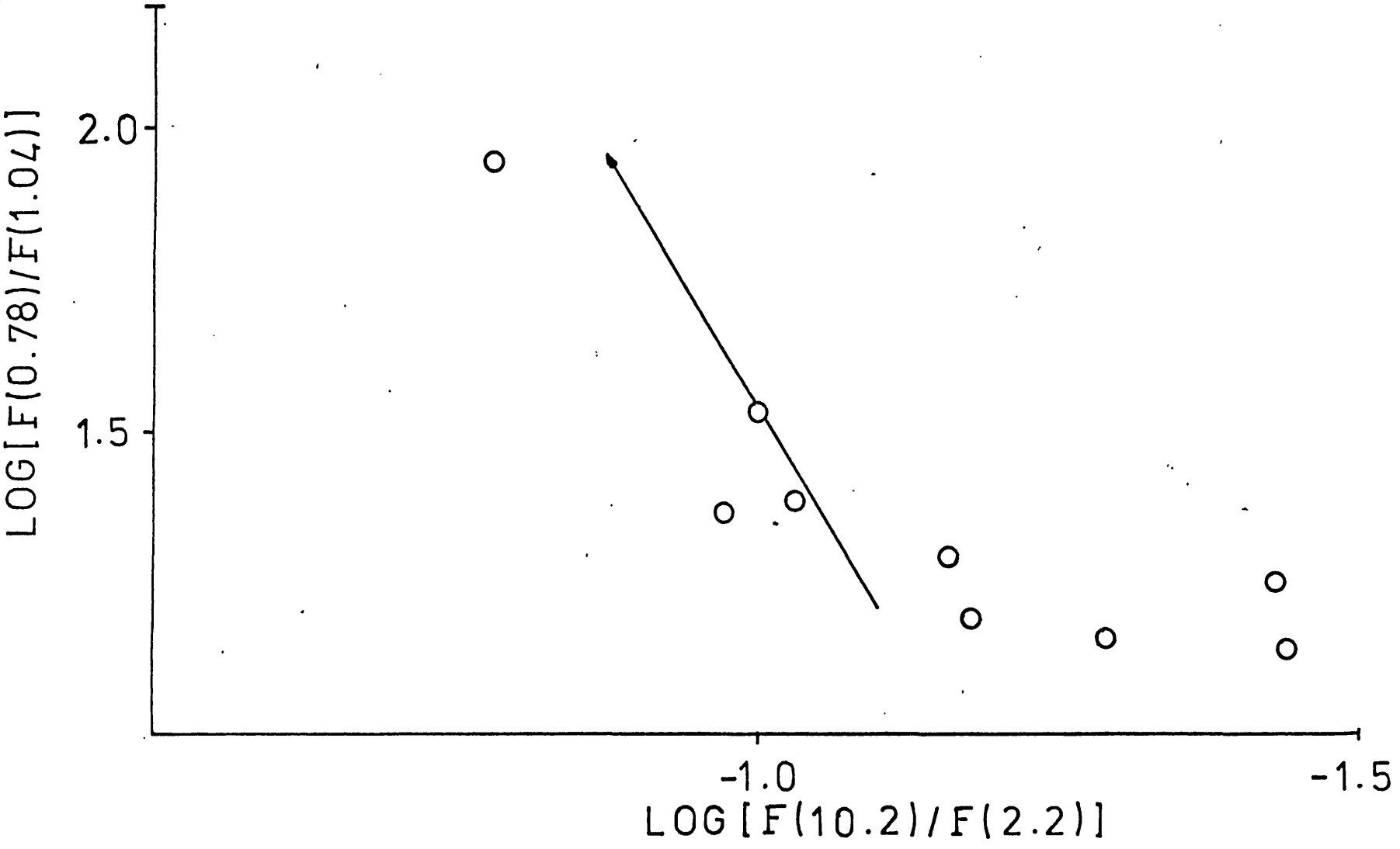

FIGURE A1.1

RELATIVE VARIATION OF COLOUR INDICES FOR M9 IRC STARS. ARROW INDICATES THE VAN DE HULST CURVE NO. 15 REDDENING VECTOR

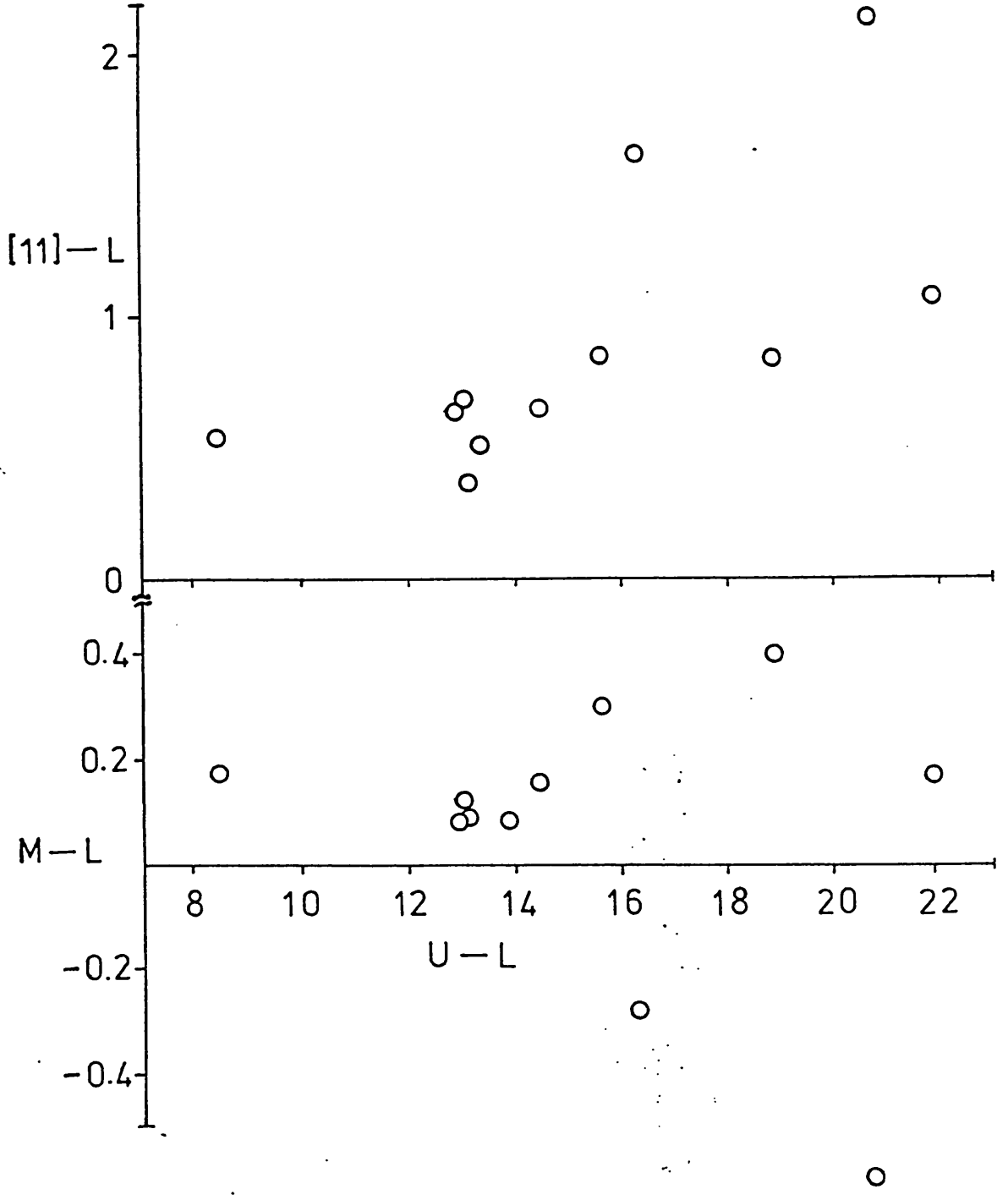

FIGURE A1.2

RELATIVE VARIATION OF COLOUR INDICES IN CARBON STARS

well the correlation between infrared "excess" and optical "depression", excluding any question of the continuum behaviour near 4.9 μm. This suggests that the index [8.4] - M is due, not to a continuum depression at 4.9 μm, but rather to a continuum elevation at 8.4 μm relative to shorter wavelengths. If this is the case, then L-M should show only small systematic variations with U-L. Figure A1.2 demonstrates this to be the case. It seems therefore clear that for carbon stars also, a changing infrared continuum is reasonably well correlated with optical variability, for which optical dust absorption is perhaps the most attractive and obvious explanation.

APPENDIX 2

COMET WEST

The discovery of comet West was first announced at the European Southern Observatory on November 5th 1975. It was subsequently to become the brightest naked eye comet since comet Ikeya Seki in 1965. Fortunately, its observational availability with the Tenerife flux collector coincided with an observing trip by the Imperial College infrared group. Although short wave observations ($\lambda \leq 4.8$ μm) were precluded because of instrumental defects, numerous observations were acquired by the writer at $\lambda = 10.2$ μm Early instrumental help by P. R. Jorden is gratefully acknowledged, as is the sacrifice of ~1 hour of photometry by J. D. Needham at the termination of several of his observing periods.

The comet was usually acquired at about ~6 a.m. G.M.T., as soon as it became available. 10.2 μm photometry was then performed upon the nucleus, and small scale mapping then completed. This latter proved a necessary precaution in view of the daily power cuts at the observatory, and subsequent difficulties in retrieving the comet during daylight hours, when the local generator became operational. Despite these problems a considerable amount of useful data was acquired, and on several occasions observations were possible until ~4 p.m., when the comet again became unavailable because of large zenith angle. The observations began on 7.3.76, and continued through to 18.3.76, the last day of allocated telescope time.

Initial mapping took the form of scans at a rate 1.2 arcsecs. sec^{-1}, using the hand guide control. The nucleus was first centred in the beam, and then displaced in right ascension and declination to the first scan origin. The comet was then moved across the beam in right ascension. On relocating scan origin, a new origin was established by offsetting 5 arcseconds in declination towards the nucleus. A provisional map of the nuclear region was obtained by continued offsetting in declination after each right ascension scan. Confirmatory maps using declination scans were then procured, using a similar procedure. The size of these preliminary maps was primarily determined by the rate of motion of the comet (~1 arcsecond.$minute^{-1}$), and the desire to reduce intrinsic motion of the comet over the scan periods; time limits were also imposed by the need for larger scale mapping later. The initial scans were therefore limited to areas ~1 arcminute square.

The main scans were longer, and made use of the comet motion. The nucleus was again offset to a location ~3 arcminutes distant in R.A. Declination scans were then initiated of length ~5 arcminutes, centred on the scan origin. No further change in the scan location was required, the comet being allowed to progress through the beam by its own motion. Scan length was determined by the requirement that adjacent scans overlap at all points, where scan width was $\simeq 10''$. Sampling was at one second intervals, and scan rate was again 1.2 arcsecs.sec^{-1}.

An example of a complete run is presented in figure A2.1. The comet emission was first detected as weak, and non-point-like, as the tail passed through the beam. The nucleus was eventually encountered as a strong (point-like) signal, which subsequently

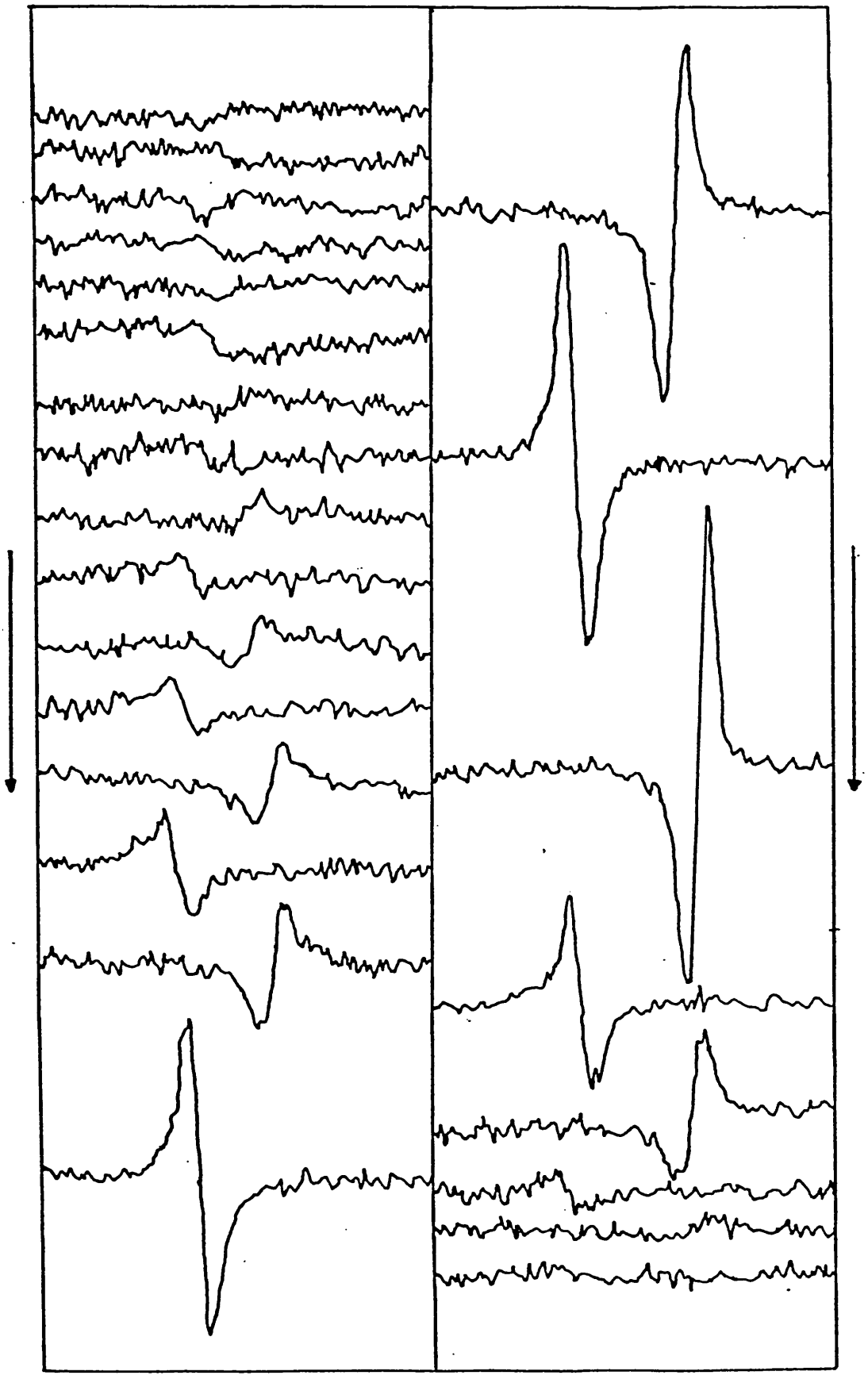

FIGURE A2.1

DECLINATION SCANS THROUGH COMET WEST. ARROWS INDICATE INCREASING RIGHT ASCENSION

faded rapidly. There is therefore no infrared spike (unlike comet Kohoutek (c.f. Sekanina 1974)) and this agrees with the visual appearance of the comet; rather, infrared emission terminates rapidly on the solar side of the nucleus. The tail, on the other hand, appears to lead to weak emission, gradually fading with distance from the nucleus.

At the same time as the infrared observations, photographic plates were also acquired with the 50 cm Mons telescope, and 60 inch flux collector. These have fairly high dynamic range, and it is hoped that a comparison of optical and infrared isophotal maps will prove instructive.

A thorough analysis of the data has been retarded by commitment of the principal investigators to other programs, and lack of ancillary help. The recent acquisition of a technical assistant (C. Ebdon) is now permitting some headway to be made, and it is hoped to have our first contour maps out in the near future. The ideas behind the reduction technique to be employed are as follows. The discussion benefits considerably from talks with Dr. M. J. Selby, who has given this question particular attention.

If $i_p(K)$ is the Fourier transform of $I_p(x)$, the observed instrumental function, and $s(K)$ is the Fourier transform of the source function $S(x)$, then the measured intensity $I_{Ml}(x)$ is given by

$$I_{Ml}(x) = S(x) \otimes I_p(x)$$

or $$i_{ml}(K) = s(K) \cdot i_p(K)$$

In principle, $S(x)$ may be retrieved by determining $s(K) = i_{ml}(K)/i_p(K)$. In practice, particular care should be taken to avoid

high frequency noise in $i_{m1}(K)$, which may be drastically enhanced if $i_p(K)$ falls to low values. These problems may be alleviated by applying an appropriate smoothing function to $I_{M1}(x)$, or multiplying $i_{m1}(K)$ by a suitable masking function (see in particular Brault and White 1971 for an excellent extended discussion of these problems, and techniques for their avoidance). For the present however we apply an alternative technique.

If $I_{M2}(x)$ is the signal which would be measured for a new instrumental function I(x), then

$$I_{M2}(x) = S(x) \otimes I(x)$$

$$i_{m2}(K) = s(K) \cdot i(K)$$

It follows that

$$i_{m2}(K) = i_{m1}(K).(i(K)/i_p(K))$$

and

$$I_{M2}(x) = I_{M1}(x) \otimes \text{F.T.}\{\frac{i(K)}{i_p(K)}\}$$

For the determination of the term requiring the transform operation, we note that we may write

$$i_p(K) = i_{PR}(K) + j\ i_{PI}(K)$$

where $i_p(K)$ is antisymmetric for declination scans ($j = \sqrt{-1}$). For the new instrument transfer function we take $i(K) = i(-K)$, where $i(K)$ is real, whence

$$\frac{i(K)}{i_p(K)} = C(K) - j\ D(K)$$

where $$C(K) = \frac{i_{PR}(K)\ i(K)}{i_{PR}^2(K) + i_{PI}^2(K)} \quad ; \quad D(K) = \frac{i_{PI}(K)\ i(K)}{i_{PR}^2(K) + i_{PI}^2(K)}$$

whence $D(K) = -D(-K)$ and

$$\text{F.T.}\left\{\frac{i(K)}{i_p(K)}\right\} = \int_{-\infty}^{+\infty} (C(K) - j\,D(K))\, e^{jkx}\, dK$$

$$= \int_{-\infty}^{+\infty} C(K) \cos K x\, dK + \int_{-\infty}^{+\infty} D(K) \sin K x\, dK$$

$$+ j\left\{\int_{-\infty}^{+\infty} C(K) \sin K x\, dK - \int_{-\infty}^{+\infty} S(K) \cos K x\, dK\right\}$$

The terms in parentheses correspond to integration over anti-symmetric components, and reduce to zero. The first two terms are symmetric and we may therefore write

$$\text{F.T.}\left[\frac{i(K)}{i_p(K)}\right] = 2\int_o^{\infty} C(K) \cos K x\, dK + 2\int_o^{\infty} S(K) \sin K x\, dK$$

So the Fourier transform of $i(K)/i_p(K)$ is real, and may be numerically evaluated for a given symmetric function $I(x)$. For $i(K)$ represented by a bell shaped function for instance, such that

$$i(K) = 1 \quad \text{for} \quad -K' < K < K'$$

$$= \left\{\frac{1}{2} \cos (K-K')x + \frac{1}{2}\right\} \qquad K' < |K| < K''$$

$$= 0 \qquad K'' < |K|$$

then

$$I(x) = \frac{(\sin K''x + \sin K'x)\, \pi^2}{(\pi^2 - x^2(K''-K')^2)}$$

K', K'' will be chosen to give the most reasonable and consistent results, as well as a function $I(x)$ reasonably approximating, say, optical seeing disk profiles.

To summarise, the procedure allows the evaluation of infrared

maps for a selected symmetric instrumental transfer function, $I(x)$, from original data taken with an asymmetric transfer function $I_p(x)$. This is achieved by convolving observed scan profiles with F.T.$(i(K)/i_p(K))$. The procedure is computationally cheap (in terms of time) and straightforward.

APPENDIX 3

INFLUENCE OF GRAIN SHAPE ON THERMAL BALANCE

In chapter 5, equations of grain growth and thermal balance were determined for spherical grains. This both considerably simplified the treatment, and invoked fewer assumptions. All three condensates considered are capable of developing fairly compact crystals, reasonably approximated by spheres. Whether these are the forms the condensates are likely to adopt is conjectural. In the case of graphite for instance, it is arguable that condensation will, at least initially, take the form of platelets. In this appendix we investigate some consequences of aspherical grain growth in a régime of weak gas/grain thermal coupling. Although the consequences to be noted will be considerably less severe (and problematic) where thermal coupling is strong, they may still be present on a reduced scale.

Consider the example of a graphite disk, radius "b", with axis of symmetry (AS) of length "2a". Grains generally can be considered as spinning about an axis whose direction is changing, although typically over much longer times than the spin period. At any given time, most grains can therefore be regarded as having a fixed orientation spin axis. For a disk orientated so that the AS is parallel to the stellar radial vector $\underset{\sim}{r}_*$ (the face-on (FO) case), the total absorption coefficient is

$$C_{aFO} = - \frac{2 \pi V_g}{\lambda} I_m (m^2 - 1)$$

where V_g is grain volume, m the complex refractive index. For AS

perpendicular to r_* (the edge-on (EO) case) we have

$$C_{aEO} = -\frac{\pi V_g}{\lambda}\left\{I_m\left\{\frac{m^2-1}{m^2}\right\} + I_m\,(m^2 - 1)\right\}$$

where for graphite (Wickramasinghe and Guillaume 1965)

$$m^2 = (n^2 - k^2) - 2nki \simeq 4 - 10\lambda_i \qquad (\lambda \text{ in } \mu\text{ms})$$

for $\lambda \gtrsim 0.4$ μm, whence $nk \simeq 5\lambda$. So

$$C_{aFO} \not\simeq C_{aFO}(\lambda)$$

C_{aFO} is therefore essentially temperature independent (for low temperatures) and

$$\sigma\, T_*^4 \left\{\frac{r_*}{r}\right\}^2 \overline{C}_{aFO}(T_*) \simeq 2\,\overline{C}_{aFO}(T_{gr})\,\sigma\, T_{gr}^4$$

$$T_{gr} \simeq \frac{T_*}{2^{\frac{1}{4}}} = 2523 \text{ K} \qquad (T_* = 3000 \text{ K})$$

A value significantly higher than the value $T_{gr} \simeq 2360$ K determined for spherical grains. Grains with this orientation would require emmersion in a total gaseous pressure of $>3 \times 10^3$ dynes.cm^{-2} to avoid appreciable sublimation.

The appropriate equation of thermal balance for an EO configuration gives however

$$T_{gr} = \frac{T_*}{2^{\frac{1}{2}}} \simeq 2120 \text{ K} \qquad (T_* = 3000 \text{ K})$$

requiring a total gaseous pressure of only 2.96 dynes.cm^{-2}. Thus, if graphite platelets form in a low pressure environment, there is little probability of them acquiring appreciable grain size; high sublimation in FO spin configurations is likely to dominate over grain growth at an early stage of development. Similar arguments will apply for other

materials and grain shapes. For closure, the argument strictly requires a demonstration that spin axis orientation will change appreciably over the period of grain growth. This may be given as follows.

The time taken to cause a significant change in the orientation of the spin axis of a grain of mass M is

$$\tau_o \sim \frac{M}{m\ dN/dt}$$

where dN/dt is the atomic number flux incident to the grain

$$\frac{dN}{dt} = 4\ \pi\ a^2\ \left\{\frac{kT}{2\pi m}\right\}^{\frac{1}{2}} .\ n$$

where n is the number density of atoms with mass m. Whence

$$\tau_o \sim \frac{2\ \pi\ a\ \rho_{gr}}{3n\ (2\ \pi\ m\ kT)^{\frac{1}{2}}} \simeq \frac{2\ \pi\ a\ \rho_{gr}\ \mu^{\frac{1}{2}}\ m_H^{\frac{1}{2}}}{3\ \rho\ (2\ \pi\ kT)^{\frac{1}{2}}} \qquad \ldots(A3.1)$$

The rate of accretion of atoms/molecules corresponding to the condensate is

$$\frac{dN}{dt} = 4\ \pi\ a^2\ \frac{\rho\ X}{A_T\ m_H}\ \left(\frac{kT}{2\ \pi\ A_T\ m_H}\right)^{\frac{1}{2}}$$

since $$N = \frac{4}{3}\ \frac{\pi\ a^3\ \rho_{gr}}{A_T\ m_H}$$

$$\frac{dN}{da} = \frac{4\ \pi\ a^2\ \rho_{gr}}{A_T\ m_H}$$

and $$\frac{da}{dt} = \frac{X\rho}{\rho_{gr}}\ \left(\frac{kT}{2\ \pi\ A_T\ m_H}\right)^{\frac{1}{2}} \qquad \ldots(A3.2)$$

The time taken to acquire radius a, all other conditions being constant, is then given by

$$\tau_{gg} = \frac{a\ \rho_{gr}}{X\ \rho} \left(\frac{2\ \pi\ A_T\ m_H}{kT}\right)^{\frac{1}{2}} \qquad \ldots(A3.3)$$

from equation A3.1 and A3.3 we then obtain

$$\frac{\tau_{gg}}{\tau_o} \simeq \frac{3}{X} \left\{\frac{A_T}{\mu}\right\}^{\frac{1}{2}}$$

Evidently, $\tau_{gg}/\tau_o >> 1$ for any likely condensate, and this is a lower limit. τ_o here is the time required to change the spin axis orientation of a grain already fully evolved to radius "a".

For an appropriate time averaged value of the ratio τ_{gg}/τ_o, note that $\tau_o \propto M/a^2 \propto a$. Since da/dt = constant (equation A3.2), $\langle\tau_{gg}/\tau_o\rangle \simeq 6/X \left\{\frac{A_T}{\mu}\right\}^{\frac{1}{2}}$.

It is clear therefore that certain spin orientations may well be excluded, or occupied by grains with mass greatly depreciated through sublimation. This would result in a rather novel mode of grain polarisation. A similar effect may well be responsible for an attenuation in the numbers of larger grains.

As grains become larger, so their spin rate will decline. At a certain stage, it no longer becomes permissible to regard the grain as having a mean temperature for fixed axis of rotation, and both grain temperature and sublimation rate may vary appreciably over a rotation cycle. This will occur if cooling time $\tau_{COOL} > \tau_{ROT} \simeq \omega_{SP}^{-1}$, where ω_{SP} is the spin angular velocity of the grain:

$$\tau_{COOL} \simeq \frac{E_{gr}}{4\ \pi\ a^2\ \sigma\ T_{gr}^4}$$

where E_{gr} is the grain internal energy given by

$$E_{gr} \simeq \frac{3}{2}\ kT_{gr}\ \frac{\dot{N}_A}{A_T}\ \rho_{gr} \cdot \frac{4}{3}\ \pi\ a^3$$

whence

$$\tau_{COOL} \simeq \frac{k\, N_A\, \rho_{gr}\, a}{2\, \sigma\, T_{gr}^{3}\, A_T}$$

where N_A is the Avogadro number. An alternative form for E_{gr}, involving the Debye temperature, is given by Greenberg (1968). For a grain with moment of inertia I_{gr}, and in thermal equilibrium with its surroundings, we have

$$\frac{1}{2}\, I_{gr}\, \omega_{SP}^{2} \simeq \frac{3}{2}\, kT_{gr}$$

For illustrative purposes we use $I_{gr} = \frac{2}{5}\, Ma^2$ (appropriate for a sphere), whence

$$\omega_{SP}^{2} = \frac{15\, k\, T_{gr}}{2\, M\, a^2}$$

and

$$\tau_{ROT} \simeq \left\{\frac{8\, \pi\, \rho_{gr}\, a^5}{45\, k\, T_{gr}}\right\}^{\frac{1}{2}}$$

whence

$$\frac{\tau_{COOL}}{\tau_{ROT}} \simeq \frac{0.67\, K^{3/2}\, N_A\, \rho_{gr}^{\frac{1}{2}}}{\sigma\, T_{gr}^{2.5}\, A_T\, a^{1.5}}$$

For $A_T = 12$, $T_{gr} \simeq 2000$ K, $\rho_{gr} \simeq 2$ gm.cm^{-3} we then have

$$\frac{\tau_{COOL}}{\tau_{ROT}} \simeq \frac{7.6}{a^{1.5}} \qquad \text{(a in μms)}$$

Since we require $\tau_{COOL}/\tau_{ROT} > 1$ it is clear that the assumption of a mean grain temperature is reasonable providing the grains are submicron in size.

REFERENCES

Abt, H.A., Jeffers, H.M., Gibson, J., Sandage, A.R., 1962. Ap. J. 135, 429.

Adams, W.S., MacCormack, E., 1935. Ap. J., 81, 119.

Adel, A., 1939. Ap. J., 89, 1.

Adel, A., 1940. Ap. J., 91, 487.

Alexander, D.R., Johnson, H.R., 1972. Ap. J., 176, 629.

Allen, C.W., 1973. Astrophysical Quantities, Athlone Press, London.

Aller, L.H., 1956. Gaseous Nebulae, Chapman and Hall, London.

Andrews, P.J., 1967. Ap. J., 147, 1183.

Andriesse, C.D., Wierstra, T., 1973. Astron. Astrophys., 24, 465.

Appenzeller, I., Hiltner, W.A., 1967. Ap. J., 149, 353.

Arp, H.C., 1965. In "Stars and Stellar Systems", Vol. V, Eds. A. Blaauw and M. Schmidt, University of Chicago Press, Chicago.

Ashbrook, J., 1976. Sky and Telescope, 52, 48.

Atherton, P., Reay, N.K., Worswick, S.P., 1977. In preparation.

Auman, J.R., 1969. Ap. J., 157, 799.

Bahcall, J.N., Bahcall, N.A., Weistrop, D., 1975. Astrophys. Letters, 16, 159.

Bahcall, J.N., Ostriker, J.P., 1975. Nature, 256, 23.

Baldinelli, L., Ghedini, S., 1976. Inform. Bull. Var. Stars, No. 1143.

Batten, A.H., 1973. In I.A.U. Symp. No. 51, D. Reidel Publishing Company, Dordrecht, Holland.

Batten, A.H., Sahade, J., 1973. Publ. Astron. Soc. Pacific, 85, 599.

Becklin, E.E., Neugebauer, G., Wynn-Williams, C.G., 1973. Astrophys. Letters, 15, 87.

Belcher, J.W., Olbert, S., 1975. Ap. J., 200, 369.

Bell, E.E., Eisner, L., Young, J., Oeljers, R.A., 1960. J. Opt. Soc. Am., 50, 1313.

Bernat, A.P., 1977. Ap. J., 213, 756.

Bernat, A.P., Lambert, D.L., 1975. Ap. J., 201, L153.

Bernat, A.P., Lambert, D.L., 1976. Ap. J., 210, 395.

Bidelman, W.P., 1954. Ap. J. Suppl., 1, 175.

Bolton, C.T., 1970. Ap. J., 161, 1187.

Bolton, C.T., 1972. Intern. Astron. Union Circular No. 2388.

Brault, J.W., White, O.R., 1971. Astron. Astrophys., 13, 169.

Breinhorst, R.A., 1971. Astrophys. Space Sci., 10, 411.

Cahn, J.H., Kaler, J.B., 1971. Ap. J. Suppl., 22, 319.

Caloi, V., Panagia, N., 1974. Astron. Astrophys., 36, 139.

Canizares, C.R., Neighbours, J.E., Clark, G.W., Lewin, W.H.G., Schnopper, H.W., Spratt, G.F., 1973. Ap. J., 183, L91.

Centolanzi, F.J., Chapman, D.R., 1966. J. G. R., 71, 1735.

Cester, B., Flora, U., Mardirossian, F., Pucillo, M., 1976. Inform. Bull. Var. Stars, No. 1114.

Chester, R., Johnson, L.R., 1971. Nature, 229, 105.

Christy, R.F., 1966. Ap. J., 145, 337.

Clark, B.G., Kellermann, K.I., Shaffer, D., 1975. Ap. J., 198, L123.

Clayton, D.D., Wickramasinghe, N.C., 1976. Astrophys. Space Sci., 42, 463.

Cohen, J.G., 1976. Ap. J., 203, L127.

Cohen, M., Barlow, M.J., 1974. Ap. J., 193, 401.

Cohen, M., Fawley, W.M., 1974. Monthly Notices Roy. Astron. Soc., 169, 31p.

Cohen, M., Treffers, R., 1974. Ap. J., 188, 545.

Collins, J.G., Fay, T.D., 1974. J. Quant. Spectrosc. Radiat. Transfer, 14, 1259.

Cudworth, K.M., 1974. Astron. J., 79, 1384.

Cudworth, K.M., 1975. Monthly Notices Roy. Astron. Soc., 172, 57p.

Curtis, H.D., 1918. Publ. Lick. Obs., 13, 55.

Dall'Oglio, G., Melchiorri, B., Melchiorri, F., Natale, V., 1973. Infrared Phys., 13, 169.

Demarque, P., Mengel, J.G., Aizenman, M.L., 1971. Ap. J., 163, 37.

Deutsch, A.J., 1956. Ap. J., 123, 210.

Deutsch, A.J., 1960. In "Stars and Stellar Systems", Vol. VI, Ed. J. L. Greenstein, University of Chicago Press, Chicago.

Dobronravin, P.P., 1950. Izvest. Crimean Ap. Obs., 5, 59.

Donn, B., Wickramasinghe, N.C., Hudson, J.P., Stecher, T.P., 1968. Ap. J., 153, 451.

Dopita, M.A., Gibbons, A.H., 1975. Monthly Notices Roy. Astron. Soc., 171, 73.

Dufay, J., 1968. Galactic Nebulae and Interstellar Matter. Dover Publications Inc., New York.

Dushman, S., Lafferty, J.M., 1962. Scientific Foundations of Vacuum Technique, John Wiley, New York.

Dyck, H.M., Forrest, W.J., Gillet, F.C., Stein, W.A., Gehrz, R.D., Woolf, N.J., Shawl, S.J., 1971. Ap. J., 165, 57.

Dyck, H.M., Lockwood, G.W., Capps, R.W., 1974. Ap. J., 189, 89.

Eggen, O.J., 1948. Ap. J., 108, 15.

Elsasser, W.M., 1938. Phys. Rev., 54, 126.

Essen, L., 1953. Proc. Phys. Soc. B., 66, 189.

Essen, L., Froome, K.D., 1951. Proc. Phys. Soc. B., 64, 862.

Faktor, M.M., Garrett, I., 1974. Growth of Crystals from the Vapour, Chapman and Hall, London.

Faulkener, D.J., 1970. Ap. J., 162, 513.

Fay, T.D., Johnson, H.R., 1973. Ap. J., 181, 851.

Ferch, R.L., Salpeter, E.E., 1975. Ap. J., 202, 195.

Finzi, A., 1973. Ap. J., 183, 183.

Finzi, A., Wolf, R., 1970. Astrophys. Letters, 5, 63.

Fitzgerald, M.P., 1968. Astron. J., 73, 983.

Fix, J.D., 1969. Monthly Notices Roy. Astron. Soc., 146, 37 and 51.

Fix, J.D., 1971. In Proceedings of the Conference on Late Type Stars, Ed. G. W. Lockwood and H. M. Dyck, Tucson: Kitt Peak National Observatory Contr. No. 554.

Fix, J.D., Alexander, D.R., 1974. Ap. J., 188, L91.

Flora, U., Hack, M., 1975. Astron. Astrophys. Suppl., 19, 57.

Frieboes-Conde, H., Herczog, T., Høg, E., 1970. Astron. Astrophys., 4, 78.

Fujita, Y., 1965. Vistas in Astronomy, Ed. A. Beer, Oxford Pergamon, 7, 71.

Fujita, Y., 1970. Interpretation of Spectra and Atmospheric Structure in Cool Stars, University of Tokyo Press, Tokyo.

Gabovits, J., 1936. Publ. Obs. Tartu, 28, No. 5.

Gabovits, J., Öpik, E., 1935. Publ. Obs. Tartu, 28, No. 3.

Gallagher, J.S., Code, A.D., 1974. Ap. J., 189, 303.

Gaposhkin, C.P., 1957. The Galactic Novae, North Holland Publishing Company, Amsterdam.

Gehrz, R.D., Hackwell, J.A., Jones, T.W., 1974. Ap. J., 191, 675.

Gehrz, R.D., Woolf, N.J., 1970. Ap. J., 161, L213.

Gehrz, R.D., Woolf, N.J., 1971. Ap. J., 165, 285.

George, D., Kaftan-Kassim, M.A., Hartsvijker, A.P., 1974. Astron. Astrophys., 35, 37.

Gillet, F.C., Merrill, K.M., Stein, W.A., 1971. Ap. J., 164, 83.

Gilman, R.C., 1969. Ap. J., 155, 485.

Gilman, R.C., 1972. Ap. J., 178, 423.

Gilman, R.C., 1974. Ap. J. Suppl., 28, 397.

Gilra, D.P., 1973. I.A.U. Symp. No. 52, Ed. J. M. Greenberg and H. C. van de Hulst.

Glasby, J.S., 1968. Variable Stars, Constable, London.

Glass, I.S., Feast, M.W., 1973. Monthly Notices Roy. Astron. Soc., 163, 245.

Golden, S.A., 1969. J. Quantit. Spectrosc. Radiat. Transfer, 9, 1067.

Grasdalen, G.L., 1974. Astron. J., 79, 1047.

Greenberg, J.M., 1968. In "Stars and Stellar Systems", Vol. VII, Ed. B. M. Middlehurst, L. H. Aller, University of Chicago Press, Chicago.

Greig, W.E., 1971. Astron. Astrophys., 10, 161.

Greig, W.E., 1972. Astron. Astrophys., 18, 70.

Grindlay, J.E., Liller, Wm., 1977. Ap. J., 216, L105.

Grinin, V.P., Zvereva, A.M., 1968. In I.A.U. Symp. No. 34, Ed. D. E. Osterbrock, C. R. O'Dell, D. Reidel Publishing Company, Dordrecht, Holland.

Grotrian, W., 1937. Z. Astrophys., 13, 215.

Günther, O., 1959. Astron. Nachr., 285, 97, 105.

Gurzadyan, G.A., 1969. Planetary Nebulae, Gordon and Breach, New York.

Hack, M., Hutchings, J.B., Kondo, Y., McClusky, G.E., Plavec, M., Polidan, R.S., 1974. Nature, 249, 534.

Hack, M., Hutchings, J.B., Kondo, Y., McClusky, G.E., Plavec, M., Polidan, R.S., 1975. Ap. J., 198, 453.

Hack, M., Hutchings, J.B., Kondo, Y., McClusky, G.E., Tulloch, M.K., 1976. Ap. J., 206, 777.

Hall, D.S., 1974. Acta Astron., 24, 7.

Hansen, O.L., Hesser, J.E., 1975. Nature, 257, 568.

Härm, R., Schwarzschild, M., 1975. Ap. J., 200, 324.

Hazlehurst, J., 1970. Monthly Notices Roy. Astron. Soc., 149, 129.

Herczog, T., 1969. In "Mass Loss from Stars", Ed. M. Hack, D. Reidel Publishing Company, Dordrecht, Holland.

Hicks, T.R., Phillips, J.P., Reay, N.K., 1976. Monthly Notices Roy. Astron. Soc., 176, 409.

Hill, G., Barnes, J.V., Hutchings, J.H., Pearce, J.A., 1971. Ap. J., 163, 443.

Hjellming, R.M., Webster, E., Balick, B., 1972. Ap. J., 178, 439.

Hoffleit, D., 1964. Catalogue of Bright Stars, Yale University Observatory, New Haven, Connecticut.

Hoyle, F., 1956. Ap. J., 124, 482.

Hoyle, F., Wickramasinghe, N.C., 1962. Monthly Notices Roy. Astron. Soc., 124, 417.

Hromov, G.S., Kohoutek, L., 1968. Bull. Astron., 19, 1.

Hua, C.T., Louise, R., 1970. Astron. Astrophys., 9, 448.

Huang, S-S., 1963. Ap. J., 138, 342.

Huang, S-S., 1973. In I.A.U. Symp. No. 51, D. Reidel Publishing Company, Dordrecht, Holland.

Huang, S-S., Brown, D.A., 1976. Ap. J., 204, 151.

Huang, S-S., Struve, O., 1956. Astron. J., 61, 300.

Huang, S-S., Struve, O., 1960. In "Stars and Stellar Systems", Vol. VI, Ed. J. L. Greenstein, University of Chicago Press, Chicago.

Humphreys, R.M., 1974. Ap. J., 188, 75.

Hulst, H.C. van de, 1949. Rech. Astr. Obs. Utrecht, 11, Part 1, 1.

Humphreys, R.M., Strecker, D.W., Ney, E.P., 1971. Ap. J., 167, L35.

Humphreys, R.M., Strecker, D.W., Ney, E.P., 1972. Ap. J., 172, 75.

Hunter, J.H., Sofia, S., 1971. Monthly Notices Roy. Astron. Soc., 154, 393.

Huruhata, M., 1952. Publ. Astron. Soc. Pacific, 1952, 64, 200.

Hutchings, J.B., 1972. Monthly Notices Roy. Astron. Soc., 158, 177.

Hutchings, J.B., Hill, G., 1971. Ap. J., 167, 137.

Iben, I. Jr., Rood, R.T., 1970a. Ap. J., 159, 605.

Iben, I. Jr., Rood, R.T., 1970b. Ap. J., 161, 587.

Jacchia, S., 1941. Harv. Bull. No. 915.

Jameson, R.F., Longmore, A.J., Crawford, B., 1973. Nature, 242, 107.

Jameson, R.F., Longmore, A.J., 1976. Monthly Notices Roy. Astron. Soc., 174, 217.

Jeans, J.H., 1928. Astronomy and Cosmology, Cambridge, Cambridge University Press.

Jedrzejec, E., 1969. MS. Thesis, Warsaw Univ.

Jeffries, J.T., Pottasch, S., 1959. Ann. d'ap., 22, 318.

Johnson, H.L., 1966. Ann. Rev. Astron. Astrophys., 4, 193.

Johnson, H.L., 1966b. Sky and Telescope, 32, 73.

Johnson, H.L., 1968. In "Stars and Stellar Systems", Vol. VII, Eds. B. M. Middlehurst and L. H. Aller, University of Chicago Press, Chicago.

Johnson, H.L., Mendoza V, E.E., 1966. Ann. d'ap., 29, 525.

Johnson, H.L., Mitchell, R.I., Iriate, B., Wisniewski, W.Z., 1966. Comm. Lunar Planet. Lab., No. 63.

Johnson, H.L., Mitchell, R.I., Latham, A.S., 1967. Comm. Lunar Planet. Lab., No. 92.

Johnson, H.R., 1974. Model Atmospheres for Cool Stars, NCAR-TN/STR-95, January.

Jorden, P.R., Long, J.F., MacGregor, A.D., Selby, M.J., 1976. Astron. Astrophys., 49, 421.

Joy, A.H., Wilson, R.E., 1949. Ap. J., 109, 231.

Kahn, F.H., 1968. In Planetary Nebulae, Eds. D. Osterbrock and C. R. O'Dell, D. Reidel, Dordrecht, Holland.

Kaiser, C.B., 1968. N.C.A.R. Cooperative Thesis No. 10, University of Colorado and High Altitude Observatory, NCAR.

Kaler, J.B., 1970. Ap. J., 160, 887.

Kaler, J.B., 1974. Astron. J., 79, 594.

Kaminsky, M., 1965. Atomic and Ionic Impact Phenomena on Metal Surfaces, Academic Press, New York.

Kanagy II, S.P., Wyatt, S.P., 1975. Bull. American Astron. Soc., 7, 259.

Kaplan, S.A., Pikelner, S.B., 1970. The Interstellar Medium, Harvard University Press, Cambridge, Massachusetts.

Kaye, G.W.C., Laby, T.H., 1966. Tables of Physical and Chemical Constants, Longmans, London.

Kirkpatrick, R.C., 1976. Astrophys. Letters, 17, 7.

Kondo, Y., Hack, M., Hutchings, J.B., McClusky, G.E., Plavec, M., Polidan, S., 1975. Astrophys. Space Sci., 38, 353.

Kondo, Y., McClusky, G.E., Eaton, J.A., 1976. Astrophys. Space Sci., 41, 121.

Kopal, Z., 1959. Close Binary Systems, Chapman and Hall, London.

Kopal, Z., Shapley, M.B., 1956. Jodrell Bank Annals, 1, 141.

Kopp, I., Lindgren, R., Rydh, B., 1974. Table of Band Features of Diatomic Molecules in Wavelength Order, Version A, Institute of Physics, University of Stockholm, Tables Internationales de Constantes, Paris.

Kovach, W.S., 1971. Ap. J., 168, 423.

Kraft, R.P., 1962. Ap. J., 135, 408.

Krishna Swamy, K.S., 1970. Ap. J., 162, 259.

Krizewski, A., 1967. Acta Astron. 17, 297.

Kubiak, M., 1966. Acta Astron., 16, 275.

Kuhi, L.V., 1964. Publ. Astron. Soc. Pacific, 76, 431.

Kukarkin, B.V., Kholopov, P.N., Efremov, Yu.N., Kukarkina, N.P., Kurochkin, N.E., Medvedeva, G.F., Perova, N.D., Fedorovich, V.P., Frolov, M.S., 1970. General Catalogue of Variable Stars, Moscow, 2.

Kukarkin, B.V., Paranego, P.P., Efremov, Yu.I., Kholopov, P.N., 1958. General Catalogue of Variable Stars, Parts I and II, 2nd ed., Moscow.

Kukarkin, B.V., 1974. The Globular Star Clusters, USSR Academy of Sciences, Moscow.

Kutter, G.S., 1970. Ap. J., 160, 369.

Kutter, G.S., Sparks, W.M., 1974. Ap. J., 192, 447.

Kwok, S., 1975. Ap. J., 198, 583.

Langmuir, I., 1913. Phys. Rev., 2, 329.

Lee, T.A., 1970. Ap. J., 162, 217.

Lee, T.J., 1972. Journal of Vacuum Science and Technology, Jan/Feb.

Leroy, J.L., Auriére, M., Laques, P., 1976. Astron. Astrophys., 53, 227.

Longmore, A.J., Jameson, R.F., 1975. Monthly Notices Roy. Astron. Soc., 173, 271.

Louise, R., 1973. Mém. Soc. Roy. Liége, 5, 465.

Louise, R., 1974. Astron. Astrophys., 30, 189.

Low, F.J., Riecke, G.H., 1974. In "Methods of Experimental Physics", 12A, Ed. N. Carleton, Academic Press, New York and London.

Lucy, L.B., 1968. Ap. J., 151, 1123.

MacGregor, A.D., 1973. Thesis, University of London.

MacGregor, A.D., Phillips, J.P., Selby, M.J., 1973. Monthly Notices Roy. Astron. Soc., 164, 31p.

Maciel, W.J., 1973. Astrophys. Letters, 15, 177.

Maciel, W.J., 1976. Astron. Astrophys., 48, 27.

Maciel, W.J., 1977. Astron. Astrophys., 57, 273.

Manson, J.E., 1965. In "Handbook of Geophysics and Space Environments", Ed. S. L. Valley, p. 5-22.

Marlborough, J.M., Roy, J.-R., 1970. Ap. J., 160, 221.

Matthews, W.G., 1966. Ap. J., 143, 173.

McCrea, W., 1937. Observatory, 60, 277.

McLaughlin, D.B., 1939. Pop. Astr., 47, 410, 481, 538.

McLaughlin, D.B., 1960. In "Stars and Stellar Systems", Vol. VI, Ed. J. L. Greenstein, University of Chicago Press, Chicago.

McLaughlin, D.B., Dijke, S.E.A.v., 1943. Ap. J., 100, 63.

McNamara, D.H., 1951. Publ. Astron. Soc. Pacific, 54, 244.

Melnick, G., Harwit, M., 1975. Monthly Notices Roy. Astron. Soc., 171, 441.

Mèndez, R.H., 1975. Ap. J., 199, 411.

Mendoza, E.E., Johnson, H.L., 1965. Ap. J., 141, 165.

Menzel, D.H., 1968. In I.A.U. Symp. No. 34, Ed. D. E. Osterbrock and C. R. O'Dell, D. Reidel Publishing Company, Dordrecht, Holland.

Mezger, P.G., 1972. In Interstellar Matter, Geneva Observatory, Switzerland.

Minkowski, R., Aller, L.H., 1954. Ap. J., 120, 261.

Minkowski, R., Osterbrock, D., 1960. Ap. J., 131, 537.

Moss, D.L., Whelan, J.A.J., 1970. Monthly Notices Roy. Astr. Soc., 149, 147.

Mould, J.R., 1976. Astron. Astrophys., 48, 443.

Münch, G., 1968. In I.A.U. Symp. No. 34, D. Reidel Publishing Company, Dordrecht, Holland.

Murray, B.C., Wildey, R.L., 1964. Ap. J., 139, 734.

Mustel, E.R., 1951. Izv. Krymsk. Astrophys. Obs., 7, 118.

Mustel, E.R., 1957. I.A.U. Symp. No. 3, Ed. G. H. Herbig, D. Reidel Publishing Company, Dordrecht, Holland.

Mustel, E.R., Boyarchuk, A.A., 1970. Astrophys. Space Sci., 6, 183.

Naftilan, S.A., 1976. Ap. J., 206, 785.

Neugebauer, G., Leighton, R.B., 1969. Two Micron Sky Survey, NASA SP-3047.

Newell, B., Da Costa, G.S., Norris, J., 1976. Ap. J., 208, L55.

O'Dell, C.R., 1962. Ap. J., 135, 371.

O'Dell, C.R., Peimbert, M., Kinmann, T.D., 1964. Ap. J., 140, 119.

Oort, J.H., van Herk, G., 1959. B.A.N., 14, 299.
Osterbrock, D.E., 1974, Astrophysics of Gaseous Nebulae, W.H. Freeman and Co., San Francisco
Paczynski, B., 1971. Ann. Rev. Astron. Astrophys., 9, 183.

Paczynski, B., 1971. Astrophys. Letters, 9, 33.

Parker, E.N., 1960. Ap. J., 132, 821.

Parkin, D.W., Phillips, D.R., Sullivan, R.A.L., Johnson, L.R., 1972. Quart. J. R. Met. Soc., 98, 798.

Pearse, R.W.B., Gaydon, A.G., 1976. The Identification of Molecular Spectra, Chapman and Hall, London.

Perek, L., Kohoutek, L., 1967. Catalogue of Planetary Nebulae, Acad. Publ. House, Prague.

Peterson, A.W., 1973. Bull. Am. Astron. Soc., 5, No. 1, 13.

Peterson, A.W., 1976. Astron. Astrophys., 53, 441.

Petrosian, V., Dana, R.A., 1975. Ap. J., 196, 733.

Phillips, J.P., Reay, N.K., 1977. Astron. Astrophys., 59, 91.

Phillips, J.P., Reay, N.K., Worswick, S.P., 1977. Astron. Astrophys. (in press).

Phillips, J.P., Selby, M.J., 1977. Astrophys. Space Sci., 49, 339.

Plass, G.N., Yates, H., 1965. In "Handbook of Military Infrared Technology", Ed. W. L. Wolfe, Office of Naval Research, Department of the Navy, Washington, D.C.

Pohl, E., Kizilirmak, A., 1975. I.A.U. Inform. Bull. Var. Stars, No. 1053.

Proisy, P.E., 1974. Astron. Astrophys., 35, 37.

Reay, N.K., Worswick, S.P., 1977. Monthly Notices Roy. Astron. Soc., 179, 317.

Reddish, V.C., Lawrence, L.C., Pratt, N.M., 1966. Publ. Roy. Obs. Edinburgh, 5, 111.

Reimiers, D., 1975. In Problems in Stellar Atmospheres and Envelopes, Ed. B. Bascheck, W. H. Hegel and G. Traving, Springer-Verlag, New York.

Rigterink, P.V., 1972. Astron. J., 77, 230.

Roberts, M.S., 1960. Astron. J., 65, 457.

Rosebury, F., 1965. Handbook of Electron Tube and Vacuum Techniques, Addison-Wesley, Reading, Massachusetts.

Rubbra, F.T., Cowling, T.G., 1959. In 9th Internat. Ap. Symp. (Liege); Cointe-Sclessin, Belgium: Institut D'Astrophysique.

Sahade, J., 1958. Étoiles a raies d'emission, Cointe-Sclessin: Institut D'Astrophysique.

Sahade, J., 1960. In "Stars and Stellar Systems", Vol. VI, Ed. J. L. Greenstein, University of Chicago Press, Chicago.

Salpeter, E.E., 1971. Ann. Rev. Astron. Astrophys., 142, 855.

Salpeter, E.E., 1974a. Ap. J., 193, 579.

Salpeter, E.E., 1974b. Ap. J., 193, 585.

Sandage, A.R., 1957a. Ap. J., 125, 422.

Sandage, A.R., 1957b. Ap. J., 125, 435.

Sandage, A.R., 1970. Ap. J., 162, 841.

Sanchez Magro, C., Needham, J.D., Phillips, J.P., Selby, M.J., 1977. Monthly Notices Roy. Astro. Soc., 180, 461.

Sanner, F., 1976. Ap. J. Suppl., 32, 115.

Scheffler, H., 1966. Z. f. Astrophys., 63, 207.

Scheffler, H., 1967. Z. f. Astrophys., 65, 60.

Schild, R.C., Peterson, D.M., Oke, J.B., 1971. Ap. J., 166, 95.

Schwarzschild, M., 1970. Quart. J. Roy. Astro. Soc., 11, 12.

Scott, P.F., 1973. Monthly Notices Roy. Astron. Soc., 161, 35p.

Seaton, M.J., 1966. Monthly Notices Roy. Astron. Soc., 132, 113.

Sekanina, Z., 1974. Sky and Telescope, 47, 374.

Selby, M.J., 1973. Publ. Roy. Obs. Edinburgh, 9, No. 1, 48.

Shklovsky, I.S., 1956. A. Zh., 33, 222.

Shulov, O.S., 1967. Astrofizica, 3, 233.

Simoda, M., Iben, I., 1968. Ap. J., 152, 509.

Slutz, S., 1976. Ap. J., 210, 750.

Smak, J.E., 1966. Ann. Rev. Astron. Ap., 4, 19.

Smart, W.M., 1971. Textbook on Spherical Astronomy, Cambridge University Press, Cambridge.

Smith, H., 1976. Monthly Notices Roy. Astron. Soc., 175, 419.

Smith, M.G., Hesser, J.E., Shawl, S.J., 1976. Ap. J., 206, 66.

Smith, R.L., Rose, W.K., 1972. Ap. J., 176, 395.

Smyth, M.J., Dow, M.J., Napier, W.McD., 1975. Monthly Notices Roy. Astron. Soc., 172, 235.

Sparks, W.M., Starrfield, S., 1973. Monthly Notices Roy. Astron. Soc., 164, 1p.

Spinrad, H., Vardya, M.S., 1966. Ap. J., 146, 399.

Spitzer, L., 1968. Diffuse Matter in Space, Interscience Publishers, New York.

Stanyokovich, K.P., 1958. Vvedenic v Kosmischeskuiv Gazodinamiku, Moscow: Izd.-Vo. Fisiko-Mathematicheskoi, Sec. 20.

Starrfield, S., Truran, J.W., Sparks, W.N., Kutter, G.S., 1972. Ap. J., 176, 169.

Sterne, T.E., 1937. Monthly Notices Roy. Astron. Soc., 97, 582.

Stothers, R., 1972. Nature, 238, 5.

Strohmeier, W., 1972. Variable Stars, Pergamon Press, Oxford.

Strom, S.E., Strom, K.M., Brooke, A.L., Bregman, J., Yost, J., 1972. Ap. J., 171, 267.

Strong, J., 1941. J. Franklin Inst., 232, 1.

Struve, O., 1950. Stellar Evolution, Princeton University Press, Princeton.

Struve, O., Horak, H.G., 1950. Ap. J., 112, 178.

Struve, O., Sahade, J., 1957. Publ. Astron. Soc. Pacific, 69, 41.

Taylor, R.J., Wood, P.R., 1975. Monthly Notices Roy. Astron. Soc., 171, 467.

Tchudovitchev, G., 1939. Engelhardt Bull., No. 17.

Tchudovitchev, G., 1943. Engelhardt Bull., No. 17.

Tsuji, T., 1966. Publ. Astron. Soc. Japan, 18, 127.

Tsuji, T., 1969. In "Low-Luminosity Stars", Ed. S. S. Kumar, Gordon and Breach, New York.

Tsuji, T., 1971. Publ. Astron. Soc. Japan, 23, 553.

Underhill, A.B., Fahey, R.P., 1973. Ap. J. Suppl., 25, 463.

Voelcker, K., Elsasser, H., 1973. In I.A.U. Symp. No. 52, D. Reidel Publishing Company, Dordrecht, Holland.

Wade, C.M., Hjellming, R.M., 1972. Nature, 235, 270.

Warner, B., 1972. Monthly Notices Roy. Astron. Soc., 160, 35p.

Warner, J.W., Ruben, V.C., 1975. Ap. J., 198, 593.

Walter, K., 1973. Astrophys. Space Sci., 21, 289.

Weedman, D.W., 1968. Ap. J., 153, 49.

Westerlund, B.E., Henize, K.G., 1967. Ap. J. Suppl., 14, 154.

Weymann, R., 1960. Ap. J., 132, 380.

Weymann, R., 1961. Ann. Rev. Astron. Astrophys., 1, 97.

Weymann, R., 1962a. Ap. J., 136, 476.

Weymann, R., 1962b. Ap. J., 136, 844.

Wickramasinghe, N.C., 1967. Interstellar Grains, Chapman and Hall, London.

Wickramasinghe, N.C., 1972. Monthly Notices Roy. Astron. Soc., 159, 269.

Wickramasinghe, N.C., 1973. Light Scattering Functions for Small Particles with Applications in Astronomy, Adam Hilger, London.

Wickramasinghe, N.C., Guillaume, C., 1965. Nature, 207, 366.

Wickramasinghe, N.C., Donn, B.D., Stecher, T.P., 1966. Ap. J., 146, 590.

Wildey, R., Murray, B., 1964. Ap. J., 139, 435.

Wilson, O.C., 1958. Rev. Mod. Phys., 30, 1025.

Wilson, O.C., 1960. Ap. J., 131, 75.

Wilson, R.E., 1971. Nature, 234, 406.

Wilson, R.E., 1974. Ap. J., 189, 319.

Wood, P.R., 1973. In Mem. Soc. Roy. Sci. Liége, 5, 419.

Woodsworth, A.W., Hughes, V.A., 1976. Monthly Notices Roy. Astron. Soc., 175, 177.

Woolf, N.J., 1965. Ap. J., 141, 155.

Woolf, N.J., 1969. Ap. J. (Letters), 157, L37.

Woolf, N.J., 1973. Ap. J., 185, 229.

Woolf, N.J., 1973b. In I.A.U. Symp. No. 52, Ed. J. M. Greenberg and H. C. van de Hulst, D. Reidel Publishing Company, Dordrecht, Holland.

Worden, S.P., Whelan, J.A.J., 1973. Monthly Notices Roy. Astron. Soc., 163, 391.

Woyk, E., 1968. In I.A.U. Symp. No. 34, Ed. D. E. Osterbrock and C. R. O'Dell, D. Reidel Publishing Company, Dordrecht, Holland.

Yamashita, Y., 1962. Publ. Astron. Soc. Japan, 14, 390.

Young, A.T., 1974a. In "Methods of Experimental Physics", 12A, Ed. N. Carleton, Academic Press, New York, London.

Young, A.T., 1974b. Ap. J., 189, 587.

Zaikowski, A., Knacke, R.F., Porco, C.C., 1976. In "Solid State Astrophysics", Ed. N. C. Wickramasinghe and D. J. Morgan, D. Reidel Publishing Company, Dordrecht, Holland.

Ziolkowski, J., 1976. Ap. J., 204, 512.

Mon. Not. R. astr. Soc. (1973) **164**, *Short Communication*, 31P–33P

THE DETECTION OF M15 AT 10·2 μ

A. D. MacGregor, J. P. Phillips and M. J. Selby

(Received 1973 July 24)

SUMMARY

The detection of emission at 10·2 μ from the central regions of M15 is reported, and some possible origins are examined.

1. INTRODUCTION

Few globular clusters are found to be positionally associated with infra-red sources. A comparison between the positions of the 119 globular clusters listed by Arp (1965) and the infra-red sources given in the 2·2-μ catalogue of Neugebauer & Leighton (1965) reveals only three relatively close coincidences. One (IRC–20528), close to the centre of NGC 6717, is the K1 star BS 7120 of visual magnitude +4·98. Of the remaining two IRC–20498, which may be variable in the K band, has been discussed by Cohen (1971) who suggests as a possible origin an extended infra-red source within the globular cluster M22. The other, IRC–10402, lies in the outer regions of I 1276 and has a large (I–K) of $+5{\cdot}43 \pm 0{\cdot}09$, but has not as yet been identified with any optical object. Apart from these sources, IRC–20385 has been provisionally identified by Warner & Wing (1971) and Wray (1971) as a heavily reddened globular cluster very near the galactic plane.

In this paper, the discovery of infra-red radiation from the metal deficient globular cluster, M15, is reported. The detection is the first to be made of a globular cluster at the longer wavelength of 10·2 μ, and is of the central 0·5-pc diameter region alone. It is the only globular cluster known to contain a planetary nebula (O'Dell, Peimbert & Kinman 1964), Ps1. The planetary nebula is unlikely to contaminate our results because it is metal weak, small ($\sim$1 arcsec), distant from the centre of M15 ($\sim$30 arcsec), and weak at radio wavelengths (Higgs 1971). Indeed, if it had been detected, it would have resulted in a negative contribution to the observed flux.

2. OBSERVATION

M15 was observed with the 60-in. infra-red telescope at Tenerife during one night in 1972 October. A 4·2 K, copper-doped germanium photoconductor with a similarly-cooled broad band filter centred on 10·2 μ was used in a conventional infra-red photometer. A sky beam of 10 arcsec was accepted by the detector and a vibrating mirror provided the sky chopping, on this occasion with a peak–peak amplitude of 10 arcsec in declination. An oscillating image of the sky is produced by the chopper on the detector so that it measures the difference in emission between two adjacent sky beams of 10 arcsec diameter and 10 arcsec separation. For M15 the telescope was ' nodded ', i.e. alternately set in two positions, so that the differ-

ence in emission was taken between the central 10-arcsec diameter containing the core of the cluster, and the adjacent 10-arcsec diameter regions north and south. Two hundred and thirty pairs of integrations were taken representing a total integration time of about 25 min.

Visually, M15 has a fairly well-defined core of approximately 10-arcsec diameter. It was estimated that we were able to define and position the centre of the core to better than 3 arcsec. Extinction was measured by observing various standard calibration stars. On the night in question an extinction of $\sim 0{\cdot}9$ mag air mass^{-1} was recorded, a value which is not unreasonable when it is considered that the edges of the filter passband overlap the edges of the 8–13 μ atmospheric window. The measurements were calibrated by taking the 10·2-μ magnitude of α Tau to be $N = -2{\cdot}97$ (Gillett, Merrill & Stein 1971), and the flux corresponding to $N = 0{\cdot}0$ to be $4{\cdot}3 \times 10^{-25}$ W m^{-2} Hz^{-1} (Johnson 1966).

After correction for extinction we measured a flux for M15 of $(+1{\cdot}0 \pm 0{\cdot}3) \times 10^{-25}$ W m^{-2} Hz^{-1}, which at 10·2 μ corresponds to $N = {}^{+}1{\cdot}6 \pm 0{\cdot}3$ mag, the quoted error representing one standard deviation of the photometry. Various ways in which this flux might originate are now considered.

3. DISCUSSION

Of the stellar population in the core of M15 the red giants should give the largest contribution at 10·2 μ, but we estimate that they are in total not brighter than $N \simeq +8{\cdot}5$ for the central 10 arcsec diameter region. It is therefore clear that even a substantial population of stars with Mira-like excesses would not account for the observed flux. If a stellar source is to explain the observed emission at all, objects having extremely large infra-red excesses such as NML Cyg are required. If we were to transpose NML Cyg from a distance of $\sim 0{\cdot}5$ Kpc (Stein *et al.* 1969) to that of M15 (~ 10 Kpc), the infra-red 10·2-μ magnitude would change from $\sim -5{\cdot}5$ to $\sim +2{\cdot}0$. This latter value is comparable to the 10·2 μ flux measured from M15. If on the other hand a distance $\sim 0{\cdot}2$ Kpc is adopted for NML Cyg (Herbig & Zappala 1970), then several of these highly reddened sources would be required to explain the measured flux.

It is also possible that the 10·2-μ flux from the cluster may originate in an extended, cool dust cloud in the central 10 arcsec region. The temperature of dust heated by the local stellar population is unlikely to exceed 50 K, and assuming an emissivity at 10·2 μ of 0·1 for the grains, then the mass of the dust cloud would be $\sim 5 \times 10^4 M_\odot$. If the grains originate from stellar mass loss within the cluster, and a value of 0·4 per cent is adopted for the fraction by mass of ejected matter which eventually forms dust, then a total mass loss of $10^7 M_\odot$ is required. The latter value is a lower limit since it assumes that all dust grains are retained by the cluster and all the dust is contained within the central 10 arcsec diameter. In any case a total mass loss of $10^7 M_\odot$ is unrealistically high; Oort & van Herk (1959) estimate a total mass loss of $3 \times 10^5 M_\odot$ for M3. It is interesting to note that such a dust cloud would give substantial reddening in the centre, which would lead to an estimated absorption $E(B-V) \gtrsim 1{\cdot}3$ mag in excess of that for the outer regions of the cluster. Unfortunately, there seem to be no measurements available for the integrated $(B-V)$ at the very centre of M15.

4. CONCLUSION

The preceding discussion indicates that although the 10·2-μ flux from M15 is unlikely to be from a cool extended dust cloud, it can be explained in terms of a hot, compact dust cloud. The heating mechanism may be a single red giant, placing the source in the category of NML Cyg, or perhaps a small ensemble of closely packed stars. In either case, only relatively small dust masses of $\sim 10^{-5}\ M_{\odot}$ (for a grain temperature ~ 300 K) are required. With the present state of information about M15, arguments concerning the nature of the source must necessarily be rather tentative, however, and it would clearly be valuable to observe this globular cluster at other wavelengths, and investigate the spatial distribution of infra-red emission.

ACKNOWLEDGMENTS

JPP and ADM are in receipt of SRC research studentships. We are indebted to M. Douma for valuable assistance with the detector and other equipment, and are grateful to F. Quist of MIT Lincoln Labs. for the loan of the Cu Ge detector elements.

Astronomy Group, Department of Physics, Imperial College of Science and Technology, London SW7 1NA

Received in original form 1973 *May* 13

REFERENCES

Arp, H. C., 1965. *Stars and stellar systems, Vol. V*, p. 401, eds A. Blaauw and M. Schmidt, University of Chicago Press, Chicago.
Cohen, M., 1971. *Astrophys. Lett.*, **9**, 95.
Gaustad, J. E., 1963. *Astrophys. J.*, **138**, 1050.
Gillett, F. C., Merrill, K. M. & Stein, W. A., 1971. *Astrophys. J.*, **164**, 83.
Herbig, G. H. & Zappala, R. R., 1970. *Astrophys. J. (Letters)*, **162**, L15.
Higgs, L. A., 1971. *Publ. astrophys. Branch. Nat. Res. Council Canada*, **1**, No. 1.
Johnson, H. L., 1966. *A. Rev. Astr. Astrophys.*, **4**, 193.
Neugebauer, G. & Leighton, R. B., 1965. Two micron sky survey: a preliminary catalog, *NASA, SP.*3047.
O'Dell, C. R., Peimbert, M. & Kinman, T. D., 1964. *Astrophys. J.*, **140**, 119.
Oort, J. H. & Herk, G. van, 1959. *Bull. astr. Inst. Nethl.*, **14**, 299.
Stein, W. A., Gaustad, J. E., Gillett, F. C. & Knacke, R. F., 1969. *Astrophys. J.*, **155**, L177.
Warner, J. W. & Wing, R. F., 1971. *Astrophys. J.*, **167**, L53.
Wray, J. D., 1971. *Astrophys. J.*, **168**, L97.

THE STRUCTURE AND INTERNAL EXTINCTION OF NGC 7027

T. R. Hicks, J. P. Phillips and N. K. Reay

REPRINTED FROM

Mon. Not. R. astr. Soc. (1976) **176**, 409–420

PUBLISHED BY

BLACKWELL SCIENTIFIC PUBLICATIONS

OXFORD LONDON EDINBURGH MELBOURNE

Mon. Not. R. astr. Soc. (1976) **176**, 409–419.

THE STRUCTURE AND INTERNAL EXTINCTION OF NGC 7027

T. R. Hicks, J. P. Phillips and N. K. Reay

Physics Department, Astronomy Group, Imperial College of Science and Technology, London SW7 2BZ

(Received 1976 February 13; in original form 1975 December 8)

SUMMARY

We have measured the [O III] λ 5007 Å emission line at several points in the planetary nebula NGC 7027, and obtained monochromatic electronographs of this nebula in Hβ λ 4861 Å and [O III] λ 5007 Å. These data are used to investigate the internal extinction and gaseous structure of the nebula.

1. INTRODUCTION

Morphological studies of planetary nebulae usually distinguish a group of objects with irregular structure. These are planetaries which do not have any symmetry, or distinguishing features which would enable them to be classified as 'ring'-like, 'ellipsoidal' or 'bipolar' (Westerlund & Henize 1967; Hromov & Kohoutek 1968). Rather, they are highly irregular, the only common factor between members of this group being their total lack of common distinguishing morphological features. The planetary nebula NGC 7027 is such an object (Minkowski 1968). Although its optical form appears to reflect a variation of gaseous density, the 5-GHz radio map of Scott (1973), shows a highly regular bipolar structure, implying that the optical irregularity of the nebula is due to heavy extinction.

Observations at 10·2 μm indicate an emission excess, presumably from dust grains within the nebula, and mapping at this wavelength (Becklin, Neugebauer & Wynn-Williams 1973) shows the distribution of this emission also to have a regular bipolar structure. The close similarity of radio and infrared maps argue for a uniform mixture of gas and dust; quite at variance with the observed optical extinction. If this is the case then preferential absorption of radiation from the back of the shell, by dust in the front part of the shell, would lead to a red/blue asymmetry in emission line profiles. The precise interpretations of any observed asymmetry would also depend upon the structure which is adopted for the nebular envelope and the presence or otherwise of temperature or density inhomogeneities. It may therefore be feasible to measure the extinction due to dust within NGC 7027 by observing the detailed shape of a spectral line and adopting a suitable model for the nebular envelope.

Osterbrock (1974) has already tried to resolve components in the Hα, Hβ and Hγ lines from NGC 7027 using high dispersion spectra, but with little success. The purpose of this communication is to report the results of observing the less thermally-broadened [O III] λ 5007 Å line, in an attempt to resolve line components and further investigate internal extinction.

2. OBSERVATIONS

Observational evidence indicates that for density bounded planetary nebulae the [O III] λ 5007 Å and Hβ λ 4861 Å radiations originate from the same regions (Weedman 1968). Furthermore, expansion velocities measured from these two lines are usually in close correspondence.

For NGC 7027, measurements at the 21-cm wavelength (Thompson & Colvin 1970) have failed to detect any significant neutral hydrogen component. If it were concluded from this that the nebula is density bounded we would expect the Hβ and [O III] radiations to come from the same region. Fig. 1 shows contour maps of NGC 7027 produced from electronographs obtained using a Spectracon image converter on the 50-cm Mons telescope, Tenerife. Fifteen contour levels are equispaced between the highest and lowest intensities in the electronographic images, and the angular resolution is limited by ' seeing ' to approximately 2 arcsec. The exposure for the [O III] λ 5007 Å electronograph was 2 min compared with 30 min for the Hβ electronograph and we see the two emitting regions are essentially identical.

In the following we assume the emitting regions truly are identical, implying that the spatial structure and dynamics of the [O III] region closely resemble those of the H II region.

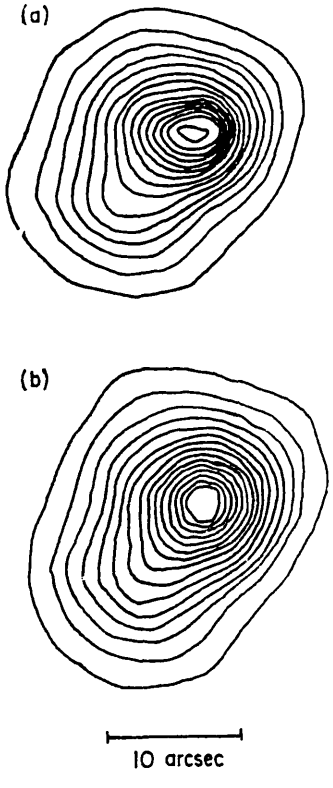

FIG. 1. *Contour maps for (a) [O III] λ 5007 Å, and (b) Hβ λ 4861 Å. Fifteen contour levels are equispaced between the highest and lowest intensities in the electronographic images. The similarity of the maps indicate that the radiations are from a common emitting region.*

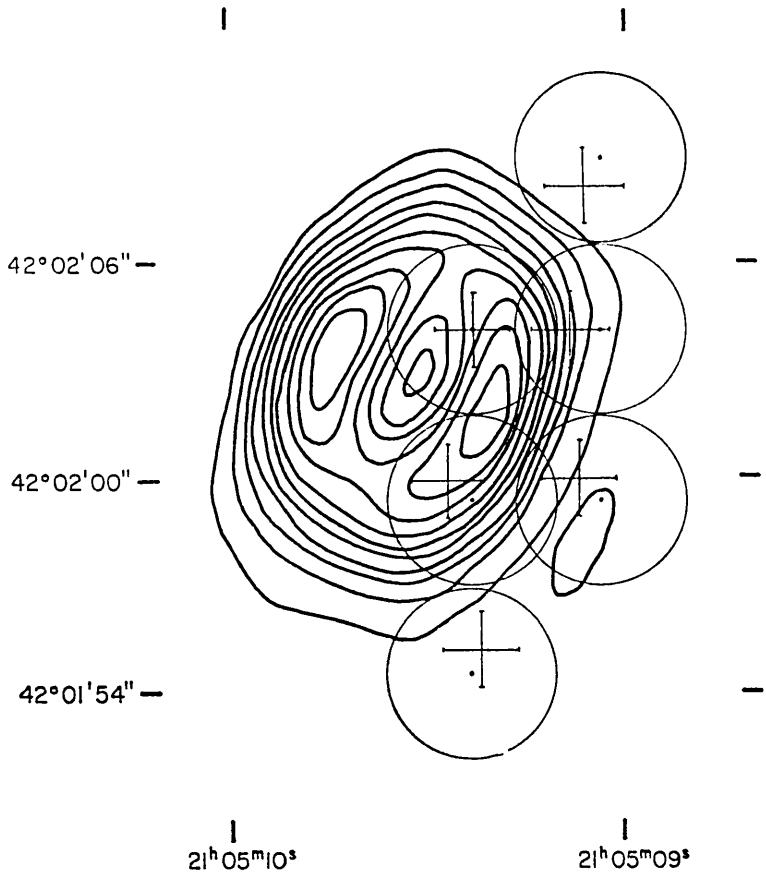

FIG. 2. *Locations of points at which spectral profiles were obtained, plotted on the 5 GHz radio map (Scott 1973). The circles represent the size of the 5 arcsec diameter telescope beam and the crosses are the effective points of observation. The size of the crosses represent the errors in the positions of these points.*

[*O III*] *line profiles*

A servo-controlled Fabry–Perot interferometer (Hicks, Reay & Scaddan 1974) was used to obtain line profiles for a number of points across the nebular envelope. The spectral resolution was 70 000 and the data were obtained using the Isaac Newton telescope at the Royal Greenwich Observatory. Fig. 2 shows the locations at which the profiles were measured plotted on the 5-GHz radio map (Scott 1973). The circles represent the 5-arcsec diameter entrance diaphragm projected on to the nebula. Positioning was accomplished by accurately offsetting the telescope from nearby reference stars to the radio centre of the nebula. A further small offset from the radio centre then located the diaphragm at the point to be observed. The ' bright knot ' in the visual image of NGC 7027 was used as a reference point for guiding, and frequent checking of the offsets ensured image rotation and telescope drift errors were kept small. The effective positions, derived by appropriately weighting each point within the entrance diaphragm with the [O III] intensity distribution, are indicated by the crosses within the circles (Fig. 2). The positional accuracy of these effective positions is $\pm 1{\cdot}5$ arcsec (indicated by the size of the

crosses) made up by errors in telescope setting and small errors in the weighting procedure.

Fig. 3 shows examples of the recorded line profiles. Clearly a double peak structure is just detectable, particularly near the nebular centre. A curve fitting programme was used to fit to each profile two gaussian components and a variable continuum level, and Table I gives the velocity separations and relative heights of the fitted components.

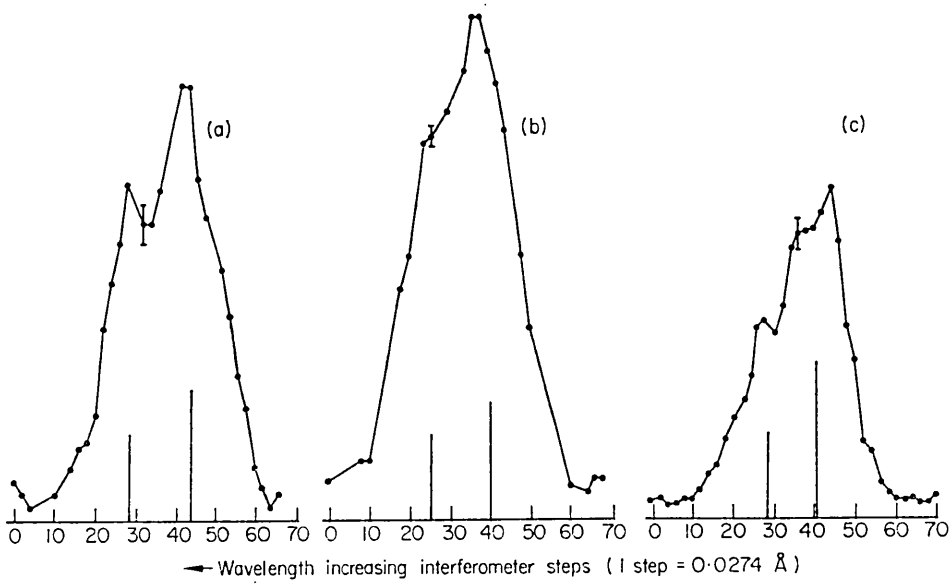

FIG. 3. *Typical line profiles (a) and (b) were recorded near the centre 'c' of the radio nebula at telescope coordinates (c −0·15) sec RA and (c +1·7) arcsec Dec. Profile (c) was recorded near the edge of the nebula at (c −0·15) RA and (c −8·3) arcsec Dec. The vertical lines represent the relative heights of fitted components.*

A number of points can be made in relation to Fig. 3 and Table I.

(1) All profiles show evidence for two blended components.

(2) In the direction of the bright knot the component separation corresponds to an expansion velocity of 13·5 km s^{-1}. This is much smaller than the value of 20·45 km s^{-1} reported by Wilson (1950) for the centre of the nebula and explains the failure of Osterbrock to find significant structure in the thermally-broadened Balmer lines (Osterbrock 1974).

(3) Although errors on some of the measurements near the nebular edge are large, the component separation is consistently greater at points nearest the nebular centre than for outlying points.

(4) The intensity ratios I_B/I_R are consistently greater than unity, suggesting either a non-uniform density or temperature structure in the envelope, or internal extinction amounting to ~0·34 mag near the nebular centre.

Line profiles were also taken to the north and east of the nebular centre, which showed at least qualitative agreement with the details presented above, but these were unfortunately erased by a malfunction of the computer disk system.

TABLE I

[O III] observations and parameters of fitted curves

	Position on nebula						Details of fitted curves		
	Telescope* position		Effective† position		No. of scans	Intensity‡	Intensity‡	Ratio	Separation
Date	(sec)	(arcsec)	(sec)	(arcsec)	co-added	(red)	(blue)	I_B/I_R	(km s^{-1})
1974 Sept. 29	−0·15	+1·7	−0·15	+1·7	9	1153 ± 60	1578 ± 65	1·37 ± 0·13	24·4 ± 1·4
1974 Sept. 30	−0·15	+1·7	−0·15	+1·7	2	107 ± 14	338 ± 10	1·63 ± 0·16	27·0 ± 1·6
1974 Sept. 30	−0·15	+1·7	−0·15	+1·7	1	189 ± 14	286 ± 12	1·51 ± 0·18	27·0 ± 1·9
1974 Sept. 29	−0·15	−3·3	−0·08	−2·6	4	88 ± 37	242 ± 24	2·75 ± 1·42	23·1 ± 5·6
1974 Sept. 30	−0·48	+6·7	−0·41	+6·0	4	34 ± 12	121 ± 13	3·55 ± 1·64	14·0 ± 3·7
1974 Sept. 30	−0·48	−3·3	−0·41	−2·6	6	148 ± 25	218 ± 39	1·47 ± 0·51	17·6 ± 2·1
1974 Sept. 30	−0·15	−8·3	−0·15	−7·3	3	220 ± 94	388 ± 54	1·76 ± 1·00	21·0 ± 2·6
1974 Sept. 29	−0·48	+1·7	−0·38	+1·7	3	362 ± 123	422 ± 111	1·16 ± 0·70	21·9 ± 5·7

* Direction at which telescope was pointing with respect to the centre of radio nebula. Expressed in seconds of RA and arcseconds of declination.

† Effective position on nebula, weighted to account for the 5 arcsec entrance diaphragm.

‡ Peak intensity of fitted components, expressed as photoelectron pulse counts. The intensity error is derived from the least squares fitting procedure, and represents the uncertainty in the fitted peak height.

We now examine the consequences of these comments for the density and temperature structure of the nebular envelope and for the question of extinction within the nebula.

3. DISCUSSION

The only model the authors know as having been specifically applied to NGC 7027 is that of Scott (1973), who proposed that the nebula has the form of a tilted cylinder; a model that had been suggested previously by Hromov & Kohoutek (1968) and Zanstra & Brandenburg (1951), and subsequently again by Scott (1975) for other planetary nebulae. From the evidence presented here, it is clear that the apparent diminution of the red-shifted component of the central line could be due either to temperature or gaseous inhomogeneities, or absorption by dust. With the cylindrical model, however, the amount of gaseous inhomogeneity required to explain the spectral line would seriously compromise the spatial symmetry of the radio emission. Furthermore, spectra of the three density bounded nebulae NGC 6210, 7009 and 7662 (Osterbrock, Miller & Weedman 1966) show that where the emission lines have well resolved blue- and red-shifted components, the ratios I_B/I_R (Hβ) and I_B/I_R ([O III]) are identical within experimental error. Because the intensity of [O III] λ 5007 Å increases almost linearly, and that of Hβ declines slowly, with temperature in the range 7500–15 000 K, we would expect even small changes in this parameter across the nebular envelope to give discernibly different values of I_B/I_R (Hβ) and I_B/I_R ([O III]). Also, if this were the case the intensity distributions of Hβ and [O III] would differ, whereas our own observations for NGC 6210 and 7662 and those of Aller (1956) (in Hα and [O III]) for NGC 7009 show the isophotes to be identical.

Because, as already noted, the Hβ and [O III] isophotes for NGC 7027 are also essentially identical, it seems therefore reasonable to assume that there is little temperature structure within the Hβ+[O III] emitting region of this nebula. The inevitable proviso must be made, however, that temperature inhomogeneities have not been conclusively eliminated, and there remains a chance, albeit slim, of some contribution to line asymmetry from this source.

If dust extinction is considered as a more likely alternative explanation, then because of the geometry of the Scott cylindrical model there would be no way of distinguishing between absorption by dust lying within the nebula or differential absorption across the face of the nebula by external dust. Internal dust would, however, have to be within the inner boundary of the cylindrical shell (Fig. 4). For the dust grains in NGC 7027 to have the relatively substantial ultraviolet absorption bands suggested by the work of Becklin *et al.* (1974) and to lie within the high temperature radiation field characteristic of central stars in planetaries, would imply the need for radii greater than 5 μm if they are not to be accelerated into the nebular shell by radiation pressure. Such grain sizes are very much larger than those usually associated with interstellar or circumstellar extinction, which in turn are probably submicron in size (*cf.* Greenberg 1973; Capps & Dyck 1972). This, if the Scott model were correct, might suggest that the asymmetry line profile is due to differential extinction across the object by dust external to the nebular shell: probably the same dust which causes the nebula to appear irregular in the visible. From a comparison of the 5-GHz intensity profiles taken along the major axis of this nebula (Scott 1973) and the Hβ profile (Fig. 5) it is apparent that this proposition is viable if the model proposed by Scott is simply inverted.

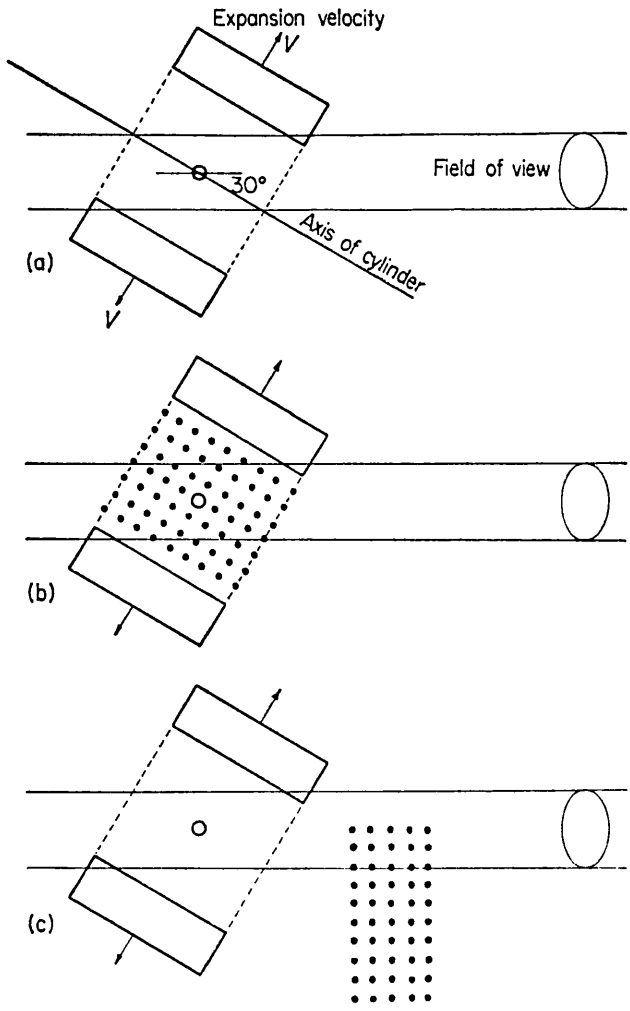

FIG. 4. (*a*) *Cylindrical model viewed with* 2*-arcsec telescope beam. The upper front edge and lower rear edge would give blue and red spectral components respectively.* (*b*) *Internal dust would attenuate radiation from the lower rear edge of the shell, i.e. the* '*red*' *component would be attenuated.* (*c*) *External dust could cause variable extinction across the face of the nebula and give the same effect as internal dust in* (*b*). *For this particular model these comments are generally true for fields of view* $\lesssim$ 2 *arcsec.*

It is clear from the above how strongly the model adopted influences the interpretation of the spectral line profiles. The question therefore arises as to how valid this model is. There are in fact several objections to the cylindrical model.

The first concerns the splitting of the spectral lines, which should remain roughly constant and independent of position along the major axis if as is commonly supposed for other nebulae (*cf.* Aller & Liller 1968) the expansion velocity of the nebula is roughly proportional to the radial distance from the star. The exception to this is where tilting of the cylinder enables us to view either the front or the back of the shell in isolation; as does the cylindrical model of NGC 7027 at positions on the major axis away from the nebular centre. In that case one or other of the line

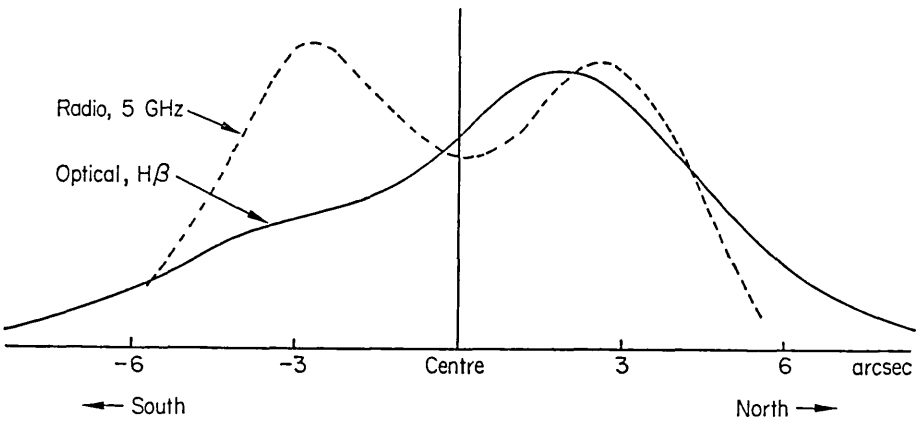

FIG. 5. *Relative 5-GHz and Hβ intensities plotted along the major axis of the 5-GHz radio map.*

components would disappear, depending on which side of the minor axis of the nebula the line was observed. In fact the lines measured away from the centre of NGC 7027 and along the major axis still indicate two relatively strong components (Fig. 3) which appear to have a reduced separation compared to the central line. Furthermore, lines measured on opposite sides of the minor axis of the nebula also show similar relative heights for the spectral line components, behaviour which is again at variance with a simple cylindrical model.

We propose instead that the nebula is an oblate spheroid, a form first suggested for planetaries by Curtis (1918). This would present a bipolar configuration when viewed from appropriate angles, and for reasons first given by Wilson (1958), would be able to account for the spectral line behaviour of this and many other planetaries In comparison, few planetary nebulae have spectral line data which indicates a cylindrical configuration.

To further investigate the properties of an oblate nebula, we have constructed a model in which the nebula exists within a region defined by two concentric ellipsoids. The ellipsoids are created by rotating ellipses of differing axial lengths, but identical eccentricities, about their minor axes. Contour maps of a number of such nebulae in which the gas density varied as $r^{-\alpha}$ ($\alpha > 0$) were computed for a range of nebular orientations. The ratio between the major and minor axes was taken to be 1·7, and between the axial lengths of outer and inner ellipsoids as 1·625. These values are not critical; the former depends on the value of α adopted, and increases as α increases. Changes in the latter have little effect on the computed contour map for values of shell thickness below the diameter of the resolution element. The model we adopt is not therefore unique, but gives a rather better fit to the radio data than most other models investigated. A circular resolution element of diameter 2·0 arcsec was assumed, to present a realistic comparison with the radio map. A value of $\alpha = 1$ was found to give a reasonable representation of the radio contours and an example of this model for which the plane containing the minor axis is normal to the line of sight is presented in Fig. 6. The bipolarity evident in this map is maintained even if the model is tilted such that the minor axis presents an angle of up to 45° with the line of sight. The close resemblance to the radio map will be noted.

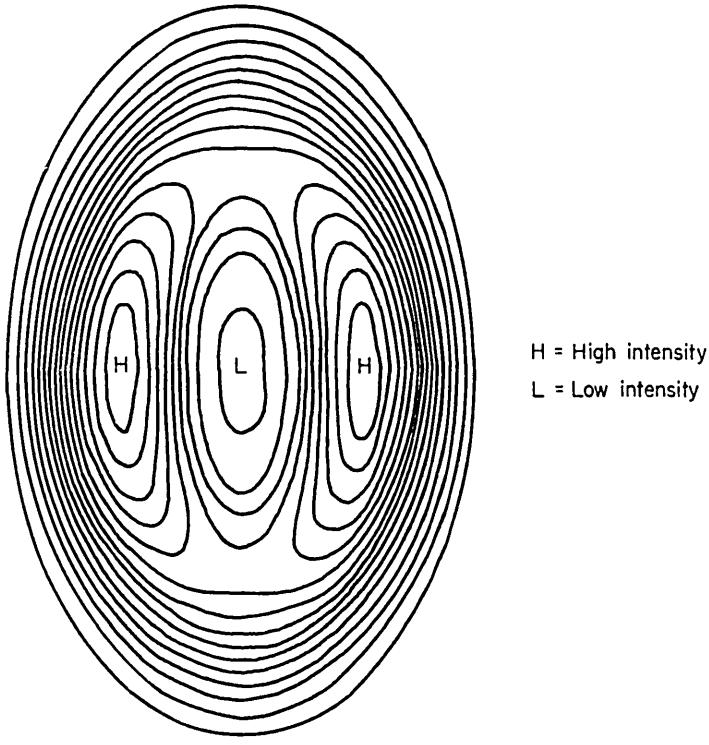

FIG. 6. *Contour map of an oblate spheroid nebular model viewed such that the minor axis is in the plane of the paper. The model shows good agreement with the radio map. The parameters of the model are discussed in the text.*

The consistent trend of spectral line ratio (Table I) would seem to rule out variations of gas density as a likely cause of spectral line asymmetry; the inhomogeneity would have to extend over the entire far side of the nebula to explain the general emission symmetry and consistent line asymmetry, but stop precisely at the nebular edge. A test of this hypothesis was nevertheless attempted with a model having the rear half at 15 per cent lower density than the front half (this would give emission components in approximately the observed ratio), the dividing plane containing the minor axis of the model. The model was orientated so that the lower density half was precisely behind the higher density half, and a regular bipolar structure was observed. Tilting the model by only $\Delta\theta \sim 5^\circ$ produced emission asymmetries very much greater than are observed in NGC 7027. It is therefore apparent that the explanation of spectral line asymmetry in terms of gaseous inhomogeneity requires of the nebula an unlikely combination of spatial orientation and density structure.

Accepting the arguments against temperature inhomogeneities presented earlier, the spectral line asymmetry is almost certainly due to dust inside the nebular shell: presumably that giving rise to the excess thermal emission at 10·2 μm. The apparent trend for an increasing absorption towards the edge of the nebula would be a consequence of increasing shell depth. If an extinction of $4{\cdot}5 \times 10^4$ mag g^{-1} is assumed for the dust, characteristic of interstellar optical extinction (Bok, Cordwell & Cromwell 1971) and the electron density at the nebular centre is taken

as $n_e \simeq 5{\cdot}9 \times 10^4$ cm^{-3} (Miller & Matthews 1972), the extinction of $\simeq 0{\cdot}34$ mag suggested by the central [O III] λ 5007 Å line measurements gives a dust:gas mass ratio of $\phi \simeq 10^{-3}$ for the oblate model adopted. This value is close to that expected ($\phi \simeq 4 \times 10^{-3}$) for efficient dust condensation in a nebula with normal elemental abundance. Similarly, although a typical optical extinction of only $\simeq 0{\cdot}2$ mag would be expected (Bless & Savage 1972) if an ultraviolet extinction of $\simeq 1{\cdot}5$ mag is adopted (Becklin *et al.* 1973) and the dust is assumed to behave like interstellar dust, the observed central extinction of $\simeq 0{\cdot}34$ mag is within the range of variability observed in these quantities.

The value of ϕ is inversely proportional to the adopted shell thickness however, and the value given here can be considered only as representative. A reduction in shell thickness by a factor of 3, for example, has little effect on the computed contour map but would increase ϕ by a similar factor.

It must also be emphasized that the application of mass extinction coefficients characteristic of interstellar grains, which derive from many sources and are probably subject to further evolution in the interstellar environment, can be considered as at best suggestive.

4. CONCLUSIONS

The observations presented here suggest that NGC 7027 may be represented by an oblate spheroid, a model first proposed by Curtis for other nebulae (Curtis 1918), and rule out a tilted cylinder model due to Scott (1973). This suggestion is supported by models of oblate nebulae, which show a bipolar structure characteristic of the radio (Scott 1973) and infrared (Becklin *et al.* 1973) maps of NGC 7027. An asymmetry noted in the observations of [O III] λ 5007 Å lines is unlikely to be due to either density or temperature inhomogeneities and is probably caused by dust within the nebular shell. The mass of dust required to explain the line asymmetry does not appear unreasonable for a nebula with normal elemental abundance.

ACKNOWLEDGMENTS

We are grateful to the Director and staff of the Royal Greenwich Observatory for their hospitality. The 50-cm Mons telescope was used by kind permission of Professor Francisco Sanchez Martinez and Dr L. Housiaux. The work was generously supported by the Science Research Council.

REFERENCES

Aller, L. H., 1956. *Gaseous nebulae*, Chapman Hall, London.

Aller, L. H. & Liller, W., 1968. *Planetary nebulae, stars and stellar systems*, Vol. VII, p. 583, eds B. M. Middlehurst & L. H. Aller, University of Chicago Press, Chicago and London.

Becklin, E. E., Neugebauer, G. & Wynn-Williams, C. G., 1973. *Astrophys. Letters*, **15**, 87.

Bless, R. C. & Savage, B. O., 1972. *Astrophys. J.*, **171**, 293.

Bok, B. J., Cordwell, C. S. & Cromwell, R. H., 1971. *Dark nebulae, globules and protostars*, p. 33, ed. B. T. Lynds, University of Arizona Press, Tucson, USA.

Capps, R. W. & Dyck, H. M., 1972. *Astrophys. J.*, **175**, 693.

Curtis, H. D., 1918. *Publ. Lick Obs.*, **13**, 55.

Greenberg, J. M., 1973. *IAU Symp. No.* **52**, p. 3, eds J. M. Greenberg & H. C. Van de Hulst, D. Reidel Publishing Co., Dordrecht, Holland.

Hicks, T. R., Reay, N. K. & Scaddan, R. J., 1974. *J. Phys. E.: Sci. Instrum.*, **7**, 27.
Hromov, G. S. & Kohoutek, L., 1968. *Bull. astr. Inst. Csl.*, **19**, 1.
Miller, J. S. & Matthews, W. G., 1972. *Astrophys. J.*, **172**, 59.
Minkowski, R., 1968. *Astr. J.*, **73**, 842.
Osterbrock, D. E., 1974. *Publ. astr. Soc. Pacific*, **86**, 609.
Osterbrock, D. E., Miller, J. S. & Weedman, D. W., 1966. *Astrophys. J.*, **145**, 697.
Scott, P. F., 1973. *Mon. Not. R. astr. Soc.*, **161**, 35.
Scott, P. F., 1975. *Mon. Not. R. astr. Soc.*, **170**, 48.
Thompson, A. R. & Colvin, R. S., 1970. *Astrophys. J.*, **160**, 363.
Weedman, D. W., 1968. *Astrophys. J.*, **153**, 49.
Westerlund, B. E. & Henize, K. G., 1967. *Astrophys. J.* (*Suppl.*), **XIV**, 154.
Wilson, O. C., 1950. *Astrophys. J.*, **111**, 279.
Wilson, O. C., 1958. *Rev. mod. Phys.*, **30**, 1025.
Zanstra, H. & Brandenburg, W. J., 1951. *Bull. astr. Inst. Netherl.*, **11**, 351.

PRINTED IN ENGLAND BY
ADLARD AND SON LTD, DORKING

REPRINT

D. REIDEL PUBLISHING COMPANY

DORDRECHT-HOLLAND / BOSTON-U.S.A.

Subscription Information

Subscriptions are entered for complete volumes only and expire with the last issue of a volume. All subscriptions are payable in advance. The publishers reserve the right to publish additional volumes and special issues.

Prices are given in Dutch guilders and in US dollars for the U.S.A., Canada, Mexico and South America. Prices are subject to change without prior notice. Subscribers to current volumes will receive advance information.
Prices do not include postage and handling. Special postal arrangements can be made. Deliveries within The Netherlands are subject to the addition of B.T.W.

Subscriptions can be sent to your regular agency or direct to:

D. REIDEL PUBLISHING COMPANY

P.O. Box 17, Dordrecht-Holland

Telephone: 35388 – Cables: Reipubco – Telex: 24245

Private subscriptions should be sent direct to the publisher. Private persons (no institutions, laboratories, libraries, etc.) may subscribe to most journals at reduced rates. They should declare that the subscription is for their own personal use, that it will not replace any library subscription and will not be put at the disposal of any library.

Payment can be made through our bankers:

Amsterdam-Rotterdam Bank N.V., Dordrecht-Holland,
Account No. 44.36.37.105

N.V. Slavenburg's Bank, Dordrecht-Holland,
Account No. 64.27.19.284

Deutsche Bank A.G., Köln, Germany,
Konto Nr. 184/6484

or via our Postal Cheque Account No. 172579.

Bank drafts, personal cheques, international money orders and UNESCO coupons are also accepted.

Claims for missing issues should be made within six months after publication. Defective issues and issues that were damaged during the mail should be returned immediately.

Please send address changes as soon as possible referring to the journal subscribed to and listing your old and new address.

Sample copies will be sent on request.

THE INCEPTION OF NOVAE TRANSITION ZONE OSCILLATIONS

J. P. PHILLIPS and M. J. SELBY
Astronomy Group, Imperial College, London, England

(Received 27 September, 1976; revised 3 November, 1976)

Abstract. The nature of semi-regular oscillations in the transition zones of certain novae is discussed. It is found that hydrostatic collapse following a reduction of radiative support for the photospheric layers is a likely explanation of transition zone inception.

1. Introduction

Some 50% of novae show semi-regular variations of luminosity in their transition zones, the nature of which is still not well determined. McLaughlin (1960), for instance, follows Grotrian (1937) in believing the novae photospheres to be continually expanding, and conjectures that the light variations originate from variations in mass ejection rates. Alternatively, Mustel (1956) contends that novae may have more or less stable photospheres, for which case any periodicity in light output may reflect actual variations in the novae radii. This last position will be adopted for the purposes of future discussion.

To proceed further it is first necessary to define a suitable nova structure. For this purpose we adopt a Roche model in which a massive and essentially singular core is surrounded by an envelope of negligible mass, in which density ϱ decreases with radius as $\varrho \propto r^{-2}$. This model has the attraction of causing least disruption to any binary system the nova may belong to: and many if not all novae appear to be components of such systems (cf. Kraft, 1964). Otherwise, for most reasonable low envelope mass cases, the model adopted will be unlikely to critically affect the subsequent discussion.

The period P of undamped radial adiabatic oscillations for the Roche model is given (cf. Sterne, 1937) by

$$P = 2\pi/\sigma, \tag{1a}$$

$$\sigma^2 = \tfrac{1}{3}(3j + q)(3j + q + 3)\left\{\frac{\Gamma G m}{R^3}\right\}; \quad j = 0, 1, 2, \cdots, \tag{1b}$$

$$q = \left\{\frac{3(3\Gamma - 4)}{\Gamma}\right\}^{1/2}, \tag{1c}$$

where m is the mass of the nova, R the radius, and Γ is the ratio of specific heats. The term is in turn dependent upon radiation pressure – a dependence having the familiar form

Astrophysics and Space Science **49** (1977) 339–348.

$$\Gamma = \beta + \frac{(4 - 3\beta)^2(\gamma - 1)}{\beta + 12(\gamma - 1)(1 - \beta)}, \tag{2}$$

where γ is the value of Γ in the absence of radiation pressure, and β is the ratio of gas to total pressure. The period P depends critically upon β for $\beta \ll 1$ if the opacity $\chi \simeq \chi_{TH}$ is the Thomson scattering opacity. This latter condition is used in the discussion of hydrostatic stability in the next section. For the moment, however, we adopt $\Gamma = \gamma = \frac{5}{3}$, although this will lead to upper limit determinations for R. For cases in which the variation of P as a function of luminosity L is not too great, this assumption is probably not too unreasonable. By adopting $m = 0.3 m_\odot$ (we shall justify this later), and using $P = 10^6$ s (characteristic of nova V 603 Aql) we obtain, using Equation (1) and $j = 0$, a nova radius at the inception of the transition zone of $R = 21.3\ R_\odot$. This will be taken as a convenient order of magnitude pulsational radius for novae in the future discussion. For initial transition zone luminosity $M_{BOL} \simeq M_v \simeq -5.0$, where M_v is the absolute visual magnitude, we then obtain an effective temperature

$$T = \left\{\frac{L}{4\pi R^2 \sigma_s}\right\}^{1/4} \simeq 11\,820 \text{ K}, \tag{3}$$

where σ_s is the Stefan–Boltzmann constant and we have assumed the photospheric and pulsational radii to coincide. The temperature corresponds to a bolometric correction B.C. $= -0.64$ which when added to M_v leads to a revised value for M_{BOL}. It is possible in this way to determine a final more accurate estimate of T by iteration (although this accuracy also depends upon the applicability of normal bolometric corrections to novae). After 10 iterations (at which the difference between successive estimates of luminosity was $< 1\%$) a temperature $T \simeq 15\,940$ K is obtained, corresponding to $M_{BOL} \simeq -6.3$. This is reasonably consistent with transition zone temperatures measured in other novae. For $j = 1$ (first mode), the corresponding values are $T \simeq 9520$ K, $R = 37.4\ R_\odot$ and $M_{BOL} \simeq -5.3$ for $I = 5$; again not unreasonable, though rather less likely. For GK Per, the same procedure may be followed, this time for $M_v \simeq -5.2$, $P \simeq 4.0 \times 10^5$ s. For $j = 0$ we thereby obtain $R = 11.5\ R_\odot$, $T \simeq 97\,507$ K and $M_{BOL} \simeq -12.8$ for $I = 47$ iterations; although because of the slow iterative convergence, the values for T and M_{BOL} are lower limits. The latter values for T, M_{BOL} are of course rather unlikely, and the excitation of the higher j modes must be considered; for $j = 1, 2, 3$ temperatures $T = 18\,700$ K, 13 490 K and 11 230 K being respectively determined. These are considerably more plausible: for comparison, Vorontsov-Velyaminov (1946) found transition zone *ionization* temperatures of between 31 000 K and 64 000 K, although these are almost certainly higher than the corresponding effective temperature for the nova. For GK Per, therefore, as for V 603 Aql, the concept that radial pulsations of a stable nova photosphere are responsible for novae transition zone oscillations appears at least reasonable and will be considered as generally valid in the foregoing discussion. Given this position, the cause of the oscillations will now be discussed.

Several mechanisms seem possible. For instance, it can be shown that large photospheric convective cells with circulation periods similar to those of transition zone luminosity variations are plausible, although the mode of radial oscillatory excitation is obscure. The Schwarzschild stability criterion for convection is fairly readily satisfied for the kind of envelopes discussed in Section 2 ($\varrho \simeq 10^{-11}$ g cm^{-3}, $R \simeq 20\ R_\odot$), and although the resultant Rayleigh numbers ($R_e \simeq 10^{10}$) are about six orders of magnitude too great for cell formation, eddy viscosity could possibly reduce R_e substantially.

More obvious would be resonant excitation of radial motions through the tidal forces of a stellar companion, although yet again, the absence of spectroscopic evidence for companions with appropriate periodicities in either GK Per or V603 Aql is restrictive. A more tenable hypothesis involving hydrostatic instability may be available, however, and we discuss this in more detail in the following section.

2. Mechanism Invoking Hydrostatic Instability

The equation of momentum conservation for the outer layers of a nova may be written as

$$\varrho \frac{\mathrm{d}\mathbf{v}}{\mathrm{d}t} = -\{\nabla p + \varrho \mathbf{g}\} - \mathbf{N}, \tag{4}$$

where ∇p is the pressure gradient (including radiation and gas terms), $\mathbf{g}$ is the gravitational potential gradient, $\mathbf{v}$ is velocity and $\mathbf{N}$ is a viscous dissipative term, assumed for the moment to be negligible. The term in parentheses is a restorative term, and for hydrostatic equilibrium we have $(\nabla p + \varrho \mathbf{g}) = 0$.

For small deviations from hydrostatic equilibrium Equation (4) defines simple harmonic motion (S.H.M) about any particular radius. The solution of the Eddington adiabatic wave equation for radial motion in any particular model, assuming this S.H.M. time dependence, thus leads to particular frequency eigenvalues at which S.H.M. may occur, given in Equation (1) for the particular case of the Roche model. For novae with well defined oscillations then we presume that averaged over a pulsation cycle the surface layers are close to hydrostatic equilibrium. In fact, as Finzi (1973) first indicated, this is not necessarily true for novae at all stages as their luminosity declines, and $(\nabla p + \varrho \mathbf{g}) < 0$ (i.e., the outer layers are forced outwards) when luminosity exceeds L_0, where

$$L_0 = \frac{4\pi c G m}{\chi_0}; \tag{5}$$

whence for $\chi_0 \to \chi_{\mathrm{TH}}$, $L_0 \to L_{\mathrm{CRIT}}$, an effective upper limit to the luminosity, where χ_{TH} is the Thomson opacity given by $\chi_{\mathrm{TH}} = 0.2(1+X)$ and X is the relative hydrogen abundance. From (5) Finzi (1973), using $X = 0.7$, determined the relation

$$M_{\mathrm{CRIT}} = -6.8 - 2.5 \log_{10} \left\{ \frac{m}{m_\odot} \right\}, \tag{6}$$

where M_{CRIT} is the absolute bolometric magnitude corresponding to L_{CRIT}. If we make the reasonable assumption that $m/m_\odot \lesssim 1$ therefore it is apparent that many novae at maximum luminosity exceed L_{CRIT}, and the outer layers are *necessarily* forced out. Whenever χ_0 increases in the nova interior, this must be offset by a corresponding luminosity gradient.

Although in the above discussion $\chi_0 = \chi_{\mathrm{TH}}$ was taken as a limiting condition, there are reasons for adopting this as the actual situation in novae envelopes if hydrostatic collapse is to have any relevance to transition zone inception. Primarily, we note that for typical order of magnitude transition zone temperatures $T \simeq 10^4$ K, a density $\varrho \lesssim 10^{-11}$ g cm^{-3} would be required before $\chi_0 \simeq \chi_{\mathrm{TH}}$ (Ezer and Cameron, 1963). For these temperatures, this is precisely the order of magnitude density required for β to begin significantly departing from 1, where

$$\beta = \{1 + a_R T^3 / 3 R_g \varrho\}^{-1}; \tag{7}$$

a_R being the radiation density constant, and R_g the gas constant. Specifically, for $T = 10^4$ K and $\varrho = 10^{-11}$ g cm^{-3} a value $\beta \simeq 0.25$ is determined. Note also that the dependence of β upon ϱ and T follows almost the same form as Kramers's opacity law, so that given this β the argument is not significantly changed by varying ϱ and T. A secondary factor of some relevance is that for $L_0 \neq L_0(R)$ (as would be the case for $\chi_0 = \chi_{\mathrm{TH}}$) a substantial volume of the envelope achieves hydrostatic stability at about the same time, which would be an important factor in understanding why transition zone inception is so rapid. Finally, it will be found that novae mass values determined on the basis that $\chi_0 = \chi_{\mathrm{TH}}$ are reasonably in accord with corresponding spectroscopic estimates. For these various reasons then we adopt $\chi_0 = \chi_{\mathrm{TH}}$ in the subsequent discussion.

As the nova moves into post-maximum decline, the luminosity falls and the degree of hydrostatic imbalance will decrease until the value $L = L_{\mathrm{CRIT}}$ is reached, when hydrostatic equilibrium is temporarily attained. Beyond this stage the photospheric layers will proceed to contract more or less homologously (for $\beta \simeq 0$) as L further declines, leading possibly to the less regular transition zone light curves. For values of β significantly different from zero the argument is qualitatively similar, except that gaseous pressure is then important in restraining contraction. In consequence, transient oscillations may develop. The amplitude of these oscillations will be partly determined by the value of β during the latter stages of post-maximum decline before transition zone inception. For values of β significantly different from 0 or 1 for instance, there is the possibility of a large change of β over a short timescale, and prominent oscillations such as those observed for V 603 Aql and GK Per may occur; whereas for $\beta \simeq 1$ the hydrostatic instability consequent upon a reduction of radiative support is much smaller. Similarly, since $\mathrm{d}\beta/\mathrm{d}t$ depends upon $\mathrm{d}L/\mathrm{d}t$, the amplitude of the

oscillations depends upon the rate of luminosity decline. In contrast, the period of the oscillations depends upon the value of β *within* the transition zone, although like amplitude, it will tend to decrease as $\beta \to 1$. To summarize, then, it seems clear that for many cases typical transition zone behaviour should begin when $L \simeq L_{\mathrm{CRIT}}$, the exception being where β approaches 1 *before* inception, for which case the transition zone would start at lower luminosities. Subsequently, the oscillations may be sustained or modified through the hydrogen ionization zone, which in this respect is probably more significant than the helium ionization zone for the low density novae envelopes (Christy, 1966).

We have up to now assumed that envelope opacity is high, and this must now be verified. Along any radial direction, if τ_p is the photospheric optical depth, we have

$$\tau_p = \int_{r=r_0}^{R_0} \chi_{\mathrm{TH}} \varrho_0 \left\{\frac{r_0}{r}\right\}^2 \mathrm{d}r; \tag{8a}$$

so that

$$f_p = \tau_p / \chi_{\mathrm{TH}} \varrho_0 r_0, \tag{8b}$$

where ϱ_0 is the photospheric mass density, R_0 the pulsational radius, r_0 the photospheric radius, and f_p the fractional photospheric depth, defined by $f_p = (R_0 - r_0)/R_0$. For $\tau_p = 1$, $r_0 = 20\, R_\odot$ and $\varrho_0 = 10^{-11}$ g cm^{-3} then $f_p \simeq 0.2$. In fact, the value for ϱ_0 (and therefore f_p^{-1}) is a lower limit, since it corresponds to $T \simeq 10^4$ K, $\beta \simeq 0.25$, both of which are likely to be higher within transition zones. It seems, therefore, clear that the envelope is reasonably opaque.

Finally, it is of interest to assess the feasibility of applying Equation (6) to transition zones. Values of M_{TRANS}, the absolute visual magnitude of transition zone onset, are determined from data supplied by Payne-Gaposchkin (1957) and McLaughlin (1939), and the assumption is made that $\chi_0 \simeq \chi_{\mathrm{TH}}$. It is also assumed that before transition zone inception β is small. Transition zone bolometric corrections are uncertain; independent observations can yield colour temperatures differing by almost a factor of two (McLaughlin, 1960) although generally the relatively sparse data suggests that $T_c \simeq 15\,000$ K is probably reasonably representative. Ionization temperatures are even less informative in this respect, being invariably higher than T_c and strongly line dependent. On the basis of the colour temperatures we will later for comparative purposes use a value B.C. $\simeq 1$ mag. Certainly, B.C. $\ngtr \Delta M$, the magnitude difference between peak luminosity (B.C. $\simeq 0$) and transition zone inception, unless bolometric luminosity increases.

Eight novae were selected having well defined light curves and fairly unambiguous transition zones. The identification of transition zone onset proved to some extent subjective, except for three cases (GK Per, V 603 Aql and RR Pic) where well defined oscillations occurred. For RR Pic, the onset time was estimated using the continuum curve which, unlike the visual luminosity, oscillated strongly. The maximum oscilla-

tion luminosity was adopted as a gauge to transition zone onset, which in the less ambiguous cases is roughly the luminosity at which the light curve seriously moves into an oscillatory phase. In Table I, ΔM is the magnitude difference between peak absolute visual magnitude M_{MAX} and M_{TRANS}, and $\{m/m_\odot\}_v$ is the estimated (lower limit) nova mass using Equation (6) and B.C. $=0$. $\{m/m_\odot\}_{\mathrm{BOL}}$ is a comparative mass estimate using B.C. $=1$. The values of M_{MAX} were for consistency determined in all cases by using the McLaughlin (1939) values for t_3 and the relation $M_{\mathrm{MAX}}=-11.5+2.5\log_{10}(t_3)$ of Schmidt-Kaler (1963). For this reason, the quoted value of M_{MAX} for nova RR Pic is about one magnitude lower than the value usually adopted using nebular expansion data ($M_v=-7.3$). Even at the higher luminosity, however, nova RR Pic seems a comparatively underweight nova. More likely alternatives may be that for this case $\chi_0>\chi_{\mathrm{TH}}$, and/or that β is appreciably different from zero, or finally that the bolometric correction is uncommonly large. Apart from RR Pic and EL Aql, however, there is perhaps a surprising degree of consistency in the values of M_{TRANS},

TABLE I

Novae masses determined from transition zone data

Nova	M_{MAX}	ΔM	M_{TRANS}	$\{m/m_\odot\}_v$	$\{m/m_\odot\}_{\mathrm{BOL}}$
Dk Lac	−7.8	3.0	−4.8	0.16	0.40
V 603 Aql	−9.2	4.2	−5.0	0.19	0.48
GK Per	−8.7	3.5	−5.2	0.23	0.58
RR Pic	−6.1	3.7	−2.4	0.02	0.11
DM Gem	−8.4	3.3	−5.1	0.21	0.52
EL Aql	−8.1	1.6	−6.5	0.76	1.91
V 604 Aql	−7.8	2.6	−5.2	0.23	0.58
V 465 Cyg	$\gtrsim -6.0$*	0.6	$\gtrsim -5.4$*	$\gtrsim 0.28$	$\gtrsim 0.69$

* $\gtrsim$ Implies 'brighter than'.

considering the possible errors in M_{MAX} and ΔM, and in consequence the novae masses are seen to cluster round a value $\{m/m_\odot\}_v \simeq 0.2$, $\{m/m_\odot\}_{\mathrm{BOL}} \simeq 0.5$. For GK Per, there is an independent spectroscopic estimate of mass by Paczyński (1965) of $m/m_\odot = 0.36$, which would correspond to a transition zone luminosity $M_{\mathrm{TRANS}}=-5.7$, $\Delta M=3.0$ for B.C. $=0$, or $M_{\mathrm{TRANS}}=-4.7$, $\Delta M=4.0$ for B.C. $=1$, if the value of M_{MAX} in Table I is assumed accurate. In view of all the uncertainties, this represents a fair agreement with the light curve, the values of ΔM spanning as they do the observed value $\Delta M \simeq 3.5$. The only other nova with a mass estimate, DQ Her with $m/m_\odot \simeq 0.32$ (Kraft, 1964) is also generally in line with the values of Table I. If on the evidence of FH Ser 1970 (Gallagher and Code, 1974) we suppose generally that B.C. $\simeq \Delta M$, the novae mass estimates would require revision upwards; for GK Per, to $m/m_\odot \simeq 5.8$, which would be more in line with the Kraft (1964) value of $m/m_\odot > 1.85$. The general applicability of the result for FH Ser is, however, far from clear. These

quoted mass estimates for GK Per and DQ Her are for the nova binary systems, and not solely for the supposed progenitors of the novae. This seems valid if, as we are supposing, the novae pulsational radii are much larger than the relevant binary separations. Where this is not the case, the analysis may become considerably more complex. The internal consistency in the values of $m/m_{\odot}$ may also imply a critical range for novae binary masses, and to some extent indicates that the assumption $\chi_0 \simeq \chi_{TH}$ was, perhaps, not too unreasonable for most cases.

3. Transient Oscillations in Novae Envelopes

The consequences of assuming that the observed semi-regular oscillations in novae light curves are transient is now preliminarily discussed, with particular reference to V 603 Aql; for these purposes an uncommonly tractable example. A more realistic appraisal of oscillatory behaviour would require a more involved consideration, and at this stage many more assumptions. Short of this, the present discussion suffices for rough quantitative estimates of radial, temperature and bolometric luminosity declines.

For the Roche model, the dependence of σ^2 upon Γ has the form $\sigma^2 \propto \Phi(\Gamma)$, where for $j=0$

$$\Phi(\Gamma) = \Gamma\left\{\frac{3(3\Gamma - 4)}{\Gamma}\right\}^{1/2}\left\{\left\{\frac{3(3\Gamma - 4)}{\Gamma}\right\}^{1/2} + 3\right\}. \tag{9}$$

For $1.67 > \Gamma \gtrsim 1.4$ we have therefore

$$\Phi(\Gamma) \simeq 0.7\Gamma^{5.3}. \tag{10}$$

Similarly, from Equation (2) we obtain

$$\Gamma \simeq 1.37(1 - \beta)^{-0.06}, \tag{11}$$

for $1.0 > \beta \gtrsim 0.3$.

The temperature T may be eliminated from Equation (7) by use of Equation (3), whence for large values of β

$$1 - \beta \simeq \frac{a_R}{3R_g\varrho(4\pi\sigma_s\varepsilon^2)^{3/4}}\left\{\frac{L}{R^2}\right\}^{3/4}, \tag{12}$$

where R is the mean pulsational radius at time t, and εR is an effective radius corresponding to temperature T and luminosity L. On the basis of earlier arguments, we adopt $\varepsilon \simeq \text{constant} \simeq 1$. We have also chosen a characteristic β (and therefore Γ) for the entire envelope. This is tenable for very low density Thomson scattering envelopes, since for that case both gaseous and radiative pressures have the same radial dependence.

If

$$L = L_0 e^{-At}, \tag{13}$$

$$R = R_0 e^{-Bt}, \tag{14}$$

and

$$\varrho = \varrho_0 \left\{\frac{R_0}{R}\right\}^3, \tag{15}$$

then

$$\Phi(\Gamma) = \eta e^{0.25(2B+A)t}, \tag{16}$$

where

$$\eta = 9.7 \left\{\frac{R_g \varrho_0}{a_R}\right\}^{0.33} \left\{\frac{\sigma_s \varepsilon^2 R_0^2}{L_0}\right\}^{0.25}. \tag{17}$$

From Equation (1) we therefore obtain

$$\sigma^2 = \sigma_0^2 e^{Wt}, \tag{18a}$$

$$\sigma_0^2 = \frac{\eta G m}{R_0^3}, \tag{18b}$$

$$W = (3.50B + 0.25A). \tag{18c}$$

From Equation (18c) it is seen that the variation in periodicity is much more sensitive to radial than luminosity changes.

For the equation of motion we use

$$\ddot{\xi} + F(\xi, t)\dot{\xi} + \sigma_0^2 e^{Wt}\xi = 0, \tag{19}$$

which corresponds to damped harmonic motion with quasistatically varying frequency σ. ξ is the displacement from hydrostatic equilibrium (i.e., $\xi = r - R$, if R is the mean radius and r the instantaneous radius). $F(\xi, t)$ is a damping term, for which the simplest qualitatively reasonable form is $F(\xi, t) = \chi\dot{\xi}$, which enables a simple analytical solution for transient behaviour. Cox (1966) also points out that this leads to quantitatively similar power loss rates as more complex treatments providing that $|\chi/\sigma| \ll 1$, which is expected to be the case here.

By substituting $u = \xi e^{\chi t/2}$; $p = -\chi/W$ and $Z = e^{Wt/2}\{2\sigma_0/W\}$ we obtain the familiar Besselian form

$$Z^2\ddot{u}(Z) + Z\dot{u}(Z) + (Z^2 - p^2)u(Z) = 0, \tag{20}$$

which for boundary conditions $\dot{\xi} = 0$, $\xi = \xi_0$ at $t = 0$ leads to the general solution

$$\xi = e^{-\chi t/2}\left\{C_1 J_{-\chi/W}\left(\frac{2\sigma_0}{W} e^{Wt/2}\right) + \left[\frac{\xi_0 - C_1 J_{-\chi/W}(2\sigma_0/W)}{J_{\chi/W}(2\sigma_0/W)}\right] \times \right.$$

$$\left. \times J_{+\chi/W}\left(\frac{2\sigma_0}{W} e^{Wt/2}\right)\right\}, \tag{21}$$

where

$$C_1 = \left\{\frac{\chi\xi_0\sigma_0^{-1}J_{\chi/W}(2\sigma_0/W)}{J_{\chi/W-1}(2\sigma_0/W) - J_{\chi/W+1}(2\sigma_0/W)} - \xi_0\right\}\Bigg/ \left\{\left\{\frac{J_{-\chi/W-1}(2\sigma_0/W) - J_{-\chi/W+1}(2\sigma_0/W)}{J_{\chi/W-1}(2\sigma_0/W) - J_{\chi/W+1}(2\sigma_0/W)}\right\} \times \right.$$

$$\left. \times J_{\chi/W}(2\sigma_0/W) - J_{-\chi/W}(2\sigma_0/W)\right\}, \tag{22}$$

and $J_{\chi/W}(2\sigma_0/W)$ is a Bessel function of order χ/W and argument $2\sigma_0/W$.

From the light curve of V 603 Aql we immediately obtain $W \simeq 7.75 \times 10^{-8}$. The value A is less directly available, but may be readily estimated. Given an initial temperature of transition zone onset, and a value ΔM_{BOL} for bolometric luminosity decline, the temperature variation over the transition zone may be estimated using Equation (3); radius variation being constrained by Equation (18c). The change in bolometric correction may then be obtained using a standard relation $\mathrm{BC} = -42.54 + 10 \log_{10}(T) + (29\,000/T)$ (Allen, 1973), and this is added to the assumed decrease in bolometric magnitude to obtain the visual magnitude decrease ΔM_v. The value of ΔM_{BOL} is then varied until ΔM_v matches the observed decline. The result is a series of unique values for A, B for specific assumed transition zone onset temperatures. The procedure proves satisfactory for effective temperatures $T \gtrsim 7,100$ K, and the values of B thereby determined range from $\simeq 2.1 \times 10^{-9}$ for 7080 K to $\simeq 8.2 \times 10^{-9}$ at 10^4 K and $\simeq 10^{-8}$ at $T \simeq 15\,000$ K. For higher temperatures B increases very gradually, achieving a value $B \simeq 1.25 \times 10^{-8}$ by $T \simeq 64\,000$ K. In consequence, there is little doubt that over the entire transition zone the radial decrease is very small; almost certainly less than $\sim 10\%$ between JD2421770 and JD2421865. For very large j values the conclusion is qualitatively unchanged, although the maximum mean radial decrease is increased to $\delta R/R \simeq 0.15$. In comparison, the temperature decline and A vary from 30% and 1.9×10^{-7} at $T = 10^4$ K, to 20%, 1.3×10^{-7} at $T = 6.4 \times 10^4$ K; the rate of decline in bolometric luminosity always being less than that observed in visual brightness for initial temperatures $T \gtrsim 8000$ K.

We have assumed here that the observed oscillation frequency corresponds to the natural oscillation period of the nova – a good approximation if $|\chi/\sigma| \ll 1$. This can be roughly checked by matching the theoretical rate of linear radial amplitude decline with the observed rate of logarithmic decline in the amplitude of the luminosity variations. The consequences of a changing Γ, apart from its effect in changing pulsation frequency, will be assumed small in estimating χ. The value thereby obtained, $\chi \simeq 2 \times 10^{-7}$, is independent of the assumed temperature of transition zone onset. Thus χ, while not insignificant, is sufficiently small to justify the approximations involved in the method for its determination. In contrast, the reduction in amplitude due to frequency change alone is small; $\sim 15\%$ for a system with negligible damping, equivalent in effect to a damping constant $\chi \simeq 4.0 \times 10^{-8}$ in a system with no frequency change.

More generally, where pulsational frequency is fairly invariant the variation in pulsational radius is probably also small, and in this respect GK Per probably emulated V 603 Aql.

4. Conclusion

We have discussed in a preliminary way the manner by which transition zones exhibiting semi-periodic light variations might originate. By assuming a Roche model for the novae it was shown that a consistent picture emerged if the light variations were assumed to reflect corresponding radial variations in the novae photospheres. A discussion of the hydrostatic stability of novae indicated that the primary cause of transition zone inception could well be hydrostatic collapse following a reduction in radiative support. The onset of the transition zone would thereby depend primarily upon the nova mass, and the development of oscillatory behaviour upon the ratio of gas to total pressure (β). Finally, the specific case of V 603 Aql was investigated assuming the transition zone oscillations to be transient, from which it emerged that for the small observed frequency change, the decrease in mean radius was small, and probably less than $\sim 10\%$ over the entire transition zone. Estimates were also obtained for the variation in temperature and bolometric luminosity.

Acknowledgement

One of us (JPP) was in receipt of an S.R.C. research maintenance award in the course of this work.

References

Allen C. W.: 1973, *Astrophysical Quantities* (The Athlone Press, London) (3rd ed.).
Christy, R. F.: 1966, *Ann. Rev. Astron. Astrophys.* **4**, 353.
Cox, J. P.: 1966, in R. N. Thomas (ed.), *Aerodynamic Phenomena in Stellar Atmospheres*, I.A.U. Symposium No. 28, Academic Press Inc (London) Ltd., p. 3.
Ezer, D. and Cameron, A. G. W.: 1963, *Icarus* **1**, 422.
Finzi, A.: 1973, *Astrophys. J.* **183**, 183.
Gallagher, J. S. and Code, A. D.: 1974, *Astrophys. J.* **189**, 303.
Grotrian, W.: 1937, *Z. Astrophys.* **13**, 215.
Kraft, R. P.: 1964, *Astrophys. J.* **139**, 457.
McLaughlin, D. B.: 1939, *Pop. Astron.* **37**, 410, 481, 538.
McLaughlin, D. B.: 1960, in J. L. Greenstein (ed.), *Stars and Stellar Systems*, Vol. VI, University of Chicago Press, p. 585.
Mustel, E. R.: 1956, in A. Beer (ed.), *Vistas in Astronomy*, Pergamon Press, p. 1486.
Paczyński, B.: 1965, *Acta Astron.* **15**, 197.
Payne-Gaposchkin, C.: 1957, *The Galactic Novae*, North Holland Publishing Company, Amsterdam.
Schmidt-Kaler, Th.: 1963, *Mitt. Sternwarte Bonn* **51**, 9.
Sterne, T. E.: 1937, *Monthly Notices Roy. Astron. Soc.* **97**, 582.
Vorontsov-Velyaminov, B. A.: 1946, *Astron. Zh.* **23**, 286.

Reidel Journals

18. **The Moon**
An International Journal of Lunar Studies
Editors: H. ALFVÉN, Z. KOPAL and H. C. UREY

19. **Origins of Life**
An International Journal Devoted to the Scientific Study of the Origin of Life
(Formerly Space Life Sciences)
Editor: CYRIL PONNAMPERUMA

20. **The Philosopher's Index**
An International Index to Philosophical Periodicals
Editor: RICHARD H. LINEBACK
(Not for sale in the U.S.A.)

21. **Philosophical Studies**
An International Journal for Philosophy in the Analytic Tradition
Editor: KEITH LEHRER

22. **Problems of the Science of Science**
Editor: J. KACZMAREK
(Not for sale in the Socialist countries)

23. **Russian Linguistics**
International Journal for the Study of the Russian Language
Editor: A. V. ISSATSCHENKO

24. **Social Indicators Research**
An International and Interdisciplinary Journal for Quality-of-Life Measurement
Editor: ALEX C. MICHALOS

25. **Solar Physics**
A Journal for Solar Research and the Study of Solar Terrestrial Physics
Editors: C. DE JAGER and Z. ŠVESTKA

26. **Space Science Instrumentation**
An International Journal of Scientific Instruments for Aircraft, Balloons, Sounding Rockets, and Spacecraft
Editor: J. G. EMMING

27. **Space Science Reviews**
Editorial Committee: W. J. G. BEYNON, C. DE JAGER, S. I. RASOOL and JUAN G. ROEDERER

28. **Studies in Soviet Thought**
A Quarterly Review Published by the Institute of East-European Studies at the University of Fribourg (Switzerland), the Center for East Europe, Russia and Asia at Boston College, and the Seminar for Political Theory and Philosophy at the University of Munich.
Editors: JOSEPH M. BOCHEŃSKI, THOMAS J. BLAKELEY, and NIKOLAUS LOBKOWICZ

29. **Synthese**
An International Journal for Epistemology, Methodology and Philosophy of Science
Editor: JAAKKO HINTIKKA

30. **Theory and Decision**
An International Journal for Philosophy and Methodology of the Social Sciences
Editors: G. L. EBERLEIN, W. KROEBER-RIEL, W. LEINFELLNER and F. SCHICK

31. **Water, Air, and Soil Pollution**
An International Journal of Environmental Pollution
Editor: B. M. MCCORMAC

p.t.o.

Reidel Journals

1. **Astrophysics and Space Science**
   An International Journal of Cosmic Physics
   Editor: Z. KOPAL
2. **Boundary-Layer Meteorology**
   An International Journal of Physical and Biological Processes in the Atmospheric Boundary Layer
   Editor: R. E. MUNN
3. **Celestial Mechanics**
   An International Journal of Space Dynamics
   Editor: J. LORELL
4. **Chemical Senses and Flavor**
   A Journal Devoted to the Chemical Senses and to the Sensory Evaluation of the Gustatory, Olfactory, Tactile and Visual Properties of Materials
   Editors: E. P. KÖSTER and H. R. MOSKOWITZ
5. **Cultural Hermeneutics**
   Editor: DAVID M. RASMUSSEN
6. **Educational Studies in Mathematics**
   Editor: H. FREUDENTHAL
7. **Erkenntnis**
   An International Journal of Analytical Philosophy
   Editors: CARL G. HEMPEL, WOLFGANG STEGMÜLLER and WILHELM K. ESSLER
8. **Foundations of Language**
   International Journal of Language and Philosophy
   Editors: W. ABRAHAM, RICHARD D. BRECHT, BRUCE FRASER, MORRIS HALLE, PETER HARTMANN, K. KUNJUNNI RAJA, BENSON MATES, J. F. STAAL, PIETER A. VERBURG and JOHN W. M. VERHAAR
9. **Geometriae Dedicata**
   Chairman of the Editorial Board: H. FREUDENTHAL
10. **Geophysical Surveys**
    An International Journal of Geophysics
    Editor: WM. MARKOWITZ
11. **Journal of Chinese Philosophy**
    Editor: CHUNG-YING CHENG
12. **Journal of Philosophical Logic**
    Editor: BAS C. VAN FRAASSEN
13. **Journal of Raman Spectroscopy**
    An International Journal for Original Work in all Aspects of Raman Spectroscopy, including Higher Order Processes, and also Brillouin- and Rayleigh Scattering
    Editors: D. A. LONG and H. J. BERNSTEIN
14. **Journal of Texture Studies**
    An International Journal of Rheology, Psychorheology, Physical and Sensory Testing of Foods and Pharmaceuticals
    Editors: P. SHERMAN and A. S. SZCZESNIAK
15. **Journal of the History of Biology**
    Editor: EVERETT MENDELSOHN
16. **Marine Geophysical Researches**
    An International Journal for the Study of the Earth beneath the Sea
    Editor: B. J. COLLETTE
17. **Molecular Biology Reports**
    An International Journal for Rapid Communications in Molecular Biology
    Editor: H. BLOEMENDAL

p.t.o.

OBSERVATIONS OF β PERSEI AT 4.8 μm

C. Sanchez Magro, J. D. Needham, J. P. Phillips and M. J. Selby

REPRINTED FROM

Mon. Not. R. astr. Soc. (1977) **180**, 461–464

PUBLISHED BY

BLACKWELL SCIENTIFIC PUBLICATIONS
OXFORD LONDON EDINBURGH MELBOURNE

Mon. Not. R. astr. Soc. (1977) **180**, 461–464

Observations of β Persei at 4.8 μm

C. Sánchez Magro *Cabezón Observatory of the University of La Laguna*
J. D. Needham, J. P. Phillips and M. J. Selby *Astronomy Group, Blackett Laboratory, Imperial College, London SW7 2BZ*

Received 1977 February 3; in original form 1976 December 13

Summary. New measurements of β Persei at 4.8 μm are presented. The relatively small scatter of the results outside eclipse indicates the absence of a phase-dependent emission excess with amplitude $\gtrsim 0.1$ mag.

Jameson, Longmore & Crawford (1973) have reported the presence of a phase-dependent continuum excess from β Persei at 4.8 μm. They argue that this originates from optically thin free–free emission by a plasma situated between primary and secondary stars (components *A* and *B*). Subsequently, Smyth, Dow & Napier (1975) were able to show much of this excess to be spurious, the consequence of an underestimate of the stellar contribution to the infrared flux. Even when corrected for this, however, the 4.8-μm results of Jameson *et al.* indicated an emission excess of $\simeq 0.3$ mag near secondary minimum. All likely physical mechanisms for this excess were consequently shown to lead to emission excesses at shorter wavelengths, which are not observed.

More recently, Longmore & Jameson (1975) have reported further results at 2.2, 3.6, 4.8 and 8.6 μm. A phase-dependent excess is again reported at 4.8 μm, as well as 8.6 μm, although except for one point at 8.6 μm the claimed variability in their (smoothed) results has barely 2σ significance, where σ represents one standard deviation. The maximum excesses are also of order 0.3 mag, which, as Smyth *et al.* have already indicated, is of a size readily attributable to uncertainty in extinction at these wavelengths. In view of this latter possibility, and the low statistical significance of the claimed excesses, considerable caution must clearly be exercised before accepting them as real. In addition it should be noted that the revised model of Longmore & Jameson (1975) developed to explain these excesses conflicts with the measurements of Hα emission by Andrews (1967). This model, in which a gaseous stream (optically thick to Hα) passes from secondary to primary components, would predict a broad peak at secondary minimum for Andrews' emission parameter $R\alpha$, and a narrower peak at primary minimum. This behaviour would be a consequence of the greater Hα emission from the high-temperature region of stream proximate with stellar component *A*. The observed behaviour of $R\alpha$ is the opposite of this, however, with a wider peak for $R\alpha$ at primary minimum. Similarly, displacements of $\simeq 0.05$ in phase would be anticipated

for the peaks of $R\alpha$ at primary and secondary minima, for which there is little evidence in the data of Andrews.

Because of these reservations, and the importance of possible excesses to our understanding of gas dynamics in binary systems, we have taken further observations of this binary at $\lambda = 4.8$ μm in an attempt to further elucidate the characteristics of the light curve. The observations were obtained during several trips in 1976 to the 1.5-m Tenerife flux collector in the course of a continuing program of infrared measurements of elipsing binaries. A conventional photometer with 10-arcsec aperture and 78 K ImSb detector was used. In view of the possibility of spurious excess arising from errors in measured extinction, care was taken to calibrate the results against more than 50 measurements of α Tau, which were in turn calibrated against α Lyr ($M = 0.0$). Systematic errors arising from this system calibration are probably less than 0.05 mag. In no case was β Persei measured for more than 10 min for any one observation. Phase was determined using a recent relationship for the Julian dates of primary minima, JD = 2440953.4657 + 2.8673075E, where E is the number of whole cycles since initial minimum (Ashbrook 1976). The 62 results thereby obtained are given in Table 1, and illustrated in Fig. 1(a). For comparison, the 4.8-μm results of Longmore & Jameson are given in Fig. 1(b) to the same scale.

It is evident from a comparison of Fig. 1(a) and (b) that the scatter in the results of Longmore & Jameson most probably does not reflect any substantial intrinsic variability of

Table 1. Infrared photometry of β Persei at 4.8 μm.

JD 2440000+	Phase	4.8 μm	$\sigma_{4.8}$	JD 2440000+	Phase	4.8 μm	$\sigma_{4.8}$
2845.422	0.837	2.29	0.03	3007.661	0.420	1.91	0.10
2846.372	0.169	2.02	0.02	3009.729	0.141	2.01	0.03
2846.403	0.179	2.14	0.02	3009.763	0.153	2.04	0.02
2846.424	0.187	2.01	0.01	3010.624	0.453	1.94	0.03
2846.449	0.195	2.02	0.02	3010.666	0.468	2.22	0.03
2849.357	0.210	2.05	0.01	3010.679	0.472	2.15	0.03
2849.379	0.217	1.92	0.01	3010.694	0.477	2.19	0.03
2849.399	0.224	1.93	0.01	3010.706	0.482	2.25	0.03
2849.420	0.232	2.01	0.02	3010.717	0.485	2.28	0.04
2849.447	0.241	1.96	0.02	3010.735	0.492	2.19	0.02
2850.388	0.569	2.00	0.01	3010.746	0.496	2.25	0.03
2850.408	0.576	1.99	0.02	3011.670	0.818	2.08	0.01
2850.428	0.583	1.97	0.02	3011.736	0.841	2.10	0.01
2850.445	0.589	2.01	0.02	3011.781	0.856	1.99	0.01
2851.347	0.904	2.11	0.02	3013.745	0.541	1.93	0.01
2851.376	0.914	2.02	0.02	3013.747	0.542	1.95	0.02
2852.347	0.252	1.99	0.01	3013.763	0.548	1.99	0.02
2852.367	0.259	2.01	0.02	3013.770	0.550	1.94	0.02
2853.377	0.612	2.04	0.02	3013.775	0.552	1.95	0.02
2853.398	0.619	2.00	0.02	3013.780	0.554	1.97	0.01
2853.417	0.626	1.97	0.03	3013.782	0.554	1.92	0.02
2853.438	0.633	2.23	0.05	3013.784	0.555	1.89	0.01
3001.713	0.345	1.93	0.02	3013.786	0.556	1.95	0.02
3001.735	0.353	1.95	0.02	3013.791	0.557	1.93	0.02
3004.745	0.403	1.92	0.02	3013.793	0.558	1.90	0.01
3005.724	0.744	1.90	0.02	3013.797	0.560	1.96	0.01
3006.569	0.039	1.91	0.02	3013.802	0.561	1.92	0.01
3006.643	0.065	1.92	0.03	3013.806	0.563	1.93	0.01
3006.678	0.077	1.91	0.02	3013.809	0.564	1.98	0.03
3006.720	0.091	1.94	0.02	3089.553	0.980	2.66	0.01
3006.751	0.102	1.99	0.02	3089.565	0.984	2.74	0.04

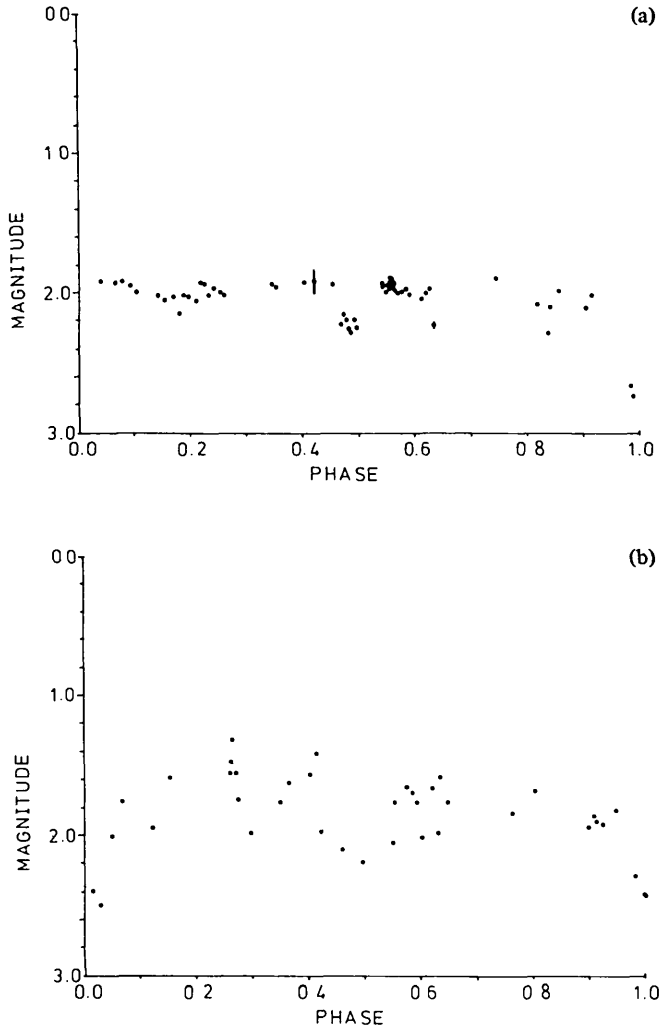

Figure 1. (a) Variation of the 4.8-μm magnitude of β Persei with phase. The vertical bars represent the 2σ error in the results. (b) Variation of the 4.8-μm magnitude of β Persei according to Longmore & Jameson (1975).

the binary. The present results indicate that a variable excess $\gtrsim 0.1$ mag can probably be excluded outside eclipse; residual scatter is attributable to variable extinction or uncertainties in the measurements thereof. The rather sparse data covering primary and secondary minima indicate eclipse depths consistent with the predictions of Smyth *et al.*, although further data are required before a more meaningful discussion becomes possible. It is nevertheless clear that any increase in eclipse depth arising from obscuration of a region of emission must also be small, and probably $\lesssim 0.1$ mag. Model 3 of Smyth *et al.* gives primary and secondary eclipse depths of 0.70 and 0.18 mag, for distance, whereas the present results suggest corresponding values of $\simeq 0.73$ and $\simeq 0.26$ mag respectively.

These negative results at least enable a possible constraint to be placed on the plasma responsible for Hα emission. If a typical dimension $2R$ is adopted for the plasma, and it is assumed to be located at the inner Lagrangian point, then the data of Andrews indicates that $0.35\,R_\odot \lesssim R \lesssim 1.3\,R_\odot$ with a most probable value of $R \simeq 1.0\,R_\odot$. The absence of emission

components at minima (Struve & Sahade 1957) also indicates $R \lesssim 1.4\,R_\odot$, because of the inclination of system A, B to the line of sight. We adopt $R \simeq 1.0\,R_\odot$ as a typical radius. To obtain the observed Hα emission strength of 5×10^{-10}erg cm^{-2}s^{-1} (Andrews 1967) then requires, for optical thickness to Hα, a plasma temperature $T \simeq 3.4 \times 10^4$K and electron density $N_e \gtrsim 10^8$cm^{-3}. Plasmas of similar dimensions but optically thin to Hα would be incapable of producing the observed Hα flux. The plasma, if optically thick to continuum, would also give a 5-μm excess of ≈ 0.2 mag, as well as respective excesses of 0.26, 0.21, 0.20 at wavelengths 2.2, 3.6 and 10.2 μm. The available data at 2.2 μm (*cf.* Smyth *et al.* 1975; Johnson *et al.* 1966) indicates that the plasma is almost certainly optically thin by this wavelength, and the present data suggests that this it probably true also at 4.8 μm, for which case $N_e \lesssim 2 \times 10^{12}$cm^{-3}. Although these density limits are not particularly informative, it is difficult to see how the plasma temperature can be significantly reduced to a value consistent with radiative excitation by the component stars without leading to conflict with the observed behaviour of the emission components of Hα. The possibility of some degree of non-radiative excitation may have to be considered therefore; not particularly surprising in view of the strong radio flares observed from this binary (*cf.* Hjellming, Webster & Balick 1972) and the models developed to account for this behaviour (*cf.* Woodsworth & Hughes 1976). Non-radiative excitation would also be a plausible consequence of theories invoking prominence activity as a mode of mass transfer within binaries (*cf.* Sahade 1960). For this latter case collisional excitation resulting from shock wave dissipation may be envisaged. Evidently, however, these ideas must remain speculative until firmer evidence is forthcoming.

To conclude, we believe that although further refinement of the infrared light curve of Algol would be of interest, the present results give no grounds for supposing an excess at $\lambda \leqslant 5\,\mu$m. It should be noted however that realistically measurable excesses at longer wavelengths are not precluded by the present measurements. An excess of $\Delta m = 0.1$ mag at $\lambda = 4.8\,\mu$m would for instance lead to respective excesses of $\Delta m = 0.42$, $\Delta m = 0.48$ mag at 10.2 μm, if optically thin free–free, or synchrotron radiation having $S_\nu \propto \nu^{-1/3}$ (*cf.* Smyth *et al.* 1975), are responsible.

Acknowledgments

We would like to thank P. R. Jorden, A. D. MacGregor, and M. Muñez for sterling instrumental and observational help during the course of this program. We also thank Professor F. Sánchez and his staff at the Institute of Astrophysics, University of La Laguna, for their assistance. JPP and JDN gratefully acknowledge SRC research grants during the period covered by this work.

References

Andrews, P. J., 1967. *Astrophys. J.*, **147**, 1183.
Ashbrook, J., 1976. *Sky Telesc.*, **52**, 48.
Hjellming, R. M., Webster, E. & Balick, B., 1972. *Astrophys. J.*, **178**, 439.
Jameson, R. F., Longmore, A. J. & Crawford, B., 1973. *Nature*, **242**, 107.
Johnson, H. L., Mitchell, R. I., Iriate, B. & Wisniewski, W. Z., 1966. *Commun. lunar planet. Lab.*, **4**, 99.
Longmore, A. J. & Jameson, R. F., 1975. *Mon. Not. R. astr. Soc.*, **173**, 271.
Sahade, J., 1960. *Stellar atmospheres*, p. 466, ed. J. L. Greenstein, University of Chicago Press, Chicago.
Smyth, M. J., Dow, M. J. & Napier, W., Mc.D., 1975. *Mon. Not. R. astr. Soc.*, **172**, 235.
Struve, O. & Sahade, J., 1957. *Publ. astr. Soc. Pacific*, **69**, 41.
Woodsworth, A. W. & Hughes, V. A., 1976. *Mon. Not. R. astr. Soc.*, **175**, 177.

PRINTED IN ENGLAND BY
ADLARD AND SON LTD, DORKING

Astron. Astrophys. 59, 91—110 (1977)

ASTRONOMY
AND
ASTROPHYSICS

On the Structural Development of the Shells of Novae and Planetary Nebulae

J. P. Phillips and N. K. Reay
Astronomy Group, Blackett Laboratory, Imperial College, London SW7 2BZ, England

Received November 3, revised December 9, 1976

Summary. An investigation of the effects of gravitational braking, differential stellar rotation and radiation pressure, upon the structural development of nebular shells, shows that the principal forms observed in planetary nebulae and novae can be readily explained in terms of these factors alone.

Key words: novae — planetary nebulae

1. Introduction

Although many of the physical processes taking place in planetary nebulae are well understood, fundamental questions concerning their origin and the evolution of the observed structural forms remain unanswered. Insofar as their origin is concerned, although the consensus of opinion would probably support red giants as the progenitors of planetary nebulae (cf. Shklovsky, 1956; Abell and Goldreich, 1966; Menzel, 1946; and more recently Pacyński, 1971; Wood, 1973; Rose, 1973), others still argue for an origin directly from the presently observed central stars (cf. Finzi and Wolf, 1970).

The mechanism by which the various observed nebular forms develop also remains controversial. A trend for the nebulae to be orientated non-randomly with respect to the galactic plane has recently been noted (Cudworth, 1975; Melnock and Harwit, 1975; Grinin and Zvereva, 1968), suggesting that their structure may be dependent to some extent upon the Galactic magnetic field. Gurzadyan (1969) and Woyk (1968) have also invoked internally generated magnetic fields to explain observed structures, although Menzel (1968) believes this to be impractical

The development of nebular shells under the combined influence of gravitation and the stellar radiation field appears not to have been treated in any detail in the literature. Most recently Kirkpatrick (1976) has considered the development of shells under the influence of a continuous accelerative process (of the kind produced by ablation from the internal surface) and concludes that prolate forms may develop: although this result is dependent upon the assumptions employed. Louise (1973) has discussed a model involving the ejection of a nebular envelope from a spherical rotating star. Although the contribution of gravity as a determinant of shell shape is discussed qualitatively the analytical treatment is confined to cases where gravitational retardation is negligible, whence nebulae acquire oblate spheroidal forms. We shall have reason to refer to this model later.

The following discussion represents a preliminary foray into the development of nebular envelopes using a model in which gravity, radiation pressure and stellar rotation are responsible for the ultimate nebular forms.

2. Mode of Shell Ejection

We shall assume that mass is ejected from the central star with sufficient energy to escape. Possible modes for this ejection process are summarised by Salpeter (1971) and more recent work on ejection through pulsational instability is given by Härm and Schwarzschild (1975), Kutter and Sparks (1974) and Smith and Rose (1972). It will be noted that this ejection mode almost cetainly requires some Mira-like star as progenitor, having as they do low escape velocities ($\sim 30\,\mathrm{km\cdot s^{-1}}$). In contrast, the presently observed central stars have escape velocities some two orders of magnitude greater, and to acquire observed nebular terminal velocities of $\sim 20\,\mathrm{km\cdot s^{-1}}$ would require ejection velocities to be unrealistically close (within $\sim 0.02\%$) to the escape velocities. This ejection mode differs from certain other treatments, which presume a transfer of entropy from the nebula to the radiation field, and a consequent steady mass loss at a rate below escape velocity (cf. Finzi and Wolf, 1970, 1971; Faulkener, 1970). A problem with this latter mechanism however is that there appear to be no obvious evolutionary tracks to the supposed progenitors (i.e. the present central stars) (Osterbrock, 1974). To acquire the

Send offprint requests to: N. K. Reay

Table 1

Planetary nebula	$(dM/dt)_{ml}$ ($\times 10^{-6} M_\odot$/yr)	t_{mu} ($\times 10^3$ yr)
NGC 2392	272.0	1.66
NGC 3242	15.9	2.45
NGC 6210	134.0	1.86
NGC 6543	61.0	3.26
NGC 6572	7.9	6.12
NGC 6720	60.3	5.15
NGC 6853	42.8	4.89
NGC 7009	96.6	2.06
NGC 7027	55.6	1.90
NGC 7662	56.8	1.17

distinctive shapes of planetary nebulae, other processes must also be invoked; possibly Kirkpatrick's mechanism, or magneto-dynamic mass redistribution.

In a similar vein Paczyński, whilst accepting Mira variables as progenitors, suggests that the weak, presumably radiatively-driven, mass loss characteristics of these stars may be the ultimate cause of planetary nebulae.

The characteristics of mass emission from M-type stars have been conveniently summarised by Wilson (1959), and these need few amendments. Specifically, it is found that mass is emitted at a unique velocity which appears to be invariant with distance from the star, and below the stellar escape velocity (suggesting that the mass flow is powered by the radiation field). The mass loss rate dM/dt for Miras has been found more recently (Gehrz and Woolf, 1971) to be $\simeq 2\,10^{-6}\,M_\odot \cdot \mathrm{yr}^{-1}$. We do not believe this continuously-driven mass flow to be a likely origin of planetary nebula shells, however, for the following reasons.

If mass flow from Miras is similar to other M-type stars, a lower limit velocity $V_{ml} \simeq 5\,\mathrm{km \cdot s}^{-1}$ may be adopted. Irrespective of subsequent accelaration by radiation pressure we may therefore assign an upper limit to the period of nebular expansion of $t_{mu} = r_n / V_{ml}$, where r_n is the outer nebular radius at time t_{mu}. This also represents an extreme upper limit for the period of nebular emission, since most observed planetaries appear to have evolved well past the stage of mass emission. A more realistic estimate for the mass emission period would be obtained by multiplying t_{mu} by the ratio of (shell radius/shell thickness).

Also, a lower limit mass loss rate $(dM/dt)_{ml}$ for the period of shell emission may be obtained from

$$\left(\frac{dM}{dt}\right)_{ml} = 4 \cdot \pi \cdot r_n^2 \cdot V_{ml} \cdot n_e \cdot M_\mathrm{H},$$

where n_e is the observed nebular electron density and M_H the hydrogen atom mass.

Values of t_{mu} and $(dM/dt)_{ml}$ are given in Table 1, assuming $V_{ml} \simeq 5\,\mathrm{km \cdot s}^{-1}$, for several well-known nebulae for which electron density and nebular dimensions are fairly well established (Allen, 1964). For comparison, we note that Paczyński (1971) uses $t_m \simeq 3.1\,10^4$ yr and $(dM/dt)_m \simeq 2\,10^{-6}\,M_\odot \cdot \mathrm{yr}^{-1}$. It will be seen that, even as respectively upper and lower limits, the values derived for t_{mu} and $(dM/dt)_{ml}$ are considerably at variance with the requirements of Paczyński.

For these, and other less substantial reasons, we have considerable doubts that the weak outflow of mass seen in Miras can be responsible for planetary nebulae, and take the view that the Miras must pass through a much more vigorous period of mass emission. Assuming this to be so, to explain the observed shell thickness we will consider three models for the ejection process; instantaneous ejection at a range of velocities (Model A), gradual ejection at a unique velocity (Model B), and finally instantaneous ejection at a unique velocity (Model C). For the latter case, we will adopt a uniform shell density with radial thickness inversely proportional to the square of the shell radius, thus approximating to the situation where much of the shell thickness arises from expansion due to turbulent, gaseous and Ly_α photon pressures. This is a severe approximation, but aids considerably the computation of non-spherical emission maps. The broad characteristics of emission structure will also be found to be fairly independent of density structure.

Clearly, the above choices represent wide extremes and it is likely that in reality a blend of these and other mechanisms will occur; it is certainly not clear from observational evidence that any of these models can be excluded. The thermal evolution of the nebulae and central stars are, for instance, almost completely conjectural, so that the tenability of Model C is unclear. On the other hand, velocity *through* the shell appears in several cases to be roughly proportional to radius (Liller and Liller, 1968; Aller and Liller, 1968), which provides some support for Model A[1]. For all models however we would roughly expect nebular shape to reflect the variation in radial velocity over the shell surface; ellipsoid-like shells should for instance be generally matched by a corresponding velocity ellipsoid. Wilson (1958) has remarked that the observational evidence for this is very strong, and Weedman (1968) has subsequently noted that generally

$$r_n = S \cdot V_n + P,$$

where S and P are constants, and r_n, V_n are the nebular radius and velocity. Typically $P \simeq 0.3 r_n$; the fact that P

[1] Since preparation of this paper, new electronographic data for NGC 6543 has enabled an interpretation in terms of a spheroidal model. Density is found to vary almost certainly as the inverse of the radius, and velocity through the shell as the radius. Both these are consequences of a Model A ejection, as will be seen later. Note that models invoking purely thermal nebular expansion (Matthews, 1966) could lead to a rather similar velocity pattern through the shell, although the density would fall with radius much more rapidly than either Model A or NGC 6543. Thin shell thermal models of this type, in which expansion around the mean shell radius occurs typically at sonic velocities can be expected to lead to emission structures intermediate between Models A and B, however

>0 suggesting some influence upon the shell motion for a finite period after ejection. It will be seen in Section 4 that radiation pressure is capable of providing this influence, so that P may be associated with the radius r_{th} at which the shell becomes optically thin. In this respect, it will be noted that the values of P are similar to although rather smaller than the values determined by Cahn and Kaler (1971) for r_{th} (i.e. $r_{th} \simeq 0.04$ pc).

3. Structural Development in a Gravitational Field

Consider a segment of nebular shell of thickness dr, subtending solid angle $d\Omega$ at distance $r(\beta)$ from the central star. The radial component of nebular acceleration may then be written

$$m \cdot \frac{d^2 r(\beta)}{dt^2} = -\frac{G \cdot m M_* \bar{r}(\beta)}{r^3(\beta)} + \frac{L_* d\Omega \cdot \bar{r}(\beta)[1-\exp(-\tau(\beta))]}{4 \cdot \pi \cdot r(\beta) \cdot C} - d\Omega[\bar{\nabla}(P_G + P_R) \cdot \bar{r}] \cdot \bar{r} \cdot dr, \quad (1)$$

where M_*, L_* are the stellar mass and luminosity respectively, β is the angle between the stellar equatorial plane and the radius vector $\bar{r}(\beta)$, $\tau(\beta)$ is the shell optical depth, and P_G, P_R are respectively gas and Lyman-α photon pressures. Generally, for the third term on the right hand side, $\bar{\nabla} \neq (d/dr)\bar{r}$, and some non-radial mass redistribution will occur. The contribution of this third term is neither clear nor analytically trivial, although initially it will be relatively small due to low $U.V.$ radiant flux, plasma temperatures, and subsequent adiabatic cooling. Its contribution will be considered only qualitatively as a postscript to Section 4. The first two terms in the equation represent the respective contributions of gravitational braking and Lyman continuum (Ly_c) radiation pressure. We consider first the development of the shell under the influence of the first term. The less certain contribution of Ly_c pressure to the shell shape will be investigated separately.

A first point to note is that we will be dealing with terminal configurations alone. Louise (1973) has argued that some nebular shells may be wholly or partially in the process of collapsing back towards the star, so that there could be cases where terminal shell shapes are not appropriate. In fact, such nebulae are most unlikely to the observed, even though they probably occur. This may be readily seen by noting that

$$\frac{\Delta V}{V_{esc}} = -\frac{1}{2} \cdot \frac{R_*}{r_n}$$

for a shell brought to a standstill in the gravitational field. ΔV is the difference between the ejection velocity and the escape velocity V_{esc}. For a nebular radius $r_n \simeq 10^{17}$ cm (below which the structure of very few planetaries has been resolved) and stellar radius $R_* \simeq 200 \cdot R_\odot$, we obtain $\Delta V / V_{esc} \simeq 7\,10^{-5}$ which, for $V_{esc} \simeq 35\,\mathrm{km \cdot s^{-1}}$ gives

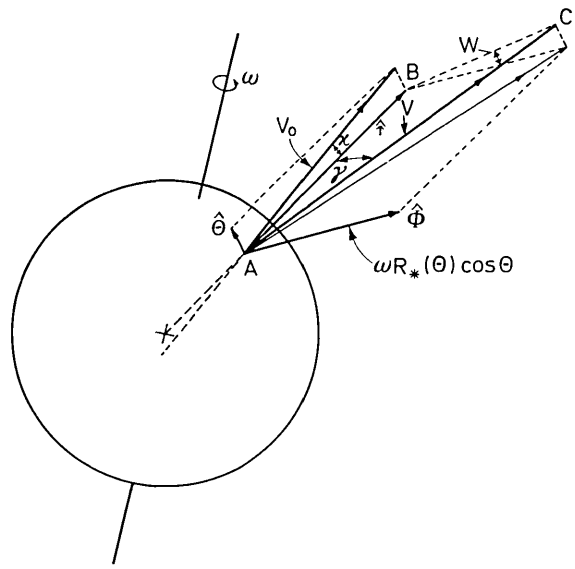

Fig. 1. Geometry of mass ejection from a rotating star (see text)

$\Delta V \simeq 2 \cdot 45\,\mathrm{m \cdot s^{-1}}$. So, unless ejection velocities are exceptionally close to the escape velocity, it is unlikely that gravitationally unstable structures of this kind will be observed.

Consider now a mass element being ejected from the surface of a star. The geometry is illustrated in Figure 1. The star is rotating with an angular velocity ω (independent of θ) and has a figure of rotation

$$R_*(\theta) = R_*(0) \cdot [1 - \omega^2 \cdot R_*^3(0) \cdot \sin^2\theta / 2 \cdot G \cdot M_*]. \quad (2)$$

This is valid for bodies with low oblation, i.e. where $\omega^2 \cdot R_*^2 / V_{esc}^2 \ll 1$, which is the case for red giants. As $\omega^2 R_*^2 / V_{esc}^2 \to 1$ higher order terms involving the moments of inertia of the star about the polar and equatorial axis become significant. We will assume the contributions from these terms to be negligible.

The velocity of the mass element ejected from the star is given by:

$$\bar{V} = \hat{r} \cdot V_0 \cos\varkappa + \hat{\theta} \cdot V_0 \sin\varkappa + \hat{\phi} \cdot \omega R_* \cos\theta \quad (3)$$

i.e.

$$V^2 = V_0^2 + \omega^2 \cdot R_*^2 \cdot \cos^2\theta,$$

where $\hat{r}$, $\hat{\theta}$ and $\hat{\phi}$ are spherical unit vectors, $\varkappa$ is the angular deviation of V_0, the ejection velocity normal to the surface, from $\hat{r}$ due to stellar oblation, and

$$\varkappa = \tan^{-1}[V_{esc}^2 \cdot \sin\theta / (V_{esc}^2 \cdot \cos\theta - 2 \cdot R_*^2(\theta) \cdot \omega^2 \cdot \cos\theta)] - \theta, \quad (4)$$

where we define

$$V_{esc} = [2 \cdot G \cdot M_* / R_*(\theta)]^{1/2}. \quad (5)$$

$\bar{V}$ is inclined at angle γ to $\hat{r}$ within the plane ABC defined by these two vectors, where

$$\gamma = \tan^{-1}[\omega \cdot R_*(\theta) \cdot \cos\theta / V_0 \cdot \cos\varkappa \cdot \cos W] \quad (6)$$

and ABC is in turn tilted at angle W to the plane containing $\hat{r}$, $\hat{\phi}$, where

$$W=\tan^{-1}[V_0\cdot\sin\varkappa/\omega\cdot R_*(\theta)\cdot\cos\theta]. \quad (7)$$

Within the plane ABC the mass element traverses a hyperbolic orbit of ellipticity

$$\varepsilon=\left\{1+\frac{4[V_0^2+\omega^2\cdot R_*^2(\theta)\cdot\cos^2\theta-V_{esc}^2]\cdot[V_0^2\sin^2\varkappa+\omega^2R_*^2(\theta)\cdot\cos^2\theta]}{V_{esc}^4}\right\}^{1/2} \quad (8)$$

and semi-major axis "a", given by

$$a=[V_{esc}^2\cdot R_*(\theta)/2\cdot(V_0^2+\omega^2\cdot R_*^2(\theta)\cdot\cos^2\theta-V_{esc}^2)]. \quad (9)$$

At infinity, the mass element subtends a terminal angle χ to the direction of the initial radius vector $\bar{R}(\theta)$, where

$$\chi=\cos^{-1}(1/\varepsilon)-\cos^{-1}(a(\varepsilon^2-1)/R_*(\theta)\cdot\varepsilon-1/\varepsilon). \quad (10)$$

The terminal angle of the radius vector of a mass element ejected from stellar latitude θ is therefore

$$\beta=\tan^{-1}\left[\frac{\sin\chi\cdot\sin W\cdot\cos\theta+\cos\chi\cdot\sin\theta}{(\sin^2\chi\cdot\cos^2W+\cos^2\chi\cos^2\theta+\sin^2\chi\cdot\sin^2W\cdot\sin^2\theta-2\cdot\sin\chi\cdot\sin W\cdot\sin\theta\cdot\cos\chi\cdot\cos\theta)^{1/2}}\right], \quad (11)$$

where β is measured between the radial vector and the stellar equatorial plane. The terminal velocity $V_t(\beta)$ at angle β is given by

$$V_t(\beta)=[\omega^2\cdot R_*^2(\theta)\cdot\cos^2\theta+V_0^2-V_{esc}^2]^{1/2}. \quad (12)$$

Equations (3)–(12) enable us to define a terminal velocity surface which, in the absence of appreciable subsequent radiative acceleration, defines the terminal shape of the nebula. Examples of these velocity surfaces are shown in Figure 2 where, for particular values of the axial ratio α, the variation of nebular shape with increasing stellar rotational velocity is shown. The axial ratio α is defined as the ratio of the nebular major axis (in the stellar rotational plane) to the minor axis, and is given by

$$\alpha^2=[1+2\cdot\omega^2R_*^2(0)/(V_0^2-V_{esc\cdot p}^2)],$$

where $V_{esc\cdot p}$ is the polar escape velocity. Another parameter of particular interest is the mass concentration coefficient ϕ. This is defined as the mass per unit solid angle at terminal angle β, divided by the mass per unit solid angle emitted from stellar latitude θ in the absence of rotation.

This parameter is given by

$$\phi=M(\beta)/M(\theta)=(\cos\theta/\cos\beta)d\theta/d\beta. \quad (13)$$

ϕ is plotted in Figure 3 as a function of terminal angle β for $\alpha=1.5$. The result is interesting, showing that for quite modest values of $\omega\cdot R_*/V_{esc}$, the mass is preferentially and substantially directed towards the minor axis ($\beta\simeq 90°$) of the nebular configuration.

At this point we digress from the main discussion to consider the consequence of this mass concentration for the Louise model. Louise (1973) considers shell density to vary as the inverse square of the nebula radius and the mass to be uniformly emitted; he does not consider a mass concentration factor. For the Louise model we can show that:

$$n/n_0=1+[(1-\alpha^2)/\alpha^2]\cdot\cos^2\beta,$$

where, in Louise's terminology, n/n_0 is the normalised shell density. This differs from the corresponding equation derived by Louise because of a confusion between terminal angle β and stellar latitude of ejection. A term allowing for tilt of the nebular surface, incorporated into Louise's equation, is not relevant to shells of finite thickness. For the Louise model, terminal angle β can be shown to be related to θ by

$$\tan^2\beta=\alpha^{-2}\cdot\tan^2\theta,$$

whence it is easy to show using Equation (13) that

$$\phi\propto r_t^3$$

$$r_t(\beta)=r_t(\pi/2)\cdot\{1+[(1-\alpha^2)/\alpha^2]\cos^2\beta\}^{-1/2}.$$

r_t is the form of the radius function at the terminal velocity V_t. So, mass is concentrated towards the stellar rotational plane, the concentration more than compensating the geometrical r^{-2} mass dilution. The gaseous density increases towards the major axis, and does not rapidly decrease as indicated by Louise.

The foregoing analysis was necessary to determine the variation of shell shapes with increasing stellar rotation, and the characteristics of mass concentration. For the purposes of modelling and further analysis, however, we will find it convenient to approximate the nebular shapes by the form

$$r_t(\beta)/r_t(\pi/2)=\{1+(\alpha^2-1)\cdot\cos^2\beta\}^{1/2}. \quad (14)$$

Corresponding, for appropriate values of α, to the innermost contours of Figure 2.

Figure 4 shows a full range of nebular shapes generated with this equation. It will be noted that for $(\alpha^2-1)<1$ "toroidal" shapes are generated, and this corresponds to the situation where, with the aid of rotation, mass escapes from the stellar equatorial regions alone. A range of toroidal shapes is given in Figure 5.

Having obtained a series of nebular forms, we must now return to a review of our basic assumptions, primarily that of constant stellar angular velocity. For the sun, the only star for which reliable data is available,

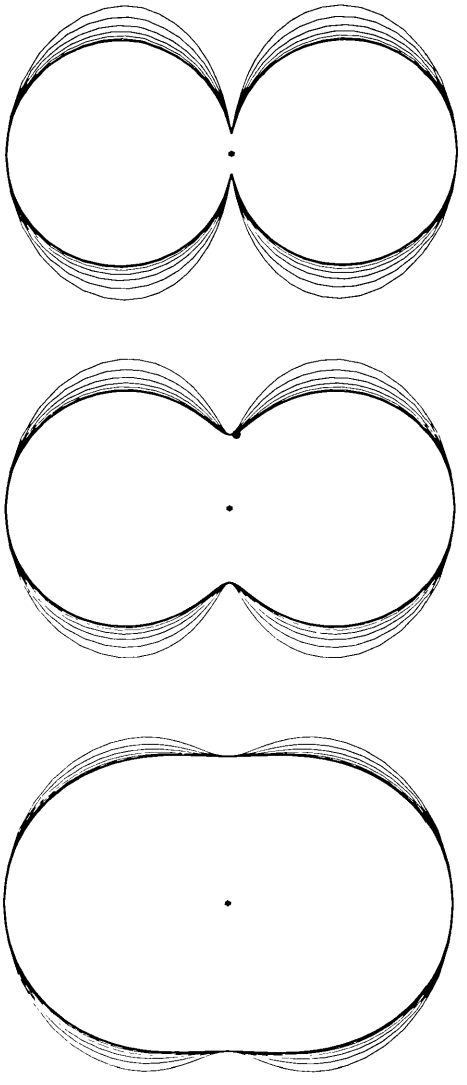

Fig. 2. Sequence of terminal shapes for shells ejected from stars with various rotational velocities. The innermost contour in each case corresponds to $\omega R_*(0) \simeq 2.5\,\mathrm{km \cdot s^{-1}}$, with $\omega R_*(0)$ incrementing 2.5 km $\cdot s^{-1}$ for each subsequent curve. Increasing axial ratios imply decreasing shell ejection velocities. The outer curve is for $\omega R_*(0) = 17.5\,\mathrm{km \cdot s^{-1}}$

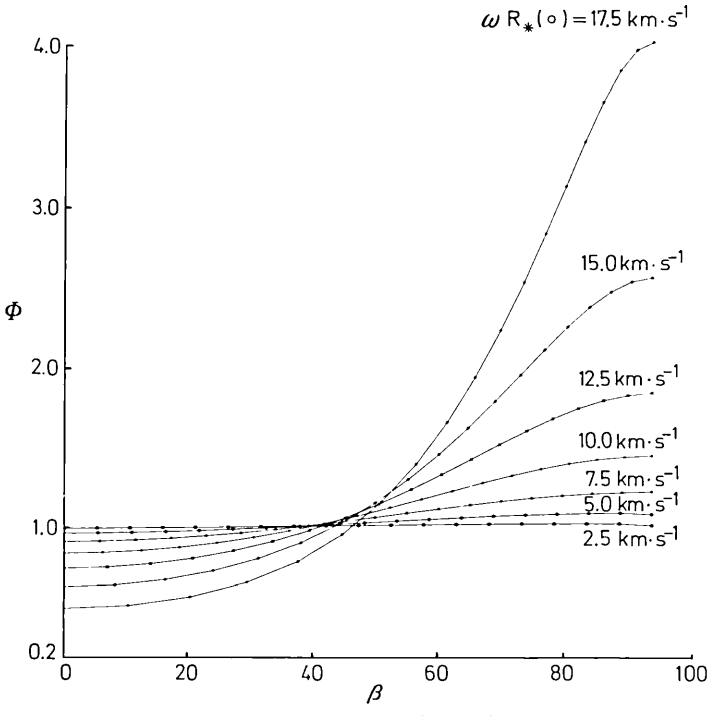

Fig. 3. The variation of mass concentration coefficient ϕ with terminal angle β, for rotational velocities $\omega \cdot R_*(0)$ ranging from $2.5\,\mathrm{km \cdot s^{-1}}$ to $17.5\,\mathrm{km \cdot s^{-1}}$. The assumed stellar polar escape velocity $V_{\mathrm{esc \cdot p}} = 35\,\mathrm{km \cdot s^{-1}}$ and the terminal axial ratio $\alpha = 1.5$

it is found that the angular velocity takes the form (Allen, 1964):

$$\omega(\theta) = \omega(0) \cdot [1 - A \cdot \sin^2 \theta], \tag{15}$$

where A is a constant. For giants the variation of angular velocity with latitude θ is unlikely to be less than in the sun, and indeed we might expect it to be greater. For illustrative purposes we have assumed Equation (15) to be generally applicable to Miras, and have investigated the influence upon nebular shape of varying the parameter A. The resulting configurations range between the forms displayed in Figure 4a and the extreme forms given in Figure 4b. The net result is seen to be an elongation of the model forms, but no substantial morphological development otherwise.

Clearly, many of the shapes displayed in Figure 4 are not commonly observed. Although ellipsoidal structures are met with frequently, the hour-glass shapes are by no means as common. There are however a number of selection effects in operation. For instance, in the case of $\omega \cdot R_* = 10\,\mathrm{km \cdot s^{-1}}$ and $V_{\mathrm{esc}} = 35\,\mathrm{km \cdot s^{-1}}$ for axial ratios between $2 \lesssim \alpha \lesssim \infty$ the ejection velocity must be within a range of $\sim 1\,\mathrm{km \cdot s^{-1}}$, whereas for $2 \lesssim \alpha \lesssim 1.3$ the corresponding velocity range is $\sim 3\,\mathrm{km \cdot s^{-1}}$. Thus, if shell ejections are equally frequent at all velocities below some fixed limit, say $V_0 < 40\,\mathrm{km \cdot s^{-1}}$, we would expect roughly three times more ellipsoidal type shapes than hour-glass configurations. Further, at elevations away from the major axis plane the hour-glass structure rapidly gives way to a strong, characteristic bipolarity within weaker ellipsoidal contours (see Figs. 10 and 12) although this itself is hardly a more common structure.

In addition, there is an observational selection effect. It is apparent from the model nebulae presented here that for many hour-glass formations gas density near the star will be very much greater than that of the more distant nebulosity. As a result, because of the restricted dynamic range of photographic plates there would in the past have been a bias for recording only the inner brighter nebular structure, at the expense of the possibly more characteristic hour-glass structure. NGC 650-1 is a case in point (see Fig. 18). Only when the outer nebular envelope was specifically investigated by taking long-exposure photographs was the intrinsic hour-glass configuration revealed. Finally, the nature of the ejecting process itself

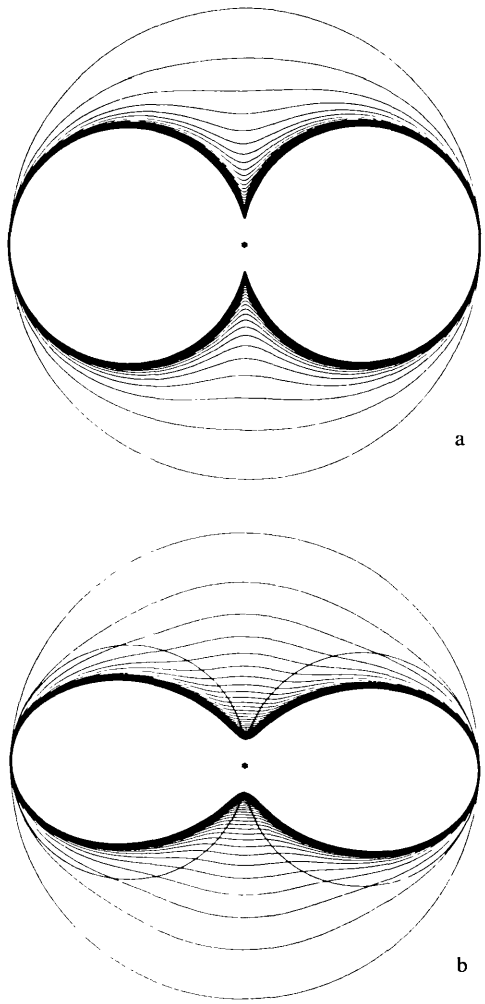

Fig. 4. a Sequence of terminal shapes for shells ejected from a rotating star, after gravitational braking. The innermost case (axial ratio $\alpha=10$) corresponds to the lowest ejection velocity. **b** Effect of differential stellar rotation upon the nebular shapes of Figure 4a. The rotation law is $\omega=\omega_0(1-0.8\sin^2\theta)$. The comparative intersecting curve is for ω = constant, $\alpha=10$

may tend to preclude the formation of nebulae with high axial ratios, if higher ejection velocities are preferred.

These clearly are factors which must be borne in mind in any future comparison of the theory with nebular statistics. A possibly more powerful discriminant against nebulae with axial ratios $\alpha>2$ however is the effect of radiation pressure upon the shells. This will be considered in more detail in the next section.

We are now in a position to determine how the resulting model nebulae would appear. Consider first Model A as defined in Section 2 and let the mass function be $\eta(V_0)$, where $\eta(V_0)\cdot\Delta V_0$ is the mass emitted at velocities between V_0 and $(V_0+\Delta V_0)$. Let the mass function terminate at a lower velocity limit V_1 and an upper velocity limit V_2, so that for $V_0>V_2$ or $V_0<V_1$ we have $\eta(V_0)=0$. Between these limits we will initially assume $\eta(V_0)$ = constant. We also assume that the mass concentration function $\phi=1$.

If the radius of the shell is $r_t(\beta)$ after a time t_s then the volume of a shell element is given by

$$v=\Delta V_t\cdot t_s\cdot A\cdot(r_t/R_*)^2, \tag{16}$$

where ΔV_t is the terminal velocity dispersion within the shell and A is the area of the element of shell when $t_s=0$. Consequently, if $\eta(V_t)$ is the terminal mass function, the density of the mass at velocity V_t is given by

$$\varrho(V_t)=\eta(V_t)\cdot\Delta V_t/v.$$

Now since

$$\eta(V_t)\cdot\Delta V_t=\eta(V_0)\cdot\Delta V_0.$$

Then

$$\varrho(V_t)=[\eta(V_0)\Delta V_t/v]\,V_t/V_0. \tag{17}$$

From (16) and (17), and noting that $r_t=V_t\cdot t_s$, we obtain

$$V_0=R_*^2\cdot\eta(V_0)/A\cdot\varrho(V_t)\cdot r_t\cdot t_s^2. \tag{18}$$

Thus taking

$$r_t=\{V_0^2-V_{esc}^2+2\cdot\omega^2R_*^2\cos^2\beta\}^{1/2}\cdot t_s \tag{19}$$

we can eliminate V_0 from Equations (18) and (19) to obtain the relation for density

$$\varrho^2(r_t)/\varrho_1^2=(r_1/r_t)^2\cdot[(r_1/t_s)^2+V_{esc}^2]/[(r_t/t_s)^2+V_{esc}^2-2\omega^2R_*^2\cos^2\beta], \tag{20}$$

where ϱ_1 is the density at the inner surface of the shell at $\beta=\pi/2$, and r_1 is the radius at this point. For the contours of equal density we readily obtain the form:

$$r_t^2=[-b+(b^2-4\cdot a\cdot c)^{1/2}]/2a, \tag{21a}$$

where

$$a=t_s^{-2}, \tag{21b}$$

$$b=(V_{esc}^2-2\cdot\omega^2R_*^2\cos^2\beta), \tag{21c}$$

$$c=[V_{esc}^2-4(V_1^2-V_{esc}^2/2)^2]/4\cdot a\cdot\varrho^2(r_t) \tag{21d}$$

and V_1 is the velocity at the inner shell surface at $\beta=\pi/2$.

Figure 6 shows a series of cross sectional views for Model A nebulae computed using Equations (14) and (21). It should be noted that for an inner shell surface of axial ratio α_2 and major axis r_2, the outer surface is constrained to a major axis r_1 for axial ratio α_1, where

$$r_1=r_2(\alpha_1/\alpha_2)[(\alpha_2^2-1)/(\alpha_2^2-1)]^{1/2}.$$

The same basic equations are used for both the non-toroidal and toroidal forms, but for the latter group the radius and density can no longer be normalised to the minor axis. For toroidal models there is also a restriction on the permitted angular range for mass ejection. Examples are given in Figure 7. Parameters for the Model A illustrated toroidal and non-toroidal nebulae are given in Table 2.

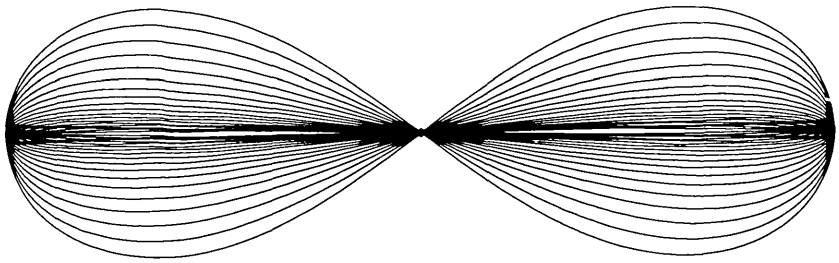

Fig. 5. Range of "toroidal" terminal shell shapes for various ejection velocities.
For these cases, the mass ejected from the poles does not achieve escape velocity

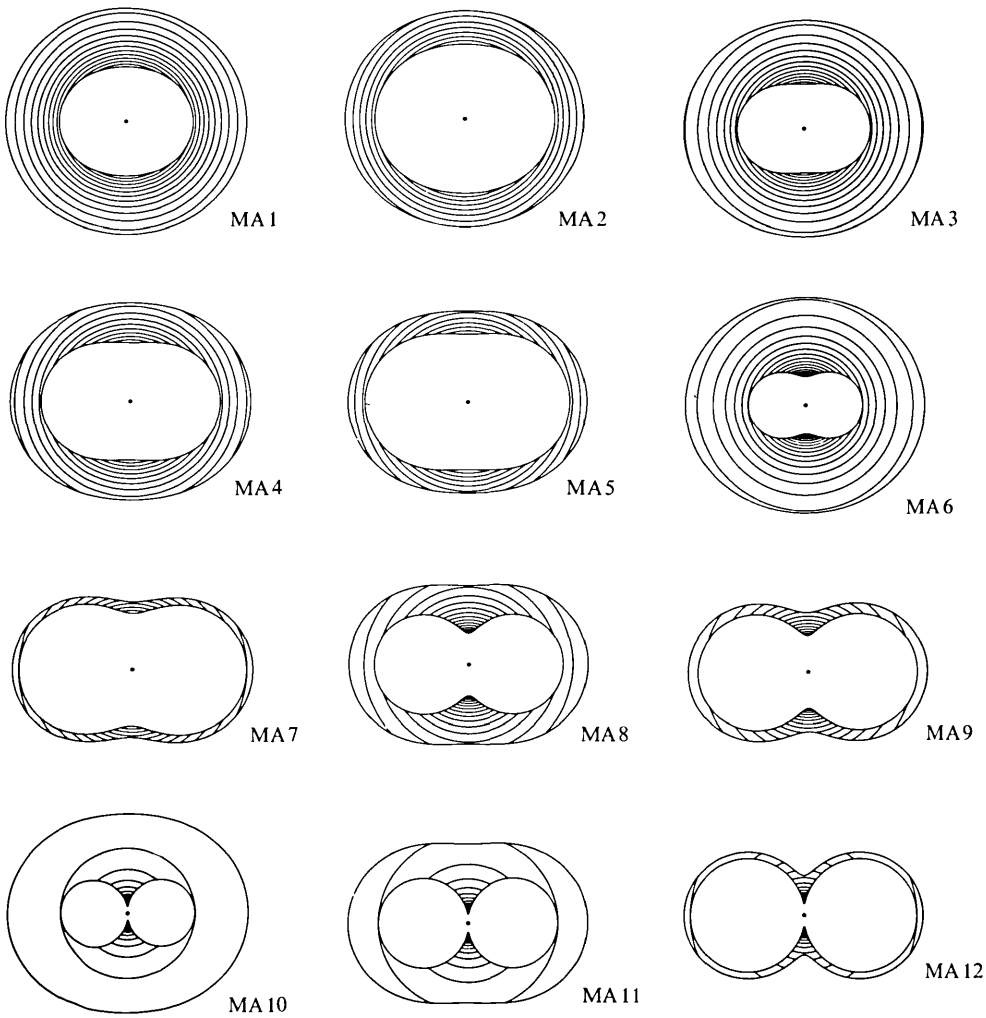

Fig. 6. Cross-sectional views of model planetary nebulae, assuming Model A ejection mechanism. The internal curves represent contours of equal density. Density is normalised to equal 1.0 at the innermost shell point on the minor axis, and adjacent density contours differ by 0.05, decreasing as distance from central star increases

In developing the foregoing models we have assumed that $\eta(V_0)$ is constant. More generally, if

$$\eta(V_0)=Q\cdot V_0^{\mu} \tag{22}$$

then

$$\varrho(r_t)/\varrho_1=(r_1/r_t)\{[(r_t/t_s)^2 + V_{esc}^2-2\omega^2R_*^2\cos^2\beta]/[(r_1/t_s)^2+V_{esc}^2]\}^{(\mu-1)/2}. \tag{23}$$

Although the density structure of the model therefore varies with μ, this only becomes significant for particularly thick shells, or for very large μ; for the specific examples considered here $\mu=0$ should suffice in representing the range of possible nebular structures.

For Model B ejection models we again use Equation (14) for the nebular shape, but assume a shell-thickness proportional to the radius $r_I(\beta)$, $(=r_t(\beta, \alpha=\alpha_I)$, $\alpha_I=$axial ratio of internal surface) of the internal shell surface.

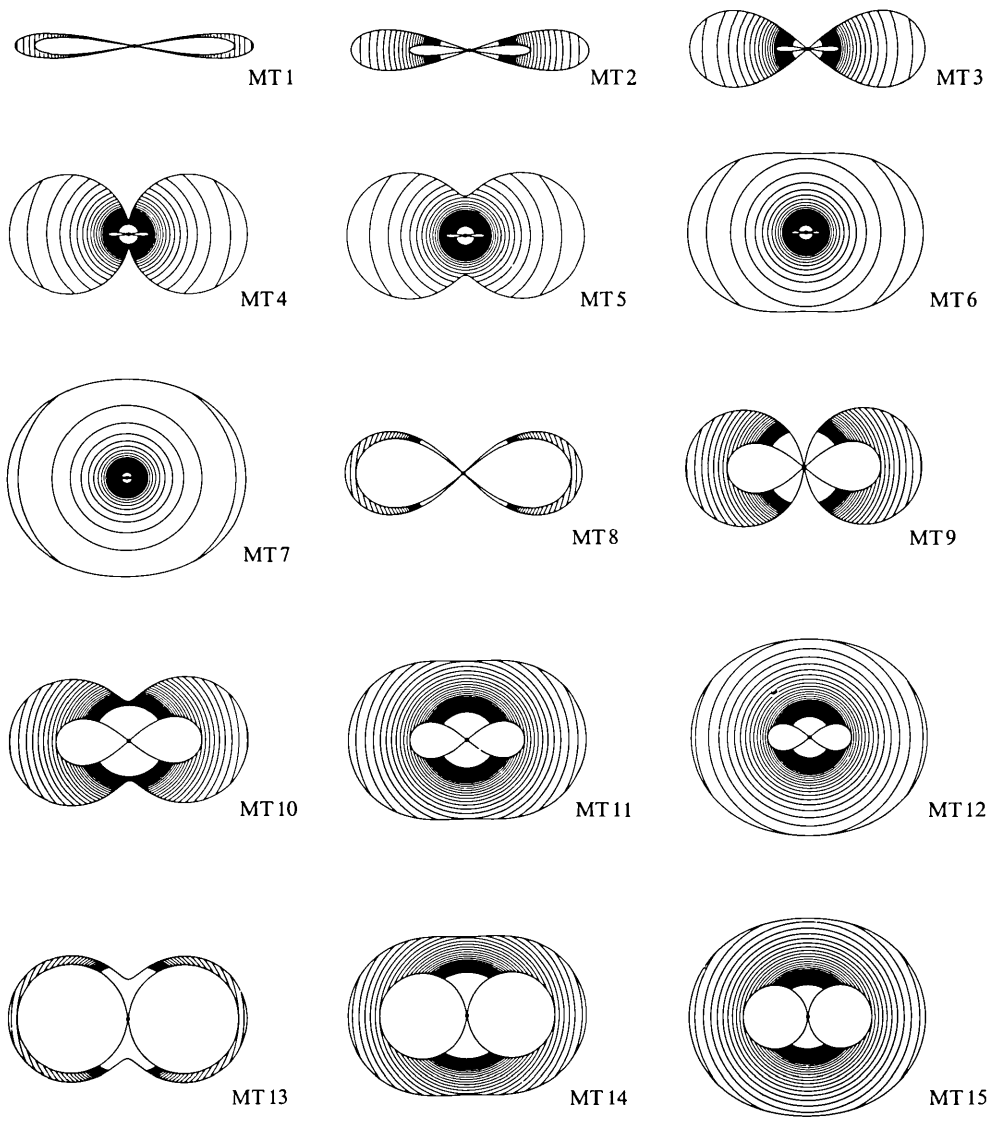

Fig. 7. Cross-sectional views of toroidal models. Ejection is Model A. Density is normalised to 1.0 at innermost shell position on the major axis. Adjacent contours differ by 0.05. Contours have been repressed at high densities

The density through the nebula is given by

$$\varrho(r_t)/\varrho_1 = 1/r_I(\beta)\cdot r_t^2, \tag{24}$$

where once again, ϱ_1 is the density at the inner shell surface for $\beta=\pi/2$. Representative cross-sections are given in Figure 8, Models MB 1–4 having respectively $(\alpha^2-1)=0.44$, 1.25, 8.0 and 99.0. For all cases, the ratio between the radii of outer and inner surfaces is 1.5.

Finally, for Model C, the density is assumed constant and the shell is considered to have expanded uniformly about an initially thin shell configuration of radius $r_t(\beta)$. Shell thickness will therefore be proportional to $r_t^{-2}(\beta)$. Selected model cross-sections are displayed in Figure 9, the defining equations for the delimiting surfaces being $r=R_0\pm A/R_0^2$; $R_0=(1+(\alpha^2-1)\cos^2\beta)^{1/2}$, where $A=0.5$, and $(\alpha^2-1)=0.44$, 1.20, 3.0 and 8.0 respectively for Models MC 1–4.

In all cases, the illustrated models represent a selection of the most distinctive examples from a more extensive range of computed models, of which only about one third are used for this paper.

In Figures 10–13 we show contour maps corresponding to selected models from Figures 6–9. In each case the model is viewed from three directions; the equatorial plane ($\beta=0$), the polar direction ($\beta=\pi/2$) and an intermediate elevation ($\beta=\pi/4$). The contour maps are produced as follows. Equations (20) and (24) are used to compute the density $\varrho(r_t)$ at a number of points along a line of sight through the nebula. These are squared and summed to give the emission measure at that position. A matrix of such points is computed covering the nebula, and this matrix is convolved with a circular aperture equivalent in size to the "seeing" limited spatial resolution achievable in astronomical photography. A

Table 2. Parameters for normalised ejection Model A toroids and non-toroids

Model	A	B	C	D $\times 10^{-3}$	E	F $\times 10^{-2}$
MA 1	1.00	0.44	4.29	84.99	0.92	−3.74
MA 2	1.00	0.44	2.10	84.89	0.92	−3.74
MA 3	1.00	1.25	5.94	31.62	0.97	−3.95
MA 4	1.00	1.25	2.84	31.62	0.97	−3.95
MA 5	1.00	1.25	1.81	31.62	0.97	−3.95
MA 6	1.00	3.00	14.28	13.43	0.99	−4.03
MA 7	1.00	3.00	1.45	13.43	0.99	−4.03
MA 8	1.00	8.00	6.40	5.08	0.99	−4.06
MA 9	1.00	8.00	2.67	5.08	0.99	−4.06
MA 10	1.00	99.0	225.0	$4.02\,10^{-1}$	1.00	−4.08
MA 11	1.00	99.0	79.19	$4.02\,10^{-1}$	1.00	−4.08
MA 12	1.00	99.0	12.37	$4.02\,10^{-1}$	1.00	−4.08
MT 1	−32.16	33.16	−31.73	1.28	1.04	−4.25
MT 2	−32.16	33.16	−29.28	1.28	1.04	−4.25
MT 3	−32.16	33.16	−19.46	1.28	1.04	−4.25
MT 4	−32.16	33.16	0.42	1.28	1.04	−4.25
MT 5	−32.16	33.16	4.15	1.28	1.04	−4.25
MT 6	−32.16	33.16	26.53	1.28	1.04	−4.25
MT 7	−32.16	33.16	75.37	1.28	1.04	−4.25
MT 8	− 1.42	2.42	− 1.21	17.28	1.02	−4.18
MT 9	− 1.42	2.42	− 0.07	17.28	1.02	−4.18
MT 10	− 1.42	2.42	0.30	17.28	1.02	−4.18
MT 11	− 1.42	2.42	1.94	17.28	1.02	−4.18
MT 12	− 1.42	2.42	5.50	17.28	1.02	−4.18
MT 13	$-3.1\,10^{-2}$	1.03	0.13	39.63	1.00	−4.09
MT 14	$-3.1\,10^{-2}$	1.03	0.83	39.63	1.00	−4.09
MT 15	$-3.1\,10^{-2}$	1.03	2.34	39.63	1.00	−4.09

$r_1=(A+B\cos^2\beta)^{1/2}$; $r_2(C+B\cos^2\beta)^{1/2}$; $\varrho=r^{-1}(Dr^2+E+F\cos^2\beta)^{-1/2}$; r = distance from central star; r_1 = Radius of inner surface; r_2 = radius of outer surface; ϱ = density; β = angle with respect to major axis.

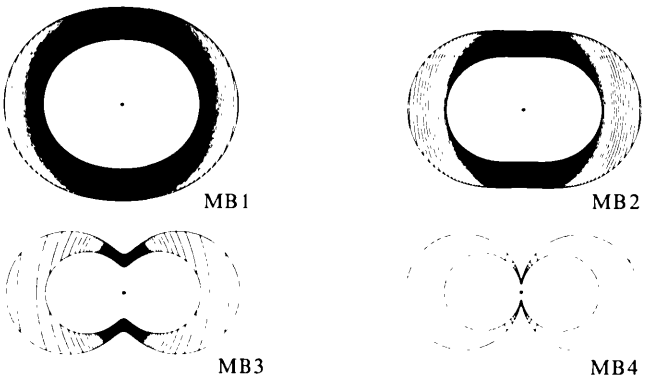

Fig. 8. Cross-sectional views of model planetary nebulae, assuming Model B ejection mechanism. Density contours are as in Figure 6

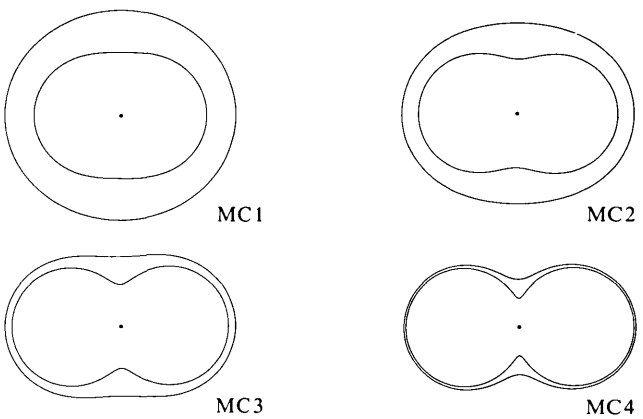

Fig. 9. Cross-sectional views of model planetary nebulae, assuming Model C ejection mechanism. Density is constant

contour map is then produced from the convolved matrix.

In Figures 10–13 we have assumed that the resolution element has a diameter of $\simeq 10\%$ of the maximum dimension of the nebula. In practice this corresponds to nebulae with dimensions $\sim 10''$ observed under conditions of 1″ "seeing".

The basic structure of the contour maps is not sensitive to the size of the resolution element, except for cases when the nebula is small and the resolution element therefore large compared with the scale size of the envelope structure. Because the contour maps are computed on the basis that the observed emission is proportional to the emission measure $n_e^2 \cdot L$, they are strictly comparable only with radio maps. They should also however be adequate for comparison with nebulae observed at Balmer wavelengths: and with some reservations at optical wavelengths in general.

The close correspondence of ejection Models B and C structures to similar Model A structures precluded the need for more extensive contouring, and illustrates a certain insensitivity of model *types* to density structure; although of course intensity levels vary in detail.

Although these models will be examined in more detail in Section 5, note that for the toroidal models (Fig. 11) there is a strong central concentration of emission, despite the fact that mass is predominantly concentrated away from the centre. In fact, although the very highly concentrated mass elements near the central star are rather unrealistic, it seems likely that even for more realistic cases there will be a strong central emission, and toroidal-like emission structures seem unlikely. In the event, the observational evidence for the existence of such emission tor oids is not conclusive (see comments concerning ring nebulae in Section 5).

To conclude, it is useful to summarise the limitations on the validity of the structures presented in Figures 6–13. These structures may be modified by mass concentration towards the poles (see Fig. 3). Appreciable stellar rotation will tend to "squash" the shell, and differential stellar rotation to extend it, in the manner illustrated in Figures 2 and 4 respectively.

Finally, the density structure through the shell will depend on the form of the mass emission function $\eta(V_0)$.

These factors can all be accounted for in discussing individual cases, and do not detract from the validity of the models presented in Figures 6–13 in describing the basic forms of nebular envelopes.

The most important influence on the shape of the nebula after gravitational braking may be radiation

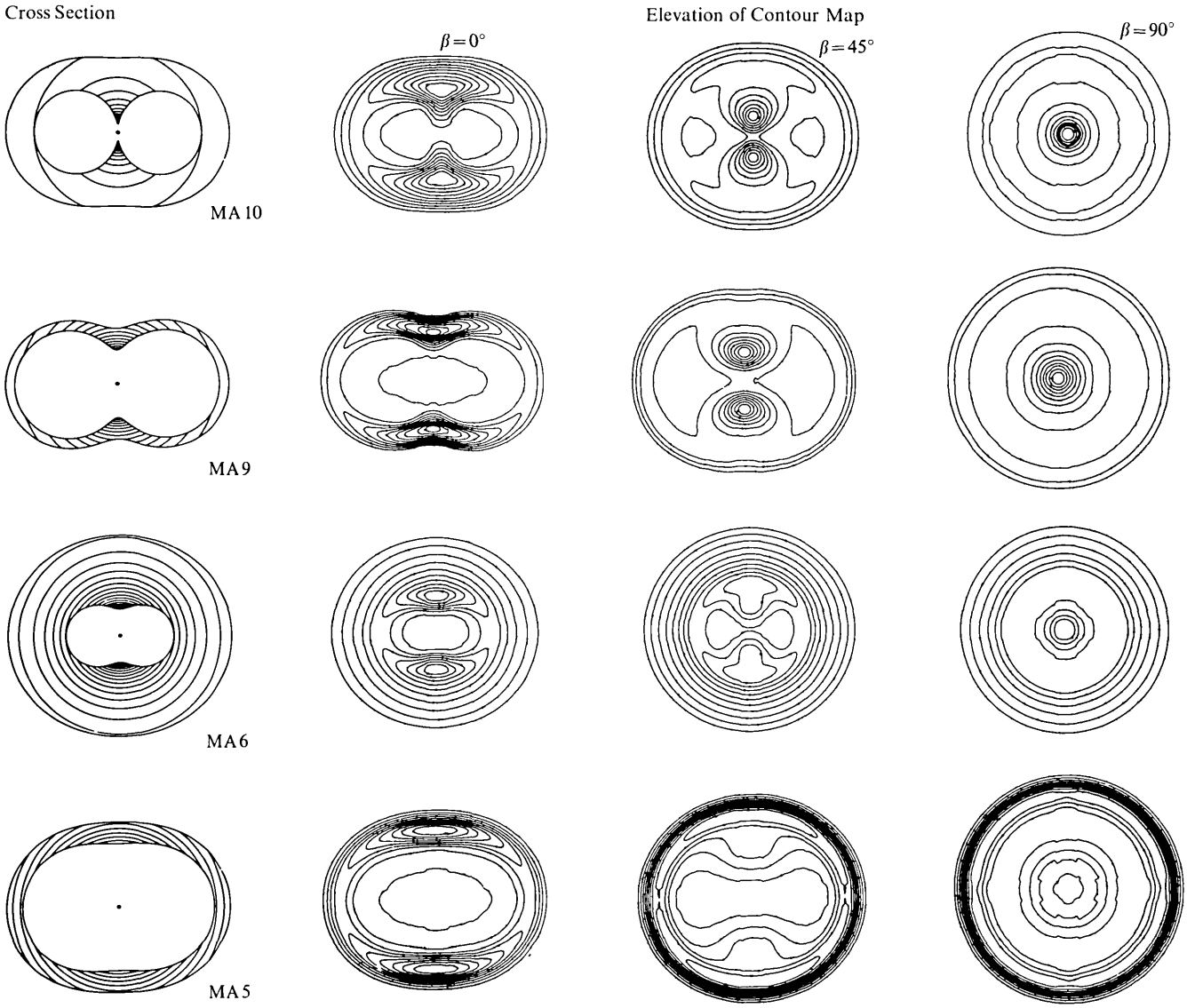

Fig. 10. Simulated emission maps at three elevations of models selected from Figure 6

pressure, the effect of which is considered in the following section.

4. Simple Theory of Radiative Acceleration

So far we have investigated the nebular shapes we anticipate will develop under the braking effect of the stellar gravitational field. The influence of radiation pressure upon the shells of planetary nebulae is not so well defined, although various studies indicate that its dynamical effect cannot be ignored (Finzi and Wolf, 1970; Mathers, 1966; Hunter and Sofia, 1971). Here we will be primarily concerned with the possible consequences of acceleration by Lyman continuum (Ly_c) radiation, either through direct capture by neutral hydrogen, or by dust grains. The results will also be broadly applicable where a stellar wind is the driving mechanism. The possible dynamical consequences of Ly_α and gas pressures present a rather less tractable problem, and these will be mentioned later.

Soon after the ejection of the nebular shell the central star proceeds to slowly contract and increase in temperature. The details of this evolution are given by Härm and Schwarzschild (1975), although this is a rather simplified theoretical treatment and subsequent formulations may be expected to differ in detail.

As the temperature increases, so does the ultra-violet flux, but at these early stages ($T_* < 10^4$ K) the Ly_c will not be capable of appreciably ionising the shell. The momentum transfer efficiency between the radiation field and the gaseous shell is at its greatest, however, and the acceleration is given by:

$$dV_n/dt \simeq E_{Lyc}/M_n \cdot c, \qquad (25)$$

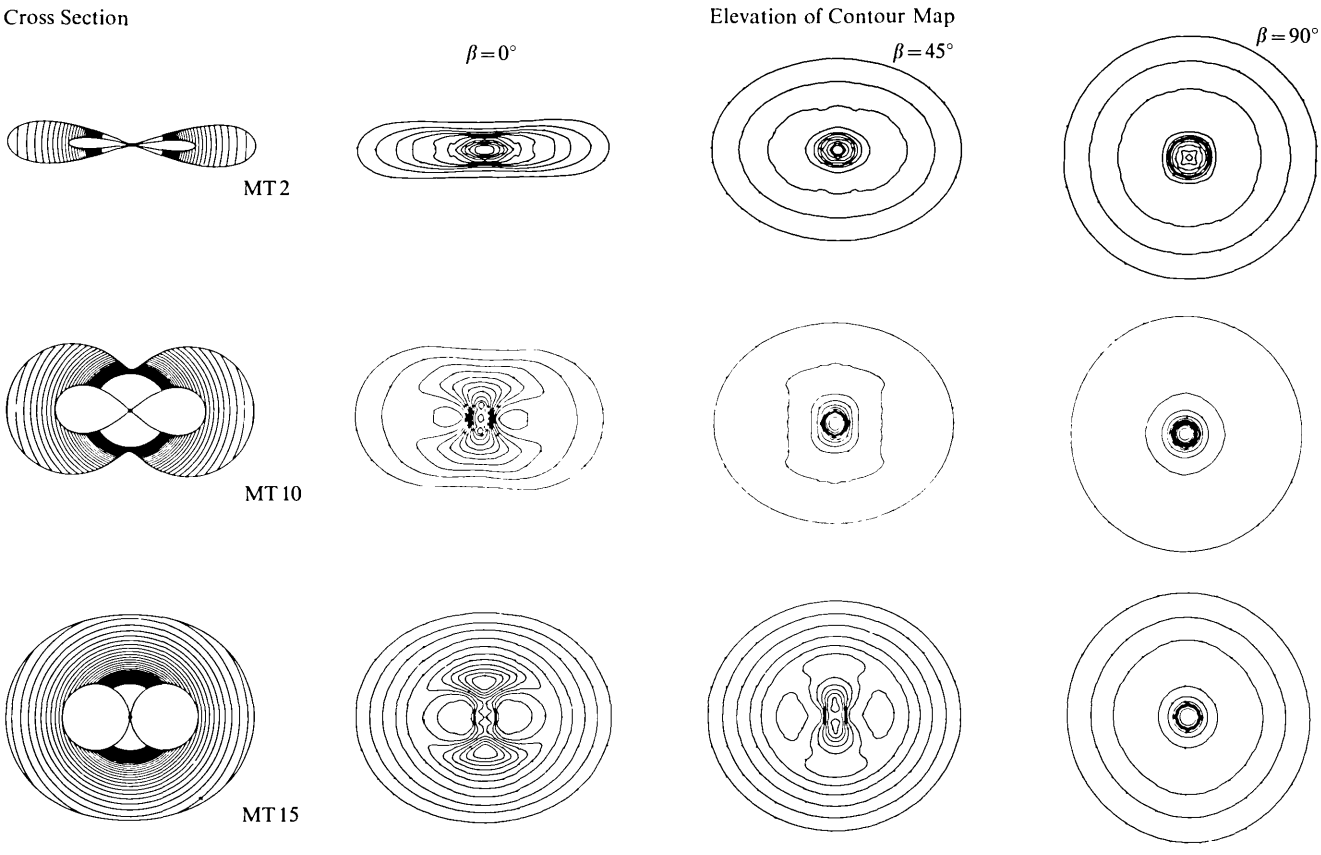

Fig. 11. Simulated emission maps at three elevations of three models from Figure 7

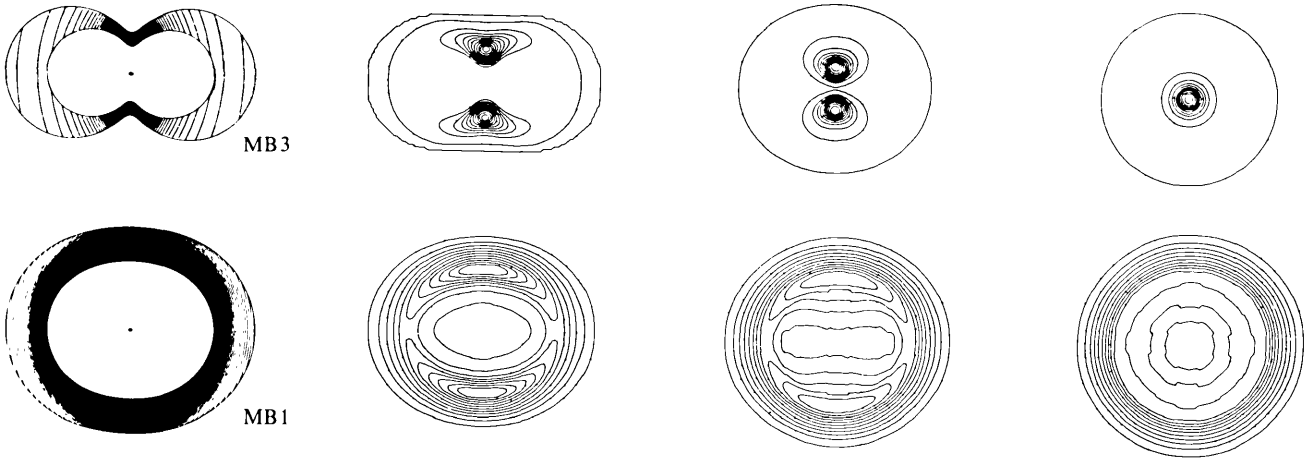

Fig. 12. Simulated emission maps at three elevations of two models from Figure 8

where E_{Ly_c} is the luminosity in the Lyman continuum, M_n the mass of the nebular shell, and c is the velocity of light. Because E_{Ly_c} is small the acceleration at this stage will be negligible. As the star evolves the total luminosity decreases, but both T_* and E_{Ly_c} continue to increase until between about 3000 and 6000 years after the ejection when $\log T_* > 4.5$. The nebular material is now much more tenuous and fully ionized. At this stage the envelope becomes increasingly transparent and the efficiency of the radiative acceleration process decreases, the acceleration declines and an asymptotic velocity is approached.

Although this picture is necessarily crude an important point emerges: the shaping of the shell occurs in the stellar gravitational field and the shell is only signi-

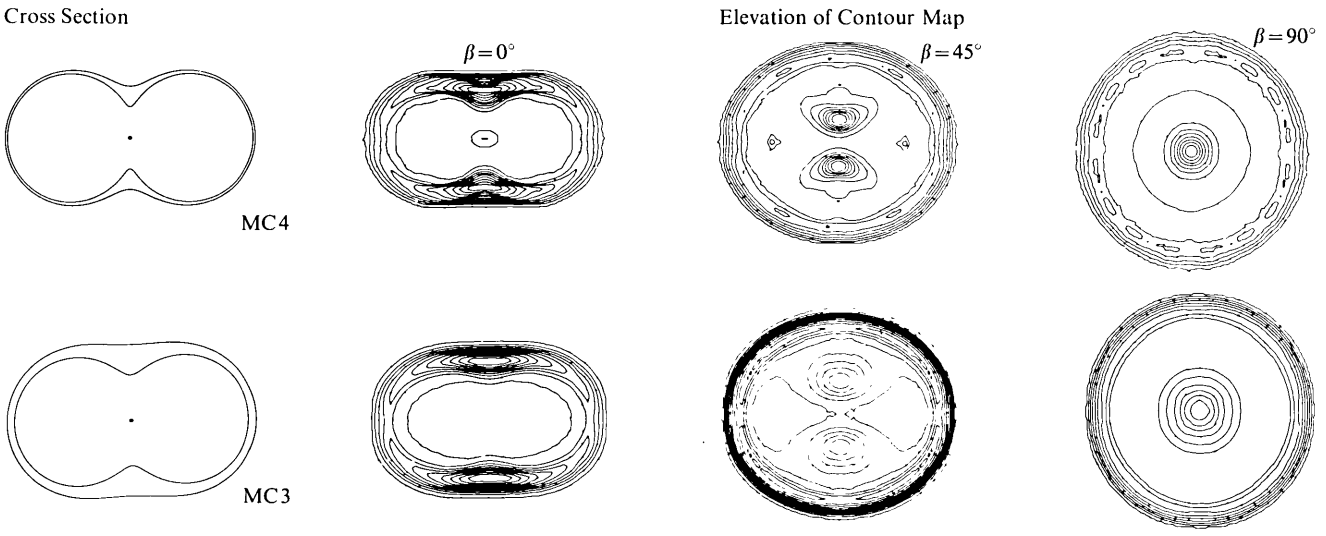

Fig. 13. Simulated emission maps at three elevations of two models from Figure 9

ficantly accelerated by radiation pressure at a later stage. This sequence will be implicitly accepted in all future discussion.

We assume a simple model in which the star has constant luminosity in the Lyman continuum, and the accelerated shell maintains a constant mass M_n. The ratio E_{Ly_c}/M_n is assumed to be the same for all parts of the shell, i.e. the mass concentration factor $\phi = 1$.

The optical depth of an element of shell ejected at an angle β to the plane of stellar rotation is $\tau(\beta)$, and the acceleration of the mass element will proceed as

$$dV_n/dt = (E_{Ly_c}/M_n \cdot c)[1 - \exp(-\tau(\beta))] \tag{26}$$

whence

$$V_r^2(\beta) = V_{R_*}^2(\beta) + \int_{R_*}^{r} (2 \cdot E_{Ly_c}/M_n \cdot c)[1 - \exp(r_{th}/r)^2] \cdot dr \tag{27}$$

where r_{th} is the radius at which the shell becomes optically thin. $V_r(\beta)$ and $V_{R_*}(\beta)$ are the shell velocities at r and R_* respectively.

We have assumed in (27) that

$$\tau(\beta) = (r_{th}/r)^2 \tag{28}$$

a form generally valid if either optically thick or optically thin shells are considered. Intermediate situations in which the shell changes from being optically thick to thin in the course of expansion will not be considered.

r_{th} is, for purely gaseous nebulae, given typically by

$$r_{th} = (M_n \cdot g \cdot f/4 \cdot \pi \cdot m_H)^{1/2}, \tag{29}$$

where g is the hydrogen atom cross-section at the Lyman series limit, f is the fractional ionisation, m_H is the hydrogen atom mass.

Where dust is present, the value r_{th} will differ (Petrosian and Dana, 1975). The solution of Equation (28) with $r/r_{th} \to \infty$ is

$$V_\infty^2(\beta) = V_t^2(\beta) + (2 \cdot E_{Ly_c}/M_n \cdot c) \cdot r_{th} \cdot \delta. \tag{30}$$

$\delta = 1$ for acceleration of an optically thick shell and $\delta = \tau_0^{1/2}(\beta)$ for acceleration of an optically thin shell. $\tau_0(\beta)$ is the initial optical depth at β. $V_t(\beta)$ is the terminal velocity after gravitational braking of the shell, and $V_\infty(\beta)$ is the terminal velocity after subsequent radiative acceleration. Non-terminal equations are readily derivable from equation (27).

The primary point to note is that for optically thick shells the terminal shapes will have the same forms as we have described in Section 3. A comparison of Equation (30) with Equation (12) for instance, shows that the effect of radiative acceleration for this case is precisely the same as if the initial nebular ejection velocity V_0 had been larger.

Considering now the case of optically thin shell acceleration, we note that for ejection Models A, B and C we may write

$$\tau_0(\beta) \propto r_m^{-2}(\beta), \tag{31}$$

where r_m is the mean shell radius, of the form represented by Equation (14). After some manipulation it is possible to show that the terminal radius has the (normalised) form

$$r_\infty^2 = \{1 + (\alpha^2 - 1)\cos^2\beta + [\alpha^2 - \alpha_\infty^2]/[(\alpha_\infty^2 - \alpha^{-1}) \cdot (1 + (\alpha^2 - 1)\cos^2\beta)^{1/2}]\}/\{1 + (\alpha^2 - \alpha_\infty^2)/(\alpha_\infty^2 - \alpha^{-1})\}, \tag{32}$$

where α is the axial ratio before radiative acceleration and α_∞ is the terminal axial ratio after radiative acceleration. Terminal shapes for several initial values of α are presented in Figure 14.

It is also found that

$$E_{Ly_c} \cdot r_{th} \cdot \tau_0^{1/2}(\beta)/M_n \cdot c = [\omega^2 R_*^2 \cdot (\alpha^2 - \alpha_\infty^2)]/[(\alpha^2 - 1) \cdot (\alpha_\infty^2 - \alpha^{-1})] \tag{33}$$

from which it may be deduced from inspection that α_∞ has a lower limit value $\alpha_{\infty l}$ given by

$$\alpha_{\infty \cdot l} = \alpha^{-1/2}. \tag{34}$$

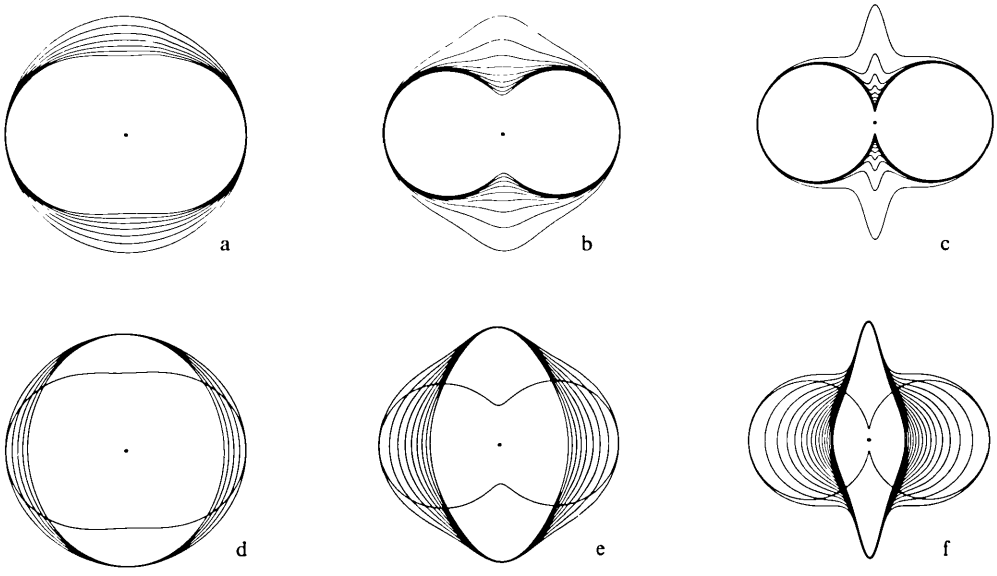

Fig. 14. Influence of radiation pressure upon optically thin shells of various initial configurations. The innermost contour is the initial shape, outer contours represent effects of increasing radiation pressure. For cases (*a*)→(*c*), the terminal axial ratios are limited to $\alpha = 1$. For cases (*d*)→(*f*), the shell development has been represented from $\alpha = 1$ to the limiting minimal axial ratio. For these latter cases, the intersecting contour is the initial configuration

Thus it is possible for the terminal axial ratio α_∞ to be less than 1, where we emphasize that α_∞ is the ratio between the nebular axis in the stellar rotational plane divided by the nebular axis in the polar direction. From Figure 14 we see that this implies prolate-like spheroids may develop, forms that have been suggested several times for planetary nebulae (Weedman, 1968). If however it were presumed that much of the significant radiative acceleration in planetary nebulae occurs when the nebula is optically thick, as certain evidence would indicate (cf. Weedman, 1968), prolate forms would be unlikely to be commonly produced in this manner.

In the following sections we will see some examples of the less extreme cases of optically thin radiative acceleration. For the particular case of nova DQ Her, we find a confirmation that the more extreme form of optically thin radiative acceleration can also occur.

Accepting that the principal radiative acceleration occurs whilst the nebula is optically thick, if we let

$$V_l^2 = 2 \cdot E_{\mathrm{Ly}_c} \cdot r_{th} / M_n \cdot c. \tag{35}$$

The maximum possible axial ratio is given by

$$\alpha_{\infty u}^2 = 1 + 2 \cdot \omega^2 R_*^2 / V_l^2.$$

For $E_{\mathrm{Ly}_c} = 2.3\,10^{29}$ W (i.e. $T_* = 50000$ K), $M_n = 0.05\,M_\odot$, $r_{th} = 0.1$ pc and $\omega R_* = 5\,\mathrm{km\,s^{-1}}$ we obtain $\alpha_{\infty u} \simeq 1.8$. Clearly, these parameters could be varied. Doubling the stellar temperature for instance produces more than an order of magnitude increase in E_{Ly_c}. The basic point to note is that radiative acceleration of the shells is likely to be quite influential, and is an important discriminant against envelopes with large axial ratios. Subsequent acceleration of the optically thin shells will therefore be of configurations with low axial ratios and, as can be seen in Figure 10, this leads to unremarkable pseudo-ellipsoidal terminal shapes.

Finally, for purely gaseous nebulae Ly_α scattering seems likely to be a dominant accelerative factor (Kovach, 1971) where nebulae are optically thick to Ly_c. For expansion of nebulae which are optically thin to Ly_c, Ly_α densities would be much lower. Recent infrared observations (cf. Cohen and Barlow, 1974) have also shown that many if not all planetary nebulae contain some proportion of dust, for which case the importance of Ly_α as an accelerative mechanism could again be greatly reduced (Kovach, 1971; Ferch and Salpeter, 1975). If for simplicity we follow Kirkpatrick in considering the shells as containing a uniform pressure Ly_α photon (or a particle) gas, it seems clear that for Models A, B and C there is a consequent equatorial distension of the kind determined for differential stellar rotation. In short, the result is likely again to be a modification of the original gravitationally braked morphological sequences but no serious development of new nebular forms. In contrast, the turbulent, radiant. and gaseous pressures within a shell may all conspire, given an adequate time scale, to severely modify the density structure of the nebulae.

To some extent this eventuality is covered by Model C. Clearly though, the problem of structural modifications due to Ly_α and gaseous pressure needs to be considered within the framework of a more rigorous discussion.

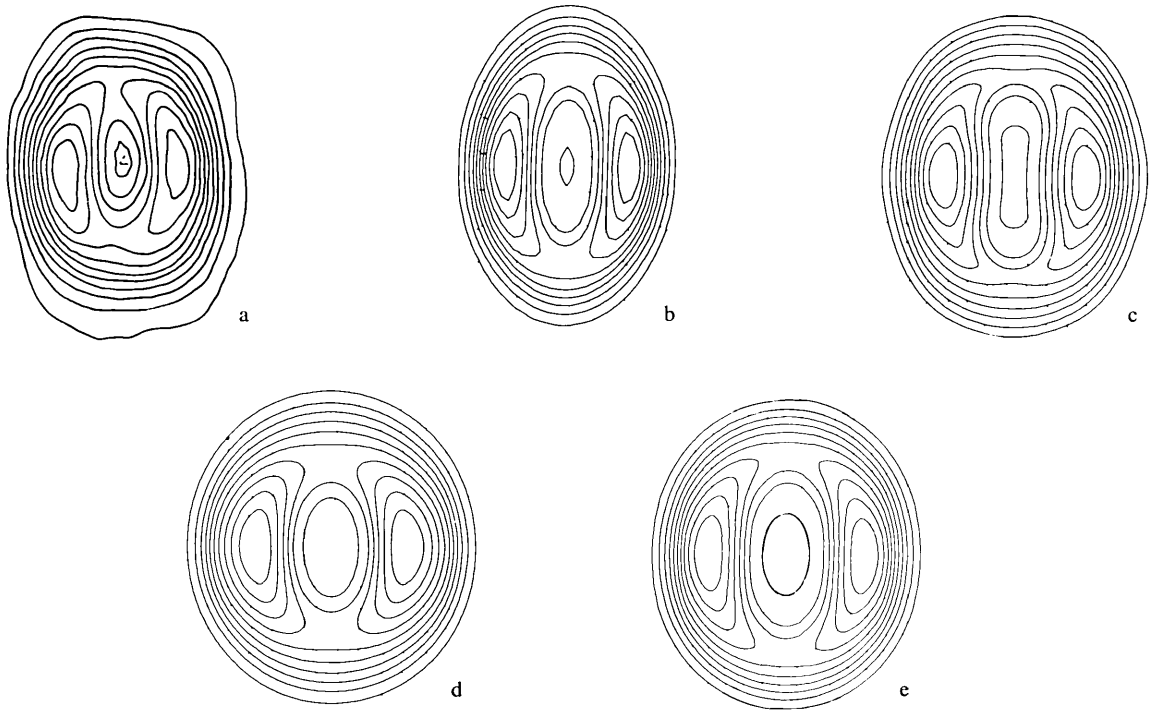

Fig. 15a—e. NGC 7027. **a** 5 GHz radio map from Scott (1973). **b** Ellipsoidal model from Hicks et al. (1976). **c** Model C ejection model using equations for delimiting surfaces and density as defined in Section 3, with $A = 1.5$, $(\alpha^2 - 1) = 3.0$. **d** Model B ejection model. Inner surface as for Model A ejection (defined in Section 3 and Table 2), outer radius 1.5 × inner radius. A = 2.25, B = 0.99. **e** Model A ejection. Inner radius, outer radius and density as defined in Section 3 and Table 2. A = 1.00, B = 1.25, C = 2.84, D = 0.0316, E = 0.97, F = −0.0395

5. Observational Comparison with Theory

We have established many of the basic nebular configurations that may be expected to occur when gravitational braking, radiative acceleration and stellar rotation are the principal physical determinants of shape. Whether these alone are capable of accounting for observed nebular structures must now be investigated through comparison with representative nebulae.

For this purpose, we identify several morphological categories, within each category discussing representative nebulae and their relationship to particular model structures. This discussion is by no means exhaustive; a more complete morphological and structural classification of planetary nebulae will be published at a future date.

Bipolar Nebulae

In bipolar nebulae the principal nebular intensity is concentrated within two "bars", one each on eitherside of the central star and most often at the ends of the nebular minor axis. These constitute a large fraction of known planetary nebulae, and can be well represented by models with axial ratios $\simeq 1.5$ (e.g. see Fig. 10). An example of this type is NGC 7027. In Figure 15 we present the radio map (Scott, 1973), models based on the foregoing theory, and a strictly ellipsoidal model. The latter model was first discussed by Hicks et al. (1976) and although the two show similar bipolar structures, the new models are significantly better at accounting for the squarer shape of NGC 7027. In particular, note that apart from relatively minor differences, all three ejection modes enable reasonable representations of this nebula. This illustrates forcibly the point made, earlier in the paper. that the morphological characteristics of model nebulae are relatively insensitive to the large differences in density structure that characterise the various ejection modes.

More generally, Hromov and Kohoutek (1968) describe a morphological sequence strongly dominated by the bipolar structure, of which they identify two basic kinds: a structure in which the "bars" are straight, and a structure in which the intensity bars are slightly curved. In terms of the theory presented here this is seen as a natural consequence of a structural development from nebulae with $\alpha \lesssim 1.5$ (which have straight sides) to nebulae with lower values of α, for which the curvature at the minor axis increases. We believe that the forms of the outer envelopes identified by Hromov and Kohoutek are more probably indicative of ionisation than density structure, and therefore outside the scope of this paper.

Another point to note here is that the strength of the bipolarity, as indicated by the variation of relative intensities between the ends of the major and minor axes, is observed to vary widely. For instance, nebula A 66 has a higher degree of bipolarity than A 70. This can be understood in terms of a variation in the mass concentration factor between nebulae, and since intensity is

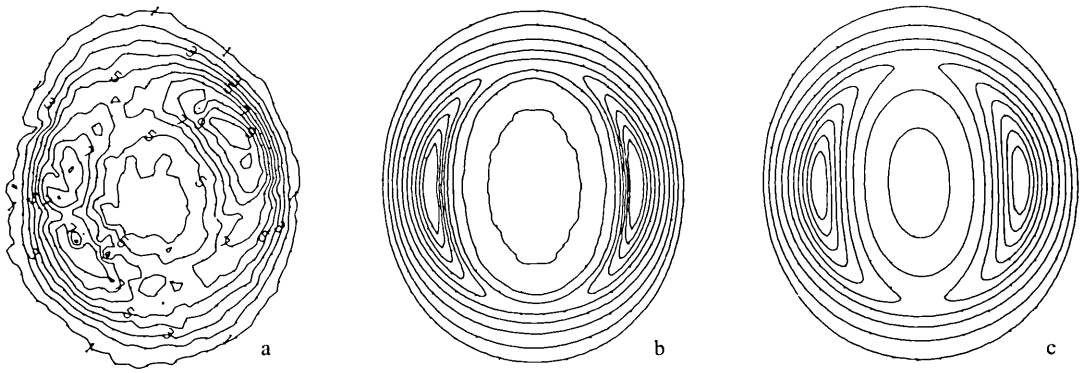

Fig. 16a—c. NGC 6720. **a** Isophotal contour map produced from Hβ electronograph. **b** Model B ejection model with A = 2.25, B = 0.99. **c** As **b** but with density falling as r^3 from its value at the inner surface to zero at the centre of the nebula. This approximately simulates the situation where ablation from the shell is operative, or a gradual diminution in the rate of mass loss from the star has taken place

roughly proportional to the square of the electron density, a relatively small variation in ϕ will suffice to cause quite large modifications to the emission structures of nebulae.

Axial ratios $\alpha > 1.5$ will tend to produce hour-glass (elevation $\beta = 0$, see Fig. 7) or diskoidal structures ($\beta = 90°$) depending upon the nebular elevation. At intermediate elevations however a strong bipolarity is evidenced whereby two high intensity, roughly circular regions are enclosed by a lower intensity halo. An example of this, similar to Models MB 3 (Fig. 12) or MA 9 (Fig. 10) viewed at $\beta = 45°$ is NGC 2440. Figure 17 shows for comparison an isophotal map (Aller, 1956) of this object produced from an H_β exposure. The same figure shows an isophotal map of IC 418, and we note that the characteristic central anvil shape is well reproduced by Model MT 15 (Fig. 17) when viewed at an elevation of $\beta = 45°$. Care should be exercised in comparing IC 418 and NGC 2440 directly with the theoretical models, however; the contour levels reproduced in Figure 17 are set at logarithmic intervals, whereas the model contours are at linear intervals.

Ring Nebulae

Although these have long been recognised as a separate category, the borderline between ring and bipolar nebulae is by no means clear. Where essentially spherical rings of even intensity are encountered, no problems in categorisation arise. These are usually interpreted as spherical shells (cf. Gurzadyan, 1969) with a certain quantity of central gas filling, and can be so considered here. Cases such as NGC 6720 however, although usually classified as rings, show unmistakable evidence of bipolarity. Latterly there has been a trend to explain NGC 6720 and a similar nebula, NGC 7293, in terms of tilted tor oids, or rings (Minkowski and Aller, 1954; Warner and Rubin, 1975; Hua and Louise, 1970; Louise, 1974; Minkowski and Osterbrock, 1960). The structures are reasonably well explained in terms of the models formulated here, however; we follow Gurzadyan in taking these also to be essentially spheroidal structures. The ratio between the peak ring brightness and the central hole of NGC 6720 is $\simeq 3:1$ for the electronograph presented in Figure 16. This is in close agreement with the model structures shown in Figure 16, which emulate reasonably well the general appearance of NGC 6720. On this basis NGC 6720, and probably NGC 7293 [which has a similar shape and ring/hole intensity ratio (Gurzadyan, 1969)] can be seen as intermediate structures with axial ratios neither too large to lead to extreme bipolarity ($\alpha \gtrsim 1.5$, say), nor so low as to produce simple rings ($\alpha = 1$).

Hour-glass Shapes

NGC 2474-5 (Fig. 18) has been previously described (Minkowski and Aller, 1954) as evidence for peculiar ejection processes whereby masses of gas were ejected in opposite directions from the central star; a natural model to adopt in view of the observed configuration. In fact, the nebula can be seen to be in many ways a classic example of the Hour-Glass type of structure shown in Figure 6 (Model MA 8). Note that the two bright regions correspond in the model to the minor axis "lobes" on the inner surface. The greatly increased brightness of these lobes is a direct consequence of their spatial proximity to the central star and, more important, the increased density in these parts of the shell. Although the internal arcs formed by the rest of the shell are rather less circular than in the model, it is possible to understand this variation in terms of the stellar rotational effect illustrated in Figure 2. In truth, this nebula from its physical appearance might well be classified more as a bipolar nebula than an hour-glass nebula, and its inclusion in this section is on the basis solely of the shape of its innermost surface.

Other distinctive examples of hour-glass structures reminiscent of models illustrated in Figures 6, 8–10, 12

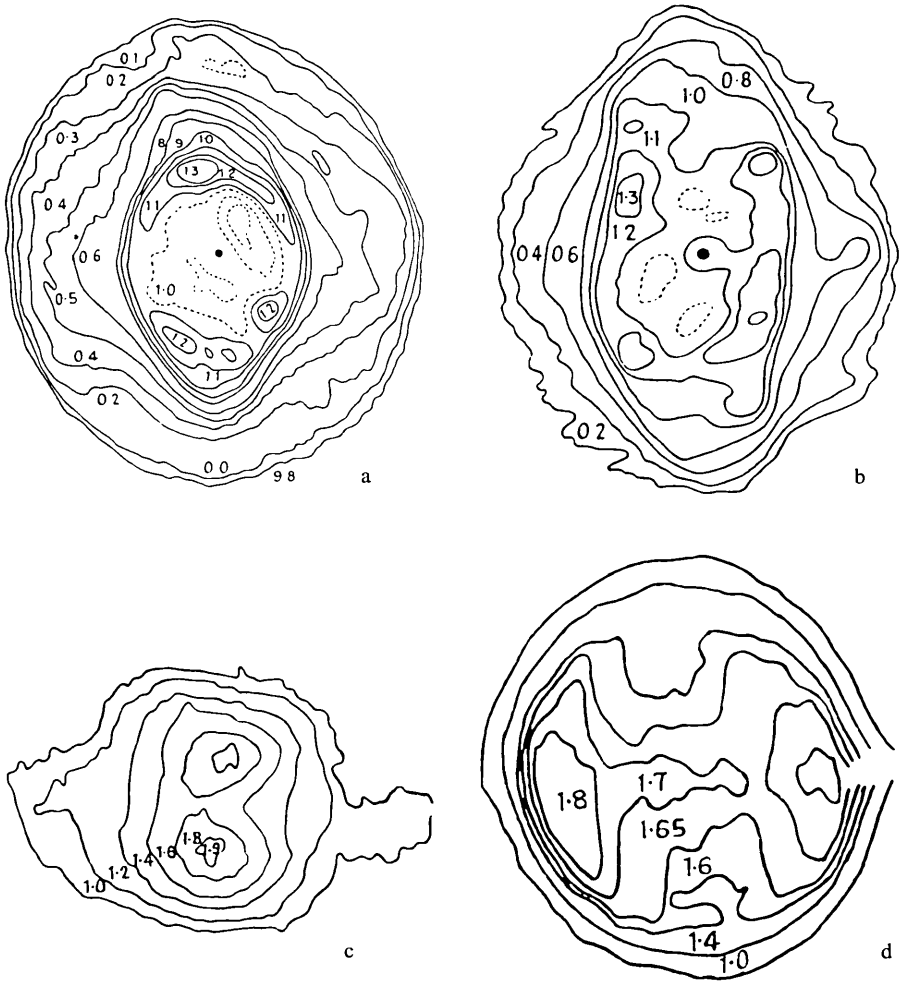

Fig. 17a—d. Miscellaneous isophotal maps of planetary nebulae adapted from Aller (1956). The significance of these in the context of the models is described in the text. **a** NGC 3242 in white light. **b** NGC 7009 in H_α. **c** NGC 2440 in λ4861 H_β. **d** IC 418 in λ4861 H_β. The contours are logarithmic

and 13 are NGC 2346 (Fig. 18), Henize 30 (NGC 2899) described by Henize as "peculiar", NGC 650-1 (Fig. 18), NGC 6772, NGC 6537 and MHα 362. LkHα 208 also shows this characteristic structure, although this nebula would not usually be classified as a planetary; the central star is almost certainly very young.

Diskoid and Other Nebular Types

A third common morphological category is the "diskoid", in which surface brightness is either uniform, or falls from the nebular centre outwards. It is not possible to define a unique structural form for this type of nebula; both toroidal and non-toroidal structures appear capable of emulating this behaviour, and it is not therefore surprising that this constitutes an important nebular grouping (cf. Westerlund and Henize, 1967). Consider in particular two examples of the genre, however: NGC 3042 and NGC 7009 (Fig. 17). An interesting feature of these particular nebulae is the peculiar distortion of the internal isophotes along the minor axes.

This is a distinctive sign of optically thin radiative acceleration (see Fig. 14) and may possibly be taken as evidence that radiation pressure has a significant influence upon nebular shapes.

Finally, a close look at the simulated emission maps of several of our models (cf. Figs. 11 and 13) reveals that many display a strong central concentration of emission, surrounded by a weak and sometimes extensive halo, leading in some cases to a peripheral brightening and the development of a weak secondary ring. This is highly reminiscent of the halos found round many nebulae, which have previously been ascribed to multiple ejections (Kaler, 1974), shell splitting due to internal Ly_α pressure (Gurzadyan, 1969) and ionisation of the interstellar medium (cf. Kaler, 1974). It appears that a further explanation may now be given in terms of the structural forms adopted by shells under the circumstances investigated by this paper.

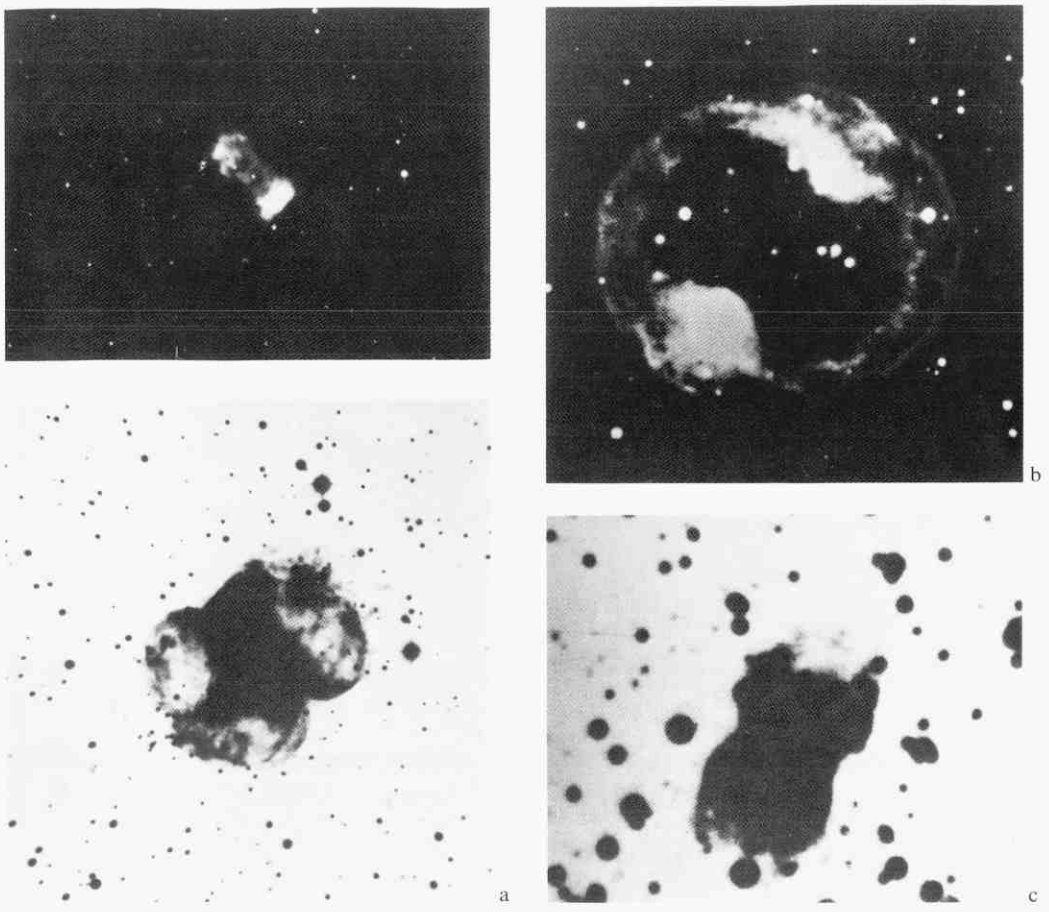

Fig. 18a—c. Three hour-glass nebulae. **a** NGC 650-1 in H_α λ6563 + [N II] λ6548, λ 6583. Note that the top left short exposure photograph only reveals a rather irregular structure, whereas the longer exposure photograph reveals the hour-glass structure. From Minkowski and Aller (1954). **b** The planetary nebula NGC 2474-5. The nebula has a structure strongly reminiscent of model MA 8 in Figure 6. **c** The planetary NGC 2346, which shows the hour-glass form particularly well

Novae

Finally we consider the development of novae shells in the context of nebular development as discussed in the preceeding sections. We will concern ourselves in particular with Nova DQ Her, which appears to illustrate well the action of radiation pressure upon optically thin shells in a manner not likely to be observed in planetary nebulae. The most recent attempts to explain the structure of this nebula have been by Warner (1972) who suggested that non-radial stellar pulsations are responsible, by Mustel and Boyarchuk (1970) who suggested magnetic guiding of the nebular material, by Hutchings (1972) who suggested interaction of the expanding nebula with the secondary component of the DQ Her system, and finally by Sparks and Starrfield (1973) who suggested an interaction of the expanding nebula with a pre-nova circumstellar ring.

The nebula will be explained here in terms of at least two principal ejections of mass, the first being more energetic than the second. Assuming this course of events, the subsequent evolution of the shell can readily be determined if both shells reached a terminal radius in the gravitational field during the nova pre-maximum phase. For simplicity, we also assume that there is no mass concentration ($\phi = 1$), that the shells are optically thin, and that the outer shell reaches a more or less minimal terminal axial ratio, whereas the inner shell achieves an intermediate configuration. This might for instance arise if the fractional ionisation of the inner shell were greater than that of the outer shell. Different shell masses would not account for this behaviour because a greater inertia to radiative acceleration would be offset by an increase in optical depth, which commensurately increases the radiation pressure upon the shell.

Finally, it will also be assumed that radiation pressure is the predominant accelerative factor for novae shells. This, it will be noted, has been questioned by Mustel (1962), who proposes that high energy particles are the dominant factor in shell acceleration. The consequences in this model of electromagnetic and particulate radiation need not differ greatly, however, and for this reason the choice of one or other accelerating mechanism may not necessarily be critical.

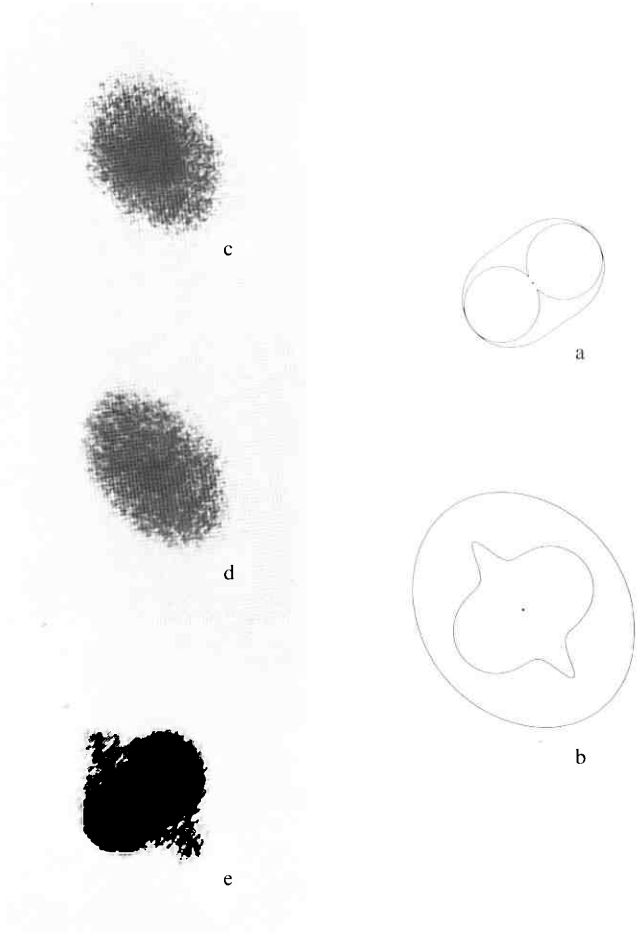

Fig. 19a–e. Model of DQ Her nebular shells: **a** Initial shell shapes: the relative positions are not critical. **b** Terminal shell shapes: relative shell dimensions are critically determined by the final axial ratios adopted. **c** Star and Nebula in blue light. **d** Nebula in [O III]. **e** Nebula in [N II] λ 6548, λ 6584. The photographs are by Baade (McLaughlin, 1946) and show a close similarity to the model

The shell shapes prior to radiative acceleration are shown in Figure 19, where the inner lower velocity shell has an axial ratio $\alpha = 10$, and the outer shell an axial ratio $\alpha = 1.5$. Subsequently, as Equation (34) indicates, the terminal axial ratio of the outer shell may achieve a minimal value of $\alpha_{\infty l} = (1.5)^{-1/2} \simeq 0.8$. For the inner shell, an intermediate terminal axial ratio of $\alpha_{\infty} = 1$ is adopted, based on the photographic evidence. The resulting shells after radiative acceleration are shown in Figure 19, and may be compared to the photographs obtained by Baade (McLaughlin, 1946). A comparison is persuasive. The dominance of [N II] λ 6548, λ 6584 for the inner shell must in some way relate to differing physical conditions between the two shells.

Using this model for the development of the envelope, it is also possible to learn something about the star at the time of ejection.

For novae generally the principal spectrum, evident in the period subsequent to maximum light, is preceded by a much lower velocity line system. McCrea (1937) and Mustel (1957) have argued that the transformation from one line system to the other is a consequence of radiative acceleration of the envelope, for which case the pre-maximum velocity may be identified with the shell terminal velocity after gravitational braking but before radiative acceleration. From the observed orientation of the nebula of DQ Her, it may be further presumed that the pre-maximum velocity coincides closely with the expansion of the nebula in the stellar equatorial plane, whence the equatorial rotational velocity of the ejecting star, V_{rot}, is given by

$$V_{\text{rot}} = V_{\text{exp}} \cdot [(\alpha^2 - 1)/2\alpha^2]^{1/2},$$

where V_{exp} is the pre-maximum velocity, and α the nebula terminal axial ratio before radiative acceleration. For nova DQ Her we have $V_{\text{exp}} \simeq -180\,\text{km}\cdot\text{s}^{-1}$ if we assume the outer shell (axial ratio $\alpha \gtrsim 1.5$) to be primarily responsible for the pre-maximum spectrum, whence we obtain $V_{\text{rot}} \gtrsim 95\,\text{km}\cdot\text{s}^{-1}$.

If the inner shell (axial ratio $\alpha \simeq 10$ before radiative acceleration) was responsible for the pre-maximum spectrum, then a rotational velocity $V_{\text{rot}} \simeq 127\,\text{km}\cdot\text{s}^{-1}$ is determined.

Several investigators (Herbst et al., 1974; Bath et al., 1974; Swedlund et al., 1974) have recently suggested that a 142 sec light periodicity in the post-nova refers to the rotation period of the star, in which case the stellar equatorial velocity would be in excess of $10^3\,\text{km}\cdot\text{s}^{-1}$. This is clearly very much greater than the values determined above, if applicable to the pre-nova star, and suggests that the principal envelope detached itself after a period of nova expansion. Applying conservation of angular momentum to the nova photospheric layers gives a ten-fold increase in nova radius before principal shell ejection; that is, a radius of $\sim 1\,R_{\odot}$. For this case, $\omega R_{*}/V_{\text{esc}} \lesssim 0.3$, and the analysis developed for planetary nebulae would also be applicable for shell ejection here. Further, since a maximum nova radius of $\simeq 10^2\,R_{\odot}$ is finally achieved (Arhipova and Mustel, 1975), the primary envelope would be ejected well before light maximum; another pre-requisite of the analysis. In principle, it seems therefore possible to at least partially understand the structural development of the nebula of DQ Her.

Although we have so far confined ourselves to discussing DQ Her, it is clearly of interest to know whether other novae display envelopes which can be similarly accounted for.

Data for pre-1957 novae has been collated by Payne-Gaposhkin (1957). Of the eight novae for which nebular disks were observed during this period, only one (RR Pictoris) appears to have displayed features reminiscent of the internal envelope of DQ Her; although an elliptical nebula was observed for T Aur (Mustel and Boyarchuk, 1970). At least three others however (V603 Aql, CP Lac and T Aur) showed spectra that have been interpreted

fairly unambiguously in terms of an expanding equatorial toroid, or disk, with polar jets; a description which fairly accurately represents the kind of nebular structure we propose for DQ Her. In the case of V603 Aql, the symmetry of the observed nebula appears to reflect a fortuitous nebular orientation whereby the polar jets are directed more or less towards the observer. Hutchings (1972) describes spectra of three more recent novae; Nova Delphini 1967, Nova Volpeculae 1968 (1) and Nova Serpentis 1970, all of which appear likely to have ejected similar nebular structures.

It therefore seems probable that the majority of novae eject shells during the low luminosity pre-maximum stage which through gravitational braking acquire high axial ratios, but which are subsequently radiatively accelerated to form the characteristic equatorial toroid—polar jet structure displayed so clearly in the nebular form of DQ Her.

6. Conclusion

We have investigated the structural development of nebular shells ejected from rotating stars where the principal mechanism determining shell development is gravitational braking. The resulting forms are found to be adequately represented by a simple analytical expression, which enables the further contributions of radiation pressure and differential stellar rotation to be conveniently assessed for a wide range of nebular forms. Various model planetary nebulae have also been constructed, assuming particular shell ejection modes, and we have contoured a wide range of such models to determine the range of nebular types which may be expected in these circumstances.

It is found that most commonly observed nebular shapes can be readily accounted for, as well as some less common forms of nebulae. A preliminary understanding of the statistics of nebular shapes also seems to be possible. Under these circumstances, it is not clear that magnetic fields are required to explain the morphology of most planetary nebulae, although a statistical tendency for the major axis of planetary nebulae to orientate themselves parallel to the galactic plane, for nebulae near the galactic plane, may indicate that the galactic magnetic field plays some formative influence in certain cases. The physical mechanisms behind this orientation, if indeed it exists, are still extremely uncertain however.

By way of a final caveat, we must repeat that the present treatment has done no more than broadly introduce certain mechanisms possibly influencing shell shape, and their likely consequence for the generality of observed nebulae, and this must clearly be eventually superceded by a much more detailed and specific analysis. Unfortunately, many important aspects upon which such an analysis must be based are at present so conjectural as to probably make such specificity at this stage premature. It is undoubtedly at least partly for these reasons that the sophistication of certain spherically symmetric hydrodynamical treatments is exceeded only by the inadequacy of the resultant models in explaining observed nebulae; the ultimate arbiter of relevance.

References

Abell, G.O., Goldreich, P.: 1966, *Publ. Astron. Soc. Pacific* **78**, 232
Allen, C.W.: 1964, Astrophysical Quantities, Athlone Press, London
Aller, L.H.: 1956, Gaseous Nebulae, Chapman and Hall Ltd., London
Aller, L.H., Liller, W.: 1968, Stars and Stellar Systems VII, University of Chicago Press, Chicago, p. 483
Arhipova, V.P., Mustel, E.R.: 1975, Novae in "Variable Stars and Stellar Evolution", IAU *Symposium No.* 67, ed. V. E. Sherwood and L. Plant, D. Reidel Publishing Company, Dordrecht-Holland, p. 305
Baade, W.: 1942, *Publ. Astron. Soc. Pacific* **54**, 244
Bath, G.T., Evans, W.P., Pringle, J.E.: 1974, *Astrophys. J.* **193**, L11
Cahn, J.H., Kaler, J.B.: 1971, *Astrophys. J. Suppl.* **22**, 319
Cohen, M., Barlow, M.J.: 1974, *Astrophys. J.* **193**, 401
Cudworth, K.: 1975, *Monthly Notices Roy. Astron. Soc.* **172**, 57p
Faulkener, D.J.: 1970, *Astrophys. J.* **162**, 513
Ferch, R.L., Salpeter, E.E.: 1975, *Astrophys. J.* **202**, 195
Finzi, A., Wolf, R.: 1970, *Astrophys. Letters* **5**, 63
Finzi, A., Wolf, R.: 1971, *Astrophys. J.* **165**, 285
Grinin, V.P., Zvereva, A.M.: 1968, On the Orientation of the Majors Axes of Planetary Nebulae in "Planetary Nebulae", IAU *Symposium No.* 34, ed. D. E. Osterbrock and C. R. O'Dell, D. Reidel Publishing Company, Dordrecht-Holland, p. 287
Gurzadyan, G.A.: 1969, Planetary Nebulae, Gordon and Breach, New York
Härm, R., Schwarzschild, M.: 1975, *Astrophys. J.* **200**, 324
Herbst, W., Hesser, J.E., Ostriker, J.P.: 1974, *Astrophys. J.* **193**, 679
Hicks, T.R., Phillips, J.P., Reay, N.K.: 1976, *Monthly Notices Roy. Astron. Soc.* **176**, 409
Hromov, G.S., Kohoutek, L.: 1968, *Bull. Astron.* **19**, 1
Hua, C.T., Louise, R.: 1970, *Astron. Astrophys.* **9**, 448
Hunter, J.H., Sofia, S.: 1971, *Monthly Notices Roy. Astron. Soc.* **154**, 393
Hutchings, J.B.: 1972, *Monthly Notices Roy. Astron. Soc.* **158**, 177
Kaler, J. B.: 1974, *Astron. J.* **79**, 594
Kirkpatrick, R.C.: 1976, *Astrophys. Letters* **17**, 7
Kovach, W.S.: 1971, *Astrophys. J.* **168**, 423
Kutter, G.S., Sparks, W.M.: 1974, *Astrophys. J.* **192**, 447
Liller, M.H., Liller, W.: 1968, Observed Angular Motions in Planetary Nebulae in "Planetary Nebulae", IAU *Symposium No.* 34, ed. D. E. Osterbrock and C. R. O'Dell, D. Reidel Publishing Company, Dordrecht-Holland, p. 38
Louise, R.: 1973, *Mém. Soc. Roy. Liège* **5**, 465
Louise, R.: 1974, *Astron. Astrophys.* **30**, 189
Matthews, W.G.: 1966, *Astrophys. J.* **143**, 173
McLaughlin, D.B.: 1946, *Sky and Telescope* **5**, No. 7
McCrea, W.: 1937, *Observatory* **60**, 277
Melnick, G., Harwit, M.: 1975, *Monthly Notices Roy. Astron. Soc.* **171**, 441
Menzel, D.H.: 1946, *Physica* **12**, 768
Menzel, D.H.: 1968, The Role of Magnetic Fields in the Origin and Structure of Planetary Nebulae in "Planetary Nebulae" IAU *Symposium No.* 34, ed. D. E. Osterbrock and C. R. O'Dell, D. Reidel Publishing Company, Dordrecht-Holland, p. 279
Minkowski, R., Aller, L.H.: 1954, *Astrophys. J.* **120**, 261
Minkowski, R., Osterbrock, D.: 1960, *Astrophys. J.* **131**, 537
Mustel, E.R.: 1957, Physical Processes in Novae in "Non-Stable Stars", IAU *Symposium No.* 3, ed. G. H. Herbig, D. Reidel Publishing Company, Dordrecht-Holland, p. 57
Mustel, E.R.: 1962, *Astron. Zh.* **39**, 185
Mustel, E.R., Boyarchuk, A.A.: 1970, *Astrophys. Space. Sci.* **6**, 183
O'Dell, C.R.: 1962, *Astrophys. J.* **135**, 371

Osterbrock, D.E.: 1974, Astrophysics of Gaseous Nebulae, W. H. Freeman and Company, San Francisco
Paczyński, B.: 1971, *Astrophys. Letters* **9**, 33
Payne-Gaposhkin, C.: 1957, The Galactic Novae, North Holland Publishing Company, Amsterdam
Petrosian, V., Dana, R.A.: 1975, *Astrophys. J.* **196**, 733
Rose, W.K.: 1967, *Astrophys. J.* **150**, 193
Rose, W.K.: 1973, *Mém. Soc. Roy. Sci. Liège* **5**, 419
Salpeter, E.E.: 1971, *Ann. Rev. Astron. Astrophys.* **142**, 855
Scott, P.F.: 1973, *Monthly Notices Roy. Astron. Soc.* **161**, 35p
Shklovski, I.S.: 1956, *Astron. Zh.* **33**, 515
Smith, H.: 1973, *Monthly Notices Roy. Astron. Soc.* **164**, 321
Smith, R. L., Rose, W.K.: 1972, *Astrophys. J.* **176**, 395
Sparks, W.M., Starrfield, S.: 1973, *Monthly Notices Roy. Astron. Soc.* **164**, 1p
Swedlund, J.B., Kemp, J.C., Wolstencroft, R.D.: 1974, *Astrophys. J.* **193**, L11
Warner, B.: 1972, *Monthly Notices Roy. Astron. Soc.* **160**, 35p
Warner, J.W., Ruben, V.C.: 1975, *Astrophys. J.* **198**, 593
Weedman, D.W.: 1968, *Astrophys. J.* **153**, 49
Westerlund, B.E., Henize, K.G.: 1967, *Astrophys. J. Suppl.* **14**, 154
Wilson, O.C.: 1958, *Rev. Mod. Phys.* **30**, 1025
Wilson, O.C.: 1960, *Astrophys. J.* **131**, 75
Wood, P.R.: 1973, Dynamical Properties of a Red Supergiant Envelope in *Mem. Soc. Roy. Sci. Liège* **5**, 419
Woyk, E.: 1968, Explanation of Different Shapes of Planetaries in Terms of Movement in Magnetic and Gravitational Fields, in "Planetary Nebulae", IAU *Symposium No.* 34, ed. D. E. Osterbrock and C. R. O'Dell, D. Reidel Publishing Company, Dordrecht-Holland, p. 275

Astron. Astrophys. 61, 695—703 (1977)

ASTRONOMY
AND
ASTROPHYSICS

The Structure of NGC 6543

J. P. Phillips, N. K. Reay and S. P. Worswick
Astronomy Group, The Blackett Laboratory, Imperial College of Science & Technology, Prince Consort Road, London SW7 2BZ, England

Received February 2, revised June 2, 1977

Summary. New monochromatic electronographic data are presented which, along with previous data, enables a re-assessment of the nature and origins of the structure of NGC 6543. It is suggested that the nebula may be represented by an intrinsically simple spheroidal structure, with three axes of differing lengths.

Key words: planetary nebulae — structure

1. Introduction

NGC 6543 has previously been described in terms of a helical structure (Münch, 1968) similar in many ways to the structure of the Helix nebula, NGC 7293. Recently however NGC 7293 has been alternatively described in terms of a toroidal structure (Warner and Rubin, 1975) with an interpretation in terms of a spheroidal structure being perhaps even more likely (Phillips and Reay, 1977). In the following we review the data upon which the helical interpretation of NGC 6543 was based, and present new electronographic data, in an attempt to further elucidate the structural characteristics of this nebula.

2. The Emission Structure

A spectracon electronographic image tube has been used to obtain narrow band exposures of NGC 6543 at various wavelengths. The electronographic detection process has the advantage, over conventional photography, of linearity and large dynamic range. The observations, summarised in Table 1, were made on the 42-inch telescope at the Lowell Observatory, Flagstaff, Arizona.

The electronographs were digitised using a PDS microdensitometer and isophotal maps were produced for each wavelength using the University of London CDC 6600 computer. A detailed account of the reduction technique is given by Coleman et al. (1975). In Figures 1 to 7 we present maps for wavelengths Hα λ6563 Å, HeI λ5876 Å [OIII] λ4959/5007 Å, [OI] λ6300 Å, [OII] λ3726/29 Å, [NII] λ6583 Å and [SII] λ6731 Å. Details of the exposures are given in Table 1. Fifteen contour levels are set at equispaced intervals between the highest and lowest points in the digital matrix and alternate levels are numbered, with the lowest numbers corresponding to the lower levels. Markers on the contour lines point in the direction of reducing intensity.

Table 1. Exposure details for NGC 6543

Ion	Wavelength Å	Passband Å	Emulsion	Exposure Time Mins
OII	3726/29	24	L4	20
HeI	5876	10	G5	5
OIII	4959/5007	50	L4	5
OI	6300	9	G5	60
HI	6563	10	L4	5
NII	6583	9	L4	20
SII	6731	10	G5	30

An important detail to note from Figures 1 to 7 is the difference in emission structure between the Hα, HeI and [OIII] maps and the remaining forbidden line maps. The Hα, HeI and [OIII] maps show a weak internal bipolarity orientated at position angle (p.a.) $\simeq 165°$, which for the remaining forbidden line maps transforms to a much stronger and more extended bipolarity at p.a. $\simeq 12°$. This must clearly reflect ionisation structure within the nebula, a point also made by Dopita and Gibbons (1975). A feature which is not so readily accounted for is the twisting of the bipolarity in the Hα, HeI, [OIII] and radio maps (Terzian, Balick and Bignell, 1974) with respect to the major axis of the outer layers. The p.a.'s of the bipolarity and major axis in the Hα, HeI, [OIII] and radio maps also differ from the p.a. of the bipolarity in the forbidden line maps. Measure-

Send offprint requests to: J.P. Phillips

Fig. 1. Hα 6563 Å. North is vertically up and east to the left, for all the non-simulated maps

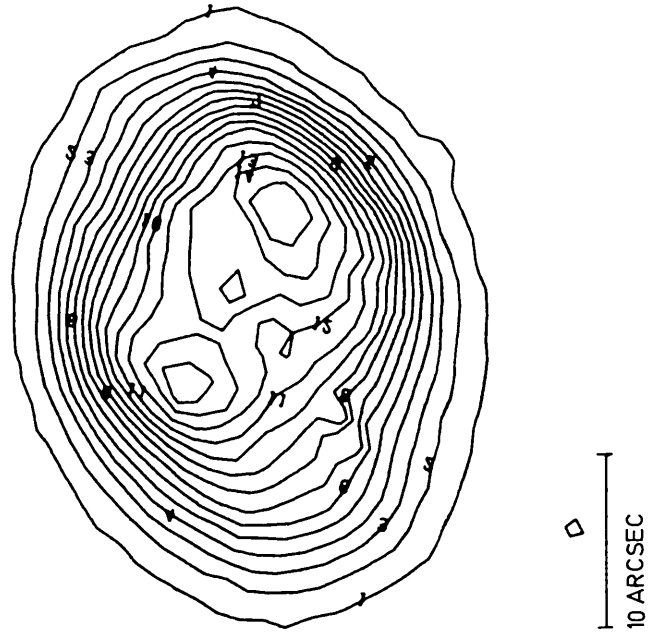

Fig. 3. [O III] 4959/5007 Å

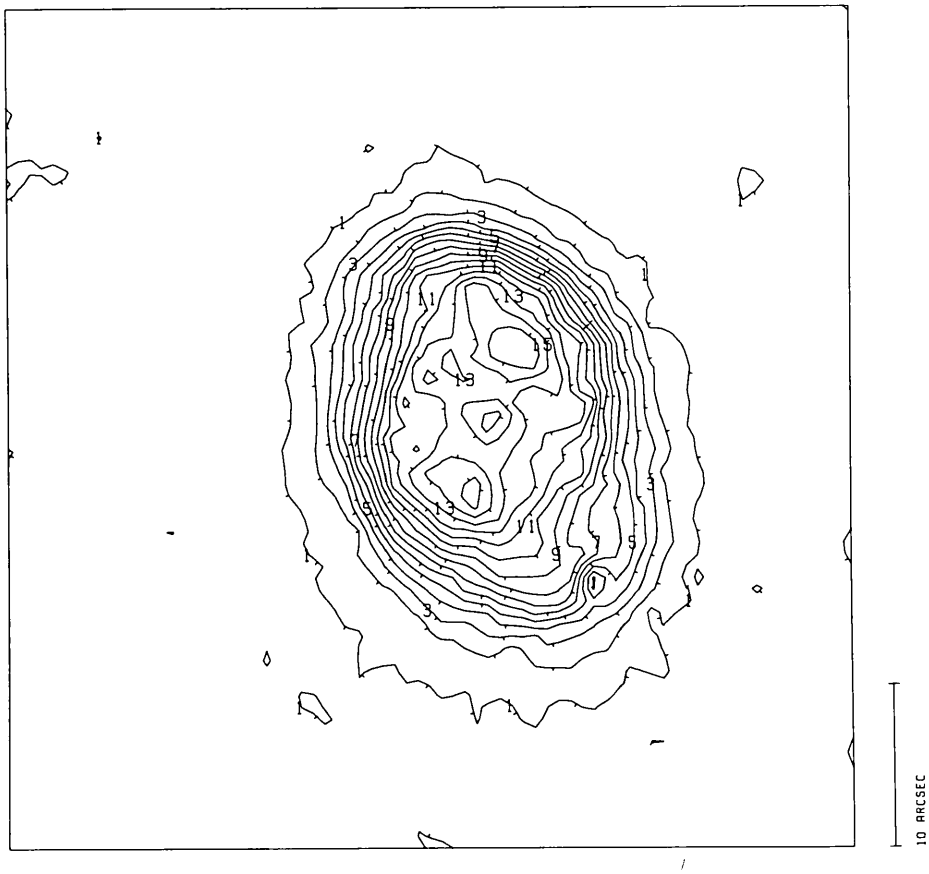

Fig. 2. He I 5876 Å

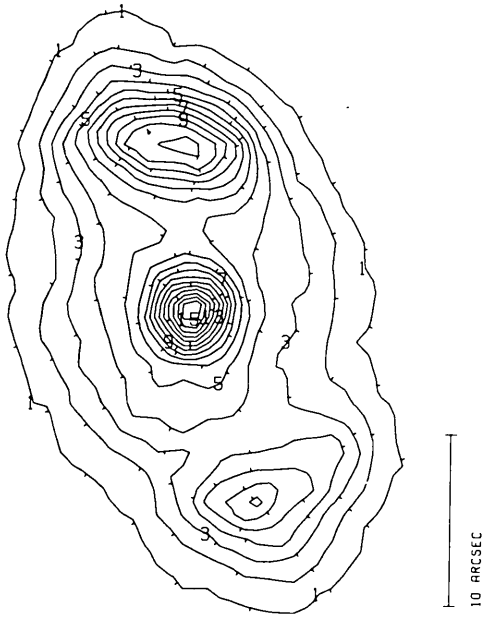

Fig. 4. [O I] 6300 Å. The central maximum in this and the [O II] λ 3726/29 Å map is due to continuum emission from the central star

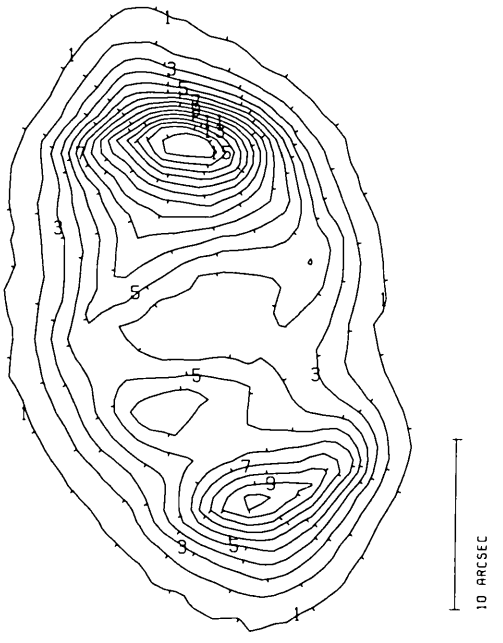

Fig. 6. [N II] 6583 Å

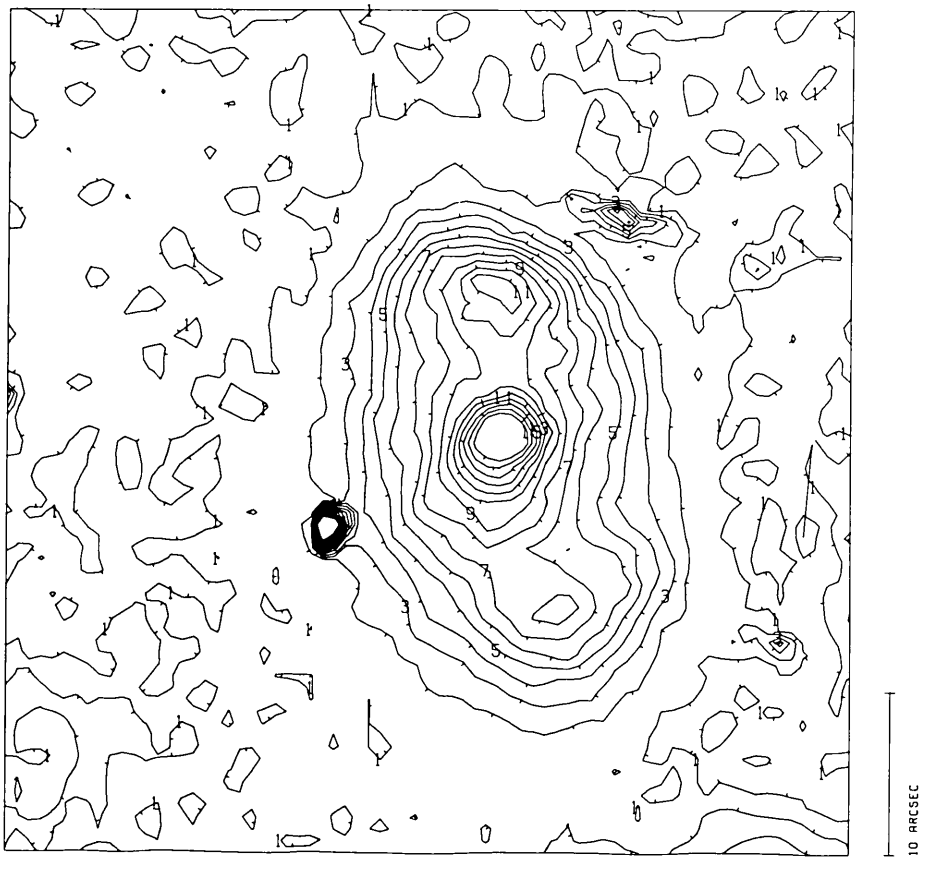

Fig. 5. [O II] 3726/29 Å

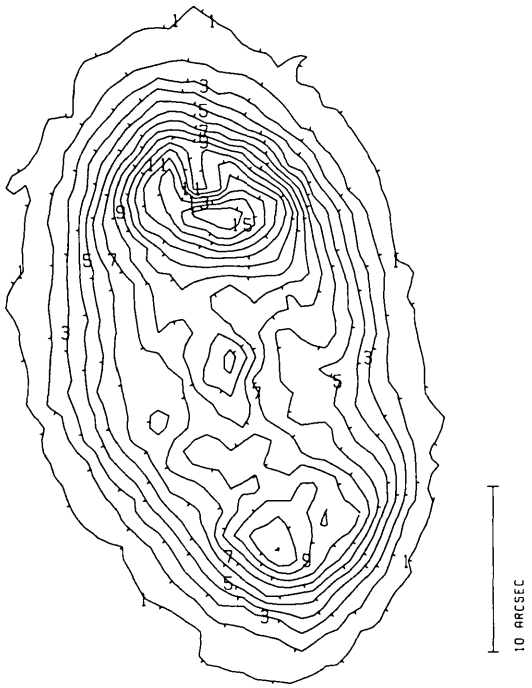

Fig. 7. [SII] 6731 Å

Table 2. Wavelength Dependence of Position Angle in NGC 6543

Map	Position Angle	Axis[a]	Reference
[OI]	12°±2°	*P*	—
[SII]	12°±2°	*P*	—
[NII]	11°±2°	*P*	—
[OII]	10°±2°	*P*	—
[OIII]	22°±4°	*M*	—
HeI	22°±4°	*M*	—
HeI	159°±5°	*P*	—
Hα	16°±2°	*M*	—
Hα	167°±2°	*P*	—
—	23°	*M*	Munch (1968)
8085 MHz	23°±2°	*M*	Terzian et al. (1974)
8085 MHz	156°±5°	*P*	Terzian et al. (1974)
4995 MHz	27°±10°	*M*	Scott (1975)
4995 MHz	154°±6°	*P*	Scott (1975)
4995 MHz	35°±5°	*M*	George et al. (1974)
1407 MHz	40°±2°	*M*	Elsmore (1968)

[a] *M* = Major Axis Position Angle; *P* = Position Angle of Axis of Bipolarity

ments of the relevant position angles are presented in Table 2. Clearly, both differential twisting and structural differences must be accounted for in any model which is to realistically represent NGC 6543.

3. The Physical Structure

A primary problem that any model for NGC 6543 must come to grips with is the rather complex radial velocity pattern of this nebula, as observed by Münch (1968). It is by no means clear that a helical structure is an obvious consequence of this pattern, and some degree of faith must be exercised in relating this pattern to Münch's model; the proposed structure was probably suggested as much by the rather contorted appearance of the broad band optical emission structure as by the radial velocity data. In an attempt to clarify the situation, the velocity data near the major and minor axes of the emission structure has been plotted with respect to distance from the central star (Fig. 8). We have adopted a mean nebular radial velocity of -65 km.s^{-1}, implicitly used by Münch, and consistent with other measures (Keeler, 1894; Campbell and Moore, 1918; Scheiner and Wilsing, 1905). It is immediately apparent that although the radial velocity points are somewhat scattered they occupy distinct tilted regions, as indicated roughly by the rectangles in Figure 8. If velocity is taken as proportional to radius, the result can be interpreted in terms of emission from elements within a tilted spheroidal volume. A possible implication would be for the presence of small-scale condensation within the nebula, a concept also supported by the work of Dopita and Gibbons (1975). The Hα map suggests a macrostructure in which mass is distributed quite regularly, so that an homogeneous microstructure without condensations would be expected to lead to broad spectral lines displaying little of the observed variability in radial velocity over short projected spatial distances. The suggestion that velocity be taken as proportional to radius is consistent with observed behaviour in other nebulae (cf. Aller and Liller, 1968; Liller and Liller, 1968). Its validity for this nebula may be assessed by the accuracy with which the implied physical structures account for nebular emission characteristics. In particular, note that the absence of radial velocity measurements within a radius of $\simeq 3''$ of the central star indicates the possible presence of a corresponding centrally evacuated region with these dimensions. A low emission central zone also appears to be required to account for the observed Hα, HeI bipolarity, although in itself this may be alternatively explainable in terms of a higher temperature central region (or, for the HeI, a higher state of ionisation). The latter hypothesis would be expected to result in stronger central [OIII] emission however, in contradiction both to the [OIII] electronograph and the sense of the central [OIII] radial velocity measures by Münch. It seems likely therefore that this hypothesis would require a central [OIV]/[OV] zone. However this may be resolved, for the present discussion we simply assume the presence of a central region of reduced hydrogenic emission, which in combination with the shape and orientation of the outer nebular boundary will be expected to play a crucial role in determining nebular emission structure.

To assess the plausibility of such structures, we have tested various models with axial ratios and angles of

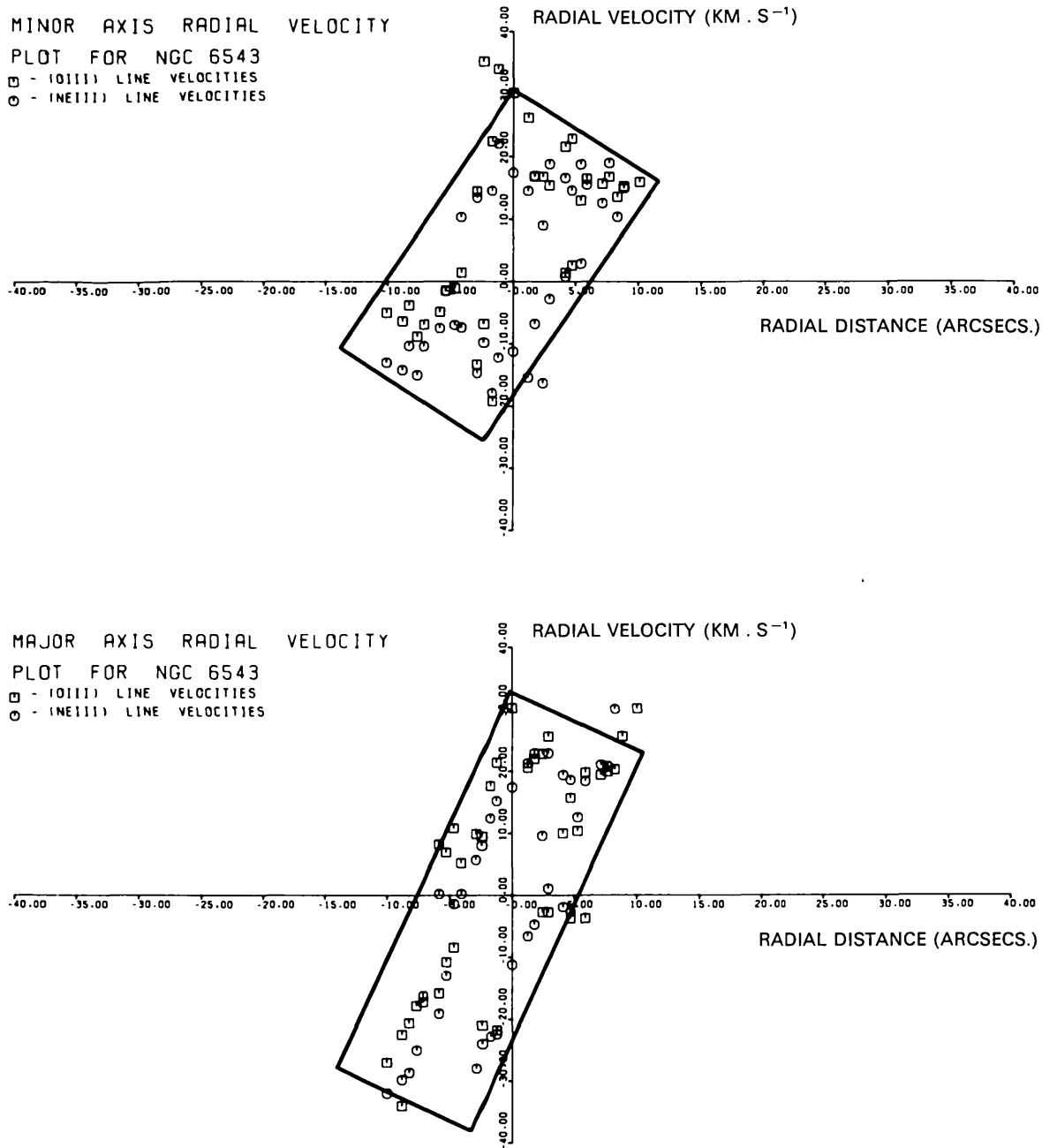

Fig. 8. Variation of radial velocity along p.a. 20°, the approximate orientation of the major axis of the emission structure, and p.a. 110° (the corresponding minor axis), using the Munch (1968) data for NGC 6543. Although the relative scales of the axes are uncertain, the radial velocity data is seen to occupy distinct regions of the maps, indicated approximately by the tilted rectangles

tilt to the line of sight consistent with the radial velocity data. The models chosen were spheroids (in Cartesian coordinates defined by $x^2/a^2+y^2/b^2+z^2/c^2=1$) with axes $a>b>c$, where "a" is tilted at angle θ to the line of sight, and ϕ is the angle of tilt of "b" to the line of sight for $\theta=0°$. Although the value of θ is conjectural, for any given θ the ratios $a:b:c$, and angle ϕ can be reasonably well assessed. On this basis we have computed isophotal contour maps for various angles θ and ϕ, and Figure 9 shows a map which resembles NGC 6543 reasonably well. Emission is taken as proportional to $N_e^2\,L$, where N_e is electron density and L is path length. Density is taken to vary as the inverse of the radius. Temperature in this approximation is assumed constant throughout the nebula, and a seeing disc of diameter $\simeq 3''$ is assumed for direct comparison with the observed maps. Further details of the modelling procedures are given by Phillips and Reay (1977). The differential

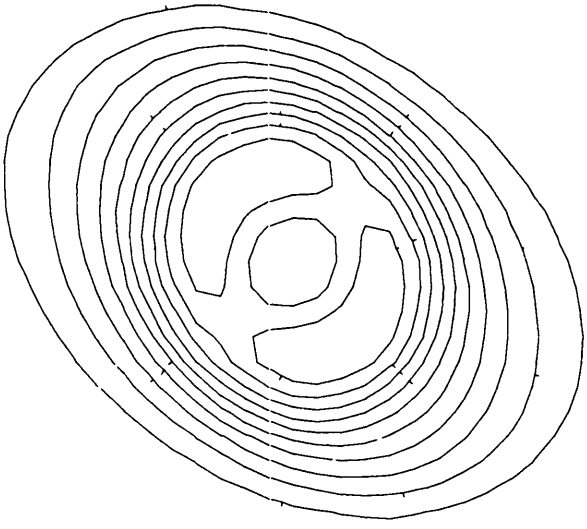

Fig. 9. Simulated Hα map using a model with $\theta = 30°$, $\phi = 55°$, $a = 18{,}0''$, $b = 8.85''$, $c = 4.4''$, $\alpha = 1$. Terms are explained in the text

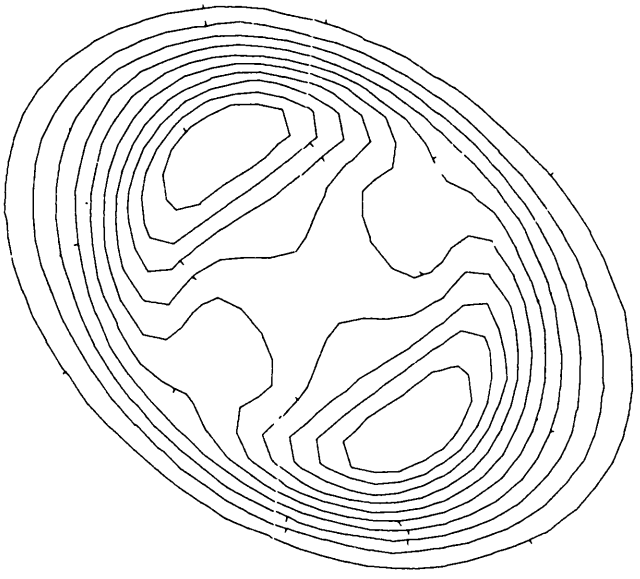

Fig. 10. Simulated forbidden line map. Reasonable representation of the forbidden line maps can be achieved by increasing the size of the central zone in which emission is zero

nebular twist characteristic of the observed emission structure is seen to be reasonably well reproduced. The twist between internal and external contours is a peculiar consequence of tilting a nebular configuration in which $a \neq b \neq c$, and $\alpha > 0$, where the exponent α is defined by $\rho \propto r^{-\alpha}$, ρ and r being respectively the density and radius. When $b = c$ (a prolate spheroid), ϕ or $\theta = n\pi/2$ ($n = 0,1,2$), or $\alpha = 0$, this differential twist disappears. A zero emission zone of diameter $6''$ has been adopted. This is consistent as noted previously with radial velocity data, and leads to a bipolarity reasonably close to the observed form. Trials with slightly smaller ($5''$) and larger ($7''$) central holes led to less successful structures.

Attempts were also made to test for the forms of the density variation with radius. The case $\alpha = 0$ produced too large a bipolarity and, more critically, no differential twisting. For $\alpha = 2$, it was also found impossible to reproduce the observed twist, as well as the projected axial ratio of the observed emission structure. Irrespective of the length of the physical major axis, the $\alpha = 2$ model led to structures with too small an axial ratio. In comparison, the $\alpha = 1$ structure reproduces reasonably well both the observed twist and bipolarity of NGC 6543.

A further point to note concerning this model is that both the inner and outer regions are twisted with respect to the physical major axis of the nebula which does not lie along the major axis of the emission structure, but along a horizontal direction in Figure 9. A comparison of model with observed nebula suggests that the projected major axis of the physical structure of NGC 6543 probably lies close to p.a. $\simeq +50°$ compared with a p.a. of $+20°$ for the major axis of the emission structure. When Münch's radial velocity data is replotted for this new axis, the model parameters require only marginal revision. The models presented in this paper are based on the radial velocity data for p.a. $= 50°$.

Finally, any model for NGC 6543 must also be capable of accounting for the observed differences in emission structure between Hα and the forbidden lines. To approximately simulate the situation relevant to forbidden lines, we have again assumed an emission proportional to $N_e^2 L$ (valid supposing constant temperature throughout the region of nebula containing the ions), and a central region of zero emission with diameter $D_c = 10''$, corresponding to that region where the atomic species responsible for the observed radiation is in a higher state of ionisation. The resulting contour map, illustrated in Figure 10, shows that the observed bipolarity and relative intensity levels of the forbidden line maps are tolerably well reproduced, considering the approximations. So far as can be assessed values of D_c for the observed forbidden lines (excluding [O III]) also appear to be very similar, differing by less than $\sim 2''$.

We may therefore state that the principal features (as well as some more subtle characteristics) of the observed emission structure of this nebula can be accounted for in terms of an intrinsically simple spheroidal model, and no recourse appears necessary to more complex models.

4. Origin of the Physical Structures

We would finally like to briefly indicate various anomalies in the observed emission, and deduced physical

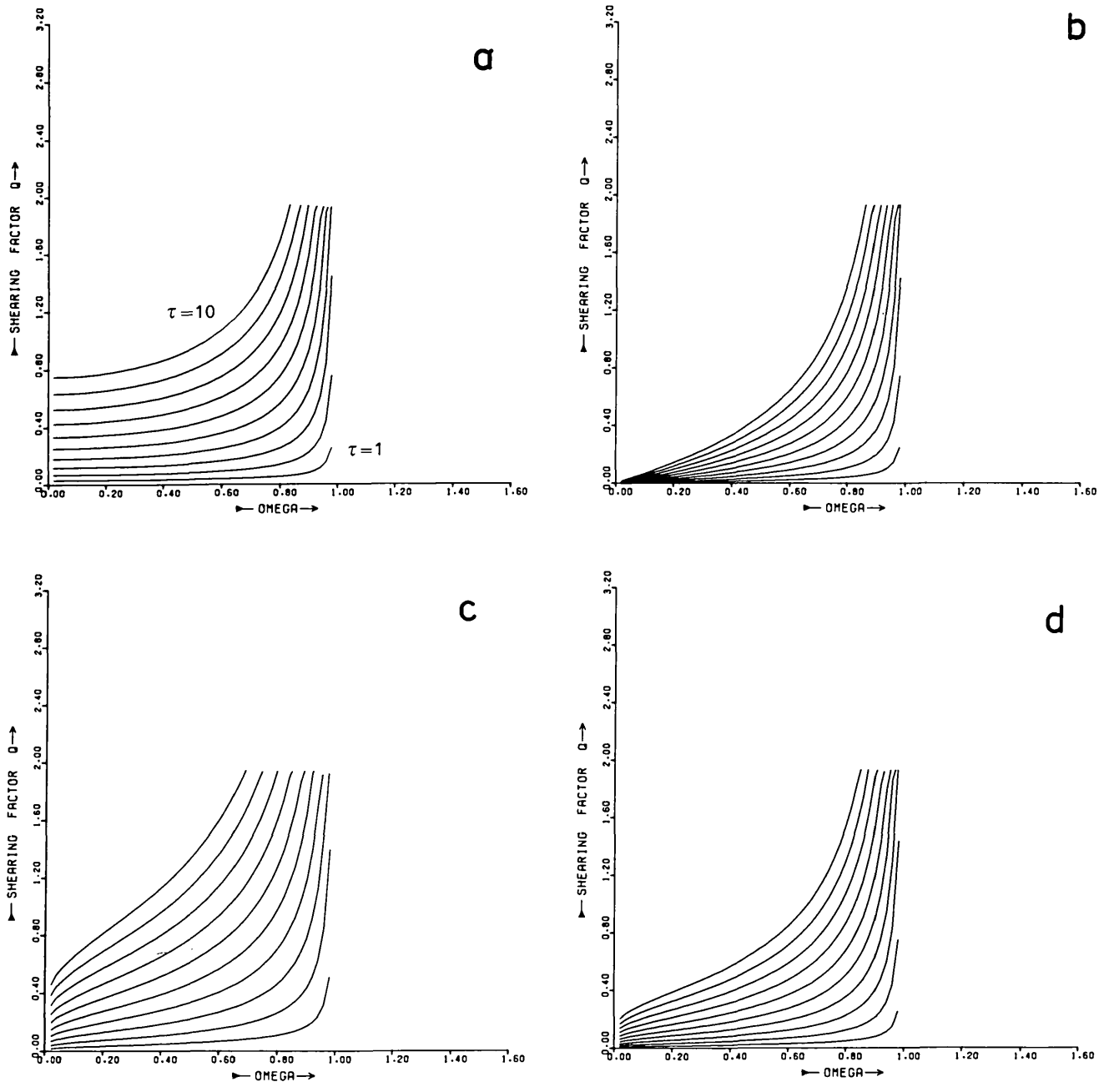

Fig. 11a—d. Graphs indicating the interdependence of various shearing parameters discussed in the text. **a** $\alpha = 0.0$, $u = 5.0$, **b** $\alpha = 2.0$, $u = 5.0$, **c** $\alpha = 1.0$, $u = 2.0$, **d** $\alpha = 1.0$, $u = 5.0$. For graphs, τ increments by unity for each curve, varying from $\tau = 1$ to $\tau = 10$

structures of the nebula, which appear to be coherently explainable in terms of interaction between the nebula and an external medium.

First is an apparent compression of the outer isophotes in the northeastern sector of the Hα, HeI and [OIII] maps, relative to those in the southwest. This is closely matched by a similar displacement of the northeastern poles of the forbidden line maps towards the central star, relative to the southwestern poles. This degree of retardation would be a plausible consequence of motion through interstellar clouds, and probably applies to a significant number of observable nebulae. The northeastern pole of the forbidden line maps is also distinctly brighter than its southwestern counterpart; a criterion used by Gurzadyan (1969) to adduce the presence of shell compression by the interstellar medium in other nebulae.

The behaviour of the Hα, HeI and [OIII] maps is also shared by the radio maps, where another interesting feature becomes apparent. In a direction almost directly

opposite to the side of the nebula showing compression is an extended tail, seen particularly clearly in the 4995 MHz map of George et al. (1974) but also evident in the 1407 MHz map of Elsmore (1968) and the 4995 MHz map of Scott (1975). If the tail is assumed to represent material removed from the main nebula shell, it is possible to go some way towards accounting for the deduced shape and orientation of the nebula. The length of the tail (~length of the nebular major axis) is consistent with the observed nebular expansion velocity of $0.5 \pm 0.1''$ · century^{-1}. It will be incidentally noted that Liller's expansion rate is also consistent with the kind of nebular orientation proposed for the nebula in Section 3 if a distance of 1.50 kpc is adopted (Cahn and Kaler, 1971).

If nebular shearing is responsible for the radio tail, and is an important determinant of the peculiar nebular structure deduced in Section 3, then at least one consequence might be to expect a similar orientation of the central star velocity vector; the major axis of the physical structure; and the radio tail.

The non-zero values of proper motion claiming greatest significance (Perek and Kohoutek, 1967) are those of Kozlov (1935), who obtains $\mu_\alpha \cos\delta = +(80 \pm 11)\ 10^{-2}$ arc s · century^{-1} and $\mu_\delta = +(30 \pm 9)\ 10^{-2}$ arc s · century^{-1}. This corresponds to motion along the direction defined by p.a. 69°.4. Assuming just 2σ errors in $\mu_\alpha \cos\delta$ and μ_δ, the position angle could be 50°.4, very close to the expected projection of the physical major axis in the plane of the sky, and of course not too different from the reverse of the direction defined by the radio tail. Note that the precise orientation of the radio tail also depends upon the relative motion of the interstellar medium at NGC 6543 with respect to the sun—although the r.m.s. random velocity of clouds relative to the sun in the line of sight is only ~9 km s^{-1} (Allen, 1973), whereas the velocity of NGC 6543, and planetary nebulae generally (Delhaye, 1965; Cudworth, 1974) is many times larger. It will be further noted that the proper motion of $\simeq 40$ km s^{-1} in combination with a radial velocity of $\simeq -65$ km s^{-1} leads to an angle between the velocity vector of the central star and the line of sight of 31.6°. This is almost exactly the value for major axis orientation (θ) found to give reasonable model characteristics in Section 3, although the degree of agreement must be considered fortuitous in view of the uncertainties. *If* the proper motion measurements used here are anywhere near accurate, therefore, the major axis of the nebular structure is almost certainly proximate with the velocity vector of the central star, as required by our model.

A rough idea of the relevance of nebular shearing can be obtained using a snowplough model. An initially spherical nebula of radius R_0 has density ρ varying with radius R as $\rho = \rho_{0n}\{R/R_0\}^{-\alpha}$. Consider a column at perpendicular distance z from the central star, parallel to the velocity vector of the central star, of length L, and presenting a time-averaged cross-sectional area $\bar{A}$ to the direction of motion. If central star velocity is V_s, and initial nebular expansion velocity is $V_{\exp} < V_s$, then the component of distance "s" moved by the column in the direction of motion of the central star is given through

$$M_0 V_0 \simeq (M_0 + \rho_0 \cdot \bar{A} \cdot s) \cdot ds/dt \tag{1a}$$

$$V_0 = V_s + V_{\exp} \cos\eta, \tag{1b}$$

where M_0 is the initial column mass, η the angle between radius vector of column intercept with shell surface and V_s, ds/dt is column velocity, ρ_0 is the density of the interstellar medium and $\bar{A} = \int_0^T A(t)dt / \int_0^T dt \simeq A(T)/3$. Note that $M_0 = AL\bar{\rho}_n$, where $\bar{\rho}_n$ is the mean column density. If we let $s = s_0 + R_0 \cos\eta - r$; $R_0 = V_{\exp} t$; $\omega = Z/R_0$, $\tau = S_0/R_0$, $q = r/L$, $p = \bar{\rho}_n/\rho_0$ and $u = \rho_{0n}/\rho_0$, where r is the retardation of the front of the column, and $s_0 = V_s t$ is the distance moved by the central star, then integration of Equation (1) leads to

$$q = 3p\left\{\left[(\tau + (1-\omega^2)^{1/2}) \cdot \frac{1}{6p(1-\omega^2)^{1/2}} + 1\right] - \left[1 + \frac{1}{3p(1-\omega^2)^{1/2}} \cdot (\tau + (1-\omega^2)^{1/2})\right]^{1/2}\right\},$$

where

$$p(\alpha = 0) = u$$

$$p(\alpha = 1) = \frac{u\left\{\ln\left[\left(\frac{1}{\omega^2} - 1\right)^{1/2} + \frac{1}{\omega}\right]\right\}}{(1-\omega^2)^{1/2}}$$

$$p(\alpha = 2) = \frac{u\left\{\omega^{-1} \cdot \tan^{-1}\left[\frac{1}{\omega^2} - 1\right]^{1/2}\right\}}{(1-\omega^2)^{1/2}}.$$

Representative graphs illustrating the relation between q and ω for various values of τ, α and u are illustrated in Figure 10. It should be noted that the approximation for $\bar{A}$ means that the graphs become only indicative as $q \to 1$. It is required that the shearing factor q is reasonably large at $\omega \simeq 0.5$, and drops to $q \simeq 0.1$ at $\omega = 0$. The graphs suggest that the requisite shearing is plausible if $\alpha = 1$. $\alpha = 2$ probably gives too small a retardation q at $\omega \simeq 0$, although the presence of a central hole would tend to accentuate q above graphical values for small ω, depending upon the precise mode of shell development. For $\alpha = 0$, the retardation at $\omega \simeq 0$ is certainly too great, being close to the value at $\omega \simeq 0.5$. Graphs at different values of u lead to the same conclusions. Note generally that if the shell was ejected over an extended temporal period, shearing for any given set of parameters can be expected to be more severe. The important result however is that shearing with the kind of density structure ($\alpha = 1$) deduced in Section 3 for NGC 6543 is at least a plausible mechanism

for explaining much of the shell structure, although the reason for $b \neq c$ must probably be sought in the original velocity indicatrix of the ejected shell. A more realistic formulation is required before more definite conclusions can be drawn, however.

Finally, since the observed retardation would certainly require passage through a dense region of the interstellar medium, a halo would be expected to develop where the interstellar medium became ionized, if the nebula were optically thin. NGC 6543 is surrounded by such a halo, which is roughly circular, extended (diameter $\simeq 5'$) and of low intensity. This was first discovered by Minkowski (Aller, 1956) and has since been well photographed by Millikan (1972).

If for the central star we take an equivalent blackbody Zanstra temperature $T_* \simeq 66000$ K (Harman and Seaton, 1966), distance $\simeq 1.50$ kpc and extinction $\simeq 0.63$ magnitudes (Cahn and Kaler, 1971), visual magnitude $\simeq 9.74$ (Kostjakova et al., 1968) (in fact an upper limit brightness because of possible nebular contamination), and bolometric correction $\simeq 4.4$ (Aller and Liller, 1968), the observed size of the external halo leads to an upper limit gaseous density $n_H \lesssim 110 \varepsilon^{-1/2} \text{cm}^{-3}$, where ε is the filling factor. This corresponds to a mean spatial density $\bar{n}_H = \varepsilon n_H \lesssim 110 \varepsilon^{1/2} \text{cm}^{-3}$. We have assumed the halo to be an homogeneous stabilised Stromgren sphere irradiated by the full central star U.V. flux shortward of 912 Å. These assumptions lead to a distinct upper limit for $\bar{n}_H \varepsilon^{-1/2}$, and since from the optical evidence (Millikan, 1972) we expect $\varepsilon < 1$, it is clear that the mean density is indeed likely to be comparable with interstellar clouds. This is further confirmed by the radio map of George et al. (1976) which enables a rather generous upper limit of $\bar{n}_H < 200 \varepsilon^{1/2} \text{cm}^{-3}$ to be assigned to the mean halo density.

Taken individually, then, these various pieces of evidence can be regarded as providing only partial support for the hypothesis that NGC 6543 is interacting with the interstellar medium. Taken as a whole, however, we believe the case has much to recommend it. If this proposal were to be confirmed, then NGC 6543 would indeed prove to be very interesting.

5. Conclusion

We have presented electronographic data which, combined with available radial velocity data (Münch, 1968) has enabled us to construct a relatively simple model for NGC 6543 which displays the vital characteristics of the Hα, HeI, radio and forbidden line emission maps. We have speculated upon the likely origin of nebular asymmetries and structure, and conclude that there is a strong possibility that NGC 6543 is significantly interacting with the interstellar medium.

Acknowledgements. We thank Dr. M. J. Selby, Prof. J. Ring and our colleagues in the Blackett Laboratory, Imperial College, for their support during the course of this research.

The electronographic data was obtained using the 42″ telescope at the Lowel Observatory, Flagstaff, Arizona. We thank the director Dr. J. Hall for his hospitality and Dr. W. A. Baum, director of the Planetary Research Center, who obtained the observing time on our behalf and with whom we collaborated in the observational program.

The work was generously supported by the Science Research Council (SRC). S. P. W. is supported by an SRC Research Fellowship.

References

Allen, C. W.: 1973, Astrophysical Quantities, 3rd Ed. Athlone Press, London

Aller, L. H.: 1956, Gaseous Nebulae, Chapman and Hall, London

Aller, L. H., Liller, W.: 1968, Nebulae and Interstellar Matter, p. 483, eds. B. M. Middlehurst and L. H. Aller, University of Chicago Press, Chicago

Cahn, J. H., Kaler, J. B.: 1971, *Astrophys. J. Suppl.* **22**, 319

Campbell, W. W., Moore, J. H., 1918, *Publ. Lick Obs.* **3**, 161

Coleman, C. I., Reay, N. K., Worswick, S. P.: 1975. *Monthly Notices Roy. Astron. Soc.* **171**, 45

Cudworth, K. M.: 1974, *Astron. J.* **79**, 1384

Delhaye, J.: 1965, Galactic Structure, p. 61, eds. A. Blaauw and M. Schmidt, University of Chicago Press, Chicago

Dopita, M. A., Gibbons, A. H.: 1975, *Monthly Notices Roy. Astron. Soc.* **171**, 73

Elsmore, B.: 1968, 'High-Resolution radio observations of five planetary nebulae' in Planetary Nebulae, eds. D. Osterbrock and C. R. O'Dell, D. Reidel, Dordrecht, p. 108

George, D., Kaftan-Kassim, M. A., Hartsvijker, A. P.: 1974, *Astron. Astrophys.* **35**, 219

Gurzadyan, G. A.: 1969, Planetary Nebulae, Gordon and Breach, New York

Harman, R. J., Seaton, M. J.: 1966, *Monthly Notices Roy. Astron. Soc.* **132**, 15

Keeler, J. E.: 1894, *Publ. Lick Obs.* **3**, 161

Kostjakova, E. B., Savel'eva, M. V., Dokuchaeva, O. D., Noskova, R. I.: 1968, UBV photometry of the bright nuclei of the planetary nebulae, in *Planetary Nebulae*, eds. D. Osterbrock and C. R. O'Dell, D. Reidel, Dordrecht, p. 317

Kozlov, V. I.: 1935, *A. N.* **254**, 137

Liller, M. H., Liller, W.: 1968, Observed angular motions in planetary nebulae, in *Planetary Nebulae*, eds., D. Osterbrock and C. R. O'Dell, D. Reidel, Dordrecht, p. 38

Liller, W.: 1968, Planetary Nebulae, eds. D. Osterbrock and C. R. O'Dell, D. Reidel, Dordrecht, p. 266

Millikan, A. G.: 1972, *Mercury, J. Astron. Soc.* **1**, 13

Münch, G.: 1968, Internal motions in the planetary nebula NGC 6543, in *Planetary Nebula*, eds. D. Osterbrock and C. R. O'Dell, D. Reidel, Dordrecht, p. 259

Perek, L., Kohoutek, L.: 1967, Catalogue of Planetary Nebulae, Acad. Publ. House, Prague

Phillips, J. P., Reay, N. K.: 1977, *Astron. Astrophys.* **59**, 91

Scheiner, J., Wilsing, J.: 1905, *Publ. Potsdam* **15**, No. 47

Scott, P. F.: 1975, *Monthly Notices, Roy. Astron. Soc.* **170**, 487

Terzian, Y., Balick, B., Bignell, C.: 1974, *Astrophys. J.* **188**, 257

Warner, J. W., Rubin, V. C.: 1975, *Astrophys. J.* **198**, 593